Forschungszentrum Karlsruhe
Technik und Umwelt

Wissenschaftliche Berichte
FZKA 6653

Programm Nukleare Sicherheitsforschung

Jahresbericht 2000

B. Mühl (Hrsg.)

Programm Nukleare Sicherheitsforschung

September 2001

FORSCHUNGSZENTRUM KARLSRUHE

Technik und Umwelt

Wissenschaftliche Berichte

FZKA 6653

Programm Nukleare Sicherheitsforschung

Jahresbericht 2000

Herausgegeben von B. Mühl

Programm Nukleare Sicherheitsforschung

Forschungszentrum Karlsruhe GmbH, Karlsruhe

2001

Als Manuskript gedruckt

Forschungszentrum Karlsruhe GmbH
Postfach 3640, 76021 Karlsruhe

Mitglied der Hermann von Helmholtz-Gemeinschaft
Deutscher Forschungszentren (HGF)

ISSN 0947-8620

Summary

The reactor safety R&D work of Forschungszentrum Karlsruhe (FZK) had been part of the Nuclear Safety Research Project (PSF) since 1990. In 2000, a new organisational structure was introduced and the Nuclear Safety Research Project was transferred into the Nuclear Safety Research Programme (NUKLEAR). In addition to the three traditional main topics – Light Water Reactor safety, Innovative systems, Studies related to the transmutation of actinides –, the new Programme NUKLEAR also covers Safety research related to final waste storage and Immobilisation of HAW. These new topics, however, will only be dealt with in the next annual report.

Some tasks related to the traditional topics have been concluded and do no longer appear in the annual report; other tasks are new and are described for the first time.

Numerous institutes of the research centre contribute to the work programme, as well as several external partners. The tasks are coordinated in agreement with internal and external working groups.

The contributions to this report, which are either written in German or in English, correspond to the status of early/mid 2001.

Zusammenfassung

Seit 1990 sind die F+E-Arbeiten des Forschungszentrums Karlsruhe (FZK) zur Reaktorsicherheit im Projekt Nukleare Sicherheitsforschung (PSF) zusammengefasst. Im Jahr 2000 wurde infolge der Einführung einer neuen programmatischen Struktur im FZK das Projekt Nukleare Sicherheitsforschung in das Programm Nukleare Sicherheitsforschung (NUKLEAR) überführt. Neben den bisherigen Arbeitsschwerpunkten Leichtwasserreaktorsicherheit, Innovative Systeme und Studien zur Aktinidenumwandlung beinhaltet das Programm Nukleare Sicherheitsforschung nunmehr auch die Sicherheitsforschung zur Endlagerung und die Immobilisierung von hochradioaktivem Abfall. Diese beiden neuen Arbeitsschwerpunkte werden aber erst im kommendem Jahr im Jahresbericht berücksichtigt werden.

Die konkreten Forschungsthemen und -vorhaben werden laufend mit internen und externen Fachgremien abgestimmt. Die Arbeiten zu einigen Vorhaben der bisherigen Schwerpunkte konnten abgeschlossen werden und erscheinen daher nicht mehr im vorliegenden Jahresbericht 2000. Andere Vorhaben kamen neu hinzu; über diese wird im vorliegenden Bericht zum ersten Mal berichtet.

An den beschriebenen Arbeiten sind die folgenden Institute und Abteilungen des FZK beteiligt:

Institut für Hochleistungsimpuls- und Mikrowellentechnik	IHM
Institut für Instrumentelle Analytik	IFIA
Institut für Kern- und Energietechnik	IKET
Institut für Materialforschung	IMF I, II, III
Institut für Nukleare Entsorgungstechnik	INE
Institut für Reaktorsicherheit	IRS
Institut für Technische Chemie	ITC
Hauptabteilung Informations- und Kommunikationstechnik	HIK
Hauptabteilung Versuchstechnik	HVT

sowie vom FZK beauftragte externe Institutionen.

Die einzelnen Beiträge stellen den Stand der Arbeiten im Frühjahr/Sommer 2001 und sind entsprechend dem F+E-Programm 2000 nummeriert.

Inhalt

Contents

32.21 LEICHTWASSERREAKTORSICHERHEIT

32.21.01 Wasserstoffverhalten und Gegenmaßnahmen

I. Model Development and Validation of GASFLOW II

(P. Royl, J.R. Travis, G. Necker, IKET)

Abstract

The 3D CFD code GASFLOW is developed at FZK as an integral analysis tool for the calculation of steam/hydrogen distribution with simulation of mitigation in nuclear reactor containments. Improvements in modeling and validation of GASFLOW during this year include a new model for the simulation of turbulent heat transfer, implementation of a new model for the simulation of hydrogen recombination on catalytic foils, modeling of composite structures with a thin layer of an insulating liner on top of a heavy concrete stucture. GASFLOW was also used for the analysis of selected experiments from the FZK tests PASCO to validate the combined modeling of radiative and convective heat transfer and compare the results with those from the CFD code FLUTAN which had succesfully analyzed these tests before. A new composite structure of a plastic liner and concrete has been modeled in GASFLOW and a 3D visualization option for the structure temperatures has been implemented. The existing sump model in GASFLOW has undergone major revisions and was used in test calculations for the small break loca in the Konvoi plant Neckarwestheim 2.

1. Turbulent Heat Transfer

A consistent turbulent heat transfer model has been implemented into GASFLOW II [1]. It is well known that a developing turbulent boundary layer begins with region of laminar flow, then proceeding to a fully turbulent boundary layer flow through a so called transition region. Observations of certain flow structures within a fully developed turbulent boundary layer flow show an immediate region next to the wall as the "laminar" or "viscous" sub-layer and the far field zone away from the wall as the "turbulent zone" or "Turbulent Core". These regions are joined by what many researchers call the

"Buffer Zone". New wall functions were implemented into GASFLOW, that fully evaluate the stress tensor for a no slip boundary condition and determine the turbulent heat and momentum exchange for a coupled three zone model with a laminar sub layer, a buffer zone and a turbulent zone. The model interfaces the turbulent kinetic energy and dissipation in the boundary layer with the turbulence parameters from the standard k-ε model implemented into GASFLOW. The wall functions for no slip boundary conditions are derived for heat transfer to smooth walls and to walls with a defined surface roughness. The simulation of heat transfer for a no slip boundary condition still needs to be generalized to also include the simulation of mass transfer. This holds for the steam condensation which is still simulated on basis of the Reynolds analogy and does not yet account for the momentum loss for a no slip boundary condition.

2. Catalytic Foil Model

A new model for simulating catalytic foils has been implemented into GASFLOW. It models specially marked structure surfaces to recombine hydrogen and oxygen from the fluid node adjacent to this structure. It removes the mass and enery of oxygen and hydrogen from the fluid node, adds their heat of recombination to the heat conduction node on the surface of the structure and returns 1 mole of steam per removed 1.5 moles of hydrogen and oxygen with the steam energy of the foil surface temperature. If not enough oxygen is available, the oxygen concentration controls the reaction rate. One dimensional heat conduction into the structure and radiative and convective cooling of the structure surface determine the structure surface temperature. A fluid node can be bounded in the limit by up to 6 different catalytically coated structure surfaces. The structure underneath the catalytic foil is considered as composite material with thermal conductivities and heat capacities that can differ in each heat conduction node. The catalytic foil model was succesfully applied to interprete the foil recombiner test HDR E11.8.1. The results are documented in [1].

Three dimensional scoping calculations with the foil model were performed with the GASFLOW code for a hypothetical large break loca (surge line loca) in a Konvoi type containment with a rapid steam/hydrogen release. The idea

behind is the development of a catalytic coating of all structures. The recombination rates on such coated structures were compared to a previous analysis for the same scenario in this containment in which hydrogen mitigation was simulated with 62 catalytic Siemens recombiner boxes [3]. The scoping calculation assumed a homogeneous catalytic coating of all containment structures inside of the steel sphere including the inside of the spherical steel shell itself. The total catalytically active area for this simulation was 39,000 m^2. The hydrogen recombined according to its local concentration near the structures and the applied correlation for the recombination rate was the same as for the foils applied in the HDR test E11.8.1 [4]. The global catalytic coating lead to a much faster reduction of the hydrogen inventory compared to the simulation with the Siemens boxes. The available large catalytic area limited the maximum hydrogen inventory to 220 kg compared to 400 kg with the Siemens boxes out of a total hydrogen release of 550 kg (fig. 1). Note that the catalytic coating of the structures is particularly helpful in limiting the further hydrogen accumulation resulting from the second release peak around 6000 s. The peak recombination rates from all foil surfaces were 0.2 kg/s compared to peak hydrogen release rates of 2.8 kg/s for this scenario. They were five times higher than with the Siemens boxes. This demonstrates that such catalytic coating could indeed have a significant mitigation potential. The temperature on the inside of the recombining spherical steel shell peaks around 410 K. It is limited by the convective and radiative heat transfer from the inside and outside of the steel shell to the air gap and the outer concrete shell. The highest steel shell temperatures occur around the apex as consequence of a temporary accumulation of a stratified steam/hydrogen/air cloud in the dome (fig. 2). The maximum heat flux into the containment steel shell is 0.25 kW/cm^2 and occurs in the region where the hydrogen jet from the source is impinging at the time of this snap shot. The maximum concrete temperature in the inner component rooms around the source doesn't exceed 650 K and stays below the limit of self ignition due to the radiative and convective cooling of the structure and the large heat capacity of the concrete. Further analysis with the foil model is foreseen in cooperation with Jülich where such new structure coatings are developed and tested in the frame of a joint project that is supported by the Helmholz Gemeinschaft (HGF-Project).

3. Simulation of Pasco Tests

The PASCO (passive containment cooling) tests were performed at FZK 8 years ago. They simulate the passive cooling by radiation and air convection in the annulus between the steel shell and the outer concrete shell of an innovative PWR containment under hypothetical accident conditions. The well instrumented tests study basic phenomena of combined convective and radiative heat transfer. They study the heat transfer by convection and radiation from an electrically heated plate -with a rather homogeneous distribution of the surface temperature- to air flowing in a rectangular channel and to the unheated walls on the sides and back of the rectangular channel. The heated plate is 50 cm wide and has a height of 8 m. Two channel depths of 50 and 100 cm were simulated (fig. 3). A natural convection air flow builds up with cold air entering at the bottom and warm air leaving at the top with stationary flow rates that depend on the applied heating power of the plate. The tests measured the velocity and temperature fields in the gas and the wall temperatures. Heating powers were adjusted to yield wall temperatures of 100, 150, and 150 C applying powers of 3.3, 6.6, and 8.2 kW, respectively. The test conditions for 4 seleced Pasco tests are summarized in the table in fig. 3.

Detailed evaluations and interpretations of these tests with Flutan have been made by Cheng et al [5]. They applied a k-epsilon turbulence model with logarithmic wall functions for determining the wall shear stress and developed an analytic model for the description of the radiative heat exchange between the heated and unheated walls for the simple test geometry. Their simulations were performed for a wide range of hot wall temperatures and give stationary heating powers that agree well with the test data. All their calculations demonstrated that the heat that radiates away from the heated plate significantly exceeded the heat removal from the hot plate by convection.

We have analyzed the Pasco experiments listed in the above table to test the combined simulation of convection and radiation in GASFLOW using the GASFLOW model for radiation transport [6]. This model determines the radiation tranport in a P1 approximation for the direction dependent radiation

intensity. It calculates the radiation heat flux without view factors for an arbitrary arrangement of structures inside a 3D mesh with interconnected computational cells. The simulation made use of the above discussed new wall functions for turbulent heat transfer. The turbulent flow was simulated in the rectangular channel with a no slip boundary condition and full evaluation of the wall shear stress using the k-ε turbulence model in GASFLOW. The measured stationary mass flow rates for the analyzed tests from fig. 3 were applied as input. The GASFLOW prediction for the overall heat removal from the heated plate under stationary conditions (fig. 3) systematically exceeds the measured power input from the experiment by 10-20 %. The predictions from FLUTAN for the heating power are in better agreement with the test data. The convective heat removal calculated in GASFLOW with the wall functions for the no slip boundary condition agrees well with the predictions from the FLUTAN analysis. The major difference is that GASFLOW overpredicts the radiative heat removal from the hot plate. The P1 approximation for the radiation transport in GASFLOW has some limitations when applied in an optically thin medium like air where the radiation absorption is very small. The total emitted radiation power from the heated plate systematically exceeds the impinging radiation heat flux on the unheated walls in GASFLOW by about 50 %. The analytic solution for the radiation heat fluxes in FLUTAN fully neglects absorption, so the emitted radiation heat fluxes balance the impinging heat fluxes by definition. The difference between the emitted radiation heat from the hot plate (Qrad in fig.3) and the impinging radiation on the unheated plates (Qrad impinge) is absorbed heat in the gas. As shown in fig. 4 the calculated gas temperatures at the upper exit of the test channel exceeds the measured data points (crosses) due to the overprediction of radiation absorption in the P1 approximation for the radiation transport. The difference in temperatures becomes smaller near the unheated wall (y=0). The convective heating of air from the unheated wall balances the impinging radiation heat flux under stationary conditions. Because the impinging radiation heat flux is attenuated too much by absorption there is too little convective heat transfer from the unheated walls and the temperature points from GASFLOW and from the test data near this wall move closer together. The velocity profile in fig. 4 shows a pronounced increase from the local buoyancy due to the convective heating

from the unheated and heated plates on both sides. This buoyancy induced velocity peak is less pronounced in GASFLOW on the unheated side compared with the test data (circles in fig. 4). The full velocity profile at the exit of the test channel (fig. 5) shows a pronounced buoyancy effect near the heated and unheated walls. The colors which represent the gas temperatures all show local peaks near the corners due to convective heating of the fluid from two sides. Also shown in fig. 5 are the temperatures of the unheated walls which increase along the channel due to the accumulated energy in the air and which show the lateral heat transport along the length of the test channel. The calculated profiles from GASFLOW agree quite well with those calculated in FLUTAN.

There are some limitations in describing the radiation transport in an optically thin medium with the implemented P1 approximation in GASFLOW. But in an optically thicker steam enriched atmosphere, which is representative of a reactor containment during severe accident conditions this model for radiation transport should be better applicable to describe the interaction of radiation and absorption and the resulting radiation heat fluxes on the structures. This is of particular importance for the simulation of hydrogen combustion loads in an atmosphere with a lot of steam which cannot be well simulated with a view factor model.

4. Simulation of composite heat conduction structures and visualization of thermal combustion loads on structures

The mapping of the heat conducting structure surfaces in the 3D GASFLOW mesh has been generalized. The code now defines the coordinates (x,y,z) of the four corners for each structure surface (wall front and back side and slabs) and creates facettes as areas in space so-called "Quads", which can be given a certain color according to their temperature or another characterizing result like heat flux or film thickness. The facettes can also be applied to display an envelope of the geometry model like a wrapping paper that is put around the 3D fluid meshes. They can be defined for selected material numbers (concrete, steel, and or composite materials like a liner). This allows to selectively visualize certain structures (p.e. the inner

containment surface, but also structure components like pumps and steam generators and their surface temperatures). Output is prepared for the 3D visualization programs GMV [7] and Kismet [8]. Kismet now displays different gas clouds together with selected surrounding structures that are colored according to their temperatures. This allows the visualization of thermal combustion loads on containment structures together with the hot cloud of burnt gases.

The displayed surface temperatures in figure 6 of the inner concrete shell, the surface temperatures of the steam generators and pumps inside a PWR containment with four loops during a continuous deflagration of hydrogen give an example of this new possibility for the visualization of structure temperatures. The red ring shows a composite concrete structure of 30 cm thickness at the upper end of the cylindrical part of the concrete containment that is covered with a 0.8 cm thick insulating plastic liner. The standing flame from hydrogen combustion leads to the hot gases displayed in the transparent yellow cloud with T>800K. It causes higher local thermal loads by radiation and convection indicated by the red color at the upper end of the steam generator above the source. Its impingement on the containment dome also leads to the locally higher surface temperatures indicated in the left part of the picture. The composite structure with the insulating liner that is exposed to the same gas temperatures as the pure concrete structure above and below is heated to significantly higher surface temperatures. During the analyzed 400 sec of continuous hydrogen deflagration with a standing flame the heat cannot propagate more than 2.5 cm into the concrete. 1D heat conduction into concrete of 30 cm thickness was simulated with 20 nodes that increase in size from a thickness of 0.1 cm at the surface to 6 cm at the outer boundary of the concrete. The profiles in fig. 6 only show the inner 4 cm region of the 30 cm thick concrete structure and compare the surface temperatures of the pure concrete (pos. B) with those of the adjacent concrete insulated with the liner on top (pos. A). Note that the insulated concrete underneath the liner doesn't show any temperature increase during this analysis. The calculation is a succesful test of the GASFLOW option to simulate composite structures which hasn't been applied before. It helped to define the liner model that was later applied in EPR calculations performed by Siemens.

5. A new sump model for GASFLOW II

The simulation of sumps in GASFLOW was limited so far to have sumps on walls only where the sump temperature could be prescribed by table input. As a first approach to a new sump model this restriction was removed and sumps were allowed to be positionned on thick structure surfaces (slabs) with a tabular input of the sump surface temperature. We have extended GASFLOW then to parametrically define a sump during an ongoing transient containment analysis without the need to restart from scratch. We have used this new option to analyze the impact of steam vaporization from a sump on the bottom of the containment of Neckarwestheim in the late phase of a small break loca simulation between 27,000 and 30,000 sec. During this time the documented GASFLOW simulation [9] without the sump model had predicted hydrogen/air sedimentations from condensing steam on concrete walls leading to the accumulation of hydrogen/air clouds near the bottom of the containment (see red cloud in the right part of fig. 7). The design of the Konvoi plant actually foresees that the water deposited on the containment structures is collected through drainage pipes and accumulates in one large sump at the bottom. According to RALOC analysis from GRS the sump water which contains also many heat sources from washed out fission products is continuously boiling in the late phase of the accident. Our analysis with the new sump model on the bottom of the containment (left side of fig. 7) shows indeed that a boiling sump can largely prevent such hydrogen accumulations in particular on the source side where the sedimentation is weaker due to the more preheated structures. Therefore there is a need for including the sump modeling also in future conatinment analysis in particular in the late phase of hydrogen sedimentation.

Meanwhile the sump model in GASFLOW has been refined further [10] and now allows for a deterministic determination of the sump mass and energy from four sources: the droplet depletion or rainout of the liquid component from the fluid field, liquid films draining from slabs and walls directly into the sump, phase change (condensation and/or evaporation at the sump surface, and sump to sump mass and energy exchange. The sump is treated in a "Lumped parameter sense". The parametric definition of the sump surface

conditions is no longer necessary. The new model has just been implemented into GASFLOW in a first version and is now undergoing further testing.

6. References

1. J. R. Travis: "A Model for Turbulent heat Transfer for the GASFLOW Computer Code", Work Report, August 2000

2. P. Royl, G. Necker, J. R. Travis: "GASFLOW Simulation of Hydrogen Recombination with Radiation Transport from Catalytic Foils in the Recombiner Foil Test HDR E11.8.1", Procs Jahrestagung Kerntechnik, Dresden May 15-17, 2001

3. P. Royl, H. Rochholz, W. Breitung, J. R. Travis, G. Necker, A. Veser: "GASFLOW-Analysen zur Wirksamkeit eines Rekombinatorkonzepts bei einem postulierten Surge-line LOCA im Kernkraftwerk Neckarwestheim-2, FZKA 6333, März 2000

4. P. Royl, J. R. Travis, E. A. Haytcher, and H. Wilkening: "Analysis of Mitigating Measures during Steam/Hydrogen distributions in Nuclear Reactor Containments with the 3D Field Code GASFLOW," presented at the OECD/NEA CSNI Workshop on the Implementation of Hydrogen Mitigation Techniques, Winnipeg, Canada, May 13–15, 1996.

5. X. Cheng, U. Müller: "Turbulent natural convection coupled with thermal radiation in large vertical channels with asymmetric heating",International Journal of Heat Mass Transfer, Vol 41, No. 12, p.1681-1692

6. J. R. Travis: "A computationally efficient Thermal Radiation Transport Model for the GASFLOW Code", Procs. Seminar on Containment of Nuclear Reactors held in conjunction with 15th International Conference on Structural Mechanics in Reactor Technology, Seoul, Korea, August 23-24, 1999

7. F. A. Ortega:"GMV Version 1.6 General Mesh Viewer User's Manual", report LAUR 95-2986, Los Alamos National Laboratory 1995

8. U. Kühnapfel: FZK-Nachrichten 2-3, 1996

9. P. Royl, J. R. Travis, W. Breitung: "Ergebnisse der GASFLOW Analysen für einen hypothetischen Kühlmittelverlustunfall mit kleinem Leck (Small Break Loca) im Kernkraftwerk Neckarwestheim-2 mit sekundärseitigem Abfahren der Dampferzeuger", IKET Bericht Nr. 3/00, Februar 2000

10. J. R. Travis: "A Sump Model for the GASFLOW II Computer Code", Work Report December 19, 2000

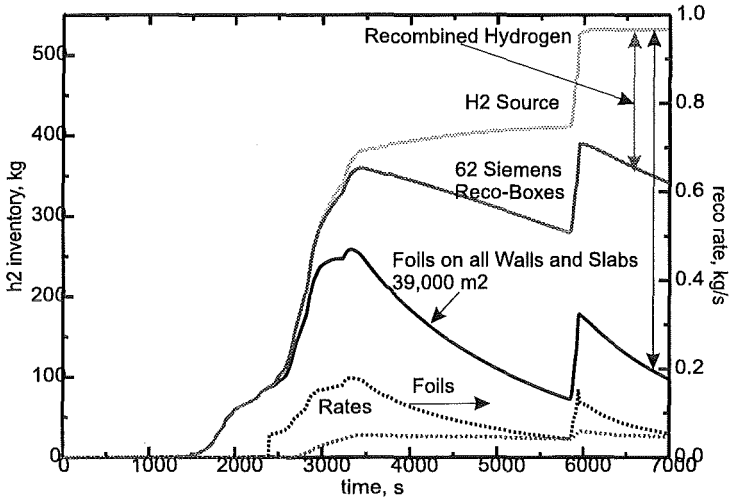

Fig.1: Surge Line LOCA in Neckarwestheim 2 with mitigation. Hydogen inventory and recombination rates from scoping calculations with catalytic foils on slabs and walls vs. recombination by 62 Siemens recombiner boxes

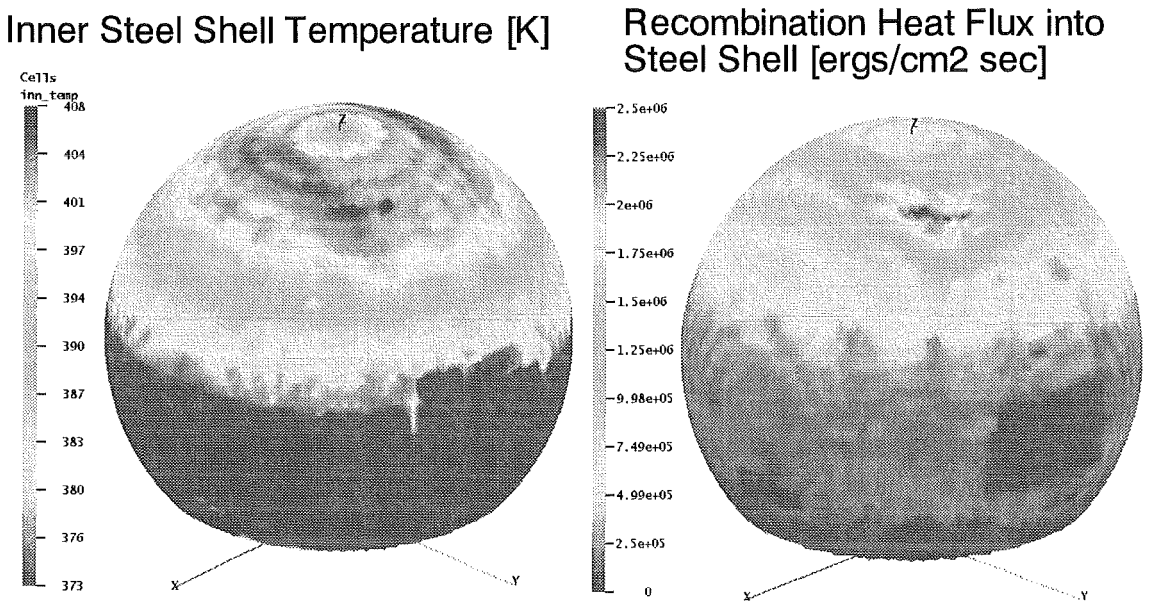

Fig.2 : Surge line LOCA in GKN, scoping calculations with catalytic foil coating of all internal containment structures (39,000 m2). Distribution of temperatures and recombination heat fluxes on inner steel shell at 6000 s.

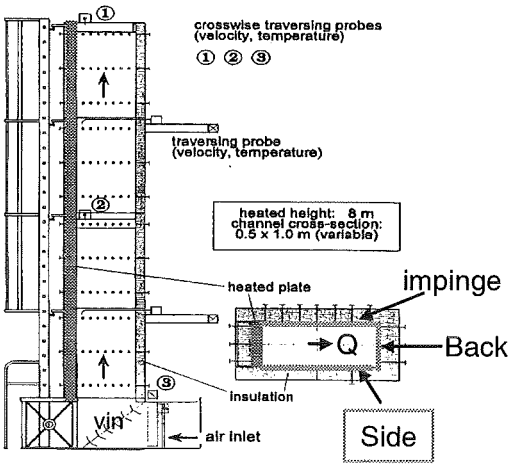

			M014	M019	M022	M040
Test Data	Test Section	-	0.5mx1m			0.5mx0.5m
	Heater Temp	C	100	150	175	150
	Inlet Temp	C	23.34	22.4	23.04	14.3
	mdot	g/s	332	410	540	304
	Q	kW	3.33	6.58	8.23	6.57
Flutan	Q	kW	3.38	6.97	9.03	6.92
	Qconv	kW	1.56	3.05	3.79	3.24
	Qrad	kW	1.82	3.92	5.24	3.68
	Qrad/Qconv	-	1.17	1.29	1.38	1.14
	mdot	g/s	278	392	462	304
GASFLOW	vin	cm/s	58.3	78.7	90.8	101
	Q	kW	3.90	7.93	10.47	7.87
	Qgasf/Qtest		1.17	1.21	1.27	1.20
	Qconv	kW	1.53	3.02	3.90	3.29
	Qrad	kW	2.37	4.91	6.57	4.58
	Qrad impinge	kW	1.26	2.74	3.59	2.69
	Qrad/Qconv	-	1.55	1.63	1.68	1.39

Fig. 3: Experiment setup of the FZK Pasco experiments and GASFLOW results for selected tests in comparison with FLUTAN analysis [5]

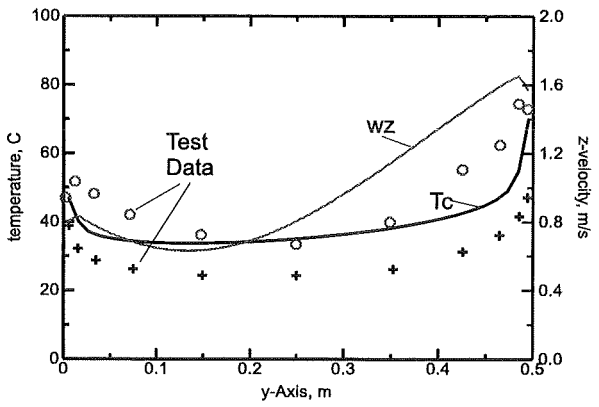

Fig. 4: Pasco Test M040, axial velocity and temperature profile at the exit of the test section (z=7.9 m, x=0.25 m), GASFLOW vs. test data

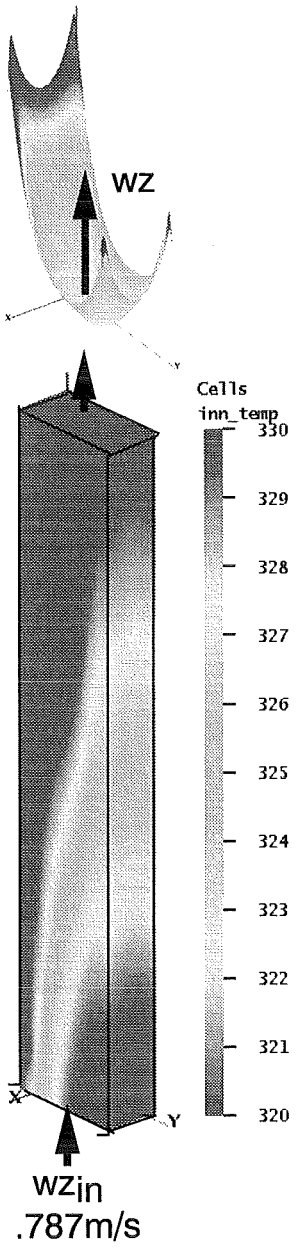

Fig. 5: Wall temperature and velocity/gas temperature profile from GASFLOW at the exit of the test section, range T:307-398K,wz:0.3-2.6 m/s (Pasco Test M019, heated wall temp. 423K)

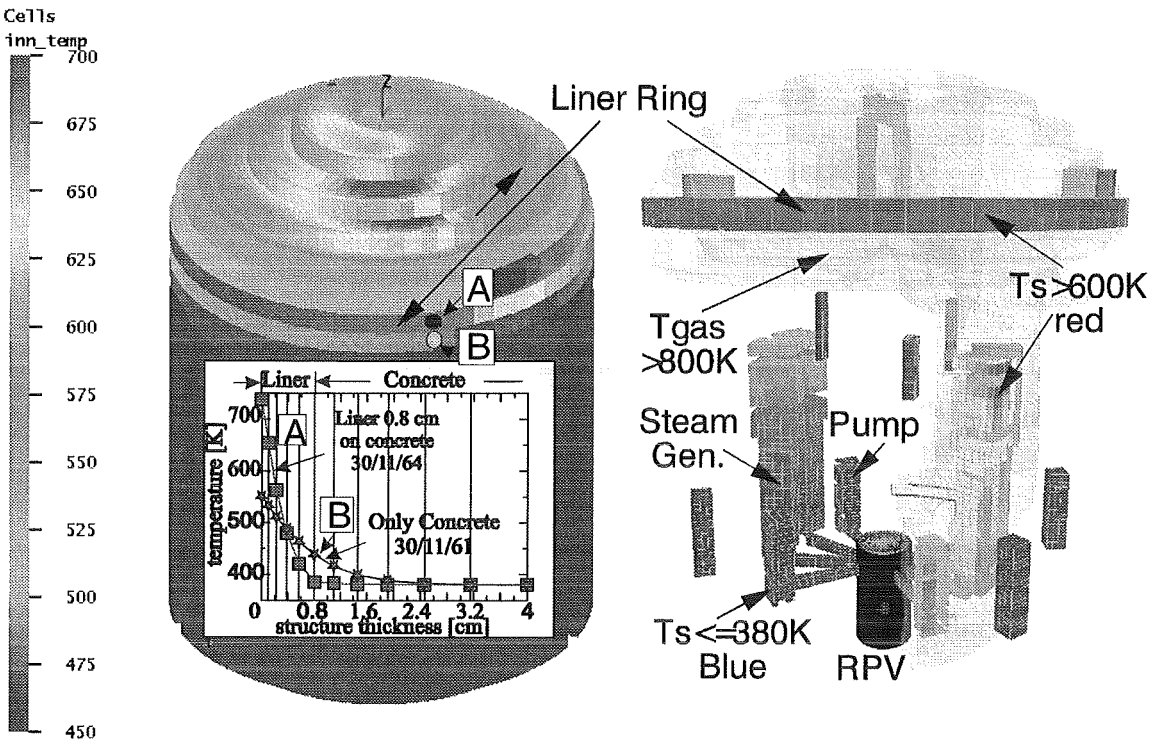

Fig. 6: 3D Visualization of structure temperatures. GASFLOW test calculations with a ring of an insulating liner at the upper end of the cylinder of a concrete model conctainment (liner thickness 0.8 cm, with $\lambda = 1.5$ e-3 /cm K, concrete thickness 30cm with λ =3.e-2 W/cm K)

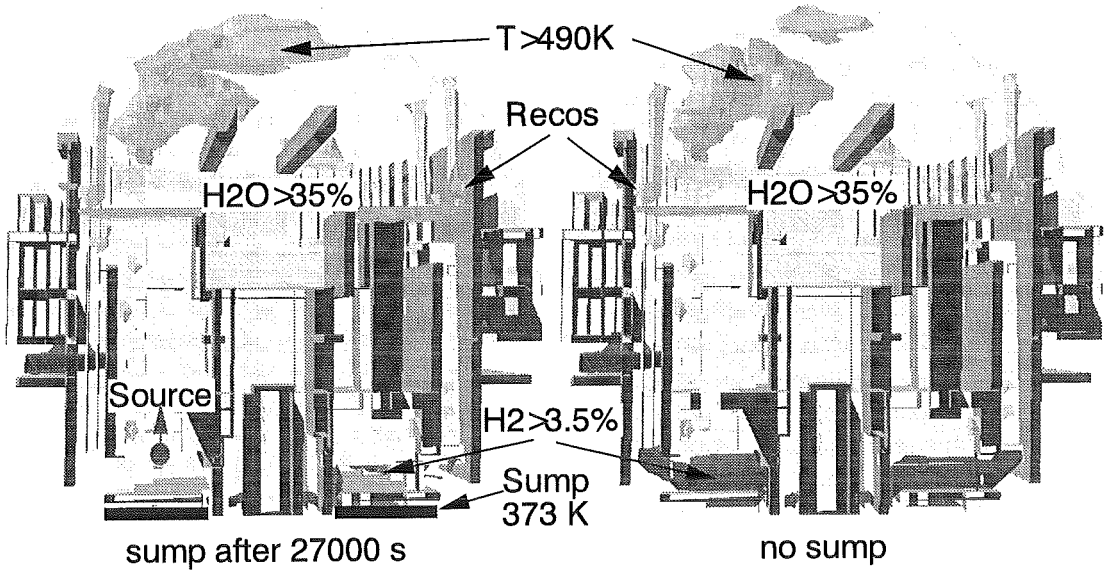

Fig. 7: Hydrogen sedimentation with and without sump modeling after 30,000 s (final phase of small break LOCA in Neckarwestheim 2

II. Combustion Tests at FZK 12m Tube

(A. Veser, G. Stern, J. Grune, W. Breitung, IKET)

Abstract

At the Research Center Karlsruhe, an experimental program has been started in the 12 m Hydrogen Combustion Test Tube Facility (Figure 1) to investigate the combustion behavior of H_2-CO-air mixtures under different conditions.

1. Regimes of premixed combustion

Different regimes are realizable in premixed combustion. They are not only influenced by the mixture composition (e.g. H_2, CO and steam concentration in air) but also by details of the geometrical structure, e.g. obstacles, free volumes. There is a complicated interplay between hydrodynamics flow and chemistry.

Figure 2 shows Schlieren pictures of different combustion modes in homogeneous H_2-air mixtures. Dark areas indicate high density gradients. Figure 2a depicts a laminar flame in which unburned and burned gas are separated by a smooth, very thin flame front. The flame surface travels with a constant velocity up to the top. The continuity of the combustion is maintained by diffusion of heat and radicals. Figure 2b shows a typical fast turbulent flame. Instead of a smooth flame surface, pockets of unburned and burned gas are surrounded by the respective other medium. The heat and mass transport are governed by turbulence, not by molecular diffusion. The turbulent combustion velocity S_t may often be described by the laminar combustion velocity S_L and the turbulent fluctuation velocity u' according to:

$$S_t/S_L=1+u'/S_L \quad (u'/S_L < 40)$$

u' is a measure for the mean turbulent kinetic energy per mass. At very high turbulence levels, quenching causes a decrease of the turbulent combustion velocity. An even faster combustion form, a so-called quasi-detonation, can be seen in Figure 2c. The movement of the flame-front is extremely fast so that the associated shock wave causes a temperature rise in the unburned gas in front of the flame beyond its ignition temperature within microseconds. The pressure waves were created by the rapid expansion of the burned and compressed gas during the combustion. The complex of fast flame and pressure waves reaches in lean H_2-air mixtures velocities

of about 1300 m/s (15 % H_2). In stoichiometric H_2-air mixtures well developed stable detonations with coupled flame- and shock- structures reach about 2000 m/s.

2. FZK experiments

FZK experiments performed so far concentrated on the turbulent combustion in fully confined, partially obstructed geometry. To this end the tube was equipped with an array of obstacles of a blockage ratio (BR) 45 % and a distance of 0.5 m. Mixture composition and initial pressure are the parameters the test series.
By varying the hydrogen concentration in the mixture with air the three combustion regimes described above can indeed be observed in the experiments. The results of these experiments are displayed in a velocity-distance diagram (Figure 3). Lean H_2 concentrations (9-10 % H_2 in air) lead to a subsonic flame (v<200 m/s) with almost no flame acceleration. This regime can be regarded as an intermediate state of the situations displayed in Figure 2a and b. An increase of the H_2-concentration (12 % H_2 in air) entails, after an initial acceleration phase a fast turbulent combustion, comparable to the one depicted in Figure 2b. The maximum flame speed is close to the sound velocity in the burned gas (shoked flow). By further increasing the H_2-concentration (15 % H_2 in air), again after an acceleration phase, the flame speed reaches the level of a quasi-detonation (comparable to Figure 2c). Mixtures with even higher H_2 concentrations (>20% H_2 in air) develop into a stable detonation with a velocity close to the theoretical Chapman-Jouquet speed.

Starting from these previously obtained results for H_2-air mixtures, experiments were performed in the FZK-tube in order to quantify the influence of CO-concentration on the combustion process of H_2-CO-air mixtures. In Table I the initial conditions of these experiments are listed. So far H_2-CO-air mixture experiments have been performed with 11 % and 18 % fuel gas concentration, the results are presented in the v-x diagrams below (Figure 4 and 5). Replacing half of the H_2 by CO (5.5 % H_2 + 5.5 % CO = 11 % fuel gas) results in a subsonic flame (< 200 m/s), without no acceleration, in contrast to the combustion of pure hydrogen in air, which reaches after an acceleration phase the regime of a choked flame (500-700 m/s flame speed)

Table I: Initial conditions of experiments with H_2-CO-air mixtures

Experiment	H_2 [%]	CO [%]	**Air [%]**	p_0 [bar]	BR [%]
R0799_10	11	-	89	1	45
R0799_11	5,5	5,5	89	1	45
R0999_35	5,5	5,5	89	0,5	45
R0999_34	5,5	5,5	89	2	45
R0999_00	18	-	82	1	45
R0999_01	9	9	82	1	45
R0999_37	9	9	82	0,5	45
R0999_36	9	9	82	2	45

Some influence of the initial pressure can also be observed. An increase of the initial pressure (0.5, 1.0, 2.0 bar) leads to a decrease of the flame speed and finally results in an unstable flame propagation due to local flame quenching near the end of the tube. Analogous experiments with 18% fuel gas concentration reveal a different picture in the v-x diagram (Figure 5). The combustion of pure H_2 causes a rapid flame acceleration up to the quasi-detonation regime, while more moderate and longer lasting acceleration up to detonation speed is the outcome of the experiments with 9 % H_2 and 9 % CO. The influence of a initial pressure rise (0.5, 1.0, 2.0 bar) is noticeable only at beginning of the experiment through a faster acceleration of the flame front with increasing pressure.

3. Conclusions

The results obtained so far clearly demonstrate a damping effect of CO on the turbulent combustion speed of H_2-CO-air mixtures when compared to turbulent combustion in pure H_2-air mixtures. This effect, is probably caused by the relatively long induction and reaction time of the complicated oxidation mechanism of CO. This process requires as an initiating component OH-radicals, which have to be provided in a sufficient amount by the H_2 oxidation. The resulting time delay between hydro-

gen and CO oxidation could be detected in the H_2-CO-air experiments with the installed photodiodes, which showed two spatially separated flame zones moving along the tube.

With respect to safety analysis, the mitigation effect of CO additions on the observed flame speed and the resulting pressure loads should be taken into account. Treating CO simply as H_2 in the analysis would lead to overconservative load estimates.

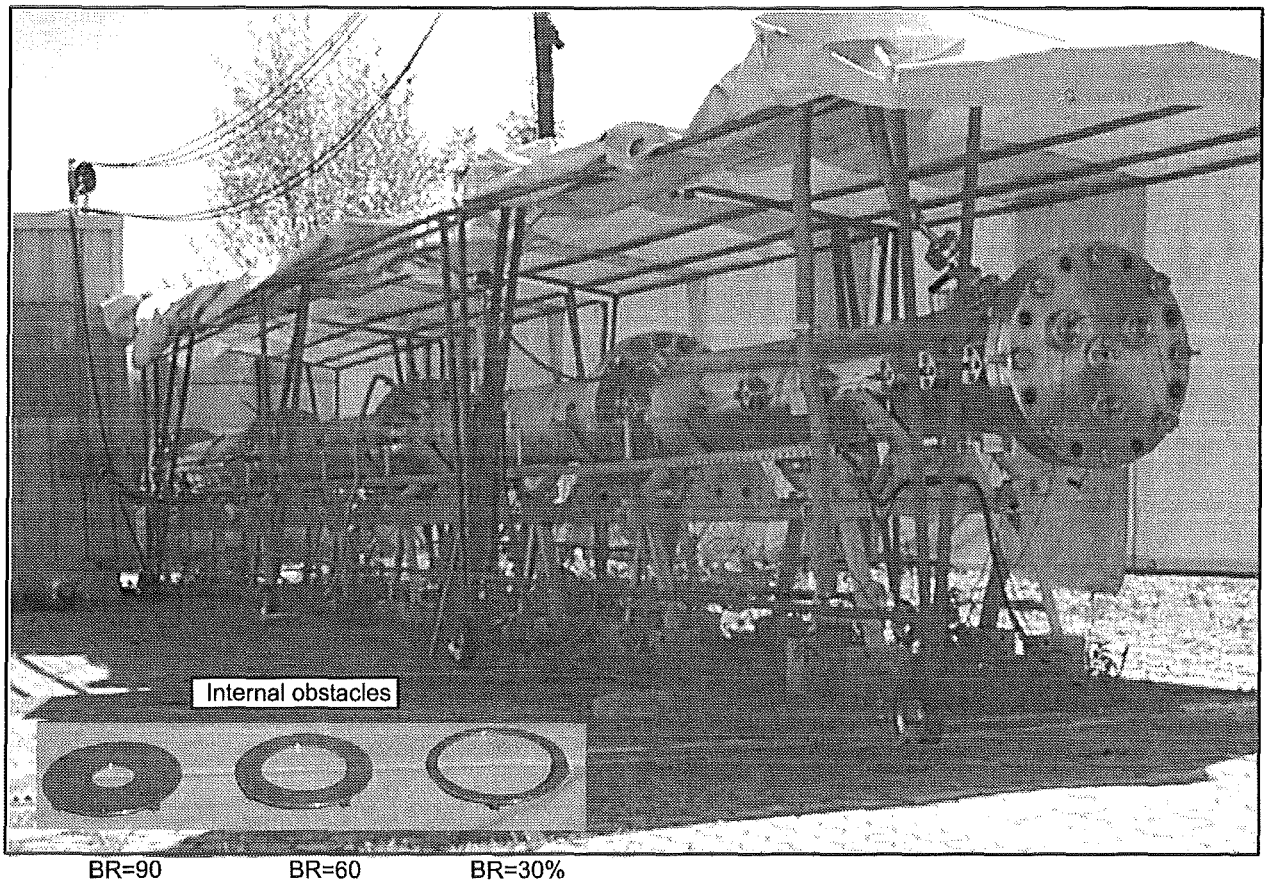

Figure 1: FZK 12m –tube

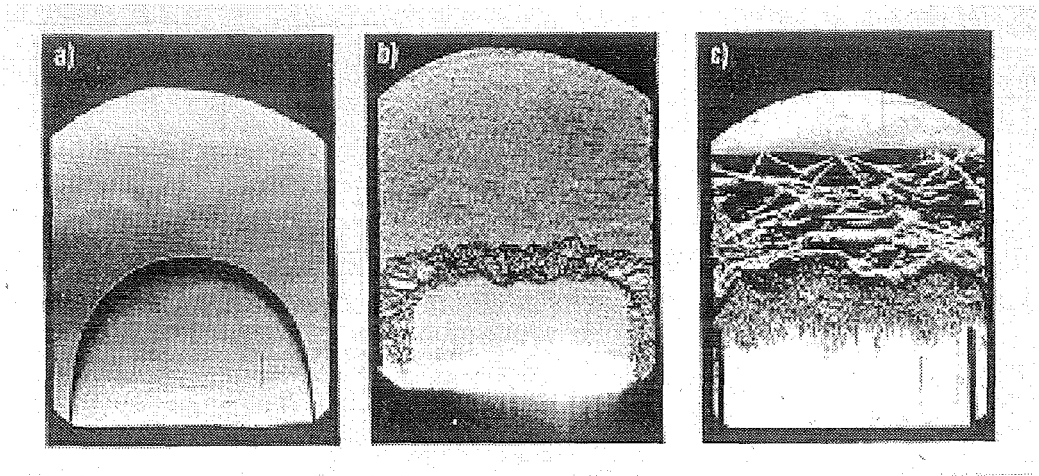

Figure 2: Schlieren pictures of a laminar deflagration (a), turbulent deflagration (b) and quasi- detonation (c) (F.-J. Wetzel, DLR, 1993)

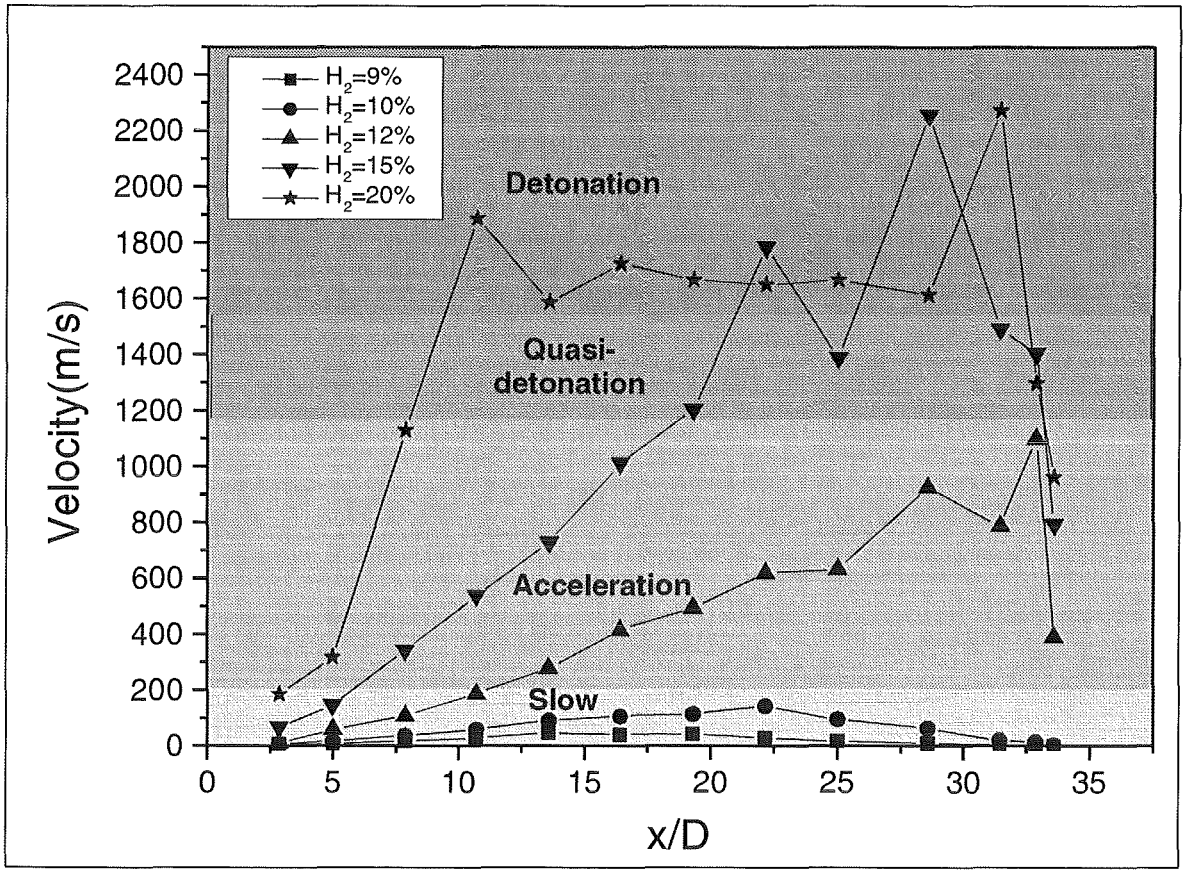

Figure 3: V-x diagram of FZK-tube experiments with various H2-air mixtures (BR = 45 %)

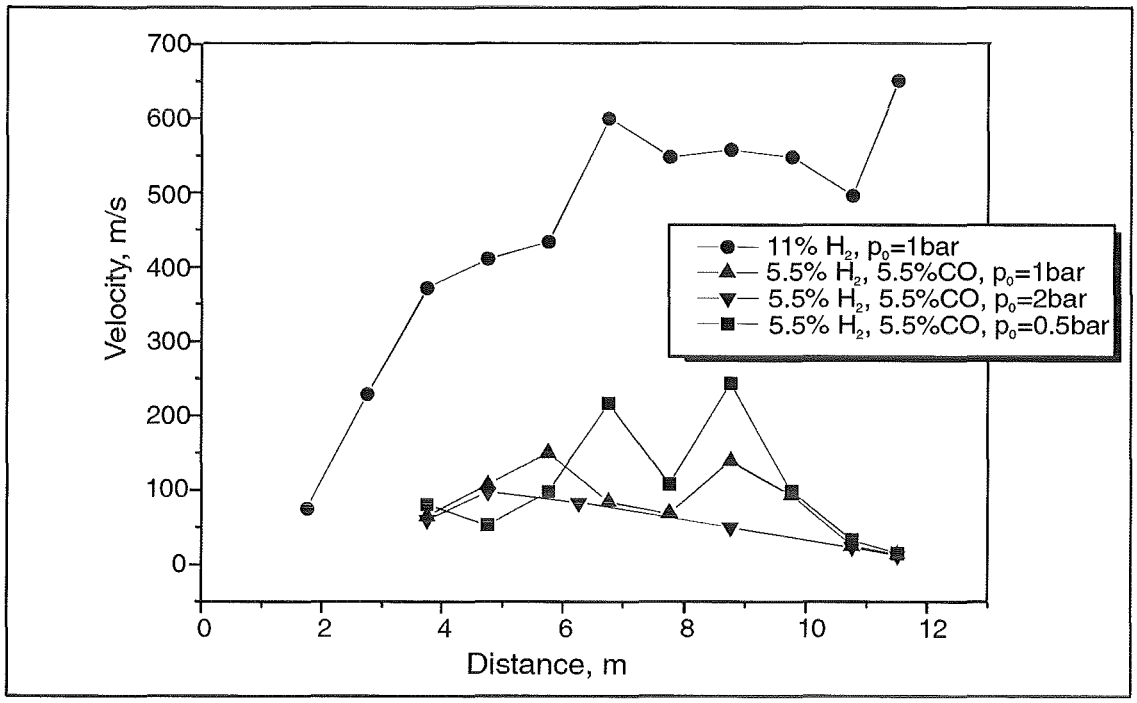

Figure 4: V-x diagram with 11% fuel-gas.

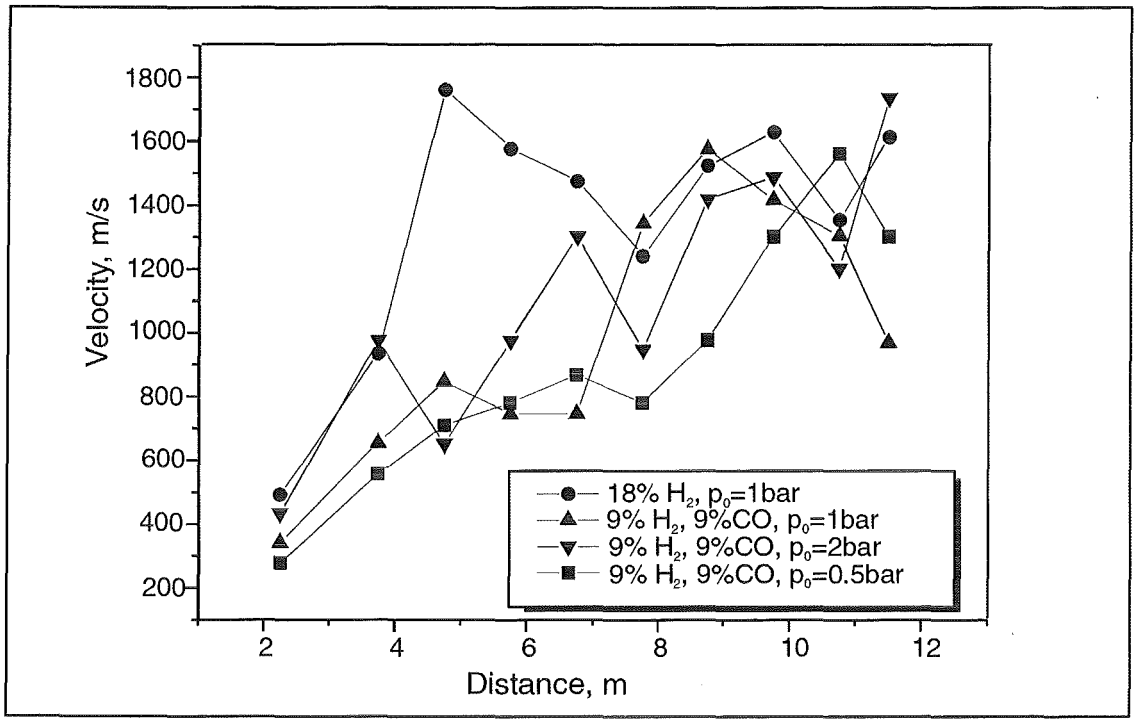

Figure 5: V-x diagram with 18% fuel-gas.

III. Numerical Simulation of Combustion with COM3D and B0B

(U. Bielert, A. Kotchourko, A. Veser, W. Breitung, IKET)

Abstract

During the last year various numerical simulations were performed as part of the HYCOM project. The fast turbulent combustion code COM3D was used in pre-test calculations of large scale experiments in the RUT facility. These computations were performed on a very fine grid to provide the highest possible accuracy. Additional calculations of experiments performed in the DRIVER tube were done with the combustion code B0B. This code uses a simplified combustion model, but is faster than COM3D. Parameter variations were performed to study the behaviour of the combustion model in limiting conditions.

1. Fast turbulent combustion simulation of RUT facility using COM3D

A test calculation of test case HYC02 was performed using COM3D. In this test only the curved section and the canyon part of the RUT facility was used. The straight channel was closed of for this test. The initital conditions for the test were a uniform mixture of 10 % hydrogen in air. The ignition occured near the end of the curved section.

The computational grid used in this calculation consists of 98 x 94 x 416 cells. This results in a cell size of 0.0667m x 0.0667m x 0.0667m. The total grid consists of about 3.8 million cells. With this grid it was possible to resolve not only the main obstacles but also the supporting metal structures which hold the obstacles and other equipment in place. The geometry used in the actual calculation is shown in Figure 1. The resolution of the modell is sufficient to include even such details as the fans on the ground and the grids at the walls.

For a simulation of this large size the use of a powerful computer was necessary. A parallel version of COM3D has been developed and implemented to make use of massive parallel machines. Using the parallel version the

blind simulation was performed on a Cray T3E. Using 80 CPUs, a total of approximately 8000 CPU hours were needed for the calculation. Some results of this calculation are presented in the following figures.

Figure 2 shows a 3D view of the hydrogen concentration at a fixed point in time during the combustion process, 0.111 seconds after ignition. The mixture was ignited in this calculation near the curved end of the RUT facility. At the instance shown, the flame has already moved through the channel and has entered the canyon. In the upper part the flame continues to propagate horizontally. Only later burns the flame downwards into the canyon and consumes the remaining hydrogen there. This is due to the fact, that the flow in the upper part of the canyon is essentially horizontal. Near the entrance into the canyon it can be observed how the shape of the flame is modified by the obstacles and the confinement. It can also be observed that the flame produces a tongue shape as it moves through the hole in the first obstacle. In the calculation the region between the unburned reactants shown in red color and the completely burned products shown in blue is rather thick. The details of this flame region depend on the combustion and turbulence models and the numerical methods used.

Figure 3 shows the distribution of the turbulent kinetic energy [Pa] for the same instance in time shown in figure 2. It can be observed that behind the opening of the first obstacle in the cavity,where the flame just arrived, a high level of turbulence has already been created. A similar region of high turbulence is already building up behind the hole in the second obstacle which is still well before the flame front. High levels of turbulence are also present at the top of this obstacle where a kind of shear flow is created by the expansion flow of burned gases. All these regions are in front of the flame. Thus the turbulence levels will effect the further flame propagation and further enhance combustion according to the used EBU model. In the burned gases high turbulence levels are observed near the curved end of the channel. It seems as if the turbulence decay between the obstacles in the curved section is somehow delayed by the flow redirection.

Pressure histories for the probe positions used in the experiments are shown in Figures 4 and 5. All probes in figure 4 are located
in the upper region of the RUT facility. The probes PP05 and PR05 are located at the right side above the canyon. The probes PP11 and PR11 are located at the left side near the end of the curved section. The other probes are located in between with numbers increasing from right to left. Figure 5 shows similar data for the probe positions located in the lower part of the RUT facility , the so called canyon. Again the numbers increase from right to left. At all locations peak pressures between 3.5 bar and 4.5 bar are observed. The differences between the calculated pressure histories at the positions of the piezo resistive transducers and the piezoelectric transducers is very small. However, the temporal response at different locations is quite different. At position PP05 the pressure history shows a pronounced maximum at about 0.15 sec. After that some low frequency oscillations are observed. At postion PP07 a relatively smooth pressure rise is observed. In the upper part of the canyon the pressure remains at a relatively low level, then rises very quickly to 3.5 bar overpressure and remains almost constant on that level. At location PP11, also above the canyon, a peak pressure of 4.5 bar is reached. The peak is rather wide and is followed by a low frequency oscillation. The same peak pressure is also reached in position PP12. But here the peak is much sharper.

The large variety of computed pressure histories clearly shows the importance of temporal and spatially resolved calculations. The calculations indicate that different parts of the test facility see very different load conditions. While some regions are subjected to high frequency loads and short pressure peaks, other regions see a more static loading. These differences are due to complex reflections and superpositioning of different waves in the facility.

In order to determine the structural response of the walls and to maintain the structural integrity of a containment the time history of the pressure loads must be known locally.

While the discussion of the simulation results gives a consistent picture of the combustion process for this test case, only the comparison to the experimental results will allow to evaluate the quality of the simulation in a conclusive way.

2. Calculation of small scale tests using B0B

The computer code B0B was jointly developed by KI and FZK to calculate combustion processes in large complex structures in a fast way. It was used for the RUT facility. These calculations are part of the blind test calculations discussed in the next paragraph. The same code was used by FZK for simulations of small scale experiments. A major advantage of B0B over COM3D is computation time. With B0B parameter studies are much cheaper than with COM3D. However, the modeling approach of both codes is quite different.

The computer code B0B combines a 3D hydrodynamics flow solver with a simple empirical combustion model. In this combustion model the burning rate is defined by a burning rate constant Kc which must be defined approriately. This burning rate constant is related to the turbulent burning velocity ST and the expansion ratio sigma. This allows to estimate values for Kc based on models for ST and a calculation of sigma, which is a mixture property.

To gather experience with the B0B code a parameter variation of Kc is performed for test 1 in configuration 1 of the driver tube (L=12m, D=0.174m). In this test the tube is closed and a constant blockage ratio of 0.6 is used in the whole tube. A mixture with a hydrogen concentration of 10 % is ignited at one end. This experiment has been simulated with a wide range of Kc values. The resulting velocity profiles along the tube are shown in Figure 6. In this figure the flame velocity is plotted as function of distance from the ignition location for the different Kc values. For all Kc values a constant final flame velocity is observed. This final velocity increases with increasing Kc values. For higher Kc values the final flame velocity value is reached earlier and closer to the ignition point, thus indication a shorter acceleration phase of the combustion process. The figure shows that using different values for Kc the whole range

of combustion regimes can be obtained. For very high values detonation velocities can be achieved. Lower values of Kc result in fast flames and even lower values allow to stay in the regime of slow turbulent flames.

In Figure 7 the final quasi-constant value for the flame velocity is plotted as function of the burning rate constant Kc. With decreasing Kc the final flame velocity decreases. Given the experimentally observed flame velocity, the curve in figure 7 helps to estimate the appropriate value for the constant Kc in the simulation, reproducing the experimental result.

Figures 8 and 9 show pressure histories for the different simulations at two locations in the tube. Figure 8 gives data for a location 1.18m from the ignition location. At this location only the fastest flames have reached the final value of the flame velocity. The pressure histories clearly show the different combustion regimes. For the two slowest simulations with Kc=500 and Kc=1000 the pressure rises slowly and steadily. No distinguished pressure waves are observed. For values of Kc=2000 and Kc=3000 the initial presure rise rate increases and some small oscillations can be observed before reaching the final pressure plateau. For higher values of Kc a very fast pressure rise with a pressure peak much larger than the final equilibrium pressure is observed. This clearly indicates the interaction of pressure waves. It seems that the peak pressure increases further with increasing Kc value. However, the simulation with the highest value for the burning constant Kc=200000 is not in line with this observation. For this simulation only a moderate initial pressure peak was observed. Figure 9 gives similar data for a location 8.76m from the ignition location. At this location all simulations have reached the final values of the flame velocity. The profiles for the faster simulations are quite similar to the profiles in figure 8. The peak values are similar and the oscillations following the first pressure peak are somewhat more pronounced and decay a little faster. For the slower simulations (e.g. Kc=1000) a wave interaction causing a small plateau in the pressure curve can be observed. The final flame velocity for this case is about 400 m/s. Thus we see some hydrodynamic effects in these curves also. For higher values of Kc the computation was stopped before this effect could be observed.

If the pressure peaks were generated by interactions of reflected pressure waves alone, the peaks for the different fast simulations should be different at

the two locations. The time and location were these interactions take place depend on the generation of the pressure waves and thus on the combustion model and the burning constant Kc. At a fixed location we should see different phases of the wave interaction for different simulations. These patterns should change if we choose a different position for the observation. Since we see the same pattern at both locations, this indicates that the pressure peaks are caused locally by the energy release in the combustion wave. Increasing Kc values release the energy faster and thus cause higher peak values, which travel with the flame velocity through the tube. This would then indicate that for the highest value of Kc=200000 some other limit has been reached.

The purpose of this systematic parameter variation of Kc was to build some expericence using the B0B code and to better understand the effects of such parameter variations. The simulations performed so far indicate that the code B0B is able to simulate to very different combustion regimes. However, it is crucial that an appropriate value for the burning constant Kc is choosen. Based on a large body of experimental data in widely different experimental facilities correlations for the burning constant Kc have been developed at the Kurchatow Institute. Using these correlations a value of Kc can be calculated based on the expansion ratio sigma and the turbulent burning velocity of the mixture, and can be used to predict tubulent combustion.

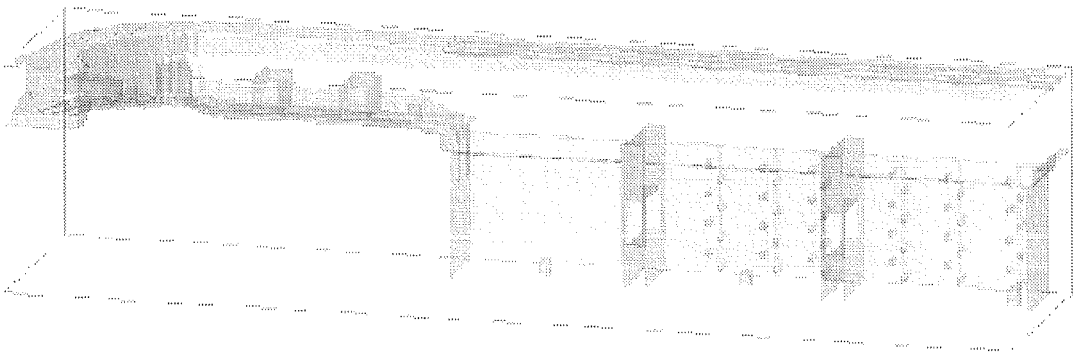

Figure 1:Geometry for blind test calculation HYC02.

Figure 2: Calculated hydrogen concentration during combustion process at 0.111 seconds after ignition for blind test calculation HYC02. Scale 0 - 10 vol% H_2

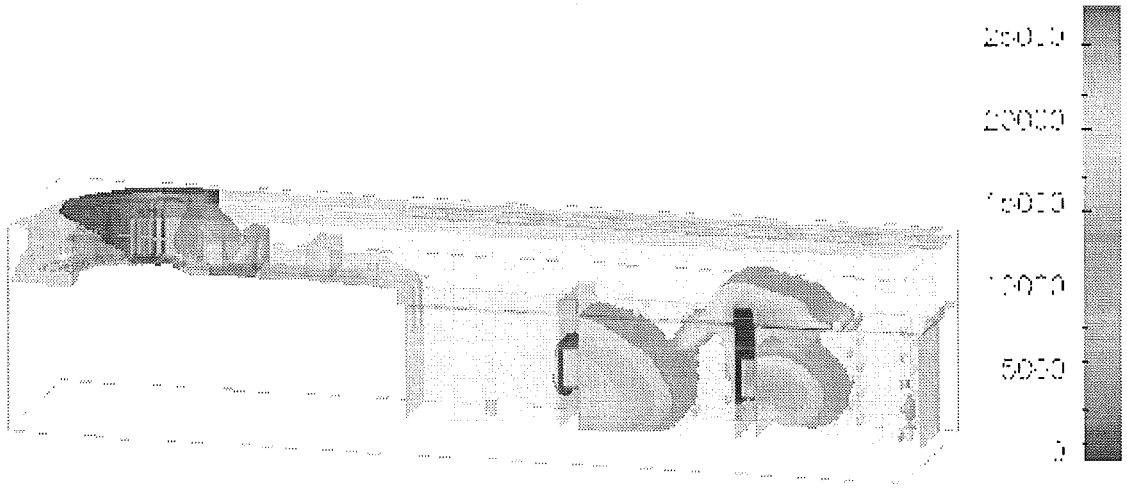

Figure 3: Calculated turbulent kinetic energy during combustion process at 0.111 seconds after ignition for blind test calculation HYC02. Scale 0 - 25000 Pa

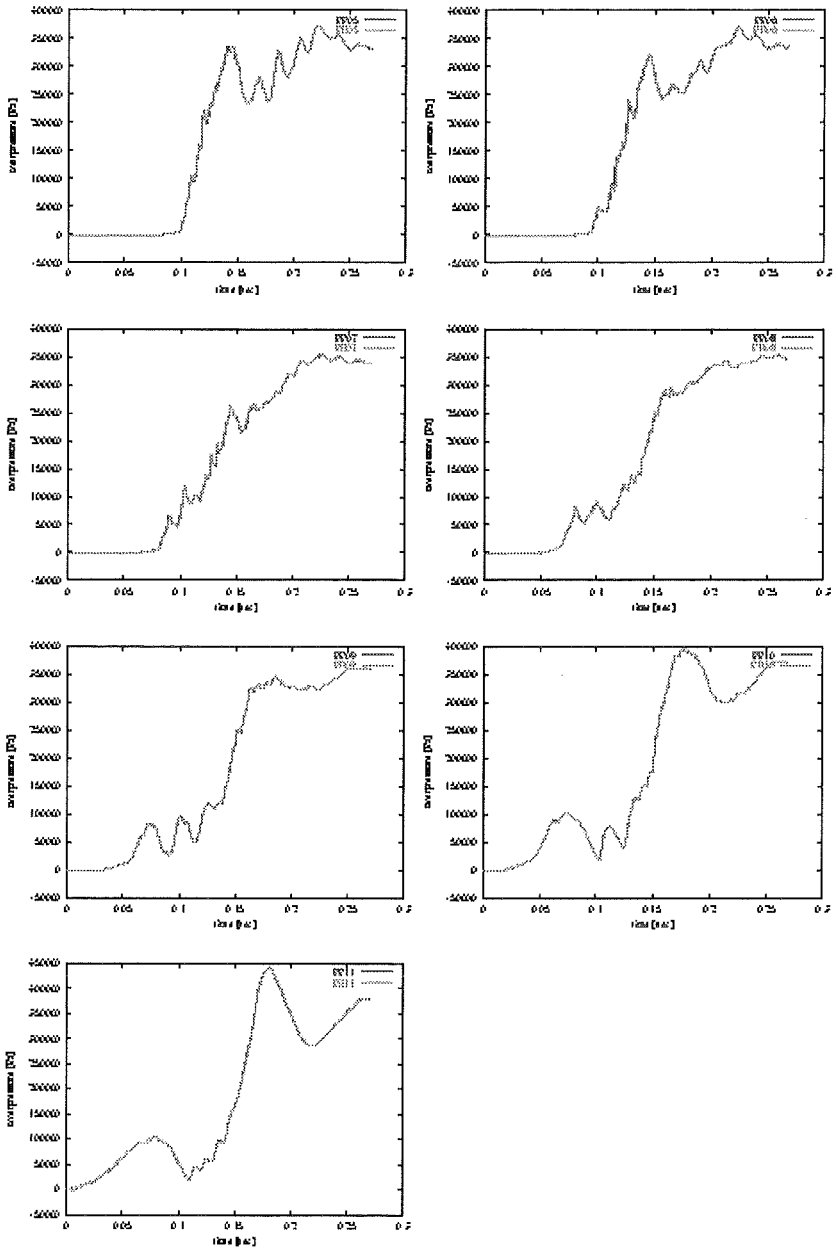

Figure 4: Pressure histories for probes in the upper part of the RUT facility for blind calculation of test HYC02 with COM3D code.

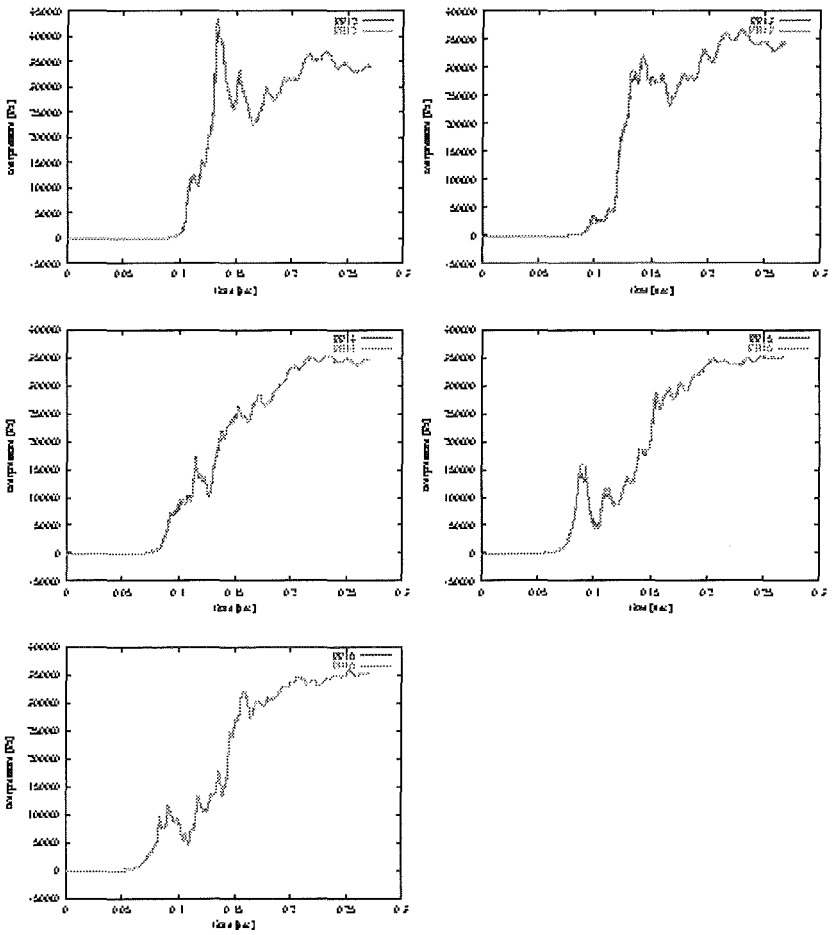

Figure 5: Pressure histories for probes in the lower part of the RUT facility for blind calculation of test HYC02 with COM3D code.

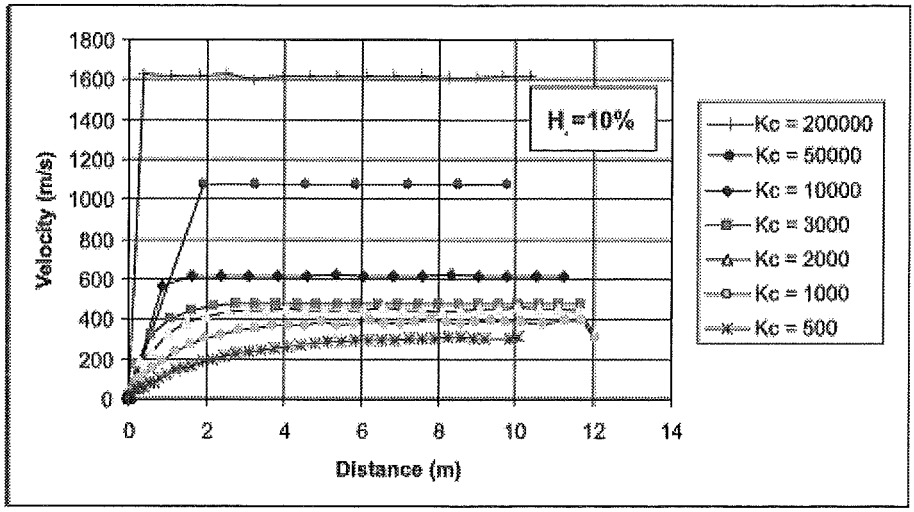

Figure 6: Test calculation in Driver tube with 10 % H_2, BR = 0.6, ignition at end wall. Flame velocity as function of position for different values of the burning constant Kc.

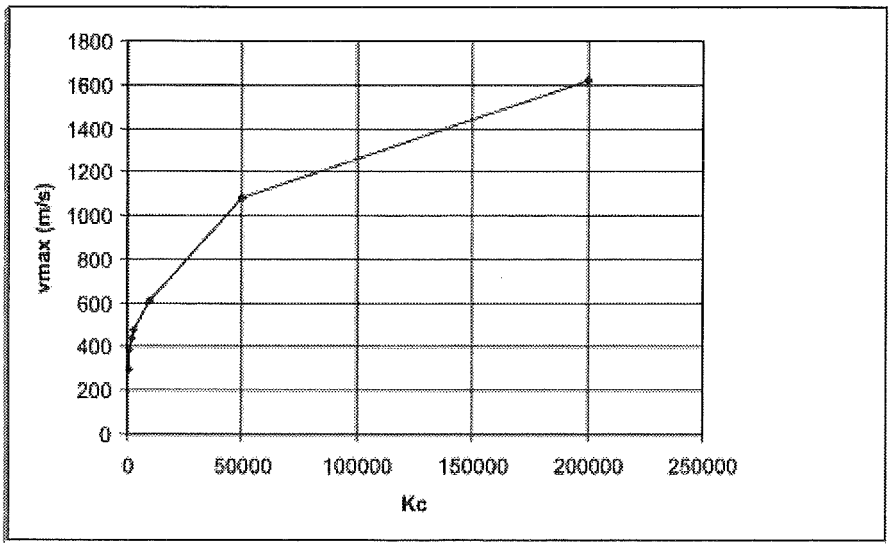

Figure 7: Test calculation in Driver Tube with 10 % H_2, BR = 0.6, ignition at end wall. Maximum flame velocity as function of burning constant Kc

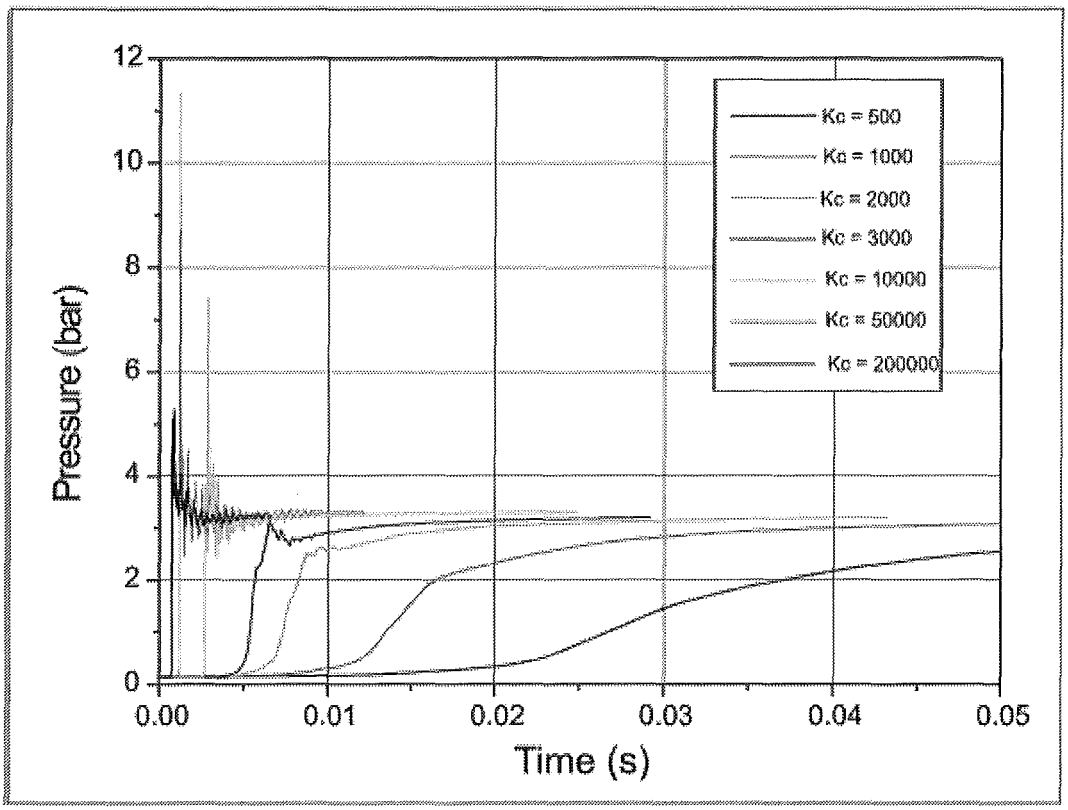

Figure 8: Test calculation in Driver tube with 10% H_2, BR = 0.6, ignition at end wall. Pressure histories at 1.18m behind the ignition location for different values of the burning constant Kc.

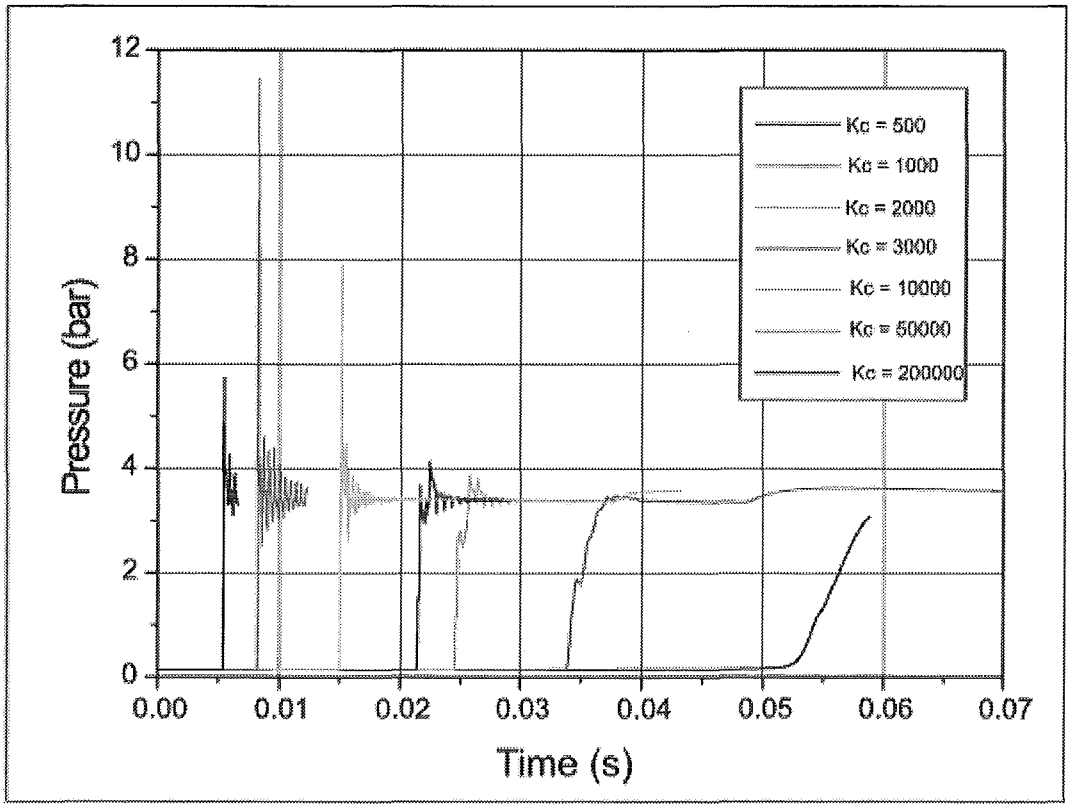

Figure 9: Test calculation in Driver tube with 10% H_2, BR = 0.6, ignition at end wall. Pressure histories at 8.76m behind the ignition location for different values of the burning constant Kc.

IV. Ein strukturdynamisches Modell zur Interpretation realer dynamischer Drucklasten

(B. Burgeth, A. Veser, IKET)

Abstract

Structural components of containments perceive dynamic pressure loads differently according to their eigenfrequencies. The linear undamped oscillator has been employed as a structural dynamic model to analyse these perceived pressures and hence to estimate the damage potential of the original pressure loads. This investigation is based on a detailed representation of local pressure loads, calculated with a 3d CFD code (B0B) for the combustion of a homogeneous hydrogen-air mixture inside a reactor containment.

1. Einleitung

Ein wesentlicher Bestandteil nuklearer Sicherheitsanalysen ist es, die Auswirkung dynamischer Drucklasten, die bei verschiedenen Szenarien der Wasserstoffverbrennung in einem Containment auftreten können, einzuschätzen. Diese Szenarien bestimmen sich vor allem durch die Gemischzusammensetzung und die komplexe Containmentgeometrie. Die auftretenden Verbrennungsformen reichen von der langsamen über die schnelle Deflagration bis hin zur Detonation, zu deren Simulation eine Reihe von Codes zur Verfügung stehen [1]. Um die sehr komplexen Phänomene bei der turbulenten Verbrennung zu simulieren, wurde der B0B-Code herangezogen [2]. Die hierbei zum Einsatz kommenden Modelle liefern konservative Abschätzungen der bei der Verbrennung entstehenden Lasten. Die Containmentgeometrie wurde mit hohem Detailgenauigkeit dargestellt (Δx, Δy, Δz = 0.4m, 1.8 Millionen Rechenzellen). Abbildung 1 zeigt als Beispiel die Verbrennung einer 8 % H_2-Luft Mischung, 0.17s nach der Zündung im Dom des Containments.

2. Strukturdynamische Bewertung von dynamischen Drücken mit dem Einmassenschwinger-Modell

Mit dem B0B-Code wurden Rechnungen durchgeführt, die sich hinsichtlich Wasserstoffkonzentration und Zündort unterscheiden [3]. In Abbildung 2 sind die zeitlichen Druckverläufe an vordefinierten Stellen in dem Containment dargestellt, die sich aus der Simulation der Verbrennung mit dem Code unter den angegebenen Bedingungen ergeben.

Die relativ niedrige H_2-Konzentration bedingt zwar eine langsame Deflagration (anfangs ca. 50 m/s), führt aber dennoch zu relativ hohen, lokalen Druckspitzen von bis zu etwa 8 bar. Verursacht werden diese mehrfachen Druckmaxima durch Fokussierungs- und Reflektionseffekte an Wänden und inneren Strukturen. Der Fokussierungs- und Reflektionscharakter der Druckkurven wird deutlich, wenn die Drücke in dimensionsloser Form über der durch die Schallgeschwindigkeit im verbrannten Gas normierten Zeit aufgetragen werden und die Druckamplitude auf den AICC-Druck der homogenen Gasmischung bezogen wird. (Abbildung 3). Bedingt durch die komplexen Geometrien und Strömungsverhältnisse im Containment wird unverbranntes Gas vorkomprimiert und anschließend verbrannt. In der Rechnung werden dadurch Drücke bis zum doppelten AICC-Druck erreicht.

Die zeitliche Lage der Druckspitzen im Diagramm spiegelt die relative Entfernung zwischen dem lokalen Druckaufnehmer und benachbarten baulichen Strukturen wieder. Diese regelmäßigen Reflektionen können bei bestimmten Bauteilen zu Resonanzeffekten führen, die das Schädigungspotenzial der ursprünglichen Druckwellen stark vergrößern können.
Um die mechanische Auswirkungen dieser realen Druckverläufe auf die Gebäudestrukturen besser beurteilen zu können ist ein dynamischer Analyseschritt nötig.

Ausgehend von dem Modell eines linearen ungedämpften Einmassenschwingers [4,5,6] (Abbildung 4) wurden die durch die berechneten lokale Druckverläufe auf die Gebäudestrukturen ausgeübten Kräfte simuliert.

Dabei wurde angenommen, dass ebene Druckwellen senkrecht auf die Strukturfläche einfallen und dann elastisch reflektiert werden. Das Verhalten eines ungedämpften Einmassenschwingers mit der Eigenfrequenz ν wird beschrieben durch eine gewöhnliche lineare Differentialgleichung zweiter Ordnung:

$$\frac{1}{4\pi^2}\frac{1}{\nu^2}\ddot{q}_\nu(t) + q_\nu(t) = p(t) \qquad (1)$$

p(t) steht für den durch den B0B-Code bereitgestellten aber um einen Offset p_0=1bar bereinigter Druckverlauf. Er liegt nicht in Form einer Funktionsvorschrift, sondern als eine

Menge diskreter Datenpunkte vor. Der Antwortdruck $q_\nu = q_\nu(t)$ repräsentiert unter den oben gemachten Annahmen die lokale dynamische Belastung einer Struktur mit der Eigenfrequenz ν. Aus strukturdynamischer Sicht ist besonders der maximale statische Antwortdruck q_ν^{max} wichtig.

Von großer Bedeutung bei der Berechnung von q_ν bzw. q_ν^{max} ist die detaillierte Erfassung des Zwangsterms p(t) durch eine geeignete Approximation. Die anschließend gewonnenen analytischen Lösungen von Gleichung (1) lassen sich mit dem Computer Algebra System (CAS) Maple 6 [7] auswerten und darstellen [8]. Als ein Beispiel ist der in Abbildung 2 hervorgehobene Zwangsterm p(t) mit der zur Eigenfrequenz ν =10 Hz korrespondierenden Lösung q_{10} dargestellt. Zusätzlich sind die theoretisch ermittelten Nieder- ($\nu \rightarrow 0$) und Hochfrequenz- ($\nu \rightarrow +\infty$) Limits eingetragen (Abbildung 5).

Die nachfolgenden Abbildungen 6 und 7 zeigen für das gleiche Beispiel q_ν^{max} in Abhängigkeit von Oszillatorfrequenz ν. Zum Vergleich ist in den Graphiken auch ein angepasster idealisierter in analytischer Form darstellbarer Druckverlauf und der dazugehörige maximale Antwortdruck dargestellt.

3. Ergebnisse und Ausblick

Der Vergleich von original berechneten diskreten Druckpunkten und idealisierten analytischen Druckverläufe verdeutlicht die große Sensitivität des ungedämpften Einmassenschwingermodells. Kleine Abweichungen in den Zwangstermen p(t) führen zu großen, schwer vorhersagbaren Veränderungen in den maximalen Antwortdrücken. Wie bereits erwähnt, ist daher die detailgetreue Abbildung des Zwangstermes, der in Form numerischer Daten vorgegeben ist, notwendig. Aus dem gleichen Grund ist auch eine Verfeinerung des Modells durch das zusätzliche Einführen einer Dämpfung empfehlenswert. Dies erscheint auch sinnvoll im Hinblick auf eine Anpassung des jetzt noch konservativen Modells an reale Strukturverhalten [5,6].

4. Referenzen

[1] OECD State-of-the-Art Report on Flame Acceleration and Deflagration-to-Detonation Transition in Nuclear Safety. Report NEA/CSNI/R (2000), (August 2000)

[2] A. Efimenko, A. Lelakin, A. Denkevits and S. Dorofeev; Development and evaluation of Computer Code for 3D Simulation of Combustion Processes in Complex Containment Geometry, Final report for FZK, Moscow, November 1999

[3] A. Veser; Simulation of Combustion in Complex 3d-Geometry with BOB; unpublished (2000)

[4] W. Breitung, R. Redlinger; A Model for structural Response to Hydrogen Combustion Loads in Severe Accidents; Nuclear Technology, Vol 111, Sep. 1995

[5] J. Eibl; Zur bautechnischen Machbarkeit eines alternativen Containments für Druckwasserreaktoren, Stufe 2, Dezember 1991

[6] J. Eibl; Zur bautechnischen Machbarkeit eines alternativen Containments für Druckwasserreaktoren, Stufe 2, Dezember 1994

[7] Maple6, The Standard for Analytical Computation; Waterloo Maple, Advancing Mathematics

[8] B. Burgeth; On the Numerical Treatment for Forcing Terms in the Linear Oscillator Equation; unpublished (2000)

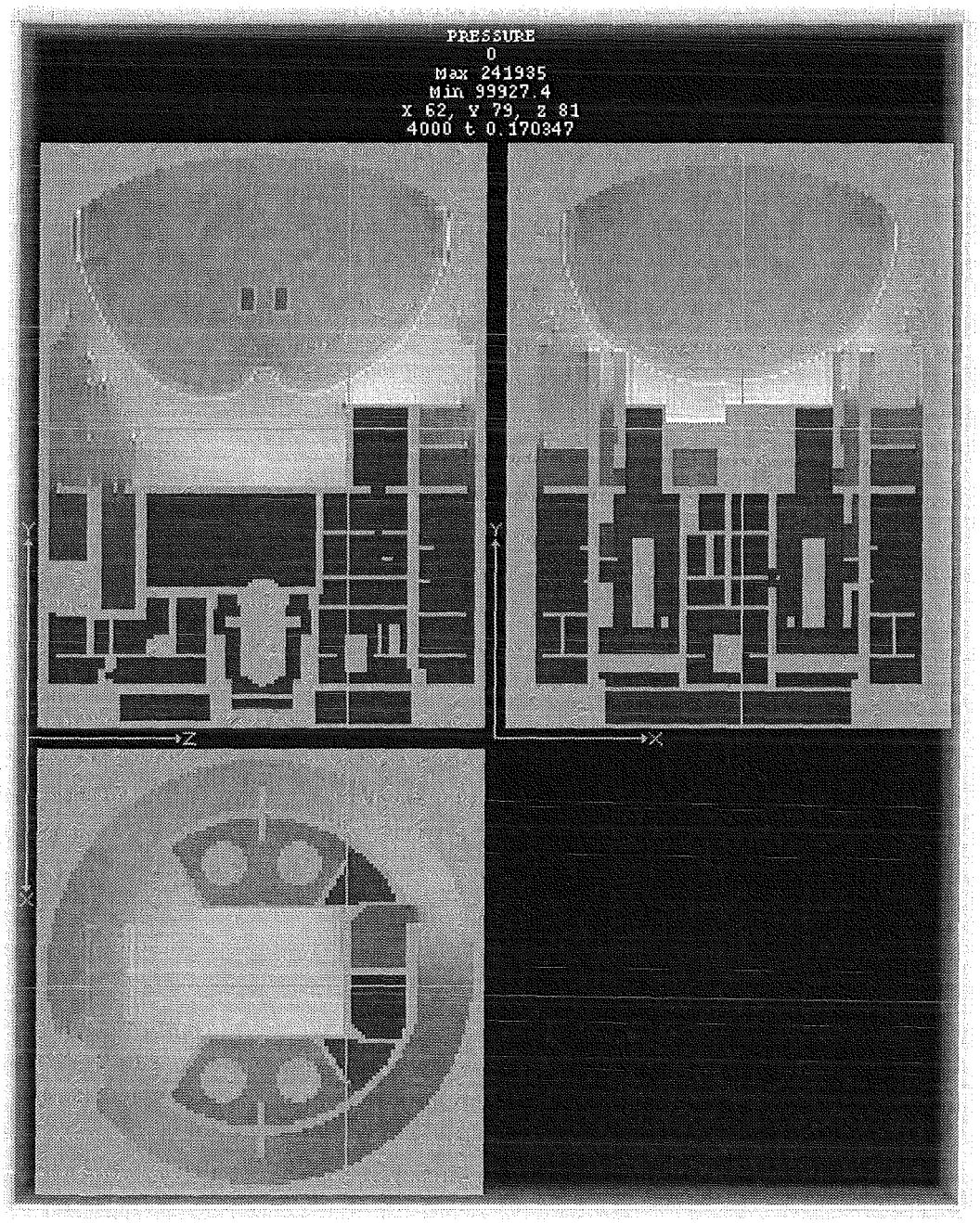

Abbildung 1: Berechnetes Druckfeld aus Simulation mit CFD-Code B0B bei Verbrennung einer 8 % H_2-Luft Mischung in einem komplexen 3d Containmentmodell. Zündung im Nordpol des Doms, Zeitpunkt 0.17s nach der Zündung, maximaler Druck 2.42 bar.

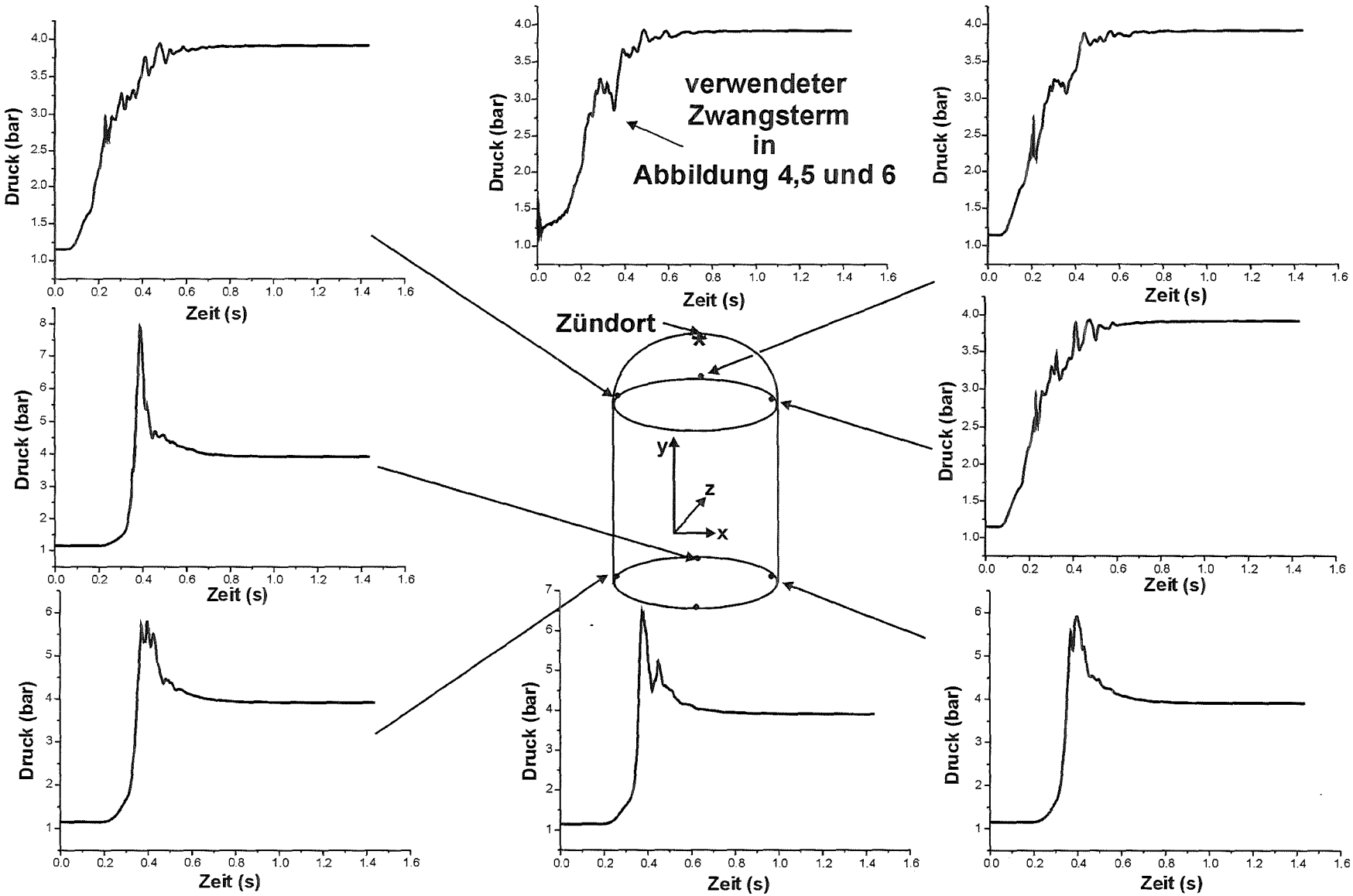

Abbildung 2: Berechnete lokale Druckverläufe bei Verbrennung einer 8% H_2-Luft Mischung in einem komplexen 3d-Containment- Modell, Zündung im Nordpol des Doms. Im unteren Containmentbereich führen Reflektionen und Fokussierungseffekte zu hohen lokalen Druckspitzen.

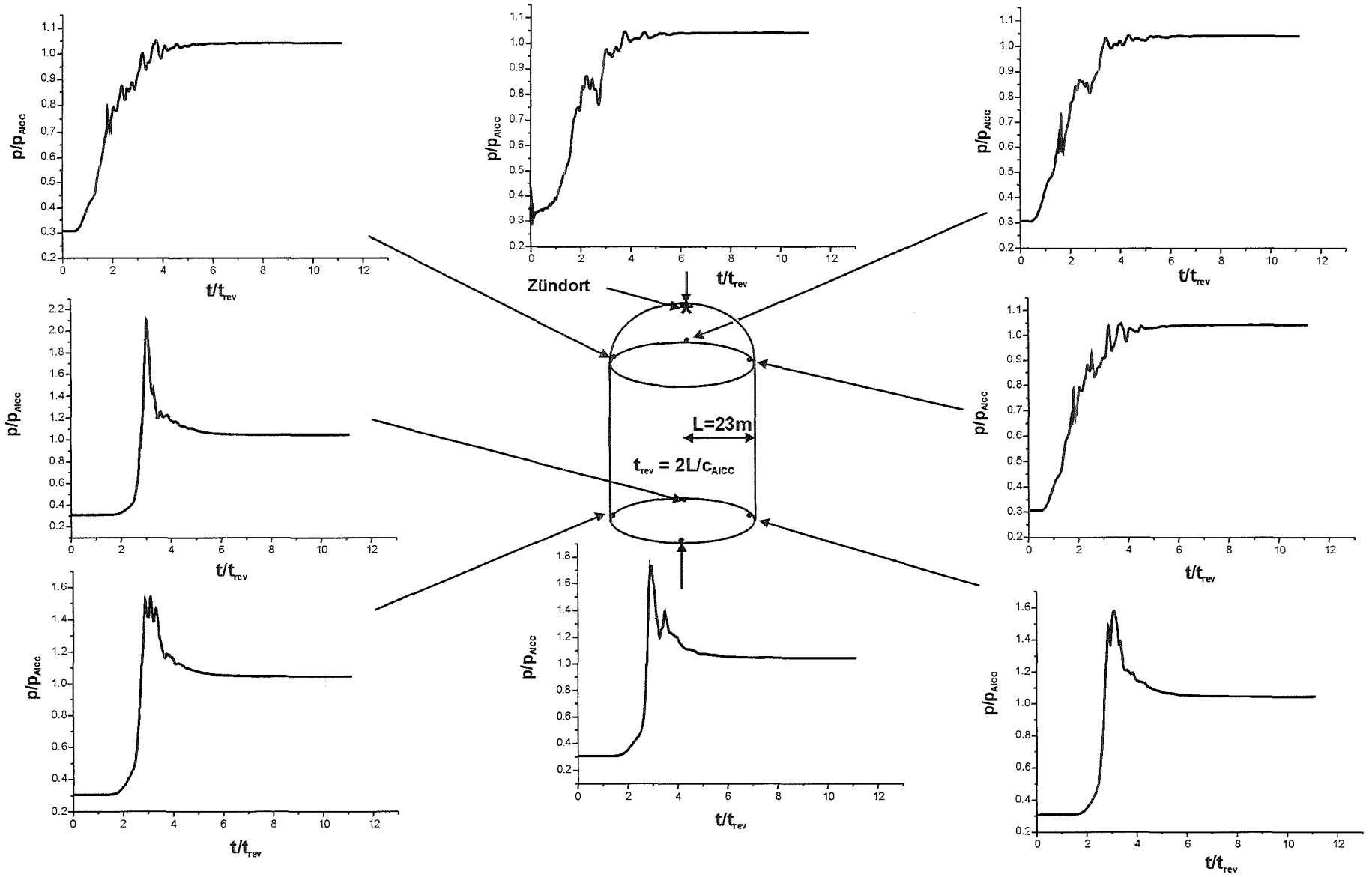

Abbildung 3: Dimensionslose Darstellung der berechneten lokalen Drücke durch Normierung mit dem AICC-Druck der Mischung p_{AICC} und der Laufzeit von Druckwellen im verbrannten Gas (p_{AICC}= adiabatic isochoric complete combustion pressure, c_{AICC}= Schallgeschwindigkeit im verbrannten Gas)

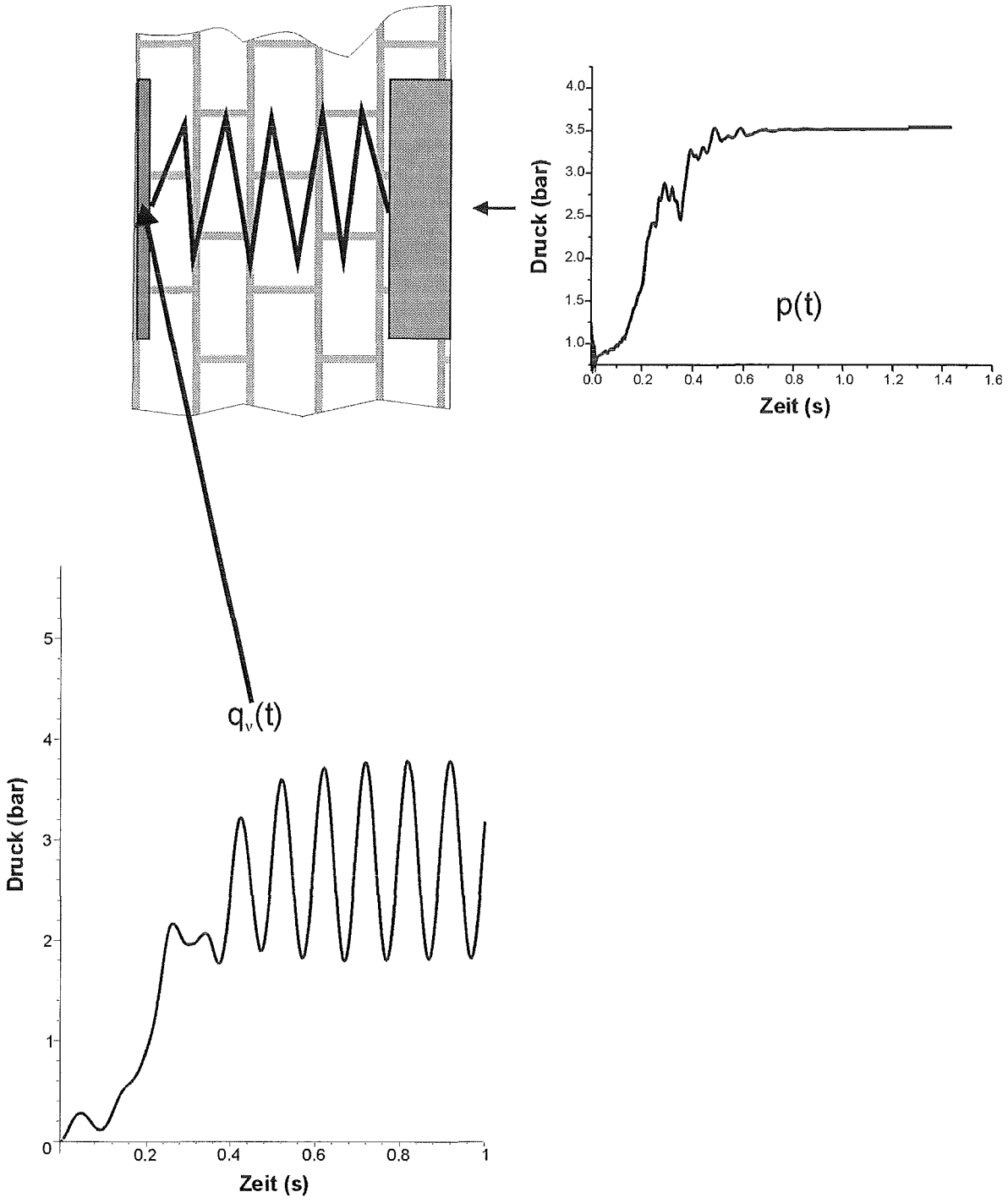

Abbildung 4: Eine lokale Struktur in der Modellvorstellung eines Einmassenschwingers. Der Zwangsterm p(t) beschreibt die einfallenden Druckwellen auf einen Oszillator mit Eigenfrequenz ν . Die Antwort $q_\nu(t)$ kann als die vom Rückstellmechanismus (Feder) aufzunehmende Drucklast interpretiert werden.

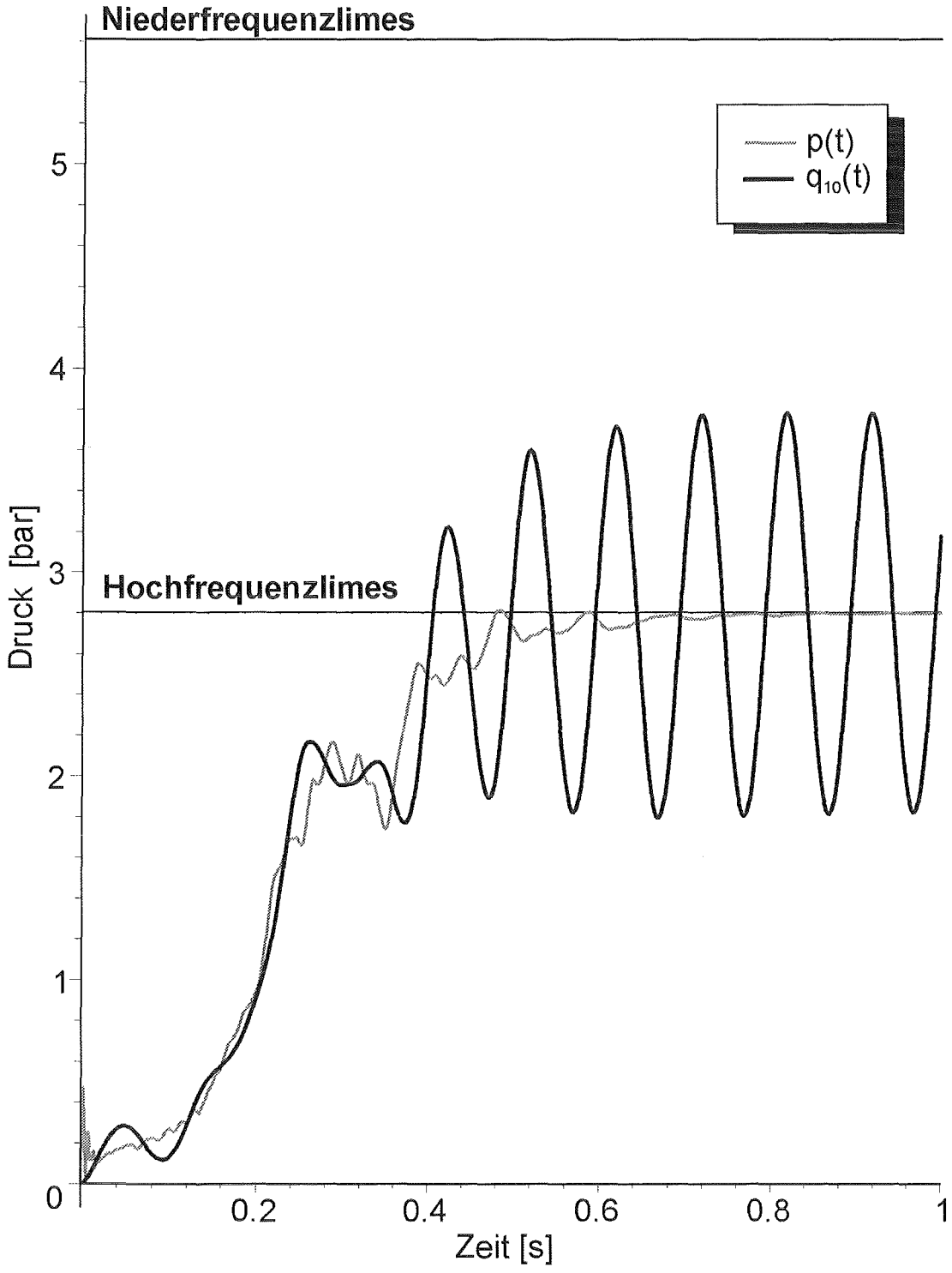

Abbildung 5: Der Zwangsterm p(t) und der effektive zeitliche Druckverlauf $q_{10}(t)$, der sich als Antwort des Einmassenschwingermodells für die Eigenfrequenz ν=10Hz ergibt.

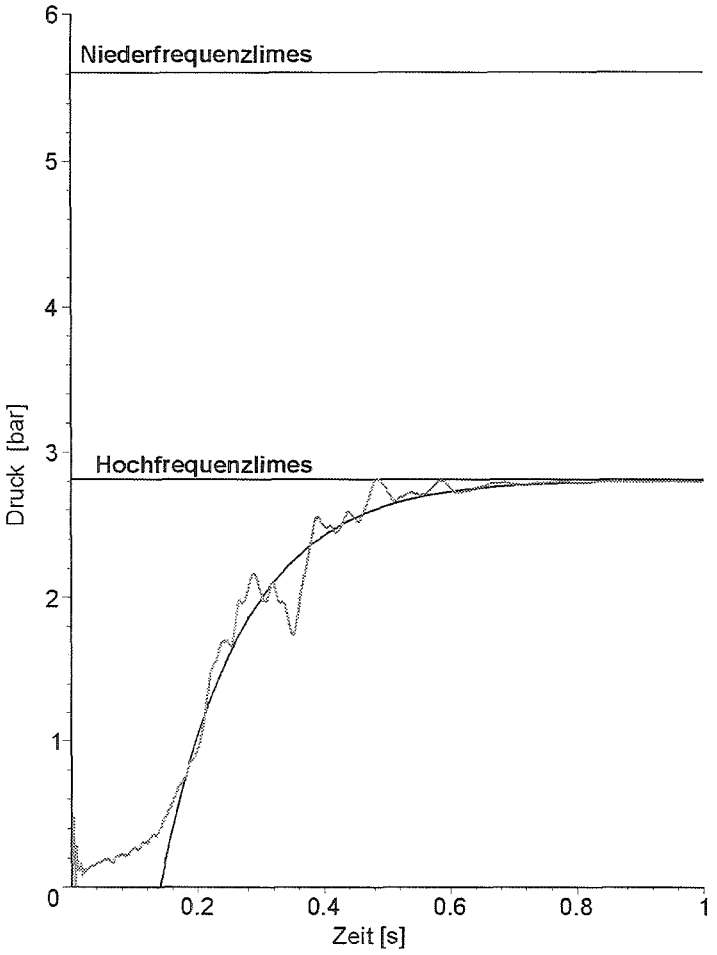

Abbildung 6: Numerisch vorgegebener Zwangsterm p(t) im Nordpol der Containmentkuppel (grauer Graph) und angepaßte analytische Vergleichsfunktion.

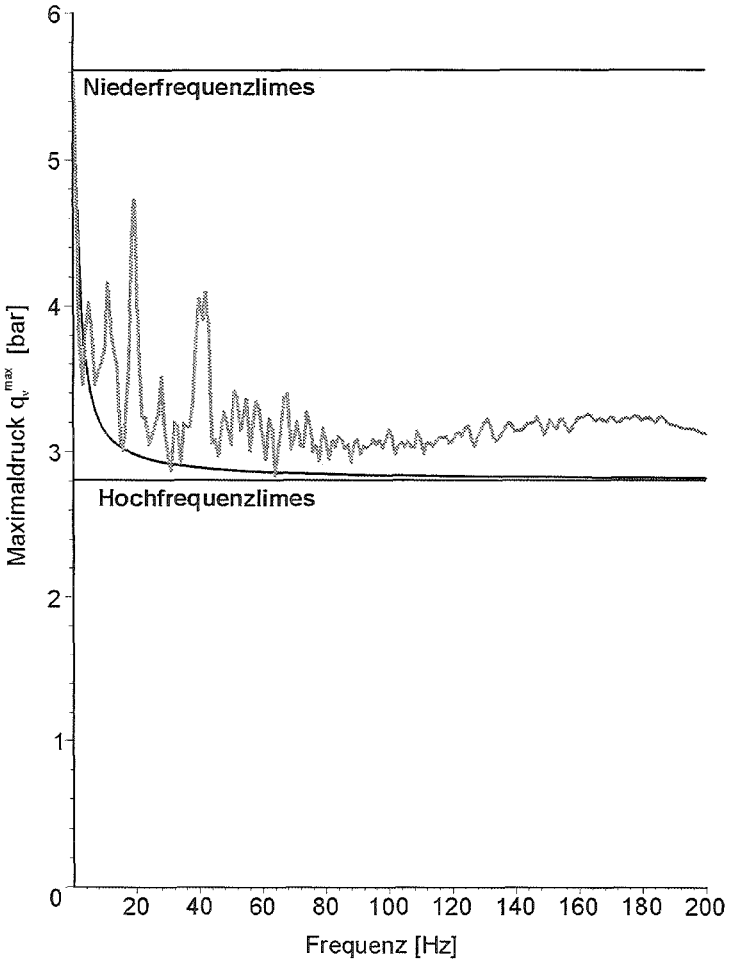

Abbildung 7: Der graue, stark oszillierende Graph zeigt den zum Beispiel gehörende maximale Antwortdruck q_ν^{max} als Funktion der Frequenz ν; Zum Vergleich ist der maximale Antwortdruck aufgetragen, der aus dem idealisierten Zwangsterm (schwarzer Graph) entsteht. Selbst kleine Unterschiede zwischem idealisiertem und realen Zwangsterm führen durch Resonanzeffekte zu Druckspitzen beim maximalen Antwortdruck q_ν^{max}, bei diesem Beispiel besonders im Frequenzbereich zwischen 0 und 50 Hz.

V. Einsatz von Gassensorik zur sicherheitstechnischen Überwachung

(M. Harms, J. Goschnick, IFIA)

Zusammenfassung

Um im Falle eines Störfalls die Wasserstoffkonzentration schnell bestimmen zu können, wurde auf der Basis der Gradienten-Mikroarray-Technologie der Karlsruher Mikronase KAMINA ein Wasserstoffdetektor hoher Dynamik (Messbereich 0,1 ppm-100 %) und weitgehender Selektivität mit Wolframtrioxid als gasempfindlichem Material entwickelt. Aufgrund der eingesetzten Gradiententechnik werden gas-spezifische Muster erhalten, die eine Differenzierung unterschiedlicher Gas-komponenten ermöglichen. In Laboruntersuchungen konnte eine Nachweisgrenze für Wasserstoff von < 1 ppm ermittelt werden. Mit der speziell für hohe H_2-Konzentrationen entwickelten KAMINA-Betriebselektronik, die einen zu niedrigen Widerständen erweiterten Messbereich bis 500 Ohm aufweist, lässt sich eine Nachweisgrenze von 400 ppm realisieren. Diese neuartige KAMINA ermöglicht Messungen bis weit in den Explosionsbereich hinein. Wechselnde Feuchte im Bereich von 20 – 80 % hatte dabei keinen Einfluss auf das Wasserstoff-Signal. Will man den gesamten Dynamikbereich des Mikroarrays ausschöpfen, bietet sich eine Tandemlösung aus zwei Betriebselektroniken und zwei identischen Chips an, um Wasserstoff sowohl hochempfindlich in Spuren bei hohen Messwiderständen zu detektieren als auch hohe Wasserstoffkonzentrationen bei niedrigen Widerständen mit der Niederohm-Elektronik zu bestimmen.

1. Einführung

Für die frühzeitige Erkennung sich entwickelnder Störfälle und die Störfall-überwachung selbst wird an einem einfachen gasanalytischen Sensorsystem hoher Robustheit und großer Zuverlässigkeit gearbeitet, das eine ständige empfindliche Kontrolle der Atmosphärenzusammensetzung im Reaktor erlaubt. Zudem soll das Gerät auch in der Detonationsapparatur des INR während der Untersuchungen dort eingesetzt werden können. Verwendet wird dazu die KAMINA (**Ka**rlsruher **Mi**kro**na**se). Sie ist ein Komplettsystem zum Betrieb eines Gassensor-Mikroarrays mit integrierter Elektronik inklusive einem über serielle Standardschnittstelle ange-

schlossenen 586er Laptop, dessen Software eine momentane Kontrolle des Messsystems und eine on-line-Datenauswertung erlaubt. Die Entwicklung eines Systems wird angestrebt, das seine Messdaten leitungsgebunden oder per Funk an eine Überwachungszentrale weitergeben kann. Die Messungen, d. h. die Abfrage aller Sensorelemente des Chips, erfolgen jede Sekunde.

Das hier benutzte Gassensor-Mikroarray (GSMA) besitzt eine Detektorschicht aus Wolframtrioxid. Zu den Vorzügen solcher Gassensoren auf Halbleitermetall-Basis gehören neben dem sehr schnellen Ansprechen - welches meist im Sekundenbereich liegt - auch die große Bandbreite der detektierbaren Gase und die besonders hohe Empfindlichkeit des Nachweises. Die große Vielfalt detektierbarer Gase ist für einen einzelnen Metalloxid-Gassensor ein erheblicher Nachteil, wenn hohe Selektivität für eine bestimmte Atmosphärenkomponente verlangt wird. Es lässt sich aber ein Sensorsystem mit der Fähigkeit zur Gasunterscheidung aufbauen, wenn eine Vielzahl unterschiedlicher Sensoren zu einem sog. Sensorarray zusammengefasst wird, dessen Sensoren unterschiedlich auf Gase ansprechen, so dass deren Signale bei verschiedenen Gasatmosphären charakteristische Signalmuster liefern. Mit Hilfe von Musteranalyseverfahren ist eine Unterscheidung und Wiedererkennung von Gasmischungen möglich.

Das Karlsruher Gassensor-Mikroarray realisiert das Prinzip eines Sensorarrays in besonders einfacher Weise dadurch, dass auf einem fingernagelgroßen Sensorchip (genau 9 x 10 mm) ein Metalloxidfeld durch Streifenelektroden in eine Vielzahl von Segmenten unterteilt wird. Durch Messung des Widerstandes zwischen zwei benachbarten Elektroden resultiert je ein Sensorsignal. Die Betriebstemperatur des Sensorchips - die im Fall der H_2-Detektion bei 300 – 350 °C liegt - wird durch vier Heizmäander erzeugt, die auf der Rückseite des Chips angebracht sind. Die Regelung der Heizleistung erfolgt mit Hilfe zweier Widerstandstemperaturfühler auf der Chipoberseite. Die unterschiedliche Empfindlichkeit der Sensorelemente wird durch die sogenannte Gradiententechnik erzielt. Das bedeutet, dass bestimmte Einflussgrößen auf das Detektionsverhalten gezielt von Sensorelement zu Sensorelement variiert werden. So wird zum einen ein Temperaturgradient über die Länge des Chips eingestellt, indem jedes der vier Heizelemente mit einer unterschiedlichen Heizleistung betrieben wird. Zum anderen wird die gesamte Chipoberfläche mit einer gaspermeablen Membran aus SiO_2 beschichtet, die über das gesamte Sensorarray eine ansteigende Dicke aufweist. Auf diese Weise können je nach dem mit der

Metalloxidoberfläche in Kontakt tretenden Gas unterschiedliche Signalmuster erhalten werden. Zur Signalauswertung stehen verschiedenste Varianten der multivariaten Datenanalyse in der KAMINA-eigenen Software zur Verfügung.

2. Experimentelles

2.1 KAMINA mit erweitertem Messbereich

Die Untersuchungen mit der Standard-KAMINA an der Detonationsapparatur des INR im Bereich von 15 – 80 % Wasserstoff zeigten, dass der Messbereich der bisher eingesetzten Elektronik unterschritten wurde. Deshalb wurde für Anwendungen, bei denen Messwiderstände unter 20 kOhm ermittelt werden, in Zusammenarbeit mit der HPE eine KAMINA entwickelt, die einen Messbereich von 500 Ohm bis 1,5 MOhm aufweist. Mit dieser KAMINA wurden Messungen im Bereich 10 – 15.000 ppm Wasserstoff durchgeführt.

Die Bestimmung der Kenngrößen des Sensorsystems für Wasserstoff in diesem nicht-explosiven Bereich erfolgte durch das sogenannte Pulsexpositionsverfahren im Untersuchungslabor des IFIA. Dabei wird der Sensorchip zunächst synthetischer Luft definierter Luftfeuchte ausgesetzt, worauf ein Konzentrationspuls des Zielgases mit möglichst kurzen Anstiegs- und Abklingzeiten erfolgt. An einen Expositionspuls schließt sich eine Erholungsphase an, bei der der Sensor wieder mit synthetischer Luft angeströmt wird. Es wurden mehrere Pulsexpositionen bei verschiedenen Gaskonzentrationen durchgeführt. Zu deren Durchführung wurde ein computergesteuertes Gasmischsystem eingesetzt, welches durch Massendurchflussmesser und pneumatische Ventile eine gezielte Einstellung der Gaskonzentration und der Luftfeuchte ermöglicht.

Zusätzlich wurde bei einer Wasserstoff-Konzentration von 400 ppm die relative Feuchte im Bereich von 20 – 80 % variiert, um den Einfluss dieses Parameters auf das Sensorsignal zu ermitteln.

3. Ergebnisse

3.1 H_2-Messungen im nicht-explosiven Bereich

Mit der neuartigen KAMINA wurde aufgrund des erweiterten Messbereich Wasserstoff bis zu einer Konzentration von 15.000 ppm durch das Gassensor-Mikroarray auf Wolframtrioxid-Basis detektiert. Höhere Konzentrationen konnten aufgrund der Explosionsgefahr im Labor nicht untersucht werden. Konzentrationen oberhalb der Explosionsgrenze ab 80 % bedürfen einer zusätzlichen Erweiterung des Messbereiches. Durch die obere Begrenzung des Messbereiches von 1,5 MOhm ergibt sich eine Nachweisgrenze von ca. 400 ppm. Diese Nachweisgrenze beruht einzig auf der elektronischen Beschränkung der Auslesung der Messwiderstände. Wie im vorherigen Bericht bereits beschrieben wird mit dem Gradientenmikroarray auf WO_3-Basis eine Nachweisgrenze von < 1 ppm erzielt.

Da das Sensorsignal S jedes Arrayelements definiert wird als die relative Leitfähigkeitsänderung

$$S = (G_c - G_o) / G_o = (G_c / G_o) - 1 = (R_o / R_c) - 1$$

G_c = Leitfähigkeit bei der Konzentration c
G_o = Leitfähigkeit bei c = 0
R_c = Widerstand bei Konzentration c
R_o = Widerstand bei c = 0

eines Sensorelementes bei einer bestimmten Prüfgaskonzentration c, bezogen auf den Leitfähigkeitswert $G_o = G_{c=0}$ in prüfgasfreier Luft, muss bei Einsatz der hier angepassten KAMINA eine andere Referenz definiert werden oder der Widerstand bei c = 0 zuvor mit einer herkömmlichen KAMINA bestimmt werden. R_0 wurde bei den hier vorgestellten Untersuchungen mit konventionellen Laborgeräten (Keithley 2001) gemessen. Um den gesamten Messbereich abzudecken, bietet sich eine Kombination der herkömmlichen Variante und der Niederohm-KAMINA in einem Gerät an, die jeweils mit identischen Chips ausgerüstet sind.

Die Ansprechzeit charakterisiert das zeitliche Ansprechverhalten des Sensors und wird als t_{90}-Wert angegeben. Die t_{90}-Zeit ist als diejenige Zeit definiert, nach der das Sensorsignal bei einem Rechteckgaspuls 90 % des stationären Signalendwertes erreicht hat. Für die H_2-Detektion wurden t_{90}-Werte von wenigen Sekunden ermittelt.

3.2 Wechselnde Feuchte und potentielle Störgase

In weiteren Pulsexpositionen wurde bei konstanter Wasserstoff-Konzentration von 400 ppm die rel. Feuchte von 20 bis 80 % variiert, um den Einfluss wechselnder

Feuchte auf die H_2-Detektion zu ermitteln. Es konnte festgestellt werden, dass in diesem Bereich kein Einfluss auf die Detektionseigenschaften festgestellt werden kann. Es wurden immer die gleichen Widerstände gemessen.

Diese Unabhängigkeit von der rel. Feuchte beweist auch das Ergebnis einer Linearen Diskriminanzanalyse (LDA), bei der Wasserstoff und die potentiellen Störgase Kohlenmonoxid und Kohlendioxid unterschieden werden sollen (Abb. 1). Die Grundlage der Auswertung bilden Messungen von 2.000 ppm Wasserstoff bei wechselnder Feuchte (35 – 80 %) sowie 2.000 ppm H_2 bei 1 - 10 % CO bzw. 1 – 40 % CO_2. Aus dem Diagramm wird deutlich, dass zum einen die Messpunkte von den Untersuchungen mit CO und CO_2 von denjenigen des reinen Wasserstoffs getrennt werden, aber weiterhin alle Messpunkte der Wasserstoff-Untersuchung trotz wechselnder Feuchte in einem Cluster zusammengefasst werden.

Eine Quantifizierung der einzelnen Gase kann mit Hilfe der eigens entwickelten KAMINA-Software durchgeführt werden. Dazu wurde die Partial Least Square-Methode (PLS) integriert und steht nun als Auswertetool neben den qualitativen Methoden zur Verfügung.

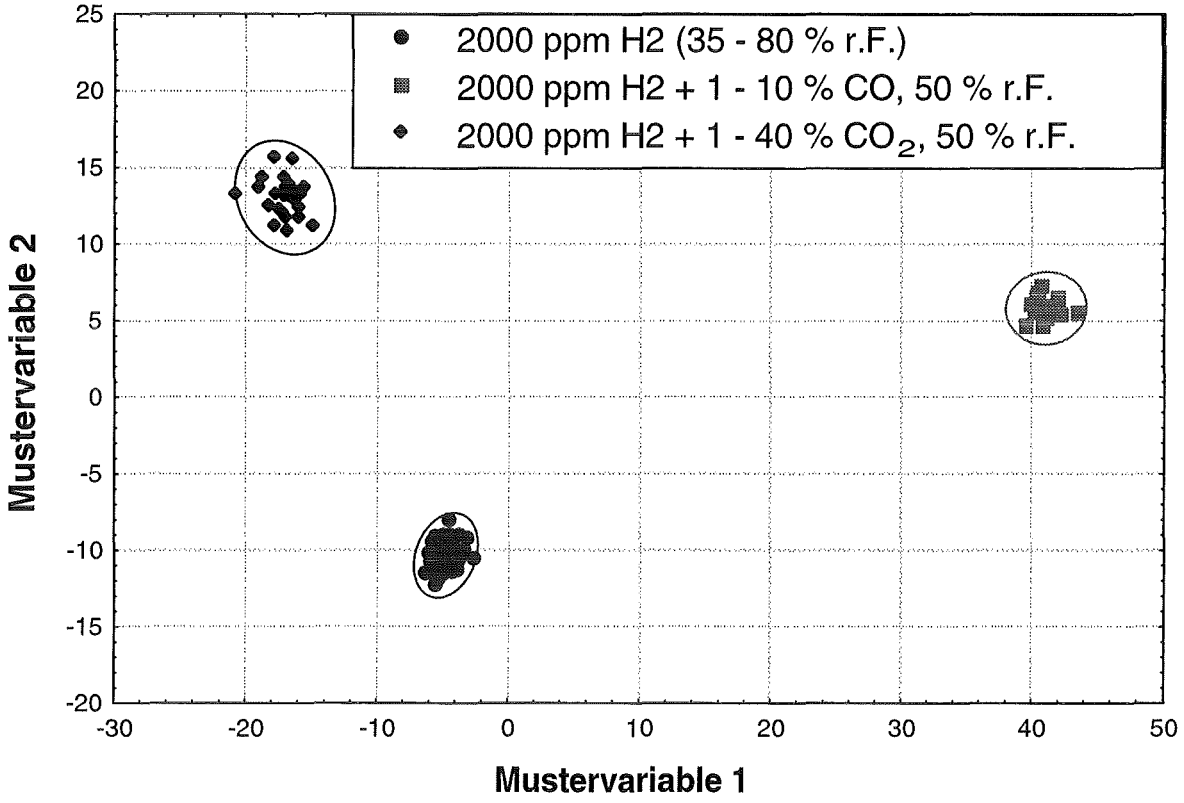

Abb. 1: Ergebnis einer LDA zur Unterscheidung von H_2 und den Störgasen CO und CO_2. Ferner wird deutlich, dass wechselnde Luftfeuchte von 35 – 80 % r. F. keinen Einfluss auf die H_2-Erkennung hat.

32.21.02 Thermische Wechselwirkung von Kernschmelze und Kühlmittel

I. ECO-Experimente zur Energiekonversion bei Dampfexplosionen

(G. Albrecht, H. Brüggemann, W. Cherdron, E. Jenes, A. Kaiser, N. Prothmann, D. Raupp, W. Schütz, H. Will, IRS)

Abstract

The ECO experiments have been launched in 2000 to measure the conversion of thermal into mechanical energy in confined steam explosions under well-defined conditions. The design of the facility is such that mechanical work done on quite resistant surroundings is directly measured.

Aluminum oxide is used to simulate the core melt. The internal dimensions of the test facility as well as major test conditions are similar to the previous PREMIX tests.

The facility consists mainly of a cylinder and a piston enclosing the melt generator and the test volume. Under the action of an increased pressure, the piston can move downwards against a stepwise increasing force provided by crushing material. There are three independent ways to measure the mechanical energy release: Two of them are time resolved and are based on pressure and force measurements in combination with measurements of the piston displacement by transducers and high-speed cameras. The third measurement is provided by the crushing material itself, giving the total amount of work. The conditions within the melt-water mixing zone are observed by thermocouples and arrays of void probes.

The melt is released from the melt generator which is fixed to the stationary cylinder. The exit nozzle is equipped with a fast acting slide valve that is closed prior to triggering the explosion or when the pressure in the test volume exceeds a preset limit. A small explosive device is installed at the test vessel bottom for triggering the explosion.

Two exploratory tests (ECO-01 and ECO-02) were carried out in 2000. In the first test, an artificially triggered explosion occurred, whereas it was a self-triggered explosion in the second tests. The energy conversion was very small in both cases, i.e. below 0.1 percent.

1. Purpose and test conditions of ECO

The PREMIX experimental programme on coarse melt-water mixing without triggering a steam explosion was finished at the end of 1999. A final, detailed documentation on the second test series (PM12-18) has been completed recently /1/.

The ECO experiments have been launched in 2000 to actually measure energy conversion in confined steam explosions under well-defined conditions. The design of the facility is such that only work done on quite resistant surroundings by lasting pressure is measured.

Like in PREMIX, alumina melt is used to simulate the core melt. The internal dimensions of the test facility as well as major test conditions are similar to PREMIX. Until now, two partly exploratory tests have been performed and will be described here. Their initial conditions are detailed in Table 1.

The ECO facility, see Figure 1, consists mainly of a cylinder and a piston enclosing the melt generator and the test volume. The latter is 0.59 m wide and initially 1.38 m high. Under the action of an increased pressure, the piston can move downwards against a stepwise increasing force provided by crushing material. There are three independent ways to measure the mechanical energy release: Two of them are time resolved and are based on pressure measurements inside the test volume and force measurements in the support columns, respectively, and on measurements of the piston displacement which are performed by displacement transducers and by the visual observation of the facility by video and high-speed cameras. The third measurement is provided by the crushing material. It only gives the total amount of work.

The conditions within the melt-water mixing zone are observed by thermocouples and arrays of void probes like in PREMIX. Here they are especially important since visual observation is very difficult.

The melt is released from the melt generator which is fixed to the stationary cylinder after melt-through of a steel foil as in PREMIX. However, in order that no water enters the melt generator, the exit nozzle is equipped with a fast acting slide valve that is closed prior to triggering the explosion or when the pressure in the test volume exceeds a preset limit. To make sure that a steam explosion is obtained in every experiment, a small explosive device is installed at the test vessel bottom for triggering the explosion. It is fired when two out of three selected void probes near the vessel bottom indicate void, i.e. the presence of melt, or when the pressure exceeds a preset limit, or after a preset time delay after the onset of melt release.

As the experiments have just begun and data analysis including numerical simulations with MC3D are still ongoing, the data reported here are still preliminary.

2. ECO-01: Description and results

For ECO-01 the calculation of the velocity of melt release gives a maximum value of 8 m/sec at the onset. Figure 2 shows the development of the multiphase zone around the melt jet as a function of time (zero time is the onset of melt release as detected by a devoted thermocouple). During the mixing process, the pressure in the (closed) test vessel rose by about 0.23 MPa. This together with the strong initial subcooling explains the narrow multiphase zone which had the intended low void fraction. However, the melt velocity in the water was so high (around 7 m/sec) that only 5.76 kg of melt had left the melt generator when melt was detected close to the bottom, the melt generator was closed, and the trigger fired (at 0.169 sec).

Some representative pressure traces are shown in Figure 3 (note that the axial heights are not equally spaced). In higher resolution, the trigger peak can be identified in the trace of PK01 with a width of 0.1 msec and a height of almost 4.5 MPa. One can derive that this pulse moves upwards at a speed of about 1000 m/sec, apparently essentially in the single-phase water surrounding the mixing zone. But no strong, coherent or clearly propagating, steam explosion was triggered. The explosion rather seems to be composed of several quite localized events at different elevations. The explosion was essentially terminated after 8 msec.

After the test, most of the debris was found in the size range 0.20...0.32 mm, see Figure 4. This debris size is normally taken as indicating a steam explosion. (By contrast, see the much larger debris found in PREMIX test PM18 that is also shown in Figure 8.) Still energy conversion has been extremely small. The piston moved by 2 mm at best. This gives a work of W = 5.6 kJ. Compared to the total thermal energy, Q, of 24.2 MJ, a conversion factor $\eta = Q/W = 0.02$ % is obtained – an almost negligible result. We think that this is due to the large amount of cold water present which led to fast condensation of the steam.

3. ECO-02: Description and Results

The main idea for ECO-02 was to get more melt into the test vessel. Therefore the nozzle diameter was increased to 60 mm and the water level was slightly decreased.

The plate closing the cylinder was provided with two venting holes in order to keep the pressure nearly constant during the premixing phase. Of course, these holes were equipped with fast sliding valves to close them prior to triggering the explosion or when the pressure rose before that.

In the test, actually a spontaneous interaction occurred after 0.211 sec when the melt had penetrated into the water almost 0.4 m. The total melt mass released prior to closing the melt generator nozzle was 2.78 kg. Nevertheless, the explosion appears to have been more violent than in ECO-01. The thermal interaction started close to the free surface at about 1.0 m height and propagated downwards. (The pool bottom is at 0.1 m.). The maximum pressures amounted to 20 MPa. They were measured at the levels of 0.6 m and 0.75 m. This spike was about 1 msec wide. It was reflected at the bottom reaching 32 MPa (and destroyed the trigger device). It then propagated upwards again, gradually dying out to about 10 MPa. This whole process took 2 msec. The event was finished before it could be influenced by the fact that the test vessel was still open (closing the relief paths takes about 10 msec). But only small amounts of melt and water were ejected.

As compared to ECO-01, the range of the debris size is extended towards somewhat larger values, 0.2...0.71 mm, see Figure 4. The work done in this experiment is similar to that of ECO-01. So the energy conversion factor is about twice as high - still extremely small.

REFERENCES

/1/ A. Kaiser, W. Schütz, H. Will
PREMIX Experiments PM12-PM18 to Investigate the Mixing of a Hot Melt with Water,
FZKA-6380(2001), in print.

Table 1 ECO-01 and ECO-02 test conditions

		ECO-01	ECO-02
Melt			
mass released	kg	5.76	2.87
temperature	K	2600	2600
Melt release			
driving pressure diff.	MPa	0.22-0.04-0.17[1]	0.09
nozzle diameter	m	0.045	0.06
height of fall	m	0.275	0.325
max. speed[2]	m/s	7.4	5.9
Water			
temperature	K	293	293
pool depth	m	1.10	1.05
System pressure	MPa	0.1-0.3[1]	0.1
Trigger pressure	MPa	12	-[2]

[1] varies during mixing
[2] self-triggered steam explosion.

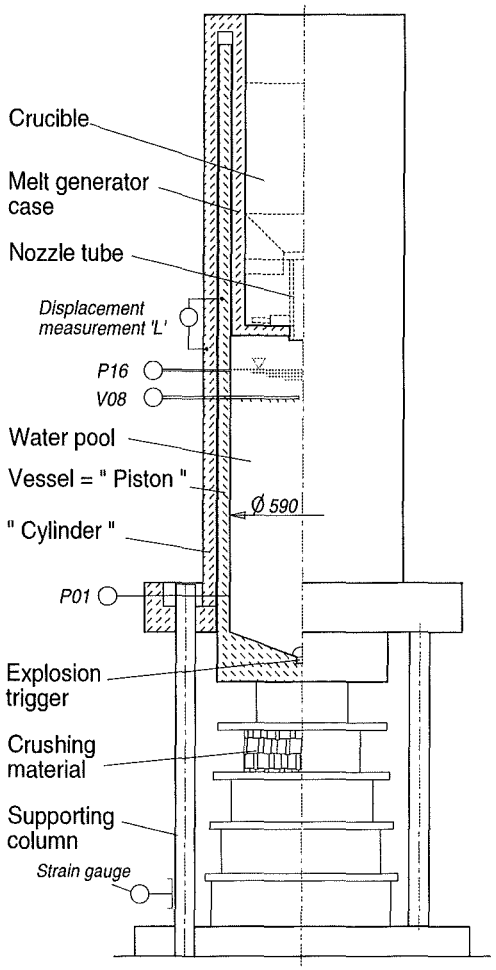

Fig. 1: Test facility in ECO-01, schematically

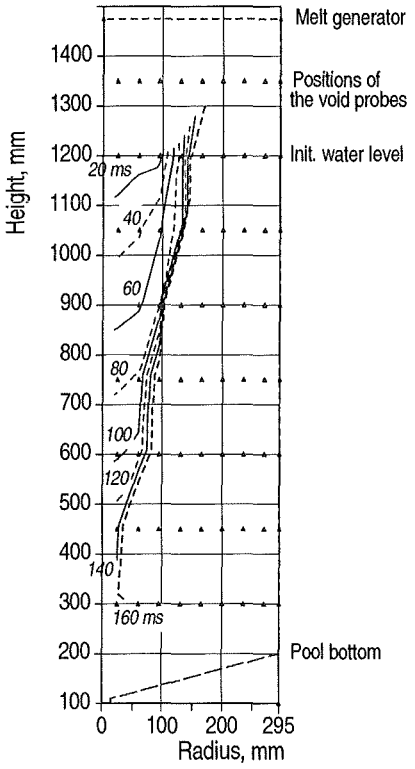

Fig. 2 Progression of the mixing zone into the water, ECO-01

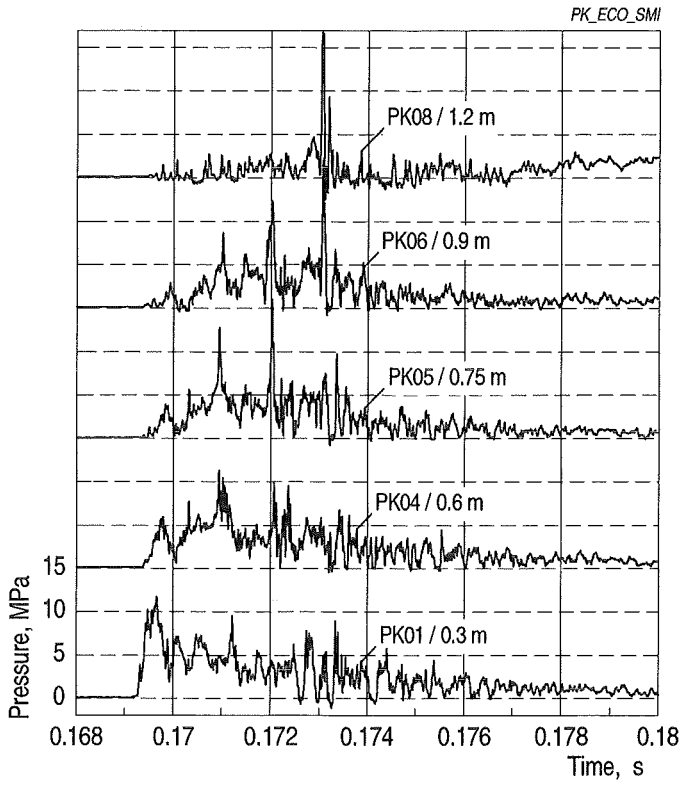

Fig. 3 Pressure data obtained at different levels in the water pool

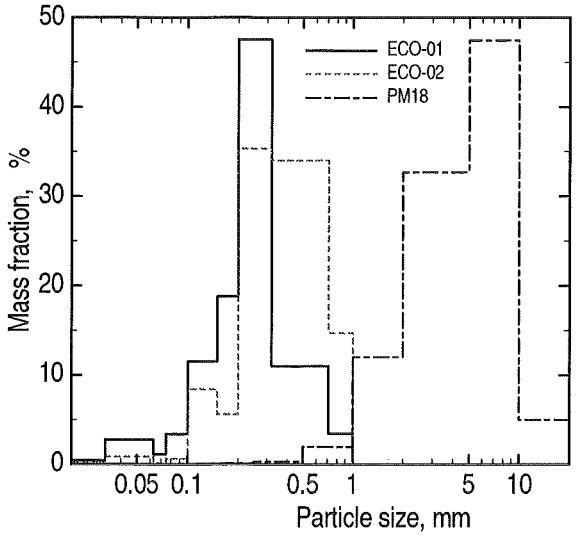

Fig. 4 Post test particle size distribution in ECO-01 and ECO-02 compared with PM18 in PREMIX (without explosion).

II. Theoretische Arbeiten zur Schmelze-Kühlmittel-Wechselwirkung

(H. Jacobs, P. Ruatto, B. Stehle, E. Stein, IKET; M. Böttcher, U. Imke, D. Struwe IRS; H. Marten, HIK)

Abstract

Work in 2000 concentrated on further numerical development of MATTINA and the extension of MC3D in the scope of strongly sub-cooled water premixing and the simulation of the first ECO vapour explosion experiments. In addition some BILLEAU experiments were simulated to verify the modifications of the MC3D 3.2 base version.

Zusammenfassung

Im Jahr 2000 konzentrierte sich die Arbeit auf die weitere numerische Entwicklung von MATTINA und die Erweiterung von MC3D im Bereich der Vorvermischung mit stark unterkühltem Wasser und der Simulation der ersten ECO Dampfexplosions-experimente. Außerdem wurden einige BILLEAU Experimente nachgerechnet, um die durchgeführten Änderungen der Basisversion von MC3D 3.2 zu überprüfen.

I. NUMERICAL SIMULATION OF BILLEAU EXPERIMENTS (MC3D)

BILLEAU [1] is a series of experiments performed in France to investigate the premixing of cold and hot particles with water. The small spheres are released into a water filled facility formed by two parallel polycarbonate walls. In order to guarantee a 2D geometry the distance between the plates is only a few millimetres larger than the spheres diameter. The essential experimental parameters are the particles diameters and temperature as well as their falling height. The experimental data are well suited to verify numerical simulations concerning the time dependent position of the interaction zone and the space distribution of particles. In the experiment DPZ11 1.03 kg of zirconium spheres at a temperature of 2000 °C and a diameter of 10 mm are released into water of 18 °C. The free fall distance to the water surface is 0.3 m. The depth of the water pool is 0.8 m. Figure 1 shows the front position of the spheres in the experiment and the numerical simulation with the FZK version of MC3D 3.2. The position of the water surface is marked by a dotted line. After 0.8 s the spheres reach

the bottom of the facility, whereas in the experiment the front is at a position of 0.2 m above the bottom. The smaller front propagation velocity might be explained by friction effects between the particles and the walls of the facility as well as numerical diffusion.

II. PREMIXING IN STRONG SUB-COOLED WATER(MC3D)

The simulation of premixing in strongly sub-cooled water is an important prerequisite for the understanding of the initial conditions in the ECO-experiments and the calculation of vapour explosions in that environment. Extensive changes in the modelling of premixing in sub-cooled water were necessary to achieve successful simulations of the PREMIX-experiments PM17 and PM18 (about 100 K and 30K sub-cooling) [2]. In the boiling model of the original version the heat transferred from the melt to the water is used to produce steam at the interface which leads to strong condensation effects in sub-cooled water causing numerical problems. Reduction of the condensation effects gives to much steam separating melt from water leading to reduced heat transfer. To solve the problem the boiling model was changed and now the heat is directly transported to the bulk water until a weak sub-cooling is reached. A smooth transition to the boiling model under saturation conditions with steam production at the interface is included. In experiments with sub-cooled water the space above the water level is filled with air and not with saturated steam. So the behaviour of an ideal non-condensable gas which mixes with the produced steam has to be simulated. The solution given in the original MC3D 3.2 version fails and a new description was introduced including the calculation of decreased condensation of steam in a mixture with a non-condensable gas. Adding the above mentioned modifications to the FZK-Version of MC3D 3.2 it is possible to calculate the pressure curve of PM17 and PM18 satisfactorily for the initial mixing phase. Figure 2 shows the result for PM17, which has the larger sub-cooling.

III. SIMULATION OF VAPOUR EXPLOSION EXPERIMENTS (MC3D)

Up to now the MC3D explosion module was mainly used as stand alone model in the domain of simulating experiments using initial conditions given by input. But there exists an interface to the premixing module reading the result of a premixing calculation and re-adjusting some values to start the explosion simulation. It was necessary to extend and to improve the interface to make consistent simulations of KROTOS [3]

and ECO experiments starting with premixing followed by an explosion. In many cases the restart of the explosion calculation from premixing runs into numerical problems due to very low void fractions in some regions. An input was created to add some minimum void fraction in the whole domain. In addition fine particles can be added in the trigger zone to initiate a trigger pulse, even if there are no coarse melt droplets. The deviations from saturation equilibrium give also problems in starting the explosion calculation, which could be caused by the different equation of states used in the explosion module. The coding was changed so that sub-cooled steam and overheated water are set to saturation in the transition from premixing to explosion. In the explosion application itself the physical models for heat transfer, drag and fragmentation are not exactly the same as the models used in premixing. In the first time steps of an explosion calculation the physical conditions are changed leading to a different base state as given in the last steps of the premixing calculation. Sometimes a steep pressure rise appears which then initiates an explosion at a location totally different from the trigger position in the experiment. To avoid such spontaneous explosions the heat transfer, drag and fragmentation models in the explosion module were changed to render as good as possible the situation of premixing. In addition a pressure condition is introduced to allow fine fragmentation only, if a threshold pressure value is reached. The first calculations of ECO1 showed much too strong pressurization and we detected that the fragmentation of water droplets was limited to a diameter of 0.5 mm, whereas the melt droplet could become much smaller depending on input. The original coding was changed to have the maximum and minimum diameters of bubbles and droplets as input. Using small water droplets with strongly sub-cooled water gives heavy condensation effects leading to convergence problems which could not be resolved totally until now. Condensation at large interface areas can lead to local depressurisation reaching pressures lower than one bar. That gives problems with the equations of state used in the explosion module. So we reduce the condensation coefficient in the low pressure range to be zero at one bar. For the simulation of KROTOS experiments the condensation effects are not as important as in the case of ECO because in KROTOS the water is pushed out of the test vessel. For ECO experiments a closed container is used, so the water cannot escape and the steam is intermixed with sub-cooled water after the explosion. The explosion module of MC3D contains several empirical parameters, which are not all well known. An important one is the direct hot liquid-cold liquid heat transfer

coefficient. For the ECO1 and ECO2 recalculation we use parameters determined by KROTOS simulations. The two ECO experiments cannot be simulated using the same value for the above mentioned heat transfer parameter. Until now the large difference cannot be explained. The contact mode of fine particles with water in ECO1 and ECO2 seems to be very different. Figure 3 shows the result for the pressure near the bottom of the vessel for ECO2. To get the same quality of pressure course in ECO1 the liquid-liquid heat transfer coefficient has to be multiplied by a factor of about 0.05.

IV. Development of MATTINA

While the testing of MATTINA was continued with recalculations of selected QUEOS experiments and some other test cases, the basic version of the program was converted from FORTRAN 77 to FORTRAN 95. This allowed the testing of the code portability and code performance with different compilers and on different platforms. The test case used was quite typical for the intended applications of MATTINA: a stream of particles of molten corium (10 % volume fraction of corium, particle diameter 5 mm) entering a water pool. Some results of these performance tests are listed in Table 1.

An especially comforting result of these tests is that it was possible to obtain identical results with different compiler options on the same platform (system) and even with different compilers on different platforms. However, this didn't come automatically. MATTINA uses an automatic system to adjust the time steps in such a way that important variables (pressure, temperatures) do not change too much within one time step. This system uses in some cases factors for varying the time step that are derived from the actual results. So even minor changes in the numerical results that may e.g. result from different sequences of arithmetic operations or from different representations of numbers (different number of bytes) will lead to (slightly) different time steps. But occasionally, local results may vary quite importantly with time step length. So, calculations with different compilers and/or platforms will deviate soon from each other. But it was possible to suppress this effect by narrowing the variability of the time steps by e.g. allowing a limited number of significant digits only in the factors applied to the time steps or in the time steps themselves. This technique allowed to perform calculations with identical results after almost 3000 time steps.

System and compiler options	real [s]	user [s]	sys [s]	Number of time steps	Comment
1) unisp RS/6000 pwr2 77 MHz					
a) -qnoopt	2812	2680	89	2738	
b) -qnoopt -qfloat = nomaf:nofold	3029	2879	89	2810	
c) -O3 -qhot -qstrict	1496	1298	67	2738	ident. 1a)
2) inrrisc7 RS/6000 7013-591					
a) -O3 -qhot -qstrict	4206	1341	81	2738	ident. 1a)
3) intsp RS/6000 pwr3 222 MHz					
a) -qnoopt	761	716	44	2738	ident. 1a)
b) -qnoopt -qfloat = nomaf:nofold	845	785	60	2810	ident. 1b)
c) -O3 -qhot -qstrict	335	298	36	2738	ident. 1a)
4) hikau1c PII 400 MHz, PGI Compiler					
a) -Kieee -pc64 -Mnobuiltin -O0	2595	2577	17	2725	
b) -Kieee -pc64 -Mnobuiltin -O2	1172	1158	13	2725	ident. 4a)
c) -O2	1144	1131	14	2725	
5) inrcblx2 PIII 600 MHz					
a) Fujitsu Fortran Compiler	466	418	24	2728	
6) hikhpc PIII 700 MHz, PGI compiler					
a) -Kieee -pc64 -r8 -O2	245	240	5	2725	
7) vpp300					
a) -O0,-Wv,-an	9817	8557	1191	2774	
b) -O2,-Wv,-an	3923	2727	1162	2718	
8) vpp5000					
a) Binary from vpp300	3025	2766	243	2774	ident. 7a)
b) -O0,-Wv,-sc neu comp.	2613	2337	262	2783	
c) -O2,-Wv,-an neu comp.	666	407	245	2735	

Table 1: Computing times and numbers of time steps required for 0.2 sec problem time in a test case (corium drop fragmentation)

Of course, this experience highlights the fact that sometimes local results may depend quite importantly on the actual time step length. This means that the timing of certain events and local values must not be taken as strictly reliable. On the other hand, the experience with the code is that overall results change very little (or in a physically reasonable way) when changing the time steps or the initial conditions. As an example we may consider the test case described above in which the total surface of the corium is a controlling variable. Two calculations were performed on completely different platforms (an IBM work station and a Linux PC). For 1 sec problem time they required about 69 700 and 93 600 time steps, respectively. The corium surface developed in the same way in both calculations up to about 0.2 sec. At 0.26 sec a steaming event occurred in both calculations which fragmented the particles so that the surface increased by factors of 2.88 and 3.04, respectively. After that the total surface oscillated (due to coalescence and fragmentation) in a very similar way but the higher starting value in the second calculation translated into a time shift that amounted to about 12 msec in the beginning and disappeared gradually before 1 sec problem time was reached. The corium surface remained about 10 % larger in the second case. This indicates that 10...20 % uncertainty apply even to global results.

The exercise also indicated that the code is not suited for running it on a vector computer (vpp300 or vpp5000). The degree of (automatic) vectorization remained very low. On the other hand, the performance on the HIK high performance Linux cluster (of which hikhpc is the front end) is quite good. So this will be the system used preferably in the future.

In 2000 also the first tests of the newly developed second order differencing scheme in MATTINA could be run. This scheme is second order in space only and it is of the MUSCL (Monotonic Upwind Scheme for Conservation Laws) type [4] that was first proposed by van Leer [5]. As expected, this improved differencing scheme reduces the numerical diffusion considerably without removing it completely or nearly so. An example is given in Figure 4. It is derived from the actual simulations of QUEOS tests, i. e. we assume a cloud of solid particles to fall from a height of 2.3 m. But in contrast with the experimental situation, the cloud is assumed to have a volume fraction of particles of 10 % only and to have a height of 30 cm. The figure shows the situation after 0.5 sec of free fall, i. e. the rectangular curve labelled 'analytical' is the

initial distribution moved downward by s = g/2 t^2 = 1.226 m. At this time the 'analytical' leading edge has passed 49 mesh cells. The effect of the second order scheme is quite obvious. It will be incorporated into the basic code because it allows for higher accuracy without reducing the size of the mesh cells.

REFERENCES

[1] G. Berthoud, T. Oulmann, M. Valette, Corium water interaction studies in France, Int. Seminar on Heat and Mass Transfer in Severe Accidents, Cesme, Turkey, May 21-26, 1995

[2] A. Kaiser, W. Schütz, H. Will, PREMIX Experiments PM12-PM18 to Investigate the Mixing of a Hot Melt with Water, FZKA-6380, 2001.

[3] H. Hohmann, D. Maggalon, H. Schins, and A. Yerkess, FCI experiments in the aluminumoxide/water system, Nuclear Engineering and Design, 155, 391-403,1995.

[4] C.-D. Munz, Theorie und Numerik nichtlinearer hyperbolischer Differentialgleichungen; I. Die skalare Erhaltungsgleichung. Bericht des Kernforschungszentrums Karlsruhe, KfK 4805 (Dezember 1990), p. 98

[5] B. van Leer, Towards the ultimate conservative difference scheme; V. A second order sequel to Godunov's method, J. Comp. Phys. **32** (1979) 101-136

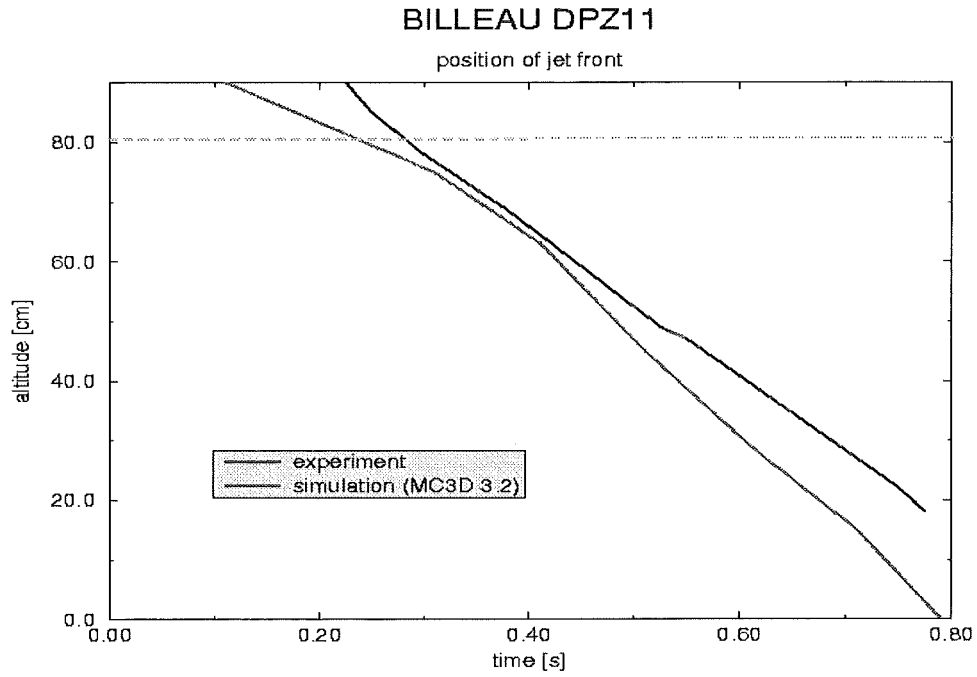

Figure 1: Front propagation of spheres in BILLEAU DPZ11.

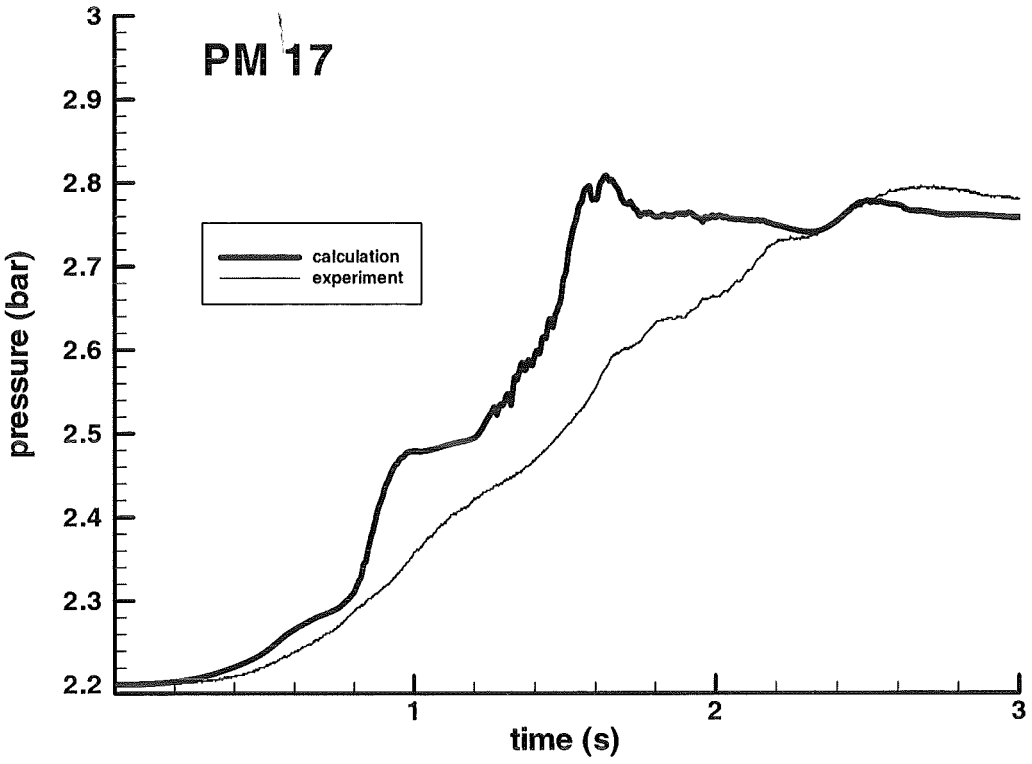

Figure 2: Pressure in the vapour space of PREMIX 17

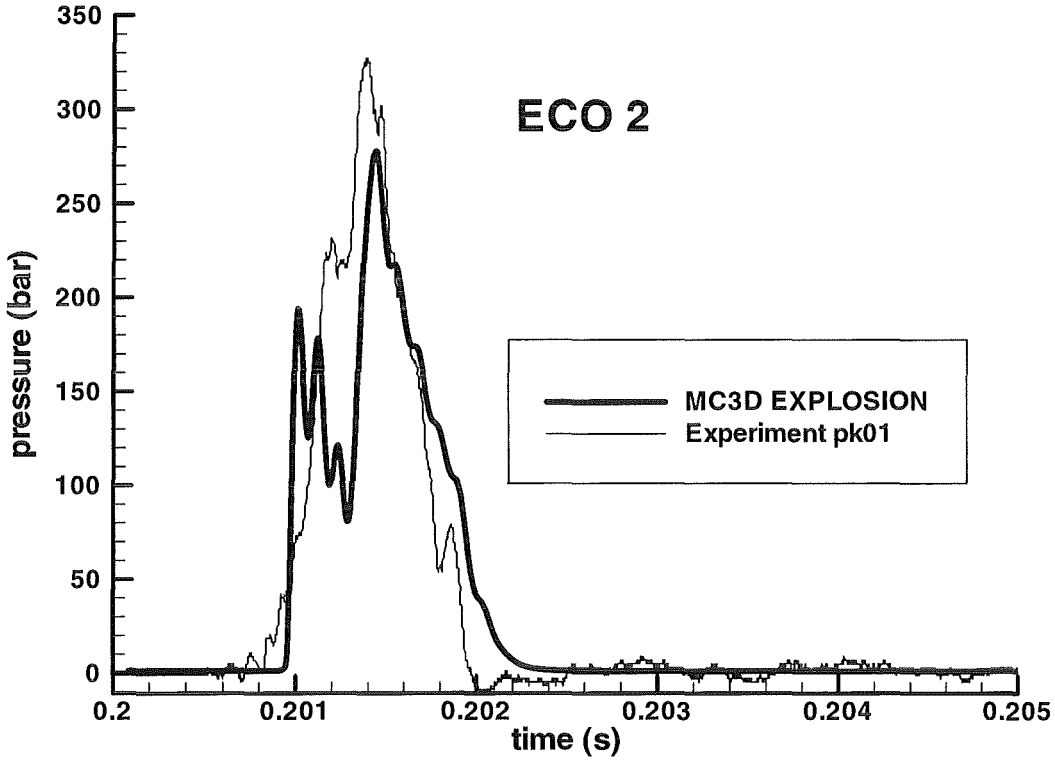

Figure 3: Pressure near the bottom of the test vessl for ECO 2.

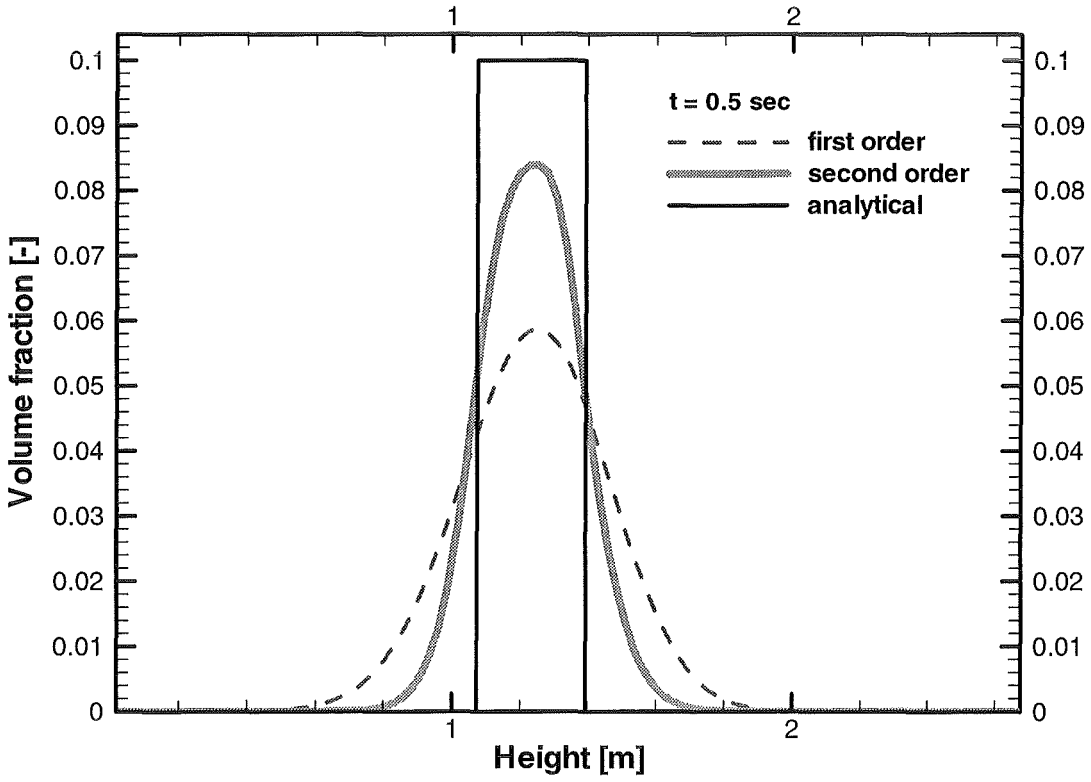

Figure 4: Spatial distribution of particle density after a free fall during 0.5 sec

32.21.03 Versagen des Reaktordruckbehälters und Dispersion der Kernschmelze

I. Versagen des Reaktordruckbehälters infolge thermoviskoplastischer Instabilität

(E. Diegele, D. Hofer, IMF II)

Abstract

Im Rahmen des EU-Projektes LISSAC (Limit Strains for Severe Accident Conditions) wird die Übertragbarkeit von Prüfungen im Labormaßstab auf große Komponenten (typische Abmessung eines Reaktordruckgefäßes) untersucht. In Experimenten mit lokalen Dehnungsgradienten werden bei geometrisch ähnlichen Abmessungen unter denselben Belastungen größenabhängige Effekte beobachtet. Diese lassen sich mit den klassischen Modellen der Plastizitätstheorie nicht erklären. Das Ziel des Vorhabens ist die Entwicklung von Materialmodellen zur Beschreibung des Verformungsverhaltens mit nichtlokaler Plastizität; insbesondere (a) die Entwicklung eines thermodynamisch-konsistenten Modelles für große Deformationen und dessen Einbau in einen Finite-Element-Code, (b) die Untersuchung der qualitativen und quantitativen Möglichkeiten eines solchen Modells, (c) die Anwendung zur Beschreibung der Experimente, die bei den Projektpartnern durchgeführt werden.

Aktueller Stand der Arbeiten:

Im Berichtsjahr wurde eine Theorie ausgearbeitet, bei der jedem materiellen Punkt eine (lokale) Substruktur zugeordnet wird. Nichtlokale Einflüsse erhält man durch die Berücksichtigung der räumlichen Ableitung des Deformationsgradienten für diese Substruktur. Die Evolutionsgleichungen der Verfestigungsvariablen sind als hinreichende Bedingungen für die Gültigkeit des zweiten Hauptsatzes der Thermodynamik hergeleitet worden. Außerdem kann gezeigt werden, dass sich bei reiner Elastizität die Theorie auf das Modell des mikromorphen Kontinuum reduziert, das in den letzten beiden Jahren (in einem anderen Projekt des Institutes) als sogenanntes 'benutzerdefiniertes Element' in das FE-Programm ABAQUS eingebaut wurde .

Die Arbeiten erfolgen in enger Zusammenarbeit mit der TU Darmstadt.

1. Introduction

Internal length scales may be elaborated in the constitutive theory in a natural way by assuming the hypothesis of "substructure" assigned to every material point. If this substructure deforms homogeneously the continuum is called micromorphic. The aim of the paper is to present a micromorphic plasticity theory, which satisfies the second law of thermodynamics in every admissible process. For the sake of simplicity only kinematic hardening is considered.

2. Preliminaries – decomposition of deformation

2.1 Notation

In the following we consider isothermal deformations and write $\dot{\varphi}(t)$ for the material time derivative of a function $\varphi(t)$, where t is the time. We use bold face letters for second order tensors. In particular **1** represents the identity second order tensor and $\mathbf{A}^T$ denotes the transpose of a second order tensor **A**. We write tr**A** for the trace of **A**, $\mathbf{A}^D = \mathbf{A} - 1/3\ (\mathrm{tr}\mathbf{A})\mathbf{1}$ for the deviator of **A** and $\mathbf{A}\cdot\mathbf{B} = \mathrm{tr}(\mathbf{A}\mathbf{B}^T) = \mathrm{tr}(\mathbf{A}^T\mathbf{B})$ for the inner product of **A** and **B**. Also we use the notation $\mathbf{A}^{T-1} = (\mathbf{A}^{-1})^T$ provided that $\mathbf{A}^{-1}$ exists.

2.2 Decomposition of deformation

Consider a material body B which occupies a region $\mathrm{P_P}$ in the three dimensional Euclidean point space E in the reference configuration (t=0). Each particle of the material body B can be identified by a position vector X to the place X in $\mathrm{P_P}$ after having chosen a fixed point (origin) in E. A configuration at time t is called actual configuration $\mathrm{P_t}$. The position of a particle is identified by a position vector **x** to the place x in this configuration.

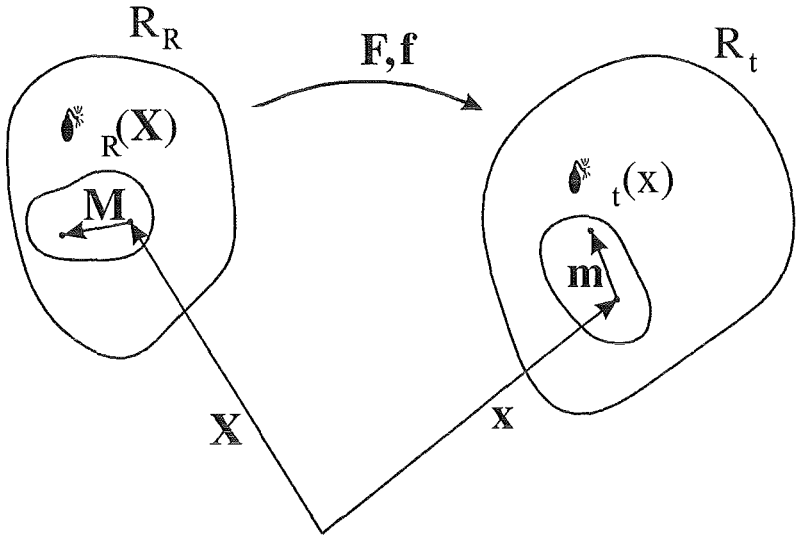

Fig. 1: Motion, reference and actual configuration

A motion is described by the equation

$$\mathbf{x} = \hat{\mathbf{x}}(\mathbf{X},t)\,. \tag{2.1}$$

The deformation gradient tensor is denoted by

$$\mathbf{F} = \mathbf{F}(\mathbf{X},t) = \frac{\partial \hat{\mathbf{x}}}{\partial \mathbf{X}} = GRAD\hat{\mathbf{x}}\,. \tag{2.2}$$

For **F** (det **F**>0) the polar decomposition

$$\mathbf{F} = \mathbf{RU} = \mathbf{VR}, \tag{2.3}$$

applies, where **R** represents a proper orthogonal second-order tensor.

Following Eringen et al. [2, 3, 4], (cf. also Mindlin [5]), we define a micromorphic continuum to have attached to every material point a substructure. The substructure itself behaves like a material body, which undergoes homogeneous micro-deformations. These are described by a deformation gradient tensor **f** (det **f**>0) for which the polar decomposition

$$\mathbf{f} = \mathbf{ru} = \mathbf{vr}. \tag{2.4}$$

holds.

In order to introduce some strain measures we first concentrate on pure elasticity. In this case the specific free energy function ψ is supposed to depend on **F**, **f** and *GRAD* **f**:

$$\psi = \overline{\psi}(\mathbf{F}, \mathbf{f}, GRAD\mathbf{f}) \tag{2.5}$$

GRAD **f** introduces an internal length scale in the constitutive theory; with respect to convective coordinates, it is given by

$$GRAD\mathbf{f} = \frac{\partial \mathbf{f}}{\partial \theta^k} \otimes \mathbf{G}_k \tag{2.6}$$

so that *GRAD* **f** represents a third order tensor. By using the principle of material objectivity, it is a routine matter to obtain the reduced form

$$\psi = \overline{\overline{\psi}}(\tilde{\boldsymbol{\varepsilon}}, \tilde{\boldsymbol{\beta}}, \tilde{\mathbf{K}}) \tag{2.7}$$

where

$$\tilde{\boldsymbol{\varepsilon}} = \mathbf{f}^{-1}\mathbf{F} - \mathbf{1} \tag{2.8}$$

$$\tilde{\boldsymbol{\beta}} = \frac{1}{2}(\mathbf{u}^2 - \mathbf{1}) \tag{2.9}$$

$$\tilde{\mathbf{K}} = \mathbf{f}^{-1} GRAD\mathbf{f}\,. \tag{2.10}$$

In these equations, $\tilde{\boldsymbol{\beta}}$ is the classical Green strain tensor with respect to the reference configuration and the curvature tensor $\tilde{\mathbf{K}}$ renders a nonlocality to the constitutive model. Rate-dependent or rate-independent elastic-plastic material properties may be described by assuming the multiplicative decompositions

$$\mathbf{F} = \mathbf{F}_e \mathbf{F}_p, \qquad \mathbf{f} = \mathbf{f}_e \mathbf{f}_p, \tag{2.11}$$

which introduce a so-called plastic intermediate configuration (see Fig. 2).
Moreover, det $\mathbf{F}_p$>0 and det $\mathbf{f}_p$>0 are assumed to apply so that the polar decompositions

$$\mathbf{F}_p = \mathbf{R}_p \mathbf{U}_p, \tag{2.12}$$

$$\mathbf{f}_p = \mathbf{r}_p \mathbf{u}_p \tag{2.13}$$

apply as well.

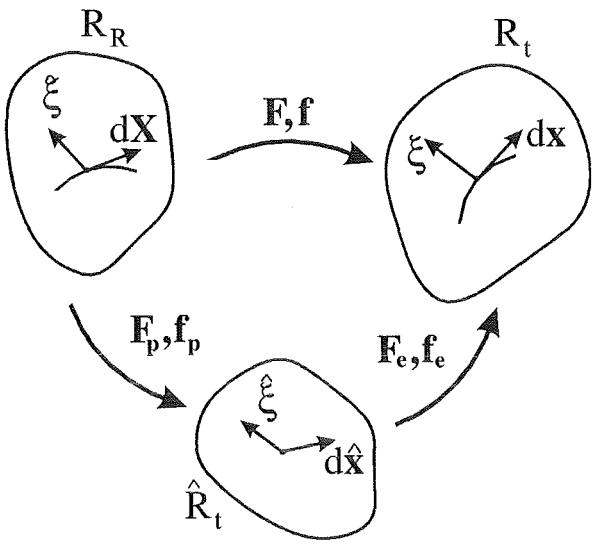

Fig. 2: Motion, decomposition of deformation

It can be shown (see Grammenoudis et al. (2000)) that the multiplicative decompositions of **F** and **f** imply additive decompositions for $\tilde{\varepsilon}$, $\tilde{\beta}$ and $\tilde{\mathbf{K}}$ in the form

$$\tilde{\varepsilon} = \tilde{\varepsilon}_e + \tilde{\varepsilon}_p, \tag{2.14}$$

$$\tilde{\beta} = \tilde{\beta}_e + \tilde{\beta}_p, \tag{2.15}$$

$$\tilde{\mathbf{K}} = \tilde{\mathbf{K}}_e + \tilde{\mathbf{K}}_p. \tag{2.16}$$

Also, these decompositions of strains may be transformed to the actual and the plastic intermediate configurations, the counterparts of $\tilde{\varepsilon}$, $\tilde{\beta}$, $\tilde{\mathbf{K}}$ being ε, β, $\mathbf{K}$ and $\hat{\varepsilon}$, $\hat{\beta}$, $\hat{\mathbf{K}}$, respectively.

3. Second law of thermodynamics

We assume isothermal deformations with uniform distribution of temperature. Then, the generalized Clausius-Duhem inequalitiy for micromorphic materials (cf. Eringen et al. [2, 3, 4]) reads as follows:

$$\mathbf{S} \cdot \overset{\Delta}{\varepsilon} + \boldsymbol{\Sigma} \cdot \overset{\Delta}{\beta} + \mathbf{M} \cdot \overset{\Delta}{\mathbf{k}} - \rho_R \dot{\psi} \geq 0 \tag{3.1}$$

Here, ρ_R is the mass density in the reference configuration, **S** the classical Cauchy stress tensor, $\boldsymbol{\Sigma}$ the stress tensor induced by the microstructure and **M** the so-called couple stress tensor, respectively; $\overset{\Delta}{\varepsilon}, \overset{\Delta}{\beta}, \overset{\Delta}{\mathbf{k}}$ denote specific objective derivatives as

defined in Grammenoudis et al. (2000). Note in passing that $\mathbf{S}$, ε and Σ, β are non-symmetric and symmetric second order tensors. Also $\mathbf{M}\cdot\overset{\Delta}{\mathbf{k}}$ is an appropriately defined inner product for third order tensors. As above, ψ is the specific free energy function, which now is supposed to obey the decomposition

$$\psi(t)= \psi_e(t)+ \psi_p(t). \tag{3.2}$$

3.1 Elasticity laws

The free energy function ψ is supposed to exhibit, with respect to the reference and plastic intermediate configuration, the following representations:

$$\psi_e = \hat{\psi}_e\left(\hat{\boldsymbol{\varepsilon}}_e,\hat{\boldsymbol{\beta}}_e,\hat{\mathbf{K}}_e\right)=\tilde{\psi}_e\left(\tilde{\boldsymbol{\varepsilon}}_e,\tilde{\boldsymbol{\beta}}_e,\tilde{\mathbf{K}}_e,\tilde{\boldsymbol{\varepsilon}}_p,\tilde{\boldsymbol{\beta}}_p\right) \tag{3.3}$$

By inserting (3.2), (3.3) into (3.1) and using standard arguments according to Colemann and Noll, the potential relations

$$\begin{aligned}
\hat{\mathbf{S}} &= \rho_R \frac{\partial \hat{\psi}_e}{\partial \hat{\boldsymbol{\varepsilon}}_e} \neq \hat{\mathbf{S}}^T \\
\hat{\boldsymbol{\Sigma}} &= \rho_R \frac{\partial \hat{\psi}_e}{\partial \hat{\boldsymbol{\beta}}_e} = \hat{\boldsymbol{\Sigma}}^T \\
\hat{\mathbf{M}} &= \rho_R \frac{\partial \hat{\psi}_e}{\partial \hat{\mathbf{K}}_e}
\end{aligned} \tag{3.4}$$

may be established, where $\hat{\mathbf{S}}$, $\hat{\boldsymbol{\Sigma}}$ and $\hat{\mathbf{M}}$ represent counterparts of $\mathbf{S}$, $\boldsymbol{\Sigma}$ and $\mathbf{M}$, respectively in the plastic intermediate configuration. This way, after some algebraic calculations the second law (3.1) reduces to the dissipation inequality

$$D = \hat{\mathbf{P}}\cdot\overset{\Delta}{\hat{\boldsymbol{\varepsilon}}}_p + \hat{\boldsymbol{\Pi}}\cdot\overset{\Delta}{\hat{\boldsymbol{\beta}}}_p + \hat{\mathbf{M}}\cdot\overset{\Delta}{\hat{\mathbf{K}}}_p - \rho_R\dot{\psi}_p \geq 0 \tag{3.5}$$

where use has been made of the definitions

$$\hat{\mathbf{P}} := (\mathbf{1}+\hat{\boldsymbol{\varepsilon}}_e^T)\hat{\mathbf{S}} \tag{3.6}$$

$$\hat{\boldsymbol{\Pi}} := ((\mathbf{1}+2)\hat{\boldsymbol{\beta}}_e\hat{\boldsymbol{\Sigma}}+\hat{\boldsymbol{\varepsilon}}_e\hat{\mathbf{S}}+\hat{\mathbf{S}}\hat{\boldsymbol{\varepsilon}}_e^T+\hat{\boldsymbol{\chi}})_{sym} \tag{3.7}$$

$$\frac{1}{\rho_R}\hat{\boldsymbol{\chi}}_{ba} := \frac{\partial \hat{\psi}_e}{\partial(\hat{\mathbf{K}}_e)_{bcd}}\left(\hat{\mathbf{K}}_e\right)_{acd} - \frac{\partial \hat{\psi}_e}{\partial(\hat{\mathbf{K}}_e)_{cad}}\left(\hat{\mathbf{K}}_e\right)_{bcd} - \frac{\partial \hat{\psi}_e}{\partial(\hat{\mathbf{K}}_e)_{dca}}\left(\hat{\mathbf{K}}_e\right)_{dcb} \tag{3.8}$$

3.2 Kinematic hardening

We focus attention on pure kinematic hardening and define ψ_p to obey the representations

$$\psi_p = \hat{\psi}_p\left(\hat{\boldsymbol{\varepsilon}}_k, \hat{\boldsymbol{\beta}}_k, \hat{\mathbf{K}}_k\right) = \tilde{\psi}_e\left(\tilde{\boldsymbol{\varepsilon}}_k, \tilde{\boldsymbol{\beta}}_k, \tilde{\mathbf{K}}_k, \tilde{\boldsymbol{\varepsilon}}_p, \tilde{\boldsymbol{\beta}}_p\right) \tag{3.9}$$

where $\hat{\boldsymbol{\varepsilon}}_k, \hat{\boldsymbol{\beta}}_k$ and $\hat{\mathbf{K}}_k$ are strain measures responsible for kinematic hardening with geometrical meaning similar to that of $\hat{\boldsymbol{\varepsilon}}_p, \hat{\boldsymbol{\beta}}_p$ and $\hat{\mathbf{K}}_p$, respectively. The counterparts of $\hat{\boldsymbol{\varepsilon}}_k, \hat{\boldsymbol{\beta}}_k$ and $\hat{\mathbf{K}}_k$ with respect to the reference configuration are $\tilde{\boldsymbol{\varepsilon}}_k, \tilde{\boldsymbol{\beta}}_k$ and $\tilde{\mathbf{K}}_k$.

Next, we introduce the thermodynamic conjugated forces

$$\begin{aligned} \hat{\mathbf{Z}} &= \rho_R \frac{\partial \hat{\psi}_p}{\partial \hat{\boldsymbol{\varepsilon}}_k} \\ \hat{\zeta} &= \rho_R \frac{\partial \hat{\psi}_p}{\partial \hat{\boldsymbol{\beta}}_k} \\ \hat{\mathbf{M}}_k &= \rho_R \frac{\partial \hat{\psi}_p}{\partial \hat{\mathbf{K}}_k} \end{aligned} \tag{3.10}$$

and define back-stress tensors by

$$\hat{\mathbf{P}}_k := (\mathbf{1} - \hat{\boldsymbol{\varepsilon}}_k^T)\hat{\mathbf{Z}} \tag{3.11}$$

$$\hat{\boldsymbol{\Pi}}_k := ((\mathbf{1} - 2\hat{\boldsymbol{\beta}}_k)\hat{\zeta} - \hat{\boldsymbol{\varepsilon}}_k^T\hat{\mathbf{Z}} + \hat{\mathbf{Z}}\hat{\boldsymbol{\varepsilon}}_k^T + \hat{\boldsymbol{\chi}}_k)_{sym}. \tag{3.12}$$

and $\hat{\mathbf{M}}_k$, respectively. It follows that the dissipation inequality (3.5) may be recasted in the form

$$\begin{aligned} D = &\left(\hat{\mathbf{P}} - \hat{\mathbf{P}}_k\right)\cdot \overset{\Delta}{\hat{\boldsymbol{\varepsilon}}}_p + \left(\hat{\boldsymbol{\Pi}} - \hat{\boldsymbol{\Pi}}_k\right)\cdot \overset{\Delta}{\hat{\boldsymbol{\beta}}}_p + \left(\hat{\mathbf{M}} - \hat{\mathbf{M}}_k\right)\cdot \overset{\Delta}{\hat{\mathbf{K}}}_p + \hat{\mathbf{Z}}\left(\overset{\Delta}{\hat{\boldsymbol{\varepsilon}}}_p - \overset{\Delta}{\hat{\boldsymbol{\varepsilon}}}_k\right) \\ &+ \hat{\zeta}\cdot\left(\overset{\Delta}{\hat{\boldsymbol{\beta}}}_p - \overset{\Delta}{\hat{\boldsymbol{\beta}}}_k\right) + \hat{\mathbf{M}}_k\cdot\left(\overset{\Delta}{\hat{\mathbf{K}}}_p - \overset{\Delta}{\hat{\mathbf{K}}}_k\right) \geq 0. \end{aligned} \tag{3.13}$$

In order to discuss this inequality we postulate the existence of a yield function

$$f = f\left(\hat{\mathbf{P}} - \hat{\mathbf{P}}_k, \hat{\boldsymbol{\Pi}} - \hat{\boldsymbol{\Pi}}_k, \hat{\mathbf{M}} - \hat{\mathbf{M}}_k\right). \tag{3.14}$$

Plastic flow occurs for $f = 0$. Also, the associated normality rules

$$\begin{pmatrix} \overset{\Delta}{\hat{\boldsymbol{\varepsilon}}}_p \\ \overset{\Delta}{\hat{\boldsymbol{\beta}}}_p \\ \overset{\Delta}{\hat{\mathbf{K}}}_p \end{pmatrix} = \lambda \begin{pmatrix} \dfrac{\partial f}{\partial \hat{\mathbf{P}}} \\ \dfrac{\partial f}{\partial \hat{\boldsymbol{\Pi}}} \\ \dfrac{\partial f}{\partial \hat{\mathbf{M}}} \end{pmatrix} \tag{3.15}$$

are assumed to apply. Then, it can be shown (see Grammenoudis et al.) that

$$D = \hat{\mathbf{Z}} \cdot \left(\overset{\Delta}{\hat{\boldsymbol{\varepsilon}}}_p - \overset{\Delta}{\hat{\boldsymbol{\varepsilon}}}_k \right) + \hat{\zeta} \cdot \left(\overset{\Delta}{\hat{\boldsymbol{\beta}}}_p - \overset{\Delta}{\hat{\boldsymbol{\beta}}}_k \right) + \hat{\mathbf{M}}_k \cdot \left(\overset{\Delta}{\hat{\mathbf{K}}}_p - \overset{\Delta}{\hat{\mathbf{K}}}_k \right) \geq 0 \tag{3.16}$$

is a sufficient condition for (3.13). Evolution equations governing the response of kinematic hardening may be derived as sufficient conditions for the validity of (3.16):

$$\begin{aligned} \overset{\Delta}{\hat{\boldsymbol{\varepsilon}}}_p - \overset{\Delta}{\hat{\boldsymbol{\varepsilon}}}_k &= \lambda \left(b_1 tr(\hat{\mathbf{Z}}) \mathbf{1} + b_2 \hat{\mathbf{Z}} + b_3 \hat{\mathbf{Z}}^T \right) \\ \overset{\Delta}{\hat{\boldsymbol{\beta}}}_p - \overset{\Delta}{\hat{\boldsymbol{\beta}}}_k &= \lambda \left(b_1 tr(\hat{\zeta}) \mathbf{1} + b_2 \hat{\zeta} \right) \\ \overset{\Delta}{\hat{\mathbf{K}}}_p - \overset{\Delta}{\hat{\mathbf{K}}}_k &= \lambda \mathbf{A}\left[\hat{\mathbf{M}} \right] \end{aligned} \tag{3.17}$$

4. Concluding remarks

The micromorphic plasticity model proposed has to be extended in order to take into account isotropic hardening as well as damage effects. However, it is convenient, above all, to implement the theory in a finite element code. This will enable to check the capabilities of the developed theory as well as to compare the predicted responses with those according to other models involving nonlocalities, like that of Aifantis [1].

5. References

[1] Aifantis, E. C., *The Physics of Plastic Deformation,* International Journal of Plasticity, 3, 211-247, 1987.

[2] Eringen, A. C., *Microcontinuum Field Theories, I. Foundations and Solids,* Springer, New York, 1999.

[3] Eringen, A. C., *Nonlinear Theory of Simple Micro-elastic Solids - I*, Int. J. Engng. Sci. Vol. 2, 189-203, 1964.

[4] Suhubi, E. S., Eringen, A. C., *Nonlinear Theory of Simple Micro-elastic Solids - II*, Int. J. Engng. Sci. Vol. 2, 389-404, 1964.

[5] Mindlin, R., *Influence of Couple-stresses on Stress Concentrations*, Experimental Mechanics Vol. 3, 1-7, 1963.

[6] Grammenoudis, P., Hofer, D., Tsakmakis, Ch., *Micromorphic plasticity with kinematic hardening*, private communication, unpublished

II. Experimente zur Dispersion von Corium

(M. Gargallo, M. Greulich, M. Kirstahler, L. Meyer, M. Schwall, E. Wachter, G. Wörner; IKET)

Zusammenfassung

Das Versagen des RDB unter vollem Systemdruck wird durch systemtechnische Maßnahmen verhindert. Ein Versagen bei einem zu unterstellenden Druck von 10 bis 20 bar kann u.U. noch zu starker Dispersion und Umverteilung der Schmelze in die Reaktorräume und den Dom und damit zur direkten Aufheizung der Containmentatmosphäre führen. Auch wird dadurch das Konzept der Kernschmelzekühleinrichtung in Frage gestellt. Das Zusammenwirken der hierbei auftretenden Materialtransportprozesse sowie der thermischen und chemischen (Wasserstofferzeugung und -verbrennung) Wechselwirkungen ist komplex und kann derzeit mit Computercodes noch nicht oder nur bedingt berechnet werden. Notwendig sind daher Einsichten und Daten aus experimentellen Untersuchungen, insbesondere auch integrale Experimente, deren Ergebnisse mit Modellen und Coderechnungen auf die große EPR-Anlage übertragen werden können.

Im Versuchsstand DISCO-C, der die EPR-Reaktorgrube und die anschließenden Räume im Maßstab 1:18 modelliert, wurde eine zweite Versuchsreihe mit kalten Modellfluiden durchgeführt. Als Versagensart wurden seitliche Löcher und Risse verschiedener Größe in der RDB-Kalotte untersucht. Außerdem wurden einige andere Geometrieeinflüsse der Grube und des Ausströmens untersucht. Die Experimente haben gezeigt, dass ein seitliches Versagen der RDB-Kalotte zu niedrigeren Austragsraten aus der Grube führt als Löcher im zentralen Bereich der Kalotte. Versuche mit einer geänderten Geometrie der Reaktorgrube haben gezeigt, dass damit die Dispersion der Schmelze wesentlich verringert werden kann, selbst für Versagensmodes bei denen sonst ein großer Austrag stattfindet.

Abstract

Experiments are being performed in a scaled annular cavity design, typical for the European Pressurized Reactor (EPR), to investigate melt dispersal from the reactor cavity when the reactor pressure vessel lower head fails at low system pressure of less than 20 bar. In the first part of the experimental program the fluid dynamics of the dispersion process has been studied using model fluids, water or bismuth alloy instead of corium, and nitrogen or helium instead of steam. The effects of different breach sizes, - lateral failures in the lower head in this reporting period -, and different failure pressures on the dispersion have been studied systematically. The experiments have shown that lateral failures lead to smaller melt dispersal out of the reactor pit than failures in the central part of the lower head. Moreover, the geometry of the reactor pit can be modified in such a way that the dispersion is substantially reduced even for failure modes that lead to a large dispersal otherwise.

1. Introduction

At FZK the test facility DISCO-C has been built for performing dispersion experiments with cold simulant materials in an EPR-typical geometry in a scale 1:18. The fluids were water or bismuth alloy (ρ = 9.1) instead of melt, and nitrogen or helium instead of steam. Experiments with different materials are necessary to validate scaling laws. The first series of experiments with central holes in the lower head had shown large dispersal of the liquids (up to 76 %) into the pump and steam generator rooms with pressures as low as 6 bar. In the second part of the experimental program a detailed investigation of geometry effects was performed, such as lateral holes, lateral slots, and unzipping of the lower head, and changes in the cavity geometry in connection with central holes. The experimental apparatus and the test procedure were described in the last report.

2. Experimental Parameters and Results

2.1 Failure modes

Lateral hole: The first type are round holes of 25 and 50 mm diameter on the side of the lower head (Fig. 1). The inclination of the axis of the holes is 45 degrees. Their

center measured at the inside is 50 mm above the bottom of the calotte. So, the lower edges of the holes at the inside are 41.15 and 32.4 mm above the bottom of the calotte, respectively. The amount of water used was 1.8×10^{-3} m³. This scales to 10.5 m³ or approximately 85 t of corium. The liquid level was 67 mm above the bottom of the calotte and near the upper edge of the holes. With the 25-mm-hole the level was 8.2 mm above the upper edge and with the 50-mm-hole it was 0.6 mm below the edge.

Two experiments with burst pressures of 1.10 MPa were performed with holes of 25 mm (scaled 0.45 m) and 50 mm (0.90 m) diameter (R03 and R04 in Table 1). Figure 8 shows the pressure in the pressure vessel. In these experiments we do not have the pressure signal from a transducer directly in front of the hole as an indicator of the different phases of the blowdown, especially for the determination of the blow-through time. From the vessel pressure curve and the gas velocity curves (Fig. 9) we can deduce that the blowthrough occurs very early (approximately at $t \leq 0.1$ s). In Fig.8 we see that the theoretical pressure curve for single-phase gas flow is steeper than the measured one for test R04 at early times. Therefore, we can assume that the flow through the hole is two-phase at least up to $t = 0.3$ s. The maximum pressures in the cavity are similar as in the tests with central holes (not shown).

Fig. 10 shows pictures of the flow in the cavity. The main direction of the flow is not vertical as with central holes but in an angle of approximately 25 degree, except near the breach, where the jet hits the side wall and spreads in all directions. The flow into the subcompartment opposite of the hole position is shown in Figs. 11 and 12. With the smaller hole the first droplets appear at the compartment after 120 ms (Fig. 11). Droplets with diameters in the order of 1 to 5 mm carry the main liquid mass with the maximum flow in the time interval between 300 and 1000 ms. The droplet flow dies down after 1500 ms. In the test with the larger hole a gas flow with fog appears after 50 ms (Fig. 12). (The condensation of the humidity is due to the cooling of the gas during the depressurization.) Droplets appear after 100 ms. The droplet flow ends after 800 ms. The droplets have a higher velocity than in the previous test and seem to be smaller.

The ejected liquid was found mainly in the compartments opposite to the position of the hole. Not all of the liquid was ejected out of the RPV (see Table 1). The main

parameter determining the fraction that remains in the lower head is, of course, the vertical position of the lower edge of the hole. It is, however, interesting to see how much lower than this edge the water level is after the test. This number is a measure for the magnitude of the entrainment. Table 2 lists the data for the lower edge, the liquid level and the difference between the two in terms of a volume fraction (f_{entr}), that is equivalent to the liquid swept out of the lower head by entrainment. Although there is less water left in the calotte in R04 with the larger hole than in R03 with the small hole, the entrainment was somewhat smaller in R04. There are two effects reducing the entrainment. With the large hole the blowdown time is shorter, and because the water level is already lower the surface area is smaller. With the high density liquid metal the entrainment in test R05 is much smaller than with water.

The fractions ejected into the compartments are smaller than in the experiments with central holes. Due to the smaller total mass (1800 cm^3 versus 3400 cm^3) we could expect a somewhat lower dispersed mass fraction, but the differences between corresponding tests with central holes and lateral holes are larger than what we have found as an mass effect. For 25-mm holes the mass effect is approximately 20 %, i.e. the dispersed fractions f_d with 1800 cm^3 were only 80 % of those with 3400 cm^3.

Even if the dispersed fraction is determined in relation to the mass that was ejected out of the RPV, the difference is still large (f_d^* in table 2, $f_d^* = f_d/(1-f_{RPV})$). In the tests D04 and D06 almost no liquid remained on the cavity bottom, while in R03 and R04 approximately 30 % of the ejected water was found there.

Thus, for the 25-mm-hole we get the following effect on f_d:

Reducing the total mass from 3400 to 1800: f_d is reduced from 0.70 to 0.56

Moving the hole from central to the side : f_d is reduced from 0.56 to 0.36

f_d based on the mass ejected out of the RPV: f_d^* is 0.40

For the 50-mm-hole we have a similar reduction (see Fig. 7, 1.1 MPa); from $f_d = 0.76$ for a large total mass and central hole (D05), to $f_d^* = 0.50$ for the reduced dispersed fraction with smaller mass and lateral hole (R04). With higher pressure (1.6 MPa in test R06) the dispersed fraction increases also for lateral holes (Fig. 7).

The liquid metal test R05 can be compared with test M01. In test M01 with the central hole the metal mass fraction ejected into the compartments was 36 %, and 21 % was captured at the RPV support. With the lateral hole practically no metal was found in

the compartments and at the RPV support.

Lateral slot: The second type is a horizontal slot, that models a partial rip in the lower head, as it might occur with a side-peaked heat flux distribution. The flow cross section is equivalent to a 25 mm hole (Fig. 2). The slot is 12.5 mm wide (high, inclined 45 degrees), and 42.5 mm long with a 6.25 mm radius. The lower edge of the slot is 56.1 mm above the bottom of the calotte. The amount of water was the same as for lateral holes. The liquid level was 67 mm above the bottom of the calotte and 2 mm above the upper edge of the slot. Two tests with a slot were performed (R01 and R02). The vessel pressure curves of the slot and the lateral hole tests are almost identical (not shown) and therefore the gas velocities are the same also (Fig. 13).

Due to the higher location of the lower edge of the slot more water remains in the calotte. The difference between post test water level and lower edge, however, is larger (23 versus 20 mm), and therefore, the entrained amount of water. The reasons could be the larger surface area of the water pool in the calotte at this higher position, and the wider flow cross section of the slot versus a round hole. The dispersed liquid fraction is smaller with the slot. In relation to the total amount of water ejected out of the RPV (f_d^*), it is 34 % for the slot (R02) and 40 % for the hole (R03) (see Table 2). The dispersed fraction at lower pressure (R01) is small with less than 5 %. The correlation to the burst pressure is similar as that for small central holes, i.e. increasing f_d with increasing burst pressure (Fig.7). At lower pressure more water remains in the lower head, because the entrainment is smaller at lower gas velocity, lower density and shorter blowdown time.

Unzipping and tilting of the lower head: The third type models the horizontal rip propagating around the circumference of the lower head leaving only a small section attached (Fig. 3), as it was observed in the lower head failure (LHF) experiments performed at SNL. Here the calotte is a separate part that is held in position by a steel rod from below at its center. When it is released the lower head moves down on one side and is held by a hinge on the opposite side. It is stopped by crushing material on four pedestals. Two different heights of pedestals were used to obtain different flow cross sections. The maximum drop height was h = 56 mm in one case, and h = 16 mm in two other tests. The drop height at the side of the hinge was not

zero but varied between 0.5 mm and 2 mm. The total flow cross section was 220 cm^2 and 70 cm^2, respectively. For comparison, the cross section of a 100-mm-hole is 79 cm^2 and for a 50-mm-hole it is 20 cm^2. The amount of water used was 2.1×10^{-3} m^3. This scales to 12.3 m^3 or approximately 100 t of corium. The water level was 73 mm above the bottom of the calotte and 10 mm above the separating edge. Thus 500 cm^3 or 23.5 % of the total mass were above the edge.

Corresponding to the large flow cross section with the high drop height of the calotte in test K01, the time for depressurization is extremely short with 0.08 seconds (Fig. 14). The other two tests, K02 and K03, with a drop height of 16 mm show a similar blowdown curve as tests D08 and D09, with the 100-mm-hole (Fig. 15 and 16).
As for the lateral holes and slots, liquid remains in the lower head after the blowdown. The amount of liquid depends on the tilt angle of the calotte, that is higher for K01 than for the other two experiments, and on the entrainment. The entrainment is larger in test K02 compared to K01, because of the higher pressure and the larger surface area of the remaining water, and therefore, the liquid level below the lowest edge of the tilted calotte is lower. With liquid metal (K03) the entrainment is much less due to its high density.

The liquid fraction dispersed out of the cavity is very small in test K01, with $f_d = 0.011$. With the central 100-mm-hole at an even lower pressure (D14, p = 0.35 MPa) it was $f_d = 0.580$. The large break cross section does not lead to high dispersion rates, because the gas does not accelerate the liquid with the lateral break and the entrainment is small because of the extremely short blow down time. With a smaller drop height (smaller flow cross section) and a somewhat higher burst pressure of 0.8 MPa in test K02 the reduced dispersed fraction is higher ($f_d^* = 0.277$), but still less than half of that of central holes with similar cross section (D08, $f_d = 0.717$). To distinguish between the effect of the higher pressure and the different drop heights an additional test with large drop height at 0.8 MPa burst pressure will be performed. Because the entrainment process plays a major role in the case of lateral breaches, the dispersed fraction with metal is very small (K03), even at the higher pressure of 1.1 MPa.

Fig. 17 shows the pictures of the flow in the cavity of test K02. The water is ejected

through the gap horizontally all around the circumference, with the largest amount at the position opposite to the hinge. The water hits the cavity wall and initially moves upwards and downwards with equal parts. Already at 4 ms a strong upwards directed gas flow can be seen, that makes the water film very thin. In test K02, after 170 ms the water film moves due to its inertia, the gas flow has ceased. In test K01 with the larger drop height this occurs already after 80 ms.

2.2 Geometry variations

Effect of pool depth: To investigate the effect of different initial liquid pool depths a standpipe was mounted inside the pressure vessel in two experiments (Fig. 4). The standpipe can hold the same amount of liquid as the lower head (3400 cm^3). Thereby we get only two distinct stages of blow down, first the liquid jet and than the gas jet, practically without a stage of a two-phase jet in between. This geometry was used by other investigators and it is therefore interesting to see the effect on the dispersed fractions.

In these experiments the single-phase liquid outflow takes longer as in experiments with standard geometry, where the same liquid volume, failure pressure and hole dimensions were employed. For example, in test D-07 the duration of this stage was approximately of 106 ms (blowthrough time), while in test T-02 this stage takes 245 ms (Fig. 18 and 19). The total duration of the blow down is about 20 % shorter for the tests with the water in the standpipe. For both hole sizes the dispersed liquid fractions are higher in the tests with the water initially in the standpipe, about 12 % for the 50-mm-hole and 8 % for the 25-mm-hole. Code calculations have produced similar results.

Venting channel: Four holes modeling the venting openings in the reactor pit were connected by a circumferential channel and a pipe to an extra compartment modeling the spreading room (Fig.5). The four openings in the lower part of the pit had a total flow cross section of approximately ¼ of the minimum flow cross section below the RPV support girder. The four holes with the diameter of 38 mm took up 14 % of the circumference of the pit. One test (S01) with a initial pressure of 1.1 MPa and a central hole of 25 mm diameter was performed, similar as test D04. No liquid was found in the melt spreading room and only 1.3 % of the liquid was in the

circumferential venting channel after the test. Thus, the venting channel is not a preferred flow path for the melt, and the danger is low that large amounts of melt will reach the melt spreading room premature.

Wider cavity (larger annular flow cross section): The diameter of the cavity was changed from 342 mm to 386 mm for test F03 (the width of the annular gap changed from 21.75 mm to 43.75 mm, see Fig. 6, without the dispersion preventing device). In a wider cavity the average gas velocity is lower due to the larger flow cross section. The minimum flow cross section below the nozzles was kept constant. Comparison with standard tests showed that the mass fraction ejected into the compartments was reduced from 70 to 63 %. The maximum average gas velocity changed from 38 m/s to 17 m/s.

Melt trapping device: In the wider cavity an extra cylinder was inserted, that should trap the liquid mass and prevent the dispersion out of the cavity (Fig. 6). In these tests it could be observed, that the cylinder separates the liquid at the cavity wall from the gas. The gas can flow into the compartments, while the liquid is trapped between the cylinder and the cavity wall. However, the liquid falls back into the cavity as soon as the top of the gap is reached and can be entrained by the gas, but at lower gas velocities. This reduces the dispersion substantially (Table 1). With a central hole the reduction is from 63 % without trap (test F03) to 28 % with trap (F04). Combining a lateral hole with the melt trapping device like in test F06, the dispersed fraction reduces from 36 % (R03) to 10 %. If liquid metal were employed instead of water, the dispersed fraction values would be even smaller.

3. Measurements of flow parameters

In some special experiments velocities of gas and liquid droplets and droplet sizes were measured in the annular gap and at the nozzles at the entrance to the subcompartments by particle image velocimetry (PIV).

The measurements of the gas velocity in the gap show good agreement with velocities calculated from experimental pressures and temperatures. It can be concluded, that there is no fully developed flow in the annular gap. Higher velocities could be observed close to the RPV wall.

Drop sizes at the entrance to the compartments range between 220 µm and several millimeters. A tendency for the drop mean size to increase as gas velocities diminish could be observed. At a time near the end of the two-phase outflow and close to the begin of the single-phase gas outflow, a maximum number of droplets can be observed in the experiments. Drop velocities are larger than water jet velocities and have also larger horizontal velocity components. From visualization of the flow phenomena at the compartments, it could be concluded, that the water jet observed in the PIV pictures is a prolongation of the liquid film observed in the reactor cavity. Therefore, drops observed in the pictures have two possible origins:

1. Drops entrained by the gas due to the shearing force existing between gas and liquid film in the annular gap. These drops are carried out of the reactor cavity and along the main coolant lines into the compartments by the gas. They have high velocities and small diameters.

2. Drops resulting from the fragmentation of the liquid jet at the compartments. These drops have usually larger diameters and lower velocities.

Details and complete data can be found in [1] and [2].

4. Conclusions

With holes at the base of the bottom head the most important parameters governing the dispersion of melt are the hole size and the burst pressure. Practically, no liquid remains in the RPV. With lateral breaches the liquid height in the lower head relative to the upper and lower edge of the breach is an additional parameter for the dispersion process. In most cases not all the liquid is discharged out of the RPV. If the initial liquid level is above the upper edge the blowdown starts with the single-phase liquid discharge, driven by the pressure difference between vessel and cavity, as for central holes. However, the gas blowthrough occurs earlier. In the subsequent stage the liquid is carried out of the lower head by entrainment. The gas velocity at the breach may be high but the velocity above the liquid surface inside the vessel is much lower. Besides the gas velocity, the density ratio of gas and liquid, the surface area of the liquid pool, and the duration of the blowdown govern the entrainment process. Therefore, the entrained liquid fraction can be higher with a small breach

than with a large one, because the blowdown time is longer but the maximum velocity may be the same. The entrainment mechanism in such a case is not well understood and it is difficult to apply these results to the reactor case, since up to now, our experiments are the only ones with lateral breaches, and no other scale has been tested.

Shifting the break from the central position towards the side of the lower head leads to a smaller dispersion of liquid, even if the dispersed fraction is related only to the liquid mass that has been ejected out of the RPV. The main effect is probably the circumferential component of the velocity in the cavity. Also, the velocity of the entrained droplets may be lower, because of the short entrainment length within the lower head.

As for the time being, we can make the cautious statement, that taking the known similarity correlations, the results from the liquid metal tests represent the lower bound for the dispersed melt fractions, however, they are probably closer to the expected values than the results from the water tests, that represent the upper bound. So, significantly less dispersion of melt can be expected for lateral breaches at pressures below 1.1 MPa, probably less than 10 %. If higher dispersion occurs, maybe due to higher pressure at failure, simple devices to mitigate the dispersion out of the cavity may be feasible.

For the investigation of thermal and chemical effects experiments with alumina-iron melt and steam will be performed in a similar geometry.

References

1. Meyer, L., Gargallo, M., Greulich, M., Kirsthaler, M., Schwall, M., Wörner, G., Wachter, E., "Low Pressure Corium Dispersion Experiments in the DISCO-C Tests Facility with Cold Simulant Fluids", *FZK-Report 6591*, Forschungszentrum Karlsruhe, to be published in 2001.
2. Gargallo, M., Meyer, L., " Experimental Simulation of Melt Dispersion at Low Pressure in an Annular Cavity", SMiRT 16, Washington, DC USA, August 12-17, 2001
3. Meyer, L., Gargallo, M., "Experiments on Melt Dispersion with lateral failure in the Bottom head of the pressure vessel", ICONE 9, Nice Acropolis – France, April 8-12, 2001

Table 1 Parameters and dispersed liquid fractions

Test	Liquid volume (10^{-3} m^3)	Liquid	Issue	Hole Dia. (mm)	Flow cross section (cm^2)	Burst pressure (MPa)	Liquid fraction found in: compart-ments f_d	Cavity bottom f_B	RPV support f_s	Cavity total $f_c = f_B + f_s$	RPV f_{RPV}
D-20	*1.8*	*water*	*central hole*	*25*	*5*	*1.140*	*0.553*	*0.024*	*0.423*[§]	*0.447*	*0*
D-05	*3.4*	*water*	*central hole*	*50*	*20*	*1.200*	0.759	0.012	0.229	0.241	*0*
M-01	*3.1*	*metal*	*central hole*	*25*	*5*	*1.045*	*0.358*	*0.428*	*0.215*	*0.643*	*0*
R-01	1.8	water	lateral slot	equiv.25	5	0.611	0.029*	0.423	0.185	0.608	0.363
R-02	1.8	water	lateral slot	equiv.25	5	1.101	0.250*	0.244	0.244	0.488	0.262
R-03	1.8	water	lateral hole	25	5	1.100	0.358*	0.294	0.238	0.531	0.111
R-06	1.8	water	lateral hole	25	5	1.610	0.469*	0.204	0.242	0.446	0.085
R-04	1.8	water	lateral hole	50	20	1.100	0.477*	0.266	0.209	0.475	0.048
R-05	1.8	metal	lateral hole	25	5	1.050	0.0005	0.657	0.006	0.663	0.336
D-08	*3.4*	*water*	*central hole*	*100*	*78*	*0.613*	*0.717*	0.052	0.231	0.283	0
K-01	2.1	water	unzipping	h=56	220[#]	0.500	0.011*	0.851	0.043	0.894	0.095
K-02	2.1	water	unzipping	h=16	70	0.800	0.225*	0.320	0.270	0.588	0.187
K-03	2.1	metal	unzipping	h=16	70	1.100	0.008	0.455	0.124	0.579	0.413
F-03	3.4	water	wider gap	25	5	1.076	0.632	0.233	0.135*	0.367	0
F-04	3.4	water	melt trap	25	5	1.100	0.280	0.590	0.130*	0.720	0
F-05	3.4	water	melt trap	50	20	1.110	0.266	0.574	0.159*	0.734	0
F-06	1.8	water	lateral + melt trap	25	5	1.110	0.097	0.578	0.206*	0.784	0.119

* most liquid was found in the compartments opposite of the slot or hole
[#] maximum possible flow cross section (D = 245 mm) : 471 cm^2
[§] closed holes at the support girder prevented a back flow into reactor pit

Table 2 Lateral breaks data on post test liquid level in the lower head and reduced dispersed fraction f_d* (pre-test level was 67 mm for the R-tests and 73 mm for K-tests)

Test	diameter or drop height [mm]	liquid	P [MPa]	lower edge	water level	Diff. [mm]	f_{entr}	f_{RPV}	f_d	f_d^*
R-01	slot 25 equiv.	water	0.6	56	39	17	0.355	0.363	0.029	0.045
R-02	slot 25 equiv.	water	1.1	56	33	23	0.455	0.262	0.250	0.339
R-03	25	water	1.1	41	21	20	0.290	0.111	0.358	0.403
R-06	25	water	1.6	41	18	23	0.315	0.085	0.469	0.513
R-04	50	water	1.1	32	14	18	0.200	0.048	0.477	0.501
R-05	25	metal	1.1	41	39	3	0.036	0.336	0.0005	0.0008
K-01	56	water	0.5	-	-	15	0.174	0.095	0.011	0.012
K-02	16	water	0.8	-	-	25	0.401	0.187	0.225	0.277
K-03	16	metal	1.1	-	-	12	0.215	0.413	0.008	0.013

f = mass found post test in specific locations / total mass
f_d^* = mass found post test in specific locations / (total mass – mass remaining in the RPV)
f_{entr} = volume in lower head between lower edge of hole and post test water level / total liquid volume

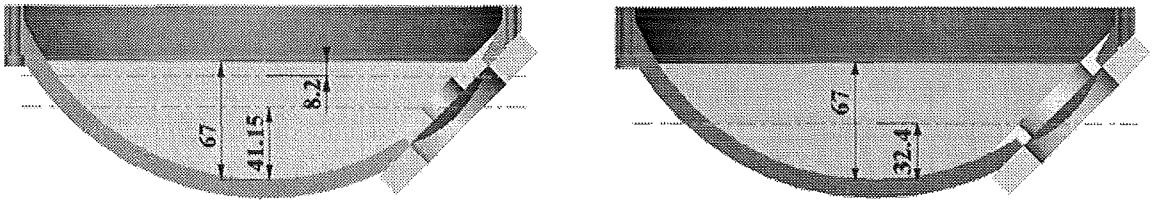

Fig. 1 Geometry of lateral holes with 25 mm and 50 mm diameter

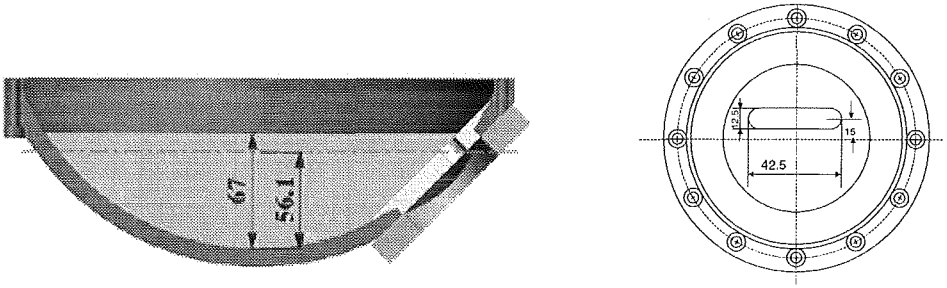

Fig. 2 Geometry of lateral slot

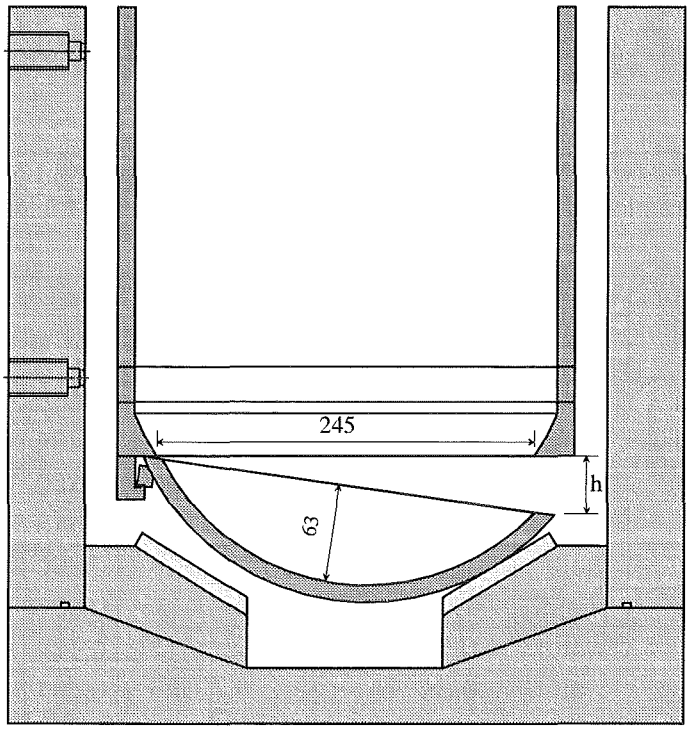

Fig. 3 Unzipping and tilting of lower head

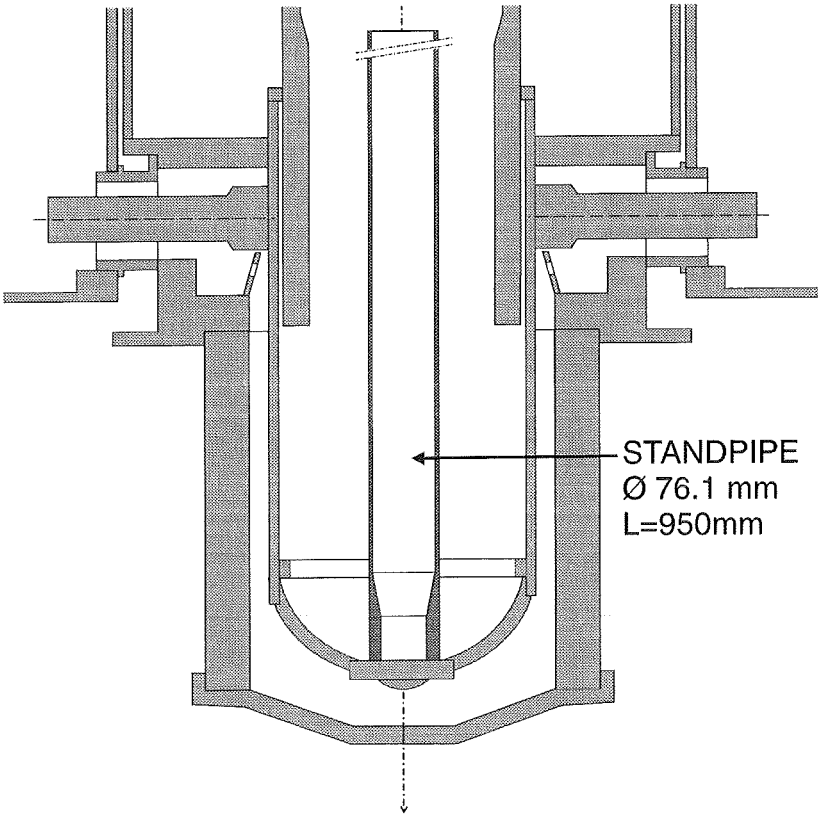

Fig. 4 Standpipe to model high pool depth

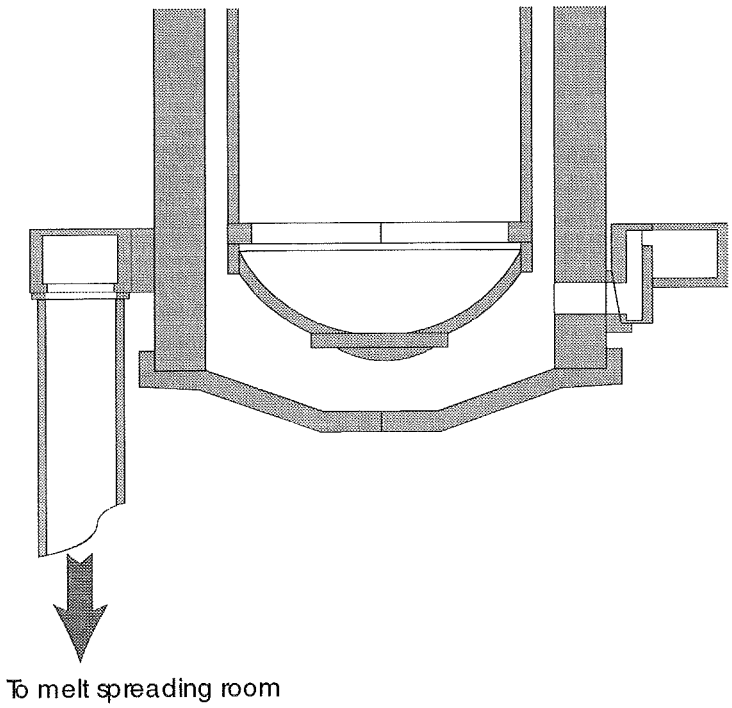

Fig. 5 Cavity with openings leading into the melt spreading room

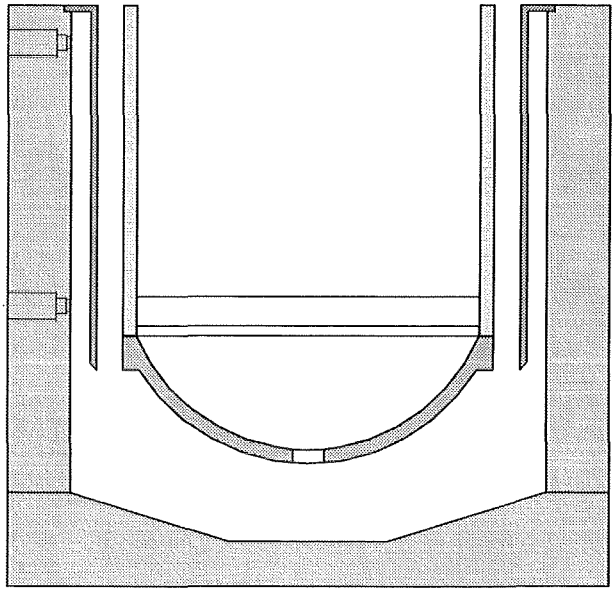

Fig. 6 Melt trapping device in the cavity

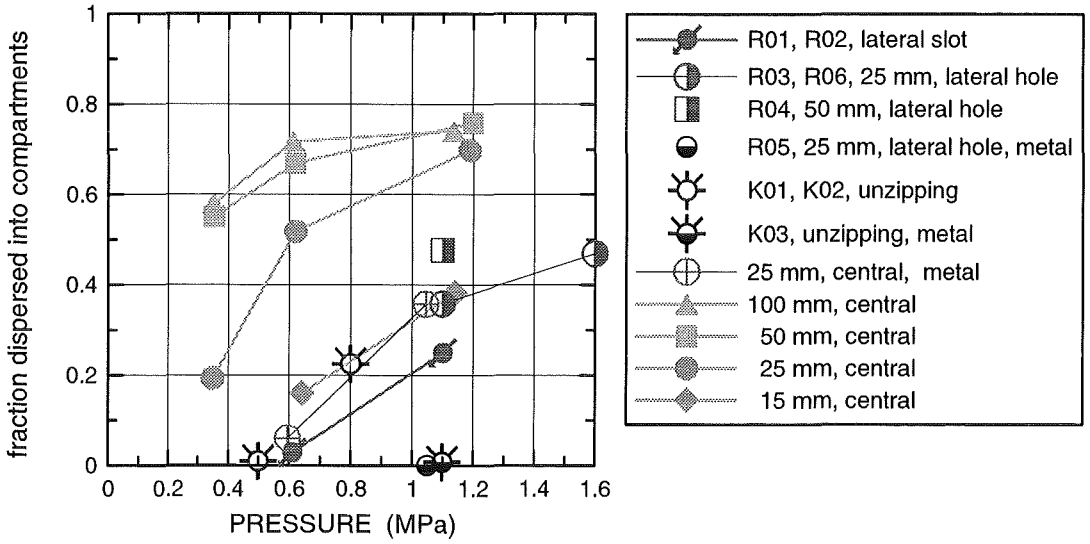

Fig. 7 Dispersed fractions for special tests with lateral breaches and changes in cavity geometry in comparison with results from tests with central holes and water.

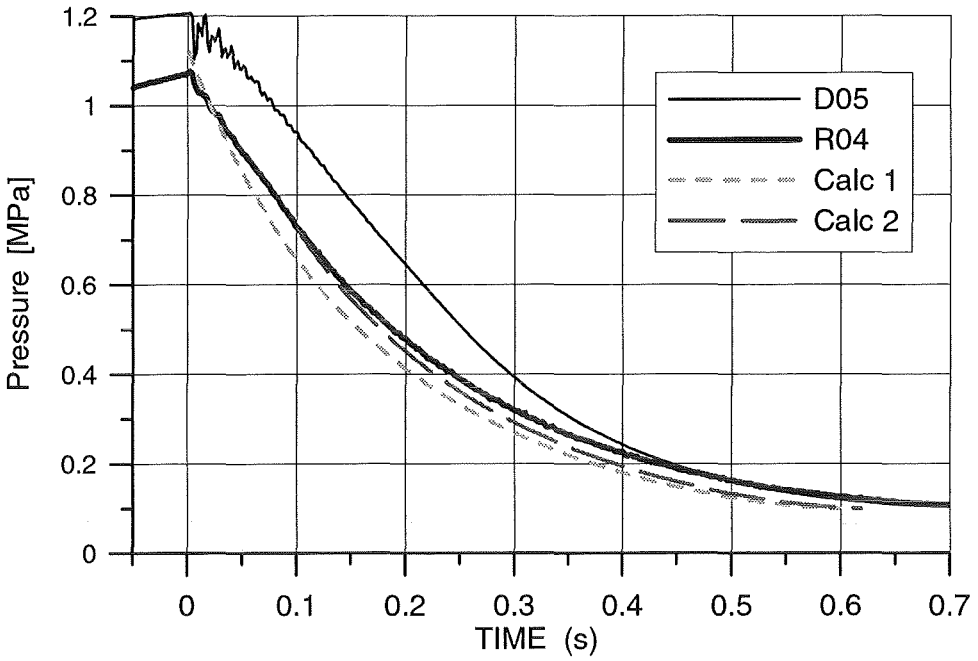

Fig. 8 Comparison of blowdown pressure of experiments with central hole (D05) and lateral hole (R04), and with single-phase gas blowdown calculated for isentropic flow

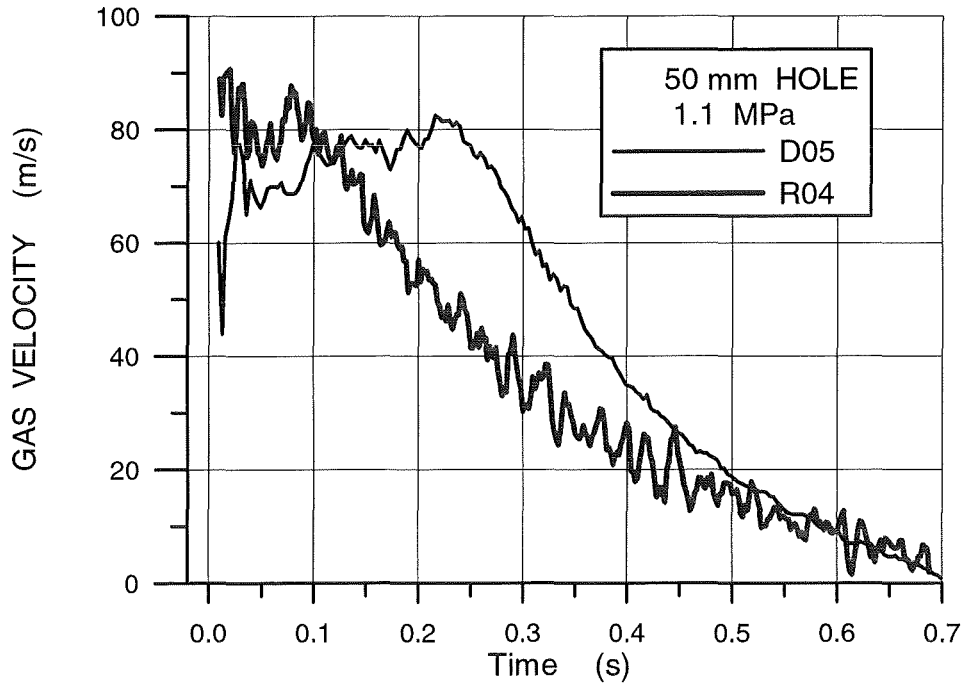

Fig. 9 Bulk gas velocities of nitrogen in the annular space in the cavity for tests with 50 mm-holes and liquid water, comparison of different hole positions (D05,central and R04)

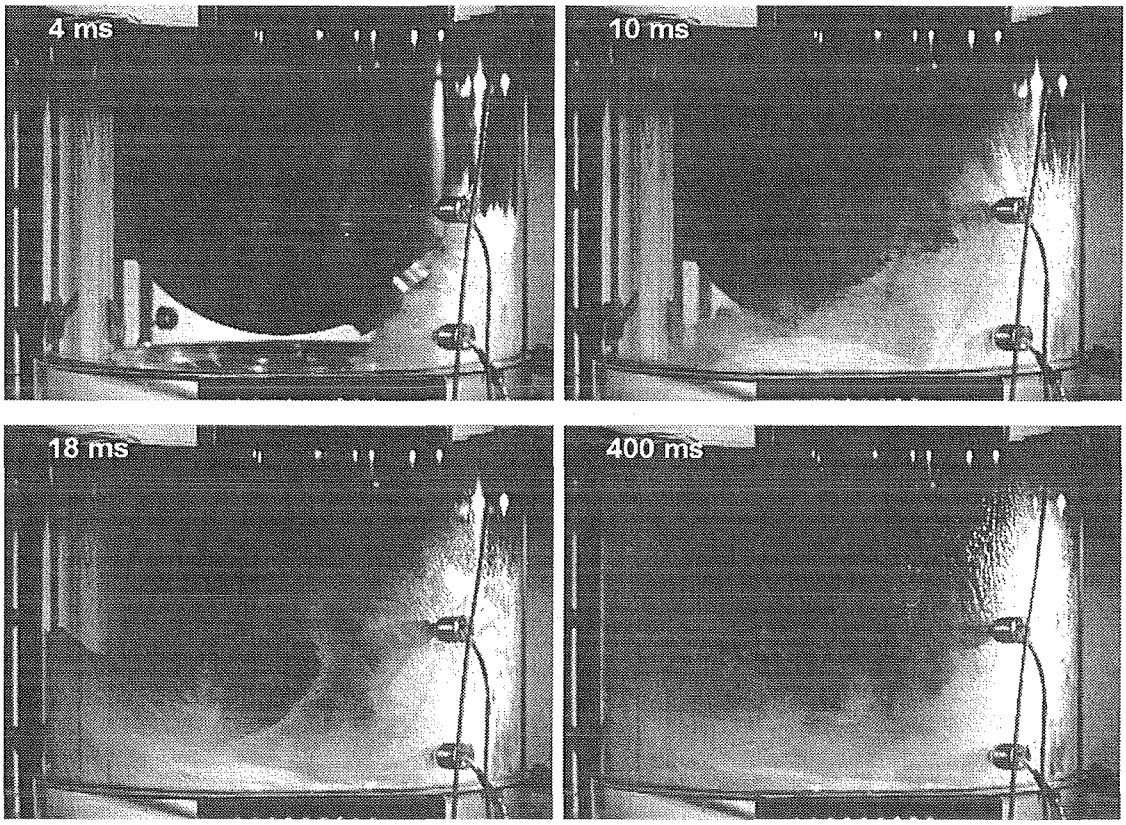

Fig. 10 Flow in the reactor pit in test with lateral hole (R03, 25 mm hole)

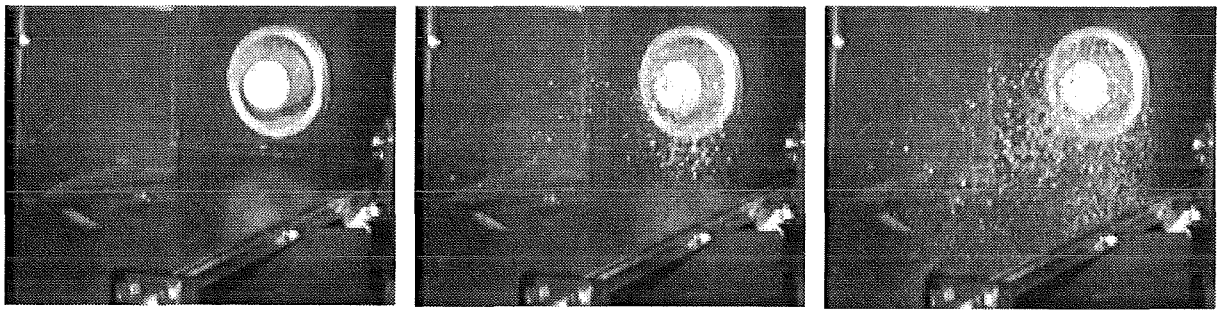

Fig. 11 Flow into subcompartment, R03, lateral hole, 25 mm

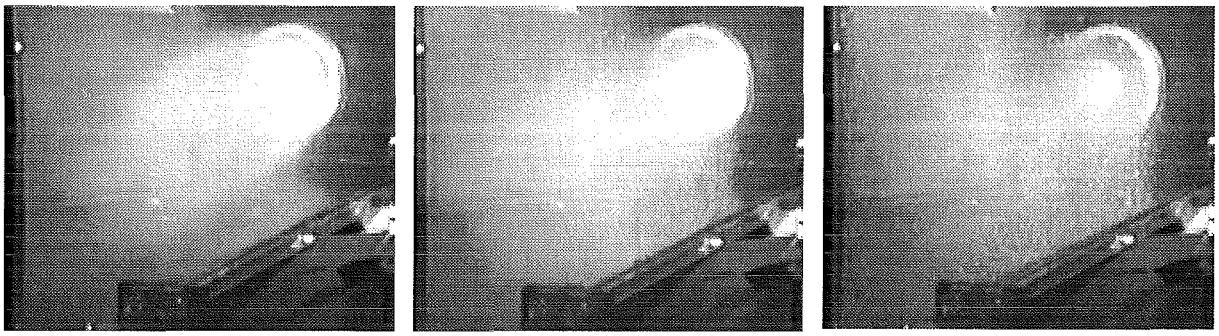

Fig. 12 Flow into subcompartment, R04, lateral hole, 50 mm

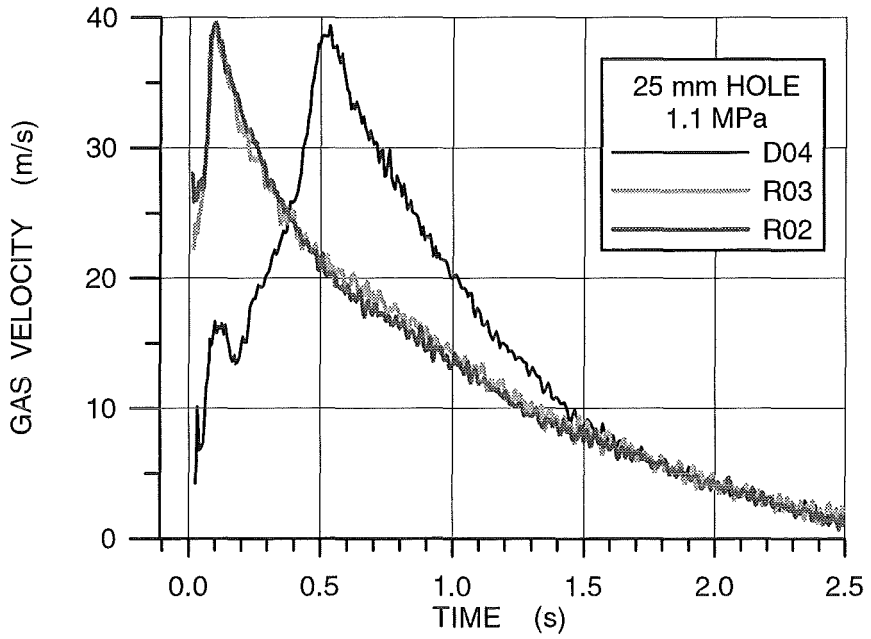

Fig. 13. Bulk gas velocities of nitrogen in the annular space in the cavity for 25 mm holes and liquid water, comparison of different hole position (D04 and R03), and different hole shape of lateral breaches (R03 and R02)

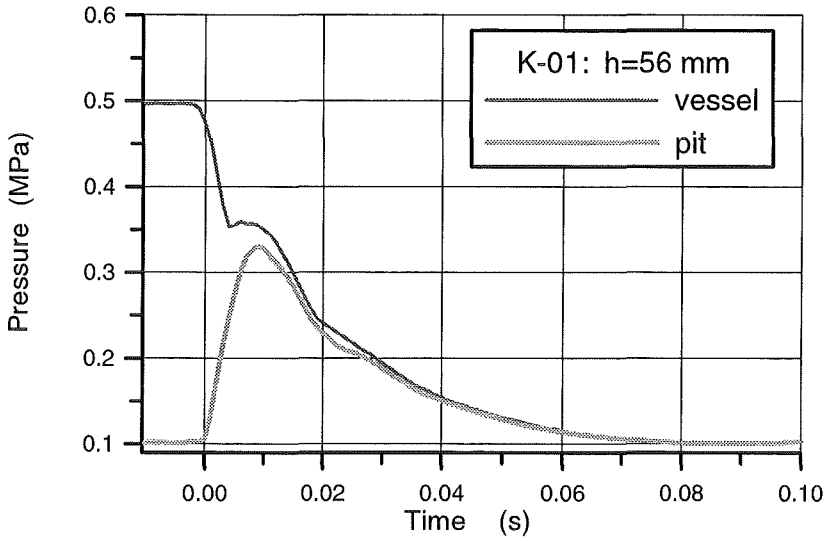

Fig.14 Pressure in the pressure vessel and the reactor pit in tests with tilting of the lower head

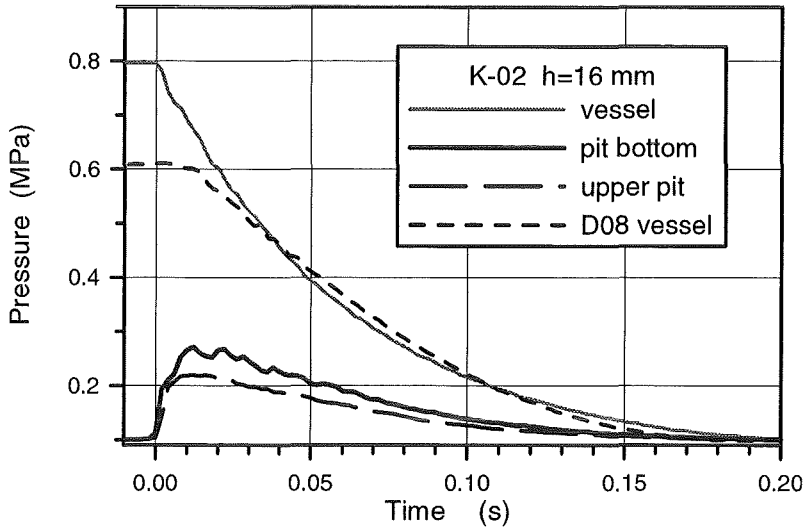

Fig.15 Pressure in the pressure vessel and the reactor pit in tests with tilting of the lower head

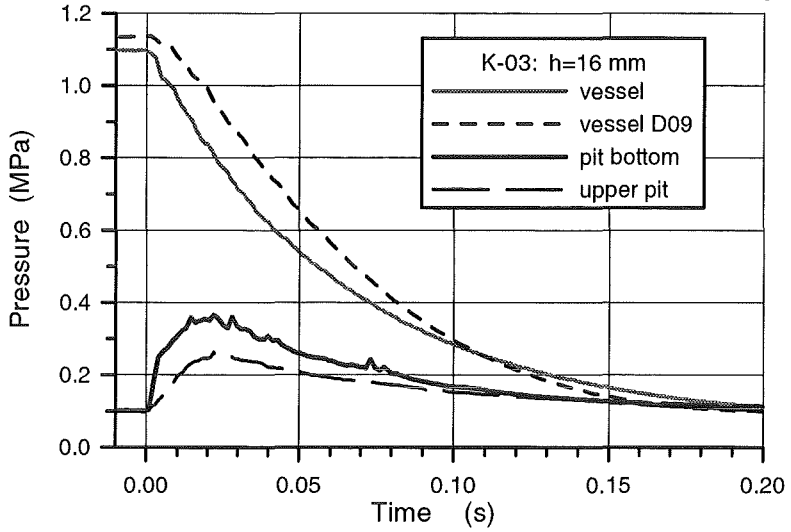

Fig.16 Pressure in the pressure vessel and the reactor pit in tests K03 (metal) and D09

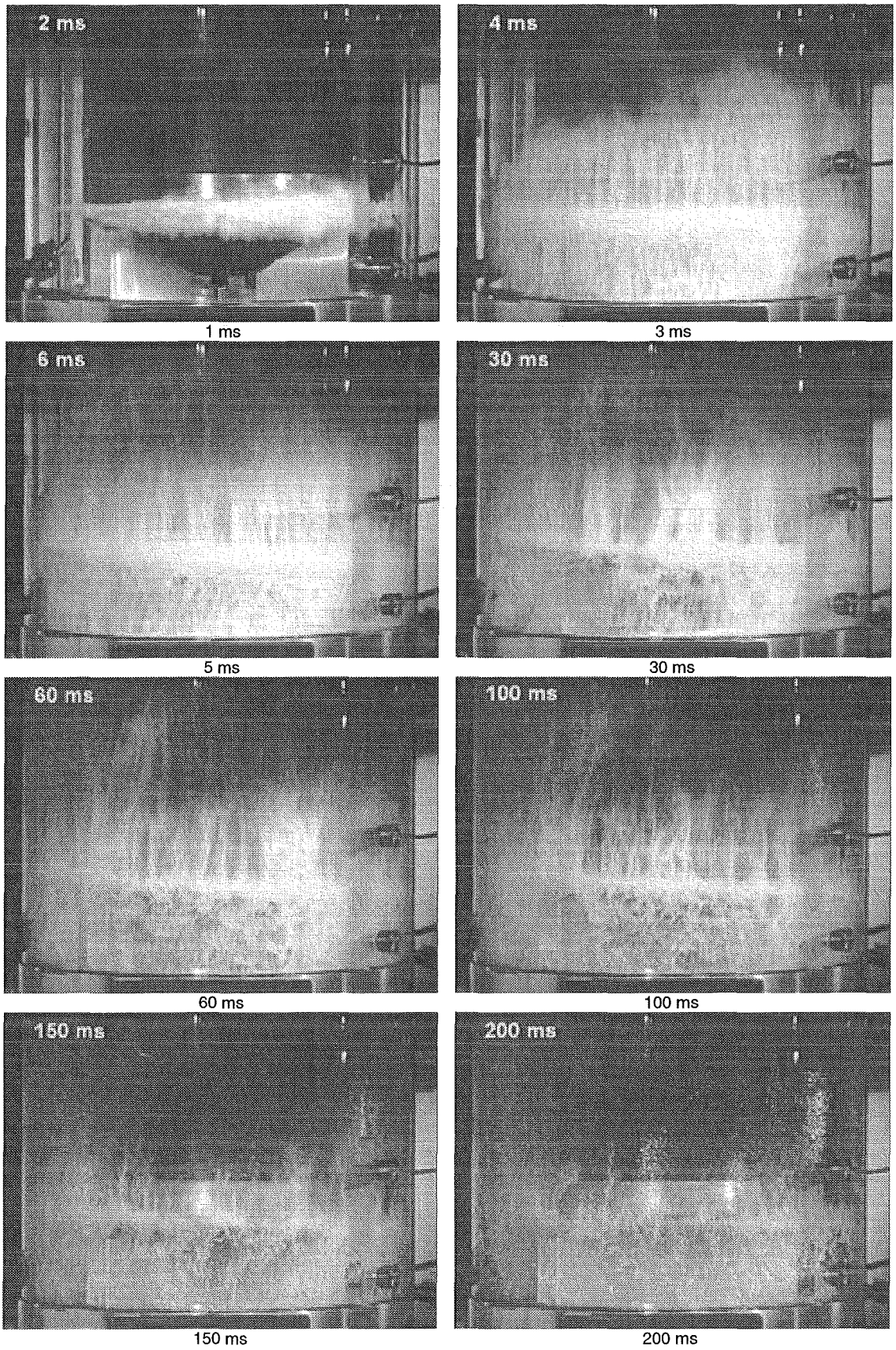

Fig. 17. Flow in the cavity, D4.2, drop height h = 16 mm

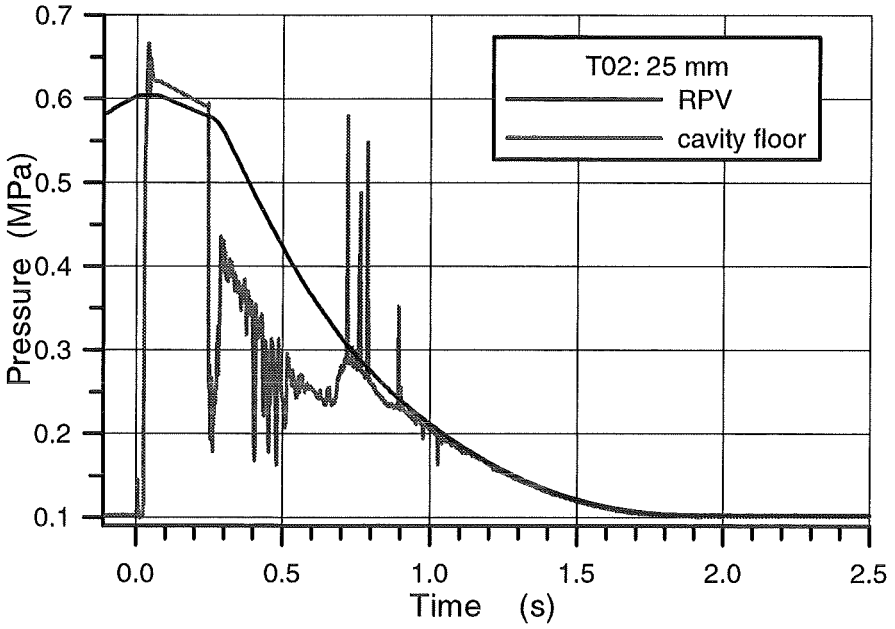

Fig.18 Pressure in the pressure vessel and the reactor pit in a test with liquid initially in a standpipe

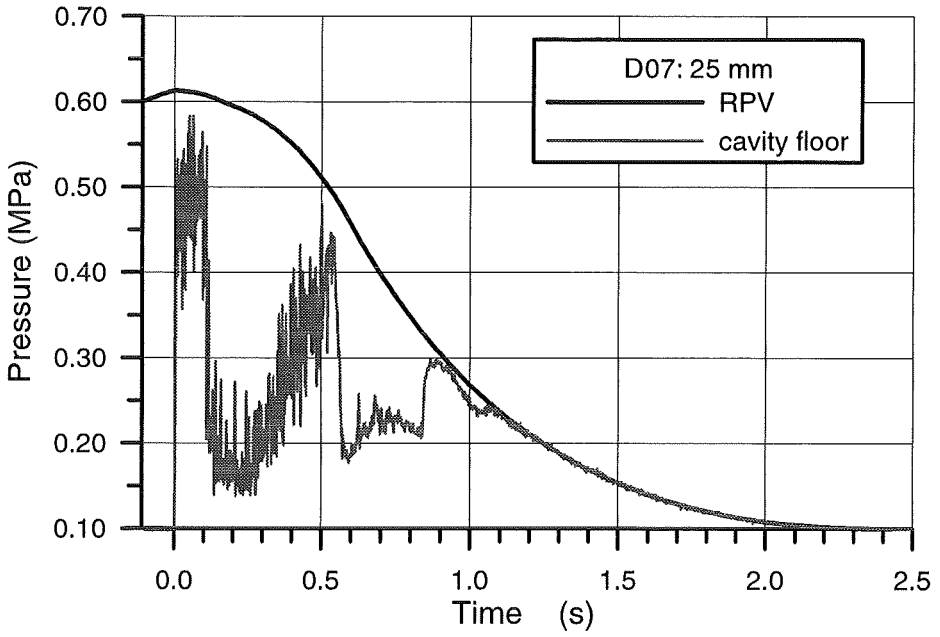

Fig.19 Pressure in the pressure vessel and the reactor pit in a standard test

III. Rechnungen zur Dispersion der Kernschmelze

(D. Wilhelm, IKET)

Zusammenfassung

Mit Hilfe eines für die Coriumdispersion erweiterten Fluiddynamik-Codes wurde ein in reduziertem Maßstab durchgeführtes Thermitexperiment analysiert, das den Auswurf von geschmolzenem Kernmaterial aus dem Druckbehälter eines Leichtwasserreaktors in die angrenzenden Räume und den Dom des Sicherheitsbehälters beschreibt. Das Experiment wurde im Rahmen einer internationalen Übereinkunft im Sandia National Laboratory, U.S.A., durchgeführt. Es wird zur Zeit mit dem DISCO Programm im Forschungszentrum Karlsruhe weitergeführt. Ein erster Versuch der Extrapolation auf den Reaktorfall wurde mit dem Code unternommen. Die Studie zeigt, daß wichtige experimentelle Resultate gemäß allgemeiner Skalierungsgesetze auf den Reaktorfall übertragen werden können, aber daß es Empfindlichkeiten vor allem beim Übergang von Thermit auf Corium gibt. Die Resultate unterliegen großen Abweichungen und Abhängigkeiten von der Geometrieauflösung und der Dynamik des Wärmeübergangs zwischen den verschiedene Komponenten.

1. Introduction

In the event of a core melt-down of a pressurized water reactor, the molten metals and oxides may collect in the lower head of the pressure vessel. Two scaled-down thermite experiments [1] were performed at the Sandia National Laboratory, Albuquerque, which simulated the discharge of the melt through a given breach of the lower head driven by steam at a moderate pressure of 1.1 MPa. Prior to these experiments, in a comprehensive program of the United States, the issue of direct containment heating was investigated. Equilibrium models and systems-level codes were successfully used [2] to predict containment overpressures for different reactor types. The present program focuses on lower pressure levels in the vessel. Therefore, the containment overpressures and the fractions of melt discharged into the containment are lower. When focussing on where and when the melt is being dispersed, it became obvious that it was necessary to resolve, different to the

previous studies, details of the geometry close to the breach. The present program not only seeks to provide results for the melt dispersion, but also for the time sequence of hydrogen generation, in-vessel pool behavior in the lower head, impact of the melt on safety components, and possibly also fission product distribution with the melt.

2. Recalculation of the experiment

The experimental program is being accompanied by calculations with a CFD code. To a code of the SIMMER family [3], models were added which were found necessary to describe the phenomena during melt dispersion. Fig. 1 shows an sketch of the reactor pressure vessel and the adjacent structures and an artist's view of the melt during dispersion. The phenomena under investigation are listed close to the location where they occur.

The flow of melt to the outside of the pressure vessel is governed by the upstream and downstream conditions. During the DISCO-C program [4], and using code calculations, the phenomena leading to a gas blowthrough have been found to play a role. The liquid melt first leaves the breach in an almost single-phase liquid flow. At a given low liquid level in the pressure vessel, the jet becomes two-phase in such a way that the center of the jet entrains vapor from the vessel. The change in flow regime has a substantial influence on the dispersion processes downstream.

Jets leaving pressure vessels at high velocities are subjected to a constriction of the jet diameter. The associated consequences on the mass flow need to be carefully modeled by the code. When leaving the breach, the jet may partly disintegrate due to the shear forces acting on it. Droplets leaving the jet may have different sizes than those being formed when the jet impinges on the cavity bottom.

Downstream of the impact area, a film of the liquid melt may be formed on the cavity bottom and the side walls. Droplets may be entrapped into the film. The rest of the droplets, especially those of a small size, may leave the cavity without contact to the cavity walls. The melt in the film exchanges heat with the colder walls. A part of the film may freeze and form a thin crust on the wall. If conditions are met, the vapor flow may entrain droplets out of the film. These droplets are generally small enough to be levitated by the vapor flow and are thus swept out of the cavity.

While the melt flows through the cavity, its surface area to the adjacent vapor is largely increased. The steam which was either in the cavity before breach opening or is flowing out of the reactor pressure vessel after gas blowthrough reacts with the metal components of the melt. The reaction is exothermic and the products are oxides and hydrogen. Inside the cavity, there is not enough oxygen for hydrogen combustion. However, when hydrogen leaves the cavity, conditions are met in the reactor dome for a steady flame which adds reaction energy to the dome atmosphere.

The code was successfully used to recalculate the more energetic of the two SANDIA experiments and to discuss effects and sensitivities of conditions which are not well known [5]. Besides the achievement of a good agreement of the pressure transients, the main findings of the post-test analyses of the experimentalists were confirmed, as there are a steam limited oxidation of metal in the cavity, a further oxidation in the containment, a constant hydrogen burning, and the limited amount of thermite dispersed beyond the cavity. The amount of thermite freezing on the cavity walls is small and has been found to have a negligible influence on the results.

Fig. 2 shows the pressure transients of the experiment (dotted lines) and the code (solid lines). The uppermost pressure is that of the pressure vessel. Pressures in the cavity and the dome start at about 0.22 MPa. The pressures of the cavity are higher and show small maxima because of thermal and chemical interactions. The pressure peak after 0.1s is lower for the code, but the general course looks similar and comes at the proper time. Subsequent pressures are well matched.

3. Extrapolation to prototypic conditions

A first attempt was undertaken to extrapolate to prototypic condition. This was done in two steps, first to prototypic scale, and then from thermite to corium. While the geometric scale-up revealed only small differences to the experiment, especially in the dynamics, the change to corium showed new sensitivities. These depend on the specification of the melt, and are thus subjected to the history of the accident. By and large, the relevant results scale as predicted, the pressures look similar to the experiment except for the cavity pressures which are higher, the relative amount of hydrogen generated depends strongly on the melt mass and the metal content in the

melt, and the fraction of melt discharged into the containment is lower but rather close to what has been measured.

Table IV shows the result of the scaling analysis and code calculations. For the experiment, the linear scale of 1:10 is arbitrary and follows the need for technical feasibility. From this scale follows directly the surface and volumes scales. Water vapor produces the driving pressure of the prototype. The experiment also uses water vapor, and the temperature frame is similar to that of the prototype, with water temperatures scaled 1:1 and thermite temperatures being close to those of a molten corium pool. The pressure of the experiment is thus scaled 1:1. The mass scaling approach of the experiments uses a comparison of thermal and chemical melt energies to find the appropriate melt mass. This yields a factor of 1900 for the prototypic melt. The scaling factors for the droplets sizes and the lines below are results of the code calculations.

	1:10 thermite	**1:1 thermite**	**1:1 corium**
Length, Time	1	10	10
Area	1	100	100
Volume	1	1000	1000
Pressure	1	1	1
Velocity	1	1	1
Mass	1	1000	1900
Droplet size	1	≈1.7	≈1
$\frac{calculated\ \ melt\ \ fraction\ \ dispersed}{measured\ \ melt\ \ fraction\ \ dispersed}$	1	≈0.9	≈0.8
Hydrogen mass produced in the cavity	1	≈450	≈240
Mass of the film frozen on the cavity walls	1	≈200	≈50

Table IV Scaling factors for 1:10 and 1:1 scale

Fig. 3 shows the calculated pressures for the corium case in 1:1 scale compared to those the calculation in 1:10 scale and the experiment. The upper abscissa stands for the protypic time, the lower for the experimental time.

Fig. 4 shows the cavity inventories of steam and gases during the first 8 s of a 1:1 scale corium calculation. The initial steam inventory is reduced before gas blowthrough which takes place around 0.6 s. Until 3.6 s, all steam flowing in is consumed by oxidation. Hydrogen inventory peaks just after gas blowthrough and when cavity pressures rise rapidly. After 3.6 s, the reaction is no longer steam limited,

but most of the metal components are already oxidized. Hydrogen production stops around 6 s.

The study of the 1:1 corium cases has shown that the dispersion scales almost 1:1 when comparing to the experiment. However, this result is not due to similar conditions during the transient. Flow conditions and chemical reactions have been found to be quite different. Besides this, the calculations show a considerable scatter of results and dependence with geometric resolution of the code and with the dynamics of energy transfer between participating components. This underlines the demand for a more important number of thermite tests which will start in the DISCO facility of the Forschungszentrum Karlsruhe.

References

[1] Blanchat T.K., Pilch M.M., Lee R.Y., Meyer L., Petit M., 1999, Direct Containment Heating Experiments at Low Reactor Coolant System Pressure in the Surtsey Test Facility, Sandia National Laboratory report NUREG/CR-5746, SAND99-1634, July 1999

[2] Pilch M.M., Allen M.D., Klamerus E.W., 1996, Resolution of the Direct Containment Heating Issue for All Westinghouse Plants with Large Dry Containments or Subatmospheric Containments, Sandia National Laboratory report NUREG/CR-6338

[3] Bohl W.R., Wilhelm D., 1992, The Advanced Fluid Dynamics Model Program: Scope and Accomplishment, *Nuclear Technology*, 99, 309-317

[4] Meyer L., 1999, Experiments to Investigate the Low Pressure Corium Dispersion in EPR Geometry, *Workshop on Ex-Vessel Debris Coolability of the Nuclear Energy Agency*, Karlsruhe, 16-18 Nov. 1999

[5] Wilhelm D., Analysis of a Thermite Experiment to Study Low Pressure Corium Dispersion, report FZKA 6602, Forschungszentrum Karlsruhe to be published

FIGURES

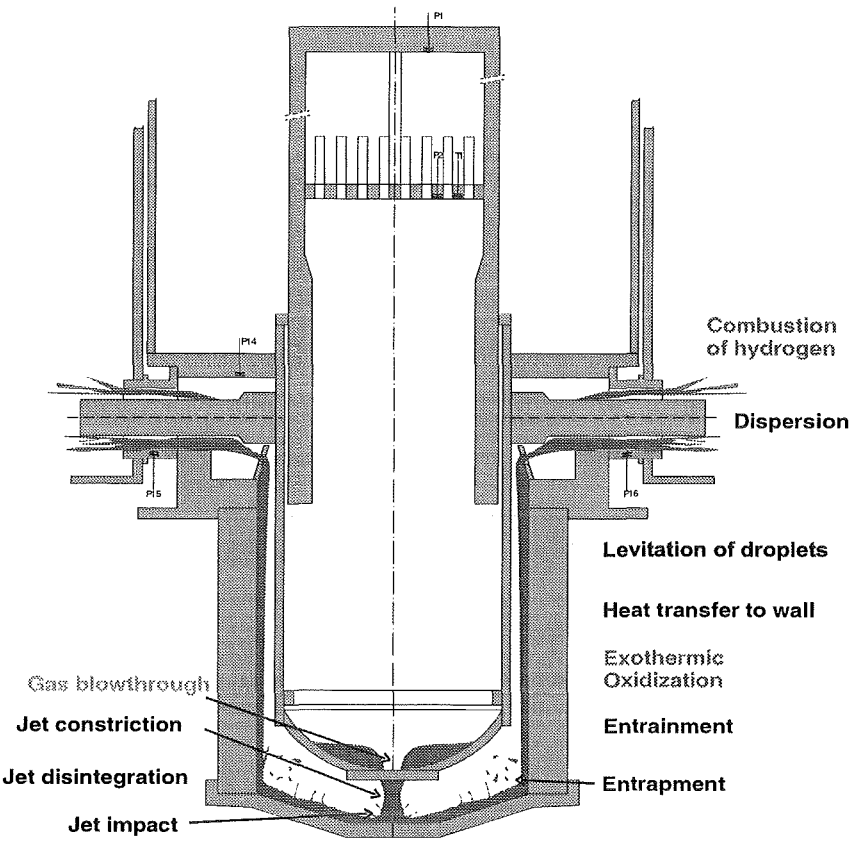

Fig.1: Sketch of a model of a reactor with symmetric cavity and dominant phenomena

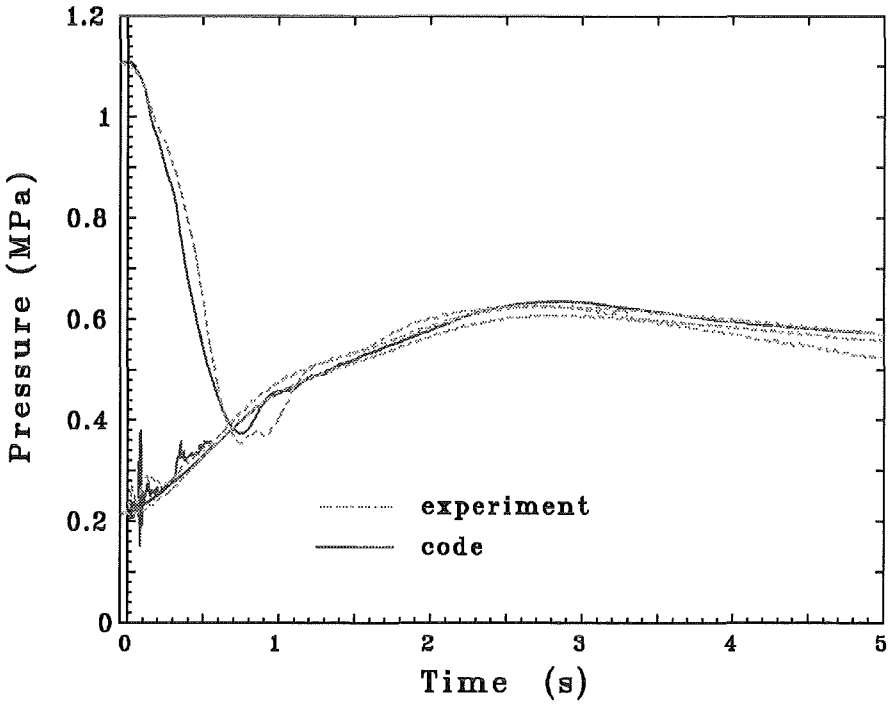

Fig. 2: Measured and calculated pressures of the SNL/Sup-1 experiment

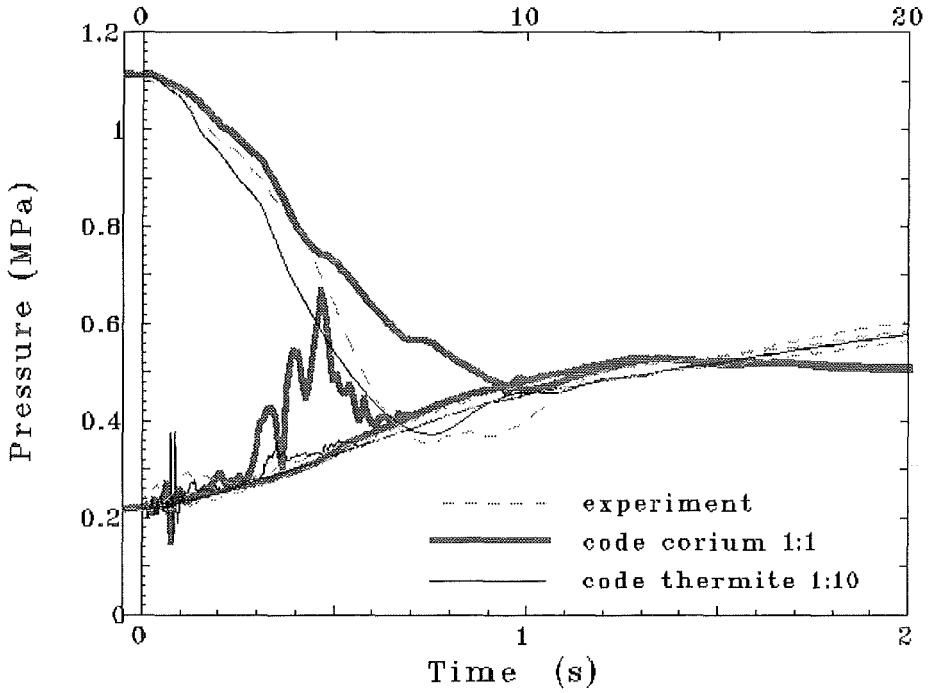

Fig. 3: Comparison of pressures of the 1:1 corium and 1:10 thermite cases

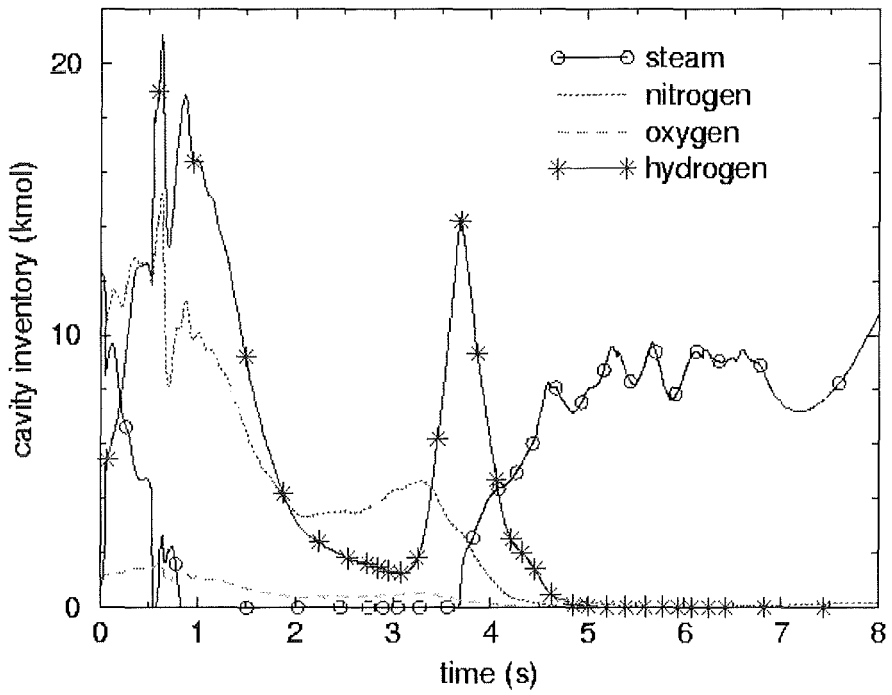

Fig. 4: Cavity inventories of the 1:1 corium case

32.21.04 Thermischer Angriff durch Kernschmelze und deren langfristige Kühlung

I. COMET - Konzept

(H. Alsmeyer, T. Cron, S. Schmidt-Stiefel, W. Tromm, T. Wenz, IKET; C. Adelhelm, IMF; H.-G. Dillmann, H. Pasler, ITC-TAB; W. Schöck, IMK; C. Grehl, G. Merkel, W. Ratajczak, HVT; Ing.-Büro F. Ferderer; Ing.-Büro G. Schumacher)

Abstract

The CometPC cooling concept is investigated to cool corium melts in a postulated core melt accident. In this concept, water is introduced to the bottom of the melt through a layer of porous concrete. Three further large scale experiments with sustained heated melts are reported, which were performed with 800 kg metal and oxide melts with an initial temperature of about 1900 °C. One experiments investigates the cooling behaviour of a 1-dimensional central section of the typical reactor scale. Two further experiments include the influence of sidewalls. After erosion of the sacrificial concrete layer, strong cooling of the melt starts with onset of passive water injection. The experiments are discussed with respect to the main results. The melts are arrested and cooled by the porous, water filled concrete when the sacrificial concrete layer and the coolant flow are adequately designed. However, distribution of the coolant water flow and the porosity of the melt are to some extend not satisfactory. In this respect, an improvement of the CometPC-cooling concept is desirable to obtain the good porosity and coolability of the melt, that were found in the original COMET-cooling concept based on an optimised array of flow channels.

Further transient tests investigate questions related to special accident scenarios for the CometPC core catcher. For the investigated scenario the low pressure pumps of the primary circuit can be restarted when the core melt has spread on the compartment. Thus, compartment and core melt are flooded through the destroyed RPV. The question is, whether crusts on the melt surface are formed and whether the fragmentation processes by water inlet from below are impeded. The experiments show that even with flooding of the melt and crust formation the melt is fragmented due water inlet from below and the flow rate is comparable to former experiments. Theoretical investigations conducted with the computer code WECHSL could demonstrate adequate agreement with the experiments. For the reactor case the calculations show that flooding doesn't lead to

crusts on top of the melt in the possible time span of concrete erosion, i.e. this scenario is not critical for the core catcher concept.

Zusammenfassung

Zur Kühlung der Kernschmelze in einem unterstellten Kernschmelzenunfall wird das CometPC-Kühlkonzept untersucht, bei dem das Kühlwasser aus einer porösen Betonschicht von unten in die Schmelze eingeführt wird. Es werden drei weitere Großexperimente mit nachbeheizten Schmelzen berichtet, die mit 800 kg Metall- und Oxidschmelze von anfangs 1900 °C durchgeführt wurden. Untersucht wird in einem Experiment das Verhalten eines 1-dimensionalen, zentralen Ausschnitts aus einer reaktortypischen Geometrie. Bei zwei weiteren Experimenten wird auch der Einfluss der seitlichen Berandung mit einbezogen. Nach Erosion des Opferbetons beginnt mit der passiven Wassereinströmung die starke Kühlung der Schmelze. Die Ergebnisse der Experimente werden in ihren wesentlichen Punkten diskutiert. Obwohl die Schmelze bei geeigneter Dimensionierung der Opferschichten und der Kühlwassermenge durch den wasserführenden Porösbeton gestoppt und gekühlt wird, sind die Gleichmäßigkeit der Durchströmung und der Fragmentierung der Schmelze durch das Kühlwasser zum Teil nicht befriedigend. Hier ist eine Verbesserung des CometPC-Kühlkonzepts wünschenswert, damit die gute Porosität und Kühlbarkeit der Schmelze erreicht wird, wie sie sich beim ursprünglichen COMET-Konzept unter Verwendung eines optimierten Feldes von Strömungskanälen ergibt.

In weiteren transienten Experimenten werden Fragestellungen zu speziellen Unfallabläufen für die CometPC-Kernfängerkonstruktion untersucht. In dem hier untersuchten Szenario wird die Niederdruckeinspeisung des Primärkreises wieder in Gang gesetzt, als sich die Schmelze im Ausbreitungsraum gleichmäßig verteilt hat. Über den zerstörten RDB wird so der Ausbreitungsraum und damit die Schmelze langsam geflutet. Es stellt sich die Frage, ob sich Krusten auf der Oberfläche der Schmelze ausbilden und ob dadurch die Fragmentation der Schmelze bei Wasserzutritt von unten behindert wird. Die durchgeführten Experimente zeigen, dass bei einer Überflutung der Schmelze mit Ausbildung einer Kruste die Schmelze durch Wasserzutritt von unten dennoch fragmentiert wird und die Wasserzutrittsraten vergleichbar mit früheren Experimenten sind. Theoretische Abschätzungen, die mit dem Computerprogramm WECHSL durchgeführt wurden, zeigen eine befriedigende Übereinstimmung mit den Experimenten. Bezogen auf den Reaktorfall zeigen die Rechnungen, dass in dem möglichen Zeitrahmen der Betonerosion

die Schmelze keine Kruste bei Überflutung ausbildet, so dass dieses Szenario für die Kernfängerkonstruktion unkritisch ist.

1. Einführung

Bei einem unterstellten Kernschmelzenunfall mit langfristigem Ausfall der Kühlung kann die Kernschmelze auf Grund ihrer Nachwärmeleistung den Reaktordruckbehälter durchschmelzen und auf das Fundament des Reaktorgebäudes austreten. Weltweit werden verschiedene Kühlmöglichkeiten untersucht, um einen weitergehenden Angriff des Fundaments zu begrenzen. Eine Überflutung der Schmelze mit Kühlwasser allein von oben kann nach bisherigen Untersuchungen das Vordringen der Schmelze in den Beton nicht stoppen, da sich eine weitgehend stabile Oberflächenkruste ausbildet, die ein weiteres Eindringen des Kühlwassers in den zentralen Bereich der Schmelze und damit eine auch in der Tiefe wirksame Kühlung und Erstarrung der Schmelze verhindert.

Im Gegensatz hierzu wird bei dem hier berichteten Vorhaben Kühlwasser von unten in die Schmelze eingeführt. Dies geschieht beim COMET-Konzept durch rein passive Maßnahmen, nachdem die Schmelze zunächst eine Opferschicht von Beton erodiert und damit Zutrittskanäle für das Kühlwasser geöffnet hat. Durch die schnelle Verdampfung des eindringenden Wassers in der Schmelze bricht die Schmelze in ein poröses, wasserdurchlässiges Bett auf, so dass große innere Oberflächen entstehen, über die die Wärme kurz- und langfristig sicher abgeführt werden kann. Diese sehr wirksame Wärmeabfuhr lässt die Schmelze schnell erstarren, so dass die angrenzenden Strukturen auf sehr niedrigen Temperaturen bleiben.

In dem ursprünglichen COMET - Kühlkonzept erfolgt der Zutritt des Kühlwassers über diskrete Kühlkanäle, die als Plastikröhrchen in einem quadratischen Raster mit 80 mm Kantenlänge angeordnet sind. Die Wirksamkeit der Kühlung unter verschiedenen Aspekten konnte experimentell nachgewiesen werden, und der Einsatzbereich der Kühleinrichtung wurde ermittelt [1].

In einer Variante dieses Kühlkonzepts, die zur Zeit weiter entwickelt wird und die mit CometPC (= Comet Porous Concrete) bezeichnet wird, wird das Feld der vorbereiteten Kühlkanäle durch eine wasserführende, poröse Betonschicht ersetzt. Experimente mit sehr heißen Thermitschmelzen von Anfangstemperaturen um 1900 °C haben zunächst in transienten Experimenten die gute Kühlbarkeit bestätigt. Zwei Experimente mit nachbeheizten Schmelzen, die im Jahre 1999 durchgeführt und berichtet wurden [2], haben die hohe Stabilität der wasserführenden, porösen Betonschicht nachgewiesen, was zum zuverlässigen Stop der Schmelze führt. Punkte, die einer weiteren Klärung und

eventueller Verbesserungen bedürfen, betreffen die Gleichmäßigkeit der Durchströmung der Schmelze und die geeignete Zutrittsrate des Kühlwassers.

Die Kühlwassermenge kann bei diesem Konzept, außer durch die Höhe des Wasserreservoirs, durch die Porosität des Betons in gewissen Grenzen gewählt werden. Als günstig im Hinblick auf das Erreichen gleicher Kühlungsbedingungen wie beim ursprünglichen Kühlkonzept wird eine Auslegung der Durchlässigkeit der Porösschicht entsprechend 1 – 2 Liter Wasser / m^2 s angesehen, wobei der treibende Überdruck des Wassers 0,1 bar beträgt. Mit dieser Auslegung erfolgten im Jahre 2000 drei weitere Großexperimente mit simulierten, nachbeheizten Kernschmelzen mit Anfangstemperaturen von 1900°C.

Abbildung 1 zeigt den schematischen Aufbau der Kühlanordnung. Dabei wurde aus den Erfahrungen der vorhergehenden Experimente eine Schicht von Keramik-Kacheln eingefügt, die den Einstrom des Kühlwassers nach Erosion der Opferschicht verbessern soll. Diese Kacheln sind nur leicht am Porösbeton befestigt, und werden durch das Fugenmaterial am Ort gehalten. Sie versagen beim Angriff der heißen Schmelze im wesentlichen durch Bruch und geben damit den Kühlwasserstrom frei, ohne dass Schmelze die Oberfläche des porösen Betons blockiert.

Abbildung 2 stellt den integrierten Versuchsaufbau für die Großexperimente mit Simulation der Nachwärme dar, mit dem umschließenden Versuchstiegel und der Induktionsspule, die sich unterhalb der Kühleinrichtung befindet und mit der die Nachwärme in der Schmelze erzeugt wird.

Die Induktionsspule wird durch Jochbleche getragen, die das magnetische Wechselfeld bündeln und so führen, dass der metallische Teil der Schmelze möglichst gleichmäßig geheizt wird. Ein Teil der Jochbleche war durch Korrosion so geschädigt worden, dass sie zum Ende des letzten Experiments im Jahre 1999 einen magnetischen Kurzschluss verursachten und durch aufwendige Reparaturmaßnahmen ersetzt werden mussten. Inbetriebnahmetests nach der Reparatur im Frühjahr 2000 haben bestätigt, dass die Induktionsheizung ihre spezifizierten Werte wieder erbringt.

2. CometPC - Experimente mit Nachwärmesimulation

2.1 CometPC-H3

Das Experiment CometPC-H3 ist das erste Großexperiment nach Reparatur der Induktionsspule. Im Hinblick auf einen sicheren Betrieb der Spule und damit eine sichere und gleichmäßige Beheizung der Schmelze wurde daher das Experiment in 1-dimensionaler Geometrie so ausgelegt, dass extreme Anforderungen an die Beheizung

nicht gestellt wurden. Dazu wurde der Abstand zwischen beheizter Schmelze und Induktionsspule so gering wie möglich gehalten. Dies geschieht durch Verringerung der Höhe der porösen, wasserführenden Betonschicht von 15 auf 10 cm und durch eine niedrigere Betonopferschicht (5 cm anstatt früher 10 cm). Dadurch werden ein früher Wasserzutritt und Beginn der Kühlung bereits 5 min nach Einguss der Schmelze erwartet.
Das Experiment verwendet eine erhöhte Schmelzenmasse von 800 kg (400 kg Fe mit einem Ni-Anteil von 15 %, 400 kg Al2O3 mit CaO) mit einer Anfangstemperatur von 1900 °C. Die Höhe der Schmelze ohne erodierten Beton beträgt 32 cm, davon 9,3 cm Metall unten und 22,5 cm Oxid oben. Die Beheizung des Experiments war bis nach Erreichen der vollen Erstarrung der Schmelze mit 300 kW netto geplant, was jedoch nicht voll realisiert werden konnte. Damit entsprechen die Versuchsdaten den typischen Bedingungen in einem Kernschmelzenunfall, die in einem 1-dimensionalen Ausschnitt einer reaktortypischen Situation nachgebildet sind.
Die erste Phase des Experiments ist durch die trockene, relativ gleichmäßige Erosion des Opferbetons charakterisiert (Abbildung 3). Die dabei auftretende, anfängliche Erosionsrate von 0,17 mm/s ist typisch für den Angriff durch eine Stahlschmelze bei Temperaturen um 1700 °C, wie sie auch von Eppinger et al. in den KAPOOL-Experimenten ermittelt wurde [3]. In dieser Phase kühlt die Temperatur der Schmelze rasch ab, so dass etwa die Erstarrungstemperatur der Stahlschmelze erreicht wird.
Nach 235 s ist die Schmelze so weit nach unten vorgedrungen, dass die Schicht der Kacheln im Osten der Kühlfläche erreicht wird, der Kühlwasserzutritt von unten einsetzt und sehr schnell eine Einströmrate von 1,3 l/s erreicht (Abbildung 4). Die hohe Einströmrate lässt darauf schließen, dass die Oberfläche der Porösschicht für den Wasserdurchtritt weitgehend freigelegt ist. Das zunächst vollständig verdampfende Wasser führt zu einer Kühlrate von nahezu 3 MW, entsprechend einer Kühlleistung von 4,5 MW/m² (Abbildung 5), und liegt damit um den Faktor 10 über dem Nachwärmeniveau. Die Einströmrate des Kühlwassers bleibt zunächst auf hohem Niveau und nimmt erst dadurch langsam ab, dass nach Überfluten der Schmelze der Wasserstand im Tiegel ansteigt und damit die wirksame Druckdifferenz des Flutwassers geringer wird (1,0 l/s bei 700 s).
Das in der Schmelze verdampfende Kühlwasser verursacht eine starke Durchströmung und Durchmischung der Schmelze. Es werden jedoch nur kleinere Schmelzepartikel von wenigen cm Größe aus der noch sehr dünnflüssigen Schmelze hochgeworfen. Trotz des hohen Wasserzutritts kommt es auch nicht zum Hochschleudern größerer Schmelzemassen, wie sie durch schnelle Verdampfung größerer, zusammenhängender Wassermengen entstehen könnten, da der Eintritt des Wassers aus dem Porösbeton in die

Schmelze verteilt über die Fläche erfolgt und sich daher keine größeren, zusammenhängenden Wassermengen bilden können. Demzufolge gibt es auch keinen messbaren Druckanstieg im Versuchstiegel, und Druckpulsationen durch kohärente Verdampfungsvorgänge treten nicht auf.

Bereits nach 280 s, also schon 45 s nach Einsetzen der intensiven Kühlung, ist die Schmelzenoberfläche teilweise von stark siedendem Wasser überflutet. Dabei sinkt auch der durch Verdampfung des Kühlwassers abgeführte Wärmestrom schnell auf etwa 500 kW. Abbildung 5 zeigt den Vergleich von durch Verdampfung abgeführten mit der in der Schmelze simulierten Nachwärme-Leistung. Ab 600 s ist jedoch die ermittelte Kühlleistung zu niedrig, da die Abgastemperatur 100 °C unterschreitet und die nun wesentliche Kühlung durch die unterkühlte Wasserschicht nicht berücksichtigt ist.

Im Zeitraum von 300 bis 360 s werden glühende Teile von oxidischer Schmelze durch vulkanartigen Auswurf in das Wasser ausgetragen. Dabei baut sich, wie die Nachuntersuchung zeigt, ein unregelmäßiger "Vulkankegel" über der zunächst ebenen, bereits erstarrten Oberfläche der Schmelze auf. Die Oberfläche der wasserbedeckten Schmelze wird ab 360 s fortschreitend dunkel, während die Schmelze in ihrem Inneren noch teilweise flüssig ist.

Bei 450 s steigt der Wirkungsgrad der Induktionsheizung, bei sonst gleichen Betriebsbedingungen der Induktionsspule, deutlich an, und zwar von zunächst 30 % auf ca. 50 %. Der Grund hierfür ist wahrscheinlich der Temperaturabfall der inzwischen zumindest in wesentlichen Teilen erstarrten Metallschmelze, die bei etwa 400 °C ferromagnetisch wird und dadurch wesentlich besser an das Induktionsfeld ankoppelt. (Für die vollständig auf Raumtemperatur abgekühlte Schmelze wurde nach dem Experiment ein Ankopplungswirkungsgrad von 55 % gemessen.) Zu diesem Zeitpunkt ist die Oberfläche der Oxidschmelze dunkel. Durch Einschalten der Beleuchtung im Tiegel wird die stark siedende Wasserschicht über der Schmelze sichtbar. Man sieht zum Teil noch geringen vulkanischen Austrag von (oxidischer) Schmelze im Osten, der nach 510 s endgültig beendet ist. Durch entsprechende Änderung der Induktorspannung wird die Nachwärmeleistung in der Schmelze auf etwa 300 kW gehalten.

Der Wasserstand im Zentralbereich des Tiegels über der Schmelze steigt stetig an und erreicht nach 13 Minuten (780 s) die Oberkante der Keramikringe (120 cm über Porösbeton). Dies vermindert den Überdruck des Flutwassers, und daher sinkt seine Einströmrate unter 1 l/s (Abb. 4).

Die kontinuierlich beheizte Schmelze hat damit in der Zeit von 450 s bis 720 s, als eine unerwartete Induktorabschaltung erfolgt, den folgenden, nahezu stabilen Zustand erreicht:

Das Vordringen der Schmelze ist durch den porösen Beton gestoppt, von dem maximal 5 mm erodiert sind. Bis auf ein Thermoelement, das bei – 5 mm durch schwache Erosion zerstört wurde, zeigen alle übrigen Thermoelemente im Porösbeton Temperaturen unter 100°C. Durch das von unten eindringende Kühlwasser und Überflutung der Oberfläche der Schmelze ist die Schmelze unten und oben erstarrt. Im inneren sind vermutlich Bereiche der Schmelze noch flüssig. Es werden noch geringe Mengen von Wasserstoff (Oxidation von Eisen durch Dampf), aber keine Aerosole freigesetzt. Die Leistung, die durch Verdampfen der Schmelze entzogen wird, entspricht etwa der Nachwärmeleistung.
Bei 720 s wird jedoch auf Grund eines fehlerhaften Kontrollsignals außerhalb des Versuchstiegels die Beheizung der Schmelze abgeschaltet und kann nicht wieder aktiviert werden. Die Kühlung der nun unbeheizten Schmelze wird durch weitere Flutung fortgesetzt. Dabei treten in der porösen, wasserführenden Betonschicht kurzfristig und lokal Temperaturen bis 650 °C auf, die allerdings, wie die Nachuntersuchungen zeigen, die Funktion des Porösbetons nicht verändern. Nach etwa 40 Minuten ab Einguss der Schmelze tritt im gefluteten Versuchstiegel kein Sieden mehr auf, da die Schmelze nur noch wenig Wärme abgibt. Der Versuchstiegel bleibt auch äußerlich völlig intakt.
Das Experiment hat, wie auch schon die vorhergehenden Experimente, den sicheren Stopp der Schmelze durch die poröse, wasserführende Betonschicht gezeigt. Durch das von unten eindringende Flutwasser (passiver Flutbeginn schon nach 4 Minuten) wurde die Schmelze bereits nach 4,7 Min auf ihrer Oberfläche überflutet und war nach 6 Minuten mit dunkler Kruste bedeckt. Nach 7,4 Minuten ist auch die Metallschmelze am Boden in wesentlichen Teilen erstarrt. Der Tiegelschnitt in Abbildung 6 zeigt allerdings, dass die Schmelze eine im Vergleich zu früheren Experimenten geringe Porosität aufweist. Daher war der Wärmeentzug insbesondere aus dem Inneren der Schmelze nicht so wirkungsvoll, wie dies in früheren Experimenten beobachtet wurde. Die Durchströmung der Schmelze mit Kühlwasser konzentriert sich im wesentlichen auf den Bereich des Vulkankegels, der sich im Nordosten der Kühlfläche ausgebildet hat. Damit sind andere Bereiche vorwiegend durch Kontakt mit Kühlwasser an Unter- und Oberseite der Schmelze gekühlt, was zur Ausbildung entsprechend erstarrter Krusten führt, die die zentrale, teilweise noch flüssige Schmelze einschließen. Trotz dieser heißen Bereiche war die Schmelze bis zur Abschaltung der Nachwärmeheizung sicher gekühlt. Leider konnte das Langzeitverhalten dieses Zustandes wegen der Fehlabschaltung der Induktionsheizung nicht untersucht werden.
Abbildung 7 zeigt den Blick auf die Oberfläche der porösen Betonschicht nach Abnehmen der erstarrten Schmelze. Man erkennt die lose aufliegenden, zum Teil zerbrochenen

Kacheln, die das Kühlwasser austreten lassen, da auch der Fugenbeton nicht mehr vorhanden ist. Im Osten der Fläche, wo keine Kacheln mehr vorhanden sind, erfolgte der erste Kontakt von Schmelze und Porösschicht. Hier ist die oberste Zone der porösen Betonschicht bis - 5 mm angeschmolzen und glasig erstarrt. Da die tiefer liegenden Zonen unverändert sind, ist die Funktion der wasserführenden Schicht nicht gefährdet. Die radialen Berandungen sind vollständig intakt und von der Schmelze nicht angegriffen.
Im Hinblick auf weitere Experimente folgt also, dass die Langzeitkühlung der Schmelze weiter zu untersuchen ist, und dass versucht werden sollte, die Homogenität der Kühlung zu verbessern.

2.2 CometPC-H4

Die spezielle Zielsetzung dieses Experiments ist die Kühlbarkeit der nachbeheizten Schmelze in einem Kühleinsatz, der erstmals auch einen seitlichen Angriff von Schmelze und entsprechende seitliche Kühlung zulässt. Abbildung 8 zeigt den verwendeten Kühleinsatz, bei dem auch die Seiten aus porösem, wasserführenden Beton gefertigt sind, die wiederum mit einer Schicht aus Opferbeton abgedeckt sind. Damit werden die Randzonen simuliert, wie sie in ähnlicher Weise in einem Reaktor gefertigt werden können. Ähnlich wie auf der Bodenplatte erfolgt die Kühlung durch Wasserzutritt von der Seite, nachdem lokal die Opferschicht abgetragen ist. In diesem Experiment ist die seitliche Opferschicht mit 4 cm weniger als halb so dick wie die 10 cm dicke Opferschicht am Boden, weil die Betonerosion vorwiegend nach unten erwartet wurde.
Das Experiment beginnt mit dem Einguss von 800 kg Schmelze, mit je 50 % metallischem und oxidischem Anteil und einer Anfangstemperatur von 1850 °C. Die Höhe der Schmelze ohne Gasanteil beträgt 35 cm. Die anfängliche Erosion des Opferbetons durch die Stahlschmelze erfolgt zunächst mit Erosionsraten bis 0,2 mm/s, und zwar sowohl nach unten, wie auch zur Seite. Dies hat zur Folge, dass die 40 mm dicke seitliche Opferschicht bereits lokal nach 180 s aufgeschmolzen ist und damit der seitliche Zutritt von Kühlwasser mit etwa 1 l/s beginnt, lange bevor die Kühlung von unten einsetzt. Dieses nicht erwartete Einsetzen der Flutung von der Seite ist für den weiteren Versuchsablauf entscheidend. Der Flutwasserstrom steigt bis 300 s auf 1,2 l/s, und fällt danach wegen des steigenden Wasserstands im Versuchstiegel langsam ab. Die mit 300 kW kontinuierlich beheizte Schmelze wird durch das nur von der Seite zutretende Kühlwasser jedoch nicht wirksam gekühlt: Das Wasser strömt zwischen Porösbeton und sich verkrustender Schmelze mit einer nur geringen Kühlwirkung nach oben und beginnt nach nur 300 s die Oberfläche der Schmelze zu überfluten. Dadurch bildet die oxidische

Oberfläche eine stabile Oberflächenkruste aus, die zwar die abströmenden Gase aus der weiter andauernden Betonerosion austreten lässt, aber gleichzeitig das Eindringen des Wassers von oben in die Schmelze verhindert.

Damit bleibt die Kühlung durch das Wasser auf den engen, seitlichen und oberen Bereich beschränkt, und die Erosion des Opferbetons am Boden setzt sich nahezu unbeeinflusst fort. Dies zeigt Abbildung 9, wo der Erosionsfortschritt an verschiedenen Stellen der ebenen Kühlfläche wiedergegeben ist. Die Streuung der Erosion an den verschiedenen Positionen weist auf Unebenheiten der Erosionsfront hin, die nach diesen Messungen etwa 20 mm betragen. Die Erosionsgeschwindigkeit im Zeitbereich 500 bis 1000s liegt bei 0,065 mm/s. Würde die gesamte simulierte Nachwärme in abwärts gerichtete Betonerosion umgesetzt, so wäre die Erosionsrate mit 0,11 mm/s etwa doppelt so hoch. Etwa die Hälfte der Nachwärme wird also nach oben oder zur Seite transportiert.

So wie die seitliche Flutung und die Überflutung der Oberfläche der Schmelze kaum einen erkennbaren Einfluss auf den Erosionsvorgang nach unten haben, verändern auch die kurzzeitigen vulkanischen Eruptionen, die nach 360 s über etwa 60 s Schmelzepartikel durch die Oberflächenkruste austreten lassen, die Kühlbarkeit nicht. Es bestätigen sich damit frühere Beobachtungen, dass allein durch Flutung von oben ein Stop der Betonerosion nicht erreicht werden kann.

Die Oberflächenkruste bleibt stabil, bis nach 20 Minuten die weiterhin flüssige Schmelze die horizontale, poröse Betonschicht erreicht (Position 0 mm in Abb. 9) und damit Kühlwasser von unten in die Schmelze eindringt. Die schnelle Verdampfung bricht daraufhin die Schmelze auf, und die Oberflächenkruste wird teilweise zerstört. Damit setzt über etwa 15 s eine heftige Eruption von oxidischer Schmelze ein, durch die etwa 1/3 des Oxids in das überschichtende Wasser ausgetragen wird. Heftiges Sieden lässt das Wasser stark aufwallen und führt kurzzeitig zu hoher Dampffreisetzung, durch die der Gasdruck oberhalb des Wassers kurzzeitig um 0,1 bar über den Umgebungsdruck steigt. Die ausgetriebene Schmelze erstarrt schnell als poröse Schicht auf der ursprünglichen Kruste. Das Vordringen der Schmelze nach unten wird nun durch die Kühlwirkung des Wasser führenden Porösbetons in größeren Bereichen gestoppt. Jedoch bleiben lokal Bereiche der Schmelze ungekühlt und dringen weiter nach unten in die poröse Betonschicht vor. Der Grund dafür ist vermutlich der niedrige Druckverlust für das Flutwasser zur seitlichen Berandung, der das zutretende Kühlwasser zum Teil nicht an die Schmelzfront und durch die Schmelze, sondern zur seitlichen Berandung strömen lässt. Nach langsam fortschreitender Erosion erreicht die Schmelze nach etwa 50 min (2955 s) die Ebene —80 mm, wo eine Sicherheitsinstrumentierung anspricht und die Induktionsheizung zur

Nachwärmeerzeugung abschaltet. Danach kühlt die Schmelze aus, ohne dass der äußere Tiegel angegriffen wird.

Abbildung 10 zeigt den senkrechten Schnitt durch die Kühleinrichtung mit der erstarrten Schmelze. Die untere Hälfte des Tiegels zeigt den porösen, wasserführenden Beton seitlich und am Boden. Im oberen Tiegel ist die Schmelze von einem Ring aus Magnesiumoxid gehalten. Während in der linken Tiegelhälfte die Schmelze auf dem feinporösen Beton gestoppt wurde, ist rechts das unerwartete Vordringen bis in den grobporösen Beton zu erkennen, wo dann die Sicherheitsabschaltung erfolgte. Sowohl der seitliche, wie auch der am Boden befindliche Opferbeton sind vollständig erodiert, so dass der Porösbeton freigelegt ist. Die auf dem Porösbeton erstarrte Schmelze mit einer Schichthöhe von 20 bis 28 cm hat außer einigen Rissen keine offene und eine nur geringe geschlossene Porosität, so dass eine Durchströmung der Schmelze kaum erfolgte. Das unten zugeführte Kühlwasser strömte überwiegend durch die seitliche Porösschicht, die eine hohe Wasserdurchlässigkeit durch Risse und einen Spalt zur erstarrten Schmelze aufweist. Diese Strömungsverhältnisse sind für das weitere Vordringen der Schmelze auch nach Kontakt mit dem unteren Porösbeton verantwortlich.

Über der kompakten Schmelze schließt sich eine große offene Kaverne von maximal 22 cm Höhe an, die eine zentrale Öffnung nach oben besitzt. Diese Kaverne enthielt den Teil der Oxidschmelze, der bei der starken Eruption nach 20 Minuten nach oben ausgetragen wurde. Dieses Material befindet sich jetzt als gut durchgängige, poröse Schicht auf der Kaverne. Gut erkennbar ist die Kruste, die den inneren Rand der oberen Kaverne bildet, und die die Begrenzung zum überschichtenden Wasser bildete, bevor die Eruption der Schmelze erfolgte. Sie ist etwa 2 cm dick, was der Wärmeleitdicke d bei einseitiger Wasserkühlung unter den vorliegenden Bedingungen entspricht, wie folgende Abschätzung zeigt:

$$d = \frac{\lambda \cdot \Delta T}{Q/A} = \frac{2\,\mathrm{W/m\,K} \cdot 1300\,\mathrm{K}}{150\,\mathrm{kW/1\,m^2}} = 0{,}017\,\mathrm{m}\,.$$

Dabei ist angenommen, dass, in Übereinstimmung mit der oben diskutierten Erosionsrate, 50 % der simulierten Nachwärme durch die Kruste nach oben in das Wasser abgeführt wurden.

Die Schlussfolgerungen aus diesem Experiment sind:

Die seitliche Berandung durch Porösbeton hat sich als sehr stabil erwiesen und ist damit für die Reaktorsituation geeignet.

Durch die falsche Reihenfolge der Flutung, d. h. seitliche Flutung vor Flutung von unten, werden aber eine ausreichende Fragmentierung und ein sicherer Stop der Schmelze

behindert. Ursache dafür sind zum einen die Ausbildung einer stabile Kruste auf der Oberfläche durch die frühe Überflutung der Schmelze vor Einsetzen der Flutung von unten, und zum anderen geänderte Strömungswege durch das Abströmen des Flutwassers in den seitlichen Bereich. Beides ist durch die Auslegung des Experiments bedingt und lässt sich durch richtige Dimensionierung der Dicken der Betonopferschicht vermeiden.

Das Experiment war - anders als geplant - über wesentliche Versuchsphasen ein Experiment, bei dem die Schmelze durch Wasseraufgabe von oben gekühlt wurde. Dabei wurde bestätigt, dass durch Ausbildung der stabilen Oberflächenkruste eine wirksame Fragmentierung und Kühlung der zentralen Schmelze verhindert werden. Auch vulkanische Eruptionen tragen wenig zur Kühlbarkeit bei, zumal sie zum Erliegen kommen, wenn sich nach einem gewissen Austrag von Schmelze ein Spalt zwischen Kruste und Schmelze gebildet hat. Hier ist aber zu erwähnen, dass im Hinblick auf reaktortypische Dimensionen von 6 m Durchmesser die Rolle von Krusten noch kontrovers diskutiert wird, wie dies z. B. bei den MACE Experimenten dokumentiert ist [4].

2.3 CometPC-H5

Dieses Experiment mit Nachwärmesimulation wurde konzipiert, um die in den beiden vorigen Experimenten aufgeworfenen Fragen zu klären. Diese sind (1.) die Homogenität und Langzeitkühlbarkeit der Schmelze und (2.) die Kühlung unter Einschluss der seitlichen Berandung. Der Aufbau entspricht daher dem 2-dimensionalen Kühleinsatz des Experiments CometPC-H4, jedoch wurde die seitliche Opferschicht mit 120 mm dicker ausgeführt als die 80 mm dicke Opferschicht am Boden (Abbildung 11), damit der Kühlwasserzutritt von unten beginnt. Eine zusätzliche Änderung betrifft eine wasserdichte Trennschicht zwischen der Porösschicht am Boden und an der Seite, die eine getrennte Wasserzufuhr für Boden und Seite ermöglicht, um den Bypass-Effekt der Kühlwasserströmung auszuschließen, wie er in H5 aufgetreten war. Der Überdruck des Wassers gegenüber der Schmelze beträgt wiederum 0,1 bar. Weiterhin ist die wasserführende, feinporöse Schicht aus Aluminiumoxid-Partikeln mit einem hochtemperaturfesten Binder hergestellt, die der zu erwartenden Temperatur der Stahlschmelze auch im flüssigen Zustand für eine ausreichende Zeit standhalten würde. Damit wird Zeit für eine weitergehende Fragmentierung und Verbesserung der Kühlbarkeit gewonnen, ohne dass die Schmelze weiter nach unten vordringt. Der folgende Bericht beschränkt sich bezüglich der experimentellen Darstellung auf die Fakten, wie sie Ende 2000 aus den Versuchsdaten ermittelt waren.

Zum Zeitpunkt null beginnt der Einguss von 800 kg Schmelze (358 kg Metall, 442 kg Oxid) mit einer Anfangstemperatur von 1890 °C. Zunächst erfolgt die trockene Erosion des Opferbetons mit der auch aus den anderen Experimenten bekannten Erosionsrate. Nach Abnahme der Übertemperatur der Schmelze zeigt sich wiederum, dass die Erosionsfront nach unten deutliche Unebenheiten aufweist, die durch ein lokal schnelleres Vordringen von einzelnen Bereichen der Schmelze verursacht sind und nach 700 s den Zutritt von Kühlwasser von unten her im mittleren Bereich der Bodenfläche auslösen. Die in die Schmelze einströmende Kühlwassermenge liegt bei 1 l/s und verursacht eine schnelle und großflächige Abkühlung der Schmelze, ihre vollständige Überflutung nach 810 s, und schließlich die Stabilisierung einer dunklen, gasdurchlässigen Oberflächenkruste auf der Oberseite der Schmelze bei 900 s, auf der sich weiterhin vom unten zuströmendes Kühlwasser ansammelt. Zu diesem Zeitpunkt ist die Kühlrate, vollständige Verdampfung des Wassers angenommen, um den Faktor 8 höher als die Nachwärmeleistung. Auslegungsgemäß tritt von der Seite her noch kein Kühlwasser zu.

Die Kühlung der weiterhin mit 300 kW nachbeheizten Schmelze führt jedoch zu diesem Zeitpunkt nicht zu deren vollständigen Erstarrung. Schwankungen der in die Schmelze eingekoppelten Induktionsleistung wie auch eine weiterhin geringe Wasserstofffreisetzung weisen darauf hin, dass ein Teil der Schmelze noch flüssig ist, da vermutlich der Kühlwasserzutritt nicht gleichmäßig über die Bodenfläche erfolgt. Ab 900 s fällt unerwartet der Kühlwasserstrom von 1 l/s stetig ab und nähert sich nach 1250 s Null. Eine mögliche Ursache hierfür ist die Umverlagerung noch flüssiger Schmelze, die dabei Strömungskanäle blockiert. Obwohl die Schmelze zu diesem Zeitpunkt von Wasser überflutet ist und das Vordringen der Schmelze durch die poröse, wasserführende Schicht gestoppt ist, würde ein Verlust der Kühlwasserströmung das Experiment in einer nicht absehbaren Weise beeinflussen. Daher wird vom Operator zum Zeitpunkt 1253 s der Überdruck des Flutwassers angehoben. Er steigt innerhalb von 15 s von 0,1 bar um 2 bar an, bis die Schmelze aufbricht und durch kurzzeitige Eruption ein wesentlicher Teil der Schmelze in die obere Wasserschicht ausgetragen wird, wo sie unter starker Dampffreisetzung schnell erstarrt. Der dabei oberhalb der Schmelze entstehende Gasdruck steigt kurzzeitig um 0,2 bar über den Umgebungsdruck an. Eine starke Wechselwirkung im Sinne einer Dampfexplosion findet also nicht statt.

Bei Aufbrechen der Schmelze wird der Überdruck des Flutwassers sofort wieder auf 0,1 bar abgesenkt. Die Flutrate liegt nun etwas über dem anfänglichen Wert von 1 l/s. Damit wird die Schmelze endgültig und vollständig kühlbar und ist daher langzeitig im erstarrten Zustand stabilisiert.

Die Beheizung der Schmelze wird über deren Erstarrung hinaus fortgesetzt, bis sie planmäßig nach 1 Stunde abgeschaltet wird. Zu diesem Zeitpunkt ist die untere Porösschicht nach den Temperaturmessungen kalt und nicht erodiert. Die seitliche Porösschicht trägt nicht zur Kühlung bei, da die Schmelze erstarrte, ohne die seitliche Betonopferschicht so weit zu erodieren, dass die dahinter liegende Porösschicht erreicht wurde.
Die Auswertung des Experiments wird im Jahr 2001 vervollständigt. Nach der bisherigen Analyse wurde eine gute und langzeitig sichere Kühlung und Erstarrung der Schmelze erreicht. Dafür war allerdings die Anhebung des Flutwasserdrucks in einer kritischen Phase des Experiments wesentlich. Wie sich das Experiment ohne diesen ursprünglich nicht geplanten Eingriff verhalten hätte, kann nicht abgeschätzt werden.

2.4 Ausblick

Die Kühlungsexperimente mit Wasserzufuhr durch eine poröse Betonschicht weisen auf Grund der neueren, großskaligen Experimente, bei denen die Schmelze entsprechend dem Nachwärmeniveau beheizt wird, die folgenden Aspekte auf:
Bei allen Kühlvorgängen verlaufen die Verdampfungsprozesse auch bei intensiver Kühlung so langsam, dass die Gasdrücke oberhalb der Schmelze nahe Umgebungsdruck bleiben. Dies gilt sowohl für das in die Schmelze eindringende Wasser, wie auch für Schmelze, die über Eruptionen in Wasser ausgetragen wurde. Insbesondere treten keine Vorgänge ähnlich zu Dampfexplosionen auf.
Die wasserführende, poröse Betonschicht hat eine sehr gute Stabilität gegen den seitlichen Angriff von Schmelze. Durch ausgedehnte Schmelzen kann jedoch in seltenen Fällen die horizontale Porösschicht lokal angegriffen werden, wenn die Zuströmung des Wassers an die Unterseite der Schmelze behindert ist. Die Möglichkeit hierzu scheint dann zu bestehen, wenn sich der Kühlwasserstrom auf wenige Strömungswege konzentriert und dadurch andere Bereiche im Porösbeton nicht ausreichend durchströmt werden.
In allen Experimenten ist die Durchströmung der erstarrenden Schmelze weniger gleichmäßig als bei dem ursprünglichen COMET-Konzept, bei dem die Verteilung des Wassers durch die einbetonierten Plastikkanäle in gewisser Weise vorgegeben ist. Die Ausbildung nur weniger Strömungskanäle in der Schmelze hängt vermutlich damit zusammen, dass die Homogenität der porösen Betonschicht keine diskreten Strömungskanäle vorgibt, ein Zufallsprozess aber wenige Kanäle bevorzugt.
In der Mehrzahl der Experimente ist die Kühlung der Schmelze trotz der erwähnten Inhomogenitäten gesichert. Die Folgen der nicht gleichmäßigen Durchströmung der

Schmelze sind eine langsamere Abkühlung von gewissen Bereichen der Schmelze. Unter ungünstigen Bedingungen kann es jedoch zu einer späteren Umverlagerung von Restschmelze kommen, die einen weiteren, ausreichenden Wasserzutritt blockieren kann.
Im Hinblick auf die in der Reaktoranwendung notwendige seitliche Berandung ist sicherzustellen, dass die Flutung der Schmelze durch Wasserzustrom von unten beginnt. Dies gelingt durch geeignete Wahl der Höhen des Opferbetons.
Als "Nebenergebnis" wurde bestätigt, dass allein durch Flutung von oben die Schmelze nicht gestoppt werden kann, weil eine stabile Oberflächenkruste das Eindringen von Wasser verhindert und Eruptionen von Schmelze bald zum Erliegen kommen.

Die oben angesprochenen, noch offenen Fragen erfordern eine Verbesserung des Kühlkonzepts. Wichtig ist eine gleichmäßigere Durchströmung der Schmelze, um eine homogenere Porosität und Erstarrung zu erzielen und Umverlagerungen von Schmelze auszuschließen. Möglichkeiten hierzu bieten eine Erhöhung des Zulaufdrucks des Flutwassers und die Segmentierung der porösen Schicht.

3. Versuchsserie CometPC-T 3

3.1 Einleitung

In diesen weiteren, transienten Experimenten werden Fragestellungen zu der CometPC Kernfängerkonstruktion untersucht, die sich aus möglichen speziellen Unfallabläufen ergeben. Den hier dargestellten Versuchen liegt folgendes Szenario im Kernschmelzenunfall zu Grunde: Nach einem Kernschmelzenunfall mit Versagen des RDB hat sich die Schmelze zunächst in der Reaktorgrube gesammelt, nach einiger Zeit versagt das Tor und die Schmelze breitet sich im Ausbreitungsraum aus. Damit beginnt die Erosion der Betonopferschicht, die ca. 10 min andauert. Prinzipiell besteht die Möglichkeit, dass die Niederdruckeinspeisung zu einem beliebigen Zeitpunkt wieder in Gang gesetzt werden kann. In diesem Szenario wird zu Grunde gelegt, dass dies gerade zu dem Zeitpunkt erfolgt, als die Schmelze in dem Ausbreitungsraum ausgebreitet ist. Damit wird über den zerstörten RDB und die Reaktorgrube der Ausbreitungsraum geflutet und somit die Schmelze überflutet. Eine Pumpe der Niederdruckeinspeisung kann dabei maximal 450 m^3/h fördern. Bezogen auf die Gesamtfläche des EPR Ausbreitungsraumes würden die 4 Pumpen 0.5 m^3/s auf 170 m^2 liefern, entsprechend 0.74 $l/s\ m^2$.
Damit ergibt sich für die Schmelze folgender Zustand: Durch die Betonerosion ist die Schmelze gasgerührt, aber der Wasserzutritt von unten hat noch nicht eingesetzt, die Schmelze ist also im Inneren noch flüssig. Durch die Flutung von oben wird sich dann

zunächst eine Wasserüberschichtung ergeben. Setzt anschließend der Wasserzutritt von unten ein, ist zu untersuchen, ob sich eine Kruste ausbilden kann und ob die Kruste gasdurchlässig bleibt. In diesem Fall kann zumindest der entstehende Dampf abströmen. Eventuell wird aber die Kruste auch wieder aufbrechen und die Fragmentation der Schmelze in ähnlicher Weise ablaufen wie in den bisherigen Experimenten beobachtet.
Diese Fragestellungen sollen in dem transienten Versuchsaufbau der CometPC-T 3 Serie untersucht werden. Die Schwierigkeit dieser Versuchsserie besteht darin, dass der Zeitraum der Betonerosion klein ist bei diesen transienten Experimenten. Diese kurze Zeit der Betonerosion muss genutzt werden, um die Schmelze zu überfluten bzw. auf der Schmelze die gewünschte Kruste zu erzeugen.
Parallel zu der Versuchsserie wurden Rechnungen mit dem Computercode WECHSL [5] durchgeführt, um Abschätzungen über die Temperaturen der Schmelze bei Überflutung während der Betonerosion zu erhalten.

Versuchsaufbau

Der Versuchsbehälter wird von der Versuchsserie der CometPC-T 2 Experimente [2] übernommen, siehe Abbildung 12. Es ist ein rechteckiger Behälter mit einer Grundfläche von 250 x 500 mm, d.h. 0.125 m². In 400 mm Höhe schließt sich auf einer Seite eine Rampe mit einem Winkel von 20 ° gegenüber der Horizontalen an. Der Behälter hat eine Gesamthöhe von 600 mm und ist mit Hochtemperaturisolationsmaterial ausgekleidet. Die unterste Schicht in dem Behälter besteht aus dem grobporösen Beton von 20 mm Höhe. Die Wasserzuführung erfolgt in diese Betonschicht. Anschließend folgt der feinporöse Beton von 100 mm Höhe zur Einstellung der Durchflussmenge. Die Porosität in dem feinporösen Beton beträgt ca. 10 %. Nach oben schließt sich die Betonopferschicht von 30 mm Höhe mit Keramikfliesen als Zwischenschicht an. In die Betonopferschicht sind 9 TE vom Typ NiCr/Ni eingesetzt, um die Erosionsfront zu detektieren. Zusätzlich werden in dem porösen Beton an 2 Stellen die Temperaturen gemessen.
Die Schmelzenmasse von ca. 160 kg besteht wie in den bisherigen Experimenten aus Thermit mit CaO Zugabe von 26 % bezogen auf die Gesamtmasse. Die Massenanteile sind damit: 65 kg Eisen und 95 kg Oxid, davon 53 kg Al_2O_3 und 42 kg CaO.
Die Wasserzuführung für den Wasserzutritt von unten erfolgt aus einem nachbespeisten Vorratsbehälter. Der Wasservordruck beträgt 0.1 bar, die Wasserzutrittsrate wird über einen Wasserzähler gemessen. Das Wasser für das Fluten der Schmelze von oben wird auf eine Temperatur von ca. 80 °C geheizt, um die Bedingungen in dem Reaktorfall zu simulieren. Der Volumenstrom wird über ein Reduzierventil auf ca. 400 ml/s eingestellt

und entspricht damit dem Volumenstrom im Realfall bezogen auf die Fläche des experimentellen Aufbaus.

3.2 CometPC-T 3.1

Versuchsablauf

Nach der Zündung setzt zunächst die Thermitreaktion ein, die nach ca. 20 s beendet ist. Bedingt durch die Betonerosion ist die Schmelze anschließend stark bewegt und dünnflüssig. Durch die Gasfreisetzung ist das Volumen der Schmelze um ca. 1/3 größer als das kollabierte Volumen. Die Schmelze fließt damit auch auf die Rampe auf, es wird aber praktisch keine Schmelze ausgeworfen. Die Thermoelemente in der Betonopferschicht zeigen, dass die Schmelze etwa nach 1 min die ersten 10 mm erodiert hat, siehe Abbildung 13. Nach 1 min wird der Wasserzufluss von oben freigegeben. Damit setzt ein leichter Schmelzenauswurf ein, des weiteren kühlt die Schmelze auf der Rampe ab und wird dunkel. Die Schmelze in dem Behälter bleibt aber gasgerührt und stark bewegt. Nach 15 s wird der Wasserzufluss gestoppt, es befindet sich zu dieser Zeit Wasser auf der Oberfläche der Schmelze. 4 s später ereignet sich durch eingeschlossenes Wasser eine schwache Interaktion mit der Schmelze an der gegenüberliegenden Seite, wodurch geringe Schmelzenmengen ausgeworfen werden. Die Aufsicht auf die Schmelze wird nicht durch kondensierenden Dampf behindert, es sind keine Flammen mehr sichtbar. Die Schmelze ist immer noch stark bewegt und es haben sich keine Krusten gebildet. Deshalb wird nach 1:40 min der Wasserzulauf erneut geöffnet für 10 s. Damit fließen insgesamt 10 l Wasser auf die Schmelze. Es bildet sich eine Kruste auf der Rampe, aber innerhalb des Behälters bleibt die Schmelze gasgerührt ohne erkennbare Kruste. Wie das Versagen der Thermoelemente zeigt, ist etwa nach 1:50 min die Betonopferschicht erodiert. Es kann aber zu diesem Zeitpunkt kein Wasser von unten eindringen, da das Ventil noch geschlossen ist. Erst 2:05 min wird der Wasserzutritt von unten freigegeben. Ca. 5 s später setzt sichtbar der Wasserzutritt ein, Schmelze wird in ganz geringen Mengen als Sprühregen ausgetragen. Hauptsächlich am gegenüberliegenden Rand wird Dampf mit Wassertropfen ausgetragen. Die Schmelze kühlt sehr schnell ab und wird damit schnell zähflüssig. Nach 2:30 min ist die Schmelze auf der Rampe erstarrt, weitere 10 s später beginnt die Erstarrung der Schmelze auf der gegenüberliegenden Seite. Nach 2:50 min ist die Oberfläche der Schmelze komplett erstarrt, weiterhin ist aus der Öffnung an der gegenüberliegenden Seite eine starke Dampfabströmung mit Wassertropfen sichtbar.
Die Wasserzutrittsrate von unten beträgt ca. 250 ml/s, siehe Abbildung 14, und entspricht damit den bisher beobachteten Werten in diesem Versuchsaufbau.

Nachuntersuchungen

Aus dem Tiegelschnitt, siehe Abbildung 15, ist deutlich zu erkennen, dass Auskleidungsmaterial von ca. 20 mm Wandstärke in die Oxidschicht eingetragen wurde. Es sind Quader von 20 x 50 mm Schnittfläche zu sehen. Dies hat aber keinen Einfluss auf das experimentelle Ergebnis. Die erstarrte Schmelze zeigt praktisch keinen Unterschied zu vorhergehenden Experimenten. An 2 Stellen haben sich deutlich Abströmkanäle im Oxid gebildet. Das Metall zeigt von unten ebenfalls mindestens 2 Öffnungen. Im Oxid ist eine Strahlerweiterung zu erkennen mit kleinen Hohlräumen im unteren Bereich und großen Hohlräumen oben. Einer dieser Abströmkanäle liegt im Randbereich des Tiegels, d.h. hier sind Randeinflüsse nicht auszuschließen. Der andere Abströmkanal ist aber in dem Innenbereich des Versuchsbehälters, Randeinflüsse spielen hier keine Rolle. Damit unterscheidet sich das Schnittbild der Schmelze nicht von vorgehenden Experimenten, d.h. die Schmelze ist trotz der Wasseraufgabe von oben fragmentiert erstarrt und damit kühlbar.

3.3 Versuch CometPC-T3.2

Bezogen auf die Geometrie des Versuchsbehälters wurde der Volumenstrom in dem ersten Experiment an die maximal möglichen Bedingungen im Reaktor für den Fall des Wiederflutens angepasst. Aber die Zeiträume sind in den transienten Experimenten sehr viel kleiner. Im Realfall können ca. 10 min. lang, die Phase der Betonerosion bis der Wasserzutritt von unten einsetzt, die Pumpen Wasser auf die Schmelze in dem Ausbreitungsraum fördern. Deshalb werden in diesem Experiment die folgenden Änderungen vorgenommen: Die Wasserzutrittsrate von oben wird nach 60 s ab Zündung gestartet und 45 s lang weiter betrieben. Damit gelangen theoretisch 20 l Wasser auf die Schmelze mit einer Volumenstromrate von ca. 450 ml/s. Der Versuchsbehälter wird von dem CometPC-T 3.1 Experiment übernommen. Lediglich die Betonopferschicht wurde von 23 mm auf 28 mm Höhe vergrößert. Mit den Fliesen von 7 mm als Zwischenschicht ist damit die gesamte Opferschicht 35 mm hoch. Sie ist gegenüber dem ersten Experiment etwas erhöht, um den Zeitraum bis Wasserzutritt von unten einsetzt zu vergrößern.

Versuchsablauf

Die Thermitreaktion kommt zunächst nur schlecht in Gang, erst nach etwa 10 s setzt die Reaktion ein und ist nach 30 s beendet. Dann folgt die Betonerosion, nach etwa 100 bis 130 s sind die ersten 15 mm Beton erodiert, wie aus dem Versagen der Thermoelemente in der obersten Ebene zu erkennen ist, siehe Abbildung 16. Nach 70 s wird der

Wasserzulauf oben geöffnet. Dies ist 10 s später als geplant, trägt aber der verspätet einsetzenden Thermitreaktion Rechnung. Der Wasserzulauf oben wurde nach 45 s wieder geschlossen zum Zeitpunkt 1:55 min. Nach 2:10 wurde der Wasserzulauf unten geöffnet. Damit strömt zunächst eine kleine Menge in den Versuchsbehälter ein. Aber erst nach 2:47 min setzt der Wasserzutritt von unten ein, siehe Abbildung 17. Dies ist auch an dem heftiger bewegten Schmelzbad zu erkennen. Kleine Schmelzenmengen werden als Tropfen aus dem Versuchsbehälter ausgetragen. Die Wasserzutrittsrate steigt zunächst auf ca. 100 ml/s an und fällt ab 3:20 min wieder auf 10 ml/s bei 3:35 min. Anschließend steigt sie wieder an auf etwa 100 ml/s bis 4:45 min und steigt dann weiter auf 240 ml/s zum Zeitpunkt 6:20 min. Diese kleine Wasserzutrittsrate ist in anderen Experimenten nicht beobachtet worden. Offenbar wurde die Betonschicht nicht vollständig erodiert aufgrund der verzögerten Thermitreaktion und der hohen Flutrate von oben. Die gemessenen Temperaturen in der Opferschicht bestätigen dieses Bild. Erst nach 100 bis 120 s werden die ersten 15 mm Opferschicht erodiert. Genaueren Aufschluss bietet hier erst der Tiegelschnitt.

Nachuntersuchungen

An der Unterseite der Metallfläche sind mehrere Öffnungen zu sehen, die einen Durchmesser von ca. 5 mm haben. An einer Öffnung sind in der geschnittenen Metallschicht einige Poren zu sehen, darüber in der geschnittenen Oxidschicht ein Hohlraum von ca. 5 cm Länge und 2 cm Breite, siehe Abbildung 18, die sich weiter oben im Oxid fortsetzt. Auch wenn ein Teil des von unten zuströmenden Wassers über die Seiten abfließt, ist ein Anteil durch die Schmelze geströmt. Damit ist auch der Eintrag von Metall in das Oxid zu erklären und die insgesamt poröse Erstarrung. Der gemessene Volumenstrom des von unten zutretenden Wassers lässt erkennen: Nach 110 s wird das Ventil geöffnet, zu sehen an der ersten Spitze, die Opferschicht ist aber erst nach 170 s erodiert und der Wasserzutritt setzt ein. Anschließend schwankt der Wasserzutritt stark über einen Zeitraum von 120 s. Die Wasserzutrittsrate ist mit ca. 50 ml/s vergleichsweise gering. Erst nach 350 s bilden sich größere Kanäle aus, wodurch der Volumenstrom auf 250 ml/s ansteigt.

3.4 Versuch CometPC-T 3.3

Mit den Erfahrungen der ersten beiden Experimente dieser Serie wird das dritte Experiment durchgeführt mit folgenden Änderungen: Die Wasserzutrittsrate von oben wird nach 60 s ab Zündung gestartet und kontinuierlich weiter betrieben, bis der Wasserzutritt

von unten einsetzt. Die Volumenstromrate beträgt ca. 450 ml/s. Der Wasserzutritt von unten wird 2 min nach Zündung freigegeben, um einen zu früh einsetzenden Wasserzutritt von unten zu verhindern. Damit kann beobachtet werden, ob die Fragmentation der Schmelze auch bei stärker abgekühlter Oberfläche abläuft wie in den ersten beiden Experimenten beobachtet. Der Versuchsaufbau wird ansonsten von dem CometPC-T 3.2 Experiment übernommen.

Versuchsablauf

Der Versuch konnte planmäßig durchgeführt werden. Die Außentemperatur lag bei ca. 10 °C mit leichtem Regen, deshalb ist die Tiegelaufsicht durch Nebelbildung stark behindert. Nach der Zündung setzt sofort die Thermitreaktion ein, die nach ca. 20 s beendet ist. Die Oberfläche der Schmelze auf der Rampe wird etwa nach 50 s zähflüssig, sie ist aber noch nicht erstarrt. Mit 1:00 min wird die Futung der Schmelze gestartet, wodurch die Schmelze bereits ca. 10 s später vollständig überflutet ist. Wassertropfen werden ausgetragen, aber nur sehr wenig Schmelze. Anschließend ist durch kondensierenden Dampf keine Aufsicht auf die Schmelze mehr möglich. Nach 2 min wird der Wasserzutritt von unten freigegeben. Ab diesem Zeitpunkt strömt kontinuierlich Wasser in den Versuchsbehälter ein, da die Betonopferschicht offenbar nicht dicht ist, siehe Abbildung 19. Nach 2:55 min setzt der Wasserzutritt kurzfristig verstärkt ein, geringfügig wird dadurch Schmelze ausgetragen. Zu diesem Zeitpunkt wird auch das Thermoelement 1 gequencht, das 20 mm oberhalb der Wasserzutrittsebene in der Betonopferschicht angeordnet ist, siehe Abbildung 20. Die darunterliegenden Thermoelemente werden davon nicht beeinflusst. Es ist damit zu ersehen, dass die Opferschicht nicht vollständig erodiert wird. Ab 3:20 min bildet sich an einer Stelle ein Vulkan aus, der auch Schmelze aus dem Inneren austrägt. Dieser Vulkan ist 4:50 min nach Zündung wieder vollständig erloschen.

Nachuntersuchungen

Wie aus der Wasserzutrittsrate von unten zu erkennen, siehe Abbildung 19, ist in diesem Experiment die Betonopferschicht nicht dicht gegenüber dem zutretenden Wasser. Ab dem Zeitpunkt Ventil öffnen, 120 s, strömt damit kontinuierlich Wasser in den Tiegel von unten ein. Dies führt dazu, dass die Opferschicht nicht vollständig erodiert wird. Dies zeigen auch die Thermoelemente in der oberen Ebene der Betonopferschicht 20 mm über der Wasserzutrittsebene, siehe Abbildung 20. Kein Thermoelement kam in Kontakt mit der Schmelze. Deshalb ist dieses Experiment bezüglich des Fragmentierungsverhaltens nicht aussagekräftig. Auf der Oberfläche bildet sich eine Kruste aus, die den Kontakt des

Flutwassers mit der Schmelze verhindert. Deshalb bleibt die Schmelze im Inneren verglichen mit anderen transienten Experimenten lange flüssig. Nach 200 s kann Wasser über die seitliche Berandung in den entstandenen Hohlraum zwischen obenliegender Kruste und der Schmelze eindringen. Durch die Verdampfungsprozesse bildet sich damit ein Vulkan aus, der ca. 8 kg Schmelze nach oben verlagert (Abbildung 21), d.h. weniger als 10 % der gesamten Oxidmasse. Es werden keine heftigen Wechselwirkungen des Wassers mit der Schmelze beobachtet. Die Schmelzenmasse, die durch diesen Vulkanmechanismus fragmentiert wird, ist aber verglichen mit der Gesamtmasse der Schmelze von ca. 160 kg klein.

3.5 Theoretische Abschätzungen mit dem Computer Code WECHSL

Der WECHSL Computer Code [5] ist ein mechanistisches Rechenprogramm, das zur Analyse der thermischen und chemischen Wechselwirkung einer Kernschmelze mit Beton entwickelt wurde. Die Energie der Schmelze wird an den aufschmelzenden Beton und in den oberen Sicherheitsbehälter abgeführt. Für letzteres werden die thermische Strahlung oder das verdampfende Sumpfwasser, das die Schmelzenoberfläche möglicherweise überfluten kann, berücksichtigt. Dieser letztere Fall wird hier für die theoretischen Abschätzungen herangezogen. Es wurden die Stoffdaten der Simulationsschmelze mit einer Anfangstemperatur von 2200 K verwendet. Das Ergebnis nach 120 s, dem Zeitpunkt des Einsetzens des Wasserzutritts von unten, zeigt: Der Wärmestrom nach oben beträgt 285 kW/m² bei einer Pooltemperatur von 1759 K und einer Oberflächentemperatur von 1356 K. Damit bildet sich zu diesem Zeitpunkt eine Krustendicke von 7.1 mm aus, siehe Tabelle 1, was in guter Übereinstimmung mit den Beobachtungen des letzten Experimentes ist.

Tab. 1: Ergebnisse der Rechnungen mit WECHSL für die experimentellen CometPC-T Stoffdaten zu verschiedenen Zeitpunkten

Zeit [s]	Betonerosion [mm]	Wärmestrom [kW/m²]	Pooltemperatur [K]	Oberflächen-temperatur [K]	Krustendicke oben [mm]
20	16	381	1760	1518	0.6
60	19	287	1758	1360	6.6
90	21	284	1758	1354	7.0
120	22	284	1758	1354	7.1

Für die Anwendung auf die Reaktorsituation mit den gegebenen Stoff- und Temperaturdaten gilt: Es gibt keine Krustenbildung in dem möglichen Zeitfenster der Betonerosion von ca. 10 min, siehe Tabelle 2. Die realen Schmelzenmassen und die Nachzerfallswärme wurden berücksichtigt bei einer Anfangstemperatur von 2603 K. Das Ergebnis nach 600 s zeigt: Der Wärmestrom beträgt 471 kW/m² bei einer Pooltemperatur von 1740 K und einer Oberflächentemperatur von 1587 K. Damit bilden sich keine Krusten aus, da die Erstarrungstemperatur bei 1453 K liegt.

Tab. 2: Ergebnisse der Rechnungen mit WECHSL für den Reaktorfall zu verschiedenen Zeitpunkten

Zeit [s]	Betonerosion [mm]	Wärmestrom [kW/m²]	Pooltemperatur [K]	Oberflächen-temperatur [K]	Krustendicke oben [mm]
120	88	549	1809	1682	-
300	97	504	1777	1630	-
600	109	471	1740	1587	-
1800	120	129	1576	903	12.6

3.6 Schlussfolgerungen

Die durchgeführten Experimente und die begleitenden Rechnungen mit WECHSL lassen folgende Schlussfolgerungen zu: Bei einer massiven Überflutung der Schmelze können sich in den Experimenten Krusten auf der Oberfläche der Oxidschmelze ausbilden. Diese Krusten werden aber bei Einsetzen des Wasserzutritts von unten wieder aufgebrochen und es bildet sich ein Vulkan aus. Durch diesen Vulkan wird flüssige Schmelze aus dem Inneren an die Oberfläche ausgetragen. Ist die Überflutung kleiner, bilden sich keine Krusten an der Oberfläche. Die Fragmentation der Schmelze und die Volumenstromrate des von unten durch die Schmelze strömenden Wassers entsprechen den bisherigen Experimenten in diesem Versuchsaufbau. Die Ergebnisse der Rechnungen mit WECHSL für eine überflutete Schmelze zeigen mit den transienten Experimenten eine gute Übereinstimmung. Zum Zeitpunkt des einsetzenden Wasserzutritts von unten würde sich eine Kruste an der Oberfläche der Oxidschmelze von ca. 7 mm ausbilden, was den Beobachtungen aus dem letzten Experiment entspricht. Für die Übertragung auf die Reaktorsituation zeigen die Rechnungen, das sich in dem möglichen Zeitfenster von 10 min für die Überflutung keine Kruste ausbilden kann. Die Temperaturen an der Oberfläche der Schmelze liegen zu diesem Zeitpunkt immer noch über 100 K über der

Erstarrungstemperatur. Erst nach 1800 s hätte sich eine Kruste von ca. 1 cm ausgebildet. Damit zeigen die durchgeführten transienten Experimente und die begleitenden Rechnungen mit WECHSL, dass dieses Szenario für diese Kernfängerkonstruktion unkritisch ist.

4. Literatur

1. H. Alsmeyer, W. Tromm, The COMET Concept for Cooling Core Melts: Evaluation of the Experimental Studies and Use in the EPR, FZKA 6186, EXV-CSC(99)-D038, Oct. 1999
2. H. Alsmeyer, T. Cron, S. Schmidt-Stiefel, H. Schneider, W. Tromm, T. Wenz, C. Adelhelm, H.-G. Dillmann, H. Pasler, W. Schöck, H. Benz, C. Grehl, G. Merkel, W. Ratajczak, F. Ferderer, G. Schumacher, Thermischer Angriff durch Kernschmelzen und deren langfristige Kühlung: COMET-Konzept, in "Projekt Nukleare Sicherheitsforschung Jahresbericht 1999", FZKA 6480, August 2000, S. 256 -287
3. B. Eppinger, F. Fellmoser, G. Fieg, H. Massier, G. Stern, Experiments on Concrete Erosion by a Corium Melt in the EPR Reactor Cavity: KAPOOL 6-8, FZKA 6453, März 2000
4. M.T.Farmer, B.W.Spencer, D.J.Kilsdonk, R.W.Aeschlimann, Status of Large Scale MACE Core Coolability Experiments, in Proceedings of the OECD Workshop on Ex-Vessel Coolability, Karlsruhe, 1999, FZKA 6475, Mai 2000
5. JJ. Foit, M. Reimann, B. Adroguer, G. Cenerino, S. Stiefel: The WECHSL-Mod3 Code: A Computer Program for the Interaction of a Core Melt with Concrete Including the Long Term Behavior, Wissenschaftliche Berichte, Forschungszentrum Karlsruhe, FZKA 5522, 1995

Abbildungen

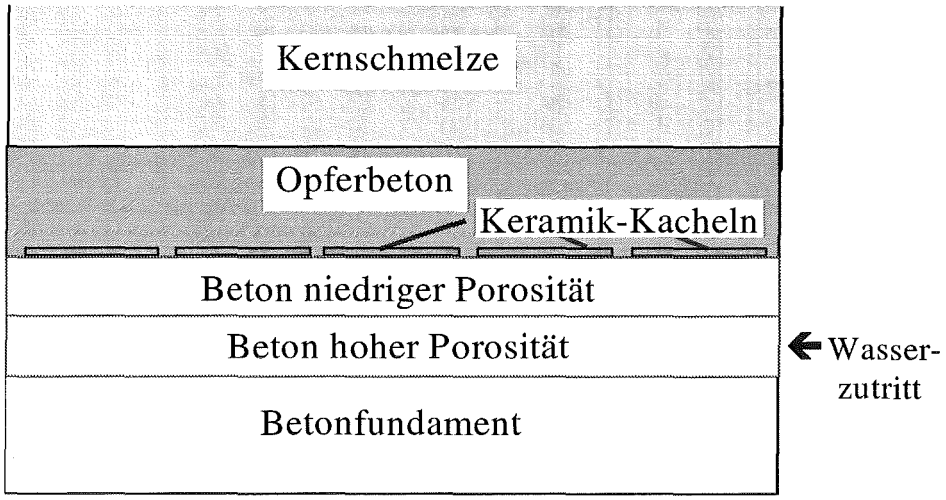

Abb. 1: Prinzip des CometPC - Kühlkonzepts zum Kühlwasserzutritt durch eine poröse Betonschicht

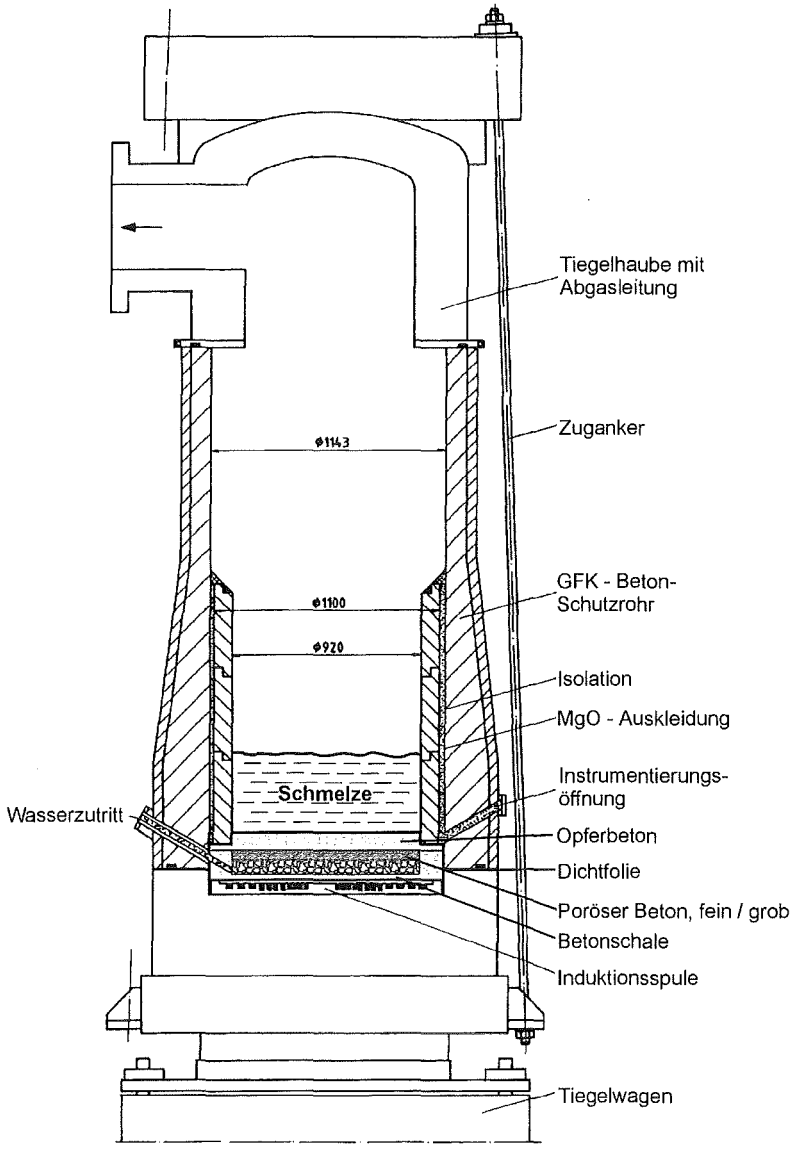

Abb. 2: Aufbau der CometPC Experimente mit Nachheizung der Schmelze durch Induktionsheizung

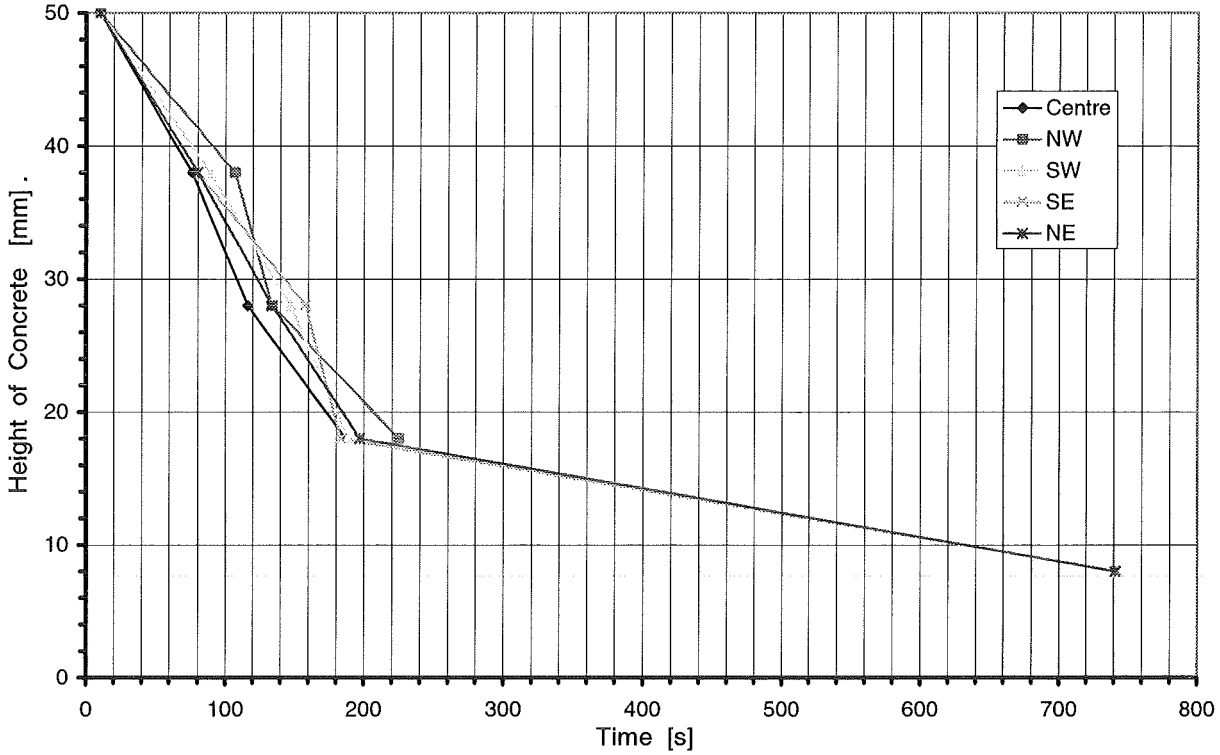

Abb. 3: Erosion der Betonopferschicht durch die Schmelze und Stop durch Einsetzen der Kühlung in CometPC-H3

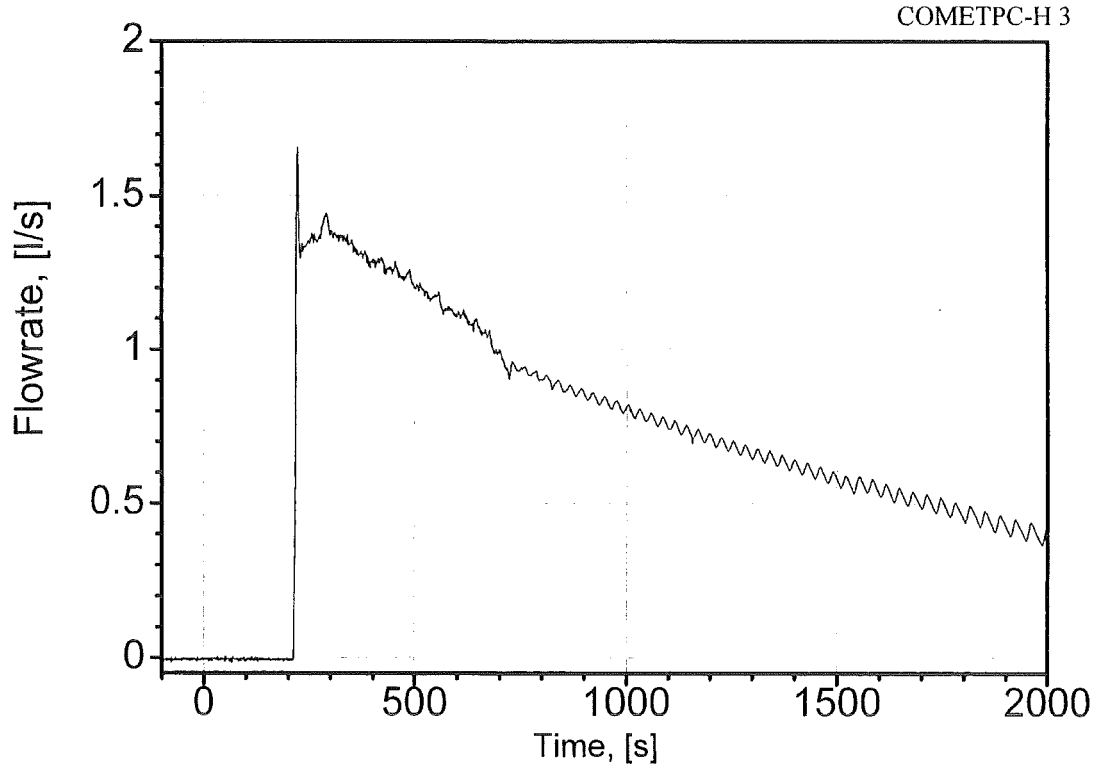

Abb. 4: Einströmrate von Kühlwasser in CometPC-H3

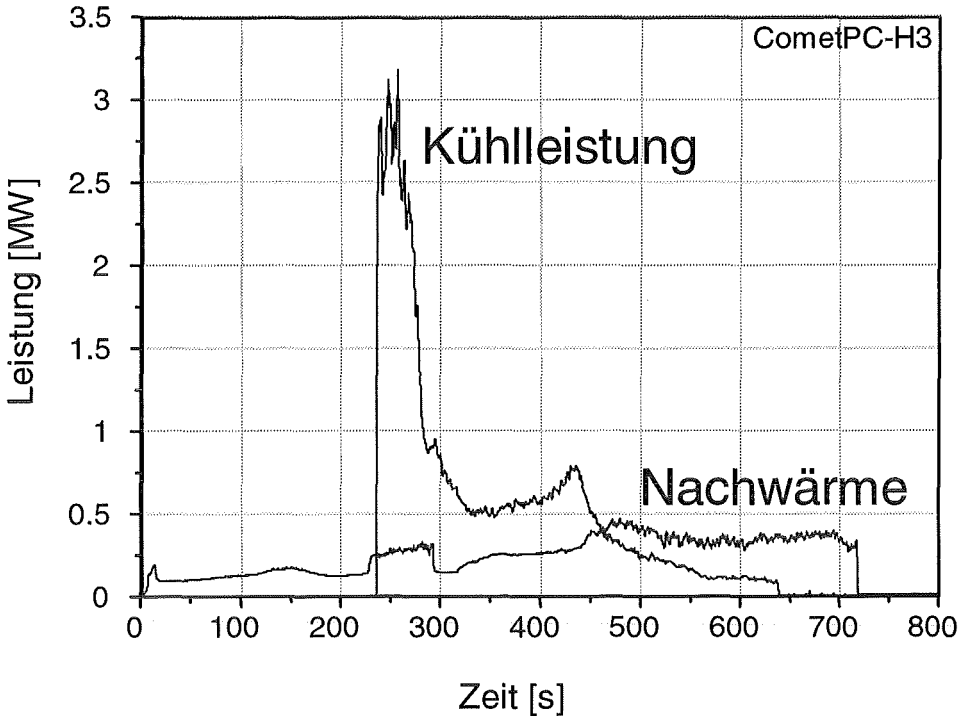

Abb. 5: Vergleich der simulierten Nachwärmeleistung und der durch Verdampfung abgeführten Kühlleistung in CometPC-H3

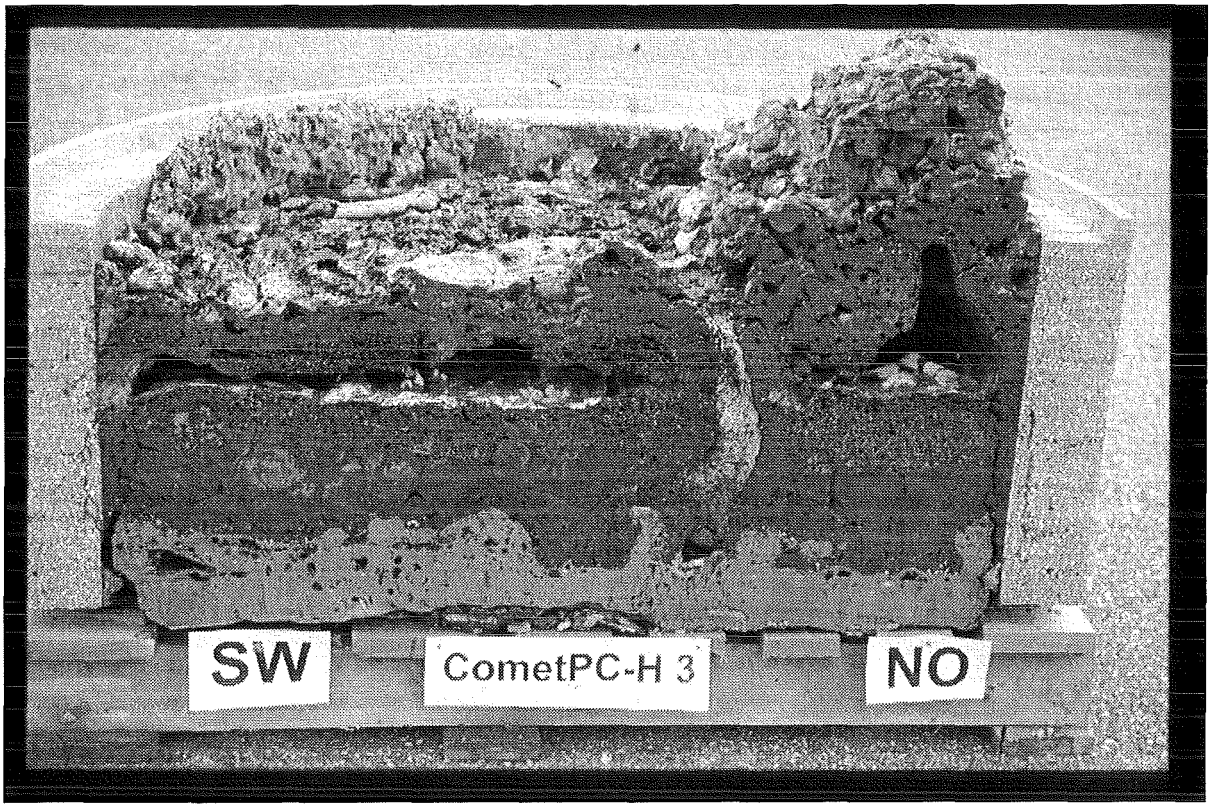

Abb. 6: Schnitt durch die erstarrte Schmelze in CometPC-H3

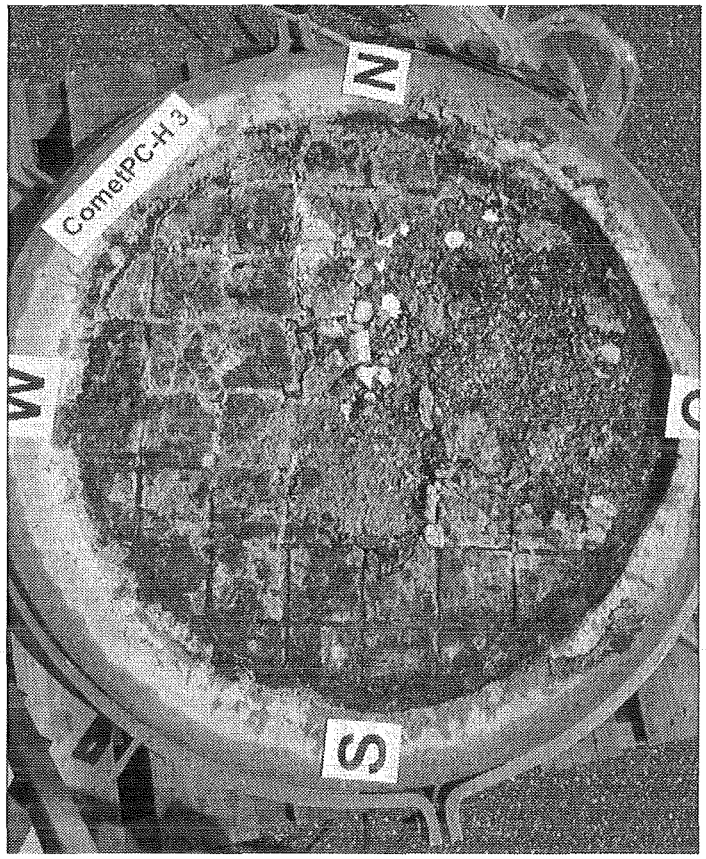

Abb. 7: Poröse Betonschicht mit lose aufliegenden Kacheln nach Abnehmen der erstarrten Schmelze in CometPC-H3

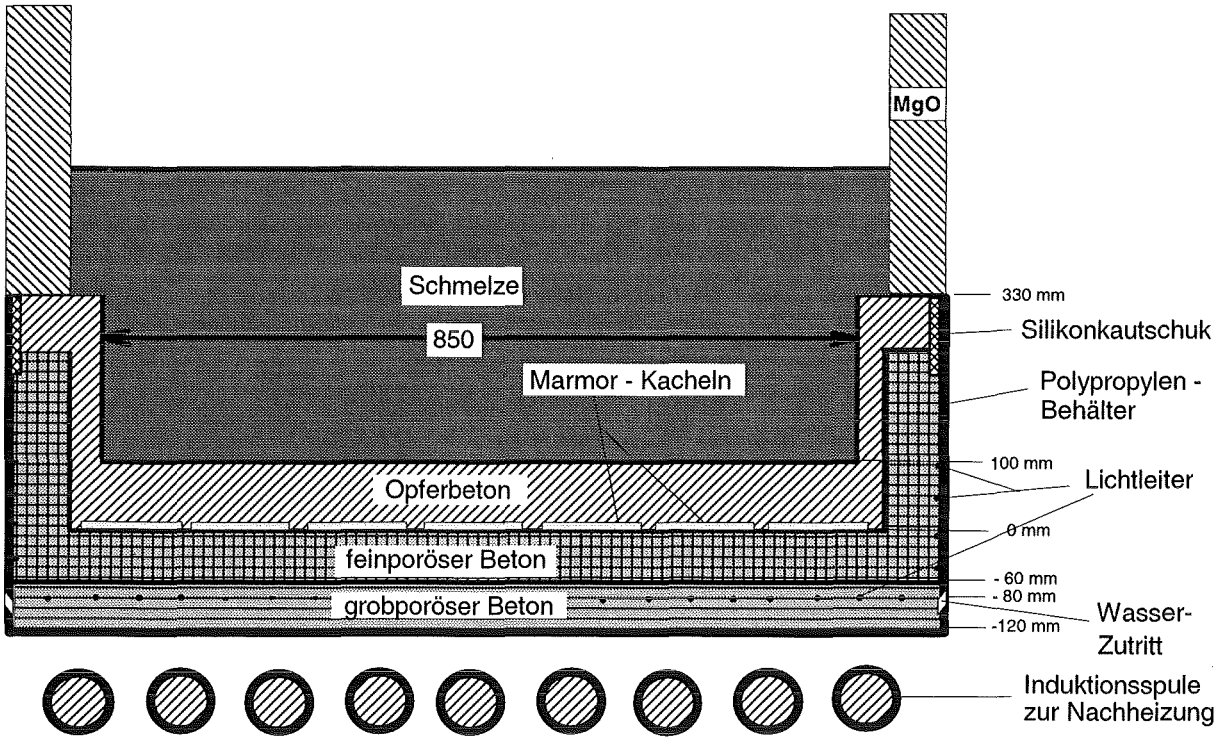

Abb. 8: Schematischer Aufbau des Kühleinsatzes unter Einschluss einer seitlichen Porösschicht in CometPC-H4

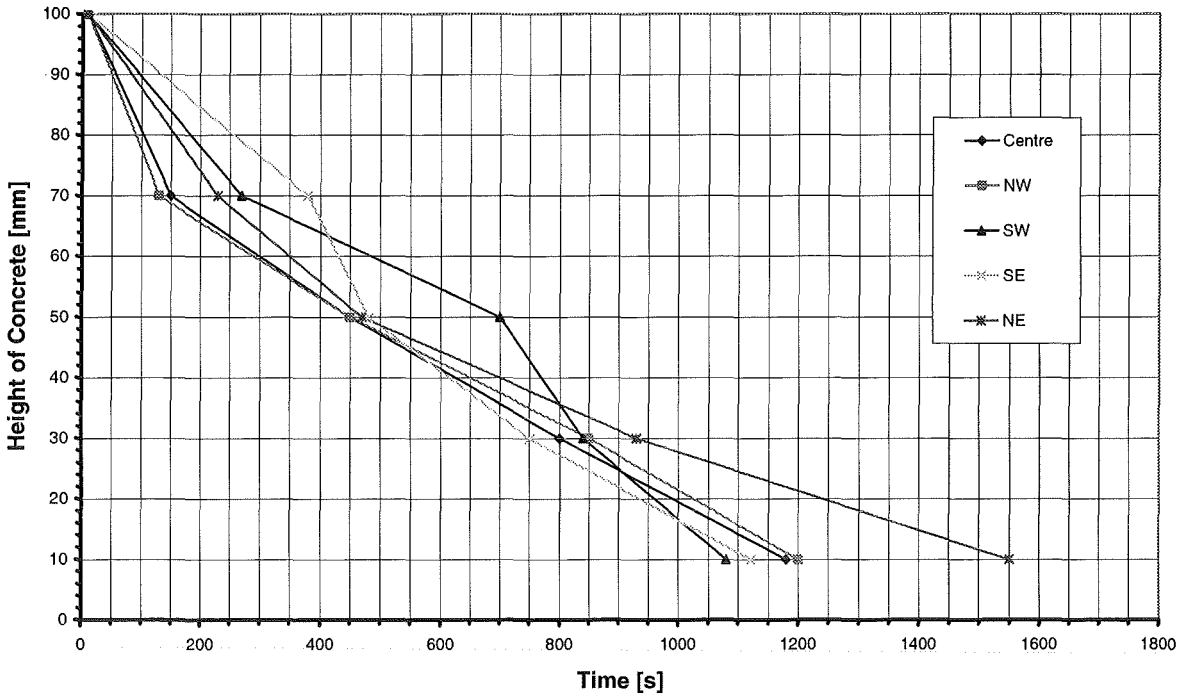

Abb. 9: Erosion der Betonopferschicht am Boden der Kühleinrichtung in CometPC-H4

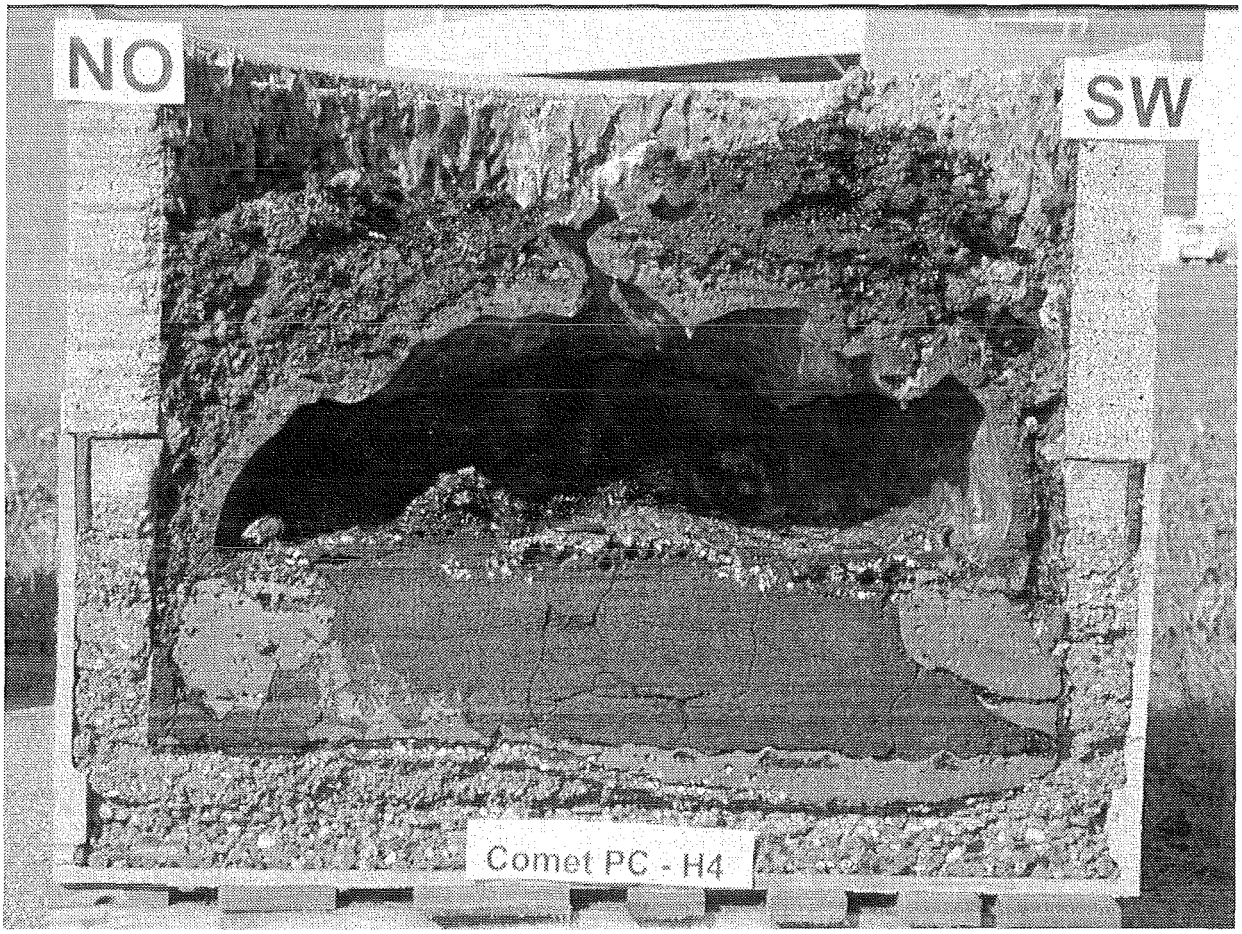

Abb. 10: Schnitt durch Versuchstiegel mit Schmelze in CometPC-H4

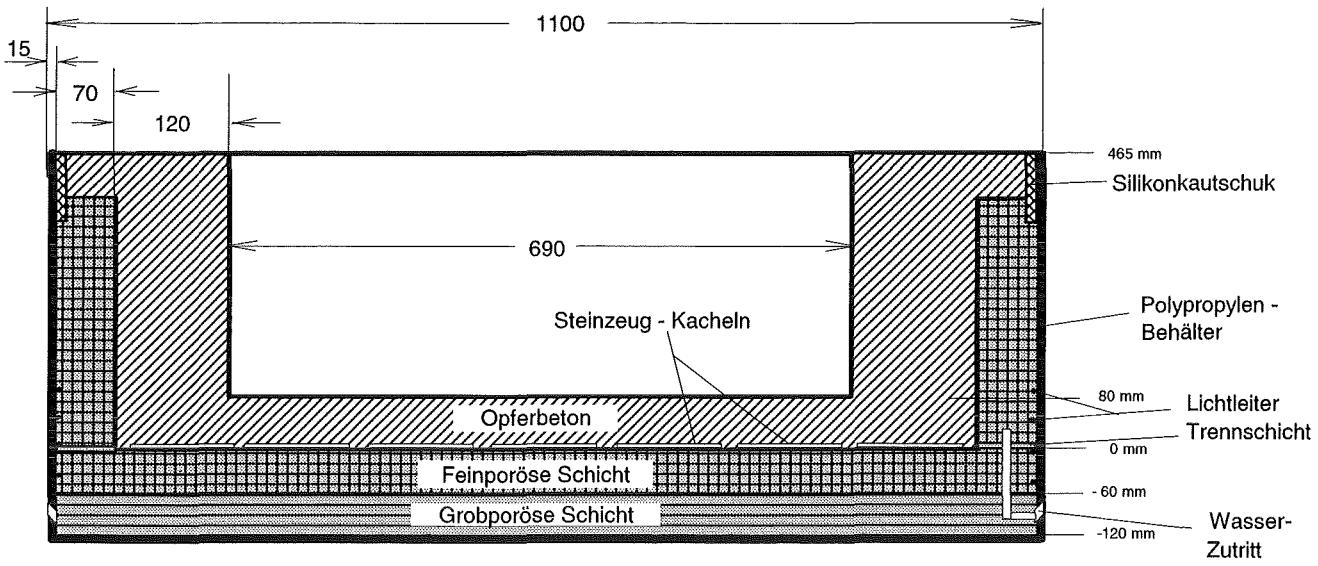

Abb. 11: Schematischer Aufbau des Kühleinsatzes in CometPC-H5

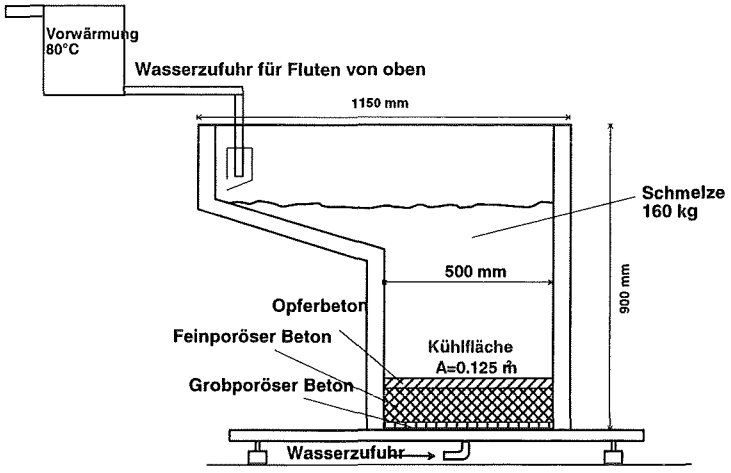

Abb. 12: Aufbau der Versuchsanlage

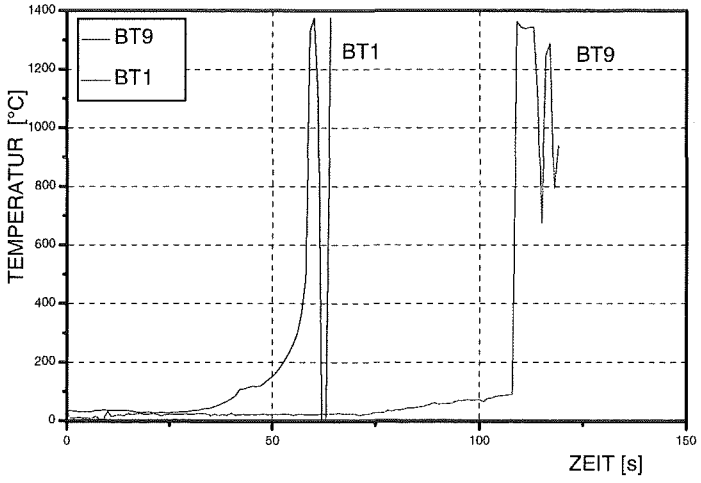

Abb. 13: CometPC-T 3.1, Temperaturen in der Opferschicht

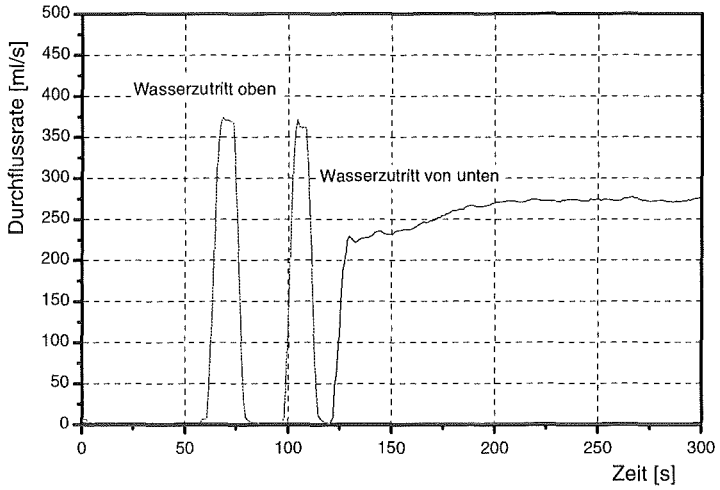

Abb. 14: CometPC-T 3.1, Wasserzutrittsrate oben und unten

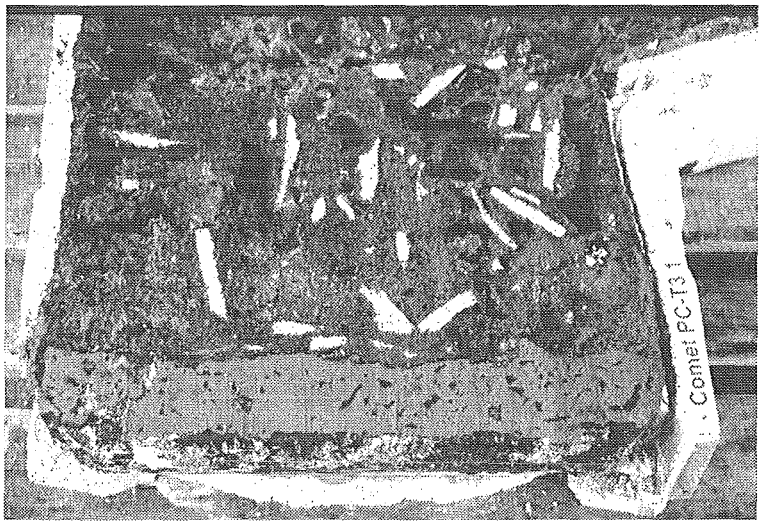

Abb. 15: CometPC-T 3.1, Tiegelschnitt

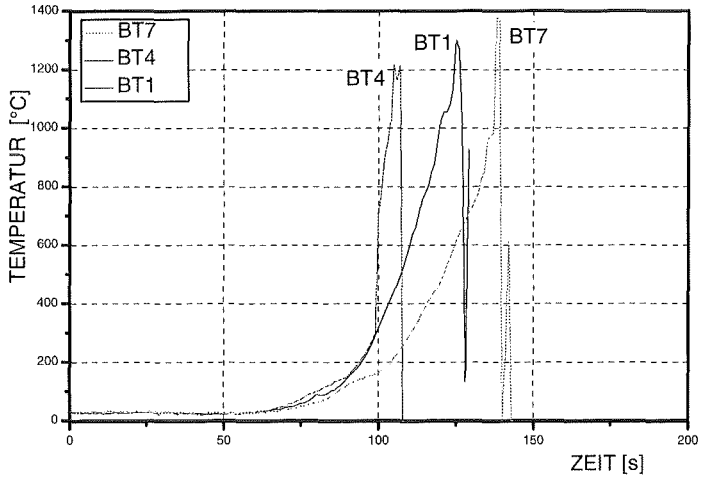

Abb. 16: CometPC-T 3.2, Temperaturen in der Betonschicht

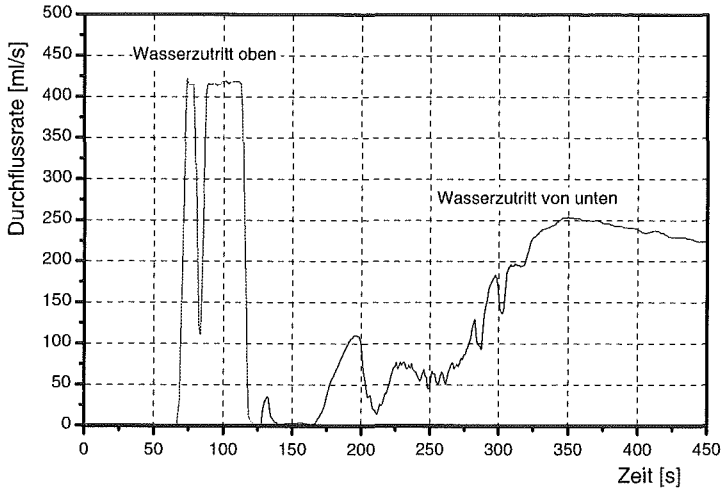

Abb. 17: Wasserzutrittsrate oben und unten, T 3.2

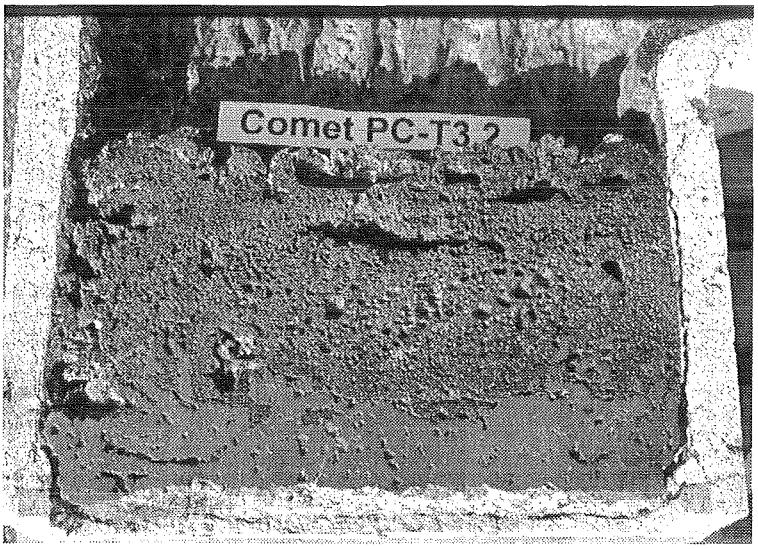

Abb. 18: Tiegelschnitt CometPC-T 3.2

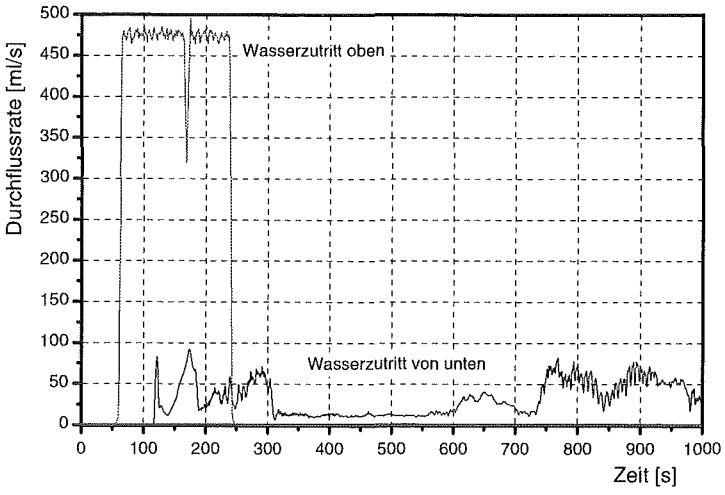

Abb. 19: CometPC-T3.3, Wasserzutrittsrate oben und unten

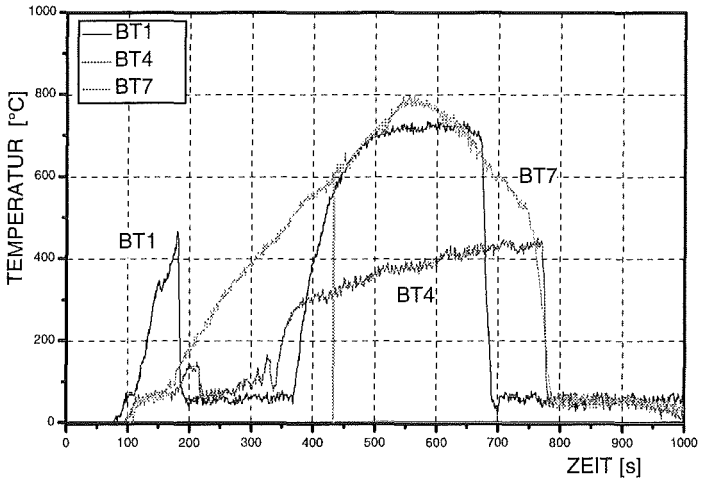

Abb. 20: CometPC-T 3.3, Temperaturen in der Betonopferschicht

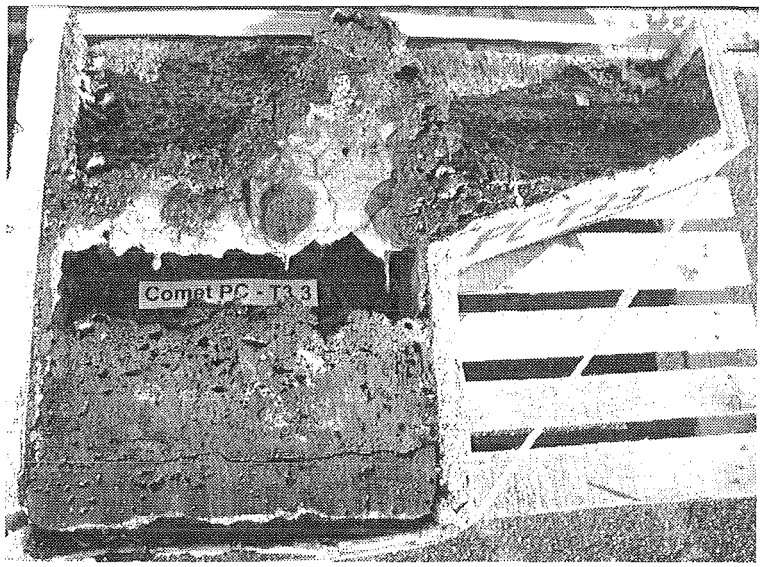

Abb. 21: CometPC-T 3.3, Tiegelschnitt

II. Investigations for the EPR-Concept – KAPOOL Experiments

(B. Eppinger, G. Fieg, S. Schmidt-Stiefel, W. Tromm, IKET; G. Stern, Fa. Pro-Science)

Abstract

The objective of the KAPOOL experiments is to investigate basic phenomena in connection with the EPR melt spreading and cooling concept. High-temperature Al_2O_3- and Fe-melts produced by the thermite reaction are used to simulate the oxidic and metallic components of the corium melt. Several KAPOOL tests have been performed to study the interaction of the oxidic melt with the release gate which is situated between the cavity and the spreading compartment. These tests have been analyzed with the HEATING-5 code and compared with the experimental results.

Zusammenfassung

In den KAPOOL-Experimenten werden grundlegende Phänomene des EPR-Konzepts zur Ausbreitung und Kühlung der Kernschmelze untersucht. Die oxidische und metallische Komponente der Kernschmelze wird dabei durch mittels der Thermit-Reaktion erzeugte Al_2O_3- und Fe-Schmelzen simuliert. In mehreren KAPOOL-Tests wurde die Wechselwirkung der oxidischen Schmelze mit dem Schmelzentor untersucht, das den Ausbreitungsraum von der Kaverne trennt. Diese Experimente wurden mit Hilfe des HEATING-5 Codes analysiert und mit den experimentellen Resultaten verglichen.

1 Introduction

Next generation LWR's shall incorporate the ability to control and retain an ex-vessel corium melt after a postulated core meltdown accident with subsequent penetration of the lower head of the reactor pressure vessel (RPV), to exclude significant radioactive release to the environment. In the case of the European Pressurized Reactor (EPR), an ex-vessel core-catcher is foreseen to meet these requirements [1, 2]. The corium melt shall first be collected temporarily (~ 1 h) in the reactor cavity under the RPV, to ensure that practically all core masses are gathered. The cavity is covered on all sides with a sacrificial concrete of relatively low water content, consisting

mainly of Fe_2O_3 and SiO_2. The zirconium present in the corium will be oxidized by the iron oxide during the concrete erosion phase. The heat production of this strongly exothermic reaction adds to the decay heat. The eroded concrete partly mixes with the corium, thereby reducing the liquidus and solidus temperatures as well as the density of the oxide melt. Eventually, the oxide density falls below the density of the metallic phase. This may result in a flipover of the two phases, if gas driven convection allows separation. After the end of the concrete erosion, a steel plate ("gate") at the bottom of the cavity will be eroded by the melt and the melt is released on the spreading area (~ 170 m^2). After spreading, the melt is flooded with water to extract the stored and the decay heat.

It is important for this concept that the melt spreads rather homogeneously over the spreading area. To achieve this, it is favorable if the melt is released in a short time (i.e. a fast opening of the gate over a large area) and the melt viscosity is low.

In the KAPOOL tests, the processes in the reactor cavity, i.e. erosion of the sacrificial concrete [3, 4, 5, 6], and meltthrough of and melt release through the melt gate are studied. Tests investigating the interaction between an iron melt and a steel plate simulating the release gate showed a rather rapid erosion of the steel plate [5, 7]. Two further tests investigating the interaction of an oxide melt with steel plates [8, 9] showed a different behavior: In any case a thermal erosion of the plate has been detected. The reason is found in the fact that the thermal contact between the oxide crust, which is formed from the very beginning, and the plate is imperfect.

A drawback of KAPOOL is the transient character of the tests: Volumetric heat production in the melt is not possible, in contrary to the realistic case of a corium melt. The possibility of a later thermal erosion of a melt gate made of steel cannot be excluded with the outcomes of these KAPOOL tests. It was the goal of further tests to study the transient behavior of the ablation process of a metallic plate in contact with a high temperature oxide melt. To do this, a low melting metal was used instead of steel. Aluminium with a melting temperature of 660 °C has been chosen as the candidate for these tests.

2 Objectives of the KAPOOL experiments

The goal of the tests KAPOOL-13 to -17 was to study the interaction of an oxide melt with aluminium plates simulating the melt gate between the cavity and the spreading compartment.

The exothermic thermite reaction 8 Al + 3 Fe_3O_4 → 4 Al_2O_3 + 9 Fe is producing an iron and an alumina melt, each with ~50 wt% and with temperatures up to 2400 °C. A thermite charge of 187 kg is ignited in a separate reaction vessel. For better conditioning of the oxide melt (decrease of the liquidus and solidus temperature), 65 kg CaO have been added to the thermite powder producing about 150 kg oxide and 100 kg iron melts. The liquidus and solidus temperatures of the melt are 1500 °C and 1395 °C resp. according to GEMINI calculations [10] and Data of the Slag Atlas [11].

The thickness of the aluminium plates at the bottom was changed between 10 and 20 mm. Pure aluminium has been chosen as material, any addition of magnesium (like the more common AlMg3) is prohibited because of a violent magnesium oxidation, which is accompanied with strong stirring of the melt; an oxide crust could easily be destroyed by these forces, which is not anticipated in these tests.

3 Test parameters of the KAPOOL experiments

The aluminium plates have been instrumented with 1 mm diameter K-type thermocouples (NiCr-Ni) at different radial and axial locations. They record the transient temperatures and the eventual plate ablation. Immersion C-type thermocouples (W-Re) [Fa. Hereaus-Nite] have been applied to record the melt temperature. For an oxide melt, the response time for these immersion thermocouples is around 8 seconds. These thermocouples are installed above the KAPOOL container and can be immersed into the melt remotely.

Several video cameras are installed around and above the facility to record the transient test. Both containers, the conical reaction crucible, in which the thermite melt is generated, and the KAPOOL test container rest on three weighing cells each to record the mass flow out of the reaction crucible and the mass flow into the test container. About 30 s after ignition the melt components are separated from each other inside the reaction crucible due to the large density difference. After release through the nozzle at the bottom about 100 kg of iron melt and several kg of oxidic melt were

dumped before the jet of pure oxidic melt was directed into the KAPOOL container. The amount of melt was recorded with the weighing cells. The temperature of the oxide melt was determined in a certain time interval by immersion W-Re-thermocouples and the transient temperatures in the steel plate were recorded by the NiCr-Ni thermocouples.

The setup of the KAPOOL container for the test KAPOOL 13 is shown in Figure 1. The KAPOOL container in KAPOOL 13 is of a strongly conical shape and is lined with a high temperature ceramics. The aluminium plate of a thickness of 20 mm is fixed at the bottom of the container, Table 1. The total diameter of the plate is ∅ 240 mm and the contact surface of the aluminium plate with the oxide melt is ∅ 200 mm. In this experiment the aluminium plate is in contact with the outer steel structures. In KAPOOL 15 to KAPOOL 17 always the same container is used. The container is of a cylindrical shape and is also lined with a high temperature ceramics. The thickness of the aluminium plate is different in the tests. The total diameter is in all tests ∅ 470 mm and the contact surface of the aluminium plate with the oxide melt is ∅ 455 mm. In these tests the aluminium plate has no contact to the outer steel structures due to ceramic insulation.

In the experiments KAPOOL 16 a 10 mm sacrificial concrete layer covered the surface of the aluminium plate. In KAPOOL 17 there is also a sacrificial concrete layer on top of the aluminium plate. The thickness of this layer was 15 mm except for the inner area of 100 mm diameter, where it was kept at 10 mm as in KAPOOL 16.

Table 1: Test Parameters for KAPOOL 13, 15, 16 and 17

KAPOOL Test #	**13**	**15**	**16**	**17**
Mass of oxide melt (kg)	92	160 [1])	150	150
Initial temperature (°C)	1860	>1800 [2])	1880	1870
Thickness of aluminium gate (mm)	20	10	10	20
Diameter of aluminium gate (mm)	240	470	470	470
Sacrificial concrete layer (mm)	No	No	10 mm	10/15 mm

[1]) 160 kg total mass. Aluminium plate eroded when ≈ 54 kg melt were poured
[2]) no temperature data

In all experiments about 190 kg of thermite powder and 66 kg of CaO were used to generate about 150 kg of oxide and 100 kg of iron melt. The composition of the thermite powder is:

25.8 wt%	Al
51.6 wt%	Fe
1.45 wt%	Si
0.8 wt%	Cu
0.35 wt%	Mn
19.2 wt%	O

The addition of CaO to the thermite powder has the effect that the liquidus and solidus temperature of the oxide melt is lowered compared to pure alumina melts. The liquidus temperature of the oxide melt is 1500 °C and the solidus temperature is 1395 °C.

4 Results of the KAPOOL experiments

4.1 KAPOOL 13

In test KAPOOL 13 the oxide melt started to pour into the KAPOOL container 54,4 s after ignition of the thermite in the crucible, about 29 s later 92 kg of oxide melt were gathered, Figure 2. The distortions of the KAPOOL container mass recordings are due to the insertion of W-Re-thermocouples into the melt pool, the loss of about 15 kg during the test was also due to the vigorous movement of the pool during insertion of the thermocouples.

The temperature of the oxide melt pool was initially 1860 °C in the beginning and dropped to about 1500 °C at 150 s, which is near the liquidus temperature, Figure 3. The temperature recordings of the NiCr-Ni thermocouples in the center of the 20 mm aluminium plate at three different vertical positions (top contact surface, in the mid-plane at 10 mm, and 2 mm above the bottom surface) are shown in Figure 4. Within 100 s after first contact of the oxide melt with the steel plate a maximum temperature of about 540 °C has been recorded at the top thermocouple. The initial contact temperature between the oxide melt (1860 °C) and the aluminium plate (initially at 20 °C) is 318 °C, much lower than the solidus temperature of the melt. A solid oxide crust is formed from the very beginning. The thermal contact between the crust and the plate may not be ideal, so thermal resistances must be assumed in modeling the problem. Post-experiment surface profiles have been measured, they show different vaulting for the oxide crust and the aluminium plate, the crust having a larger vaulting than the

plate, Figure 5. This is due to the cooling down phase when the aluminium plate changed its profile. The oxide crust surface is rough compared to the aluminium surface, which means that the thermal contact was not intimate. Heat transfer was partly conductive, partly by radiation. Additionally in this test the lateral heat losses from the 240 mm diameter aluminium plate to the outer steel structures were relatively large which may have been the reason for the vaulting of the plate, a subsequent gap formation and hence high thermal resistance.
In comparison to the tests which are discussed in the following, no aluminium gate erosion could be performed.

4.2 KAPOOL 15

Compared to KAPOOL 13, several experimental parameters have been changed to conduct test KAPOOL 15 (plate thickness reduced to 10 mm, cylindrical instead of conical container geometry and no contact to the outer steel structures due to ceramic insulation). It turned out, that already during the pouring process the 10 mm aluminium plate started to erode, probably because of the strong convective heat transfer from the highly stirred melt to the plate. The erosion started in the corner where the melt had first contact with the plate from flowing down the sidewall, and it proceeded into the direction of the melt flow, Figure 6. The size of the outflow hole grew rapidly, the final size was about 50 % of the original surface. Post test examination shows that an oxide crust of a thickness of 5 to 6 mm covers the area around the hole, Figure 7. There was no more aluminium found under this crust.

4.3 KAPOOL 16

To avoid an early leak, as happened in KAPOOL 15 a further test, KAPOOL 16, has been conducted, identical to KAPOOL 15 except for an additional 10 mm layer of boron-glass concrete on top of the aluminium plate. The height of the concrete layer was chosen that way that the calculated oxide melt/concrete interaction time is equal to the total pouring time. With this change any highly convective heat transport between the melt and the plate during the pouring interval is excluded. Post-experiment examination shows that the concrete erosion was complete. About 150 kg oxide melt was gathered in the KAPOOL container, the initial temperature was above 1800 °C. The temperature rise in the aluminium plate was rather homogeneous over the whole area except in the outer region of the aluminium plate, there the temperature rises

more slowly, Figure 8. A holding temperature at about 660 °C was recorded for about 10 seconds. Then the erosion phase started simultaneously over a large portion of the plate surface, and the oxide melt escaped from the container within 2.5 s. Figure 9 shows the structure of the aluminium plate after the test: The size of the outflow opening is given by an oxide crust of a thickness of about 4 to 5 mm and is 15 % of the original surface (∅ 455 mm of the aluminium plate is in contact with the melt). The aluminium plate is plastically deformed and strongly bent downwards except of the outer area, which is not eroded at all. The size of the hole in the aluminium plate is about 30 % of the original surface.

4.4 KAPOOL 17

In the last KAPOOL 17 test the thickness of the aluminium plate was increased to 20 mm, and the concrete layer was 15 mm except for the inner area of 100 mm diameter, where it was kept at 10 mm as in KAPOOL-16. The stepwise concrete layer was chosen to simulate an inhomogeneous concrete erosion front. The loading of the test container with about 150 kg oxide melt started 42 s after ignition and was ended 31 s later, Figure 10. The oxide melt height in the container including the concrete layer is about 47 cm. An initial concrete erosion with an erosion rate of about 0.35 mm/s was detected with NiCr-Ni-thermocouples embedded in the concrete. The oxide melt temperature was at ≈ 1870 °C. Similar erosion rates using iron melts have been measured for identical concrete at these melt temperatures. The melt temperature, as measured with the immersion thermocouples, decreases steadily to about 1700 °C at 120 s after ignition. The estimated time for a total concrete erosion is about 60 s. This is about 100 s after ignition. 20 s earlier the temperature readings of the NiCr-Ni thermocouples at the top surface of the aluminium plate started to rise. The temperature readings for the thermocouples in the central part of the plate reach the holding temperature of 660 °C after a rather long time, Figure 11. At a radius of 200 mm, close to the outer rim of the plate, this holding temperature is either reached at a much later time or not at all before the failure of the plate. 263 s after ignition the aluminium plate fails simultaneously over a large area and 150 kg oxide melt are discharged within a short time. For about 160 s the oxide melt has been in contact with the aluminium after the end of concrete erosion. During this rather long period an oxide crust was formed steadily on top of the aluminium plate. The crust thickness can be evaluated using the HEATING-V code or can be estimated with a simple enthalpy

balance. If one assumes that a gap exists between the crust and the aluminium plate, and heat transfer is purely by radiation, a crust thickness of 2.5 mm is calculated. In the case of a good thermal contact with heat conduction the thickness of the crust is 6 mm.

An analysis of these tests applying the HEATING V code is underway. The objective is to analyze the heating rates of the aluminium plates and the time of failures.

REFERENCES

[1] H. Alsmeyer et al., "Studies on the Core Melt Retention Concepts for the EPR", Proc. SFEN/KTG Conf. on the EPR Project, Strasbourg, November 1995, p. 204.

[2] H. Alsmeyer et al., "Ex-Vessel Melt Behaviour in the EPR", Proc. SFEN/KTG Conf. on the EPR Project, Cologne, October 1997, p. 161.

[3] F. Fellmoser et al., "Simulationsexperimente zum Verhalten von Kernschmelzen in der Reaktorgrube des EPR: KAPOOL 1-5", FZKA 6212, Forschungszentrum Karlsruhe, Mai 1999

[4] B. Eppinger et al., "Experiments on Concrete Erosion by a Corium Melt in the EPR Reactor Cavity: KAPOOL 6-8", FZKA 6453, Forschungszentrum Karlsruhe, März 2000

[5] G. Engel et al., "KAPOOL Experiments to Simulate Molten Corium-Sacrificial Concrete Interaction and Gate Opening in the EPR Core Catcher Concept", Proceedings of the OECD Workshop on Ex-Vessel Debris Coolability, Karlsruhe, 15-18 November 1999, FZKA 6475, pp 66-75, Mai 2000

[6] B. Eppinger, F. Fellmoser, G. Fieg, W. Tromm, "KAPOOL Experiments to Simulate Molten Corium-Sacrificial Concrete Interaction", Proceedings of ICONE-9, Nice, France, April 8-12,2001, Vol.1, Track 7-207

[7] B. Eppinger et al., "Simulation Experiment on Metallic Melt Interaction with the Melt Gate in the EPR Reactor Cavity: KAPOOL 9", FZKA Bericht, in preparation

[8] B. Eppinger, G. Fieg, "KAPOOL Experiments to Simulate Gate Opening in the EPR Core Catcher Concept", Jahrestagung Kerntechnik 2000, Bonn, 23-25. Mai 2000, pp 318-326

[9] G. Engel et al., "Investigations for the EPR-Concept- KAPOOL and KATS Experiments", Projekt Nukleare Sicherheitsforschung, Jahresbericht 1999, FZKA 6480, pp 288-300, August 2000

[10] S. Schmidt-Stiefel, 1999, private communication.

[11] Slag Atlas, Edited by the Verein Deutscher Eisenhüttenleute, Verlag Stahleisen mbH., Düsseldorf, 1981

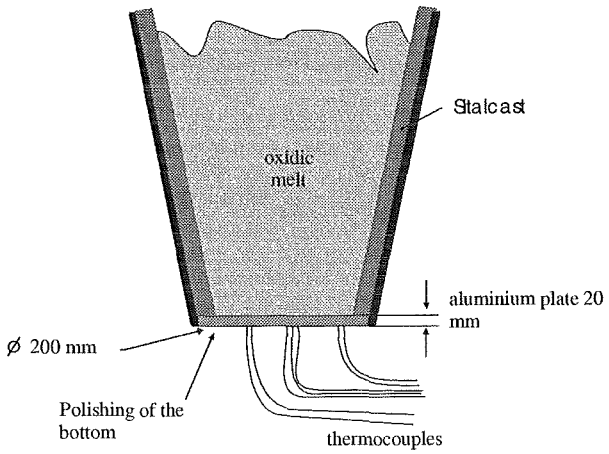

Figure 1: Setup of the KAPOOL container for the test KAPOOL 13

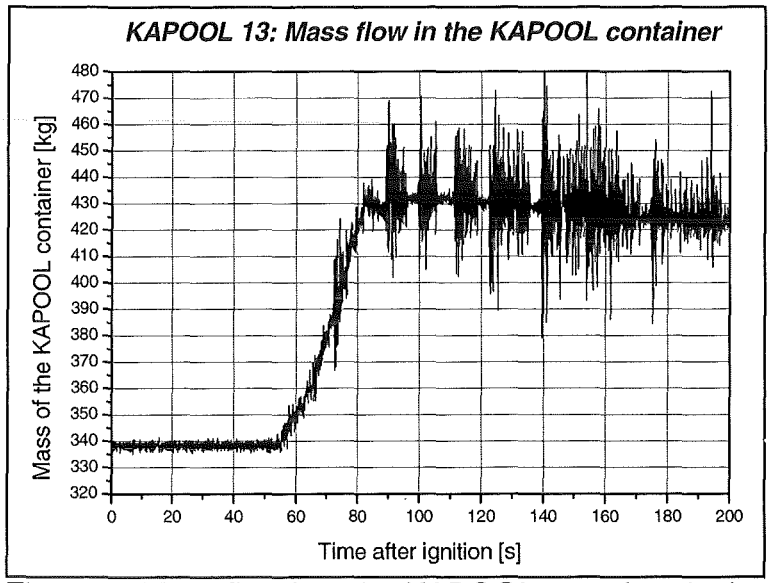

Figure 2: Mass flow into the KAPOOL container in the experiment KAPOOL 13

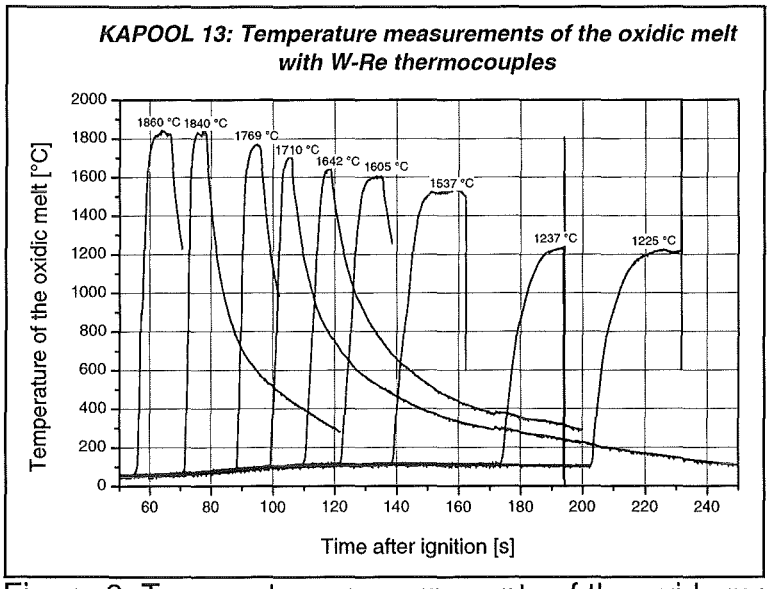

Figure 3: Temperature measurements of the oxide melt in KAPOOL 13

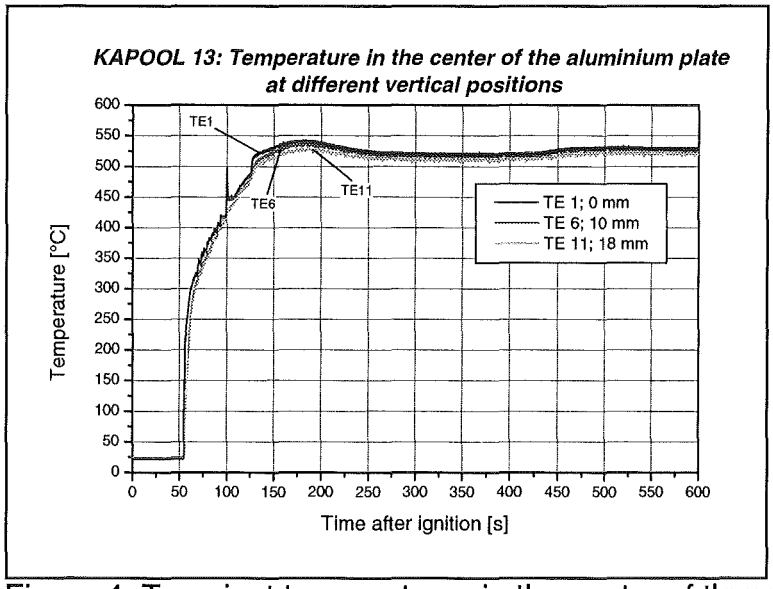

Figure 4: Transient temperatures in the center of the aluminium plate in KAPOOL 13

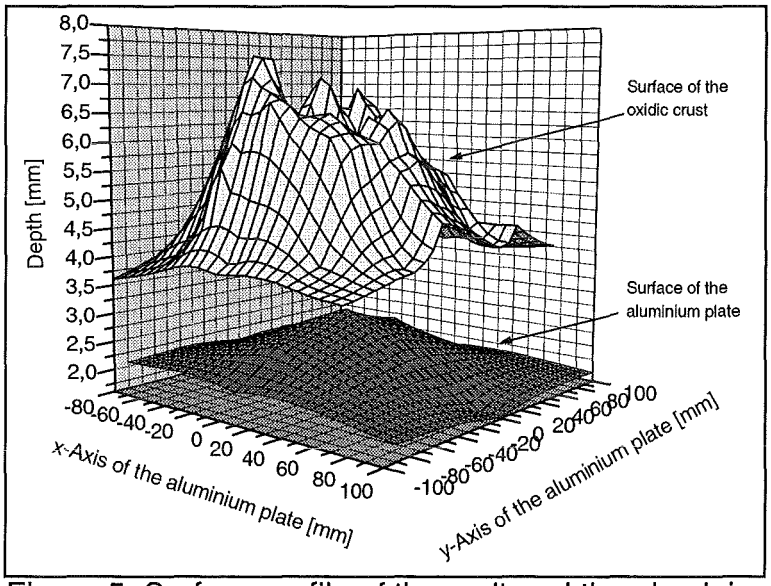

Figure 5: Surface profile of the melt and the aluminium plate at the contact surface for the test KAPOOL 13

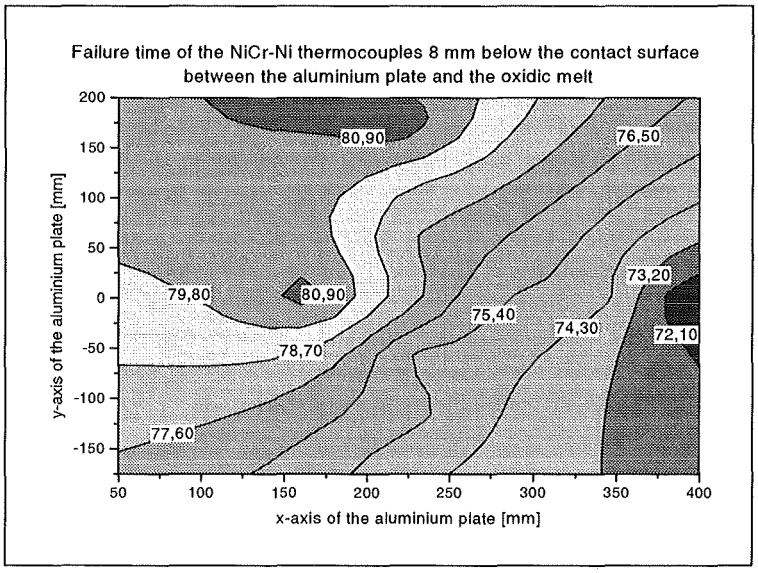

Figure 6: Failure time of the thermocouples in KAPOOL 15

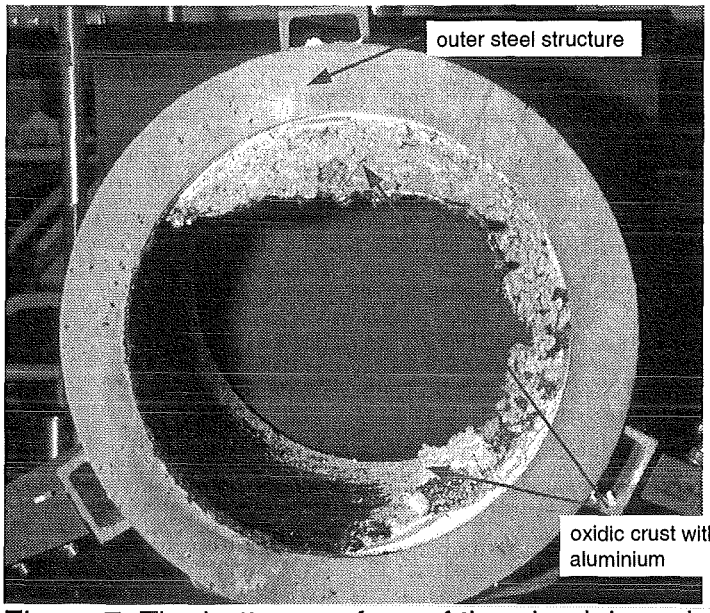

Figure 7: The bottom surface of the aluminium plate after the test in KAPOOL 15

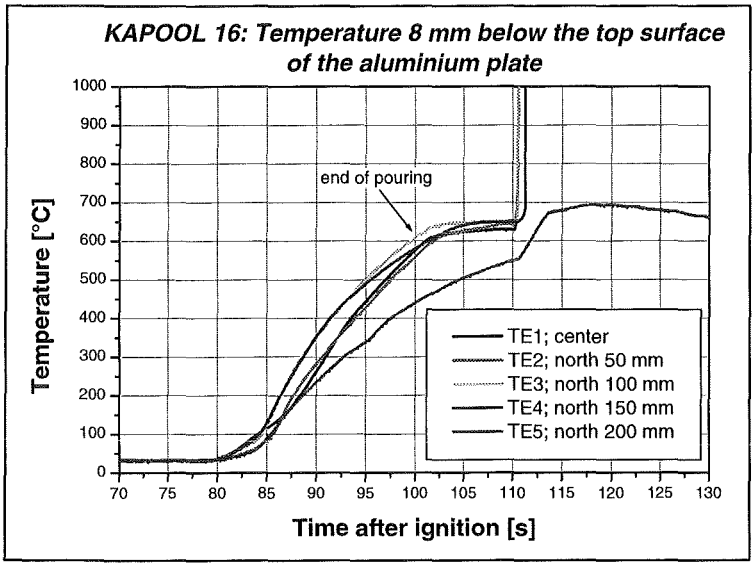

Figure 8: Transient temperatures in the aluminium plate in KAPOOL 16

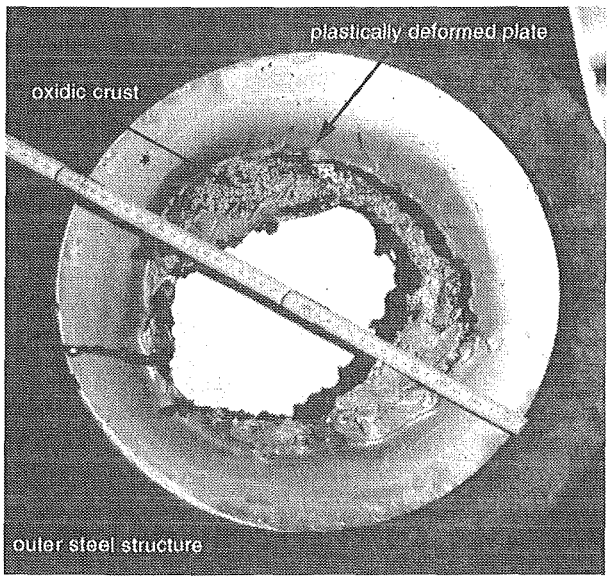

Figure 9: The bottom surface of the aluminium plate after the test in KAPOOL 16

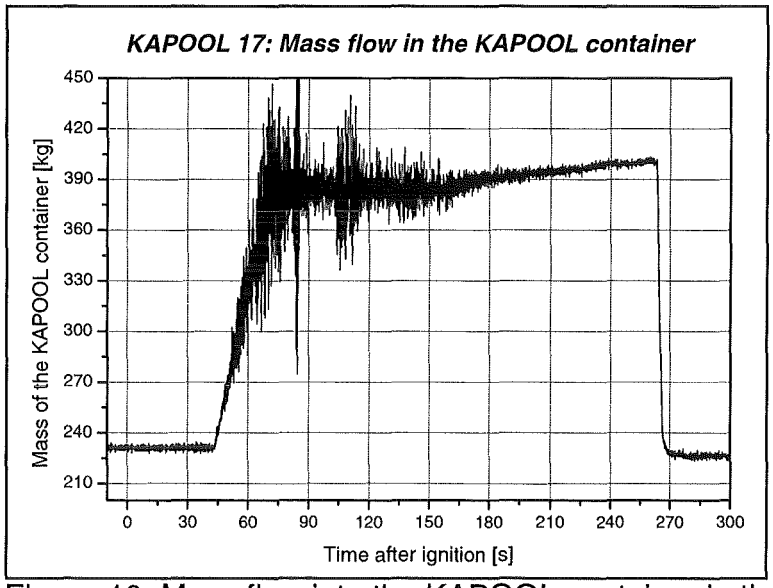

Figure 10: Mass flow into the KAPOOL container in the experiment KAPOOL 17

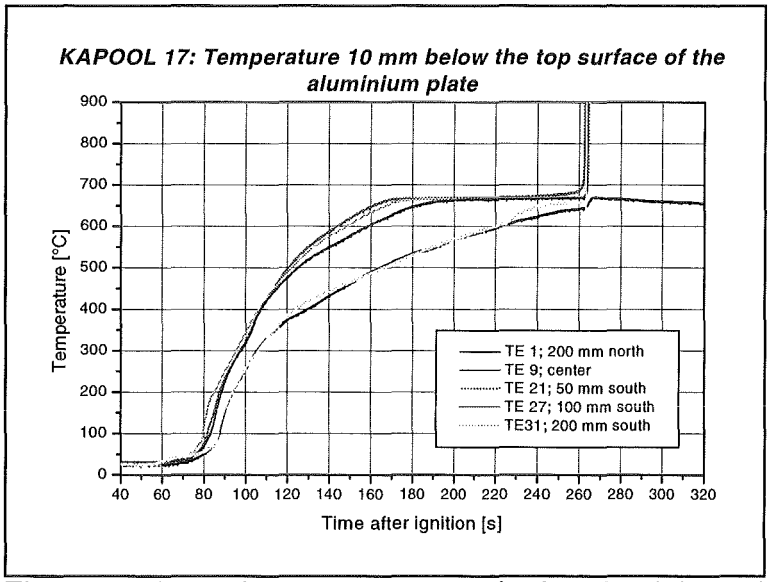

Figure 11: Transient temperatures in the aluminium plate in KAPOOL 17

III. Untersuchungen zum EPR-Konzept - KAJET-Versuche

(G. Albrecht, H. Brüggemann, E. Jenes, D. Raupp, W. Schütz, IRS)

Abstract

During a hypothetical core melt accident, the bottom of the reactor pressure vessel (RPV) may be attacked and penetrated by the melt. In case of a localised failure of the RPV, the melt expulsion into the reactor cavity may be as a compact jet for a short period, followed by a dispersed release after gas break-through. The KAJET experiments are related to the short initial phase of a compact jet. The main objective of the experiments is to establish a compact jet under driving pressures up to 2 MPa and to study its interaction with different substratum materials. The molten corium is simulated by an alumina-iron thermite melt. The gas break-through is avoided by sharply reducing the driving pressure.

In the reporting period, two KAJET experiments (KJ04, KJ05) were performed. In KJ04, about 83 kg of only alumina melt were released through a zirconia nozzle on a sample plate of construction concrete. In KJ05, 49 kg of iron and 55 kg of alumina melt were released on two separate sample plates of borosilikate-glass concrete. The maximum driving pressure was 0.5 MPa in both experiments. In KJ05 the zirconia nozzle was instrumented by thermocouples to measure the erosion rate caused by the melt jet.

In co-operation with Ruhr-Universität Bochum, a theoretical interpretation of the experiments is under way.

1. Einleitung

Im Verlauf eines hypothetischen Kernschmelzeunfalls kann die Bodenkalotte des Reaktordruckbehälters (RDB) durch die Schmelze angegriffen und in ungünstigen Fällen auch durchschmolzen werden. Bei örtlicher thermischer Ungleichverteilung in der Wärmeübertragung von der Schmelze in das RDB-Wandmaterial ist ein lokales, punktuelles Versagen möglich. Abhängig vom Unfallablauf kann zu diesem Zeitpunkt das Primärsystem unter Überdruck stehen, so dass der Schmelzeausstoß durch die RDB-Öffnung in die Reaktorgrube zunächst in Form eines kompakten Strahles erfolgt. Diese anfängliche Phase wird aber nur von sehr kurzer Dauer sein, da sich zum einen die Versagensstelle durch Wechselwirkung mit der Schmelze aufweitet und zum anderen beim Unterschreiten einer kritischen Schmelzepoolhöhe im RDB ein Durchbruch des treibenden Gases ein-

setzt. Dieser Durchbruch beendet die Phase des kompakten Strahls und führt zu einem dispergierenden Strahl. Die Wirkung des kompakten Strahls auf Auskleidematerialien der Reaktorgrube bewirkt Erosionsprozesse, deren quantitative Erfassung notwendig erscheint. Demgegenüber sind die Auswirkungen des dispergierenden Strahls eher geringfügig.

Das KAJET-Programm bezieht sich auf die (kurze) Anfangsphase des Schmelzeaustrags, während der möglicherweise ein druckgetriebener kompakter Strahl auftritt. Bei den Experimenten wird ein Schmelzestrahl mit treibendem Druck bis zu 2 MPa erzeugt und – neben der Charakterisierung des Strahls – die Wirkung auf unterschiedliche Auskleide- und Opfermaterialien untersucht. Die Kernschmelze wird simuliert durch eine Thermitschmelze aus Eisen und Aluminiumoxid. Der Einfluss der metallischen und der oxidischen Phase kann getrennt untersucht werden. Der Gasdurchbruch wird künstlich vermieden durch rasche Reduktion des Treibdrucks am Ende des Schmelzeaustrags. In früheren Versuchen zur Untersuchung des Strahlverhaltens (VJ01-VJ07 und KJ01) wurde die für die anschließenden Erosionsversuche zu verwendende Düsengeometrie bestimmt (Zirkonoxid, Austrittsdurchmesser 12 mm, Düsenwinkel 90 °, Auslaufstreckenlänge 25 mm). Mit dieser Geometrie konnten von 0-1,5 MPa sowohl mit der Eisenschmelze als auch der oxidischen Schmelze kompakte Strahle erzeugt werden.

Im Berichtszeitraum wurden zwei Erosionsversuche durchgeführt (KJ04, KJ05). Als Probenmaterial wurde bei KJ04 normaler Konstruktionsbeton und bei KJ05 Borosilikatglasbeton verwendet. Bei KJ04 wurde ausschließlich oxidische Schmelze (83 kg) eingesetzt, bei KJ05 sowohl die metallische (49 kg) als auch die oxidische Schmelze (55 kg). Der Treibdruck lag in beiden Versuchen bei max. 0,5 MPa. Bei KJ05 wurde auch die Austrittsdüse aus Zirkonoxid (ZrO_2) instrumentiert, um die Aufweitung durch den Schmelzestrahl zeitlich zu erfassen und die Wirkung auf die Düse zu untersuchen, um den Versuchsablauf genauer interpretieren zu können.

In Zusammenarbeit mit der Ruhr-Universität Bochum werden die Experimente theoretisch interpretiert, die zugrundeliegenden Szenarien analysiert und die Extrapolation auf Reaktorbedingungen vorbereitet.

2. Erosionsversuche KJ04 und KJ05

Die Versuchsbedingungen sind in Tabelle 1 aufgelistet. Bild 1 dient zur Erklärung des Versuchsablaufes. Durch eine Thermitreaktion im Schmelzengenerator entstehen zwei Schmelzephasen, Fe und Al_2O_3. Wegen der höheren Dichte sammelt sich die Eisen-

schmelze im unteren Teil des Generators an, die oxidische Schmelze sammelt sich über dem Eisen, dadurch ist die Austrittsreihenfolge physikalisch vorgegeben. Beim Versuch KJ04 trat nur die oxidische Schmelzenkomponente aus. Die Eisenschmelze wurde in einem Ringraum innerhalb des Generators aufgefangen. Unter dem Generator ist normalerweise eine drehbare Probentrommel angebracht, auf der zwei Betonproben rechtwinklig zueinander angeordnet sind (nicht bei KJ04, da nur eine Schmelzenkomponente benutzt wurde). Die Schmelze tritt unter Druck aus, trifft nach 270 mm Fallstrecke auf den ersten Probekörper und erodiert diesen. Kurz vor dem berechneten Austrittsende der Eisenphase wird die Probentrommel um 90° gedreht und somit die zweite Probe in den Strahlbereich gefahren. In der Zwischenzeit hat der Austritt der oxidischen Schmelze begonnen, die nun die zweite Probe beaufschlagt.

Beide Probekörper sind mit Thermoelementen instrumentiert, um eine zeitliche Zuordnung der Erosion zu ermöglichen. In beiden Versuchen wurden 100 mm dicke Probekörper eingesetzt, bei KJ04 aus Standardbeton, bei KJ05 aus Borosilikatglas-Beton. Jede Probe war mit 25 Thermoelementen (NiCr-Ni) instrumentiert, die in fünf horizontal angeordneten Gruppen im Abstand von 5-60 mm unter der Auftreffoberfläche angeordnet waren. Jeweils vier TE-Gruppen waren im Abstand von 15 mm konzentrisch um eine Gruppe im Zentrum angeordnet, dem wahrscheinlichen Auftreffpunkt des Schmelzestrahls.

3. Ergebnisse

Der Schnitt in Bild 2 zeigt für KJ04 die erodierte Kaverne mit einem Durchmesser von 90 bis 120 mm und 60 mm Tiefe. Insgesamt wurden ca. 360 ml erodiert.

Bild 3 zeigt die Schnitte durch die Probekörper nach dem Versuch KJ05. Teil a) zeigt die durch den Fe-Schmelzestrahl erodierte Kaverne. Die Erosionstiefe beträgt 33 mm, der Durchmesser 60 mm. Die beiden Vertiefungen auf der Unterseite der Kaverne zeigen ein unerwünschtes Vordringen der Schmelze im Bereich der Thermoelemente. Bei zukünftigen Versuchen werden deshalb die Thermoelemente horizontal angeordnet, um eine evtl. Beeinträchtigung der Messung durch die Kanalbildung zu vermeiden. Der Schnitt in Teil b) zeigt die vom Oxid erodierte Probe. Der Erosionsdurchmesser (150 mm) ist größer, die Erosionstiefe (15 mm) geringer als beim Eisen. Das erodierte Volumen durch den oxidischen Strahl war mit 120 ml dreimal größer als beim metallischen Strahl mit 39 ml, siehe auch Tabelle 1.

Bei KJ05 wurde die Austrittsdüse instrumentiert. Bild 4 zeigt die Signale von je 4, den Durchmessern 16 mm, 20 mm und 24 mm zugeordneten Thermoelementen, sowie die

Nachrechnung zur Interpretation des Versuchsablaufes. Die Streuung der zu einem Durchmesser gehörenden Signale ist relativ gering. Hieraus lässt sich folgern, dass die Aufweitung der Düse ziemlich gleichmäßig erfolgte und die runde Struktur im wesentlichen erhalten blieb. Die Erosionsrate nimmt mit der Zeit zu, bisher ist noch nicht geklärt, ob dieser Effekt von der Austrittsdauer oder der Strömungsgeschwindigkeit abhängig ist.

4. Theoretische Begleitung

In Zusammenarbeit mit der Ruhr-Universität Bochum werden die Experimente modelltheoretisch interpretiert. Dies schließt auch eine Erfassung der Unfallszenarien ein sowie Untersuchungen zur Übertragbarkeit auf Reaktorbedingungen. Die Arbeiten im Berichtszeitraum bezogen sich hauptsächlich auf die Beschreibung von Freistrahlen bzw. deren Charakterisierung durch die Reynoldszahl, die Weberzahl und Umgebungsweberzahl sowie die Ohnesorgezahl. Dabei wurde eine Einordnung des Verhaltens von Freistrahlen in den Rayleigh-, den Übergangs-, den turbulenten und den Zerstäubungsbereich möglich /1/.

Bezüglich der Erosion des Bodenmaterials durch den Strahl wurde die Erstellung eines Computercodes begonnen /2/.

Referenzen

/1/ T. Büscher, M. K. Koch, H. Unger. Betrachtungen zum Strahlverhalten. 5. Fachbericht zum Projekt RUB-E-I-263. Lehrstuhl für Nukleare und Neue Energiesysteme, Ruhr-Universität Bochum, Bochum, 2000.

/2/ M. K. Koch. Persönliche Information. Lehrstuhl für Nukleare und Neue Energiesysteme, Ruhr-Universität Bochum, Bochum, 1999.

Die KAJET-Versuche KJ04 und KJ05 sind Bestandteil eines Arbeitspaketes im EU-ECOSTAR-Projekt "Ex-Vessel-Core Melt Stabilisation Research" innerhalb des 5. Rahmenprogramms.

	KJ04 Oxid	KJ05 Eisen / Oxid
Eingesetzte Schmelzenmasse (kg)	83	49 / 55
Düsendurchmesser Austrittsbeginn (mm) Austrittsende (mm)	 12 26	 12 28
Beaufschlagungsdauer (s)	10	4,9 / 5,7
Temperatur des Schmelzestrahls (°C)[1)]	2150	2100
Max. treibender Druck (MPa)	0,5	0,5
Max. Strahlgeschwindigkeit (errechnet) (m/s)	14,4	9,9 / 14,4
Horizontale Ausbreitung der Erosion (mm x mm)	90 x 120	∅ 60 / ∅ 150
Erosionstiefe (mm)	60	33 / 23
Erodiertes Volumen (ml)	360	39 / 120
Mittlere vertikale Erosionsrate (mm/s)	≈ 4,8 - 6	6,7 / 4,0

[1)] Mit Pyrometer gemessen

Tabelle 1. Bedingungen und Ergebnisse der Versuche KJ04 und KJ05

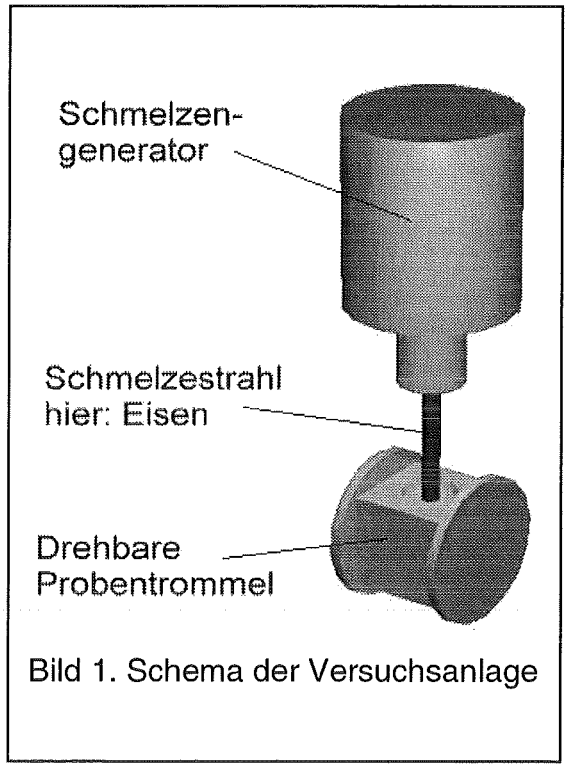

Bild 1. Schema der Versuchsanlage

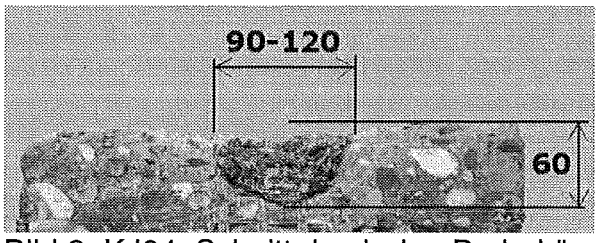

Bild 2. KJ04, Schnitt durch den Probekörper. Erosion durch Oxid-Schmelzestrahl

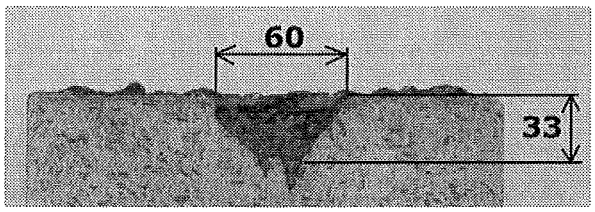

(a) Eisen

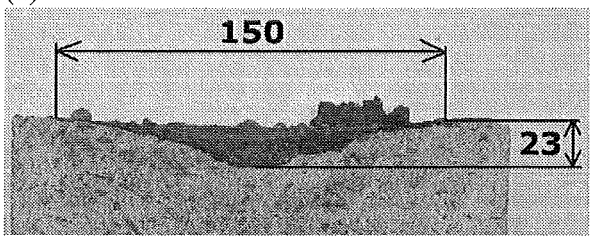

(b) Oxid

Bild 3. KJ05, Schnitte durch die Probekörper. Erosion durch a) Fe- und b) Al_2O_3-Schmelzestrahl

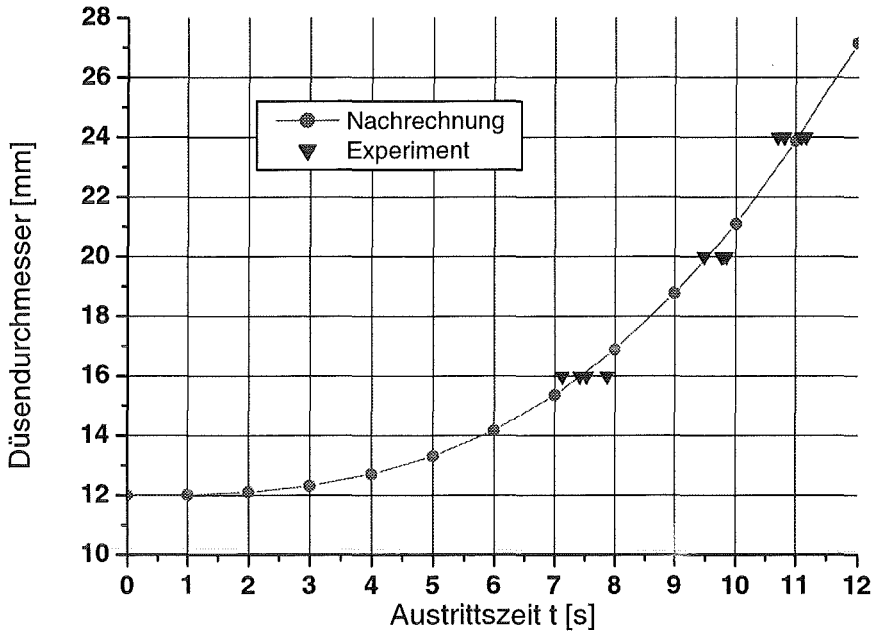

Bild 4. Aufweitung der Austrittsdüse

IV. Analysis of KATS Experiments With Two Different Melt Release Conditions

(J. J. Foit , IKET)

Abstract

The current concept of the EPR relies on a sufficiently homogeneous spreading of the melt in order to ensure its coolability after a passive initiation of flooding by water. Conditions under which a complete spreading can be expected are the subject of theoretical and experimental investigations. Derived approximate solutions are used to analyse some of the performed experiments with different melt release conditions. Results of CORFLOW simulations are also discussed.

ZUSAMMENFASSUNG

Das Konzept des EPR basiert auf einer ausreichend homogenen Ausbreitung der Kernschmelze, um deren Kühlung zu gewährleisten. Die Bedingungen, unter denen eine vollständige Ausbreitung zu erwarten ist, sind Gegenstand theoretischer als auch experimenteller Untersuchungen. Hergeleitete Näherungslösungen werden angewandt, um einige Experimente mit unterschiedlichen Einströmbedingungen zu analysieren. CORFLOW-Rechenergebnisse werden ebenfalls diskutiert.

1. Introduction

A variety of experiments have been carried out to determine the effects of cooling on the flow of fluids with different properties. The influence of the crust formation rates on the fluid flow was explored experimentally by Fink and Griffiths (1993) with the aim of understanding and classifying small-scale flow surface morphology for a fluid with weakly temperature dependent viscosity (polythylene glycol 600). This study indicated that a crust does not greatly affect the fluid flow except for very high crust formation rates. Experiments which used a fluid with strongly temperature dependent viscosity (glucose syrup) were performed by M. V. Stasiuk et al. (1993). In this case the cold, viscous fluid accumulated at the leading edge, altering the flow shape and thickness and slowing the spreading. The front became steeper and the surface behind the front was nearly horizontal. All performed experiments evolved to a stage at which the overall spreading behaviour of the flow can be approximated by a constant bulk viscosity.

In the framework of large-scale KATS experiments (Fieg et al., 1997) the non-isothermal spreading of high-temperature metallic and oxidic melts on ceramic or concrete surfaces under various conditions were studied, e. g. melt overheat and melt release conditions. The surface of the oxide melt cooled by radiation solidified, producing a thin thermal and rheological boundary layer. In all experiments the flow front stopped spreading some time later when the melt release was completed.

2. Analysis of the oxidic KATS experiments

The oxidic melt is composed of about 85 weight % Al_2O_3, 10 weight % SiO_2 and about 5 weight % FeO. For the above melt mixture there is only a limited data base of material properties available. Using an estimated phase diagram, the Stedman correlation (Stedman et al., 1990) was applied to evaluate the viscosity within the solidus-liquidus range. Above the liquidus temperature the experimental data of Elyutin et al. (1969) were used (Fieg et al., 1997).

The KATS experiments can be classified in accordance with the melt release conditions. In KATS 7 (Fieg et al., 1997) the melt was not collected but it was poured into a cavity. As soon as the cavity was filled, the melt began to spread across the channel with flow rates defined by the diameter of the pouring nozzle. In this way an almost constant volumetric flux was achieved which lasted 12 s. The melt front propagation ended at 49 s. In KATS 12 (Eppinger et al, 2001) experiment, on the other hand, the melts were gathered in a container before spreading into the channel was initiated by opening a gate in the container. Consequently, a linear decrease of the volumetric flow rate in time was obtained. The outflow of the oxidic melt from the container was completed after 10.4 s. The stop of the melt front was detected 40.s. These initial an boundary conditions are more complex than the ideal conditions for which self-similar solutions are known. However, the asymptotic behaviour of solutions of the underlying evolution equation (Friedmann, Kamin, 1980)) allows to construct approximate solutions which can be used to analyse the performed experiments or to make reasonable predictions for the melt front propagation (Foit, 2001).

One can expect that the discrete phase transition model together with the variable viscosity approach used in the CORFLOW code (Wittmaack, 1997) will predict a stop of the melt front if almost all nodes at the free boundary reach the temperature at which the value of the viscosity becomes large and if the floating crust is connected

to the basemat at the melt front. Because there is no crust failure criterion in CORFLOW, the results can depend strongly on the grid used for simulations. The sensitivity on the grid size will generally depend on the viscosity behaviour as a function of the temperature and the initial condition of the melt release.

The simulations were performed using a fine grid. The calculated front positions for the KATS 12 experiment as a function of time are compared to the measured data and to the approximate solutions for the isothermal spreading (Foit, 2001) in the following figure (Fig. 1).

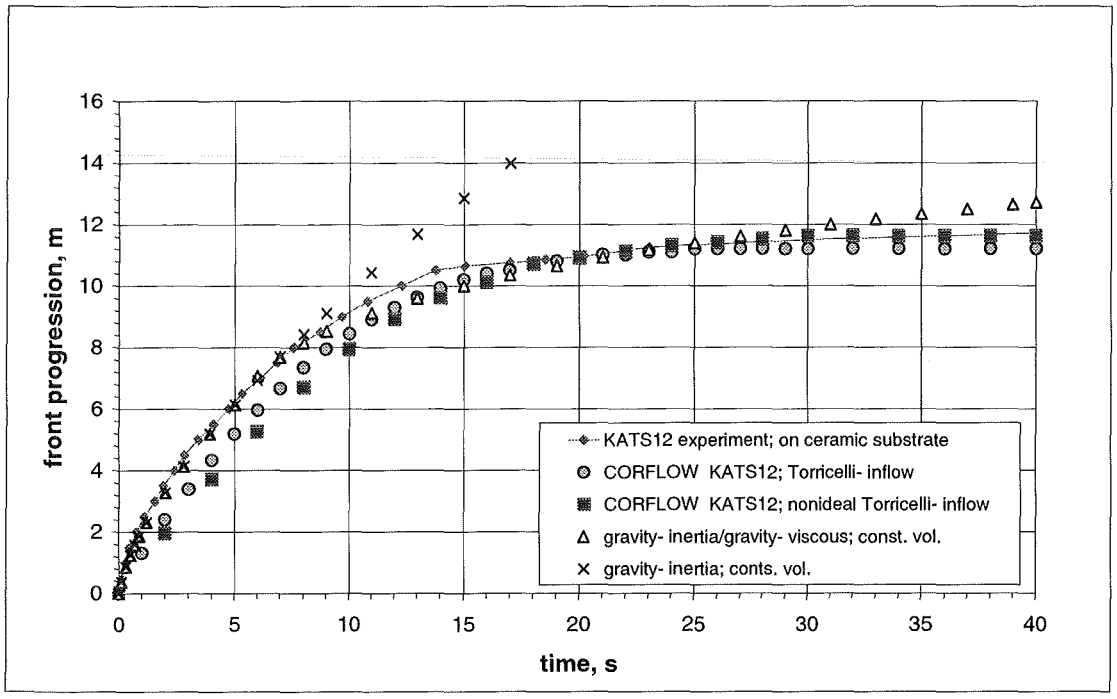

Fig. 1: Melt front progression in KATS 12 in comparison with approximate solutions and CORFLOW results

The underprediction of the melt front progression in the first stage of the spreading in the CORFLOW results is due to the experimental melt release conditions for this class of KATS experiments. The used melt release mode do not allow a reliable estimate of the melt volume flux during the release time. The final front position agrees very well with the experimental one. The approximate solutions of the underlying initial value problem (isothermal spreading of a constant volume) show the transition from the gravity- inertia spreading to the gravity- viscous spreading as well as the deviation from the isothermal spreading due to the cooling of the free melt surface.

The results of the CORFLOW simulation and the approximate solution of the second class of KATS experiments (experiments with an almost constant mass flux) (KATS 7) are shown in Fig. 2. The calculated evolution of the melt front during the melt release phase for the KATS 7 agrees very well with the measured curve, in contrast to the previous cases. The melt release mode used for this class of KATS experiments provides sufficient precise data for the inflow volume flux. The time at which the melt front stops is predicted to be much shorter than detected in the experiment: 23 s, whereas, it was measured to stop at 50 s in the experiment (Fig. 2).

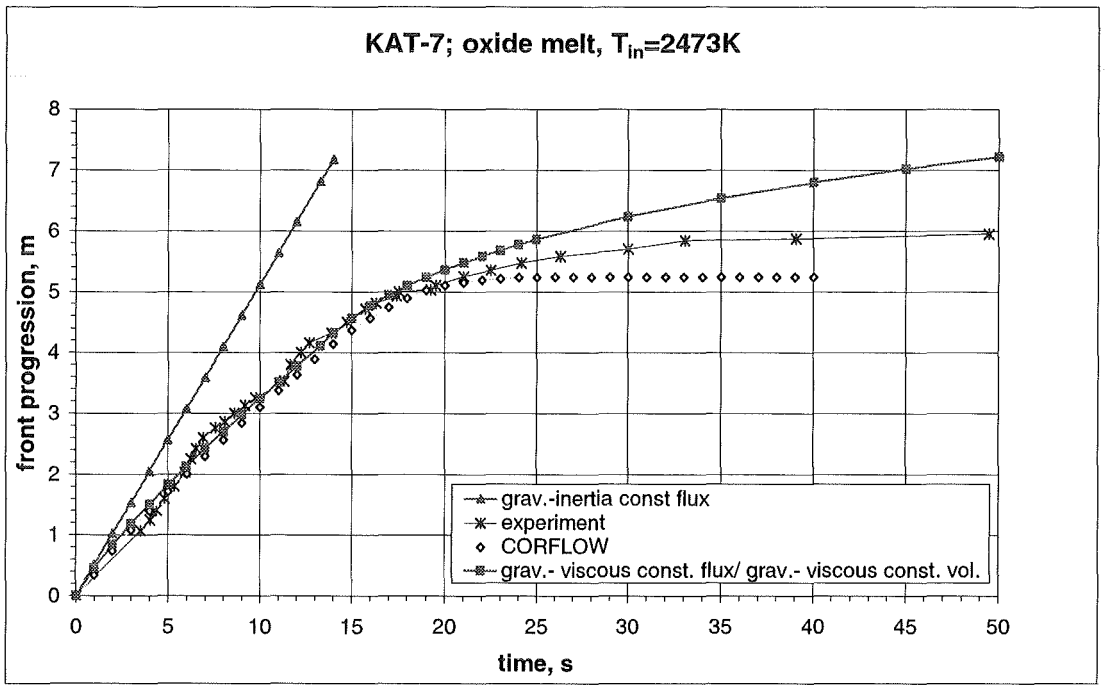

Fig. 2: Melt front progression in KATS 7 in comparison with approximate solutions and CORFLOW results

3. Conclusions

The KATS experiments are suitable for comparison with the self-similar solutions for the isothermal spreading in order to see the effects of the melt cooling on the front progression. In both experiments the final front position is located in the neighbourhood of the isothermal curve. Due to the fairly large Péclet number for the oxidic melt under consideration, the spreading melt develops only a thin thermal boundary layer at the cooled boundaries. Consequently, the influence of this thin crust on the front

propagation is weak until the time at which the gravity force is balanced by the strength of the developing crust.

The variable viscosity used in CORFLOW seems to be adequate for simulations of the oxidic KATS experiments concerning the predictions of the final front position. The CORFLOW code will predict a stop of the melt front if almost all nodes at the free boundary reach the temperature at which the value of the viscosity becomes large and if the floating crust is connected to the basemat at the melt front.

References

Bercovici, D., 1994. *Geophys. Res. Lett.* **21**, 1177.

Elyutin, V. P. et al., 1969. *Russian Journal of Physical Chemistry* **43**, 3.

Fieg, G. et al., 1997. FZKA-Report 6605, Forschungszentrum Karlsruhe.

Eppinger, B. et al., FZKA-Report 6589, Forschungszentrum Karlsruhe (2001).

Foit, J. J., 1997. FZKA-Report 6006, Forschungszentrum Karlsruhe.

Foit, J. J., 1999. Proceedings of the 7th International Conference on Nuclear Engineering, Tokyo.

Foit, J. J., 2001. To be published.

Friedman, A.; Kamin, S.: Trans. Amer. Math. Soc. 262, No. 2, 551 (1980).

Griffiths, R. W.; Fink, J. H., 1993. *J. Fluid Mech.* **252**, 667.

Huppert, H. E., 1982. *J. Fluid Mech.* **121**, 43.

Sakimoto, S. E. H.; Zuber, M. T., 1995. *J. Fluid Mech.* **301**, 65.

Stasiuk, M. V. et al., 1993. *Geology* **21**, 335.

Stedman, S. J. et al., 1990. *J. Material Sci.* **25**, 1833.

Wittmaack, R., 1997. *Nuclear Technology* **119**, 158.

Zel'dovich, Ya. B.; Kompaneets, A. S., 1950. Collection Commemorating the 70th Anniversary of A. F. Joffe, Izv. Akad. Nauk. SSR.

32.21.05 Langfristige Containmentkühlung

Two-dimensional Geysering in the Test Facility SUCOT

(G. Janssens-Maenhout, M. Daubner, H. Umekawa, T. Schulenberg, IKET)

1 Abstract

Flashing has been analyzed for a water column with an initial hydrostatic head of 0.55 bar in a vertical riser with flow cross-section of 950 x 120 mm^2 under low mass flux, low subcooling and low heat flux conditions. In this paper flashing is defined as self-evaporation due to all kind of pressure-drops, and geysering is defined as a kind of repeated vaporization, which is propagated by the pressure-drop due to a decreasing hydrostatic head. The instability phenomenon in the test facility provides information for extending the up to now one-dimensional geysering models. Due to the two-dimensional flow structure in the vertical test section one observes geysering with flow circulation. The two-dimensional geysering therefore shows smaller pressure movements and faster pressure recovery as in the case of one-dimensional geysering. In the two-dimensional case both the geysering frequency and the geysering strength enhance with increased energy input for the geysering. At reduced riser width the onset of geysering is delayed but then the geysering frequency shows an even more steep increase with increasing energy input. Furthermore the geysering frequency increases with reduced initial hydrostatic head.

2 Zusammenfassung

Das Phänomen Flashing wurde analysiert in der Versuchsanlage SUCOT unter niedrigen Massendurchsatz-, niedrigen Unterkühlungs- und niedrigen Wärmezufuhrbedingungen. Der Limit-Fall "geysering" unter Null-Durchsatz wurde insbesondere auf seine Abhängigkeit von Wärmezufuhr, Wasserstand und Kaminbreite untersucht. Spezielle Ansätze für ein zweidimensionales Geysering-Modell, basierend auf empirisch abgeleiteten Korrelationen, wurden getestet.

3 Introduction

Depending on the causing mechanism, negative resistance, time-delayed feedback or thermal nonequilibrium, flashing or boiling flow instabilities have been classified by Ozawa (1999) respectively into the three categories: (1) the Ledinegg instabilities with related

pressure drop oscillations, (2) the density wave oscillations and (3) the geysering. In the early seventies the nuclear industry analyzed flow instabilities in Boiling Water Reactors (BWR)\ and investigated the first two categories, especially the second one. For a one-dimensional description of flashing Ishii and Zuber (1970) set up a general dimensionless drift-flux model, which is still used. The criterion for instability was given as function of the Phase change number N_{PCh} and the Subcooling number N_{Sub}.

A first classification was given by Boure, Bergles and Tong (1973). The flashing types concerned mainly forced circulation and density wave oscillation with high steam quality for the BWR conditions, whereas geysering was only mentioned. Density wave oscillations have been experimentally investigated by Yadigaroglu and Bergles (1972) in large detail. Fukuda and Kobori (1978) made a subtle classification of various types density wave oscillations. Lahey and Yadigaroglu (1982) examined the relationship between Ledinegg and density wave stability criteria. They showed that to determine whether a system is stable regarding excursive instabilities, one only needs to examine the zero frequency limit of the linear model used for the analysis of density wave oscillations. This paper focuses on the third category of geysering, here defined as repeated vaporization, caused by thermal nonequilibrium due to a change in hydrostatic head. Experimental studies in a natural circulation system are scarce and mainly performed by Griffith (1962), Ozawa, Nakanishi, Ishigai and Tarui (1979) and Aritomi, Chiang and Mori (1993). Already Griffith reported geysering with periods of the order of 10 to 100 seconds, which disappears under pressurized conditions. Geysering has only clearly been defined by Ozawa, Nakanishi, Ishigai, Mizuta and Tarui (1979) as nonlinear oscillation due to the liquid superheat and self-evaporation. Ozawa noticed additionally to Griffith's findings a stabilizing effect of the inlet velocity and destabilizing effects of the riser length and the heat flux. Based on the experimental results he established a one-dimensional model, representing the principal mechanism of geysering. Later on Aritomi et al. (1993) investigated the instability by using two communicating fluid columns and explained one-dimensional geysering by a transition from bubbly flow to slug flow.

More recently Jiang, Yao, Bo and Wu (1995) pointed out that the nucleation location for the geysering and the flashing are different. In the case of geysering the self-evaporation is initiated at the bottom heated section, whereas in the case of flashing the evaporation wave starts at the top and moves then downwards. According to our definition the flashing

defined by Jiang can be interpreted as geysering. Van der Hagen, Stekelenburg and Van Bragt (1997) stated that geysering occurs in stagnant heated liquid and is dominated by gravity effects in the riser. He uses the model of Ishii but introduces a modified Subcooling number with the saturation temperature at the outlet pressure. The flashing has been mainly investigated in small, vertical tubes with a heated section and a riser section. Under the low mass flux conditions and with a free liquid surface at the outlet the flashing becomes mainly buoyancy driven and can be classified as geysering. Up to now only one-dimensional models are available in literature. However, to describe the flow behavior in real geothermal power sites or cryogenic pipelines one-dimensional models are not satisfying. Here an experimental study on geysering in two dimensions is performed. A similar principle mechanism as in the case of one-dimensional geysering is observed. The heated fluid is transported to regions at smaller hydrostatic head with lower saturation temperature and becomes superheated. When void is generated, the hydrostatic head and the corresponding saturation temperature are reduced and the self-evaporation is reinforced. However since the flow cross-section of the riser allows a two-dimensional flow behavior, the geysering does not occupy the whole cross-section. Moreover turbulent convective rolls strongly affect the extension of the vapor plume during the self-evaporation.

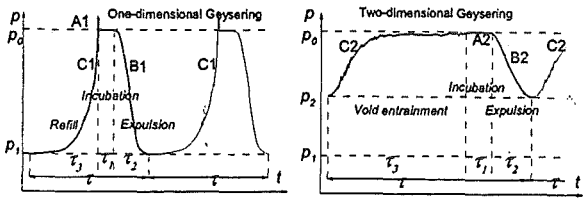

Fig. 1: Comparison between one-dimensional and two-dimensional geysering.

A division of one geysering period into three phases, analogously as in Ozawa's findings could be performed. After an incubation phase an onset of steam formation is initiated, which then expands sidely and upwards during the expulsion phase and finally ends up with a void entrainment phase. The first phase A of incubation is similar as the incubation phase in the one-dimensional geysering. The second phase B of expulsion differs in strength. In comparison to the one-dimensional geysering case the expulsion phase in the two-dimensional case is shorter and accompanied by smaller pressure movements. Therefore the pressure recovery in the third phase C shows a completely different character as the refill phase in the one-dimensional geysering case. The third phase of a

geysering period in a two-dimensional channel is identified as void entrainment phase. A fast pressure recovery with a strong mixing and entrainment of void by the turbulent convective rolls is observed. Fig. 1 shows the typical differential pressure signal during geysering with the different pressure recoveries C1 and C2 for the one-dimensional respectively two-dimensional case.

4 Experimental Setup

4.1 Test Facility

In a test facility made of glass, consisting in a horizontal section with heated bottom plate and a vertical riser section with a hydrostatic head of 0.55 bar, the geysering has been investigated under atmospheric pressure. A first description is given by Janssens-Maenhout, Daubner, Knebel and Müller (1999). The experimental test facility is shown schematically in Fig. 2 and consists of a L-shaped slab geometry with a length l = 4.50 m, a wetted height h = 5.5 m and a depth d = 0.12 m. The width of the horizontal respectively the vertical section are w_l = 0.9 m and w_h = 0.95 m. Because of the height the test facility is appropriate to investigate geysering. Moreover due to the large flow cross-section of the vertical section, two-dimensional effects on the geysering could be clearly observed.

The shape of the test facility SUCOT ("SUmp COoling Two-phase") has originally been conceived to investigate sump cooling by a passive two-phase loop in the safety concept of the European Pressurized Water Reactor. The L-shape did not disturb the measurements of the geysering phenomenon in the vertical section. The geysering was always initiated in the vertical channel and never reached the horizontal section. Two operation modes, forced circulation and natural circulation, are possible. In the forced circulation operation mode subcooled water is pumped into the horizontal lower duct and heated up by the hot bottom plate. Low heat fluxes at the bottom boundary and low mass fluxes, including zero mass flux at the inlet are envisaged.

The bottom plate of the horizontal section is heated up by 7 copper blocks, in which 4 electrical heaters of 10 kW electrical power are embedded. A maximum total wall heat flux of 150 kW/m^2 can be reached. The heat leaks thereby amount up to 5 ~ 6 kW. The heat losses are mainly caused by heat conduction over the large surface area of the flow sections, although all glass windows of the flow section are isolated. The heat leakage has

been estimated from the heat balance with the enthalpy difference measured between inlet and outlet of the flow test sections under single phase flow condition.

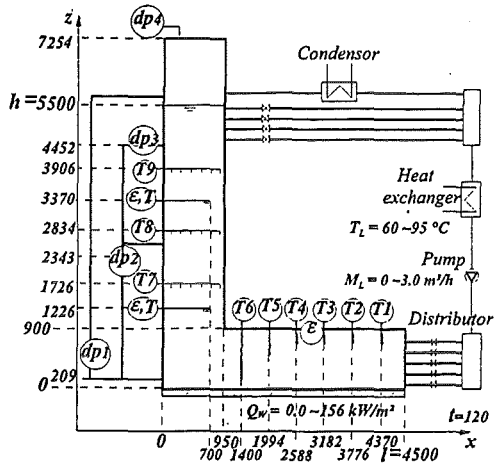

Fig. 2: Sketch of test facility SUCOT

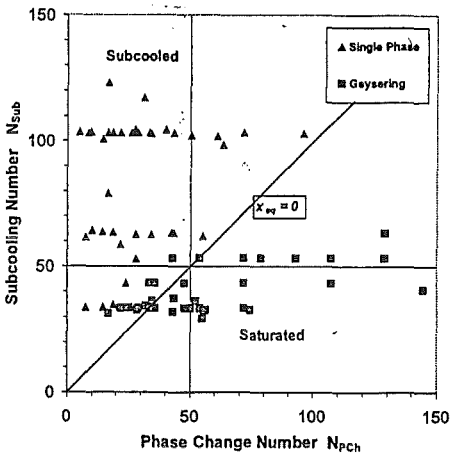

Fig. 3: Operational diagram.

In the horizontal lower duct temperature profiles have been measured by 5 times 18 traversable thermocouples of type K (indicated as T1, T2, T3, T4 and T5 in Fig. 2) and 6 fixed thermocouples of type K (indicated as T6 in Fig. 2). During the transient experiment the traversable thermocouples have been fixed at the position given in Fig.2. In the vertical riser 3 differential pressure cells measure respectively the pressure drop over the total riser (dp1 in Fig. 2), the pressure drop over the first half section of the riser with Δz = 2343 – 209 mm (indicated as dp2) and the pressure drop over the second half section of the riser with Δz = 4452 – 2343 mm (dp3 in Fig. 2). At the top of the riser also the gauge pressure in the vapor space is recorded (indicated as dp4 in Fig. 2). Additionally 3x6 thermocouples (in Fig. 2 indicated as T7,T8 and T9) and 2x4 thermocouples with 2 fibre optical probes are inserted in the riser. The transient flashing behavior has been observed by the differential pressure and temperature measurements recorded with a measuring data rate of 1 Hz during the measurement time of 1 h at different positions in the vertical and horizontal flow sections.

Exp. cond.	Set points
Hor. length	4.5 m
Inlet temp.	$50 \sim 100°C$
Inlet vol. rate	$0 \sim 0.8\ kg/s$
Wall heat flux	$0 \sim 150\ kW/m^2$
Initial level	$2.0 \sim 5.5\ m$

Dimensionless n°	Order of Magnitude
Rayleigh N°	$Ra = \beta_L g \Delta T_{Sub} w_h^3 / (\kappa_L \nu_L) \sim 1.E11$
Prandtl N°	$\mathrm{Pr} = \nu_L / \kappa_L \sim 7.E0$
Aspect Ratio	$N_R = w_h / h \sim 2.E-1$
Phase change N°	$N_{PCh} = \Delta\rho Q_W / (\rho_G M_L \Delta h_{LG}) \sim 1.E1 \sim 1.E2$
Subcooling N°	$N_{Sub} = \Delta\rho c_p \Delta T_{LSub} / (\rho_G \Delta h_{LG}) \sim 1.E1 \sim 1.E2$

Table 1: Range of experimental conditions for SUCOT.

4.2 Experimental Conditions

The working fluid is water and the range of the experimental conditions is listed in table 1. The experimental conditions, depending on the wall heat flux Q_W, liquid mass flow rate M_L and subcooling ΔT_{Sub} are specified by the Phase change number N_{PCh} and the Subcooling number N_{Sub} as derived by Ishii and Zuber (1970) from the drift-flux model, considering the three mixture conservation equations. The more detailed two-fluid model with 6 equations still suffers from incomplete closure relationships, modelling phase interaction. Moreover scaling with 1 common time scale is not any more possible with the two-fluid model.

The definition of the Phase Change and Subcooling number has been extended in order to be also applicable for the case of zero inlet mass flux. The definitions used are

$$N_{PCh} = \frac{Q_W / (\rho_G \, \Delta h_{LG})}{M_L / (\rho_L - \rho_G)} \quad \text{and} \quad N_{Sub} = \frac{(\rho_L - \rho_G)}{\rho_G} \frac{c_p \left(T_{Sat}(p_{in}) - T_{Sat}(p_{out})\right)}{h_{LG}} . \tag{1}$$

The Phase change number represents the ratio of the evaporation reaction time constant and the fluid residence time constant whereas the Subcooling number represents the enthalpy difference of the saturated fluid at the outlet to the saturated liquid at the inlet, scaled with the latent heat. The relationship between N_{PCh} and N_{Sub} is still given by the quality x_{eq} of the mixture in thermodynamic equilibrium. Additionally to N_{PCh} and N_{Sub} the classical single-phase flow dimensionless numbers are given in table 1.

An overview of all working points with non-zero inlet mass flow rate ran in different tests is given in the operational diagram of N_{Sub} versus N_{PCh} in figure Fig. 3. This operational diagram represents at one side the single phase flow regime and at the other side the geysering regime. Using the extended definition 1 the working points with zero mass flux can be situated on the line of zero mixture quality.

5 Simulation of steady state flow conditions

5.1 Model Assumptions and Equations and Closure Relations

For the numerical simulation of such dispersed two-phase flow systems the Eulerian two-fluid-model is widely used. Thereby the two phases are described separately by two interpenetrating fields, which have to be coupled by closure relationships for inter-phase

exchange of mass, momentum and energy. The two-fluid-model result in 3 transport equations in vector notation for each of the two phases with common interfacial terms.

In the horizontal duct of the test facility vapour bubbles are generated at the heated bottom plate. Therefore an extended modelling of subcooled boiling with a vapour source term at the heated wall and with a condensation source term in the subcooled bulk has been performed.

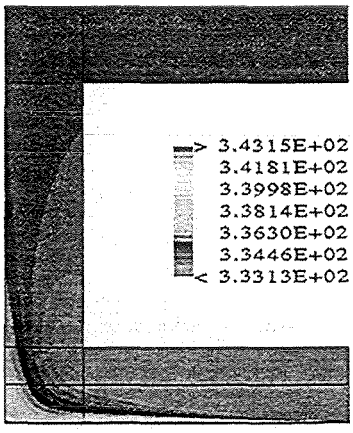

Fig. 4: Init. temp. profile (in K)

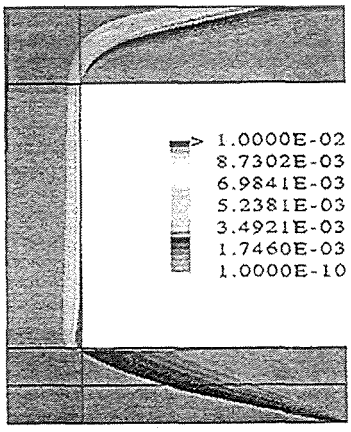

Fig. 5: Void profile

In the chimney of the test facility a bubbly flow is established, for which interfacial forces have been modelled. Under the assumption of an ideal dilute bubbly flow, with bubbles as non-interacting, small spherical and non-deformed particles, physical models for the interfacial forces have been derived from the forces on a particle volume, induced by the surrounding fluid under Lagrangian approach. Thereof a drag force, lift force, wall lubrication force, virtual mass force and turbulent diffusion force are modelled, as described by Janssens-Maenhout (1999).

5.2 Initial Single-phase Flow up to Subcooled Flow Boiling

As boundary conditions an inlet mass flux and an outlet pressure boundary are set. The walls are treated adiabatically, except the heated bottom plate, on which the heat flux $q''_W = 5.18\ W/cm^2$ is posed. In order to reduce the computational time in a first effort the set-up is confined to a simplified steady state and two-dimensional flow case. For the initial heated single-phase flow the diffusive and convective heat transport, enhanced by the buoyancy effect result in the temperature profile of Fig. 4 over the whole test facility for

the case T_{Lin} = 333 K, u_{Lin} = 0.2 m/s. Note that the characteristic time constant for the heat diffusion in the computational flow area takes $7x10^7$ s.

For the heated two-phase bubbly flow the boiling model for a smooth heated wall with imposed heat flux $q_W"$ = 5.6 W/cm^2 has been applied. After the point of onset of vapour generation a transition from a single-phase to a two-phase buoyant flow occurs and a bubbly flow establishes. For the case of a fully opened inlet with u_{Lin} = 0.2 m/s and T_{Lin} = 369 K, Fig. 5 represents qualitatively the void and velocity profiles over the whole test facility. The temperature has been kept saturated and a constant vapour source term without condensation has been modelled, as described by Janssens-Maenhout (1999).

6 Measurement Results

6.1 Characteristic Profiles

In the profile of dp_1 the three phases of incubation, expulsion and void entrainment can be clearly recognized. The total pressure drop dp_1 is mainly affected by the void entrainment and recirculation in the vertical flow section, and is therefore not mostly appropriate to count the geysering periods. The structure of the recirculation is proven by the signal dp_3 since flow accelerations cause an underpressure for downward flow respectively an over-pressure for upward flow. The pressure drop dp_2 shows that the geysering never reaches the bottom part of the vertical section and never propagates into the horizontal section.

The profile of the gauge pressure dp_4 in the vapor room above the outlet free surface shows up the highest movements. Therefore this signal is used for determining the perio-dicity of the geysering. The signal dp_4 indicates clearly the vaporization during the geysering and the therefore measures the geysering frequency. The integrated value of the condensing water at the outlet over 1 h agrees well the integral pressure movement of dp_4.

The temperature profiles indicated a gradually decrease of temperature with increasing height. The profiles T7, T8, and T9 in the middle of the riser show a strong mixing of the two-phase flow. Because of the short measurement time of fibre optical probes the void measurements did not represent the periodicity of the void behavior during geysering in SUCOT. The void measurements just confirmed the variety in size and form of some clusters of bubbles.

6.2 *Geysering Frequency as Function of the Wall Heat Flux*

The geysering frequency f_{Geyser} is determined by the number of pressure peaks N_p during the measuring time τ_p of 1 h:

$$f_{Geyser} = \frac{N_p}{\tau_p} \quad . \tag{2}$$

The frequency of the geysering has been derived applying a discrimination procedure with an exceed of 2 mbar onto the pressure signal of dp_4. The qualitative result of the geysering frequency is not affected by the chosen exceed value. This discrimination procedure has been used because the Fourier Transform of the pressure signal did not result in a spectrum indicating a specific frequency for the case of low heat flux. The frequency f_{Geyser} has been analyzed as function of the heat input Q_{Geyser} for the geysering, defined as

$$Q_{Geyser} = Q_W - M_L \, c_{pL}(102°C - T_{Lin}(°C)) \quad . \tag{3}$$

In the calculation of the geysering energy Q_{Geyser} the value of 102°C for the temperature at the onset of steam formation has been chosen because with this value the highest correlation factor of the temperature measurements was obtained. The experimental results of f_{Geyser} as function of Q_{Geyser} for all the experiments with the different inlet parameters are represented in Fig. 6. Once a minimum heat input is exceeded, the geysering frequency f_{Geyser} enhances proportionally with increased geysering energy Q_{Geyser}. This minimum heat input is needed to cover the heat losses. This result characterises the two-dimensional geysering phenomenon. In the one-dimensional case Ozawa, Nakanishi, Ishigai, Mizuta and Tarui (1979) observed a decrease of the geysering frequency with increased geysering energy. The well correlated data in Fig. 6 also illustrate the reproducibility of the experimental results.

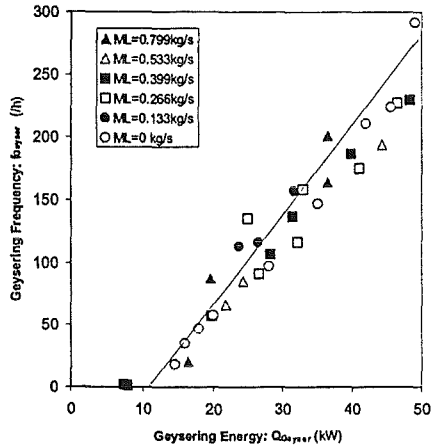

Fig. 6: Pressure peaks over energy.

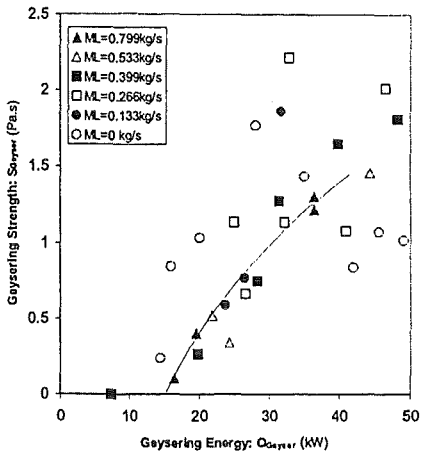

Fig. 7. Geysering strength over energy.

6.3 Geysering Strength as Function of the Wall Heat Flux

The cumulative time distribution of the pressure signal dp4 in the vapor room at the outlet allowed filtering of the pressure peaks due to geysering out of the noise in the boiling two-phase mixture. Thereby the geysering strength S_{Geyser} has been defined as

$$S_{Geyser} = \frac{1}{N_p} \sum (dp_4 - dp_{threshold}) \quad . \tag{4}$$

The geysering strength S_{Geyser} has been analyzed as function of the energy input Q_{Geyser} for the geysering. Fig. 7 shows S_{Geyser} as function of Q_{Geyser} for different inlet mass fluxes. After exceeding a minimum heat input the geysering strength S_{Geyser} starts to increase strongly with increasing geysering energy Q_{Geyser}, especially in the case of low mass flux but then tends to increase more smoothly. From Fig. 7 a threshold for a geysering of non-zero strength can be derived.

6.4 Geysering Frequency as Function of the Initial Hydrostatic Head

Additionally experiments at zero mass flux have been performed for different initial hydrostatic heads, changing the original water level z_0 from 5.5 m in steps of 0.5 m towards 2.5 m. At lower water level boiling at the heated bottom plate occurs at lower temperature. The geysering frequency f_{Geyser} enhances with decreased water level z as shown in Fig. 8. Due to the change in the volume of the vapor space, a scaled step of 2 mbar . $(z_0 - z)/z_0$ instead of the constant 2 mbar step was applied in the discrimination procedure for the signal dp_4. Additional influence of the condenser ability has been neglected. Scaling of the geysering energy Q_{Geyser} with the enthalpy of the total volume of saturated water in the riser, defined as

$$Q'_{Geyser} = \frac{Q_{Geyser}}{\rho_L \, w_h \, zd \, \Delta h_{LG}} \tag{5}$$

yields a unique correlation between f_{Geyser} and Q'_{Geyser}. This is represented in Fig. 9 and means that the total energy stored in the geysering, scaled with the initial water volume is for a given heat input constant. This confirms that the geysering in the vertical section is not disturbed by the horizontal section of the test facility.

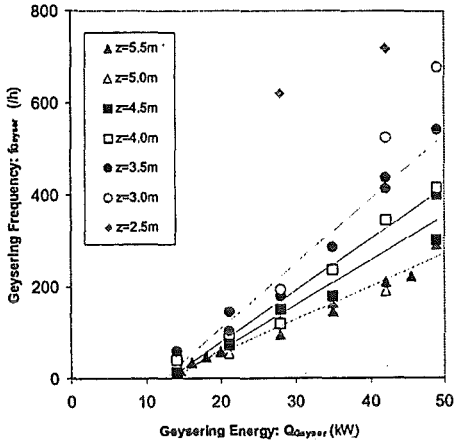

Fig. 8: Different initial water levels

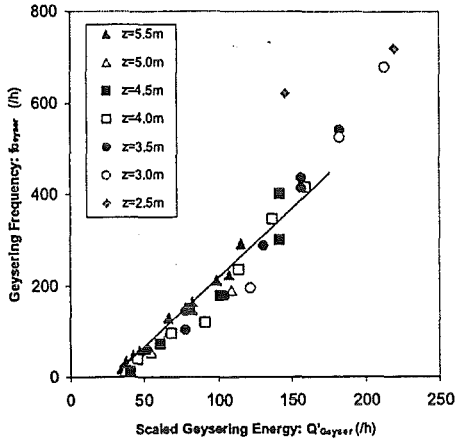

Fig. 9: Frequency over scaled energy

The general behavior that the geysering frequency decreases with increased initial water level z is related to the enlarged water volume of the riser. By increasing the water level the aspect ratio N_R is reduced and the vertical section resembles the one-dimensional channels with geysering at lower frequency. The temperature profiles of the thermocouples in the riser only depend on the distance between the thermocouples and the water level.

Below 3.0 m the strong increase in geysering frequency indicates a transition to another instability mode of the geysering. Moreover the temperature signals in the horizontal and vertical section for the cases of 3.0 m to 5.5 m water level differ completely from the temperatures recorded in the case of 2.5 m water level. The more regular temperature behavior in the case of 2.5 m water level is strongly influenced by the boiling noise of the horizontal section whereas the irregular temperature behavior in the other cases are due to the strong mixing in the void entrainment phase.

6.5 Geysering Frequency as Function of the Riser Width

The riser width has been reduced from 950 mm to 307 mm by inserting a separation plate from the bottom at z = 0.0 m until in the vapor space at z = 6.0 m. At reduced riser width the onset of geysering moved towards higher energy input for the geysering Q_{Geyser}, as represented in Fig. 10. The geysering frequency also increases with increasing energy input more rapidly in the case of a narrow riser than in the case of a wide riser since a smaller water volume is present in the riser. The comparison of the case with narrow riser

width of 307 mm and the original case with riser width of 950 mm is complicated by the difference in heat leaks. The influence of the non-active channel of 643 mm at a temperature some degrees below the temperature in the active channel of 307 mm could not be estimated.

Clearly a difference in flow behavior was observed. The convective rolls in the riser are much smaller and confirms the scaling of the diameter of those rolls with the channel width. Moreover less mixing was established. This observation was confirmed by the temperature measurements. The temperature profile in the case of narrow riser shows a much smaller fluctuation in the horizontal layers and much larger vertical temperature gradient over the different layers than the temperature profile in the case of a wide riser. Only the temperature profile T8 shows larger fluctuations around a mean temperature value, which is situated more close to the maximum value. It can be assumed that T8 is after a geysering expulsion affected by a reversal of colder water layers. This means that the geysering in the case of a narrow riser does not expand downwards so low as in the case of a wide riser.

Experiments in the narrow riser at different initial hydrostatic head are not representing the same tendency as in the original case of the wide riser. This is shown in Fig. 11. The dip in geysering frequency can be explained by a different behavior of the two-phase flow with strong flow oscillations. These flow oscillations are more expressed in the case of a narrow riser, since in the case of a wide riser the large volume of water with larger inertia damps this oscillating effect coming from the horizontal section. These flow oscillations also explain the broader scattering of measured geysering frequency data for the narrow riser case in Fig. 11.

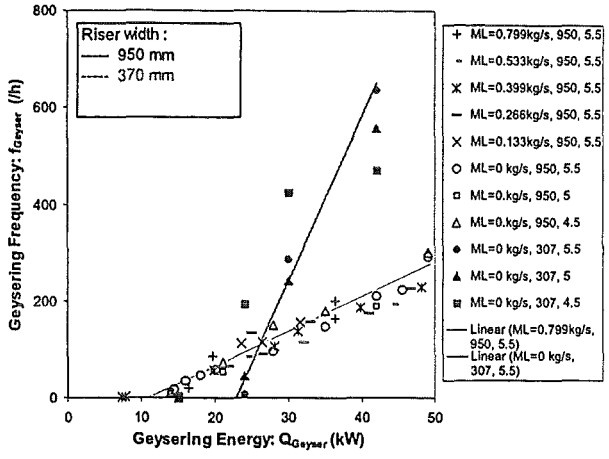

Fig. 10: Frequency in a narrow/wide riser

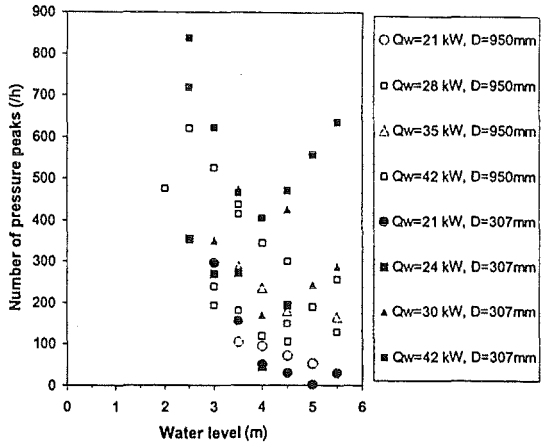

Fig. 11: Water width/height dependence

7 Conclusion and Perspective

Insteady, subcooled boiling two-phase flow in large two-dimensional geometries are still hard to be numerically simulated and need still experimental, validated correlations. The geysering phenomenon in a two-dimensional flow cross-section is strongly affected by turbulent convective rolls and therefore less explosive. One geysering period can be divided in an incubation phase, expulsion phase and void entrainment phase.

In the one-dimensional case the geysering frequency decreases by increasing the geysering energy. But in the two-dimensional case the geysering frequency increases by increasing the geysering energy. Moreover by reducing the initial water level the two-dimensional effect becomes stronger and the geysering frequency enhances even more. For high initial hydrostatic head the geysering frequency tends to approach an asymptotic value. The geysering strength enhances also by increasing the geysering energy but tends to approach an asymptotic value for high heat input.

The mixing plays a major role in the geysering phenomena. The onset of geysering can be postponed by inserting separation plates, impeding the establishment of large convective rolls. In a narrow riser the geysering frequency is not reduced proportional with the initial hydrostatic head because of a different flow oscillation behavior.

References

Aritomi, M,. Chiang, J. And Mori, M.: 1993, Fundamental study on thermal-hydraulics during start-up in natural circulation boiling water reactors: II natural circulation oscillation induced by hydrostatic head fluctuation., J. Nucl. Science and Techn. **30**(3), 203-211.

Bource, J., Bergles, A. and Tong, S.: 1973, Review of two-phase flow instability, Nucl. Eng. Design**25**, 165-192.

Fukuda, K. and Kobori, T.: 1978, Two-phase flow instability., Proc. 6th Int. Heat Transfer Conf. **FB**(17).

Griffith, P.: 1962, ASME paper 62-HT-39, K. Am. Soc. Mech. Eng. **62-HT**(39), 1.

Ishii, M., and Zuber, N.: 1970, Thermally induced flow instabilities in two-phase mixtures., Proc. 4th Int. Heat Transfer Conf., Paris pp B-5.11.

Janssens-Maenhout, G.: 1999, Beiträge zur Modellierung und numerischen Simulation von Zweiphasenströmungen mit Wärmeübertragung., PhD thesis, University of Karlsruhe. FZKA Report 6228.

Janssens-Maenhout, G., Daubner, M., Knebel, J. and Müller, U.: 1999, Boiling driven mixed convection in a L-shaped slab geometry., Proc. EUROTHERM 63 pp 189-198.

Jiang, S., Yao, M., Bo, J. and Wu., S.: 1995, Experimental simulation study on start-up of the 5 MW nuclear heating reactor, Nucl. Eng. And Design **158**, 11-123.

Lahey, R.J., and Yadigaroglu, G.: 1982, On the relationship between Ledinegg and Density Wave instability analysis, Trans. **41**, 689-691.

Ozawa, M.: 1999, Flow instability problems, Steam Power Engineering: Thermal and Hydraulic Design Principles. **Chapter 5**, 323-385.

Ozawa, M., Nakanishi, S., Ishigai, S., Mizuta Y. and Tarui, H.: 1979, Flow instabilities in boiling channels, part 2: Pressure drop oscillations, Bull. Jap. Soc. Mech. Eng **22**(170), 1113-1118.

Ozawa, M., Nakanishi, S., Ishigai, S., Mizuta Y. and Tarui, H.: 1979, Flow instabilities in boiling channels, part 2: Geysering, Bull. Jap. Soc. Mech. Eng **22**(170), 1119-1126.

Van der Hagen, T., Stekelenburg, A., and Van Bragt, D.: 1997, Reactor experiments on type-I and type-II BWR stability, Proc. NURETH 8 **1**, 397-400.

Yadigaroglu, G. and Bergles, A.: 1972, Fundamental and higher-mode density wave oscillations in two-phase flow, Int. J. Heat Trans. ASME **94**, 189-195.

32.21.06 Dynamische Beanspruchung von Reaktordruckbehälter und Containment-Strukturen unter hochtransienten Belastungen

I. Reactor Pressure Vessel Head Loaded by a Slug Impact

(B. Dolensky, B. Göller, T. Jordan, R. Krieg, M. Lux, G. Messemer, H. Rieger, M. Sidor, IRS)

Abstract

The behavior of a reactor pressure vessel head loaded by a corium slug impact which may be caused by a postulated in-vessel steam explosion has been investigated recently by means of model experiments. In this paper three key problems of this work are addressed. It is demonstrated that the formation and acceleration of a rather compact corium slug cannot be ruled out despite of various dispersion effects which may take place. Furthermore, a method is described to determine the local strain distribution in the vessel head which has been strongly deformed during the model experiments. Finally it is demonstrated that the results of model experiments describing complex liquid structure impact processes can be converted to reactor dimensions using similarity theory.

1. Description of the Problems

During a postulated in-vessel steam explosion molten core material may be accelerated as a liquid slug against the upper vessel head. If the head would fail, fragments of it could be hurled against the containment shell and endanger its integrity [1, 2]. Therefore, it is required that the liquid slug impact must not cause failure neither of the vessel head nor of the bolts connecting the head to the vessel flange.

In previous investigations [3, 4] the kinetic slug energy which can be surely carried by the vessel head and the bolts was determined to

- 0.1 GJ, if all the upper internal structures are molten,
- 0.4 GJ, if at least the upper support grid is left,
- 0.8 GJ, if the complete upper internal structures are left.

These results were based on the model experiments BERDA I, where the essential reactor dimensions were scaled down by a factor of 10. The corium slug hitting the vessel head was simulated by a liquid metal slug of about the same density. During the acceleration phase the liquid metal slug was contained in a very thin walled crucible which was supported by another rather strong crucible. Later, during the free motion phase up to the impact, the slug was contained only in the thin walled crucible. In this way a quite compact liquid slug was obtained causing the most unfavorable impact process with a relatively high impact force. In comparison to that the direct effect of the stiffness of the thin walled crucible on the impact process can be assumed to be negligible.

Here the question was raised whether these conditions might be too conservative. In reality dispersion effects should be expected to reduce the compactness of the slug and therefore also the impact force considerably. In the meantime the experiments BERDA II-DETAIL were performed. They have shown that dispersion effects will not affect the compactness of the slug significantly, provided radial dispersions are suppressed by a cylindrical constraint. More details of these experiments are presented in section 2.

In the model experiments BERDA I, among others, the deformations of the model heads were measured. According to the similarity theory described in [3, 4] the deformations of the real head are similar up to a critical limit, where severe material damage and cracking begins. Unfortunately this limit is size dependent, but reliable information is not available yet. Therefore, it was decided that only those BERDA I tests are really convertible to the reactor scale, where the resulting deformations of the model heads are mainly within the elastic region. Larger deformations might only become acceptable, if new research work yields more information on size effects in deformation and fracture [5].

In fact, a small permanent vertical displacement of the model heads up to about 5 mm was assumed to be tolerable; higher displacements reaching values up to 30 mm were not accepted. However, little information was available about the resulting local strains; the application of strain gauges was difficult and the calculation of strains using measured displacements between marked points at the head was

mostly too inaccurate. But on the other hand, the strains are the relevant quantities to describe the critical deformation limit mentioned above and to assess the structural integrity. To solve this problem, a computational procedure was developed to calculate the strain distributions in the head using the measured vertical displacements of selected points of the head. This procedure and the results are described in section 3.

Finally, the results of the model experiments BERDA I were converted to reactor dimensions using similarity theory. Although highly nonlinear effects such as classical elastic-plastic material models were included, rather simple scaling rules between quantities of the model and the related quantities of the reactor had been obtained [3, 4]. Furthermore, simplified liquid structure impact experiments in different scales were carried out, to check the scaling rules [6].

Nevertheless it was felt that additional model experiments simulating a molten core slug impact against the upper vessel head in a scale different from BERDA I could be of great help to demonstrate once more that the application of similarity theory provides indeed a satisfying solution. Therefore, the model experiments SMALL BERDA have been performed, where the essential dimensions were scaled down by a factor of 50 in comparison to reactor dimensions, i.e. a factor of 5 in comparison to BERDA I. Then the SMALL BERDA results have been converted to the BERDA I size using the above scaling rules. Comparison with the BERDA I results yields a fairly good agreement and confirms again that the reactor problem was solved adequately. A detailed description of the SMALL BERDA activities is given in [7], a discussion of the results is presented in section 4.

2. Experiments on the Compactness of a Corium Slug During its Acceleration and Free Motion Phase

The facility BERDA II-DETAIL used to perform experiments scaled down by a factor 35 is shown in Fig. 1a. The grid forming the bottom of the inner cylinder is simulating the core support plate. It was sealed by a thin membrane underneath the grid. About half the volume inside the cylinder was filled with liquid metal simulating the molten

core material. The space between the inner and outer cylinder was filled with hot water to control the temperature.

Water below the grid was suddenly pressurized simulating the loading caused by the postulated steam explosion. Thus the thin membrane underneath the grid was ruptured and water penetrated the grid and accelerated the liquid metal upwards with more than 5000 m/s^2. When the upper surface of the liquid metal had reached the upper edge of the cylinder, the water supply was stopped. Consequently, the acceleration of the liquid metal slug decayed and its movement continued with an almost constant velocity (precisely speaking, vacuum must have been occurred in the cylinder, decelerating the liquid metal slug slightly).

The acceleration and free motion of the liquid metal slug had been watched by a high speed camera. Pictures 2.8 ms, 3.6 ms and 5.2 ms after the sudden pressurization are shown in Fig. 1b to 1d.

One can clearly see that the upper surface of the slug remains relatively smooth. Dispersion effects do almost not occur. That means, the liquid metal slug can be assumed to remain quite compact during its acceleration and free motion phase. Thus the postulation of a rather molten core material slug hitting the reactor pressure vessel head seems to be not too unrealistic.

3. Calculation of the Strain Distributions in the Head Using Measured Vertical Displacements of Selected Points

As a basis of this work a three-dimensional finite element model of the head was developed, Fig. 2a. To reduce the number of the elements, advantage was taken from symmetry conditions and only one eighth of the head was modeled.

In a first approach the measured axial displacements for selected points of the tested head were used as input and the resulting strain distribution was calculated. However, the results were not satisfactory, since at the other points of the head surface the axial displacements turned out to be much smaller than the prescribed values.

In a second approach the measured axial displacements for the selected points were used to form a smooth contact surface of a "forging die". Then the finite element model was used to solve a contact problem assuming that the head is pressed again the rigid surface of the forging die, Fig. 2b. This method turned out to be successful. The pressure applied to the head had to reach a value between 100 and 400 MPa depending on the prescribed axial displacements. A pressure increase beyond this value as well as moderate variations of the constitutive equations had only very little influence on the results. Comparison of the calculated strain fields with some strains measured directly at the model heads showed good agreement.

The second approach has been used to determine the strain distributions for tests 05, 07, 09, 17, 19, 20 and 22, Fig. 3. For each case, except test 07, the maximum peak strain occurring at the edge of one of the holes and the maximum strains occurring between the holes were marked. For test 07 the head did not contain holes and the maximum strain occurring at the center of the outer surface of the head were marked.

Now the main results of the model experiments BERDA I can be extended as follows.

3.1 All the upper internal structures are assumed to be molten

The lower part of Fig. 4 shows the maximum impact force and the maximum vertical head displacement versus the slug impact velocity, alternatively versus the slug impact energy (slug mass 82.5 kg) obtained in the BERDA I tests 05, 07, 09. This has been already discussed in [3, 4]. Now the upper part of Fig. 4 shows additionally the maximum peak strain occurring at the edge of one of the holes and the maximum strain between the holes for test 05 and 09, and the maximum strain at the center of the head for test 07.

The kinetic slug energy which can be surely carried by the real vessel head and the bolts was determined to 0.1 GJ as mentioned in section 1. According to [3, 4] the corresponding value for the BERDA I scale is 0.12 MJ. It has been introduced in Fig. 4 as the admissible kinetic slug energy. Now it can be easily concluded: if this energy

condition is fulfilled, the maximum local strain expected in the head is lower than the values obtained in tests 07 and 09.

It is remarkable that for test 07 using a head without holes the maximum head deformation is larger than for test 09 using a head with holes. In previous publications this findings could be explained by random variations of the liquid slug shapes. This means, when evaluating the results a considerable scatter must be considered.

Fortunately, the assumption that all the upper internal structures are molten, was found to be not very realistic. Therefore, in this case additional tests were not performed and the results play only a minor role. For the following more realistic cases with (some) upper internal structures included significant scatter does not occur, since the upper internal structures were found to provide a certain smoothening of the impact process.

3.2 The upper support grid is assumed to be left

The lower part of Fig. 5 shows the results already discussed in [3, 4]. The upper part of Fig. 5 shows additionally the maximum local peak strain occurring at the edge of the holes and the maximum strain between the holes for tests 17, 19, 20 and 21. For the last test the other upper internal structures have been included, too; but they were made of lead. It turned out that the influence of these very weak structures was quite small.

The kinetic slug energy which can be surely carried by the real vessel head and the bolts was determined to 0.4 GJ. The corresponding value in BERDA I scale is 0.45 MJ. Thus, if this energy condition is fulfilled the maximum local peak strain expected in the head is roughly represented by the strains obtained for tests 19 and 20, which is about 7 %. The maximum strain in the middle between two holes is about 3 %.

3.3 The complete upper internal structures are assumed to be left

Fig. 6 represents the results in the same way as before. The kinetic slug energy which can be surely carried in the real scale is 0.8 GJ, in BERDA I scale it is 0.9 MJ,

which is between the kinetic slug energy for test 22 and the energies for tests 11, 12, 13 and 15. Consequently, if the energy condition of 0.9 MJ is fulfilled, the maximum local peak strain in the head is between the peak strain of 8 % for test 22 and the corresponding strains for tests 11, 12, 13 and 15 which vanish. Thus for 0.9 MJ the maximum local peak strain can be assessed to be smaller than 4 %, the maximum strain in the middle between two holes smaller than 1.6 %.

4. Checking of the Scaling Rules for Molten Core Slug Impacts Against the Vessel Head

In most of the model experiments BERDA I (with the reactor geometry scaled down by a factor of 10) the molten core slug was simulated by liquid metal. Only at the beginning for test 01 and 02 slugs consisting of a large number of lead spheres with 10 mm diameter were used. The liquid metal impact was a little bit stronger than the lead spheres impact, since the liquid metal is almost incompressible, whereas the lead spheres suffered plastic deformations which reduced the slug volume. However, the overall behavior was not very different.

Therefore, it was decided to perform the model experiments SMALL BERDA (with the geometry scaled down by a factor of 50 in comparison to reactor dimensions, i.e. a factor of 5 in comparison to BERDA I) with slugs of lead spheres, which are much easier to handle than liquid metal. First the diameter of the lead spheres was 2 mm, according to a correct geometric scaling. However, it turned out that due to different manufacturing processes the 2 mm spheres were somewhat harder than the 10 mm spheres, while available 3 mm spheres had about the same hardness. Thus 3 mm spheres were used for the SMALL BERDA tests; the total number of spheres forming the slug was still very high.

Furthermore, the material of the heads for the SMALL BERDA tests was a little bit weaker than for the BERDA I tests, but the shapes of the stress-strain diagrams were about the same. However, this deviation can be considered by the scaling rules.

Fig. 7 shows both, the results from test 01 and 02 of BERDA I and the results from test S1 to S4 of SMALL BERDA; the later values are scaled up to the BERDA I size

using the scaling rules going to be investigated here. One can see that the results obtained from both sizes of experiments yield about the same relations. Only the scatter between test S1 and S2 is not fully satisfying.

That means, similarity theory and the scaling rules can be used for an appropriate description of the impact problem under discussion.

5. Conclusions

The work presented in this paper supports the recently published values for the kinetic energies of an impacting corium slug which the reactor vessel head can reliably carry.

- If an in-vessel steam explosion happens, the formation of a compact corium slug cannot be ruled out. This had been assumed in the BERDA I experiments for determination of the kinetic slug energies which the head can carry.
- The maximum local peak strain in the vessel head, which has been assumed to be acceptable, is about 7 %, the maximum strain in the middle between two holes is about 3 %. It is likely that even higher strains may not cause fracture of the head; but the confirmation of this supposition is not available yet.
- The solution of the complex corium slug impact problem using model experiments has been confirmed. The results of the model experiments BERDA I can be converted to reactor dimensions without an undue loss of accuracy.

It should be added here that assessments of the energy releases of in-vessel steam explosions hardly exceed a kinetic slug energy of 0.4 GJ. Considering the slug energies which the head can carry and which are mentioned in section 1 and in Figs. 4 - 6, it can be concluded: An in-vessel steam explosion is not able to cause failure of the vessel head such that the integrity of the containment shell will be endangered, provided the upper support grid in the reactor is available.

References

[1] Keßler, G., Eibl, J., "Severe Accident Containment Loads and Possible Design Concepts of Future Large Pressurized Water Reactor", *Nucl Technology 111*, 358

[2] Lucas, G.E., Amarasooriya, W.H., Theofanous, T.G., "An Assessment of Steam-explosion-induced Containment Failure, Part IV", *Nucl. Sci. Eng. 97*, 316

[3] Krieg, R., Dolensky, B., Göller, B., Hailfinger, G., Jonatzke, O., Malmberg, T., Messemer, G., Stratmanns, E., Vorberg, G., Benz, H., Ratajczak, W., "Load Carrying Capacity of a Reactor Vessel Head under a Corium Slug Impact from Postulated In-vessel Steam Explosion", *Nucl. Eng. Des. 202*, 179

[4] Krieg, R., Göller, B., Hailfinger, G. Messemer, G., Vorberg, G., "Reactor Pressure Vessel Head Loaded by a Corium Slug; Results of Model Experiments BERDA I", *SMiRT-15*, Seoul 199, division P

[5] Krieg, R. et al, "Limit Strains for Severe Accident Conditions – Description of an European Research Program and First Results", *SMiRT-16*, Washington 2001, division P

[6] Stach, T., Malmberg, T., Krieg, R., "Scaled Experiments for a Simple Deformable Structure under Liquid Slug Impact", *SMiRT-14*, Lyon 1997, division P

[7] Jordan, T., "Assessment of Scaling Rules for Internal Impact Loading of a Reactor Pressure Vessel Head", to be published

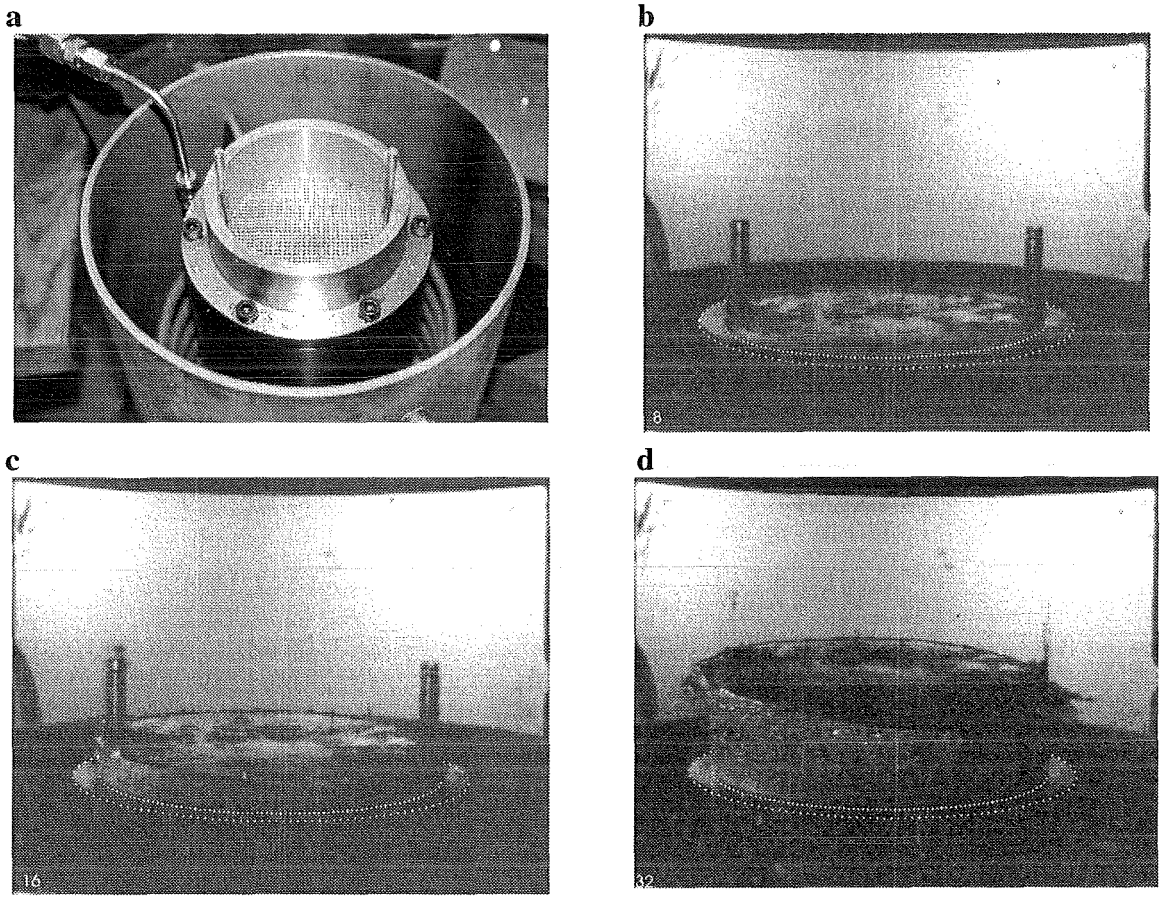

Fig 1a: Experimental facility BERDA II-DETAIL
1b: The liquid metal slug has reached the upper edge of the cylinder, the acceleration decays (2.8 ms)
1c: The liquid metal slug moves with about a constant velocity of approximately 15 m/s (3.6 ms)
1d: The liquid metal slug leaves the cylinder; no significant dispersion effects can be seen (5.6 ms)

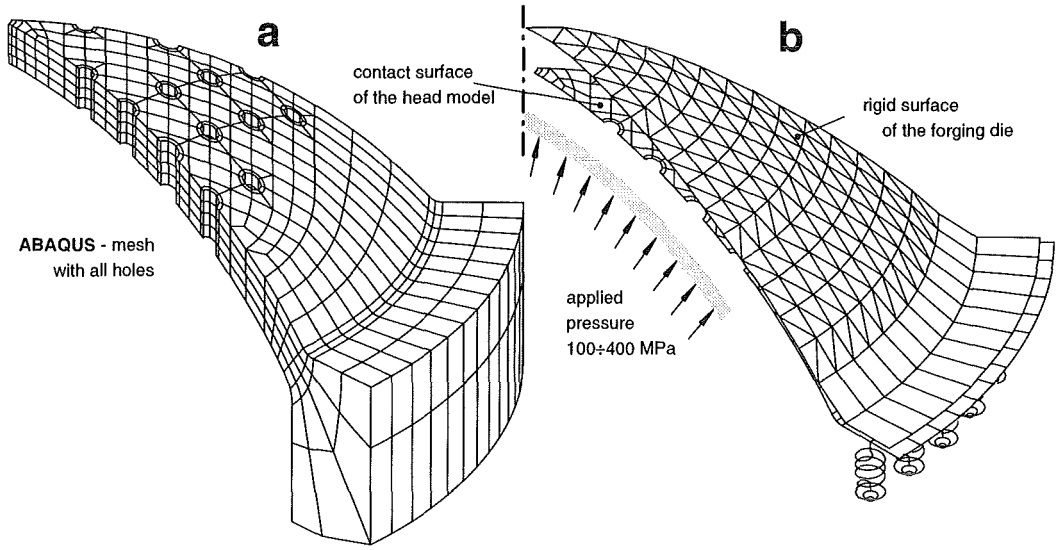

Fig.2: Calculation of the strain distributions using a finite element model and solving a contact problem

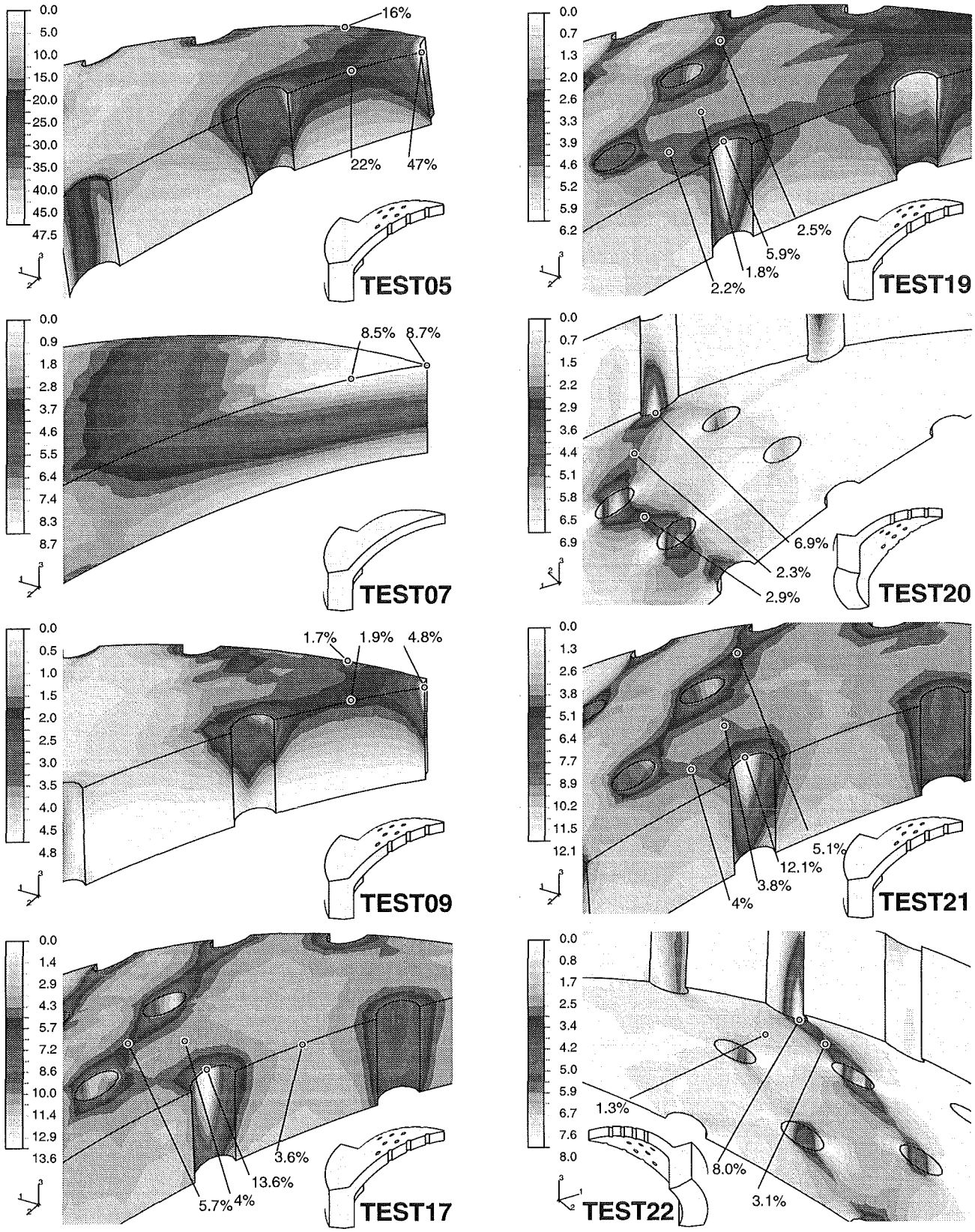

Fig. 3: Equivalent strain distributions in the head for some interesting tests

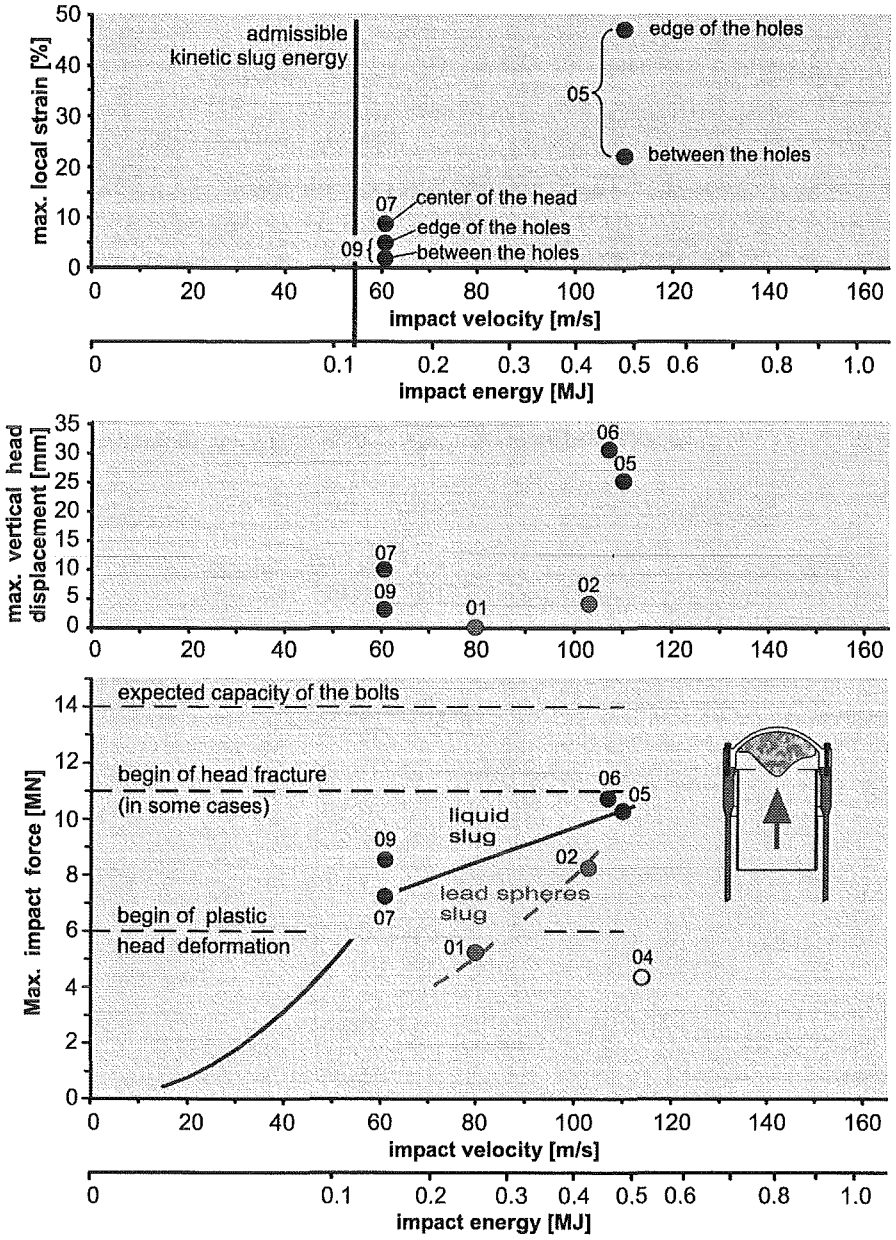

Fig. 4: Main results of the BERDA I tests assuming that all the upper internal structures are molten

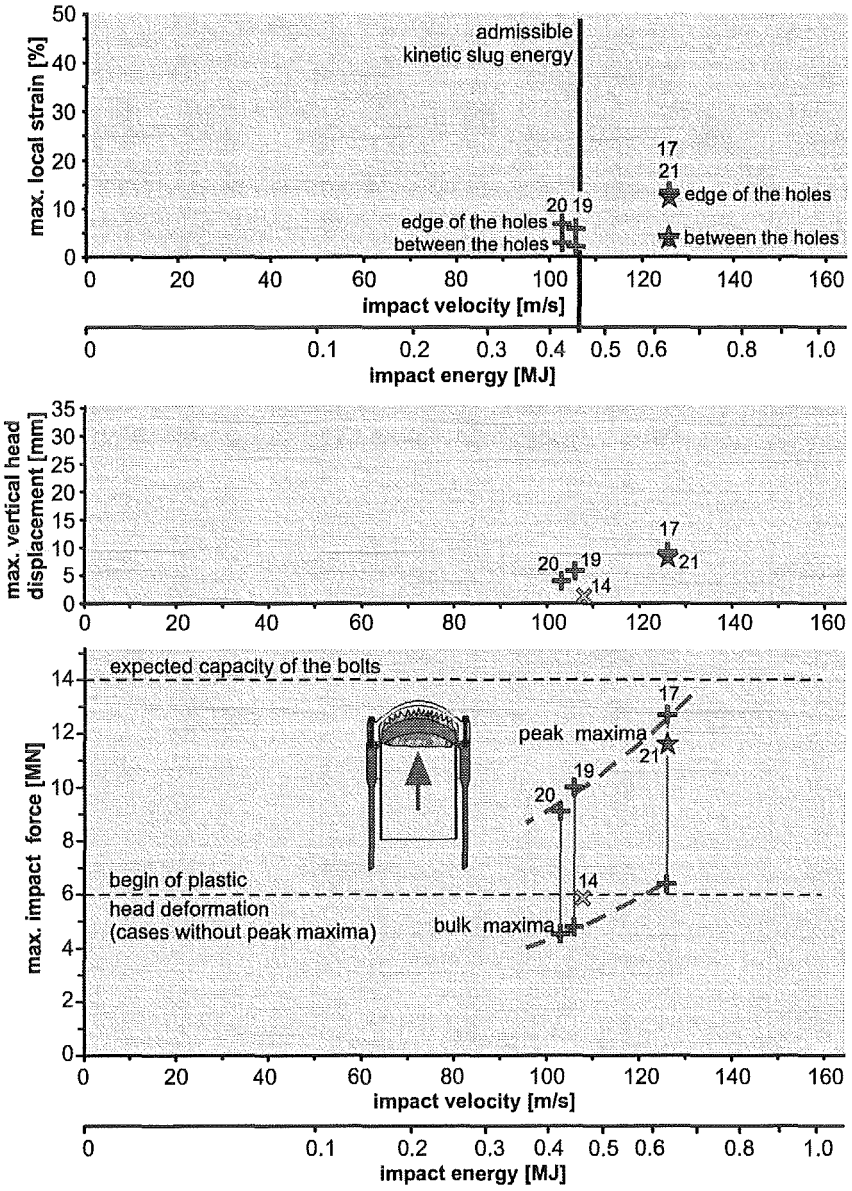

Fig. 5: Main results of the BERDA I tests assuming that the upper support grid is left

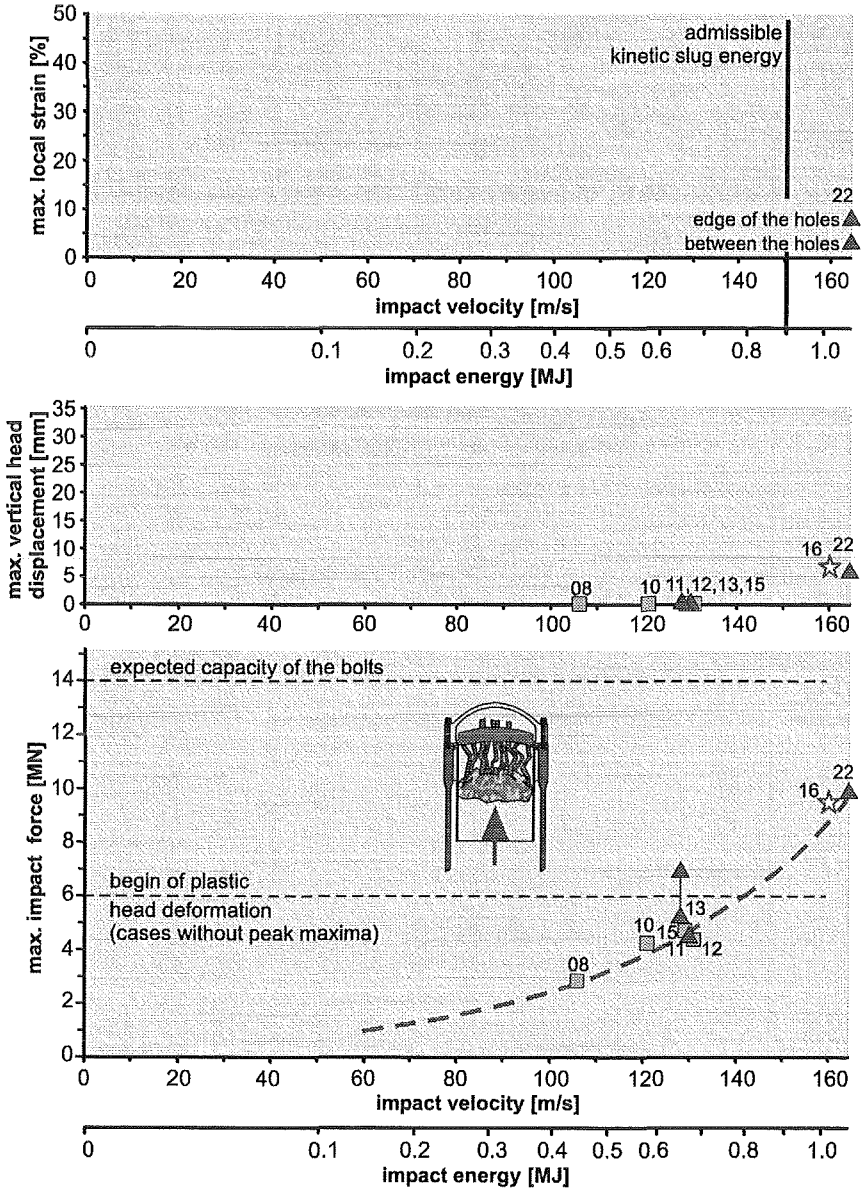

Fig. 6: Main results of the BERDA I tests assuming that the complete upper internal structures are left

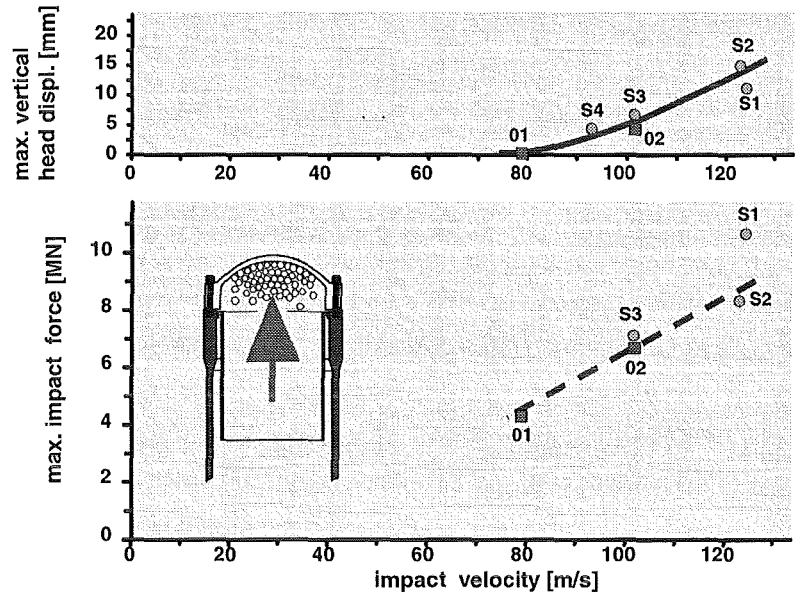

Fig. 7: Results from test 01 and 02 of BERDA I and test S1 to S4 of SMALL BERDA, scaled up to BERDA I size; the force measurement for test S4 failed.

II. Limit Strains for Severe Accident Conditions — Description of an European Research Program and First Results

(B. Dolensky, T. Jordan, R. Krieg, T. Malmberg, G. Messemer, H. Rieger, IRS; J. Aktaa, E. Diegele, R. Schmitt, IMF II; H. Plitz, NUKLEAR)

Abstract

The failure strains for a large variety of specimens from reactor pressure vessel material will be investigated. Of special interest is the dependence of the failure strains on the size of the specimens. The research program and first results are outlined. Based on the findings limit strains will be proposed which should be acceptable under severe accident conditions.

1. Introduction and Overview

The current design rules, which allow only small deformations, are appropriate for the present design basis accidents. These rules and the analyses rely on a stress based concept. Much larger plastic deformations with strains up to a certain fraction of the failure strain should be acceptable for extremely unlikely severe accidents. In this case the analyses must use a more realistic strain based concept. However, reliable information about the failure strains is lacking and therefore, larger strains which should be acceptable under severe accident conditions can hardly be defined. Among others, the influence of the component size is not known; but such information is indispensable, if results from small scale specimens and model tests are to be applied to reactor dimensions.

Therefore, an extensive research program **LISSAC** (Limit Strains for Severe Accident Conditions) with 13 European partners and **sponsored by the European Community** has been launched to determine the failure strains and to propose limit strains, i.e. acceptable strains for essential reactor vessel components under severe accident conditions. The expected results give a chance to reduce undue over-conservatisms of current severe accident analyses.

The main part of work consists of test families with different specimen shapes under uniaxial and biaxial static and dynamic loads at room temperature (RT), at 400 °C and at 850 °C. Within one test family the specimen shapes and the other conditions are the same, but the size is varied up to reactor dimensions. The material for the specimens is taken from the cylindrical section of an unused reactor pressure vessel. Special attention is given to test families where the specimens have a hole or a notch causing non-uniform stress and strain distributions typical for local structural discontinuities in reactor vessel components. There are indications that for such non-uniform distributions size effects may be more pronounced than for uniform distributions. Thus, the investigations should allow to determine size effects on the failure strains and failure processes under conditions close to design configurations.

Also the scatter of the mechanical properties of the material used is carefully studied. To provide a reliable data basis, a large number of material qualification tests including standard tension and Charpy impact tests have been carried out for specimens taken from different locations of the test material.

To deepen the understanding of structural degradation and fracture and to allow extrapolations to other loadings and geometric shapes, advanced computational methods including damage models are under development. In some cases so-called non-local concepts, in other cases the description of stochastic properties at the grain size level are considered.

Similar investigations have been carried out within the previous program REVISA, also sponsored by the European Community [1]. It covers a smaller number of specimen shapes and a reduced geometry scale factor, but it applies to several reactor steels and it includes smooth specimens as well as extensive dynamic and creep testing. Size effects of smooth specimens tested previously have been discussed in [2, 3, 4].

2. Test Families

Fig. 1 shows the different specimen shapes and the different load and temperature conditions considered. The flat specimens with a hole tested under six load and temperature conditions define six test families. The flat specimens with a slot are tested only under static loading and at room temperature and therefore, define just one test family. All together the tests listed in Fig. 1 comprise 22 test families.

Within each test family the specimens are geometrically similar; only their size is varied. The first family of the flat specimens with holes under static loading at room temperature includes five specimen sizes starting with a wall thickness of 4 mm up to a thickness of 200 mm which is almost the wall thickness of the reactor pressure vessel. Recently one partner has added two smaller specimen sizes of 0,2 and 0,8 mm wall thickness. Thus, the size scale (length scale) covers a factor of 1000! This is illustrated in Fig. 2.

The other test families cover a smaller scale factor. The largest specimen thickness is 80 mm, the largest diameter is 150 mm. The biaxial tests include only two different specimen thicknesses, 4 or 5 mm and 20 or 25 mm. The total number of family members, i.e. the total number of different test conditions is 63. Since most of the tests are going to be repeated several times, the total number of tests sums up to 162. Furthermore, in some cases additional pretests were necessary and the material qualification tests mentioned in the next section are going to be carried out, too.

As already mentioned, special attention is given to design typical strain concentrations. The flat specimens with holes can be interpreted as strutural elements of the pressure vessel head with holes necessary for the control rod drive mechanisms. The flat and curved biaxial specimens with holes are steps towards the real geometrical shape and load conditions of the vessel head; of course, the real geometric size and temperatures could not be approached at the same time; this would have been much too expensive. The specimens with notches have been introduced to study other structural elements, for instance the transition between different component cross sections.

3. Test Material

Fig. 3 shows the locations of the specimens within the cylindrical section of the unused reactor pressure vessel which was manufactured for the planned reactor Biblis C in Germany. The material of this pressure vessel is 22NiMoCr37. The locations were determined such that specimens belonging to the same test family are grouped together as closely as possible. In this way the influence of spatial variations of the material properties on the results within one test family is minimized.

In addition, specimens with thicknesses much smaller than the wall thickness t of the pressure vessel were located in the distance $t/4$ from the outside surface of the reactor pressure vessel. Thus the reduced material strength usually found in the middle of the wall and the enhanced material strength at the surfaces of the wall do not appear in the smaller specimens; that means the influence of variations of the material properties through the wall thickness of the pressure vessel has been minimized, too.

Nevertheless, the scatter of the mechanical material properties will be carefully studied by a large number of material qualification tests. Since the carbon content is known to affect the mechanical material properties strongly, the spatial distribution of the carbon content in the cylindrical section of the reactor pressure vessel was investigated. The variations over the cylindrical surface of the vessel were found to be rather small. The variations through the wall thickness were stronger. The most unfavourable variation occurred close to the material qualification test block QA; a somewhat smaller variation occurred at test block QB. The variations are shown in Fig. 4.

For test block QA standard tension tests are going to be performed in axial and circumferential direction and for several positions through the wall thickness. The results are expected soon. For test block QB the results are already available, Fig. 5. The dependence on the wall thickness is rather small. Note that the stress scale starts with 400 MPa.

To allow additional checks, further material qualification test blocks QC, QD, ..., QW have been reserved and a few further tests have already been performed or are going to be performed. From the results available it can be concluded that the scatter of the material properties is rather moderate. Its effect on the material strength within one test family is expected on the order of magnitude of ±1 %; its effect on the material ductility is expected to be in the range of ±5 %.

4. Test Equipment

For the specimens varying strongly in shape, loading and size very different testing machines are necessary.

For the small tension tests standard machines may be sufficient. However, the measurement of local maxima of strains requires sophisticated methods such as the object raster technique. For the largest tension tests a very strong machine is needed as shown in Fig. 6, upper left. For dynamic tension tests with well defined strain rates a machine is needed where the specimens are placed between very long pre-stressed steel cables; Fig. 6, upper right. For dynamic tests of shell specimens an impact machine will be used, where a large number of lead spheres is shot against the specimens; Fig. 6, lower right. Furthermore, a lot of additional test equipment and measuring techniques including micro-structure investigations will be applied, too.

5. First Results

To date specimens of the following families have been tested:

Flat specimens with holes,	static, R.T.;	thicknesses:	4, 20, 40 mm
Circular specimens with notches,	static, R.T.;	diameters:	20, 150 mm
Circular specimens with notches,	static, 400 °C	diameters:	20, 150 mm
Circular specimens with notches,	static, 850 °C	diameters:	20, 150 mm

As stated before, the maximum local strains of the specimens are of interest. Thus, the best representation of the results would be to show the tension forces versus the growing maximum local strains which occur in the holes or notches of the specimens. However, the determination of these local quantities is difficult and requires special evaluations. Here it is important to note that the growing maximum local strains are well represented by the growing vertical diameter of the holes or the growing opening

of the notches of the specimens. The determination of these integral quantities has turned out to be possible with the available measuring system.

Thus, as results, the tension forces are shown versus the growing vertical diameter of the holes or the growing opening of the notches, Figs. 7a – 7d. Results from tests belonging to the same family are shown in the same figure. To allow a comparison of the results, the forces are divided by the smallest initial cross-sections of the specimens which yields a nominal stress. If no size effect would occur, the curves for the tests of the same family would be identical.

A problem is the definition and determination of the maximum deformation of the holes or notches. It should be preferably the deformation when a macro crack starts to develop. But the curves shown in Fig. 7a for the flat specimens with holes include also the process of crack opening and crack propagation from the hole to the outer surfaces. To exclude this later phase the following procedure was used: The growth of the vertical diameter has been measured after the test and the crack opening has been subtracted as indicated in Fig. 8. The resulting values were defined as the maximum deformations and marked by stars in Fig. 7a. A similar procedure was applied for the tests with circular specimens, Figs. 7b – 7d. Here the crack opening seems to be moderate as indicated in Fig. 9; but in the center of the specimens it might be larger and corresponding corrections in the figures might be necessary.

The general finding is that the specimen size has no significant influence on the maximum nominal stress, but a rather strong influence on the maximum growth of either the vertical diameter of the holes or the opening of the notches. More details on some of the tests may be found in [5]. On the other hand, the effect of temperature on the maximum deformations seems to be moderate. However, it should be pointed out that both, the above evaluation and the conclusions are very preliminary. Additional work and test results are urgently needed for more reliable conclusions.

6. Theoretical Models

As stated above, the failure strains, i.e. the strain when a crack starts to develop and the size dependency of these strains are of main interest. This implies that the corresponding theoretical models will have to include both, the phenomenon of damage and a material related length – often called intrinsic length – affecting the deformation and damage process. The classical continuum material models for elasticity, plasticity or damage do not introduce such a length and even viscous or thermal effects do not suffice to reproduce the observed size effects. Therefore, an extension of the classical models or the development of new models is necessary. By the way such models are able to remedy the so-called ill-posedness of deformation behavior emerging when the softening effects rule out the material hardening. Actually, this ill-posedness means a malign mesh size dependency of the numerical results, which is unacceptable.

At present quite different models are under discussion. However, little is known about their success. Therefore, in the LISSAC project several models and solution methods are going to be developed in parallel.

Non-local Concepts

Here the main activities are related to higher gradient models. First steps in this direction have been made within the REVISA project. Mostly these models extend the material law, e.g. the yield function or the evolution equation for internal variables by additive terms containing strain gradients. Two directions are followed in LISSAC. One is the a more pragmatic way based on a Gurson-Tveergard damage model and a strain gradient extension proposed by Aifantis [1, 3, 4]. The relative simplicity allowed to have an early implementation in the FEM code ABAQUS. Thus first calculations of experiments revealing size effects and parameter fittings could be already provided. The other way includes the development of a thermodynamically consistent micro-morphic approach. Because of the complexity its implementation will possibly last until the end of the project.

Mathematically closely related to these approaches are the integral concepts. Here the local values of some model variables are replaced by their spatial averages. The

radius delimiting the domain for the spatial averaging can be correlated with the material intrinsic length. One easy use of this idea is the following. The critical state of a structure is reached when the damage, calculated in a conventional FEM analysis using a continuum damage model, exceeds a critical value in all points of the given domain and not only in one point.

Somehow related are the so-called advanced discrete modelling concepts. One partner has already implemented such a method. It uses the mesh size as the material intrinsic length, which is associated with the average distance of hard manganese sulphur inclusions. This procedure, combined with a Rousselier damage model, is able to model size scaled experiments even beyond the critical damage state in the domain of fracture. However, one major drawback of coupling the element sizes of the numerical scheme to microscopic quantities is that for large specimens a very large number of elements is needed.

Stochastic Concepts

In one approach a Voronoi tessellation method is used for a more direct modelling of the heterogeneous material at the meso-scale of grains. The individual grains are treated as continuous and are subdivided in finite elements. With the help of these simulations representative macro-models can be defined or statistical data on the mean values of the internal variables and on their temporal and spatial correlations may be derived. In the present state only two-dimensional simulations are possible.

With the help of the latter statistical data a stochastic extension of the conventional flow function of a continuum damage model is going to be developed. The material intrinsic length enters the model via the spatial correlation of the white noise background field. Like with the weakest link theories, which were successfully applied for brittle materials, this more empirical approach should be able not only to model size effects, but also experimentally observed scatter.

References

[1] Malmberg, T., Krompholz, K., Solomos, G., Aifantis, E.C., "Size Effects in Deformation and Fracture of a Ferritic Reactor Pressure Vessel Steel", *SMiRT-16*, Washington 2001, division F

[2] Jordan, T., Malmberg, T., "Failure Strain of the Reactor Pressure Vessel Head under Impact Loading", *SMiRT-15*, Seoul 1999, division L

[3] Malmberg, T., Krompholz, K., Solomos, G., Aifantis, E.C., "Investigations on Size Effects in Ferritic and Austenitic Materials", *SMiRT-15*, Seoul 1999, division L

[4] Malmberg, T., Tsagrakis, I., Elefteriadis, I., Aifantis, E.C., "On the Gradient Plasticity Approach to Size Effects, Part I: Reviews", *Forschungszentrum Karlsruhe*, Scientific Report FZKA 6321, Dec. 2000

[5] Aktaa, J., Hädrich, H.J., Julisch, P., Klotz, M., Schmitt, R., "Investigations to Size Effects on Plastic Deformation and Failure Behavior of In-homogenously Loaded Structures", *SMiRT-16*, Washington 2001, division F

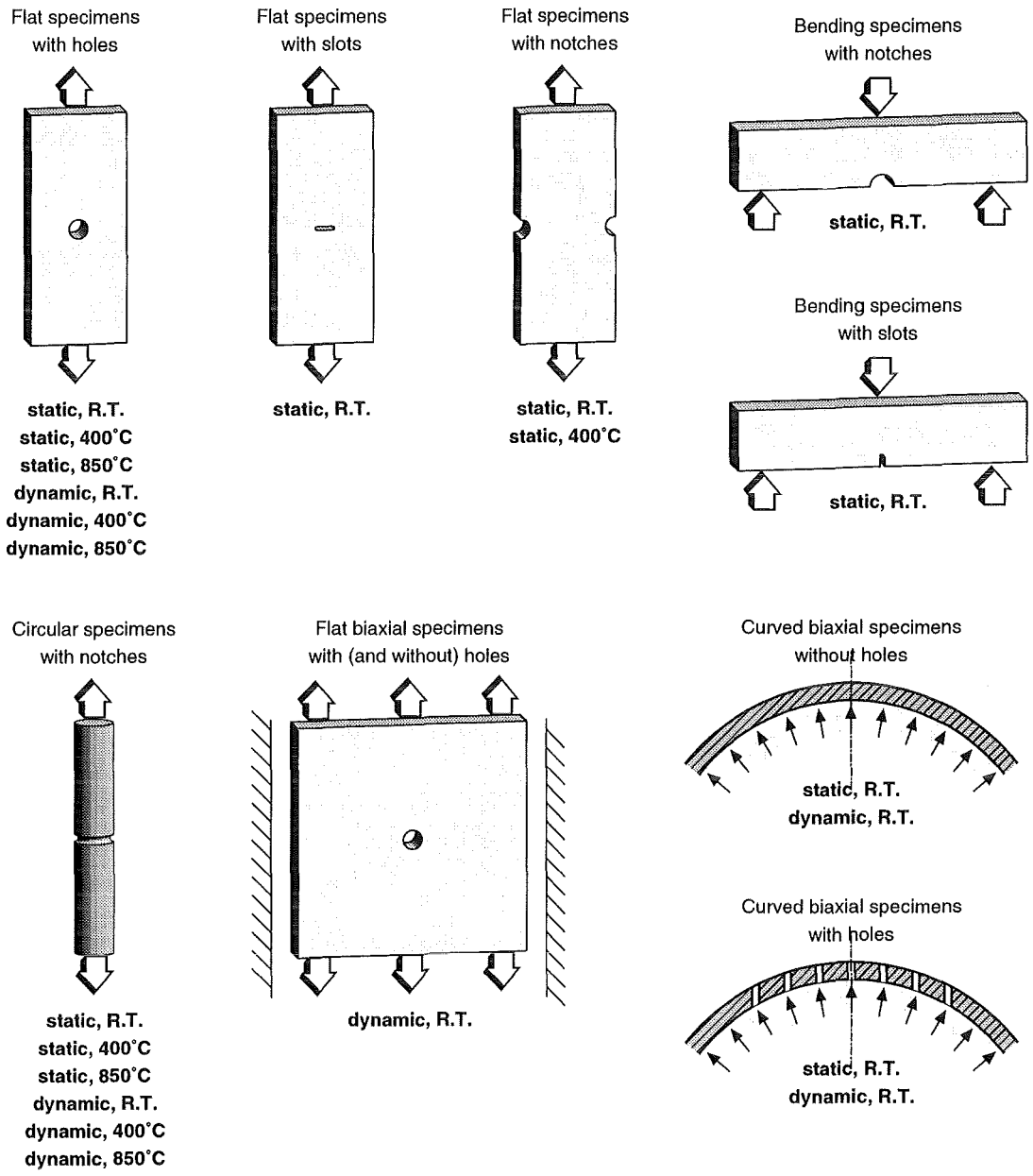

Fig. 1: The different specimen shapes under the listed load conditions define 22 test families

Fig. 2:
Flat specimens with holes to be tested statically at room temperature.

The smallest specimen has a wall thickness of 0,2 mm, expected tension force in the range of 50 N.

The largest specimen has a wall thickness of 200 mm, expected tension force in the range of 50 10^6 N

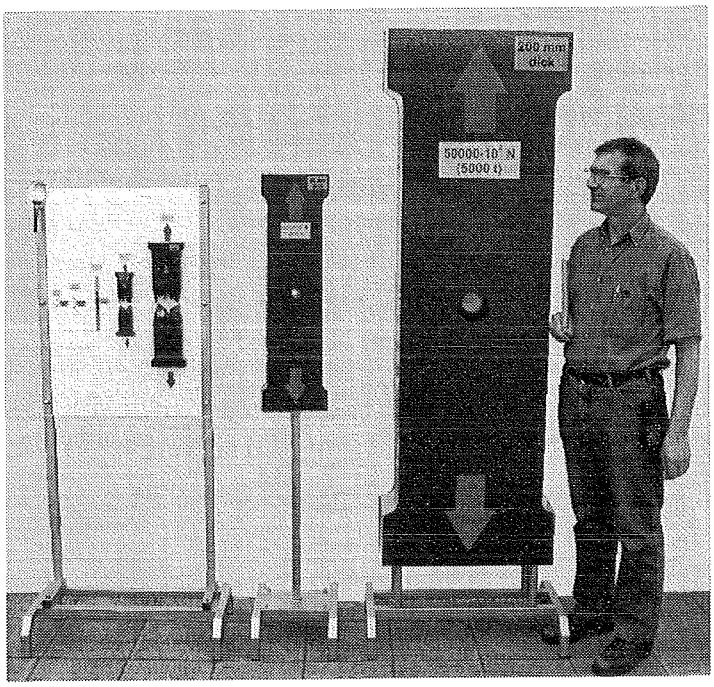

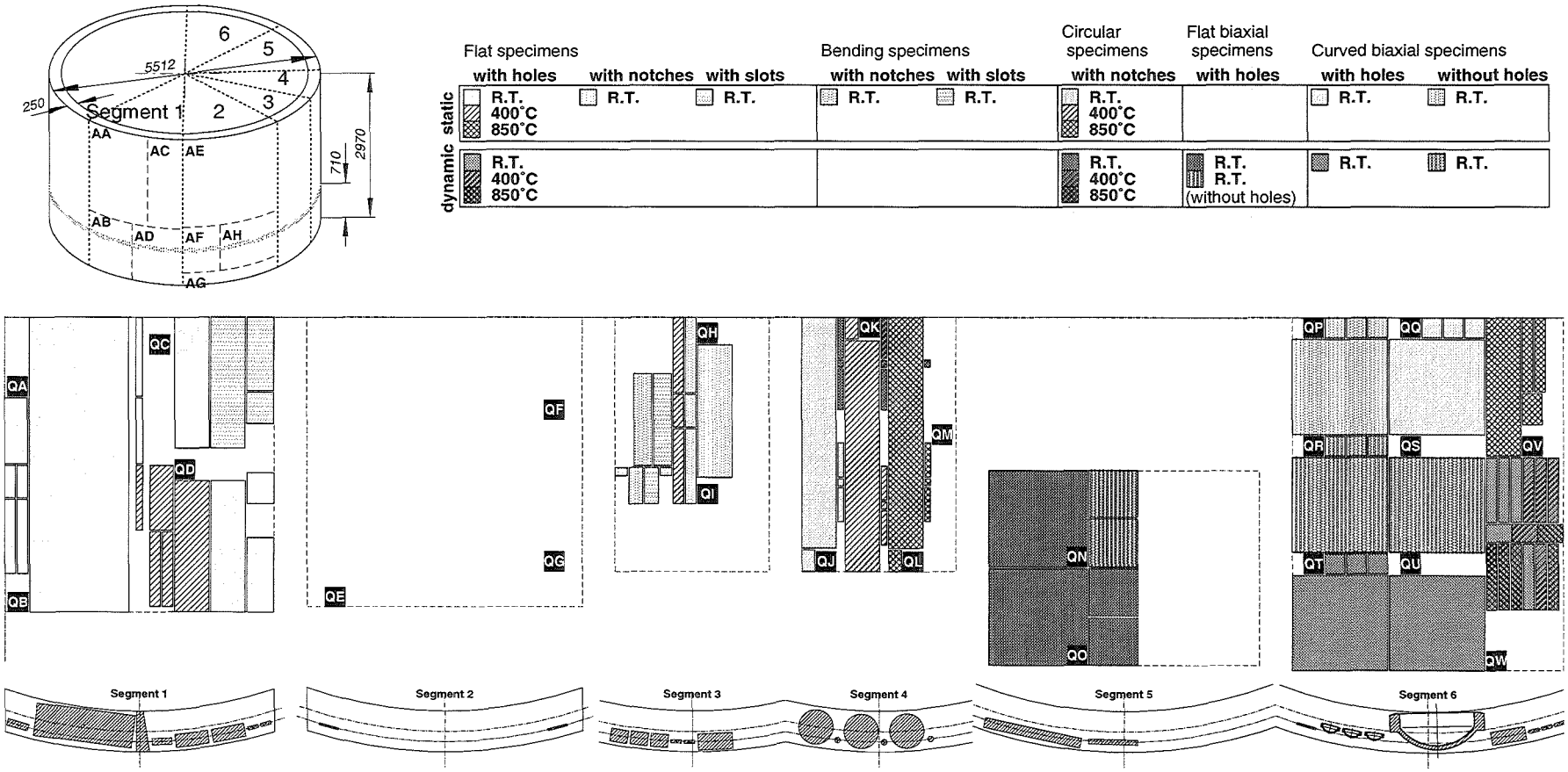

Fig. 3: Location of the specimens within the cylindrical section of the reactor pressure vessel

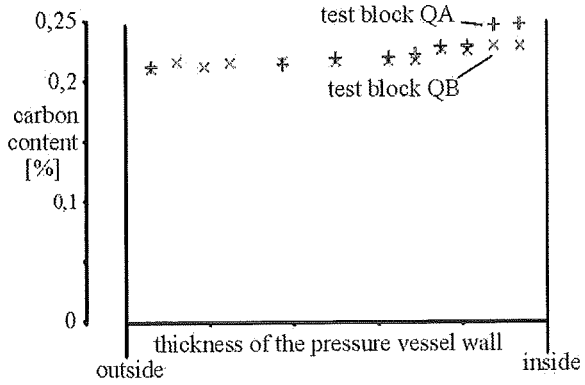

Fig. 4:
Carbon content over the pressure vessel wall.
The strongest variation occurs at test block QA

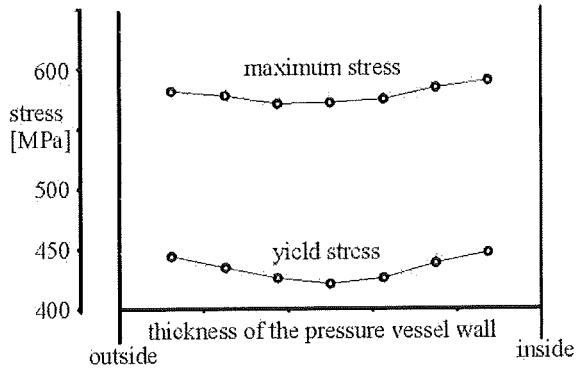

Fig. 5:
Material strength over the pressure vessel wall

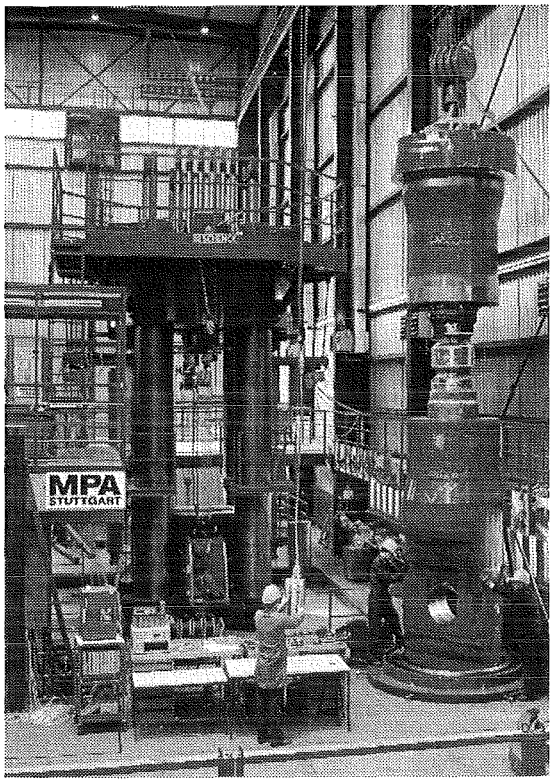

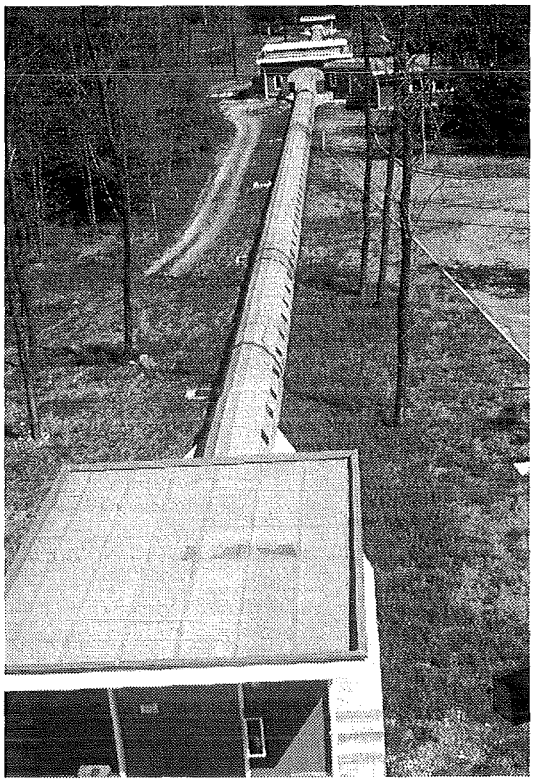

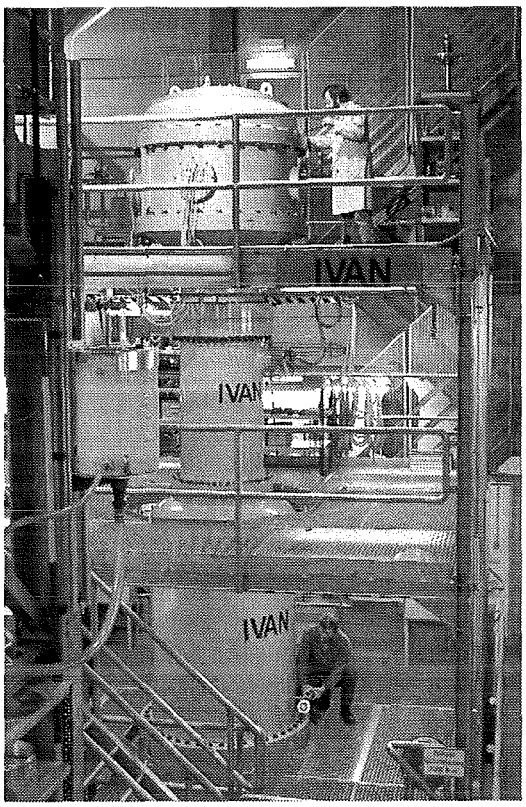

Fig.6: Testing machines used for the LISSAC experiments;

upper left: 10.000 t tension machine, Staatliche Materialprüfungsanstalt Stuttgart;

upper right: Large Dynamic Test Facility LDTF, Joint Research Centre Ispra

lower right: Impact test facility (Impakt-Versuchsanlage) IVAN, Forschungszentrum Karlsruhe;

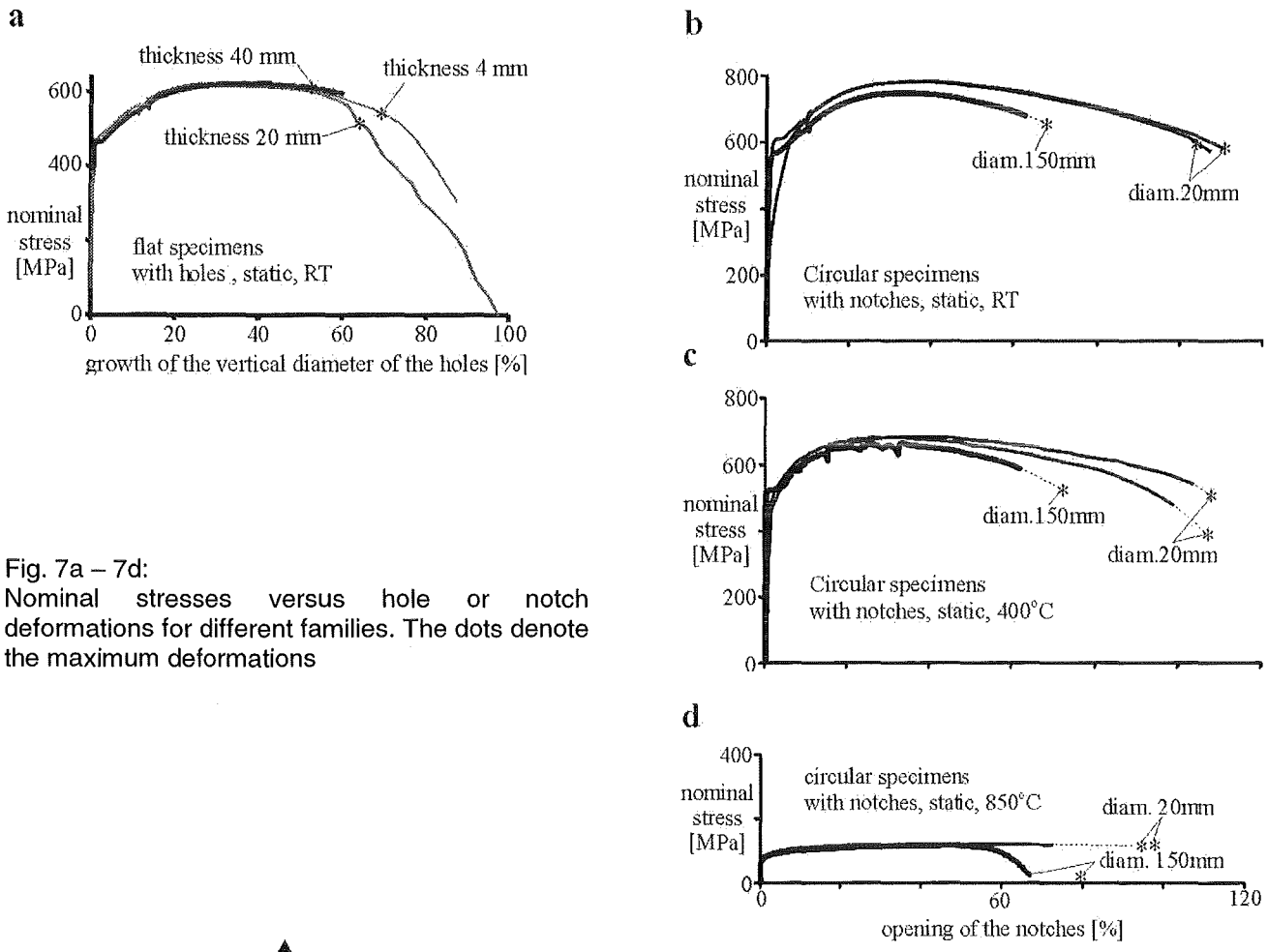

Fig. 7a – 7d:
Nominal stresses versus hole or notch deformations for different families. The dots denote the maximum deformations

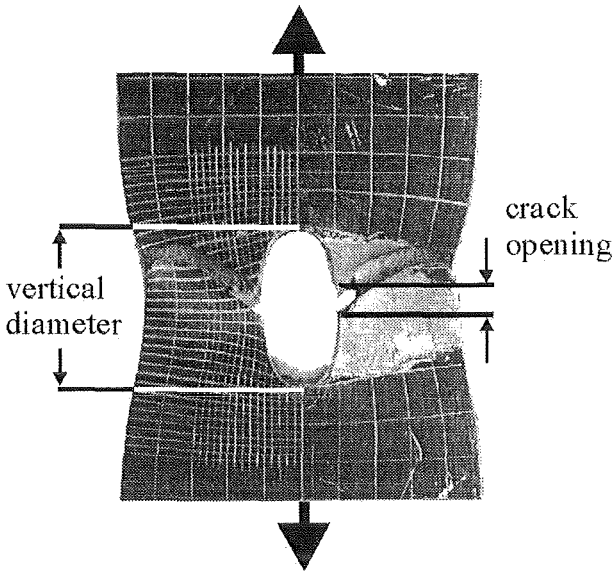

Fig. 8:
Growth of the vertical diameter and crack opening of a flat specimen of 20 mm thickness after failure

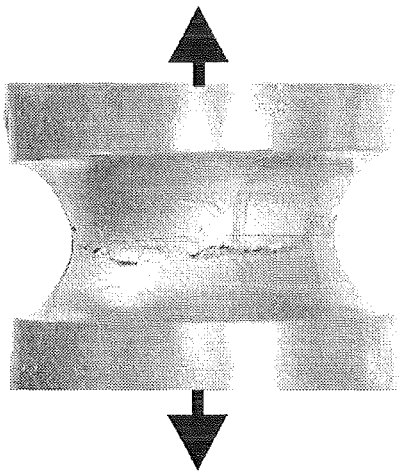

Fig. 9:
Crack opening of a cylindrical specimen with notch after failure

32.21.07 Analysen zum Containmentverhalten

I. The STEPS Process Tracking Model for Fast Calculations of Accidental Radioactive Releases

(P. Schmuck, IKET; J. Miettinen, VTT Energy, Finland)

Abstract

The STEPS system - developed in the frame of the 4th EU framework programme - is capable, at the onset of an accident, of providing estimates of the likely progression of the accident and of the current and potential magnitude and characteristics of radioactive material that may be released to the environment. It is based on information measured on-site and is used in an iterative and dynamic way aimed at constantly refining the assessment throughout the emergency, depending on how the situation develops as more detailed and complete information becomes accessible.

Fast to run, this tool enables the experts to test numerous hypotheses on how the situation will develop. Therefore, the STEPS system helps the user to provide a relatively accurate diagnosis which can be extended by several prognosis calculations. It enables the emergency response team to anticipate further failures and evaluate the possible radiological consequences in the environment in time for countermeasures of protection of the population to be set in place.

It may be noted that the STEPS system was developed as an aid to the expert. It is not intended to replace the expert who remains fully responsible for his assessment. Therefore he needs to have a thorough knowledge of the validity of the tool, and he needs to maintain a critical eye with regard to the results.

STEPS has been designed as a user-friendly and flexible system incorporating models and database for assessing Light Water Reactors status, visualizing main physical parameters evolution to follow accident development, evaluate the amount of fission products released or to be released. Its flexible structure enables it to cope with a large number of European LWR type nuclear power plants, taking into account their own specific characteristics.

In this contribution we describe in some detail the process tracking model which is the main calculational tool to follow the processes up to core uncovery and core degradation.

1. INTRODUCTION

The STEPS system is made available to European emergency organizations to equip their emergency centers for the assessment of the radioactivity released into the environment in case of an emergency situation occurring in a nuclear powered reactor. For this purpose the process tracking model including a thermohydraulic model, a fuel model and a radioactivity transport model has been developed. Using a moderately equipped PC the model can estimate in less than one minute the core status after several hours of accident time and calculate the current and potential radioactive release from the core to the containment and to the environment.

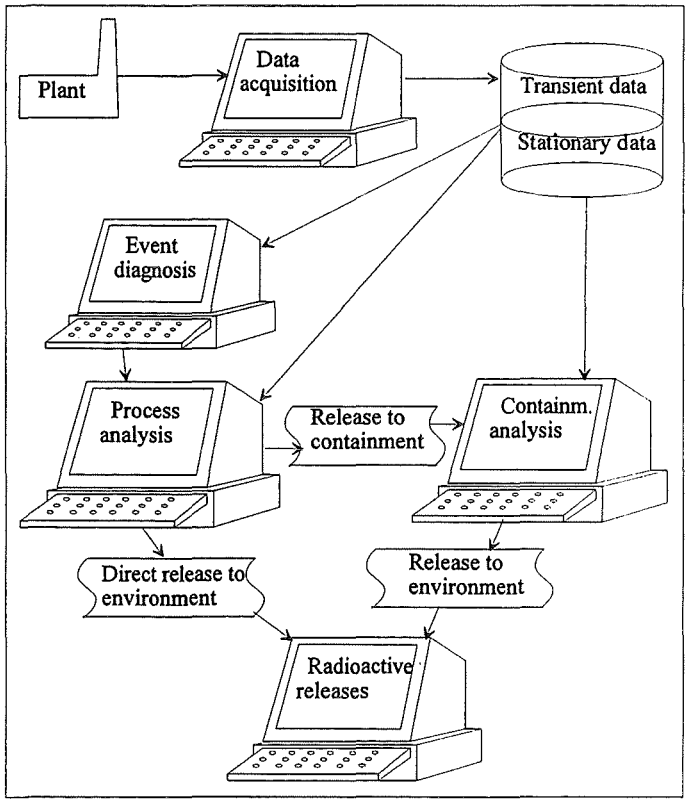

Figure 1. General principles of the STEPS system.

An illustration of the final system is presented in Fig.1. Version 1, being already in use, enables the manual input of parameters describing the plant status. Later versions will include on-line connection of plant and computing facilities to predict faster than real-time the course of the accident. The on-line status information is be transmitted from the plant to the emergency centers. The time development of main parameters is stored in a transient data file. The plant specific basic information is stored initially. After diagnosing the type of an accident the process behavior is

predicted and consequently the release of the radioactivity is estimated. The spreading in the containment is tracked by the containment model. This chain of calculations gives finally the release the environment.

The process tracking model, described is some detail in this paper, calculates the system thermohydraulics, the core heat-up, the radioactivity release from the fuel, transport of different isotopes in the primary and secondary system and the release into the containment.

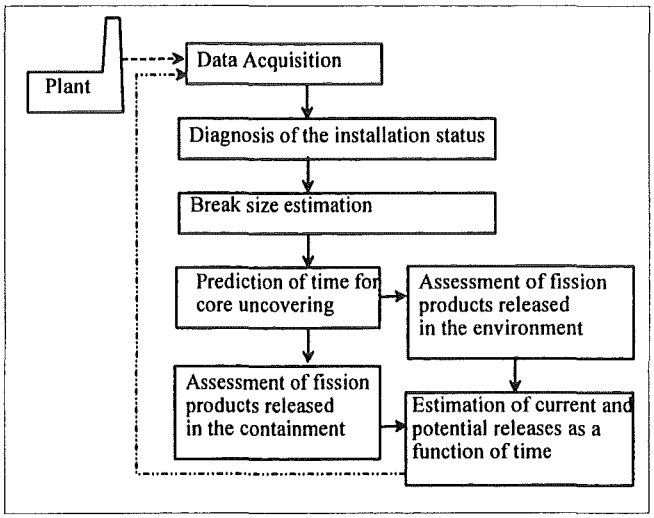

Figure 2. Flow scheme of the process tracking model

The functions included in the process tracking model have been depicted in Fig. 2. The diagnosis of the status is manual with respect to the ongoing accident, but finding the operational status of the plant systems is planned to be automatic. For a LOCA the break size needs to be estimated based on the information gathered during first minutes of the incident. By this prediction and the status of the plant systems the time for the core uncovery and the core heat-up characteristics can be calculated. In STEPS this means simulation with the process tracking model.

During international collaboration on the STEPS project independent modules were developed at different institutions and integrated together later. The interfaces between different modules are depicted in Fig. 3. The process tracking model contains the modules for PRIMARY SYSTEM and SECONDARY SYSTEM. The detailed fuel temperature distribution is calculated by the FUEL STRUCTURE module and the temperature distribution is used for estimating the release of the radioactivity to the coolant in the ACTIVITY module. The transport calculations of radioactivity in

the primary and secondary system and the releases out form an essential part of the process tracking model .

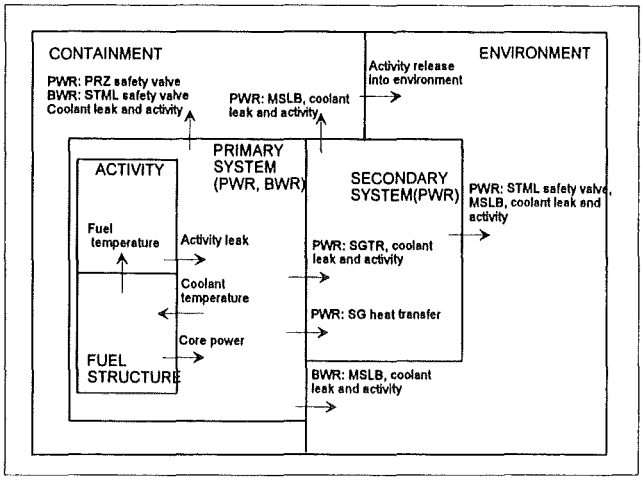

Figure 3. Data exchange between modules

The CONTAINMENT module calculates the radioactivity transport in the containment, in auxiliary buildings and the releases to the environment. Direct releases to the environment are possible in case of a steam generator tube rupture.

2. THE COURSE OF ACCIDENTS IN LWR PLANTS

Scenarios for PWRs

Core overheating and cladding rupture is quite typical for a severe accident scenario in a PWR, e.g. during a SBLOCA with insufficient ECCS injection or during a total station blackout (SBO) accident.

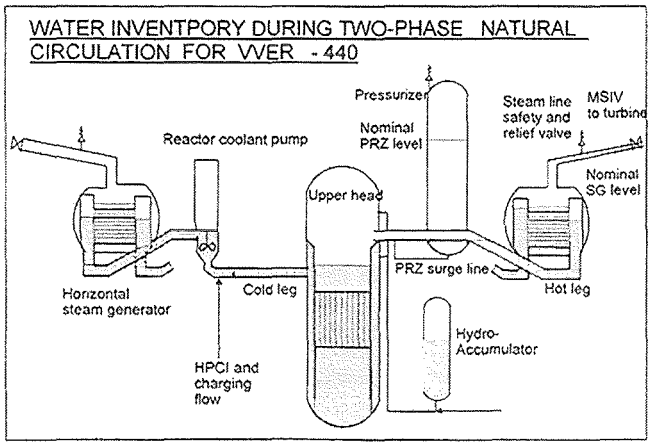

Figure 4. Coolant distribution during SBLOCA in a VVER-440

Fig. 4 illustrates the two-phase conditions in the VVER-440 plant during the SBLOCA accident or after a significant loss of the coolant during a station blackout.

The specific feature for the VVER-440 plant are the loop seals, which cause the stagnation of the two-phase natural circulation as soon as vapor is flowing into the hot leg. Fig. 4 depicts just this condition. The detailed simulation of this situation would require a multi-nodal calculation model. But core cooling is not threatened yet. More coolant has to be lost before the heat-up begins and then the loop geometry has a minor importance. The characteristics of the heat-up depends only on the total coolant inventory in the primary system, primary pressure and core power generation. From view of core temperatures the first cladding ruptures may be expected at 800 °C and radioactive releases are increasing with increasing temperatures. The cladding oxidation is accelerated significantly above 1200 °C and the oxidation process is calculated, too. Gross core degradation is expected at 2600 °C, when the oxidized cladding begins to melt.

Two-phase conditions for the Westinghouse 4-loop PWR are illustrated in Fig. 5. The natural circulation operates in the reflux-condensing mode. If the coolant inventory is increased somewhat, an efficient two-phase natural circulation is possible. Core cooling is not threatened in the depicted state.

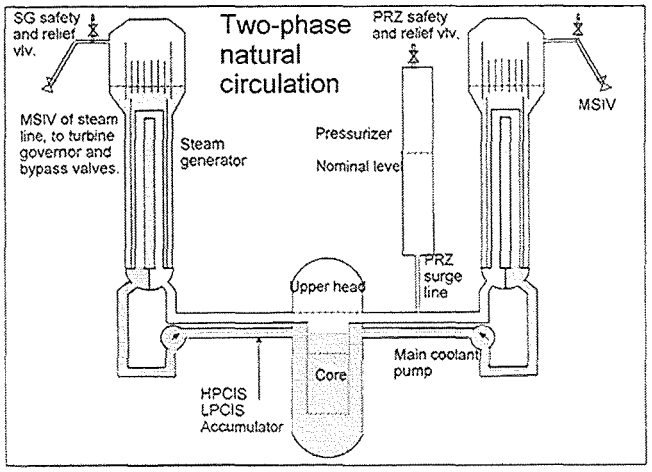

Figure 5. Coolant distribution during SBLOCA in PWR

Similar to the VVER-440 plant a significant reduction of the primary coolant is needed for the core to heat up. Its characteristics depends only on the total coolant inventory in the primary system, the primary pressure and the core power generation. This is the main argument, why a lumped process tracking

model is considered sufficient for predicting the core heat-up characteristics and further the release of radioactivity in PWR plants.

Scenarios for BWRs

The recent BWR concepts with internal circulation do not include any pipelines from the lower part of the vessel, as e.g. the ASEA BWR plant depicted in Fig. 6. The LOCA sequence is practically possible only from the steam line in this case. Another probable sequence causing core overheating is the station blackout (SBO) accident. Fig. 6 illustrates one thermohydraulic state of the blackout accident. The coolant inventory has been significantly reduced, but cooling of the core fuel is still possible. The natural circulation is completely stalled. If the coolant mass is reduced further, core cooling will eventually become impossible.

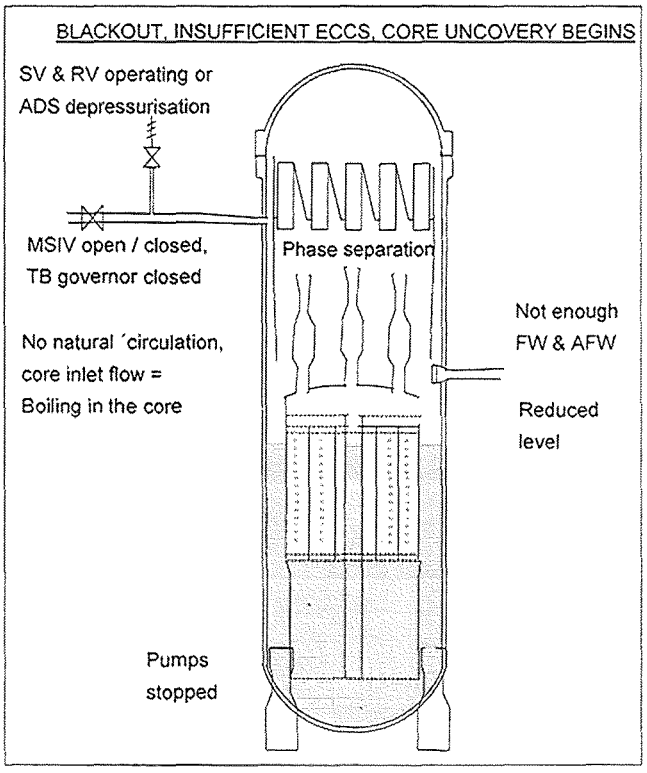

Figure 6. Coolant distribution during a SBO in a BWR

Similar to PWR plants, the core heat-up characteristics in BWR plants depends on the total coolant inventory in the vessel, vessel pressure and core power generation. Thus also for BWR plants the lumped process tracking model is sufficient for predicting core heat-up and further the release of radioactivity.

3. LUMPED PROCESS TRACKING MODEL FOR LWR PLANTS

The process tracking model is realized by a four-section description as illustrated in Fig. 7. In a PWR the section 1 means the entire primary loop except the pressurizer. Cold liquid (cold leg, downcomer, lower plenum, 1/2 core, 1/2 steam generator) and hot liquid (hot leg, upper plenum, 1/2 core, 1/2 steam generator) regions are distinguished. The BWR model uses only the single section 1. Section 2 includes the pressurizer. Section 4 describes the broken steam generator and the related steam line. It is assumed that the broken steam generator is affected by the steam generator tube rupture or by a steam line break. The rest of steam generators are lumped to the section 3, representing the intact steam generators. Sections 3 and 4 may be connected or isolated from the steam line side. This isolation enables independent pressure behavior.

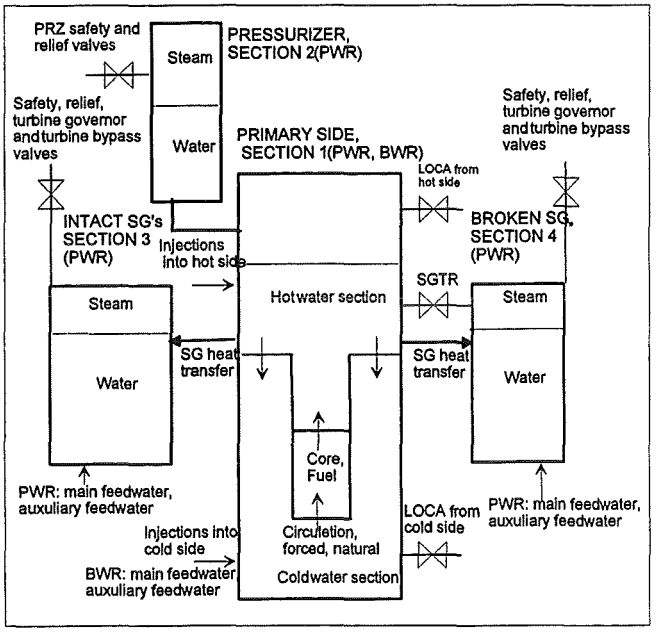

Figure 7. The four section concept.

The lumped volume considers the liquid level inside the section and it is defined by the average void fraction. The break flow rate, the core uncovery, the heat transfer of steam generators, the natural circulation and the flow into the pressurizer depends on the liquid level. The dependency from the liquid level is the feature, which complements the lumped model with the characteristics of the real geometry. The parameters related to the liquid levels and their effect in the physical calculation is described in Table 1.

The sections are rectangular regions, defined by the volume and the height. The core is a part of section 1, but in addition to the coarse hydraulic calculation, the detailed axial distribution is calculated with a fine noding for the main parameters. The core power is calculated as a nominal power during the normal operation and after the shutdown the decay power curve has been applied. The mass flow boundary conditions as inflow and outflow are important for the mass balance.

The coolant injection systems include the emergency core cooling systems as HPCIS and LPCIS, the charging injection and the accumulator injection systems. The main feedwater and auxiliary feedwater are considered for the steam generators of the PWR and for the vessel of the BWR. Steam removal is possible by the turbine governor valve, the turbine bypass valve, the steam line safety valves and the steam line relief valves. Safety and relief valves are considered for the pressurizer, too. The LOCA is considered as a primary LOCA from the section 1 (LBLOCA, MBLOCA, SBLOCA) and as a steam line break from the section 4 (MSLB, FWLB). A primary-to-secondary leak (SGTR) is possible between sections 1 and 4.

The validity of the selected four-section approach may be justified for PWR incidents as follows. The intact and broken steam generators have a different pressure behavior during SGTR and MSLB after the isolation of the steam line. Therefore the intact and broken steam generators are treated separately. The pressurizer includes void fraction in nominal operation and the liquid is saturated. The pressurizer level is used for predicting the break size. The flow quality into the pressurizer surge line is important, when the safety valve opens. These are the reasons why the pressurizer is described separately and why the elevation of the pressurizer surge line must be specified.

Table 1. Level related parameters and their effect.

Relative fraction	Affects to
Fraction of the cold liquid in primary section, F_{cw}	Core heat transfer, natural circulation
Break elevation and width, F_{brk}, D_{brk}	Quality of the break flow as liquid or vapor leak
Elevation of core bottom and core width, F_{co}, D_{co}	Start of overheating the core and the gradient of heating
Elevation of pressurizer surge line, F_{hl}	Flow into the pressurizer, liquid or vapor
Bottom of steam generator and width, F_{sg}, D_{sg}	Heat transfer mode of steam generators
Diff. elevation btw. the core and steam generator, $Z_{co\text{-}sg}$	Natural circulation flow rate (elevation as meters)

The temperature difference between the hot and cold liquid defines the natural circulation and during LOCA the temperature of the hot liquid defines the incipience of the boiling. Therefore hot and cold liquid regions are treated separately in section 1. The heat transfer to steam generators depends to what extent the steam generator tubes are covered. That is why the steam generator elevations have to be specified. Depressurization and coolant removal from the primary circuit depend on the uncovery of the pipe break. Therefore the relative break elevation has to be specified. The core heat-up depends on the elevations and consequently also the core elevations have to be specified.

4. THE FORMULATION OF THE PROCESS TRACKING MODEL

Trip and source term calculation

The timestep of accident calculations is typically 0.5 to 1.0 seconds. The rather short time steps makes the simulation of rapid depressurization and large steam generation together with the turbine pressure control possible by using the semi-implicit solution procedure. The radioactivity model has its own timestep, typically 60 seconds.

The trip signals are tested for the reactor shutdown against the given minimum and maximum pressures. The SI -signal is actuated at the given minimum pressure. These are the only safety signal considered by the trip handling. The opening of safety and relief valves is calculated automatically as a function of the pressure. The rest of the actuations are done manually through the command stream. In the command stream the time point and the command are defined. The available commands are listed in Table 2.

Table 2. Commands controlling the simulation.

Code	Function
A	Define new initial time
B	Open the defined break (LOCA, SGTR, MSLB)
C	Reactor scram
D	Blackout
E	Readjust injection efficiency
F	Readjust valve position
G	Isolate or connect steam generators in steam lines
I	Start or trip an injection
K	Apply prediction for the break size
O	Set listing or plotting time interval
R	Set valve into an automatic mode
T	Trip or start main coolant pumps
U	Update new stationary plant data
X	Update degraded core state
Z	Set stop time for the simulation

The break size prediction is one important aspect for evaluation the course of the accident. An approach was developed, which is based on three discrete readings from the plant and which may be used also with a rather coarse interval of the plant data. The principles of the method using the plant data for the break prediction is presented in Fig. 8.

The break prediction may be based on:

1: Pressurizer level for the primary LOCA and the steam generator tube rupture.

2: Primary pressure for the primary LOCA and the steam generator tube rupture.

3: Broken steam generator level for the steam generator tube rupture.

4: Reactor vessel level for the primary LOCA and the steam generator tube rupture.

5: Broken steam generator pressure for the steam line break.

The method requires that at least two or three data points are available from the plant, one point presenting the stationary state and rest the transient. The transient data points should be inside the availability range. The transient points for the pressurizer level should be collected from the period before emptying the pressurizer. The transient primary pressure points should be collected before the pressure drops down to the level of the secondary pressure. The data for the broken steam generator level should be collected, before the steam generator becomes full. The data for the reactor vessel level should include the points before the core is uncovered. The broken steam generator pressure is good for predicting the steam line break size until about 5 % of the nominal value.

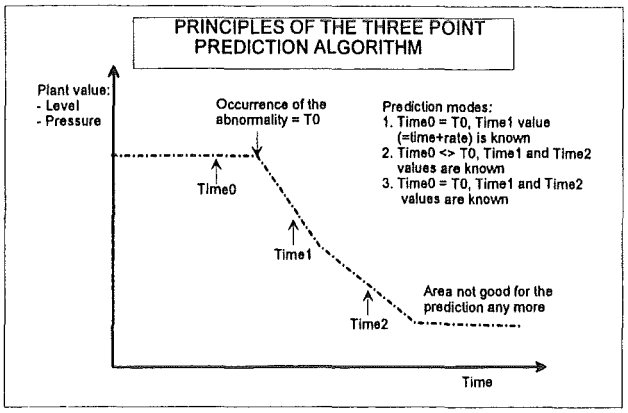

Figure 8. The break size prediction based on three data points from the plant.

The plant data points are used for the estimation of the leak flow. The break area can be estimated by dividing the estimated loss of the coolant mass by the critical flow rate per unit area. The system includes a possibility for correcting the predicted break size by iterated calculations of the accident progression. The best results are achieved by applying this correction procedure, which means repeated calculation using the break size corrected in the last iteration. The trips and safety systems are actuated by the trip logic programmed into the code or by the plant data.

Heat Transfer and Break Flow

The heat transfer from the primary side to the secondary side is calculated for three different modes: 1. single phase forced flow and natural circulation on the primary side, 2. two phase natural circulation on the primary side with primary pressure higher than the secondary pressure, 3. condensation of vapor in empty steam generator tubes, when the primary pressure exceeds the secondary pressure and 4. heat flux from the secondary side to the primary side, when the primary pressure is lower than the secondary pressure.

In the lumped volumes the flashing of the superheated liquid and the condensation due to the subcooled liquid are calculated. The heat transfer coefficients are selected appropriate for giving a reasonable pressure behavior. In principle the condensation is rather complex process in system codes.

The simplified critical break flow models are used for the primary LOCA, steam generator tube rupture and secondary steam leak. The simplified break functions have been defined for the critical flow of the subcooled liquid as

$$W_{brk,lsub}=S\sqrt{2.0\rho_l(p\ -0.9p_{sat})1.0e5} \quad (1)$$

the vapor leak as

$$W_{brk,g}=0.456S\sqrt{0.2\rho_g p\ 1.0e5} \quad (2)$$

the liquid for the steam generator tube rupture as

$$W_{brk,l}=1.73S\sqrt{0.2\rho_l max(p_l-p_4,0)1.0e5} \quad (3)$$

The total mixture flow is achieved by calculating the inlet quality x from the liquid level and relative break elevation

$$W_{brk,t}=(1-x)W_{brk,l}+xW_{brk,g} \quad (4)$$

System pressure solution

The solution of the system pressure for the lumped volumes is the most important calculation in the system, because it affects directly to the mass injections, mass leakage and the energy balance in the system. Therefore the pressure calculation will be described in more detail here.

The pressure can be derived from the volume conservation equation, which may be defined for the primary side of a PWR or for the whole BWR system through

$$\frac{d}{dt}\left[\frac{M_{li}}{\rho_{li}}+\frac{M_{gi}}{\rho_{gi}}\right]=0 \quad (5)$$

where the mass content in the section is defined by

$$M_{li}=(1-\alpha_i)\rho_{li}V_{ti} \quad (6)$$

$$M_{gi}=\alpha_i\rho_{gi}V_{ti} \quad (7)$$

The equations are written for all four sections. The volume conservation equation is further modified by differentiating the terms inside the parenthesis. The liquid and vapor density is a function of the pressure and enthalpy. The effect of the pressure is fast and the effect of enthalpy slow. That is why only the pressure derivative is considered for the pressure solution

$$\frac{d}{dt}\left(\frac{1}{\rho_k}\right)=\frac{1}{\rho_k{}^2}\left(\frac{d\rho_k}{dp}\frac{dp}{dt}-\frac{d\rho_k}{dh_k}\frac{dh_k}{dt}\right)$$
$$\approx\frac{1}{\rho_k{}^2}\frac{d\rho_k}{dp}\frac{dp}{dt} \quad (8)$$

where k means the phase, k = l for liquid g for gas. Finally the equation for the pressure may be derived as

$$\left(V_i\left(\frac{(1-\alpha_i)}{\rho_{li}}\left(\frac{d\rho_l}{dp}\right)_i+\frac{\alpha_i}{\rho_{gi}}\left(\frac{d\rho_g}{dp}\right)_i\right)\right)\frac{dp_i}{dt}$$
$$=\left(\frac{1}{\rho_{li}}\frac{dM_{li}}{dt}+\frac{1}{\rho_{gi}}\frac{dM_{gi}}{dt}\right) \quad (9)$$

The changes in the mass are defined through cumulative injection, leakage and mass transfer terms as

$$\frac{dM_{li}}{dt}=W_{lsi}{}^{n+1}-W_{lei}{}^{n+1}-\Gamma_i^{n+1} \quad (10)$$

$$\frac{dM_{gi}}{dt}=-W_{gei}{}^{n+1}+\Gamma_i^{n+1} \quad (11)$$

where the subscript "e" mean exit flow and the subscript "s" source inlet flow. The implicit estimation is applied for the mass source terms through the following general form

$$\phi^{n+1}=\phi^n+\left(\frac{\partial\phi^n}{\partial p}\right)dp \quad (12)$$

But the discretization error can not be avoided in the calculation process, where the energy equation is solved outside the pressure solution. The energy equation affects through phase densities. That is why a correction into the pressure calculation is needed in the form of a mass balance correction and this is defined through

$$E_i=\frac{M_{li}}{\rho_{li}}+\frac{M_{gi}}{\rho_{gi}}-V_{toti} \quad (13)$$

and included as a source term into Equation (9) after the discretization. The discretized Equation (9) is used for solving the system pressure on the primary and secondary side. The system pressure for the primary side and pressurizer are calculated together. The equations for the intact and broken secondary sides are solved separately. If they are connected through the steam line, the interconnecting flow is solved after the pressure solution.

Time integration of the mass and energy equations

The energy integration is done separately after the pressure solution. The energy conservation is solved for enthalpies of cold and hot liquid in the primary section, for liquid in the pressurizer, for liquid in the intact steam generators and for liquid in the

broken steam generator. The energy equations include the effect of the core power, heat fluxes of the steam generators, enthalpy added by the injection, enthalpy leaking out and energy transfer between phases. The energy equations are solved only for the liquid enthalpy. The gas overheating is calculated only for the detailed core model and added directly to the heat flux of steam generators.

The circulation momentum equation

The momentum equation is solved only for the primary circulation giving the core inlet flow and the primary flow in steam generators. If the primary main coolant pumps are running, the core circulation flow rate is set to the nominal flow. After the reactor coolant pumps have been stopped, a simplified flow decay curve is applied. The single-phase natural circulation on the primary side is assumed, if steam generator are fully covered by liquid. If the steam generators are partially empty, the two-phase natural circulation solved. For the empty steam generator the vapor condensation is calculated. The core flow is equal to the boiling rate, if the core is uncovered.
These are the simplified principles considering the circulation momentum on the primary side during different periods of the accident. The experiences have shown that the simplified model can predict rather well the transitions from the nominal flow to stagnant two-phase flow natural circulation situations.

5. DETAILED CORE REPRESENTATION

Resolution of axial distributions

The lumped model of the primary system describes the collapsed level in the average primary system. If this level is below the top of the core, a detailed core model simulates the swell level in the core and consequently the fuel heat up. The calculation takes into consideration the core power profile and void fraction due to boiling. Fig. 9 shows the heat transfer and void fraction zones considered in the detailed core model.
The detailed core model divides the core into axial nodes, typically 20 nodes. The axial profile is defined through a sinus shape function. The calculation is sweeping

from the bottom to the top. The liquid heating from the node below is calculated so far it is subcooled. For saturated liquid the heat from the core is used for boiling.

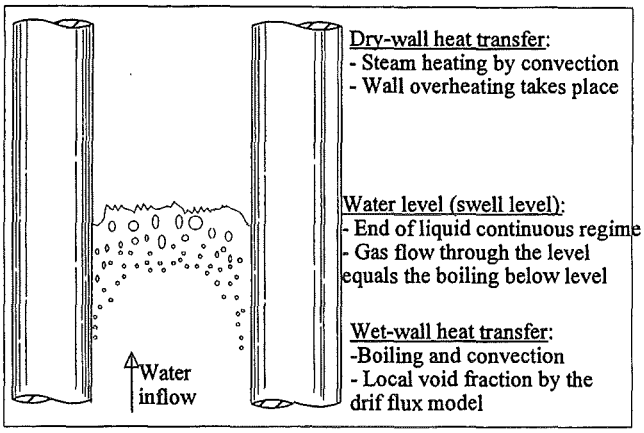

Figure 9. Heat transfer regimes for the detailed core.

The local void fraction is derived assuming stagnant flow conditions from

$$\alpha_j = \frac{W_{gj} / \rho_{gl}}{C_0 (W_{gj} / \rho_{gl} + W_{lj} / \rho_{ll}) + A_{co} V_{dr}} \qquad (14)$$

Here the drift flux formalism is used and for the simplified calculation the constant drift flux coefficients are used, $V_{dr} = 0.90$ m/s for the drift velocity and $C_0 = 1.2$ for the distribution parameter. The swell level position is defined by summing the effect of the local void fractions The steam flow through the swell level is equal to the boiling below the level. Above the swell level only single phase vapor exists and heat-up of vapor takes place.

The local fuel temperature distribution is obtained by applying the convection and boiling heat transfer below the level and convection to vapor above the level. For the fuel rods the transient heat conduction equation is solved, which takes into account the heat capacity of the fuel rod.

Inventory of radioactivity and its release

The radioactivity of core materials is caused by the radioactive decay of individual isotopes. The calculation is carried out by using both mass (gram) and activity (Becquerel = Bq) units through the whole transport chain from the fuel to the containment and environment.

The radioactivity decay law links the mass of the nuclide to the radioactivity through

$$B=\frac{N}{A}C_{Av}\lambda \qquad (15)$$

where N is the mole number, A the atom weight, C_{Av} the Avogadro number and λ the decay constant. The typical radioactivity input includes 26 elements and 73 isotopes. The isotopes are summed up to elements and finally the elements are summed up to eight groups. The radioactivity follows gas or liquid. Different isotopes may have different retention characteristics too. The transport and the retention of the radioactivity is simulated individually only for groups. The content of these groups is listed in Table 3.

Table 3. Groups of fission products.

	Fission product	Form
1	Aerosoliodine (CsI, RbI)	Gas
2	Cesiumhydroxide (CsOH, RbOH)	Liquid
3	Tellurium (Te)	Liquid
4	Oxides (Se, Zr, Nb, Mo, Tc, Ru, Rh, Sb, La, Ce, Pr, Nd)	Liquid
5	Noble gases (Kr, Xe)	Gas
6	Molecular iodine (I2)	Liquid
7	Organic iodine (CHI3)	Liquid
8	Actinides (Pu)	Liquid

The radioactivity release from the fuel consists of two phases. Immediately after the rod failure the radioactivity of the gas gap is released into the coolant. After this, radioactivity from the fuel pellet is released at higher temperatures by the activation energy law. The rod failure may be assumed taking place after the cladding reaches the threshold temperature, around 800 °C.

The continuous release of the second phase can be represented by an exponential function of the fuel temperature and element dependent release coefficient is defined in the form

$$k_m = k_0 e^{-\left(\frac{Q}{RT}\right)} \qquad (16)$$

where R is the universal gas constant (8.315 kJ/kmol/K) and Q is the activation energy (2.30×10^5) kJ/kmol.

The release of the radioactivity from the fuel to the primary system and the transport to the secondary system is calculated by using simple principles integrating the activity concentrations in liquid and gas spaces and their transport together with the

liquid and gas flow. Total radiological release is calculated by summing the leakage flow in gas and liquid form using the group scheme of Table 3.

6. VALIDATION OF THE PROCESS TRACKING MODEL

The process tracking model itself has been validated primarily independently from the STEPS system by applications to accidents in various European reactor plants. These accidents were recalculated with the integral STEPS for full system validation. The reference codes in the validation include the thermohydraulic simulator code SMABRE [1], the severe accident code MELCOR [2] and the well known RELAP5 code [3]. The SMABRE (Small Break) code [1] is a fast running simulator code which has been used extensively for independent small break LOCA calculations for the Loviisa VVER-440 plant, coupled with a 3-D core model for transient analyses of the steam line break and for ATWS cases. It has been installed into the Loviisa full scope training simulator as a model representing two-phase flow. Other applications include the simulators for the Westinghouse PWR, for the ASEA BWR with external circulation and for the ASEA BWR with internal circulation. The SMABRE code can be considered as a rather reliable reference code for the validation. The codes MELCOR and RELAP5 have been qualified by many earlier investigations. They were developed under supervision of USNRC over many years and their ability to represent accurately the accidental thermohydraulic states of the primary reactor system is well known.

The validation results obtained for BWR, VVER-440 and PWR plants demonstrate that the simplified process tracking model can make a rather good prediction for the core heat-up and the core uncovery phases. This is elaborated in more detail in our ICONE-8 paper [4].

NOMENCLATURE

α	void fraction	-	S	break area	m^2
A	flow area	m^2	W	mass flow rate	kg/s
C	coefficient	-	t	time	s
E	volume error	m^3	v	velocity	m/s
Γ	evaporation	kg/s	V	volume	m^3
h	enthalpy	kJ/kg	Subscripts		
k	release rate	1/s	g	gas	
M	mass	kg	i	section index, 1, 2, 3 or 4	
Q	heat flux	W/m^2	j	junction index	
p	pressure	bar	l	liquid	
ρ	density	kg/m^3			

REFERENCES

1. J. Miettinen, A. Hämäläinen, *Development and Validation of the Fast Running Thermohydraulic Model SMABRE for Simulator Purposes*, ICONE-8, paper 8188, April 2-6, 2000

2. R. Gauntt et al., MELCOR Computer Code Manuals, NUREG/CR-6119, July 1997

3. RELAP5 Code Development Team, RELAP5/MOD3 Code Manuals, NUREG/CR 5535, June 1995

4. J. Miettinen, P. Schmuck, K.Herviou: *A Process Model for Fast Prediction of Radioactive Releases from a LWR*, ICONE-8, paper 8190, April 2-6, 2000

II. KAREX-Experimente zum radiologischen Quellterm infolge Resuspension

(J. Minges, W. Schütz, IRS; M.K. Koch, RUB-NES)

Zusammenfassung

Die Wiederfreisetzung schwerflüchtiger Substanzen aus Flüssigkeiten (nasse Resuspension oder Reentrainment) kann als Langzeitbeitrag zum radiologischen Quellterm nach einem Unfall mit Kernzerstörung, zum Beispiel dem gefluteten Core Catcher des EPR, eine wichtige Rolle spielen. Im Rahmen des KAREX-Programms werden Laborversuche, Versuche im technischen Maßstab und modelltheoretische Entwicklungen zu dieser Thematik durchgeführt.

Die Tröpfchenbildung beim Aufplatzen von Gas- oder Dampfblasen an der Phasengrenze ist hierbei von besonderer Bedeutung.

Im Berichtszeitraum wurden vorwiegend Messungen bei Siedebedingungen mit unterschiedlichen Heizleistungen durchgeführt. Die unterschiedliche Freisetzung von festen Substanzen über aufsteigendem (vorwiegend große Blasen) und absteigendem Gebiet (vorwiegend kleine Blasen) wurde höhenabhängig bei Laborversuchen quantifiziert.

Die Versuche im technischen Maßstab umfassten überwiegend die Charakterisierung der Tropfen in der Abgasleitung, abhängig von Höhe des Flüssigkeitsspiegels und der Heizleistung. Der an der Ruhr-Universität Bochum (RUB) entwickelte Rechencode SUSANA wurde installiert und mit den eigenen Messungen verglichen.

Die theoretische Begleitung der KAREX-Experimente durch RUB wurde fortgesetzt. Da die Untersuchung der Resuspensionsmechanismen nicht nur für die Reaktorsicherheitsforschung von Interesse ist, wurde bei RUB auch eine Analyse der Anwendung in den verschiedensten Bereichen von Natur und Technik vorgenommen.

1. Überblick

Bei der Betrachtung radiologischer Quellterme nach einem schweren Störfall sind Kurzzeit- und Langzeitbeiträge zu beachten. Normalerweise gilt das Interesse den „intensiven" Kurzzeitbeiträgen. Die Langzeitbeiträge haben meist geringe Massenstromdichten (geringe Nachwärmeleistung) aber sie können über lange Zeiträume

(Monate, Jahre) aktiv sein und deshalb eine besondere Bedeutung erlangen. Die Resuspension (Wiederfreisetzung) sowohl gelöster als auch schwerflüchtiger Substanzen (Spaltprodukte) aus Flüssigkeiten wie z. B. dem Sumpfwasser oder dem gefluteten Core Catcher kann als Langzeitbeitrag zum radiologischen Quellterm nach einem Unfall mit Kernzerstörung eine wichtige Rolle spielen.

Im KAREX-Programm werden dazu Experimente zur Resuspension aus Wasservorlagen durchgeführt. Eine dominante Rolle spielen dabei Gas- und Dampfblasen, die beim Aufplatzen an der Oberfläche Tropfen bilden. Geringe Gas- oder Dampfvolumenströme setzen Tropfen beim Zerplatzen einzelner Blasen (Filmtropfen, Jettropfen) frei. Bei hohen Volumenströmen dagegen beruht die Freisetzung überwiegend aus der Flüssigkeitsabscherung mit Tropfenbildung von den Phasengrenzen zusammenhängender, an der Oberfläche aufbrechender Gaskanäle. In allen Fällen können die Tröpfchen als Träger des beigemischten partikelförmigen bzw. löslichen Materials dienen.

Das KAREX-Programm des IRS besteht aus Laborversuchen und Versuchen im technischen Maßstab. Begleitende modelltheoretische Arbeiten werden vorwiegend an der Ruhr-Universität Bochum durchgeführt. Im Berichtszeitraum lag der Schwerpunkt der Arbeiten bei der Untersuchung von Resuspensionsprozessen aus Wasservorlagen im Bereich des Siedepunktes mit unterschiedlichen Dampfvolumenströmen und der Charakterisierung der Tropfen.

2. Laborversuche

Aus vorhergehenden Versuchen, z. B. mit in Strömungsrichtung über der Phasengrenze aufgehängter Plexiglasscheibe, wurden deutliche Unterschiede im Austrag zwischen Regionen mit überwiegend großen Blasen (aufwärtsströmendes Gebiet) und überwiegend kleinen Blasen (abwärtsströmendes Gebiet) festgestellt /1, 2/. Dieses Phänomen sollte detaillierter untersucht und quantifiziert werden. Des Weiteren erfolgt ein Vergleich mit Ergebnissen des Rechencodes SUSANA /3/.

Eine Suspension aus 2 Liter VE-Wasser (VE = voll entsalztes H_2O mit pH = 7,9-8,0, Oberflächendurchmesser 135 mm) und Zinkpulver (mittl. Teilchengröße 3 µm) bzw. $SrZrO_3$-Pulver (Teilchengröße: typisch ∅ < 10 µm) wurde 15 min lang gesiedet. Die dabei entstehenden Wassertröpfchen und der Dampf wurden durch einen Filter ∅ 40 mm, dessen Höhe über der Wasseroberfläche bei den verschiedenen Durchgängen verändert wurde, abgesaugt (Absauggeschwindigkeit am Filter 1,4-2 m/sec)

und gemessen. Dabei sollte festgestellt werden, wie viel Substanz in welcher Region durch Resuspension freigesetzt wird.

Die Experimente bestätigen die in /1, 2/ festgestellten Beobachtungen und Tendenzen. Die Resuspension ist über der abwärtsgerichteten Strömung durch die zerplatzenden kleinen Blasen wesentlich höher als bei der Aufwärtsströmung mit überwiegend großen Blasen (Abbildung 1). Sie ist bei den Zn-Partikeln im Bereich von 45 mm über der Wasseroberfläche um den Faktor 8 größer und in einer Höhe von 130 mm noch um den Faktor 4. Bei kleinen Heizleistungen wird der Anteil aufsteigender kleiner Blasen (∅ < 3 mm) deutlich größer, die Anzahl großer Blasen nimmt ab. Es wurde nachgewiesen, dass ein erheblich größerer Austrag an Substanz bei schwachem Sieden erfolgt, hervorgerufen durch energiereiche Jettropfen mit geringem Durchmesser, die dann auch entsprechend hoch aufsteigen.

Zum Vergleich wurden Versuche mit Strontiumzirkonat-Pulver $SrZrO_3$ durchgeführt. Prinzipiell ist auch hier die gleiche Tendenz festzustellen: Der Verlauf der Freisetzungs-Kurve über der Phasengrenze ist der Zn-Kurve sehr ähnlich, jedoch ist der Partikel-Massenstrom um ca. einen Faktor 10 kleiner. Die Unterschiede in der Austragsmenge zwischen Zn-Partikeln und $SrZrO_3$-Partikeln zeigen deutlich, dass der Austrag materialspezifisch sein muss. So ist z. B. der Dichteunterschied zwischen den beiden Substanzen bei Zn um den Faktor ca. 3 größer, dennoch ist die Resuspension von Zn erheblich größer. Eine Vorhersage über den Austrag von festen Substanzen kann deshalb nur nach Kenntnis der spezifischen Materialeigenschaften gemacht werden. Eine einfache Verknüpfung der Resuspension mit der mittleren Konzentration im Pool erscheint nicht ausreichend.

3. Vergleich Resuspensionsmodell SUSANA und Experiment

Zur Berechnung der Tropfenfreisetzung und der damit gekoppelten Radionuklidfreisetzung ist an der Ruhr-Universität Bochum das Programmmodul SUSANA (**SU**mp water resuspension **S**ource term **ANA**lysis) erstellt worden /3/. Es soll die Bestimmung des Resuspensionsquellterms ermöglichen, z. B. für das Core Catcher-Konzept von LWR's. Die Programmversion SUSANA.MOD1 stellt dabei einen eigenständigen Code dar, dessen Ein- bzw. Ausgabe von Daten über Dateien erfolgt. In Abhängigkeit vom Dampfvolumenstrom werden dabei unterschiedliche Strömungsformen unterschieden. Bei geringen Dampfvolumenströmen beruht die Tropfenfreisetzung auf dem Zerplatzen einzelner Blasen an der Flüssigkeits-

oberfläche. Es entstehen dabei sowohl Tropfen durch die Auflösung der Blasenlamelle (Filmtropfenbildung) als auch durch den Austrag von Flüssigkeitsjets (Jettropfenbildung). Bei Einzelblasenströmung erfolgt die Berechnung der Freisetzung durch Film- und Jettopfen für den Bereich unmittelbar an der Pooloberfläche, so dass eine Höhenabhängigkeit und ein mögliches Zurückfallen eines Teils der freigesetzten Tropfen nicht erfasst wird. Bei hohen Dampfvolumenströmen, bei denen unterschiedlich große Gasbereiche unstetig und ungeordnet in der Flüssigkeit aufsteigen, beruht die Freisetzung dagegen auf einem Zerfall instabiler Flüssigkeitsbereiche an der Oberfläche infolge des Impulsaustausches zwischen Gas und Flüssigkeit. Hier kann die Nuklid-Freisetzung höhenabhängig berechnet werden.

Experiment und Berechnung werden in Abb. 1 für den Fall der Einzelblasenströmung gegenübergestellt. Zunächst zeigt die Abbildung den gemessenen Nuklid-Massenstrom über Aufwärts- und Abwärtsströmung in Abhängigkeit der Höhe über der Pooloberfläche. Ebenfalls eingezeichnet ist der mit SUSANA berechnete Massenstrom auf Höhe Null (eine Höhenabhängigkeit kann noch nicht berechnet werden, ebenso wird zwischen Aufwärts- und Abwärtsströmung nicht unterschieden). Es ist offensichtlich, dass die Extrapolation der gemessenen Werte nach Höhe Null den berechneten Wert relativ gut trifft. Dies gilt insbesondere für die Abwärtsströmung.

4. Tropfencharakteristik

Zur Messung der Jettropfengröße und –geschwindigkeit wurde eine Inline-Partikelgrößensonde beschafft. Das Messsystem ermittelt gleichzeitig die Größe und Geschwindigkeit von Partikeln, die das Messvolumen der Sonde durchlaufen. Grundlage des Systems ist ein patentiertes faseroptisches Ortfrequenzfilter-Verfahren, bestehend aus einer Gitteranordnung von Glasfaser-Lichtwellenleitern auf der einen Seite und einer Laserbeleuchtung auf der anderen Seite mit Echtzeit-Datenauswertung. Die Sonde hat den Vorteil, inline bei 100 °C und erhöhtem Druck messen zu können.

Nach einigen orientierenden Laborversuchen wurden erste Messungen im Abgasstrom des KAREX-Versuchsbehälters aufgenommen (Abb. 2). Tendenziell ist bisher festzustellen, dass mit steigender Heizleistung die Häufigkeitsverteilung abflacht und der mittlere Tropfendurchmesser (50 % Wert) sinkt (Abb. 3).

5. Resuspensionsprozesse im nicht-kerntechnischen Bereich

Einen zweiten, im RUB-Bericht /4/ diskutierten Schwerpunkt bildet die Analyse von Resuspensionsprozessen in verschiedensten Bereichen von Natur und Technik, da die Untersuchung der Resuspensionsmechanismen nicht nur für die Reaktorsicherheitsforschung von großen Interesse ist. So sind weitere Anwendungsmöglichkeiten auf dem Gebiet der Ozeanographie und Meteorologie (Klimaforschung), der Biologie (Pollen- und Bakterientransport) oder auch der Medizin (möglicher Bakterien- und Pollentransport in die Atemwege) zu finden. Schließlich stellt ein großes Anwendungs- und Nutzungsgebiet, vor allem auch aus ökonomischen und ökologischen Gesichtspunkten, die Verfahrenstechnik sowie Sekundärmetallurgie dar, wobei im letztgenannten Fall die Flüssigkeitsvorlage von der Stahlschmelze gebildet wird. Auch hierbei kann der an der Grenzfläche freigesetzte Gasstrom zu einem Austrag von Tropfen führen. Dabei ist ein Zurückfallen der ausgeworfenen Partikel aus verfahrenstechnischer Sicht durchaus wünschenswert. Untersuchungsziele liegen hier z. B. in Optimierungsmöglichkeiten des Prozesses hinsichtlich des Stoff- und Energieaustausches.

Neben dem Austrag von Flüssigkeit sind weitere Phänomene eng mit dem Blasenzerplatzen verknüpft. So wird z. B. in Bioreaktoren Luft zur Sauerstoffversorgung von Zellen eingeleitet. Insbesondere durch das Zerplatzen der Blasen an der freien Oberfläche wird ein schmales Flüssigkeitsband in der Blasenmulde abgeschert. Die bei dieser Grenzschichtströmung auftretenden großen Scherkräfte und Beschleunigungen schädigen an der Oberfläche haftende Zellen und können diese sogar abtöten. Gleiches gilt prinzipiell auch für die Auflösung der Blasenlamelle, da hier ebenfalls sehr große Beschleunigungen und Scherkräfte auftreten können. Zur Umgehung dieser unerwünschten Begleiterscheinungen können zwei Wege beschritten werden. Einerseits wird die Erzeugung bestimmter Blasengrößen angestrebt, so dass der schädigende Einfluss minimiert werden kann. Andererseits können oberflächenaktive Substanzen die Grenzflächenspannung und damit die beim Blasenzerplatzen freiwerdende Energie herabsetzen, so dass auch über diesen Mechanismus der schädigende Einfluss reduziert werden kann. Teilweise sind die Untersuchungen auch eng mit der Frage nach gesundheitlichen Auswirkungen auf den Menschen verknüpft. Als Beispiel wurde hier die Freisetzung von Legionellen aus Whirlpools (Auslöser der sog. „Legionärskrankheit“) diskutiert. Von Interesse ist bei diesen Prozessen insbesondere die Größenverteilung der gebildeten Aerosole.

Nur solche, die in einem bestimmten Durchmesserbereich liegen, können bis in die Bronchialverzweigungen gelangen und ursächlich für Atemwegsinfekte und karzinogene Erkrankungen verantwortlich gemacht werden.

LITERATUR

/1/ J. Minges, W. Schütz
KAREX-Experimente zur Resuspension schwerflüchtiger Substanzen aus siedendem Wasser
Interner Bericht IRS-Nr. 7/00 - PSF-Nr. 3337, März 2000

/2/ J. Minges, W. Schütz
Experimente zur Resuspension schwerflüchtiger Substanzen aus Wasservorlagen
Tagungsbericht Jahrestagung Kerntechnik 2000, Bonn, 23.-25.05.2000, S. 193-196

/3/ A. Voßnacke, M. K. Koch, H. Unger
Dokumentation des Resuspensionscodes SUSANA
Jahresbericht 1999 (RUB E-I-247) von RUB an FZK zum Projekt „Entwicklung des Computerprogramms RESUS"

/4/ N. Reinke, M. K. Koch, H. Unger
Theoretische Begleitung der KAREX-Experimente, Resuspensionsphänomene in Natur und Technik
Jahresbericht 2000 (RUB E-I-264) von RUB an FZK zum Projekt „Entwicklung des Computerprogramms RESUS"

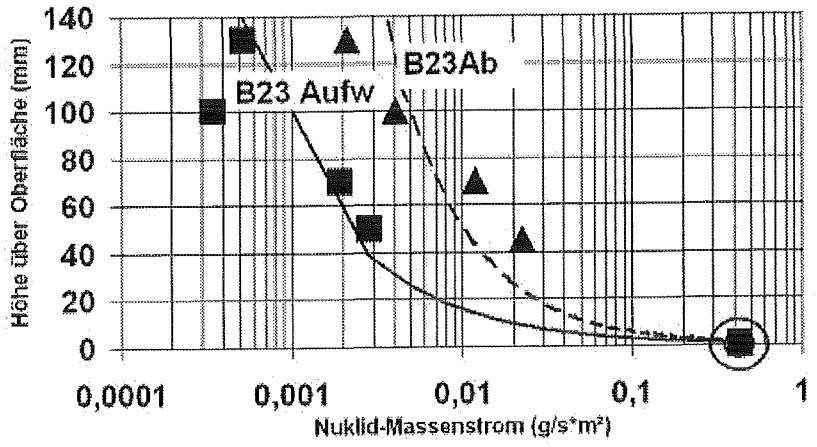

Abb. 1: Mit SUSANA berechnete Freisetzung an der Phasengrenze (umrandet) und gemessene Freisetzungen für Zn-Partikel (3 µm) über Aufwärts- und Abwärtsströmung bei 58 kW/m^2 Heizleistung

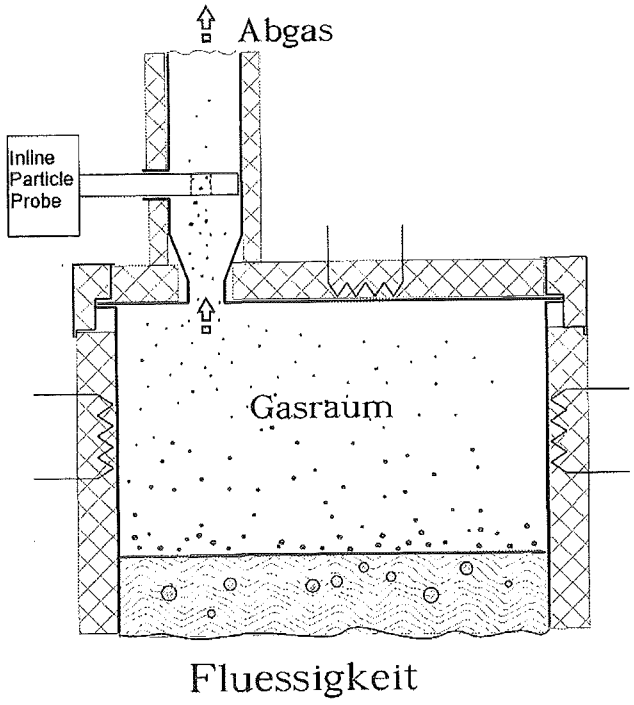

Abb. 2: Schema der Partikelmessung mit der IPP-Sonde im KAREX-Versuchsstand

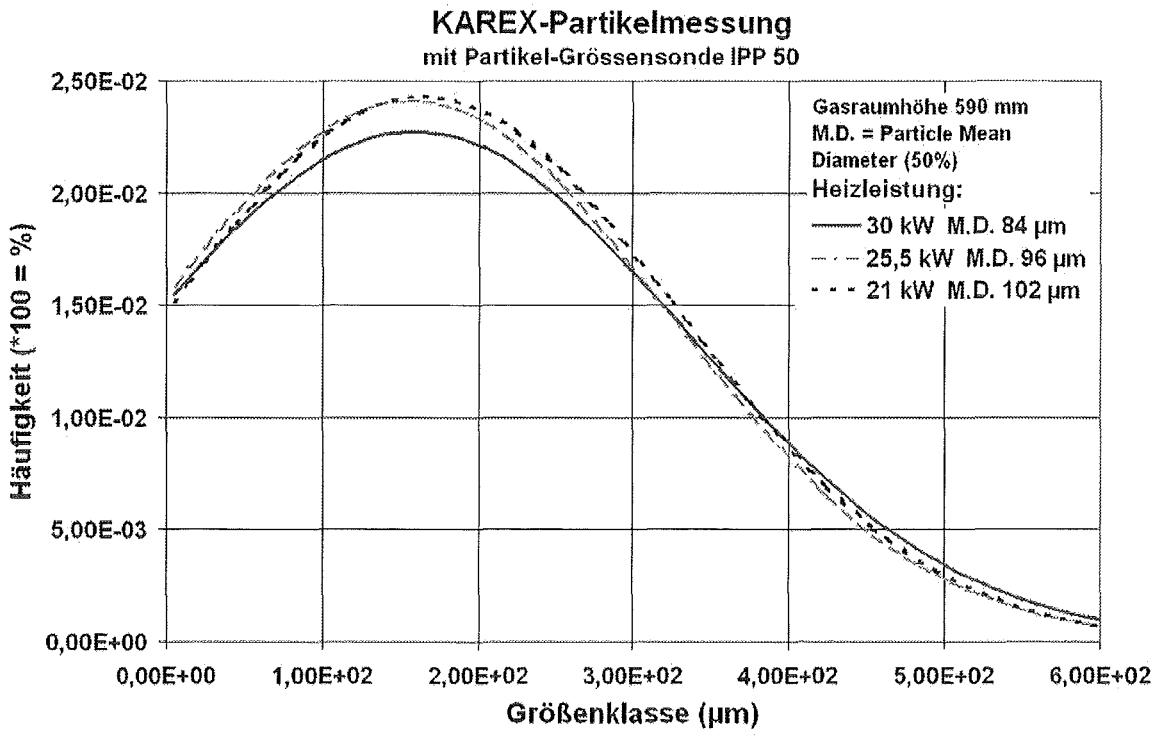

Abb. 3: Partikelmessung im Abgasstrom des KAREX-Versuchsbehälters bei verschiedenen Heizleistungen

32.21.08 Untersuchungen zur Kernzerstörung

I. Results of the QUENCH-05 and QUENCH-06 Bundle Experiments on the Investigation of Cool-Down Behaviour of Overheated PWR Fuel Rod Simulators (QUENCH-Programme)

(A. Miassoedov, D. Piel, L. Sepold, IMF III; M. Steinbrück, L. Steinbock, U. Stegmaier, IMF I)

Abstract

This report describes the test conduct and main results obtained in the bundle experiments QUENCH-05 and QUENCH-06.

Zusammenfassung

In diesem Bericht werden die Versuchsparameter und die wichtigsten Ergebnisse der Bündelexperimente QUENCH-05 und QUENCH-06 beschrieben.

Introduction

Cooling of an uncovered, overheated PWR (Pressurised Water Reactor) core by water is the main accident management measure for terminating a severe accident transient. But, before the water succeeds in cooling the fuel elements, its injection can, under certain circumstances, cause renewed oxidation of the Zircaloy fuel rod cladding, giving reheating of the rods, a sharp increase in hydrogen production and rod failure followed by the release of additional fission products. The additional hydrogen might threaten the containment, and the increased fission product release increases the source term. Evidence for these effects has been obtained from the analysis of the TMI-2 accident, in in-pile experiments such as LOFT LP-FP-2, and in out-of-pile CORA experiments. The reasons for this enhanced oxidation are not yet fully understood but it is believed that the cracking of oxide layers due to the thermal shock and subsequent exposure of fresh Zircaloy to steam are significant factors.

Because of the importance of understanding the in-vessel hydrogen source term that results during quenching, the QUENCH test facility [1] is being operated at Forschungszentrum Karlsruhe to investigate the physico-chemical behaviour of over-heated fuel elements under different flooding conditions, to improve the understanding of the effects of water addition at different stages of a degraded core and to create a data

base for model development and code improvement. The main parameters of the test program are: quench medium, i. e. water or steam, fluid injection rate, extent of pre-oxidation at onset of quenching, and the starting temperature at initiation of quenching or cool-down. Up to now six experiments have been successfully performed. The main test parameters and key results of the experiments QUENCH-01, -02, -03, and -04 [2-5] are summarised in Table 1. In the following experimental results of the QUENCH-05 and QUENCH-06 experiments are given.

	QUENCH-01	QUENCH-02	QUENCH-03	QUENCH-04
Heat-up rate, K/s	0.48 K/s	0.37 – 1.1	0.40 – 1.6	0.35 – 1.0
Maximum temperature. K	≈1830	>2500	>2500	≈2340
Cool-down medium	Water	Water	Water	Steam
Injection mass flow rate, g/s	52	47	40	50
Injection period, s	89	234	879	219
Injection velocity, cm/s	1.7	1.6	1.3	$15\text{-}20 \cdot 10^2$
Hydrogen release, total/cool-down, g	39/4	191/178	123/108	12/1.5

Table 1: Main parameters and key results of the QUENCH experiments.

Test QUENCH-05

The experiment QUENCH-05 was the second bundle experiment in the QUENCH series in which the bundle was cooled by steam, rather than being quenched by water. It differed from the first steam-cooled experiment QUENCH-04 [4] only in that the bundle was pre-oxidised before the power transient and rapid cooling began. As in the previous QUENCH experiments, the bundle was heated by a series of stepwise increases of electrical power from room temperature to ~900 K in an atmosphere of owing argon (3 g/s) and steam (3 g/s). During this time the operation of the various sub-systems was checked. The bundle was stabilised at this temperature for about 2 h, the electrical power being ~4 kW.

At the end of the stabilisation period the bundle was ramped by stepwise increases of power giving an average temperature increase of about 0.5 K/s between 900 K and 1500 K, then the temperature was stabilised at this level with a power of about 11 kW. In the following 3500 s the rods were pre-oxidised up to the desired oxide layer thickness of about 200 µm.

At the end of the pre-oxidation period the bundle was ramped at 0.3 W/s per rod to start the transient phase in the same way as in QUENCH-04. Temperature excursion started in the rod bundle at 750 mm when the temperature there reached 1900 K. The pre-planned steam cooling sequence was initiated when two rod thermocouples had exceeded 2000 K. At this time maximum measured centreline rod temperature had reached 1900 K, similarly to the temperature at cooling initiation for QUENCH-04; therefore the impact of the extent of pre-oxidation at onset of cool-down can be directly compared. Steam at ~570 K was injected at the bottom of the test section at a rate of ~50 g/s, and 20 s later the electrical power was reduced to 4 kW within 15 s, to simulate decay heat level. Cooling of the test section to below 700 K was completed about 280 s later; then the steam and electrical power were shut off, terminating the experiment (Fig. 1).

When the maximum bundle temperature reached ~1600 K, a corner rod was withdrawn to check the amount of oxidation at that time (Fig. 2).

The steam injection led to rapid cooling of the rods after a delay of 2-3 seconds (Fig. 3), except that at 750 mm a limited excursion to ~2250 K took place; this position also began to cool rapidly about 5 seconds after the start of steam injection. At these times krypton was detected in the off-gas, indicating cladding breach of at least one rod. About 30 s later, with rod temperatures from 750 mm to 950 mm being in the range 800–1400 K, reheating by about 50 K was observed, 10 s later smooth cooling was resumed. The upper shroud at elevations from 1050 to 1150 mm experienced an excursion from about 1370 K, similarly to that seen in QUENCH-01, -02 and -03 but starting at a higher temperature; in QUENCH-04 such an excursion was not so pronounced.

The total hydrogen production during the test amounted to ~27 g with 1.2 g released during the cool-down phase (Fig. 4 and 5). This low amount is consistent with the lack of large-scale temperature excursions observed in the test. Generally, the thermal behaviour of the bundle was consistent with that in QUENCH-04, and agreed well with pre-test calculations performed with SCDAP/RELAP5.

The appearance of the QUENCH-05 bundle shows practically no signs of melting. Only at the 950 mm elevation a localised failure of the shroud is observed (Figure 6). The post-test examinations of the test bundle are currently underway.

Test QUENCH-06

The sixth bundle experiment, QUENCH-06, was performed similarly to the test QUENCH-05. The only difference was that the bundle was quenched with water instead of cooling it down by steam. Also this bundle was pre-oxidized before the transient and cooling phases began. The test is also declared an International Standard Problem for blind calculations to assess the quality of severe accident codes.

The test conduct is illustrated in Fig. 7. The bundle was heated by a series of stepwise increases of electrical power from room temperature to 873 K in an atmosphere of flowing argon (3 g/s) and steam (3 g/s). At the end of the stabilization period the bundle was ramped by stepwise increases in power. The temperature was stabilized at the 1473 K level (axial maximum) with a power of about 11 kW. The temperature was maintained constant by control of the electrical power during this pre-oxidation phase for 3500 s, the electrical power being 4 kW. At the end of the preoxidation period the bundle was ramped at 0.3 W/s per rod to start the transient phase, in the same way as in QUENCH-04 and QUENCH-05. The heatup rate of the rod bundle evaluated on the basis of TCRC 13, level 950 mm, was 0.32 K/s between 1450 K and 1750 K. During the transient period, prior to any temperature excursion the withdrawal of corner rod B was started at ~1606 K to check the amount of oxidation at that time. The analysis performed after the experiment by metallographic examination resulted in a maximum oxide layer thickness of ~210 μm at the 950 mm elevation (Fig. 8).

A moderate oxidation excursion started in the rod bundle at ~7100 s at 750 mm and 850 mm when the temperature there reached ~1770-1790 K. Also at ~7100 s the upper shroud experienced a moderate excursion at the elevations from 1150 to 1250 mm.

The prerequisites for starting the quenching sequence were: a minimum of three rod thermocouples should have exceeded 1973 K, the central rod thermocouple TCRC 13 should have reached ~1873 K at this time, so that the initiation temperature for the cool-down was comparable to that of test QUENCH-05. For cooling the test bundle, the flow of 3 g/s superheated steam was turned off, the argon flow was switched over to the bundle head, and the pre-flooding sequence was initiated in that way that 4 kg of water were pre-injected within 5 s to fill the lower part of the test section. At the same time, i.e. at 7179 s, the quench pump was started to inject water into the bottom of the test section for 255 s at a mean rate of ~41.5 g/s. Before this main water injection affected the bundle

cooling an unforeseen delay was encountered in the water flow at the bundle inlet in a way that a two-step flooding occurred, firstly the pre-flooding with a fast water injection and secondly, after a delay of around 40 s, the final flooding of the bundle.

After the first water injection a prompt cooling of the test bundle started resulting from the fast pre-flooding of the lower bundle section with a total of ~4 kg H_2O. At axial levels up to 250 mm the cladding temperature drops to the saturation temperature of around 400 K. 10 – 20 s later the cladding temperatures increase again due to the evaporation of the pre-injected water at the bottom of the test section. Twenty six seconds after the injection (7179 s) the electrical power was reduced from ~18.2 kW to ~3.9 kW (to simulate decay heat levels) within 16 s. The bundle flooding was terminated when the shroud thermocouples at the 1150 mm elevation indicated local wetting. Cooling of the test section to around 400 K was complete about 250 s after its initiation; the quench water and electrical power were shut off 255 s after the water injection, terminating the experiment.

The total hydrogen production measured is ~32 g. The peak production rate of ~0.24 g/s was measured by the main mass spectrometer (Fig. 9). There is a good agreement between the Caldos analyzer and the two mass spectrometers with respect to the total values. Of the 32 g, ~2 g is estimated for the quenching phase. This compares with ~1 g for the steam-cooling phase in the QUENCH-05 test.

After the experiment the shroud showed a localized molten zone between ~870 mm and 1010 mm, between 270° and 0° orientation (Fig. 10). On the basis of the shroud thermocouples no large azimuthal differences in the shroud temperature did exist at the upper end or above the heated zone during the experiment to explain the asymmetric behavior of the shroud. Besides this failure region the shroud is intact and so are the thermocouples apart from this region. There they are still attached to the shroud surface.

References

[1] P. Hofmann, C. Homann, W. Leiling, A. Miassoedov, D. Piel, G. Schanz, L. Schmidt, L. Sepold, M. Steinbrück: "Experimental and Calculational Results of the Experiments QUENCH-02 and QUENCH-03". FZKA 6295, Forschungszentrum Karlsruhe, 2000.

[2] P. Hofmann, V. Noack: "Physico-Chemical Behavior of Zircaloy Fuel Rod Cladding Tubes During LWR Severe Accident Reflood. Part I: Experimental results of single rod quench experiments". FZKA 5846, Forschungszentrum Karlsruhe, 1997.

[3] P. Hofmann, W. Hering, C. Homann, W. Leiling, A. Miassoedov, D. Piel, L. Schmidt, L. Sepold, M. Steinbrück: "QUENCH-01, Experimental and Calculational Results." FZKA 6100, Forschungszentrum Karlsruhe, 1998.

[4] L. Sepold et.al. "Investigation of Cool-Down Behavior of the Overheated PWR Fuel Rod Simulators". FZKA 6412, Forschungszentrum Karlsruhe, 2001.

[5] G. Schanz, M. Steinbrück, U. Stegmaier, A. Miassoedov: "Post-Test Examination Results of the Water-Quenched Bundles QUENCH-01, QUENCH-02 and QUENCH-03." Proc. "Annual Meeting on Nuclear Technology 2001", Dresden, May 15 – 17, 2001, pp 197 –201.

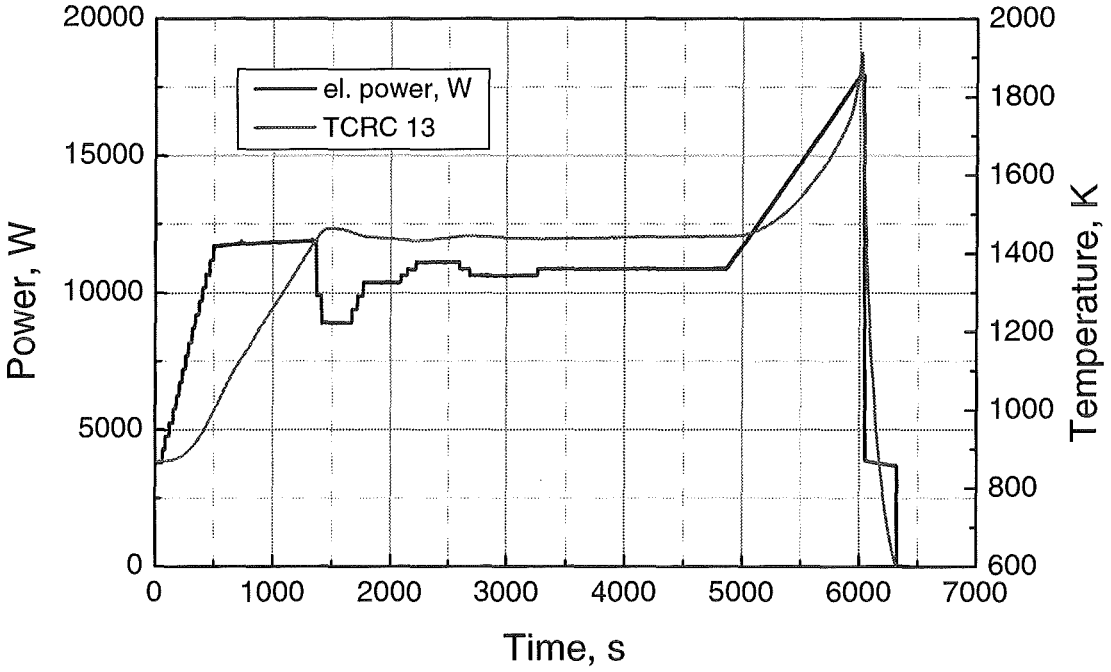

Fig. 1: QUENCH-05: Power history and temperature at elevation 950 mm

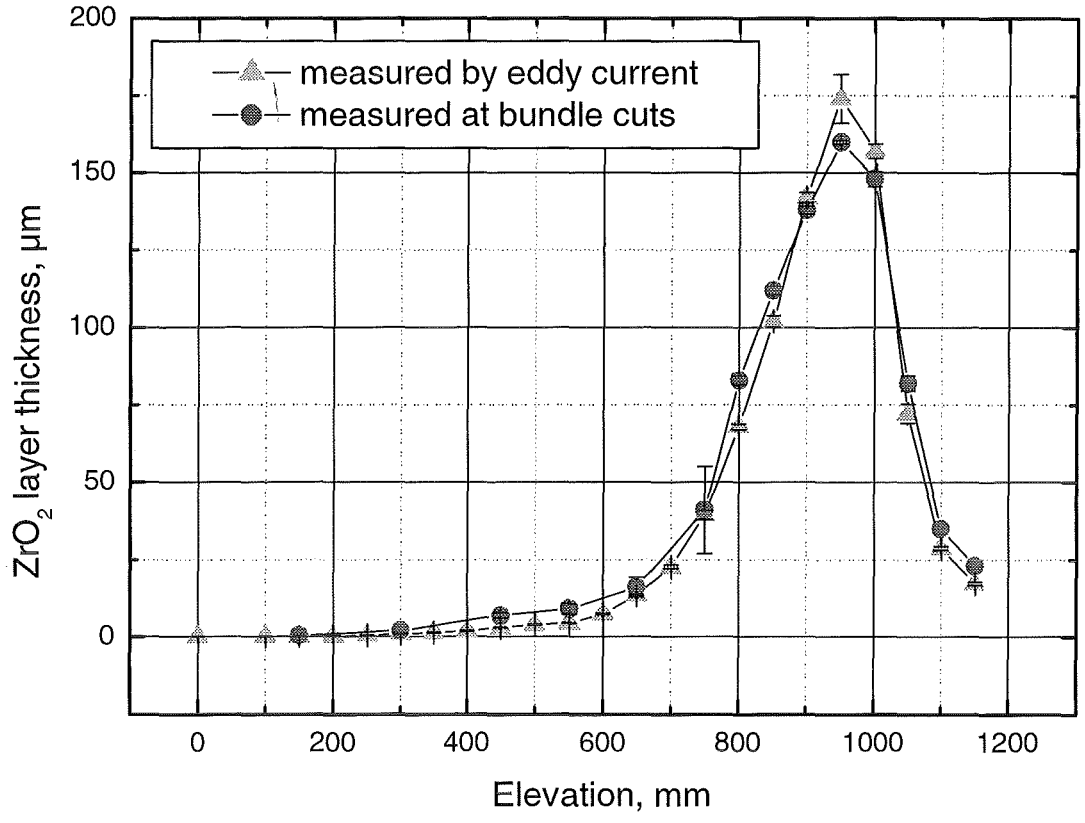

Fig. 2: QUENCH-05: Corner rod oxide layer thickness axial distribution

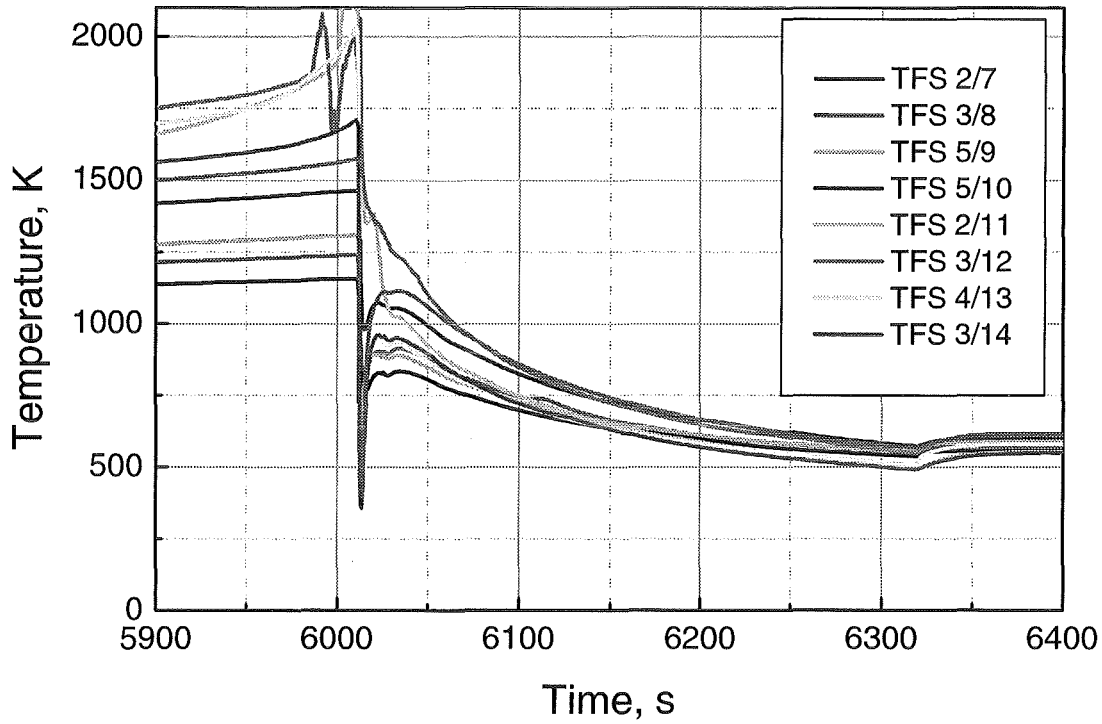

Fig. 3: QUENCH-05: Temperatures at different elevation during cool-down phase

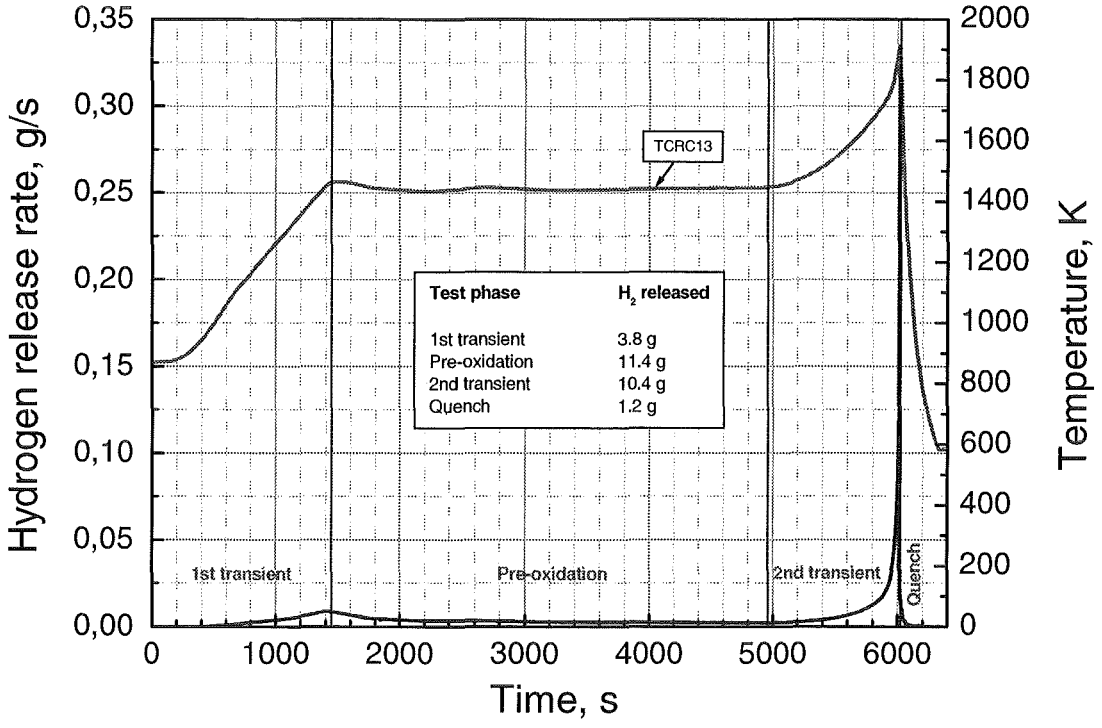

Fig. 4: QUENCH-05: Hydrogen release and bundle temperature

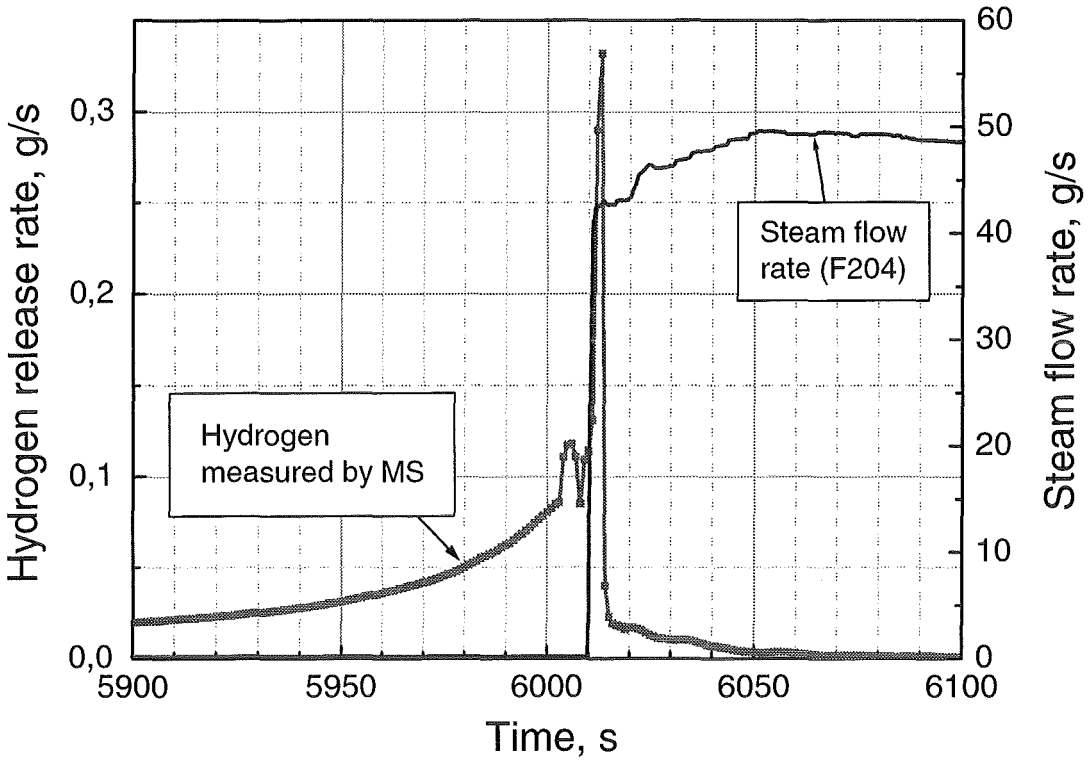

Fig. 5: QUENCH-05: Hydrogen and steam rate during cool-down phase

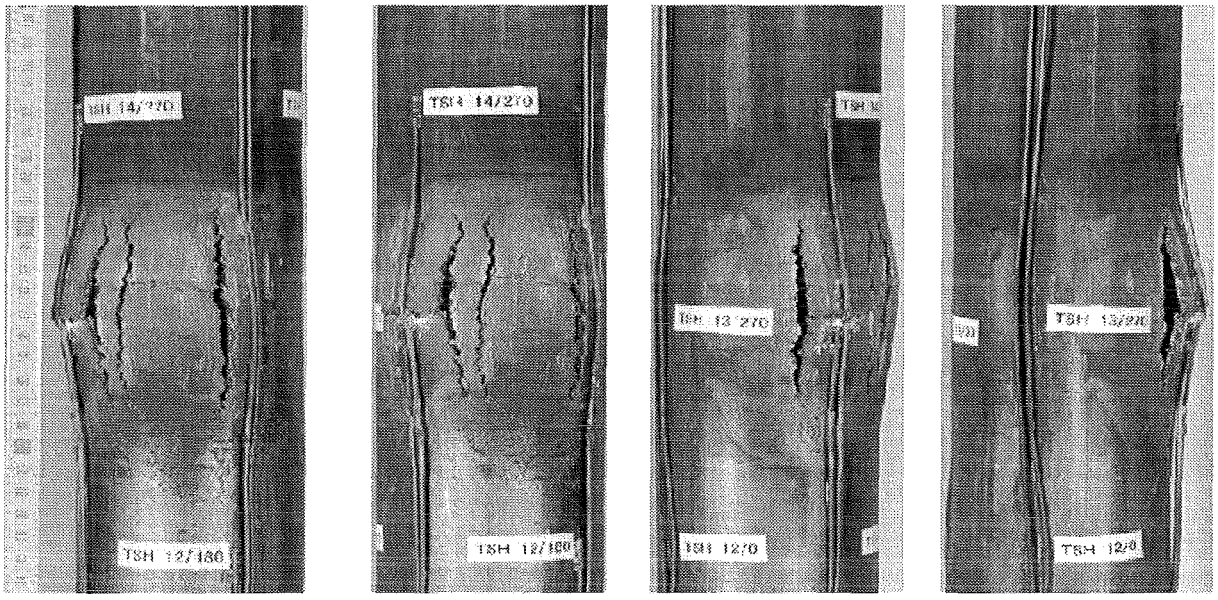

Fig. 6: QUENCH-05: Post-test appearance of the bundle

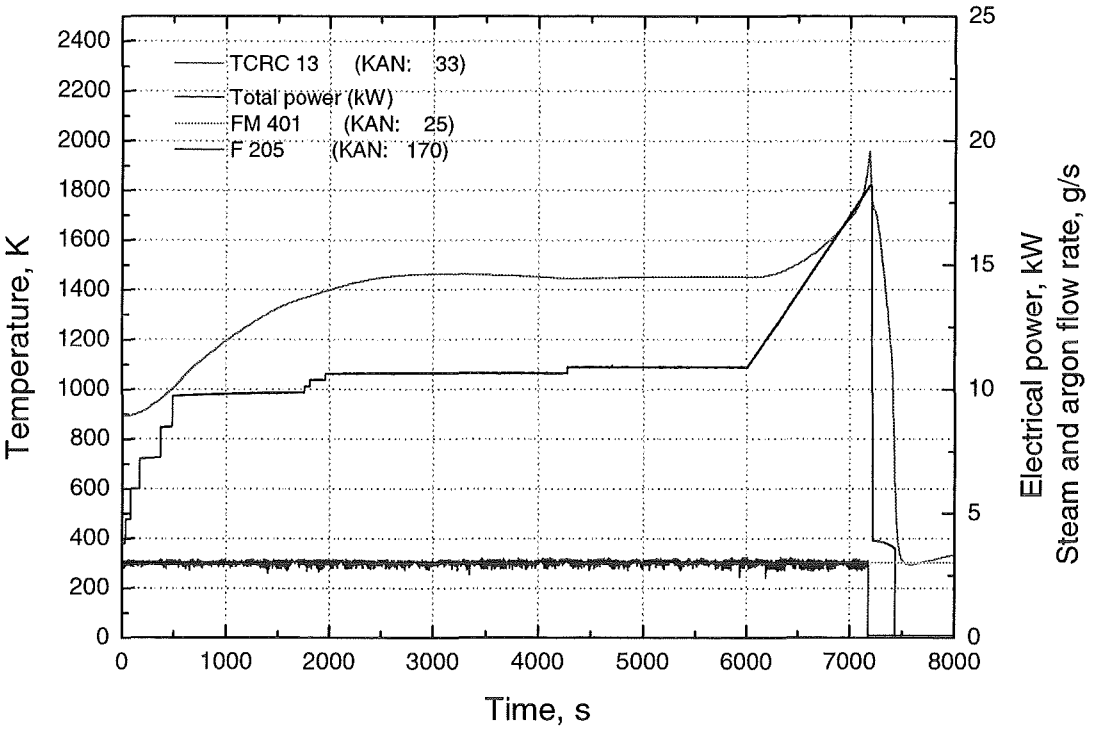

Fig. 7: QUENCH-06: Power history, temperature at elevation 950 mm and fluid injection rate

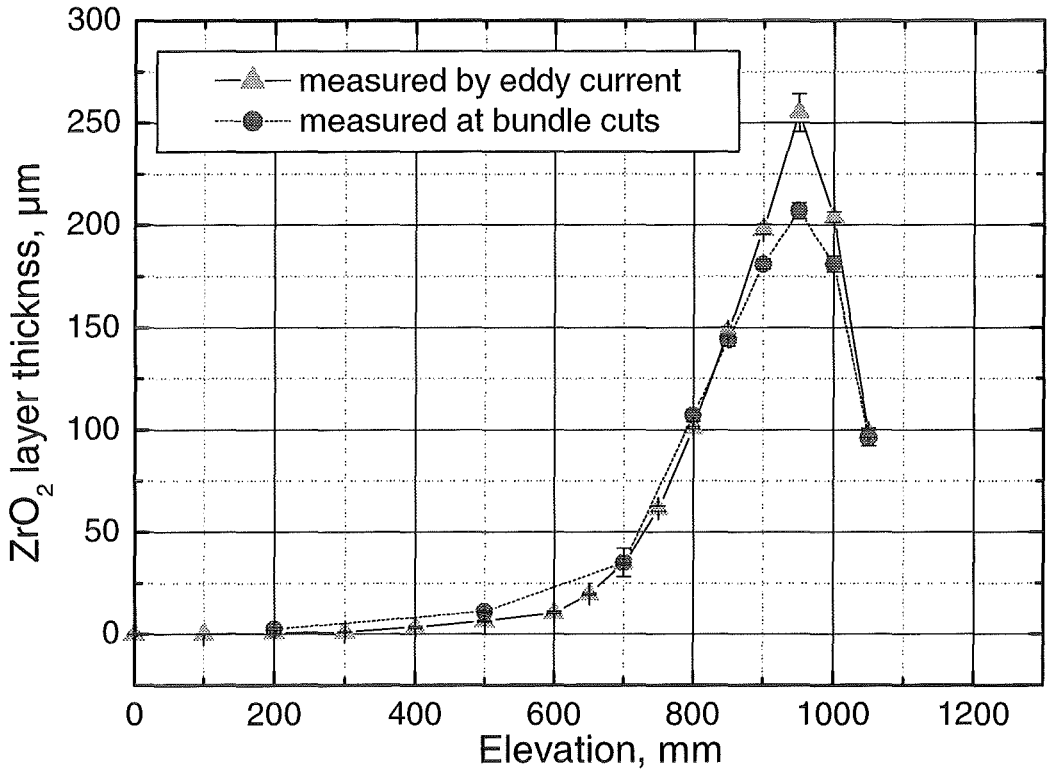

Fig. 8: QUENCH-06: Corner rod oxide layer thickness axial distribution

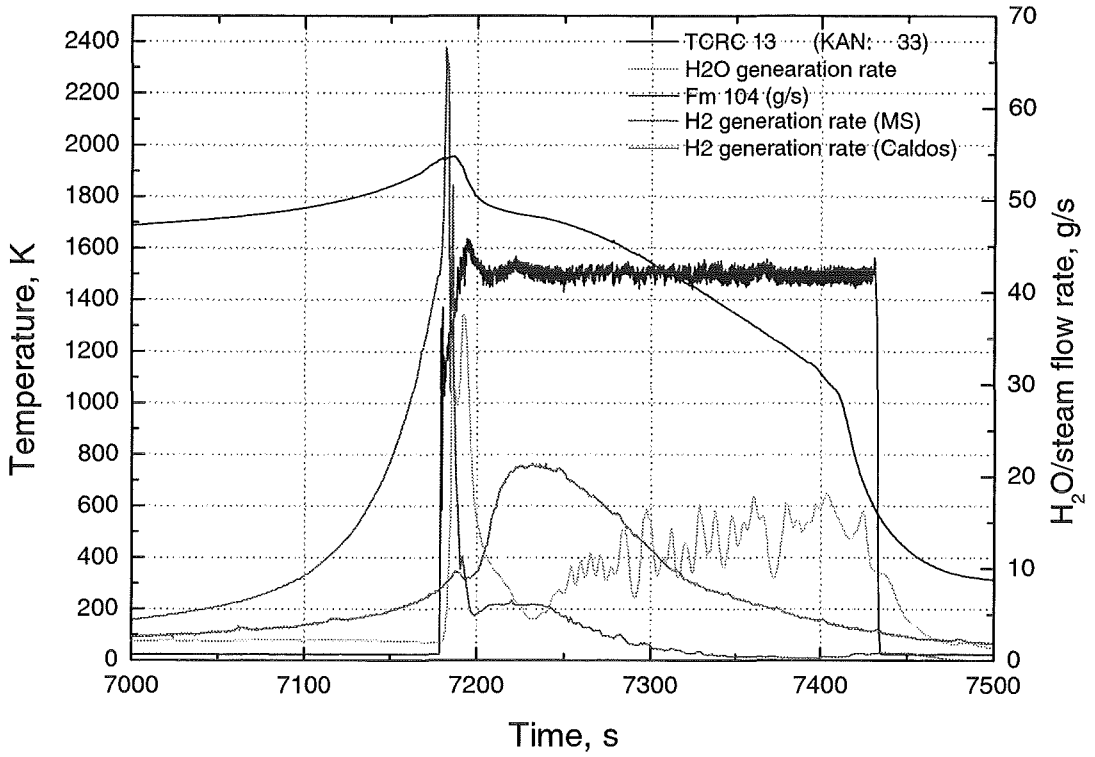

Fig. 9: QUENCH-06: TCRC 13 temperature, quench water injection rate, hydrogen and steam generation during the quench phase

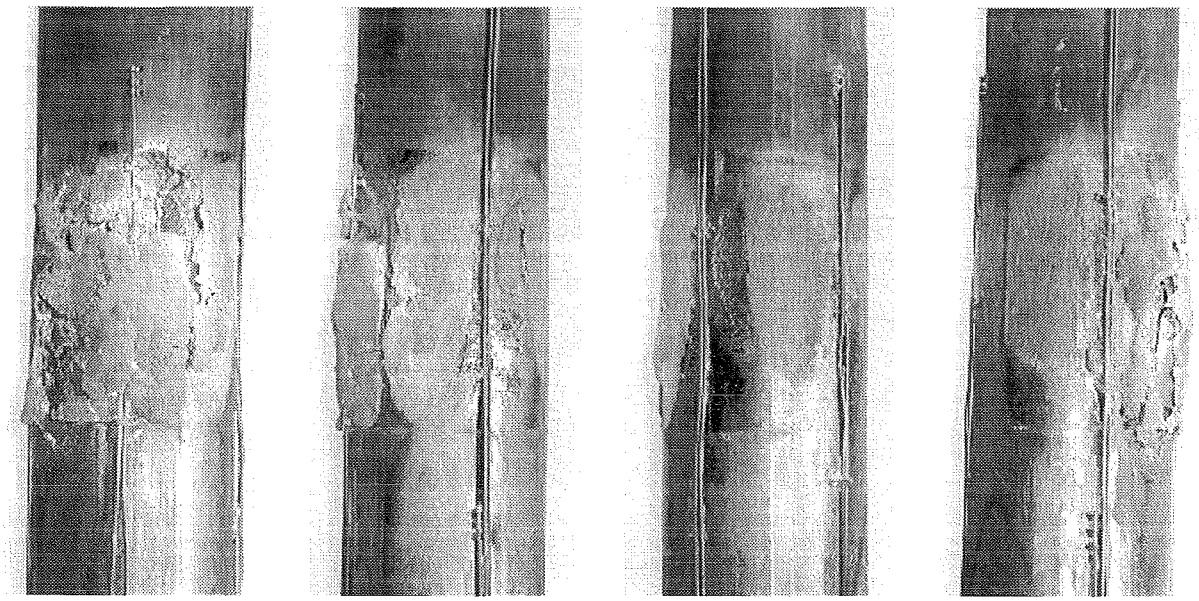

Fig. 10: QUENCH-06: Post-test appearance of the bundle

II. Metallographic Post-test Examination of QUENCH Test Bundles and Phenomenological Interpretation

(G. Schanz, M. Heck, IMF III, U. Stegmaier, IMF I)

Abstract

On the basis of the already documented results of the comprehensive metallographic post-test examination of the test bundle QUENCH-03 a mechanistic evaluation is given. In comparison with the results of the experiments QUENCH-02 and QUENCH-01 the degradation phenomena related to water quenching of transiently heated fuel rod bundles are deduced. Whereas the strongly pre-oxidised QUENCH-01 bundle showed cracking-related cladding oxidation, the bundles QUENCH-02 and QUENCH-03 responded to melt formation and relocation as the main phenomena.

Zusammenfassung

Die bereits dokumentierten Ergebnisse der umfangreichen metallographischen Nachuntersuchung des Testbündels QUENCH-03 werden mechanistisch ausgewertet. Im Vergleich mit den Ergebnissen der Experimente QUENCH-02 und QUENCH-01 werden die mit der Wasserabschreckung der überhitzten Brennstabbündel verknüpften Schädigungsphänomene abgeleitet. Während das stark voroxidierte Bündel QUENCH-01 Hüllrohroxidation im Zusammenhang mit Rissbildung zeigte, bestimmten die Phänomene der Bildung und Verlagerung von Schmelze das Verhalten der Bündel QUENCH-02 und QUENCH-03.

Phenomenological evaluation of test bundle QUENCH-03

In the following the observed results of the investigation of that bundle are summarised in the deduced temporal sequence of the identified phenomena. The oxidation and interaction of the components are interpreted on the basis of a careful inspection of the final status of the bundle QUENCH-03 [1] and the experience gained in separate effects investigations, e.g. the QUENCH RIG experiments [2]. Not all intermediate steps of development of the finally observed damage could, however, be deduced in the desired detail, since an earlier status is often obscured by later occurring and more serious events. Distinguishing between the bundle status at temperature and the status after quenching is especially difficult with respect to quench-

related mechanical fragmentation damage. Some results of the bundle experiments QUENCH-01 [3] and QUENCH-02 [1] are referred for comparison.

Scale thickness distribution

The oxide scale thickness of each rod was measured at four azimuthal directions and six axial elevations (73 to 950 mm), as far as possible; the shroud oxidation was determined for comparison. The lower elevations up to 650 mm show rather uniform thickness distribution across the bundle, indicating almost flat lateral temperature profiles. Only the outer rods have typically somewhat thinner scales at outward directions. The scale thickness ranges from ca. 1 - 2 µm at 73 mm elevation to ca. 30 - 50 µm at 650 mm. The internal shroud surface carries 1 to 40 µm at the corresponding elevations. At the external shroud surface some scale can be distinguished only in relation with the observed shroud melt-through failure and the temperature field distortion from external melt relocation. Close to those positions the internal shroud surface is oxidised up to 240 µm and adjacent rods are oxidised to 50 - 90 µm. At the higher elevations pronounced local variations of scale thickness are related with the re-distribution of metallic melt. The oxidation of the unheated central rod is stronger than that of the heated rods, due to the smaller thermal inertia and smaller axial heat conduction. The axial scale thickness profile, which reflects the cosine-shaped electric power distribution, the upward heat transfer with the atmosphere and the downward heat transfer with relocated melt, is given in Fig. 1. A sound comparison basis for the analytical treatment of the experiment is thus provided.

External cladding oxidation

Steam oxidation proceeds by formation and thickening of a ZrO_2 scale and an α-Zr(O) layer together with oxygen dissolution into the β-Zr matrix to be consumed. At temperatures above 1800 K an additional inner sub-scale of cubic ZrO_{2-x} is formed, which shows α-Zr(O) phase precipitation due to decomposition during cooling. Despite the increasing brittleness of the oxygen-containing phases the cladding/scale compound indicates self-healing tendencies against mechanical loads, e.g. the closure of wedge-shaped cracks from the surface into the scale.

Pellet/cladding interaction

At positions of solid-state contact an oxygen-rich interaction layer is growing by oxygen transfer from the ZrO_2 pellet simulator into the cladding. Since UO_2 pellets are known to behave correspondingly, the simulation quality is acceptable.

Development of cladding damage

Mechanical forces arise from the oxidation itself as well as from external constraints. Formation of cracks and fissures takes place resulting in stress relief or development of through-wall cracks according to the local extent of oxidative wall consumption. This aspect had been one of the main contributions to the quench-related hydrogen evolution in the QUENCH-01 test, in which the effect of a pronounced pre-oxidation was studied. In accordance with results of separate effects tests in the QUENCH RIG pronounced through wall cracking had been observed for scale thickness beyond ca. 300 µm [2]. In contrast to QUENCH-01 the oxidation of crack surfaces was only of minor relative importance in the experiments QUENCH-02 and QUENCH-03. Scale failure according to the anticipated "shattering" mechanism was not observed and even the scale "spalling" mechanism occurred only locally in the moderate form of a loss of external sub-scale fragments or localised scale bulging instead of a detachment of the scale in total.

Internal cladding/steam oxidation

The above mentioned mechanical scale failure gives rise to steam penetration and formation of internal scale. In this delayed and locally restricted process lenticular spots of scale are formed, obviously under oxygen supply limitation and consequently local consumption. It can be assumed from the bundle inspection that this hydrogen source term contribution is active from the later transient into the quench phase, where additional crack formation is favoured. Crack-related access of steam to the internal cladding surface is an important mechanism for QUENCH-01 and QUENCH-02 as well.

Clad Melting

Melting of cladding during oxidation is known to occur in the range of ca. 2030 (Zircaloy-4) to 2400 K (α-Zr(O) phase), in relation with the increase in dissolved oxygen. Correspondingly, incipient melting within the matrix spreads towards the

adjacent α-Zr(O) phase so that rod-internal melt relocation takes place below the scale. This melt re-distribution tends to fill pellet/cladding gaps at the expense of formation of voids at other positions. Melt oxidation proceeds by scale thickening plus homogeneous ZrO_2 phase precipitation until complete conversion to the ceramic state. Empty scale shells are apt to fracture and fragment in the attained brittle stoichiometric form, providing paths of steam access and melt escape. With the latter the melt relocation in the bundle is initiated and the possibility of enhanced melt oxidation in contact to steam is provided. The massive hydrogen release from the bundles QUENCH-02 and QUENCH-03 can be seen in relation to the melting and melt relocation processes observed in both bundles.

Bundle configuration

A bundle-typical effect is the oxidative interaction between contacting structures. In a severe accident fuel rod bending will always occur as consequence of inhomogeneous heating and steam oxidation. The pronounced and strange shroud deformation observed for QUENCH-03, a kind of bending into axially extended lobes, is not fully understood by assuming its internal oxidation to be the stress source. In any case the shroud bending effect constrains the simulator rods to mutual contact.

Rod/rod or rod/shroud contact is seen to give rise to formation of common scale shells under which metallic and axially extended "necks" are protected against oxidation. This "necking effect" is favoured by early (metallic) contact; however, a certain pre-oxidation cannot prevent it, because dissolution of scale into adjacent metal is always competing with further scale growth. Moreover, the external scale growth is retarded for geometrical reasons of supply limitation in the surrounding zone of the contact line. The net effect of external (channel side) growth and internal (neck side) dissolution of oxide is the formation of scale structures of rounded form and obviously self-healing potential (Fig 2). This argument is supported by the fact that the structures resulting from the necking process may even survive the melting event of the confined metallic component residues. The role of scale dissolution in the necking effect is illustrated by frequent observation of the corresponding dissolution process seen elsewhere in the QUENCH-02 and QUENCH-03 bundles. As function of time at temperature scales of several hundred micron thickness embedded in metallic melt show different stages of dissolution.

Neck formation together with melt dispersion/agglomeration are mechanisms which convert the originally open flow channel space into an irregular network of modified but effective flow channels, appendices under steam starvation condition, completely isolated closed voids and melt-infiltrated blockages. This geometry of the resulting bundle body is complicating the escalation behaviour as well as the response to quenching by giving rise to large local and temporal variations and gradients of temperature.

Comparative interpretation of QUENCH-01, QUENCH-02 and QUENCH-03

In the actual context the interest is focused on bundle specific and quench related phenomena [4]. In this respect the most important observation for QUENCH-03 is the formation of a more or less rigid bundle body within the hot zone by formation of necks between contacting rods and their oxidation. The flow channels modified thereby may either remain active (effective steam flow path), resistive (steam starvation tendency) or can get blocked by infiltrating melt. The necking effect, observed in QUENCH-02 as well, occurred less correlated and only localised in that bundle.

Melt formation related behaviour in QUENCH-02 and QUENCH-03 is discussed as follows: Cladding melt relocation, which is known to start within the individual rods is occurring laterally and axially within the confinement of the scale by which the surface area is diminishing and the thermal contact to the pellets is improving. This contributes to the development of large temperature variations and favours the embrittlement of bare scale, which is approaching the brittle stoichiometric composition due to the continued exposure to steam and the interrupted contact to metallic cladding. Resulting scale cracking gives access to steam, thus triggering internal steam oxidation. The oxidation of outward penetrating and dispersing melt is another hydrogen source of considerable importance, since the steam oxidation is initially not moderated by pre-existent scale. Melt accumulation in larger lumps is connected with diminishing of the surface area. The net total surface area of oxidising metallic materials and the temperature/time dependence of their oxidation are main uncertainties in the interpretation of the measured hydrogen source term.

Concerning the oxidation of metallic melts it is not possible to apply usual kinetic correlations, since the fast diffusion and convection will maintain an almost homogeneous oxygen content in the melt. Further, the LWR Severe Accident typical (Zr, U, O) melt cannot be simulated in the QUENCH program and alternative efforts

are required to quantify its oxidation kinetics in separate effect tests and to describe it mechanistically.

Melt oxidation together with melt relocation, dispersion and fragmentation are obviously the most important quench phenomena observed in QUENCH-02 and QUENCH-03 and deserve careful further consideration. In comparison "solid-state mechanisms" as cladding through-wall cracking, crack surface oxidation and internal cladding/steam oxidation are less important in the explanation of the pronounced hydrogen signals. Other mechanisms as cladding shattering into small fragments and scale or sub-scale spalling are less important.

There is no reason to modify the interpretation of the response of bundle QUENCH-01 to quenching, inasmuch as the phenomena have been found in the bundles QUENCH-02 and QUENCH-03 as well. Since no melting occurred in that test the main contributions to the hydrogen evolution are related to crack surface oxidation and internal cladding/steam oxidation.

References

[1] P. Hofmann, C. Homann, W. Leiling, A. Miassoedov, D. Piel, G. Schanz, L. Schmidt, L. Sepold, M. Steinbrück: "Experimental and Calculational Results of the Experiments QUENCH-02 and QUENCH-03". FZKA 6295, Forschungszentrum Karlsruhe, 2000.

[2] P. Hofmann, V. Noack: "Physico-Chemical Behavior of Zircaloy Fuel Rod Cladding Tubes During LWR Severe Accident Reflood. Part I: Experimental results of single rod quench experiments". FZKA 5846, Forschungszentrum Karlsruhe, 1997.

[3] P. Hofmann, W. Hering, C. Homann, W. Leiling, A. Miassoedov, D. Piel, L. Schmidt, L. Sepold, M. Steinbrück: "QUENCH-01, Experimental and Calculational Results." FZKA 6100, Forschungszentrum Karlsruhe, 1998.

[4] G. Schanz, M. Steinbrück, U. Stegmaier, A. Miassoedov: "Post-Test Examination Results of the Water-Quenched Bundles QUENCH-01, QUENCH-02 and QUENCH-03." Proc. "Annual Meeting on Nuclear Technology 2001", Dresden, May 15 – 17, 2001, pp 197 –201.

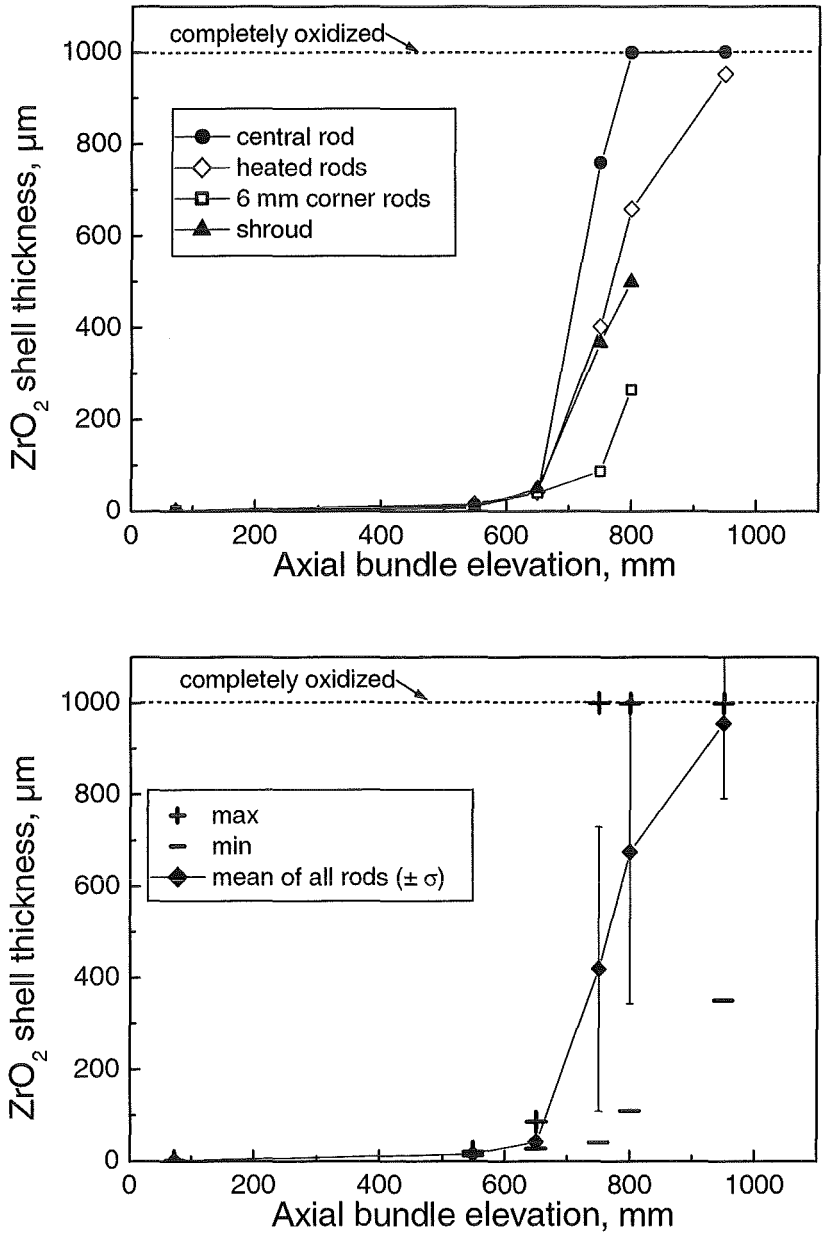

Fig. 1: QUENCH-03: Axial oxide layer thickness distribution

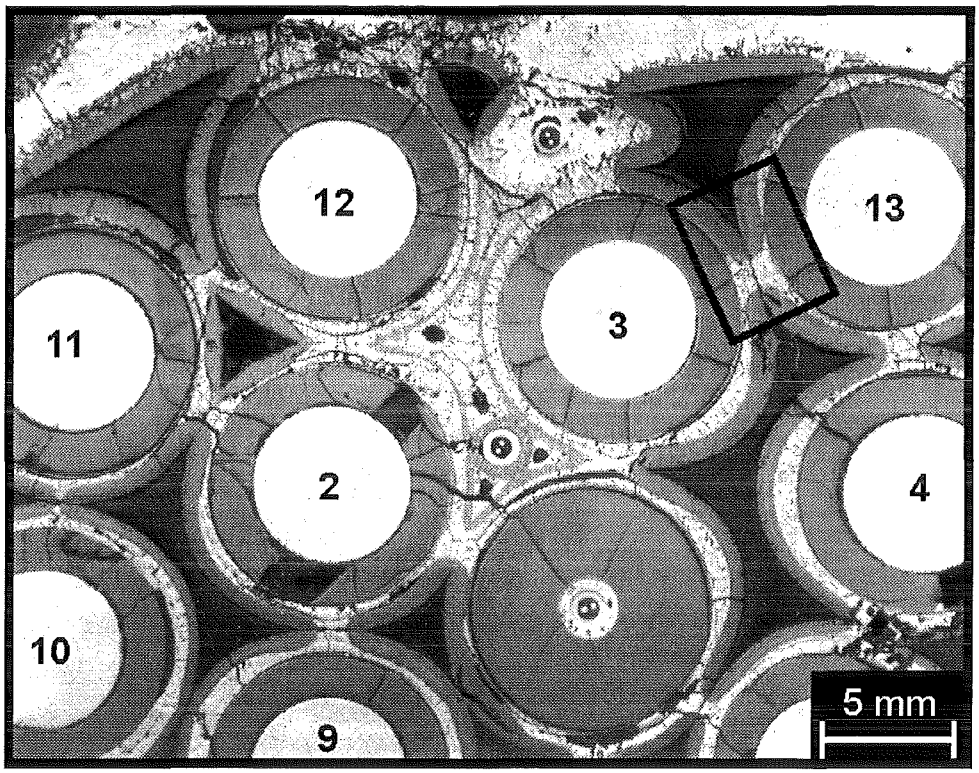

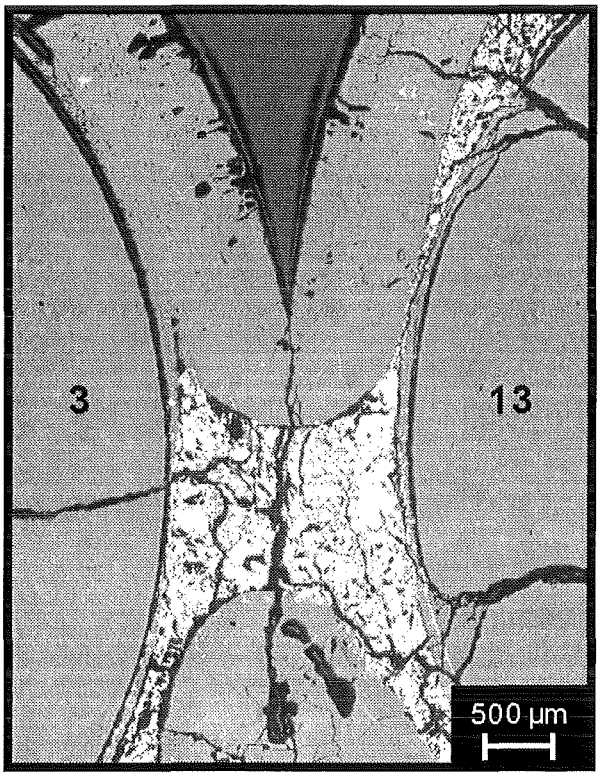

Neck of once molten material, surrounded by ZrO_2 scale and adjacent pellets

Fig. 2: QUENCH-03: Cross section at elevation 750 mm (QUE-03-5, top); formation of necks between touching fuel rod simulators

III. Recalculation of the temperature transient in QUENCH-03 with the code CALUMO

(H. Steiner, M. Heck, IMF III)

Abstract

In this contribution results of the bundle code CALUMO for the test QUENCH-01 are presented and discussed with respect to a comparison to experimental data. In the overall, a satisfying simulation of the experiment could be reached, despite some discrepancies.

Zusammenfassung

In diesem Beitrag werden Ergebnisse des Rechencodes CALUMO für das Experiment QUENCH-01 vorgestellt und im Vergleich zu den entsprechenden Daten diskutiert. Im Großen und Ganzen konnte das Experiment in befriedigender Weise simuliert werden, wenn auch im Detail noch einige Abweichungen festzustellen sind.

1. Einleitung

Im Zuge der Arbeiten zur Validierung des Bündelcodes CALUMO wurden Rechnungen für das Bündelexperiment QUENCH-01 durchgeführt. In diesem Test wurde ein voroxidiertes Bündel von Brennstabsimulatoren durch Wasser abgeschreckt. Das Bündel blieb intakt und es existieren umfangreiche Ergebnisse zur Nachuntersuchung.

Es hat sich bei den Rechnungen gezeigt, dass eine gute Simulation der Voroxidation wegen der sehr niedrigen Temperaturanstiegsraten für den Code nicht ganz unproblematisch war. Für das Wasserqueenchen auf der anderen Seite musste ein Modell neu entwickelt und in den Code eingebaut werden. Damit ist es nun möglich, neben dampfgekühlten Tests wie QUENCH-04 auch Bündel, die durch Wasser abgeschreckt werden, vollständig nachzurechnen. Die Anwendungsmöglichkeiten von CALUMO gehen nun also weit über das ursprünglich gesteckte Ziel, nämlich die Berechnung von Temperaturtransienten in Quenchtests, hinaus.

2. Entwicklung eines einfachen Modells zum Wasserquenchen

Im Sinne der bei der Entwicklung des Rechencodes CALUMO verfolgten Strategie sollte das Quenchmodell möglichst einfach sein, die wesentlichen physikalischen Aspekte aber trotzdem richtig beschreiben.

Das Modell geht davon aus, dass im Bündel drei unterschiedliche Zonen vorliegen und zwar die des Quenchwassers, ein Zwei-Phasenmischgebiet und eine Zone reinen Dampfes. Die wesentliche Annahme im Modell besagt, dass das Zwei-Phasengebiet eine konstante Länge hat, wobei im Moment drei axiale Maschen genommen werden ($\Delta zd.ph. \cong 15cm$).Berechnet werden vom Modell im wesentlichen die Dampferzeugung $\dot{m}^{st}$:

$$\dot{m}^{st} = \sum_{ique} \left(j_{ique}^{rod} + j_{ique}^{sh} \right) / \Delta \qquad (1)$$

Δ = *Verdampfungswärme*

die Geschwindigkeit der Quenchfront:

$$v^{que} = (\dot{m}^{inj} - \dot{m}^{st}) / p^{w} = F^{chan} \qquad (2)$$

$\dot{m}^{inj}$ = *eingespeister Wasserdurchsatz*

und die Position der Quenchfront.

Die Berechnung der Temperaturentwicklung geschieht mit Hilfe der in [1] beschriebenen Bilanzenverfahren, wobei die Wärmeübergangszahlen im Wasser- und Zwei-Phasengebiet fest vorgegeben sind.

3. Diskussion der Rechenergebnisse

Die für die Rechnungen mit CALUMO benötigten Eingabedaten (Massendurchsatz, Kühlmittel-Einlasstemperatur und elektrische Leistung) wurden [2] und [3] entnommen. Es hat sich dabei gezeigt, dass man den Verlauf der elektrischen Heizung möglichst genau erfassen muss, wenn man eine gute Simulation des Experiments erreichen will. Ein schematischer Leistungsverlauf wie in [3] ist nicht ausreichend.

Der Rechencode CALUMO liefert eine Vielzahl von Ergebnissen wie die zeitlichen Verläufe der mittleren Temperaturen in den Brennstabsimulatoren, im Shroud und im

Kühlmittel, die Entwicklung der Axialverteilung der elektrischen Leistung, die Oxidation im Bündel und Shroud und die Wasserstoffproduktion.

Es würde zu weit führen, alle diese Ergebnisse in diesem Beitrag darzustellen und zu diskutieren. Wir haben uns deshalb auf eine kleine Auswahl beschränkt, wobei wir hauptsächlich solche Ergebnisse zeigen, bei denen ein Vergleich mit dem experimentellen Befund möglich ist.

Die Qualität einer guten Simulation des Experiments durch den Code lässt sich in erster Linie anhand der Temperaturverläufe überprüfen. Des weiteren sind noch die Oxidschichtdicken nach dem Test und die Wasserstoffproduktion von großem Interesse. Das letztere stellt allerdings ein integraler Wert über die Oxidation dar und ist von daher kein wirklich empfindliches Kriterium, wie wir im folgenden sehen werden.

Die entsprechenden Vergleiche zwischen den Coderechnungen und den experimentellen Werten sind in den Abb.1 bis 6 dargestellt, und zwar die Temperaturverläufe an sechs axialen Höhenschritten (Abb.1 und 2), die Axialprofile der Oxidschichtdicken zu Ende des Tests (Abb. 3) und in Abb. 4 die Wasserstoffproduktionsraten zusammen mit der aufkumulierten Wasserstoffproduktion. Daneben sind in den Abb. 5 und 6 noch Ergebnisse des neu entwickelten Quenchmodells zu sehen, nämlich die Wasserdampfproduktionsraten und die Geschwindigkeit und Position der Quenchfront.

In der unteren Hälfte des beheizten Bereichs ($z < 500$ mm) findet man generell eine befriedigende Übereinstimmung zwischen gemessenen und berechneten Temperaturen. Dies deutet darauf hin, dass die elektrische Leistungsfreisetzung vermutlich korrekt modelliert ist. Im oberen Teil des beheizten Bereichs erhält man in der zweiten Hälfte der Voroxidation ein Überschwingen der berechneten Temperaturen. Vermutlich sind die bis dahin berechneten Oxidschichtdicken zu klein, was dann durch eine zu starke Temperaturerhöhung ausgeglichen wird.

Der Temperaturanstieg in der Transiente vor dem Quenchen wird generell vom Code recht gut simuliert, ebenso der Temperaturabfall in der frühen Quenchphase. Die Temperatureskalationen der Shroud-Thermoelemente auf Höhe des oberen Ar-Plenums sind vermutlich eine Folge von Konvektionsströmungen in diesen

Gasvolumen. Da die Hüllthermoelemente unbeeinflusst sind, ist es zweifelhaft, ob der Shroud tatsächlich so hohe Temperaturen gesehen hat.

Die Temperaturberechnung von CALUMO scheint auf den ersten Blick eine einigermassen zufriedenstellende Simulation des Experiments zu liefern. Falls man sich allerdings die Ergebnisse der Oxidation (Abb. 3) anschaut, stellt man fest, dass die Güte der Simulation noch nicht völlig zufriedenstellend ist. Eine Temperaturabweichung von 100 bis 150 k (was für Coderechnungen nicht dramatisch ist) führt im Bereich von 500 bis 750 mm zu deutlich höheren Oxidschichten als experimentell festgestellt. Den gegenteiligen Effekt findet man zwischen 1050 und 1200 mm.

Bei der Wasserstoffproduktion kompensieren sich diese Fehler in der Oxidation auf derart günstige Weise, dass hier wiederum sich eine relativ gute Übereinstimmung zwischen Messung und Rechnung ergibt, sowohl was die Produktionsrate als auch die kumulierte Wasserstoffproduktion anbetrifft.

Der sehr hohe Peak in der Produktionsrate, der etwa zum Zeitpunkt des Quenchens sein Maximum hat, wird allerdings in der Höhe nicht vom Code reproduziert. Da der Anstieg schon vor dem Quenchen beginnt, ist es zweifelhaft, ob dies tatsächlich ein echter Quencheffekt ist. Eine mögliche Erklärung könnte auch darin liegen, dass ein Teil des bei niedriger Temperatur produzierten Wasserstoffs in der Oberfläche der Oxidschichten zurückgehalten wird. Mit ansteigender Temperatur sollte dann dieser Anteil nach einer gewissen Zeitfunktion freigesetzt werden.

Die wichtigsten Ergebnisse des neu entwickelten Quenchmodells, nämlich die Wasserstoffproduktion und die Position der Quenchfront, sind fürs erste durchaus akzeptabel. Grob gesprochen werden ca. 50 % des eingespeisten Quenchwassers in Wasserdampf umgewandelt. Die Position der Quenchfront liegt zum Ende der Rechnung (t = 9780 s) um ca. 15 cm zu hoch.

4. Bewertung der Ergebnisse

Im Grossen und Ganzen konnten die Ergebnisse des Experiments QUENCH-01 durch den Rechencode CALUMO simuliert werden, wenn auch im Detail noch verschiedene Abweichungen festzustellen sind. Dieses einigermaßen befriedigende Ergebnis wurde dadurch erreicht, dass man eine beträchtliche Erhöhung der

Verlustleistung aus dem Shroud annahm, insbesondere in der unteren Hälfte des beheizten Bereichs.

Analysen der Thermoelement-Schriebe im äußeren Kühlmantel lassen allerdings Zweifel aufkommen, ob diese Annahme in dem Umfang zutreffend ist. Rechnungen zu QUENCH-05, die zwischenzeitlich durchgführt wurden, zeigten nun, dass man mit der Annahme einer axial abhängigen Modifikation des Wärmeübergangs zum Kühlmittel eine recht gute Simulation dieses Experiments erreichen kann. Es wird zu prüfen sein, ob dies auch für QUENCH-01 zutrifft.

Literatur

[1] H. Steiner, M. Heck:
The Code CALUMNO a Tool for the Analysis of Temperature Transients in QUENCH Tests, FZKA Bericht 6501 (Sept. 2000)

[2] L. Sepold et al.
QUENCH-01 Test Data Report, Interner Bericht (1998)

[3] P. Hofmann et al.
QUENCH-01 Experimental and Calculational Results, FZKA Bericht 6100 (1998)

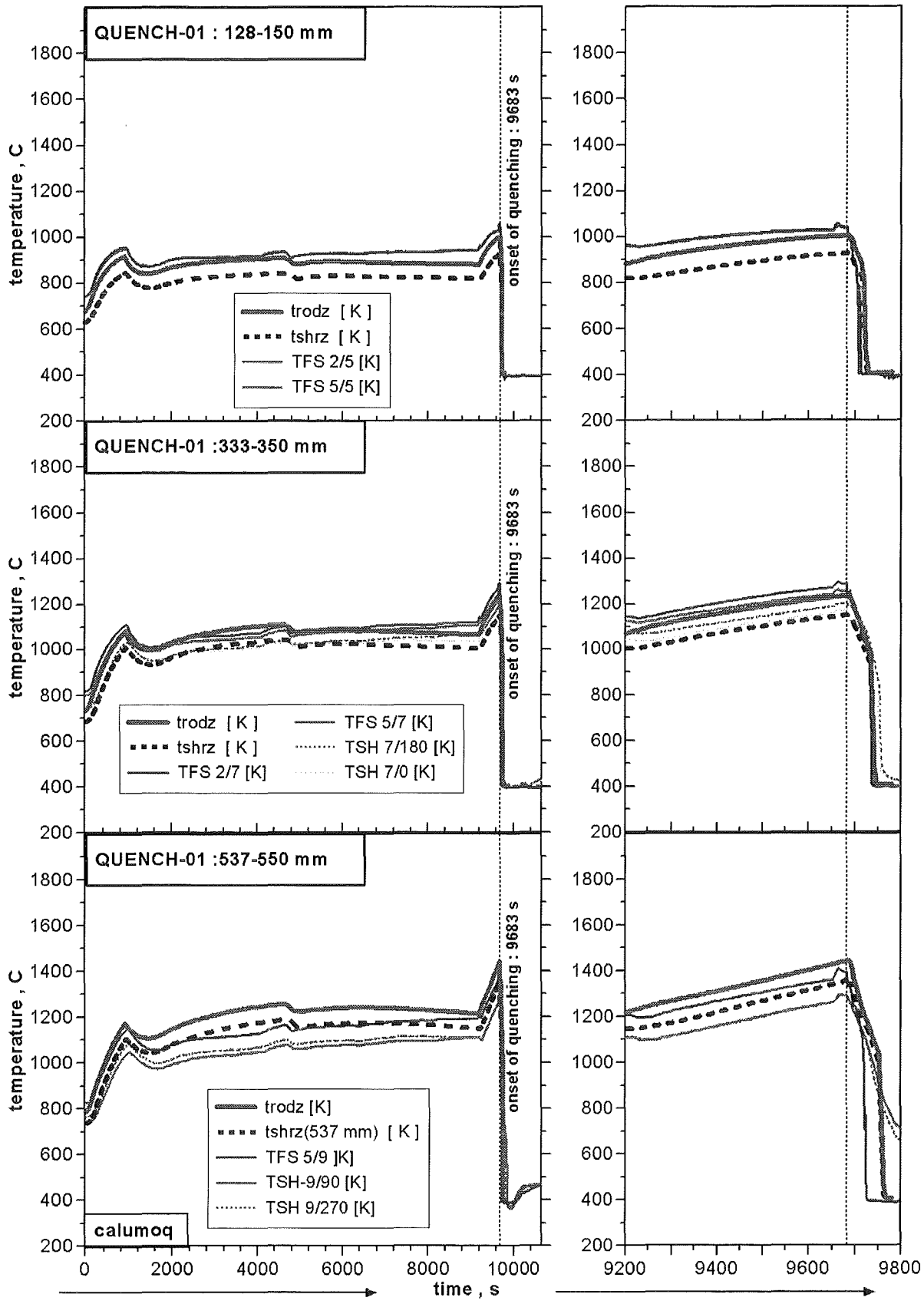

Abb. 1: Verlauf der Stab- und Shroudtemperaturen an verschiedenen axialen Positionen während der Transienten und der Quenchphase beim Versuch QUENCH-01

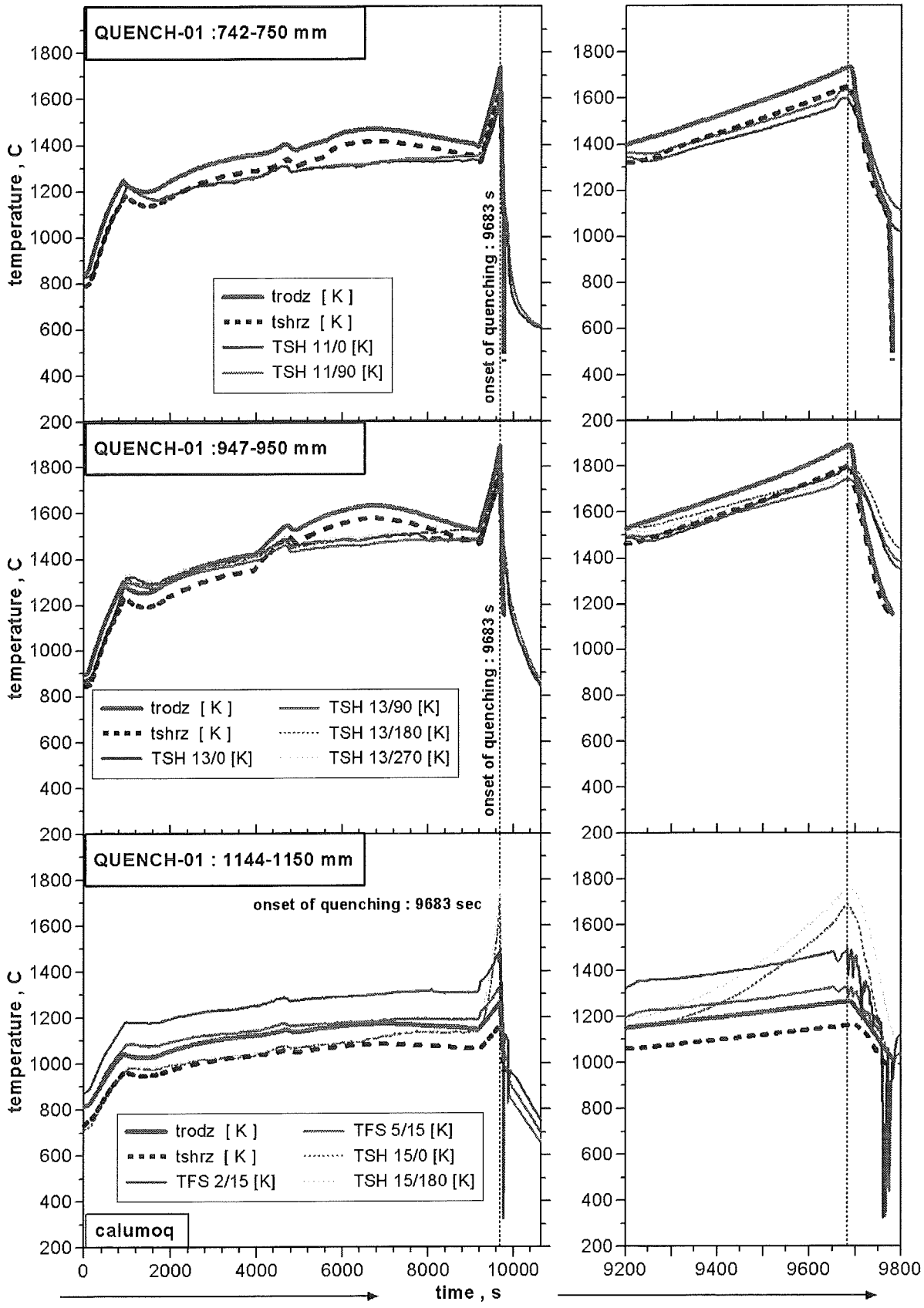

Abb. 2: Verlauf der Stab- und Shroudtemperaturen an verschiedenen axialen Positionen während der Transienten und der Quenchphase beim Versuch QUENCH-01

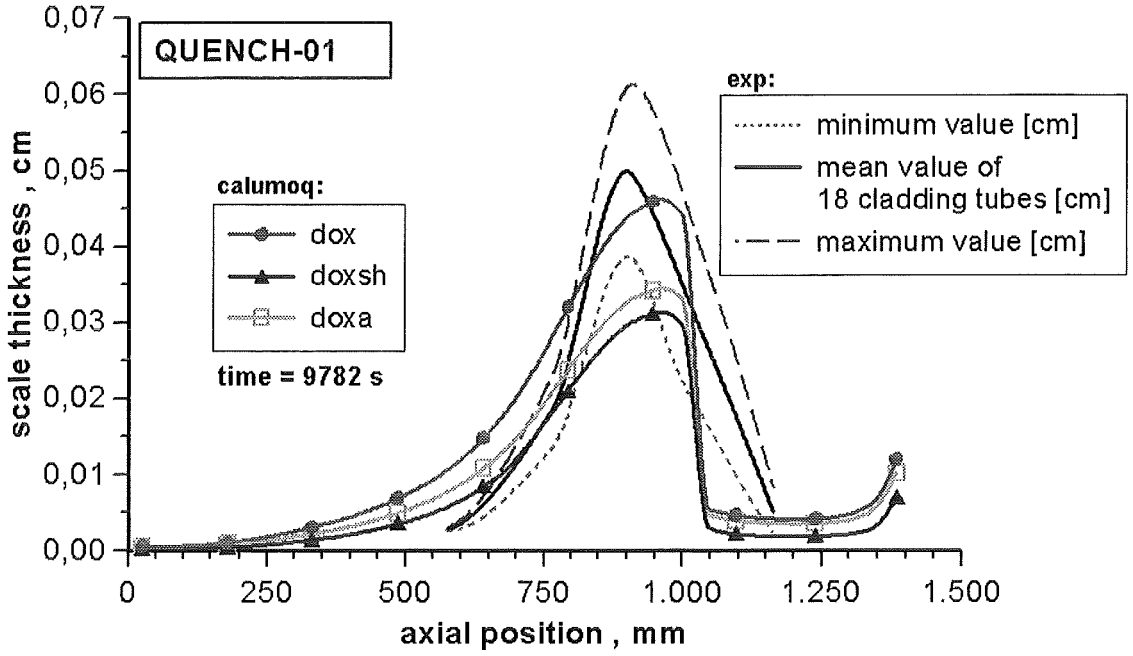

Abb. 3: Axiale Verteilung der Oxidschichtdicken nach Beendigung von QUENCH-01

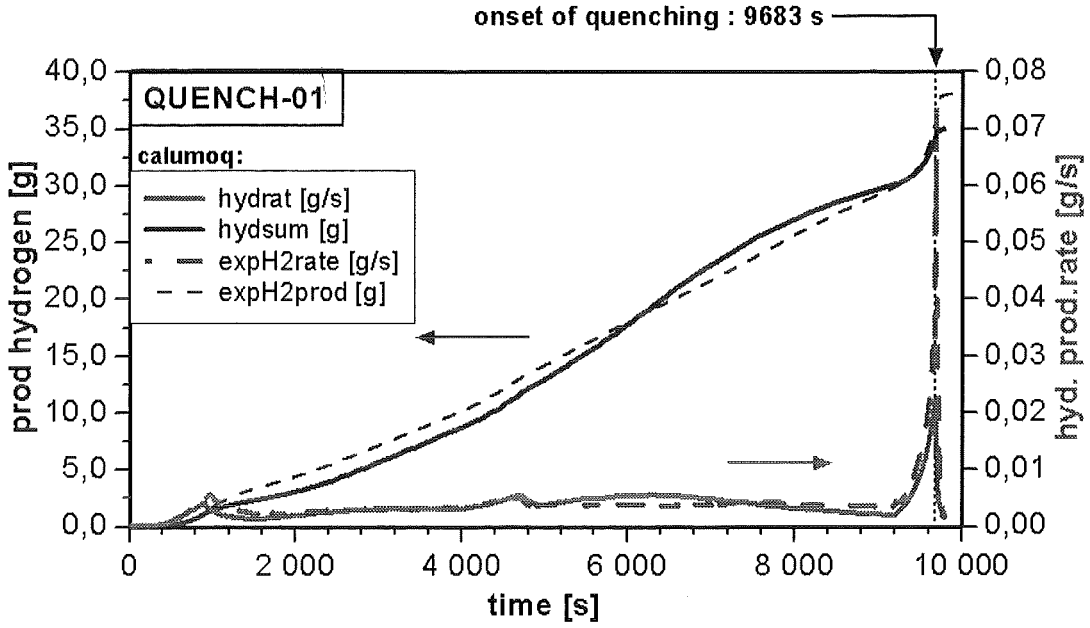

Abb. 4: Wasserstoffproduktionsrate und insgesamt produzierte Wasserstoffmenge bei QUENCH-01

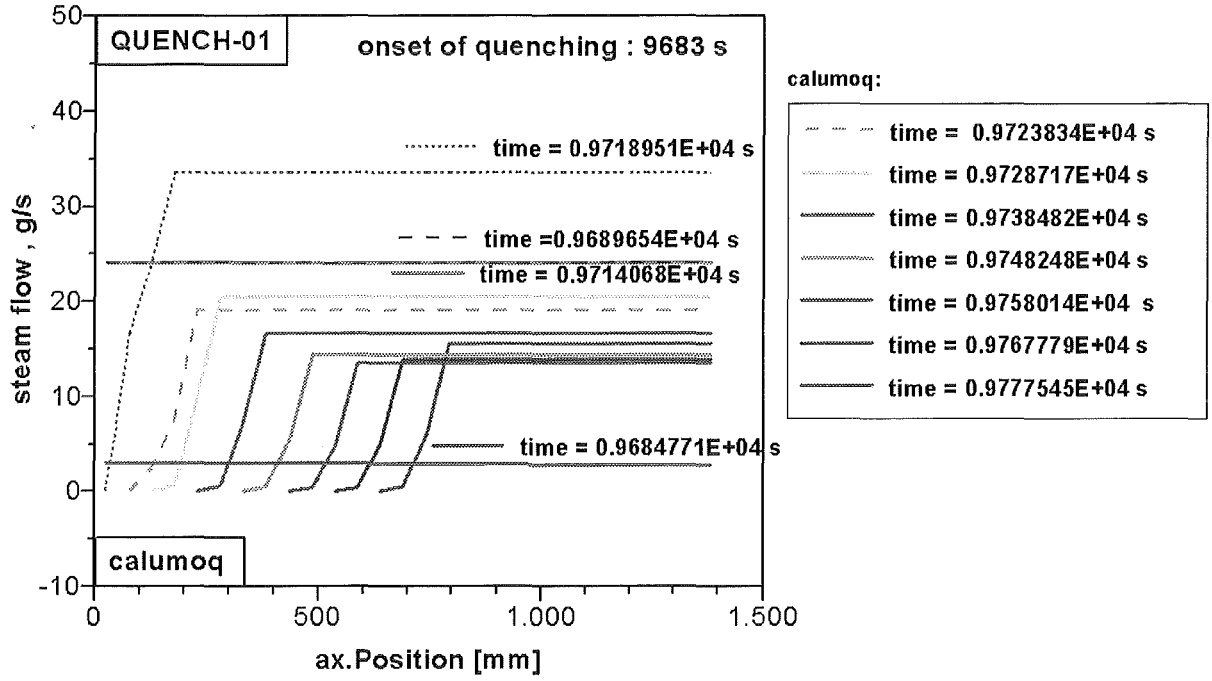

Abb. 5: Axiale Verteilung des durch Quenchen produzierten Wasserdampfes

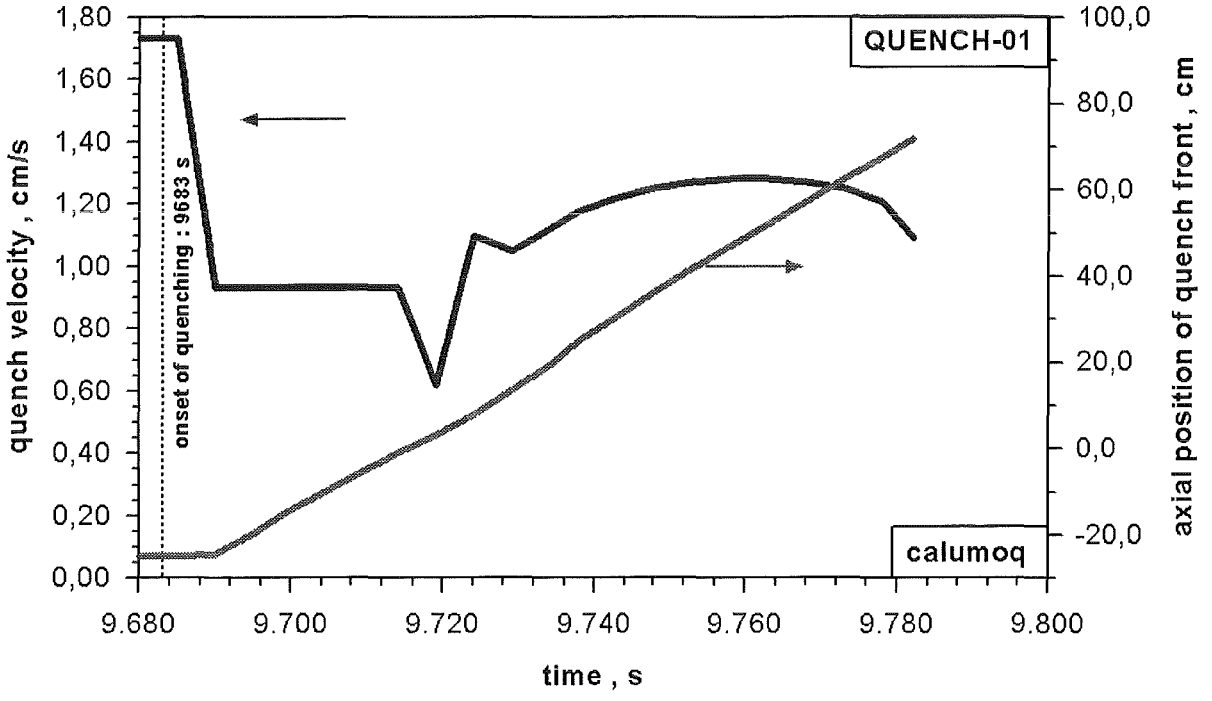

Abb. 6: Geschwindigkeit und Position der Quenchfront

IV. Separate-Effects Tests

(M. Steinbrück, L. Steinbock, A. Meier, U. Stegmaier, J. Stuckert, IMF I;
G. Schanz, W. Krauss, IMF III)

Abstract

Results of recent separate-effects tests within the scope of the QUENCH Program are presented. The main topics of the work were investigations on the quench behaviour of Russian Zr-1Nb cladding material, the oxidation of boron carbide in the temperature range between 800 and 1600 °C as well as the measurement of optical properties of pure and oxidised cladding materials.

Zusammenfassung

Es werden die neuen Ergebnisse von Einzeleffektuntersuchungen im Rahmen des QUENCH Programms beschrieben. Schwerpunkt der Arbeiten waren Untersuchungen zum Abschreckverhalten von russischem Zr-1Nb Hüllrohren, die Oxidation von Borkarbid im Temperaturbereich 800-1600 °C und die Bestimmung der Emissivität von blanken und oxidierten Hüllrohren.

1. SINGLE ROD QUENCH TESTS WITH ZR-1NB CLADDING

The injection of water to cool the degrading core down is an important accident management measure for controlling severe accident transients in the light water reactors. Reflooding of an uncovered core is the main measure of operator actions to prevent the melt down of the core. The phenomena under these conditions (complex heat transfer between cladding and water, formation of cracks in the oxidised cladding, hydrogen uptake and release during cladding oxidation) for rods with the Zircaloy-4 cladding have been studied within the QUENCH program at Forschungszentrum Karlsruhe. However, in the last time a number of new corrosion-resistant cladding materials for light water reactors with increased burnup has been proposed. A promising variant is the duplex cladding tube with the outer layer made of Zr-Nb alloy. Besides that, such alloys are being used in Russian VVER and in Canadian CANDU reactors. Therefore, an extensive separate-effects experimental database is required for Zr-1Nb claddings as a basis for the improvement of existing computer models.

Test rig and experimental procedure

For the experiments with Zr-1Nb rods the same equipment as for experiments with Zircaloy-4 rods was used. The design of the QUENCH rig is shown in Fig. 1.1.

The specimen used in the tests was a segment of VVER fuel rod cladding tube with a length of 150 mm, an outer diameter 9.13 mm (for comparison: the outer diameter of Zircaloy-4 cladding tubes is 10.75 mm) and a wall thickness of 0.705 mm (for Zircaloy-4 tube: 0.725 mm). The specimens were filled with high density yttria stabilised ZrO_2 pellets with an outer diameter 7.55 mm and a height 11 mm to simulate the fuel pellets.

Temperature at the outer surface of the cladding was measured by thermocouples at three elevations: 30 mm, 75 mm and 120 mm. The Pt/Rh thermocouples were fixed at the outer pre-oxidised tube surface by a Pt/Rh wire.

The scheme of the test conduct is presented in Fig. 1.2. The following phases for the test sequence can be distinguished. First, an initial phase, during which the facility was prepared for the actual test. The specimen was heated up to 1000°C under constant argon flow with the addition of 20% oxygen to prevent dissolution of the protection oxide layer. After establishing of the thermal equilibrium the steam was injected at a constant rate of 0.08 g/s. Second, during the enhanced pre-oxidation period, the specimen was heated up to 1400°C under a constant flow of argon and steam through the test section. The specimen was kept at this temperature until the desired oxide layer thickness is reached. Finally, the specimen was heated or cooled to the desired initial temperature at the onset of cooldown. The test was completed by increasing the steam flow rate to 1 g/s (steam temperature about 150°C) and switching off the inductive heating.

The off-gas composition was measured by "Balzers GAM-300" mass spectrometer (MS).

The amount of hydrogen absorbed by the specimens was analysed by hot extraction under flowing argon in the LAVA facility coupled with mass spectrometer.

Detailed metallographical post-test analysis of the cladding structures on the elevations, corresponding to the lower, middle and upper TC locations were performed. 1 cm long tube segments were embedded, ground, lapped and finally polished by means of STRUER's equipment.

Chemical analysis

The chemical analysis for both as received Zr-1Nb and Zircaloy-4 cladding materials was performed. The results are given in wt.% values in Table 1.1.

Temperature evolution

Temperature excursions as observed in the CORA quench tests and QUENCH bundle tests QU-02 and QU-03 were not observed in any of the reported single rod tests. One reason for that is the high radiative heat loss in the single rod QUENCH rig. Nevertheless, a temperature deviation from the regular monotonically decreasing during the cooldown phase was detected in almost all Zircaloy-4 single rod tests as well as in most tests with the Zr-1Nb cladding due to exothermic phase transitions during cooldown.

As an example, Fig. 1.3 shows the temperature evolution during cooldown from 1200 °C for the whole test and for the quench phase. The inductive heating method causes a certain axial temperature gradient with the highest temperatures in the mid zone.

Post-test non-destructive measurements

After the tests, photographs of each specimen were taken and non-destructive measurements of the following parameters were performed: oxide layer thickness, weight gain, tube diameter increase, tube length increase. The weight gains correlate well with the tube diameter increase and can be interpreted as a result of oxidation (formation of α-Zr(O) and oxide layers) .

Fig. 1.4 shows the appearance of some specimens after the cooldown from different temperatures. The oxide layer thickness at the onset of the cooldown phase was between 150 and 550 µm. Some specimens were broken during handling. Nevertheless they are mechanically quite stable and show no indications of spalling of the oxide scale. The outer surface of the cladding tubes is mostly dark which can be seen in Fig. 1.5. Here, the comparison of Zircaloy and Zirconium-Niobium claddings after the cooldown tests under the same conditions shows that at least the optical properties of oxide layers on the Zry and Zirconium-Niobium surfaces are different. It means also that these surfaces have different emissivity coefficients.

The crack pattern on the surface of the Zr-1Nb cladding tubes is not so pronounced and regular as for Zircaloy-4 tubes. For Zircaloy-4 the development of regular nets of longitudinal and circumferential through-wall cracks is typical. For Zr-1Nb tubes only some longitudinal through-wall cracks at 1100 °C, 1200 °C and 1400 °C and a lot of short surface cracks were observed. For the Zr-1Nb specimen with cooldown from 1600 °C there are only short cracks in the oxide layer.

Metallographic examination

After the tests a detailed metallographical analysis of the cladding cross-sections was performed at three elevations for each rod. A typical result of these examinations is shown in Fig. 1.6. Three typical layers (oxide layer, brittle α-Zr(O) layer, ductile β-Zr layer) were identified and measured. In contrast to the tests with Zircaloy-4 the surfaces of the through-wall cracks in Zr-1Nb tubes are practically not oxidised.

The results of the metallographical analysis allow to draw the dependence of typical layer thickness on the pre-oxidation duration. In Fig. 1.7 the measurement results for the specimens, which were cooled down from 1200 °C are presented. The local pre-oxidation temperatures were not always constant and varied from test to test. Nevertheless, a linear (for these large oxidation duration) regression dependence of oxide scale thickness vs. pre-oxidation time for each elevation acceptably fits the experimental data. The analysis shows that linear correlation of this experimental data is more precise than the parabolic one. The reason of such deviation from the parabolic law can be the formation of micro cracks and pores in the thick oxide layer.

Hydrogen release and absorption

One of main tasks of these tests was the quantitative description of the hydrogen generation kinetics. Fig. 1.3 shows the sharp increase of the hydrogen release during heat-up to 1400 °C which was observed in all tests. There is no noticeable increase of hydrogen generation during the quench phase for all the tests.

Fig. 1.8 shows the comparison of the hydrogen release between Zr-1Nb tests and corresponding Zircaloy-4 test from 1600 °C. Up to 1400 °C the oxidation kinetics for both materials are comparable. During the heat-up to 1600 °C the oxidation rate is considerably higher for Zr-1Nb in comparison to Zry-4.

Fig. 1.9 summarises the results of the analysis of the hydrogen amount absorbed in the metal phases of the rods in comparison to results obtained with Zircaloy samples. One can see that under the similar conditions the Zr-1Nb cladding tubes absorb significantly less hydrogen than Zircaloy-4 ones. This can be explained by the absence of crack oxidation in the former ones.

Table 1.1: Chemical analysis results of Zr-1Nb and Zircaloy-4 cladding materials

Element	Zr-1Nb	Zircaloy-4
Nb	0.971 ± 0.004	-
Sn	< 0.004	1.525 ± 0.011
Hf	0.0252 ± 0.0001	< 0.005
Fe	0.0079 ± 0.0002	0.221 ± 0.001
Cr	0.0022 ± 0.00005	0.105 ± 0.001
Ni	0.0023 ± 0.0001	-
Ca	< 0.005	< 0.005
Y	< 0.003	< 0.002
Cu	< 0.0003	-
Mn	0.00007 ± 0.00001	-
O	0.046 ± 0.002	0.135 ± 0.015
N	0.004 ± 0.001	0.007 ± 0.005

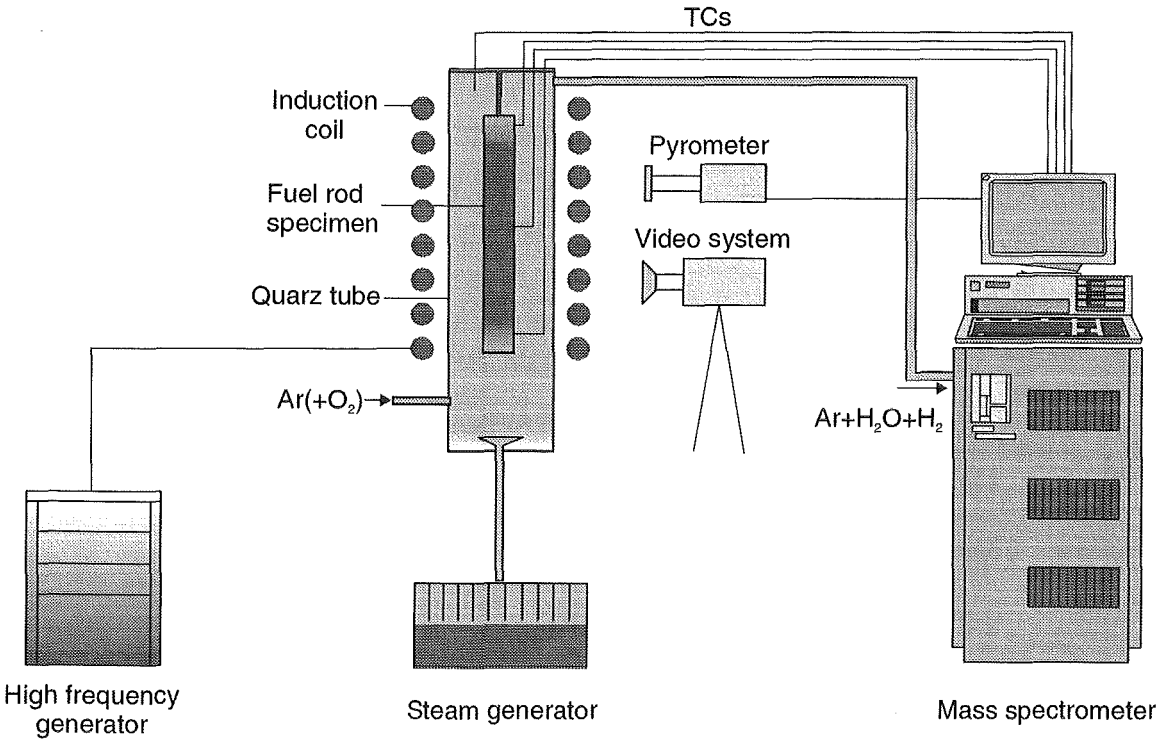

Fig. 1.1: QUENCH Rig for investigation of reflood behaviour of cladding materials

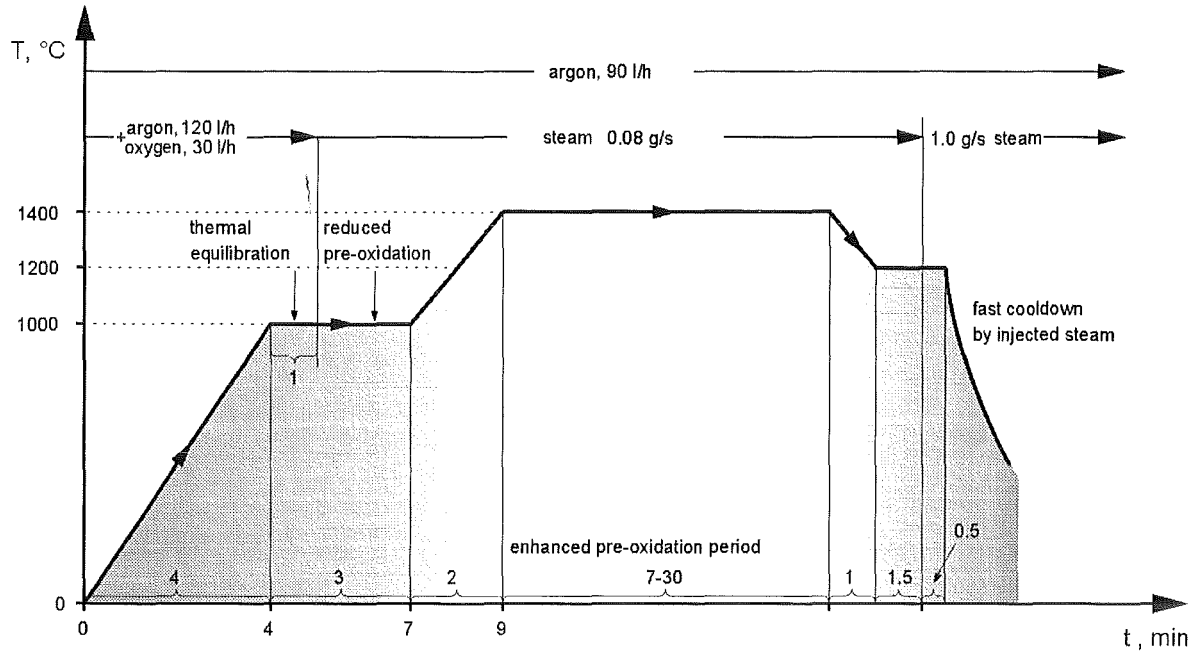

Fig. 1.2: Test conduct of single rod quench experiments

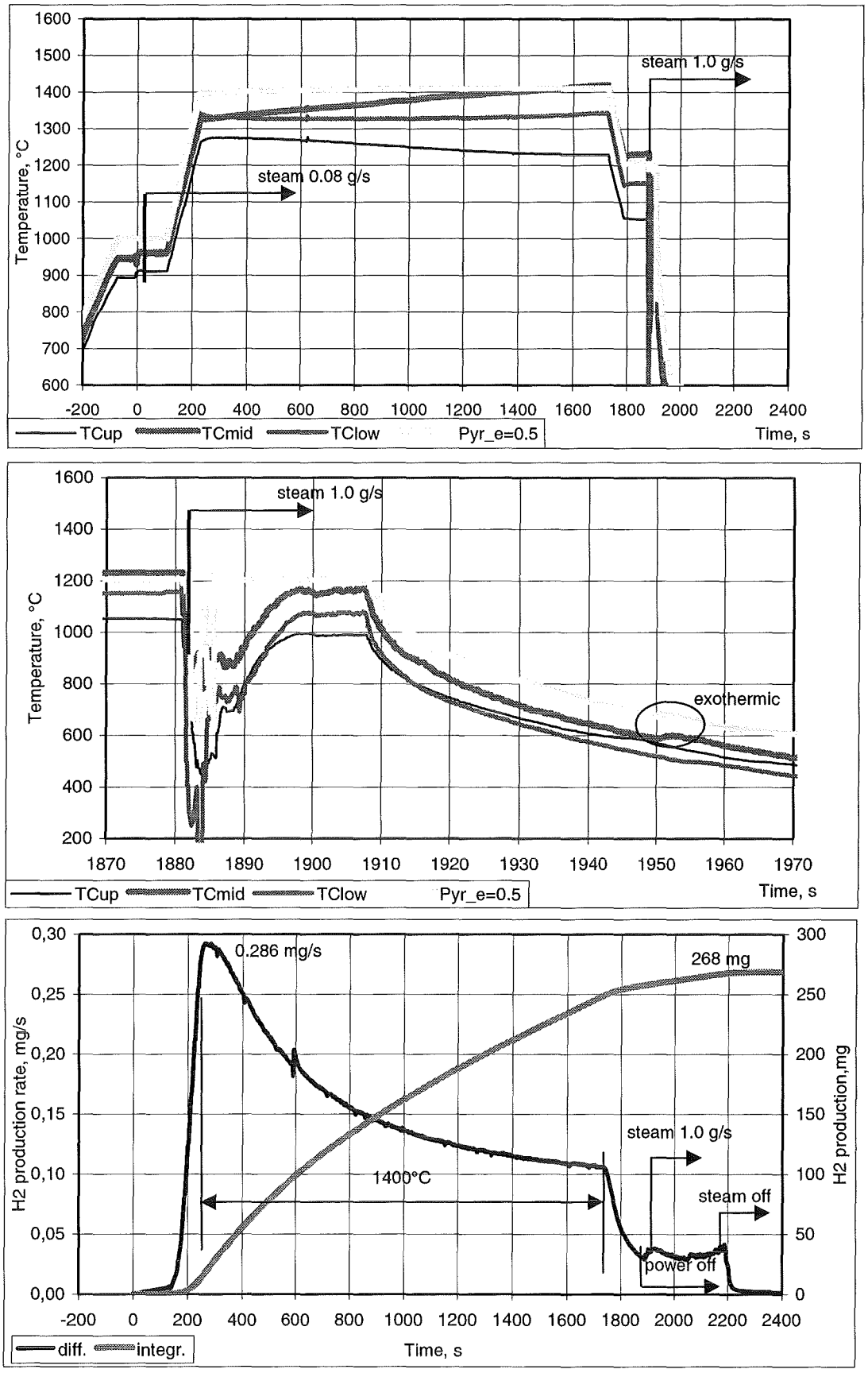

Fig. 1.3: Temperature history and hydrogen release for test 00320a with 25 min pre-oxidation and cooldown from 1200 °C

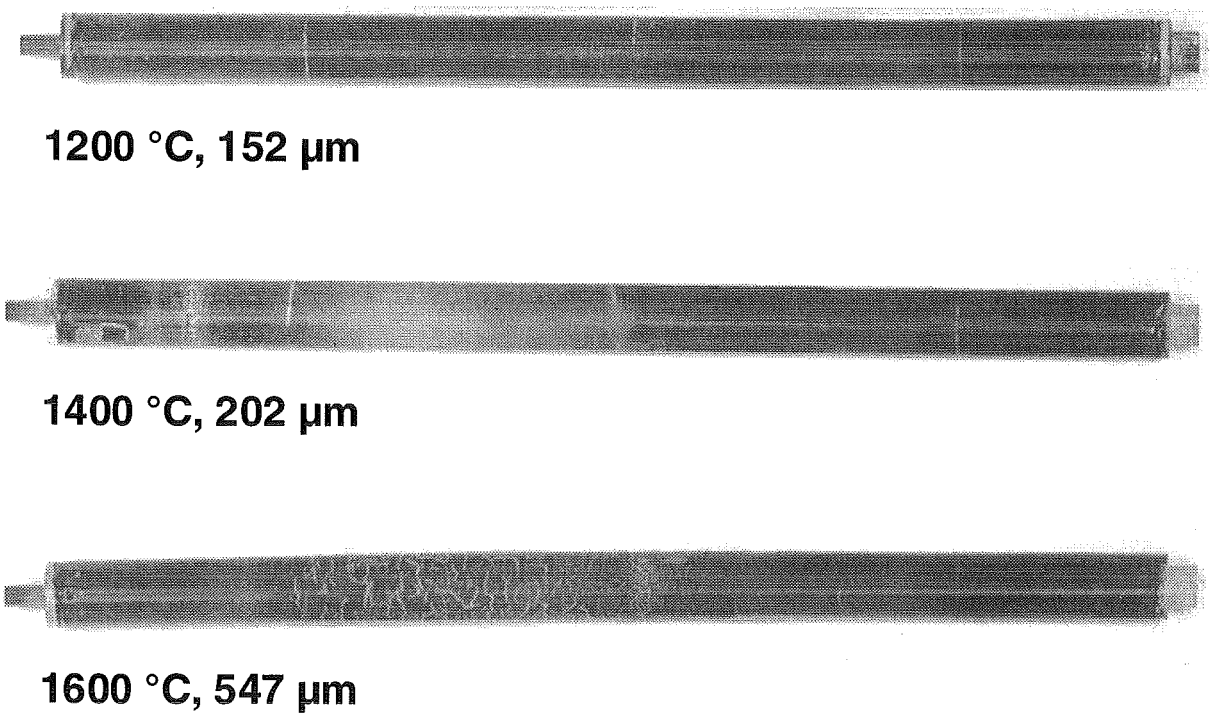

Fig. 1.4: Macroscopic post-test appearance of Zr-1Nb specimens

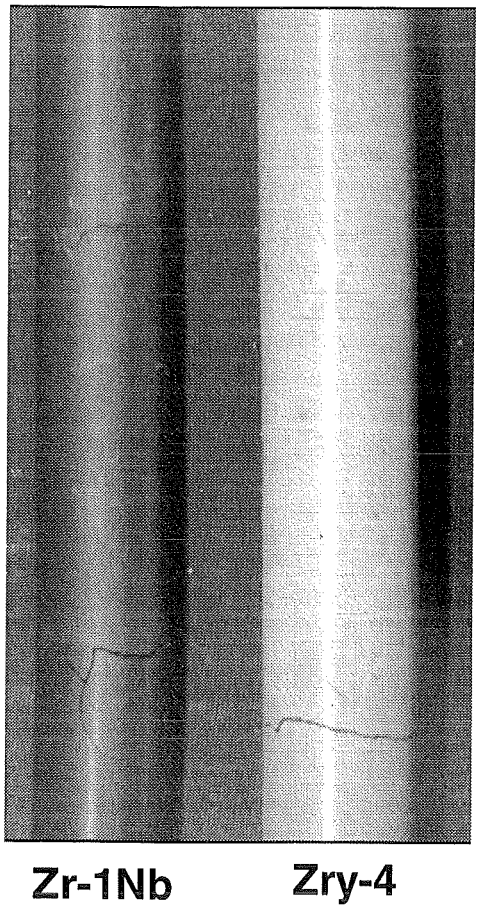

Fig. 1.5:
Comparison between macroscopic post-test appearance of Zry-4 and Zr-1Nb

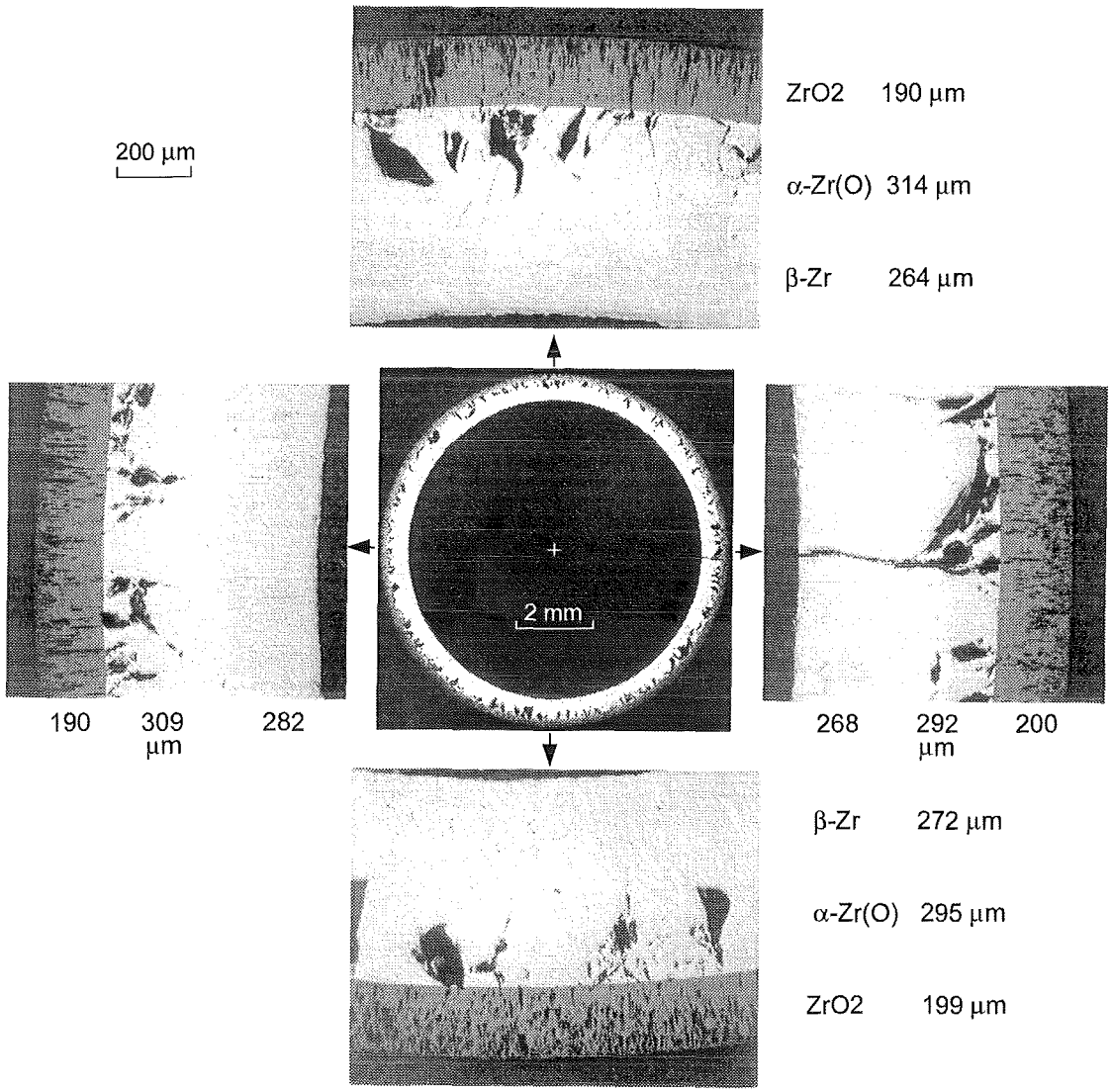

Fig. 1.6: Cross section of a specimen at mid TC elevation (18 min pre-oxidation, cool- down from 1400 °C). There are a few non-oxidised through-wall cracks

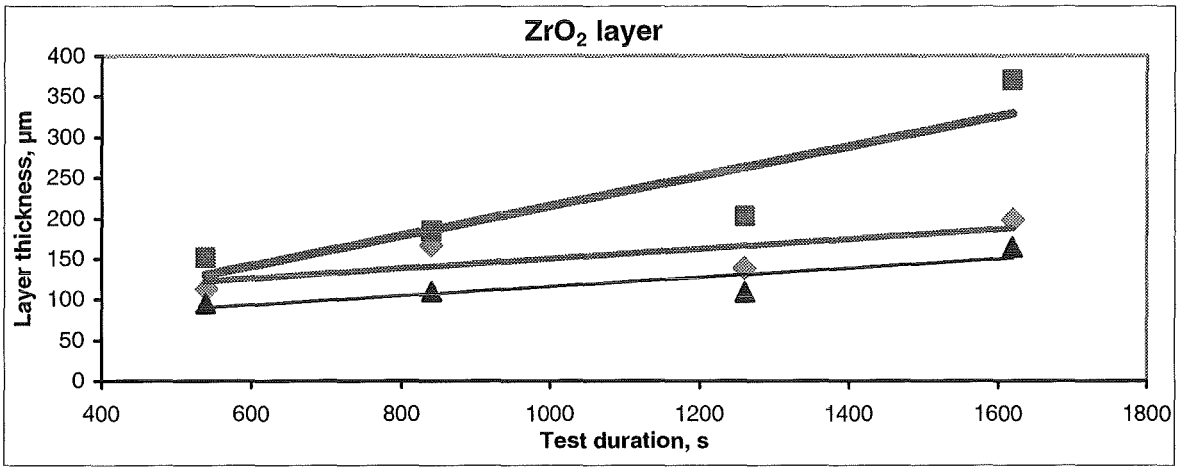

Fig. 1.7: ZrO_2 scale thickness vs. duration of pre-oxidation at 1400 °C and cooldown from 1200 °C. rhombi: lower TC, squares: mid TC, triangles: upper TC

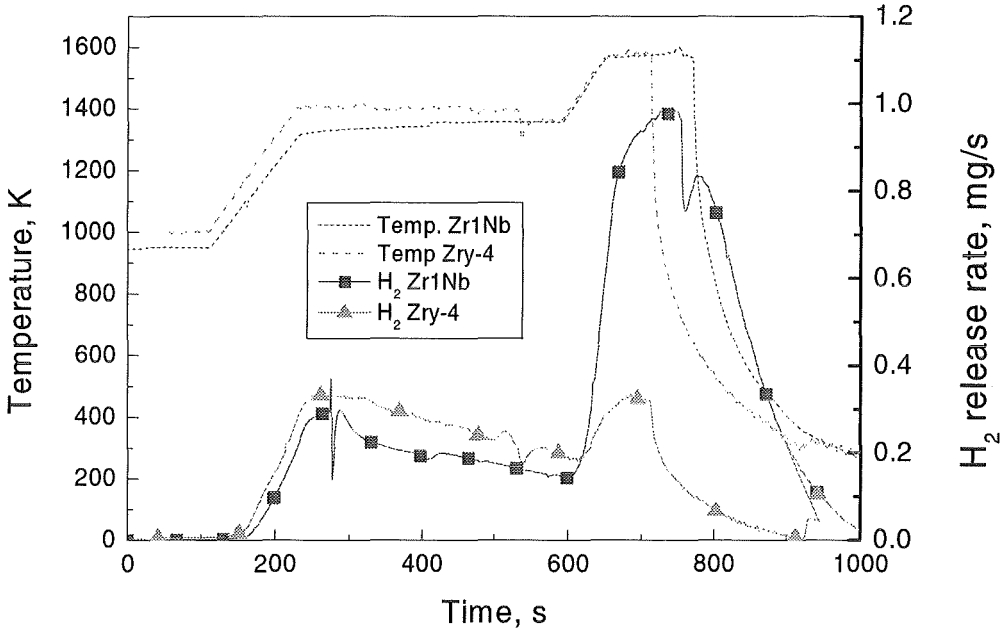

Fig. 1.8: Oxidation of Zry-4 and Zr-1Nb in steam

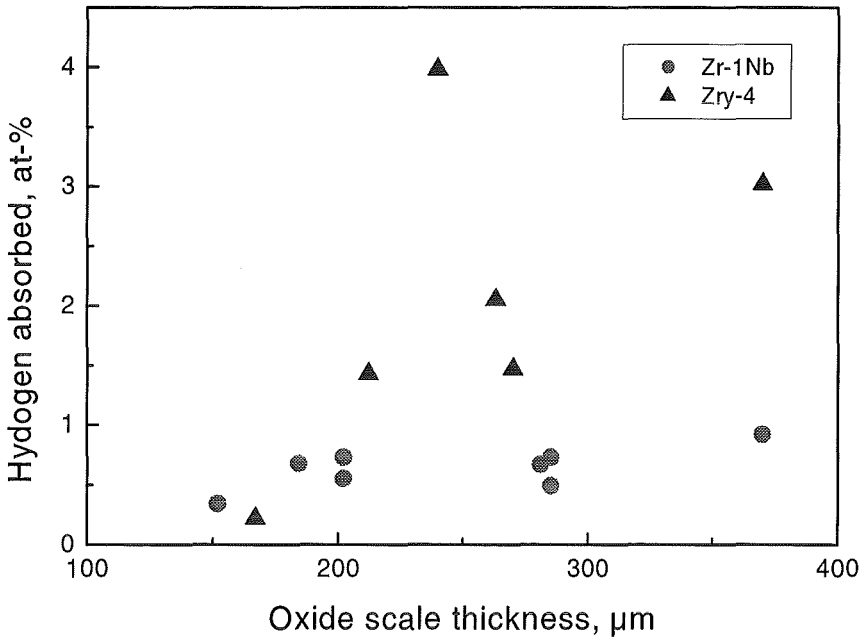

Fig. 1.9: Hydrogen absorbed by the metal phase during oxidation and steam quenching. Comparison between Zry-4 and Zr-1Nb

2. OXIDATION OF B_4C AT HIGH TEMPERATURES

Boron carbide is worldwide used as control rod material in many nuclear power plants. Previous test, e.g. within the scope of the CORA program have shown a significant influence of B_4C on the degradation and oxidation of the reactor core during a hypothetical severe accident transient due to the highly exothermic reaction with steam which leads to the formation of liquid boron oxide, hydrogen and carbon containing species like CO, CO_2 and CH_4. Methane may have a strong influence on the fission product chemistry by the formation of volatile organic iodine compounds. Presently, no data are available on the oxidation kinetics of B_4C at the high temperatures of interest. Therefore, an experimental program was launched at FZK within the scope of the 5th FP EC COLOSS Programme.

Experimental set-up

A new experimental set-up designed for the B_4C oxidation tests (BOX Rig) was put into operation. The BOX Rig consists of

- a gas supply system for Ar, H_2 and steam (0-4 mol/h each),
- a tube furnace up to 1700 °C,
- a quadrupole mass spectrometer (MS).

The system is completely computer controlled by a LabView program especially written for the BOX Rig.

The commissioning tests were performed successfully. The steam flow rate can be regulated sufficiently well and is measured accurately by the MS. Problems coming from the condensation of boric acids in the off-gas system have been solved by heating the off-gas pipes and periodical cleaning the whole off-gas system by steam.

Thermochemical pre-test calculations

Thermo-chemical pre-test calculations were performed using the equiTherm 5.0 software using the built-in Barin database for pure substances. The oxidation of B_4C in steam-containing environments can be mainly described by the following chemical reactions:

$$B_4C + 7H_2O \leftrightarrow 2B_2O_3 + CO + 7H_2 \qquad (1)$$

$$B_4C + 8H_2O \leftrightarrow 2B_2O_3 + CO_2 + 8H_2 \quad (2)$$

$$B_4C + 6H_2O \leftrightarrow 2B_2O_3 + CH_4 + 4H_2 \quad (3)$$

Further on, the boric oxide will react with excess steam to produce various types of boric acids.

According to the calculations, reaction (1) is preferred under various steam/hydrogen atmospheres in the temperature range of interest (800-1600 °C). In this temperature range it is more pronounced at higher temperatures and at higher hydrogen content in the atmosphere. A significant methane production which is of interest due to its potential influence on the iodine fission product chemistry is only obtained at low temperatures (<700 °C). At temperatures above 1200 °C and 1500 °C considerable amounts of gaseous metaboric acid HBO_2 and boric oxide B_2O_3, respectively, are calculated to evaporate. There is only a minor influence of the system pressure on the composition of the reaction products.

Experimental results

Three test series with B_4C pellets were performed up to now:

- transient tests between 800 and 1500 °C (20 K/min) under Ar/steam/(H_2) atmosphere,
- isothermal tests (30 min) at 800, 1000, 1200, 1400, 1500, and 1600 °C in Ar/steam,
- various isothermal tests under variable atmospheres from pure steam to almost pure hydrogen.

In the transient tests, the mass spectrometer shows a first peak of H_2 production just after the steam injection at low temperature and an increase of the H_2 production rate at high temperatures above 1200 °C. The CO and CO_2 production are mainly observed at high temperature, the CH_4 production is very weak and seen only at low temperature (Fig. 2.1).

In the isothermal tests (30 min), peaks of H_2, CO, and CO_2 production are measured immediately after the steam injection, followed by a plateau (Fig. 2.2). This, as well as the high reaction rates at the beginning of the transient tests, is interpreted as a rapid initial oxidation resulting in the formation of a liquid B_2O_3 layer on the B_4C pellet. The

steam supply to the B_4C material is then limited by diffusion through this layer. Again, the CH_4 production is very low, in good accordance with the thermodynamic pre-test calculations carried out by IPSN and FZK. Figure 2.3 shows a net mass gain of the specimens for temperatures up to about 1100 °C; at higher temperatures a mass loss was observed which increased with rising temperatures and reached almost 50 % at 1600 °C.

SEM images at high magnifications show an increasing roughness and porosity of the pellet surface with rising temperatures up to 1400 °C; the surface of the specimen oxidised at 1600 °C looks like molten at the high temperature. The B_4C grains of the specimens from the tests at 800 and 1000 °C are covered by a light layer, which is most probably B_2O_3.

Tests with B_4C specimens at 800 and 1200 °C and varying atmospheres (H_2/steam ratio, Ar flow rate, steam flow rate) demonstrate only a slight dependence of the off-gas composition, especially of the CH_4 release, on the composition of the atmosphere at inlet and on flow rates, as can be seen in Fig. 2.4.

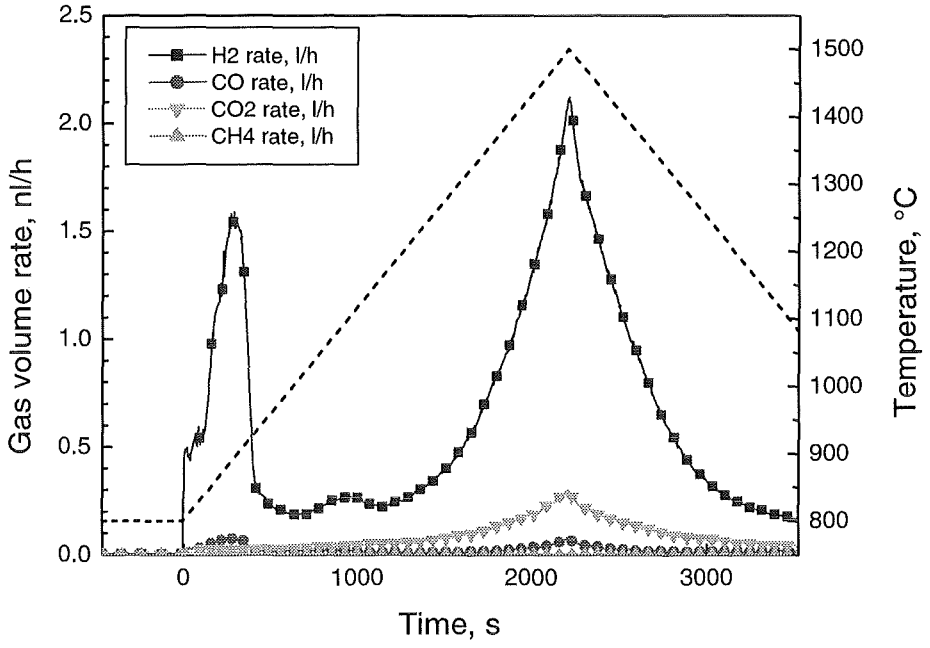

Fig. 2.1: Transient oxidation of B_4C pellets in Ar/steam atmosphere. Volume flow rate of the gases released between 800 and 1500 °C.

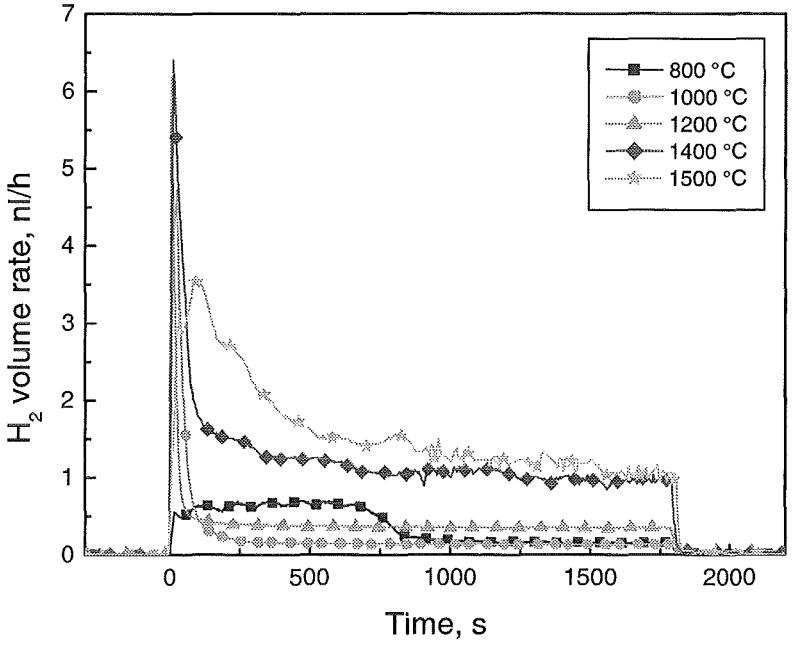

Fig. 2.2: Isothermal oxidation of B_4C pellets in Ar/steam atmosphere. Volume flow rate of the hydrogen released at 800, 1000, 1200, 1400, and 1500 °C.

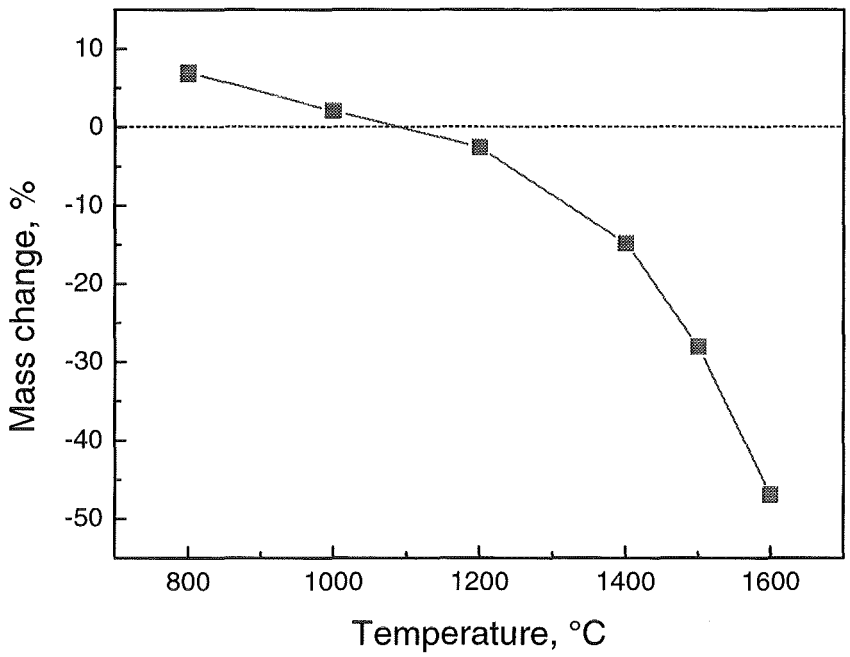

Fig. 2.3: Isothermal oxidation of B_4C pellets in Ar/steam atmosphere. Mass change in dependence on temperature.

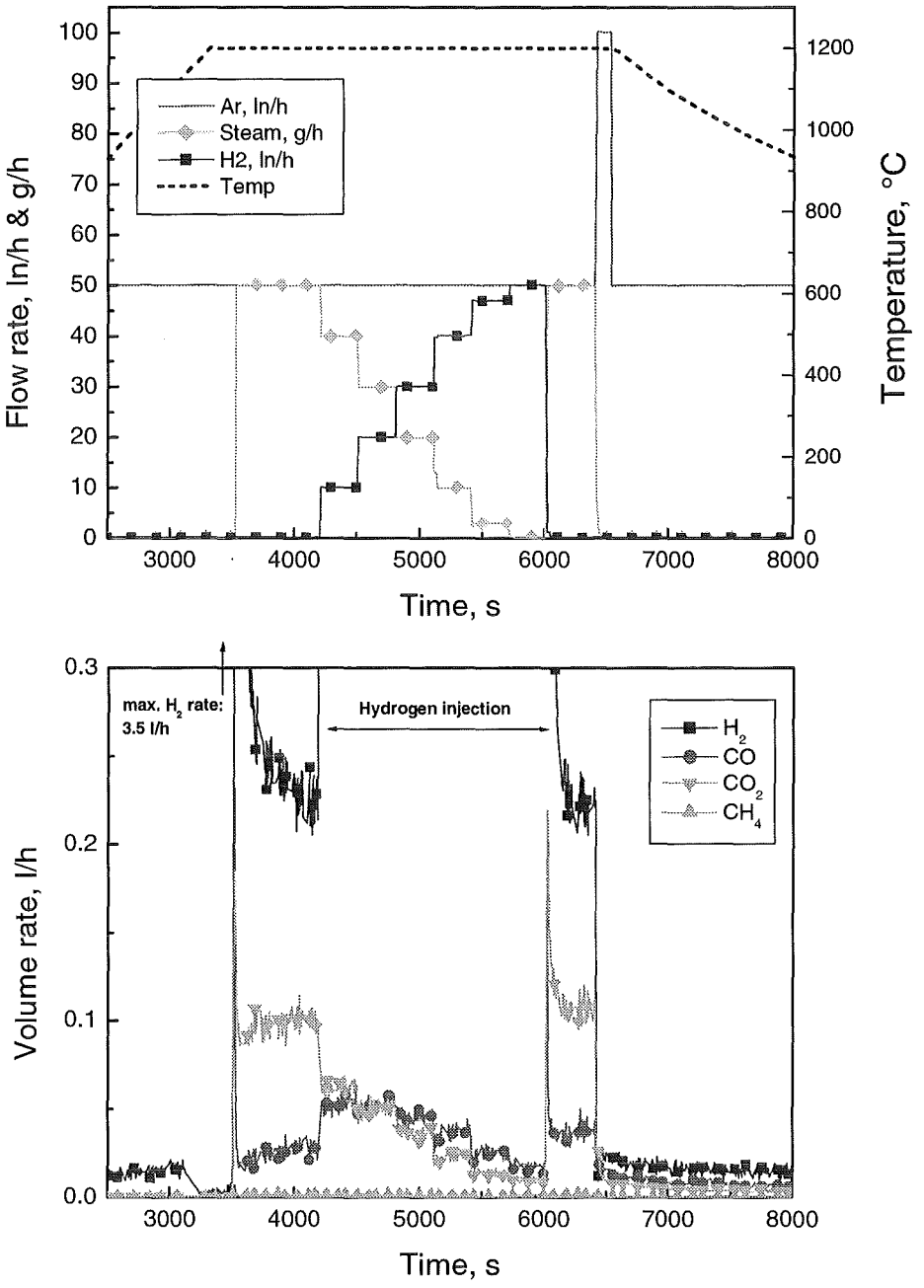

Fig. 2.4: Isothermal oxidation of B_4C pellets at 1200 °C in variable Ar/steam/H_2 atmosphere. Test conditions (upper diagram) and gas release measured by MS.

3. MEASUREMENT OF OPTICAL PROPERTIES OF REACTOR MATERIALS

The emission properties of zircaloy and its oxide determine the thermal behaviour of fuel pins during accidents. Earlier measurements of the optical properties were executed with the pure materials. The data used in code models like MATRO or SVECHA do not coincide. This necessitates a new measurement of these properties with more realistic materials. For this purpose a mirror furnace was built, which may be used to measure the optical properties at room temperature and up to 1100°C.

In this furnace a central focus line is heated with 4 line lamps inside 4 elliptical cylindrical mirrors. The lamps are controlled by a computer and have a response time of 1 second. Temperatures are measured with Pt-Rh elements. Light spectra are captured with sapphire rods and fibres and are analysed with a VIS/NIR spectrometer (500-1000 nm) and a NIR spectrometer (1100-1700 nm).

Until now spectra have been measured inside tubes of ZrO2, Al2O3 and steel during heating to 1100°C and cooling down. A remarkable result is the strong temperature dependence of the transmission of ZrO2 in the NIR at 850, 1500 and 1600 nm (Fig. 1). The transmission of zircon oxide falls sharply when the temperature rises from 500° to 1000°C. Thus a strong increase of the emission coefficient may be deducted.

This is also ascertained by an analysis of cooldown curves of oxidized zircaloy tubes, which show a maximum of the emissivity at the temperature 1150°C. The first results were obtained from as fabricated ZrO2. Future measurements will be done in a controlled atmosphere and with oxidized zircaloy tubes.

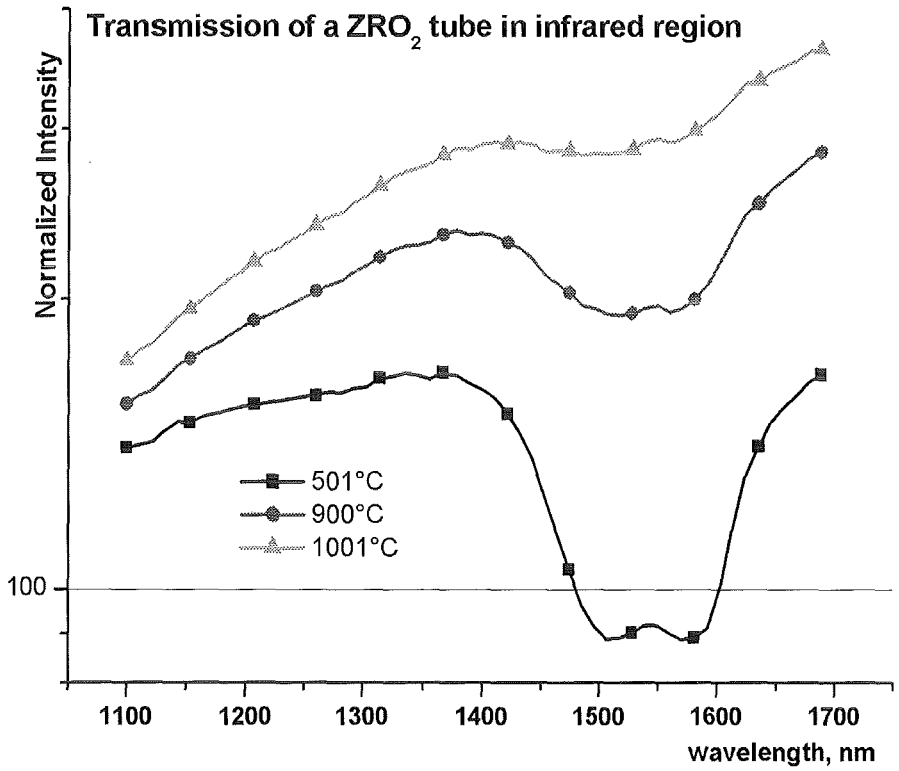

Fig. 3.1: Infrared transmission of zirconia tube

V. Einzeleffekt-Untersuchungen zum Reaktionsverhalten von Zircaloy-4 in Luft und zur Oxidation von B_4C

(W. Krauss, G. Schanz, H. Steiner, IMF III)

Abstract

The experimental separate effects test program on the Zircaloy-4 air reaction was supported by mechanistic modelling, and extended to the topic boron carbide-steam oxidation. Isothermal oxidation testing of Zircaloy-4 in air was pursued in a thermo-balance system up to 1500 °C and compared with tests in dry Ar/O_2 atmosphere. This work was done in close relation to the EU OPSA project, which is terminated meanwhile. In addition to earlier investigations using tube sections rod section specimen were included. By this it was possible to enlarge the isothermal test duration and to increase the test temperatures. This measure was necessary to provide a full data set sufficient for model development. Additionally, the more stable rod section indicated the mechanical influence on the oxidation behaviour of tube sections.

The metallographic examinations show clearly that nitrogen strongly induces morphological and mechanical phenomena. Furthermore temperature regimes can be distinguished according to the dominating oxidation mechanisms. At low temperatures (e.g. 900 °C) a self accelerating reaction takes place, whereas the reaction rates slow down at temperatures above 1200 °C. The tests indicate that passivating layers can be formed because self healing processes occur.

Modelling work on air oxidation was started using the mass increase data, and the determined scale structure for verification of the calculated actual O_2 flux through the oxide scale. The main feature of this empirical corrosion model is the separation of the oxide scale into two subscales with different O_2 transport mechanisms.

Both, experimental and theoretical results indicate, that a complete understanding of the oxidation processes and phenomena of air oxidation needs additional experimental and modelling activities on more realistic atmospheres. Without those efforts a transfer of the results to reactor safety considerations is impossible. A corresponding judgement of the air oxidation results available up to yet is given in the EU OPSA final report and the type of future work is illustrated by phenomena

detected during the performed integral tests and preliminary analytical treatment with integral code systems.

The separate effects test program on the oxidation of boron carbide with the intended expansion to the B_4C / Cr-Ni stainless steel / Zircaloy systems of special interest with respect to the production of methane. This task is performed as part of the EU COLOSS program to support the preparation of integral tests and to contribute to an international data base for application in code systems. First tests considered the oxidation of pure B_4C in dry Ar/O_2 and the evaporation behaviour of B_2O_3 in dry and wet Ar atmosphere. The temperature dependence of B_4C oxidation indicates the occurrence of regimes controlled by the formation of passivating B_2O_3 layers and their stability. Below 800 °C nearly no evaporation of B_2O_3 is detected and the oxidation can be described by a parabolic time law. In contrast above 1100 °C evaporation counteracts against growth of passivating scale. The examination, which is performed using a thermobalance system, will be supplemented in the future by mass spectrometric analysis of the gaseous reaction products.

Zusammenfassung

Das experimentelle Programm zu Einzeleffekt-Untersuchungen wurde weitergeführt mit den Schwerpunkten Zircaloy-4/Luft Oxidation, Modellierung der Einzeleffekte und Oxidationsverhalten von B_4C. Die Tests zur Zircaloy-4/Luft Oxidation erfolgten bei isothermer Versuchsführung im Temperaturbereich bis 1500 °C und wurden Oxidationstests in der Thermowaage in Ar/O_2-Atmosphäre gegenübergestellt. Diese Arbeiten wurden begleitend zum in der Zwischenzeit abgeschlossenen EU-Projekt OPSA durchgeführt. Sie ergänzen frühere Untersuchungen mit kurzen Zircaloy-4 Rohrabschnitten durch die Einbeziehung von Thermowaage-Tests an Massivproben unter strömender, trockener Ar/O_2-Atmosphäre der Zusammensetzung 80/20 oder synthetischer Luft. Mit diesen Proben konnten die Versuche zu höheren Reaktionstemperaturen und längeren isothermen Haltezeiten ausgeweitet werden. Letztere sind notwendig um einen vollständigen Datensatz für die Modellentwicklung bereitzustellen. Darüber hinaus liefern Festigkeitsvorteile von Massivproben Indizien für einen mechanischen Einfluss auf das Oxidationsverhalten von Rohrabschnitten.

Die metallographische Untersuchung zeigt, dass Stickstoff die morphologischen und mechanischen Phänomene maßgeblich bestimmt. Des Weiteren zeigen die Untersuchungen, dass Regime existieren in denen unterschiedliche Oxidationsmechanismen verschiedene Gewichtung haben. Bei niederen Temperaturen (z.B. 900 °C) wird in Luft ein sich selbst dramatisch beschleunigendes Reaktionsverhalten beobachtet. Dagegen tritt bei höheren Temperaturen (ab ca. 1200 °C) eine zeitliche Abnahme der Reaktionsgeschwindigkeit auf. Dies deutet auf die Ausbildung von passivierenden Schichten und ein Selbstheilungsverhalten hin.
Eine modellmässige Beschreibung der Oxidation in Luft wurde auf Basis der experimentell ermittelten Daten zur Massenzunahme, dem aktuellen O_2-Fluss durch die Oxidschicht und der metallographisch bestimmten Schichtstruktur begonnen. Bei diesem empirischen Korrosionsmodell wurde die Oxidschicht in 2 Teilschichten zerlegt, so dass verschiedene O_2-Transportmechanismen angesetzt werden konnten. Die ermutigenden experimentellen und theoretischen Arbeiten zeigen jedoch, dass zur guten Beschreibung der ablaufenden Prozesse, deren Verständnis und Übertragung auf Reaktorstörfallszenarien noch umfangreiche Arbeiten auch in realitätsbezogenen Atmosphären notwendig sind. Diese Ergebniseinschätzung und Forderung für zukünftige Arbeiten wird auch im extern verfassten OPSA-Bericht geteilt und am Beispiel von relevanten in Bündelversuchen beobachteten Phänomenen deutlich dargestellt.

In das Einzelleffekt-Programm wurden Untersuchungen und begleitende analytische Arbeiten hinsichtlich aktuell interessanter Störfall-Bedingungen zur Oxidation von B_4C und B_4C / Cr-Ni-Stahl / Zircaloy hinsichtlich der Produktion von Methan etc. aufgenommen. Diese Arbeiten sind eingebunden in das COLOSS-Programm und dienen der Vorbereitung von Integralexperimenten und dem Aufbau einer internationalen Werkstoffdatenbasis. Begonnen wurde in diesem Programm mit Untersuchungen zum Oxidationsverhalten von reinem B_4C in trockener Ar/O_2-Atmosphäre der Zusammensetzung 80/20 und mit Studien zum Verhalten von B_2O_3 in trockener und feuchter Ar Atmosphäre. Das Reaktionsverhalten von B_4C lässt sich in temperaturabhängige Regime unterteilen. Der diese Regime definierende Faktor ist die Ausbildung von passivierenden B_2O_3 Schichten und das stark temperatur- und atmosphärenabhänige Verdampfungsverhalten von B_2O_3. Unterhalb von 800 °C folgt die Oxidation einem parabolischen Zeitgesetz. Dagegen liegt oberhalb von 1100 °C

fast keine Passivschicht mehr vor. Die Untersuchungen, die in einem Thermowaage-system ausgeführt werden, sollen durch massenspektrometrische Analyse des Reaktionsgases und Einbeziehung der metallischen Strukturmaterial-Komponenten ergänzt werden.

1. Zielsetzung

Im Vordergrund für das Einzelleffekt-Programm und die Nutzung der Ergebnisse stehen der Wasserstoff-Quellterm, die Brennstoff-Chemie mit der Bildung von Methan sowie die Mechanismen und die Kinetik der ablaufenden Prozesse und deren Einbindung in modellmäßige Störfallszenarien. Ohne diese Kenntnisse ist eine Bewertung der Risiken wie Hüllrohrreaktion unter Lufteinbruch oder B_4C Oxidation und damit verbundene Produktion von Methan nicht möglich, wobei dieser Aspekt unabhängig von der Relevanz des Auftretens solcher Störfallszenarien ist. Beobachtete Mechanismen wie Selbstheilung könnten jedoch entscheidend zur Qualifizierung beitragen und bei der Diskussion von Risiken verwendet werden.

Wie früher bereits ausführlich dargestellt wurde, ist bekannt, dass die Hoch-temperatur-Oxidation von Zirkonium und seinen Legierungen an Luft vom Verhalten in Dampf oder in Ar/O_2-Athmospäre dramatisch abweichen kann. Insbesondere die neben der Sauerstoffoxidation ablaufende Reaktion mit Stickstoff, führt zum Wachstum morphologisch veränderter und mechanisch geschädigter Reaktions-schichten anstelle von schützenden Oxidschichten, und deshalb zu komplexeren reaktionskinetischen Randbedingungen [1-4]. Es ist somit nicht zulässig, generell ein Reaktionsverhalten zu unterstellen, das ähnlich zur Dampfoxidation ist. Darüber hinaus tritt bei der Luftoxidation im Vergleich zur Dampfoxidation eine wesentlich höhere spezifische Energiefreisetzung auf. Wesentliche Informationslücken zur Qualifizierung von Störfallszenarien bestehen mindesten noch im Bereich Verhalten von Zircaloy-4 in stickstoffhaltiger (lufthaltiger) feuchter Atmosphäre und bei Luftzutritt nach vorhergegangener Bildung intakter Oxidschichten sowie bei der Einbindung dieser Daten in die Modellierung.

Grundlegende Einzeleffekt-Untersuchungen zur Zircaloy-4/Luft-Oxidation fanden zunächst unter idealisierten und sauber definierten Bedingungen an kleinen

metallischen Zircaloy-4 Proben in Form von Rohrabschnitten und Stababschnitten statt. Nur durch den Einsatz massiver Stababschnitte und das damit verbundene große Materialangebot im Vergleich zu dünnwandigen Rohren konnte bei höheren Temperaturen eine ausreichend lange Messzeit für die Auswertung isothermer Versuche erzielt werden.

Bei den Untersuchungen zur B_4C Oxidation und der Bildung von Methan stehen wie bei der Zircaloy Oxidation Fragen wie das allgemeine Reaktionsverhalten, die Kinetik und der Einfluss von gleichzeitig oxidierenden Metallen wie Zircaloy oder Edelstahl und deren Boride im Vordergrund. Zur Separation und Bewertung konkurrierender Reaktionspfade und Reaktionsmechanismen in diesem komplexen System wurden zuerst grundlegende und einfache Reaktionssysteme ausgewählt wie das Verhalten von B_2O_3 in trockener und feuchter Atmosphäre und die Oxidation von B_4C in trockenem Ar/O_2-Strom.

2. Zircaloy – Luft Reaktion

Die Untersuchung des Reaktionsverhaltens von Zircaloy-4 in Luft wurde mit Einzeleffekttests unter transienten und isothermen Temperaturbedingungen fortgeführt. Eingesetzt wurden für diese Tests zur Gewährleistung reproduzierbarer Oberflächenbedingungen in einer Ätzlösung aus HNO_3 und HF gebeizte und in deionisiertem Wasser gereinigte Proben. Die Tests wurden in einer Thermowaage in strömender trockener synthetischer Luft oder in Ar/O_2-Atmosphäre der Zusammensetzung 80/20 ausgeführt. Aus anlagentechnischen Gründen, Kondensation von Wasser, wurde Ar/O_2 als Ersatz für Ar/Dampf gewählt. Variierte Parameter bei den transienten und isothermen Versuchsserien waren die Aufheizgeschwindigkeit (5 – 40 K/min), Zieltemperatur (650 – 1500 °C) und die isotherme Haltezeit (0.1 – 5 h).

Im Gegensatz zu früheren reinen Ofenversuchen bieten diese Experimente, ausgeführt in einem Thermowaagesystem, den Vorteil einer simultanen und kontinuierlichen Datenaufzeichnung von Probentemperatur, Massenzunahme, Reaktionsraten und der Trennbarkeit von transienter und isothermer Versuchsphase. Aus diesen Werten lassen sich die für die Modellierung notwendigen O_2-Ströme und

Oxidschichtdicken als Funktion von Zeit und Temperatur ermitteln und über die durchgeführten metallographischen Nachuntersuchungen gegenprüfen.

2.1. Experimentelle Ergebnisse zur Zircaloy – Luft Reaktion

Sämtliche ausgeführten Lufttests zeigen im gesamten Temperaturbereich einen Einfluss des zusätzlichen Reaktionspartners Stickstoff. Dieser wird immer mit in die Reaktionsschicht eingebaut und führt zu stärkeren Schichtdefekten und höheren mechanischen Spannungen. Daraus resultieren höhere Reaktionsraten, stärkeres Schwellen der Proben und verstärkte Fragmentierungstendenzen. Besonders stark ausgeprägt sind diese Phänomene im niederen Temperaturbereich bis ca. 1100 °C. Im α / β Zweiphasenbereich wird sogar superplastisches Verhalten mit sich selbstbeschleunigenden Umsetzungsraten beobachtet. Dagegen tritt bei höheren Temperaturen T >1100 °C eine Limitierung und bei großeren Expositionszeiten eine Verringerung der Reaktionsraten auf. Dieses Verhalten lässt den Schluss zu, dass Selbstheilungsprozesse einsetzen und dem ursprünglich dramatisch durch Luftstickstoff beschleunigten Oxidationsvorgang, bezogen auf die Dampfoxidation, entgegenwirken.

Morphologie, mechanisches Verhalten und Reaktionskinetik

Zircaloy-4 Proben, die nur kurze Zeit bei niedriger Temperatur der Luftatmosphäre ausgesetzt waren, unterscheiden sich im makroskopischen Aussehen nur wenig von denjenigen, die in Dampf oder Ar/O_2-Atmosphäre oxidierten. Sie weisen ebenfalls eine glatte Oberfläche mit schwarzer Färbung auf.

Bei längeren Reaktionszeiten oder gleichbedeutend dickeren Oxidschichten, treten dramatische Unterschiede zwischen der Oxidation in Ar/O_2-Atmosphäre und in Luft auf. Bei der Reaktion in Luft bilden sich bräunlich gefärbte, sehr rauhe und schollenförmig aufgerissene Oxidschichten. Dies wird besonders bei den untersuchten Rohrproben deutlich, wie es im vorgehenden Jahresbericht dargestellt wurde. Massivproben weisen infolge geringere plastischer Verformung und dadurch geringerer aktiver Oberflächen eine feinere Oberflächenstruktur auf. Beides führt bei der Luftoxidation von Massivproben, wie in der metallographischen Auswertung sichtbar ist, zu klar abgrenzbaren Schichten nämlich von Oxid mit ZrN-Partikeln, α - Zircaloy und β-Metallmatrix (Abb. 1 rechte Spalte). Bei der Oxidation in Ar/O_2 wird

eine ähnliche Schichtfolge beobachtet (linke Spalte Abb. 1). Die feinere Analyse weist jedoch deutliche Unterschiede nach. Bei der Oxidation in Luft kommt es zur Aufwölbung der Oxidhaut an Kanten, was ein Indiz für höhere Spannungen ist. Weiterhin ist diese Oxidschicht mindestens doppelt so stark wie diejenigen auf den Vergleichsproben aus der Ar/O_2-Reaktion. Trotz dickerer Oxidschicht ist die α -Schicht dünner bei Reaktion in Luft und die Grenzfläche Oxid/Metall rauher bzw. unregelmäßiger. Weiterhin zeigt diese in Luft gebildete Oxidschicht Schollenbildung und weist Poren auf. Mit wachsender Schichtdicke verstärken sich diese Defekte. Dagegen liegt bei der Reaktion in Ar/O_2-Atmosphäre, trotz Reaktionsbedingungen im Breakaway Gebiet, eine noch intakte passivierende Oxidschicht vor. Die O_2-Aufnahme, die aus den TG-Kurven der Thermowaageversuche auswertbar ist, folgt zu dieser Zeit noch gut einem parabolischen Zeitgesetz.

Beim Übergang zu höheren Testtemperaturen (T>1100 °C) treten bei der Reaktion in Luft neue Phänomene auf. In Ar/O_2-Atmosphäre verhält sich das Zircaloy-4 wie aus der Dampfoxidation erwartet, d.h. während des Aufheizvorganges steigt die Reaktionsrate mit zunehmender Temperatur erwartungsgemäß an und fällt mit Erreichen der isothermen Reaktionstemperatur parabolisch ab. Die gebildeten Oxidschichten sind defektfrei und weisen laminare Struktur auf. Weiterhin ist der Sn-reiche Saum in der Oxidschicht sowie das Durchqueren des Breakaway-Gebietes, erkennbar an einer dünnen Oberflächenschicht, sichtbar, Oxidschicht und α -Schicht haben in etwa gleiche Dicke. In Abb. 2 sind Mikrostrukturbilder von in Luft und in Ar/O_2 reagierten Zircaloy-Stababschnitten bei 1200 °C gegenübergestellt.
Dagegen steigt bei der Zircaloy-Luft Reaktion die Reaktionsrate beim Aufheizen stärker und zu deutlich höheren Werten an. Der maximale Anstieg wird bei ca. 1150 °C beobachtet. Je nach Endtemperatur kann bereits während der Aufheizphase eine Abnahme der Reaktionsraten eintreten. Das makroskopische Aussehen der in Luft reagierten Proben ändert sich ebenfalls bei dieser Temperatur. Bei niedriger Temperatur dominiert grobe Schollenbildung und tonnenförmiges Aufreißen der Oxidschicht . Oberhalb von 1100 °C werden eine weiße, feinkörnige Oberfläche und nahezu keine makroskopisch sichtbaren Risse in der Oxidschicht festgestellt. So deutlich wie im makroskopischen Bereich sind die Unterschiede im mikroskopischen Bereich bei 1200 °C noch nicht ausgebildet. Der grobe Blick zeigt eine stark gestörte Oxidschicht mit ZrN-Einlagerungen im Bereich der Grenze Oxid zu Metall. Die

Rissdichte in der Oxidschicht nimmt jedoch in Richtung aufs Metall ab und die Reaktionsschicht (Oxid + ZrN) erscheint kompakter. Wesentlich dicker ist die Oxidschicht bei Reaktion in Luft (ca. 870 µm nach 1h) im Vergleich zu ca 217 µm in Ar/O_2. Umgekehrt ist das Verhältnis bei den α -Schichten.

Die Änderungen in der Mikrostruktur der Oxidschicht luftoxidierter Proben treten bei noch höheren isothermen Reaktionstemperaturen deutlicher hervor (Abb. 3). Im Außenbereich der Oxidschicht für die bei 1500 °C reagierte Probe sind die ähnlichen Strukturen sichtbar, wie sie für niedrigere Temperaturen beschrieben wurden. Dagegen ist etwa ab der Mitte der Oxidschicht reguläres Wachstum erkennbar, jedoch mit ZrN-Einlagerungen. Diese Mikrostruktur erinnert stark an das Bild der in Ar/O_2 bei 1200°C oxidierten Probe (Abb. 2). Auch das TG Kurven-Verhalten ist ähnlich der Oxidation in Ar/O_2, jedoch auf höherem Niveau. Die Mikrostruktur und der TG-Kurvenverlauf zeigen an, dass die gebildeten Oxidschichten wieder eine nachweisbare Schutzwirkung ausüben. Mit zunehmender Umsetzung bei hohen Temperaturen werden offenbar weniger Defekte in die Oxidschichten eingebaut oder es kommt zur Ausheilung vorhandener Defekte.

2.2. Modellentwicklung zur Beschreibung der Zircaloy – Luft Reaktion

Die Untersuchungen haben durch den Vergleich der Oxidation in Argon-Sauerstoff bzw. Luft die Bedeutung des Stickstoffs als zusätzlichen Reaktionspartner und Verursacher mikrostruktureller und letztlich mechanischer Defekte und beschleunigter Kinetik eindeutig nachgewiesen. Sämtliche metallographischen Analysen zeigen eine ähnliche Schichtmorphologie für die in Luft reagierten Proben. Das Aussehen der Schichten ist vergleichbar mit den von der Dampfoxidation her bekannten Breakaway Strukturen, für die bis heute noch keine Modellierung existiert. Auf Basis der vorhandenen experimentellen Daten zu Massenzunahme und zum aktuellem O_2-Fluss durch die Oxidschicht in Abhängigkeit von Temperatur und aktiver Schichtdicke wurden zur ersten Beschreibung und die Entwicklung eines empirischen Modells vereinfachende Annahmen gemacht. Die wesentlichen Bestandteile sind die Aufteilung der Gesamtschicht in 2 Teilschichten bzw. Zonen und die Vorgabe von verschiedenen Transportmechanismen in den Teilschichten für den O_2-Fluss. Wie der metallographisch bestimmten Schichtstruktur (Abb. 4 oberer Teil) zu entnehmen ist, liegt im äußeren Bereich der Reaktionsschicht ein stark poröses Gefüge und im

inneren Teil eine eher kompakte Schichtstruktur jedoch mit ZrN Einschlüssen vor. Für die äußere Zone wurde in dem entwickelten Cracking – Corrosion – Model ein Gastransport durch Poren und Risse angenommen. Dagegen soll bei diesem empirischen Korrosionsmodell der O_2-Transport in der dichten, inneren Teilschicht diffusionskontrolliert ablaufen. Zusätzlich wird in diesem Modell unterstellt, dass der Transportwiderstand in der äußeren Schicht verschwindend gering ist. In Abb. 4, unterer Teil, sind die gemessenen Daten für Massenzunahme und O_2-Fluss den simulierten Werten gegenübergestellt. Die resultierende Massenzunahme wird mit diesen einfachen Annahmen bei der dargestellten mittleren Reaktionstemperatur in vertretbaren Fehlergrenzen simuliert, jedoch treten für den momentanen O_2-Fluss noch deutliche Abweichungen auf. Dies ist besonders gravierend im Bereich der einsetzenden Selbstheilung, für deren Qualifizierung jedoch noch nicht die notwendigen experimentellen Daten vorhanden sind.

3. B_4C -Oxidation

In das Einzelleffekt-Programm wurden Untersuchungen und begleitende analytische Arbeiten hinsichtlich aktuell interessanter Störfall-Bedingungen zur Oxidation von B_4C und B_4C / Cr-Ni-Stahl / Zircaloy – Legierungen hinsichtlich der Produktion von Methan und anderer gasförmiger Reaktionsprodukte aufgenommen. Die Arbeiten sind in das EU-COLOSS Programm eingebunden und dienen der Vorbereitung und Auswertung von Integralversuchen (QUENCH- und CODEX- Tests) und dem in-pile PHEBUS-Versuch, mit denen die Rückwirkungen der CH_4-Bildung auf die Jodchemie untersucht werden sollen.

3.1. Versuchsausführung

Aus der Kohlenstoffchemie ist bekannt, dass abhängig von den Prozessparametern wie Druck, Gaszusammensetzung, Rohmaterial, Temperatur und Gradienten Methangas produziert werden kann. Die Absorbersubstanz B_4C reagiert stark exotherm in O_2-haltiger oder dampfhaltiger Atmosphäre. Es kommt jedoch im Gegensatz zur Oxidation von reinem Kohlenstoff noch zur Bildung von Boroxid und Borsäuren, welche in direktem Kontakt mit dem Ausgangsmaterial sind, und sofern Metalle anwesend sind, auch noch zu Bildung von Boriden. Aus diesem komplexen Szenario

ist sofort ersichtlich, dass eine Bestimmung der Reaktionsbedingungen für CH_4 und eine Aussage zur Reakionskinetik von B_4C die Kenntnis der Parameter für die Einzelreaktionen einschließlich der modelltheoretischen Beschreibung erfordert.
Aus diesen Gründen wurde das Versuchsprogramm so strukturiert, dass durch Untersuchung möglichst einfacher Substanzen allgemeingültige und übertragbare Materialdaten erzielt werden können.

Basierend auf den guten Erfahrungen aus dem Zircaloy-Luft Einzeleffektprogramm wurden zur Testausführung ein Thermowaagesystem ausgewählt. Bis jetzt wurden Messungen an B_4C, B_2O_3 und C zur Wasserdampfabgabe, Massenänderung während der Oxidation und zur Verdampfung von C- und B-Verbindungen ausgeführt [5]. Die Versuche erfolgten bisher meist in trockener Ar oder Ar/O_2-Atmosphäre.

Eine überzeugende Illustration der Komplexität der bei der Oxidation von B_4C ablaufenden Vorgänge vermittelt Abb. 5. In diesem Diagramm ist die Massenänderung einer B_4C Probe wiedergegeben in Abhängigkeit von der Temperatur und Reaktionszeit während des Aufheizen auf die Endtemperatur und in der Isothermphase. Im Gegensatz zu Versuchen mit Zircaloyproben, bei denen eine monoton steigende Gewichtszunahme entsprechend der wachsenden Oxidschicht auftritt, wechseln sich beim B_4C Phasen mit positiver und negativer Massenänderung (Zone 1 – 3) mehrfach ab. Außerdem lässt sich allein aus der Massenänderung und nur aus einem Test keine Aussage zur Reaktionsrate und zum momentan ablaufenden Teilprozess machen. Nur durch Kenntnis der Teilprozesse lässt sich dieser Kurvenverlauf interpretieren.
Die drei gekennzeichneten Zonen lassen sich durch die Dominanz der folgenden Teilprozesse erklären. In Zone 1 verdampfen flüchtige Komponenten wie Wasser. Oberhalb von 550 °C setzt deutliche Oxidation von B_4C ein und die Probe überzieht sich mit einer Oxidschicht. In Zone 3 oxidiert das Material und die Reaktionsprodukte verdampfen.
Eine genauere Beschreibung erfordert die Kenntnis des Verhaltens der Reaktionsprodukte. Dazu wurden Tests mit B_2O_3 ausgeführt. Das Verhalten von B_2O_3 in trockener Atmosphäre in Abhängigkeit von Temperatur und Zeit ist in Abb. 6 dargestellt. Unterhalb von 800 °C verdampft Boroxid nahezu nicht. Deutliche Massenverluste durch Verdampfen treten ab ca. 1000 °C auf.

Dadurch kann die B_4C-Reaktion in Ar/O_2 diesbezüglich interpretiert werden. Bei Temperaturen bis 800°C kommt es in trockener Atmosphäre zur Ausbildung passivierender Boroxidschichten und die Kinetik folgt einem parabolischen Zeitgesetz. Mit steigender Temperatur nimmt die Verdampfung von Boroxid drastisch zu und seine Verdampfungsrate wird die Oxidation stark mit beeinflussen. Erste Versuche unter Anwesenheit von Dampf deuten an, dass sich die Zeitabhängigkeiten verändern und dass die TG Signalauswertung noch komplexer wird.
Im zukünftigen Einzelleffekt-Testprogramm sind weitergehende Untersuchungen in trockener bzw. feuchter und H_2-haltiger Atmosphäre geplant. Weiterhin sollen die Thermowaagetests durch eine massenspektrometrische Analyse der Reaktionsgase und eine Modellierung der Einzelprozesse und der Reaktionspfade ergänzt werden.

4. Folgerungen zur Luftoxidation und B_4C Oxidation

Die zur Zircaloy-4 Luft-Reaktion ausgeführten Arbeiten haben durch den Vergleich mit der Oxidation in Argon-Sauerstoff die Bedeutung des Stickstoffs als zusätzlicher Reaktionspartner und Verursacher mikrostruktureller und letztlich mechanischer Defekte und der in Luft beschleunigten Kinetik eindeutig nachgewiesen. Die Versuche bei höheren Temperaturen zeigen, dass Selbstheilungstendenzen auftreten und dass einzelne Reaktionsphänome in bestimmten Temperaturbereichen dominieren. Schichtbildung, ZrN-Einlagerungen und O_2-Transport tragen zu der ermittelten komplexen Kinetik der Zircaloy-4 / Luft – Reaktion bei.
Eine Fortführung dieses Programms unter Einbindung analytischer Methoden ist jedoch aus folgenden Gründen notwendig: Im experimentellen Bereich sind zusätzlich zu den Daten aus Versuchen mit idealisierten Bedingungen Informationen zum Verhalten in realitätsbezogenen Atmosphären erforderlich. Eine phänomenologische Modellierung ist zur Beschreibung der Einzelleffekttests notwendig und unablässig für die Auswertung von Integraltests und insbesondere die Übertragung auf das Brennelementverhalten in Störfallszenarien.
Die Untersuchungen zur B_4C-Oxidation wurden neu in das Programm für Einzelleffekttests aufgenommen. Die bisher erarbeiteten Ergebnisse wurden in die Datenbasis des COLOSS-Teams eingebracht und zusammen mit den Versuchsdaten der anderen Partner bewertet und für die Ausführung von Integraltests bereitgestellt. Die bisherigen Ergebnisse weisen darauf hin, dass komplexere

Zusammenhänge zwischen den auftretenden Phänomenen bei der B_4C-Oxidation hinsichtlich Reaktionskinetik und CH_4-Bildung existieren, als ursprünglich erwartet wurde.. Dies deutet an, dass für die Interpretation der Integralversuche eine gute Kenntnis der Einzelvorgänge einschließlich ihrer modellmäßigen Beschreibung erforderlich ist.

5. Literatur

[1] W. Krauss, G. Schanz
Zircaloy/air oxidation kinetics: current experiments towards future demands.
4th International QUENCH Workshop, Karlsruhe, Oct. 6-8, 1998

[2] W. Krauss, G. Schanz
Reaktionsverhalten von Zircaloy-4 in Luft, In: B. Mühl (Hrsg.), Projekt Nukleare Sicherheitsforschung, Jahresbericht 1998; FZKA 6300, Sept.1999, 32.21.08 IV, S. 460-474.

[3] W. Krauss, G. Schanz,
Comparative studies on the Zry-4/air and Zry-4/O_2 reaction behaviour towards air ingress scenarios. 5th International QUENCH Workshop, Karlsruhe, Oct. 19-21, 1999; Forschungszentrum Karlsruhe, Interner Bericht, Nov. 1999.

[4] W. Krauss, H. Steiner, G.Schanz,
Separate effect tests on Zry-4/air and Zry-4/O_2 reaction towards air ingress scenarios, including first modelling work.
6th Internatnational QUENCH Workshop, Karlsruhe, Oct 10-12, 2000,
Forschungszentrum Karlsruhe, Interner Bericht, Nov. 2000.

[5] W. Krauss, G. Schanz,
Thermogravimetric analyses towards B_4C oxidation mechanisms and kinetics.
6th Internatnational QUENCH Workshop, Karlsruhe, Oct 10-12, 2000
Forschungszentrum Karlsruhe, Interner Bericht, Nov. 2000.

Ar/O_2	Air
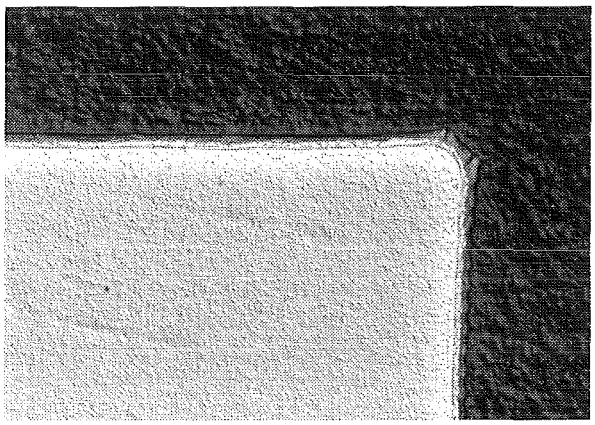	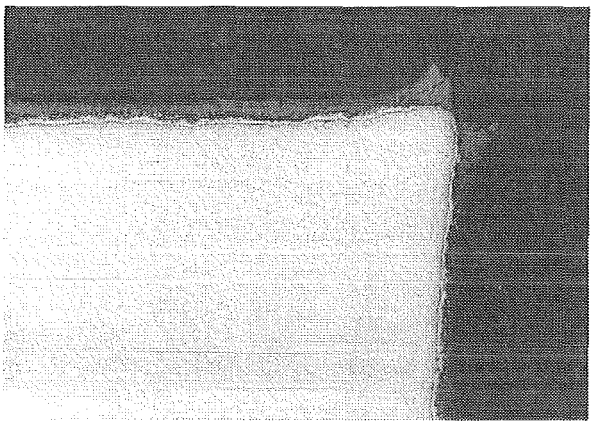
P2 O2 900 50 Magn. 50x	P7 A 900 50 Magn. 50x
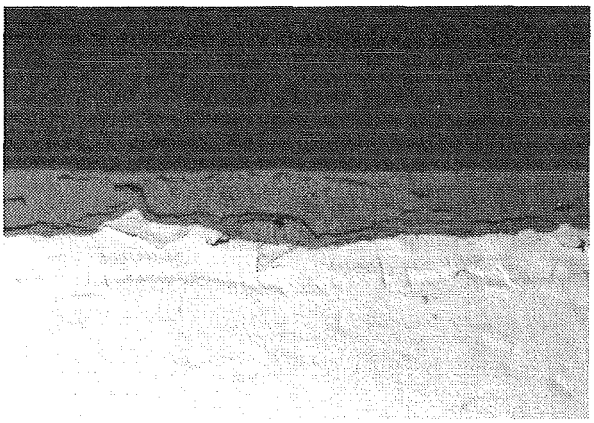	
P2 O2 900 500 Magn. 500x	P7 A 900 500 Magn. 500x
ZrO_2 scale thickness 26 µm α-Phase 20 µm	ZrO_2 scale thickness 56 µm α-Phase 17 µm ZrN particles embedded in ZrO_2

Abb. 1: Vergleich der Reaktion von Zircaloy-4 in Ar/O_2 Atmosphäre und in Luft bei einer isothermen Reaktionstemperatur von 900 °C und 1h. Die Aufheizrate betrug 20 K/min.

Probenform: Stababschnitt

Ar/O_2 | **Air**

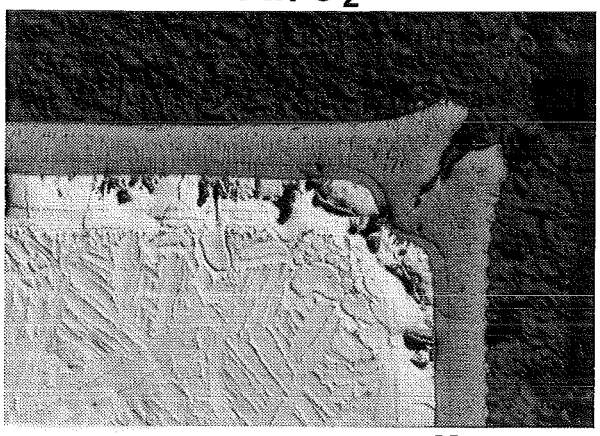

P3 O2 1200 50 Magn. 50x

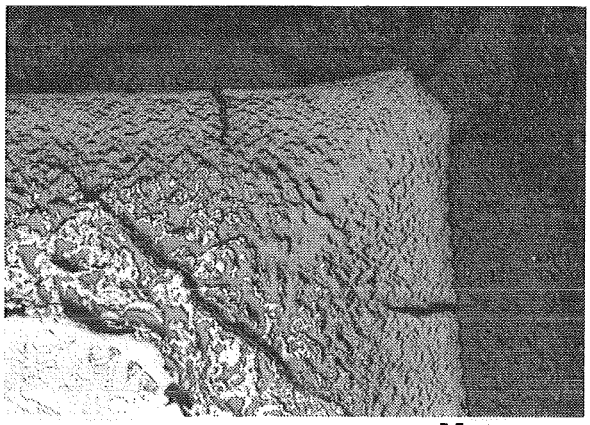

P9 O2 1200 50 Magn. 50x

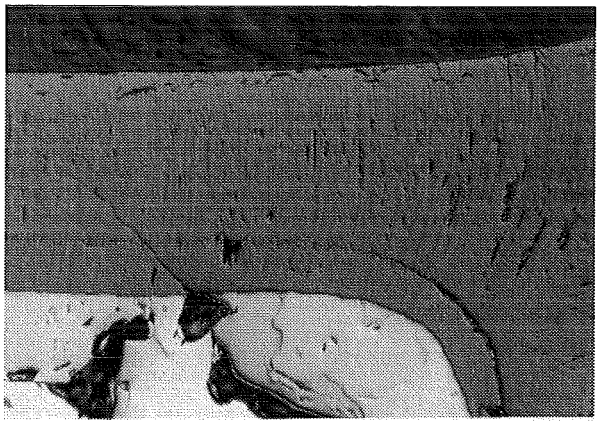

P3 O2 1200 200 Magn. 200x

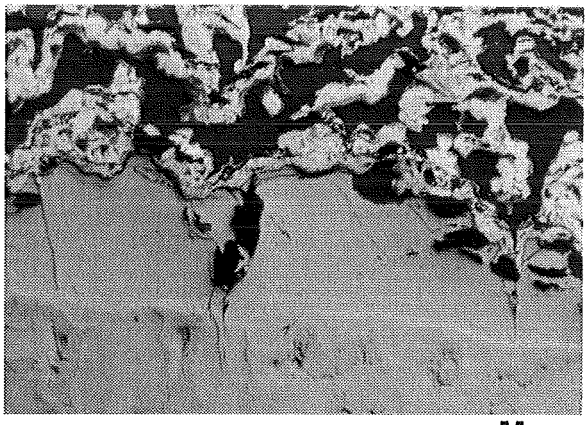

P9 O2 1200 200 Magn. 200x

ZrO_2 scale thickness 217 µm
α-Phase 222 µm

ZrO_2 scale almost regularly grown

Thin ZrO_2 layer on surface with breakaway structure

ZrO_2 scale thickness 870 µm
α-Phase 110 µm
ZrN particles embedded in ZrO_2

Abb. 2: Vergleich der Reaktion von Zircaloy-4 in Ar/O_2 Atmosphäre und in Luft bei einer isothermen Reaktionstemperatur von 1200 °C und 1h. Die Aufheizrate betrug 20 K/min.

Probenform: Stababschnitt

Air

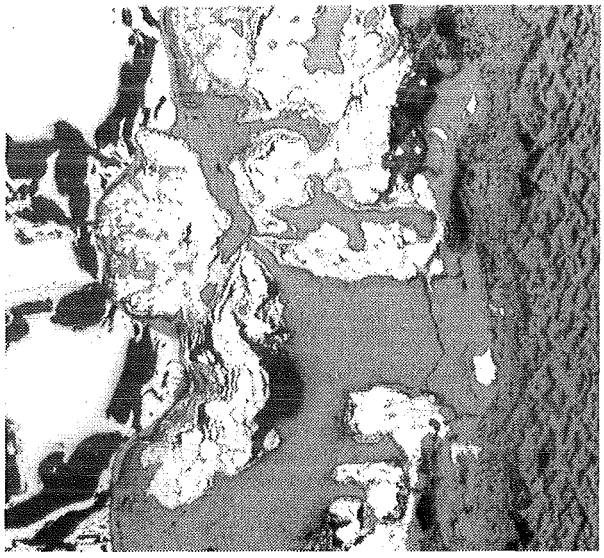

Left: **Metallic matrix**

Centre: **ZrO_2 sub-layer consisting of regularly grown oxide and ZrN grains**

Right: **Porous ZrO_2 layer similar to breakaway scales formed in steam or Ar/O_2**

Scale thickness: 1550 µm

Magn. 50x

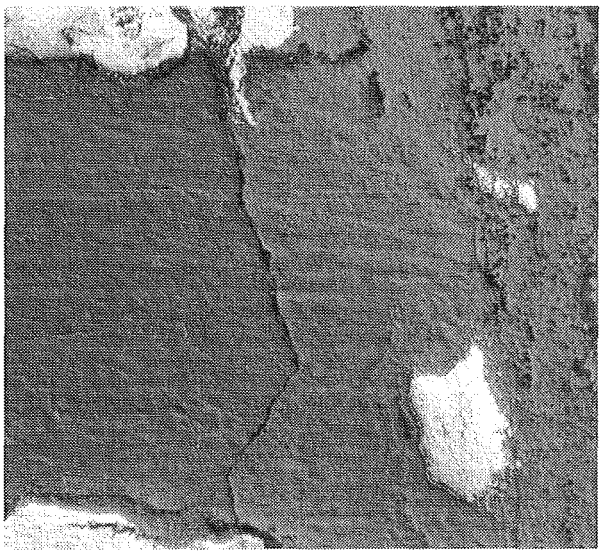

Detail from centre of overview

Change in morphology from breakaway structure (right) to regularly formed ZrO_2 (left)

Magn. 200x

Abb. 3: Zircaloy-4 – Luft Reaktion unter isothermen Bedingungen bei 1500 °C für 60 min nach transientem Aufheizen mit 20 K/min. Probenform: Stababschnitt

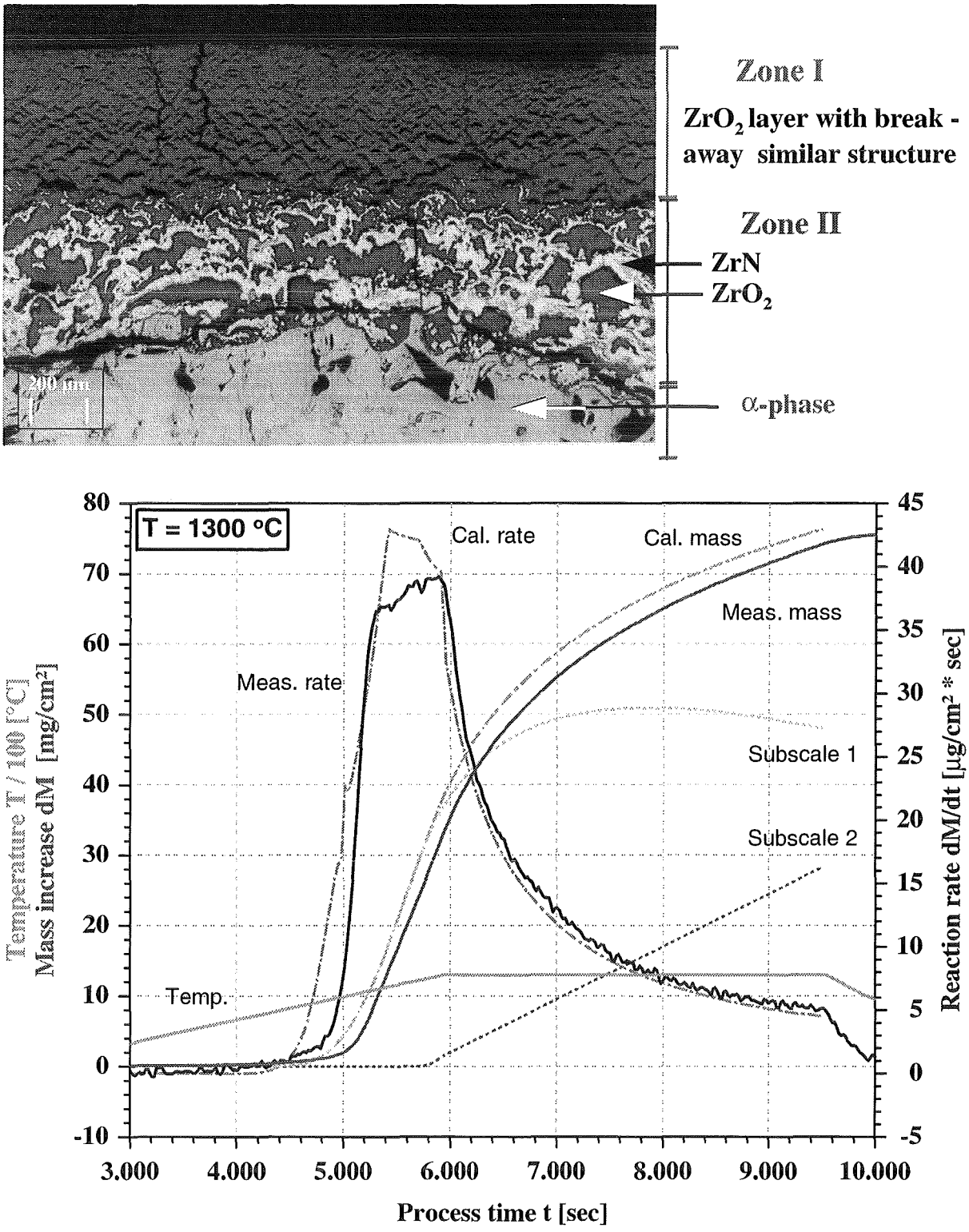

Abb. 4: Vergleich der experimentellen und modelltheoretischen Oxidationswerte (Massenzunahme und Reaktionsrate) von Zircaloy-4 in Luft bei 1300 °C nach transienter Aufheizung mit 20 K/min. Für die Modellierung wurde das Scale Cracking Model entwickelt. Es teilt die Oxidschicht in 2 Teilschichten mit verschiedenen Transporteigenschaften auf. Die Abgrenzung erfolgt dabei, wie in der Mikrostruktur oberhalb skizziert.

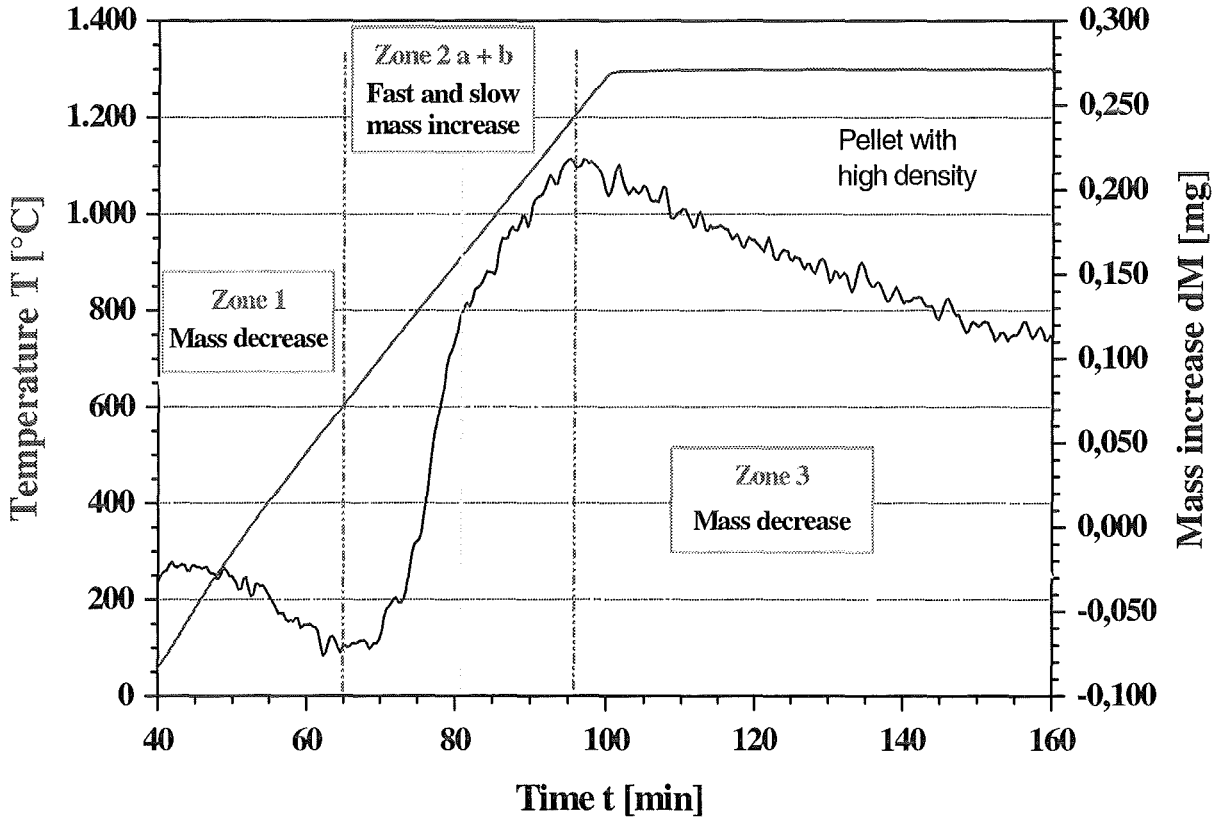

Abb. 5: Oxidation von B_4C in trockener Ar/O_2 Atmosphäre Dargestellt ist die Massenänderung der Probe in Abhängigkeit von der Temperatur während der Aufheiz- und Isothermphase. Der Massenverlauf weist auf die Konkurrenz temperaturabhängiger Reaktionsphänomene hin.

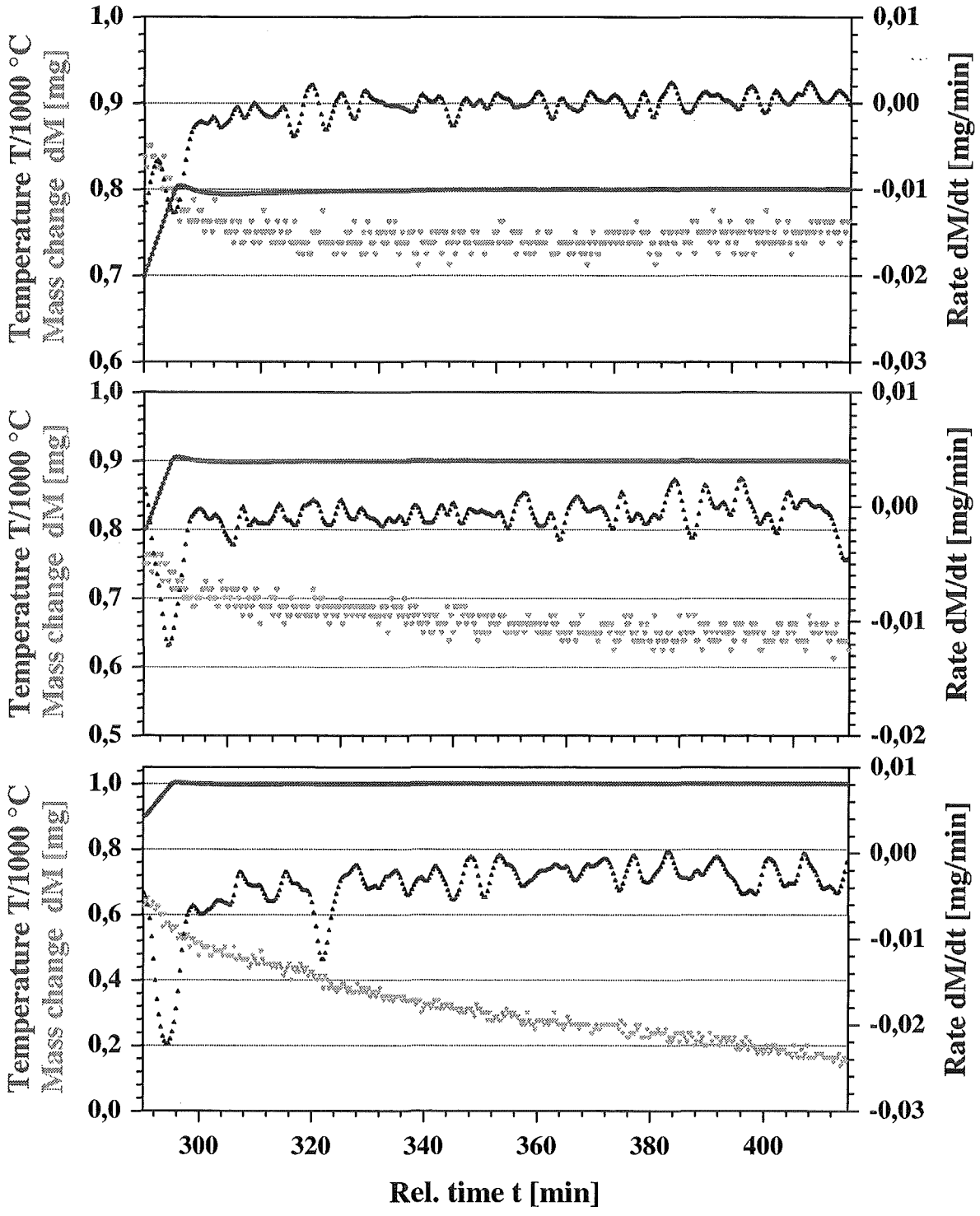

Abb. 6: Verdampfungsverhalten (Massenabnahme und Verdampfungsrate) von B_2O_3 in trockener Ar Atmosphäre bei 800, 900 und 1000 °C aus einem Tiegel mit Querschnitt 1.11 cm².

VI. Severe Accident Investigations

(W. Hering, Ch. Homann, W. Sengpiel, D. Struwe, IRS, Ch. Messainguiral, CEA)

Abstract

At the Forschungszentrum Karlsruhe (FZK) the Institute for Reactor Safety (IRS) performs accident analyses with severe core damage code systems such as SCDAP/RELAP5, ICARE2 and the thermal-hydraulic code RELAP5.

Main topic is the support of the QUENCH experiments at FZK/IMF. All test were supported by pre- and post test calculations, in this way enhancing effectively understanding of the experiment and separation of physical and facility based effects.

Besides reactor analyses for the 5th European Framework Program code validation are ongoing on and code improvements were implemented into SCDAP/RELAP5.

Zusammenfassung

Im Institut für Reaktorsicherheit (IRS) des Forschungszentrums Karlsruhe (FZK) werden Unfallanalysen mit den Kernschmelzcodes SCDAP/RELAP5 und ICARE2 sowie mit dem Thermohydraulik Programm RELAP5 durchgeführt. Der Schwerpunkt der Arbeiten liegt in der Unterstützung der QUENCH Versuche im FZK/IMF. Für alle Versuche werden Vorausrechnungen und Versuchsanalysen durchgeführt, um mit einem optimal angepassten Anlagenmodell ein verbessertes Verständnis der Experiments und die Separation von Anlagen- und physikalischen Effekten zu erreichen.

Neben Reaktoranalyen im Rahmen des 5. EU Rahmenprogramms zur Reaktorsicherheit wurden die Codes validiert und Modell-Verbesserungen eingeführt.

1.1 Accident analyses with SCDAP/RELAP5

The results of the accident analyses with SCDAP/RELAP5 /1/ for the European Pressurised Water Reactor (EPR) were documented in two reports /2/, /3/. The input decks are now used within the EU 5th Framework Program COLOSS for code comparison among severe accident codes. Also plant calculations are ongoing as part of the EVITA program to contribute to ASTEC code validation.

1.2 Code validation and improvement

For severe fuel damage best estimate analyses SCDAP/RELAP5 (S/R5) mod 3.2 /1/ and ICARE2 V3 /4/ is used, mainly for validation and support of QUENCH experiments. S/R5 mod 3.3. has been released end of 2000, however without any FZK improvements, formerly transmitted to INEEL. So the ongoing activities have to rely on S/R5 mod 3.2.irs.

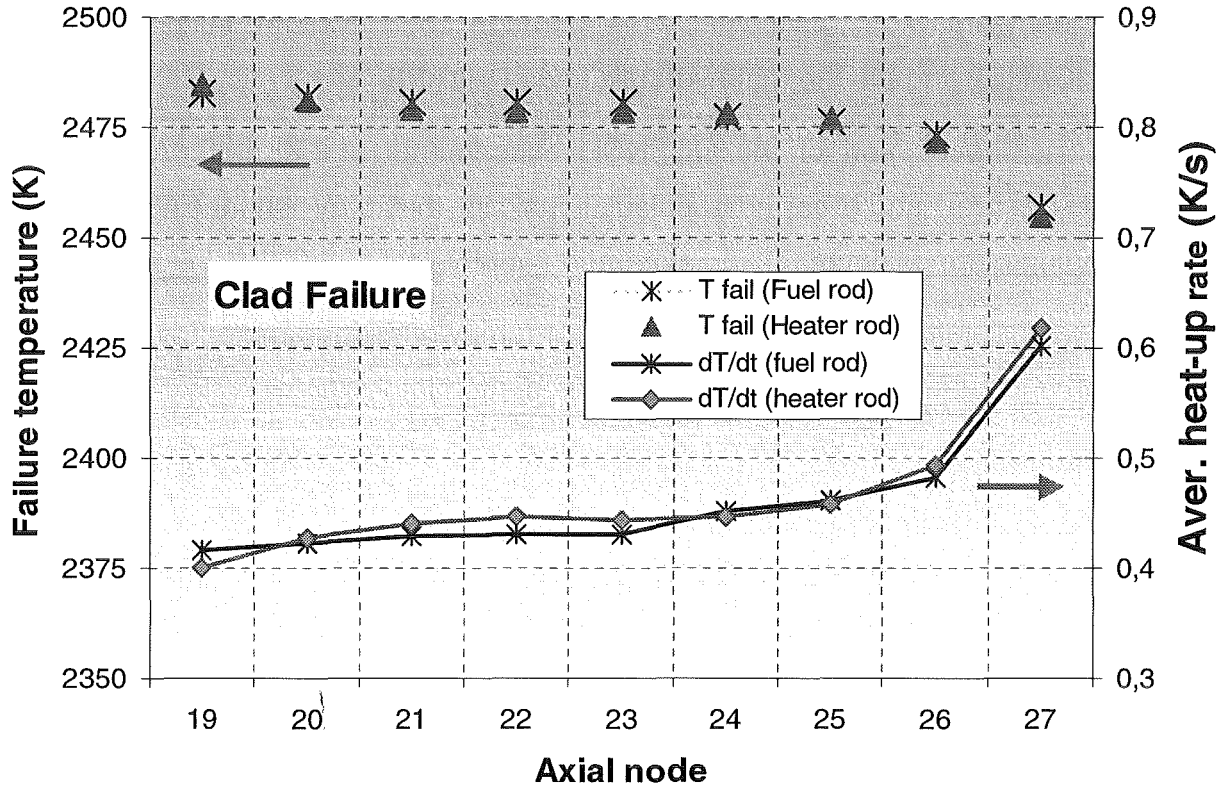

Figure 1 Failure temperature based on the average heat-up rate for various elevations in the QUENCH-01 experiment

In the present modelling in S/R5 one user defined parameter remains for the early core melt phase, the clad failure criterion, which significantly controls the hydrogen release and the character of melts (metallic/oxidic) at release. So far no general value was found for either integral experiment or reactor conditions.

To improve the modelling the oxidation history of a clad segment is calculated and compared to the results of oven experiments at FZK/IMF. This work is still ongoing, a first result for QUENCH-01 /5/ is shown in Figure 1. The main result is that each node has its individual clad failure depending on the heat-up history, which should cover all different environments from single rod to reactor size. To achieve this, validation has to include CORA, QUENCH, and Phebus FP experiments.

1.3 Activities within the CAMP agreement

The IRS participation on the international Code Assessment and Maintenance Program (CAMP) of the USNRC is mainly focused on the validation of the reflood thermal hydraulics. For this purpose different single rod and bundle experiments were analysed, e.g. the Single Rod tests (FZK QUENCH rig), the NEPTUN tests (PSI), the FLECHT and LOFT tests (INEEL) as well as the PKL tests (Siemens/KWU).

Besides the codes RELAP5/MOD3.1 and the RELAP5/MOD3.2.2γ were improved at FZK /6/ to extend the application of the RELAP5 to most relevant reflood situations, i.e. low pressure scenarios. The heat transfer mechanisms for transition boiling are described by the improved semi-mechanistic Chen-model instead of the empirical Weisman correlation /7/, improved at PSI and used in the original RELAP5 versions mentioned above. In the improved Chen correlation no additional information as the distance from the quench front is needed, as it is the case in the original RELAP5 correlation.

The modified RELAP5-code versions were used to re-evaluate different integral tests like LOFT LP-LB-1 and PKL-BII5. The results of these post-test analysis showed in general a good agreement with the measured cladding temperature, especially in the transition boiling region. The deviations of calculated temperatures with respect to experimental values at temperatures below 800 K are due to the heat transfer to dispersed droplets, modelled in the same way in the original and the FZK programme versions. As can be seen in Figure 2 the quench temperature predicted by improved RELAP5-version (322G+FZK) is closer to average experimental value of about 700 K, while the original Weisman correlation (322) predicts a lower quench temperature of around 600 K. This trend is encountered at all core elevations. The heat transfer coefficients predicted by the Weisman (322) and by the improved Chen correlation (322+FZK) are quite different from another, especially near the quench front (see Figure 3).

In sum the PSI-reflood model implemented in RELAP5/MOD3.2.2 represents an essential progress compared to the reflood model of earlier code versions. Besides the transition boiling heat transfer prediction can be improved replacing the empiric Weisman correlation by the FZK transition boiling model. The improved RELAP5 code was also successfully applied to perform plant calculations including reflood scenarios /5/.

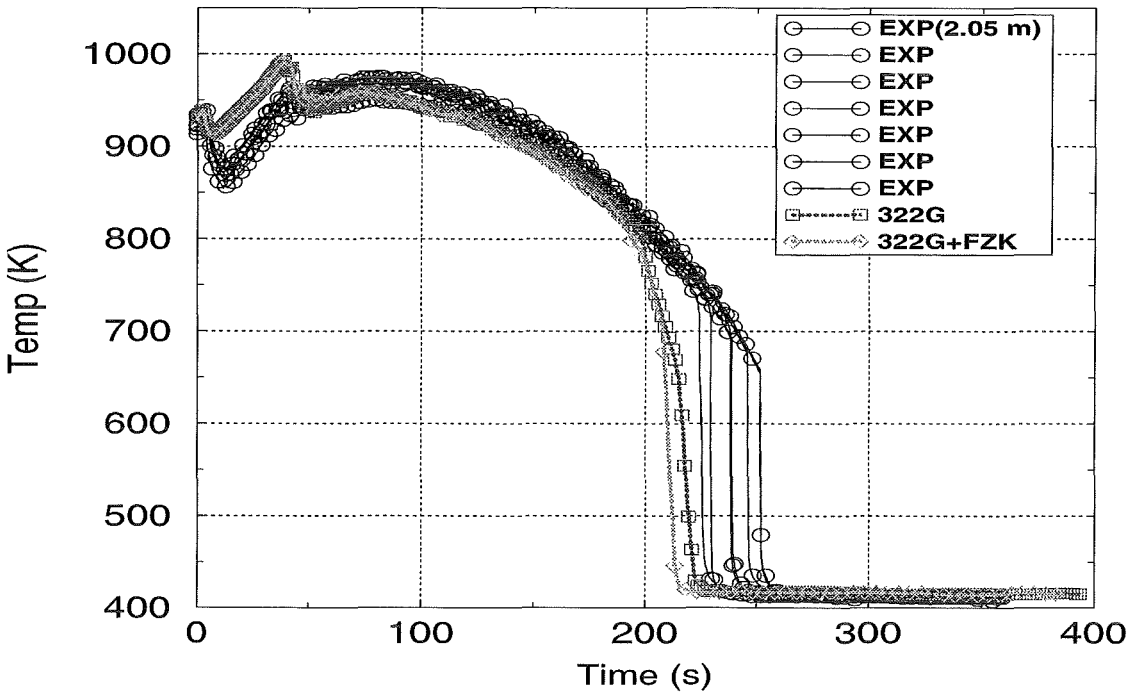

Figure 2 Comparison of calculated and measured cladding temperatures of test PKL-IIB5 at elevation 2.05 m

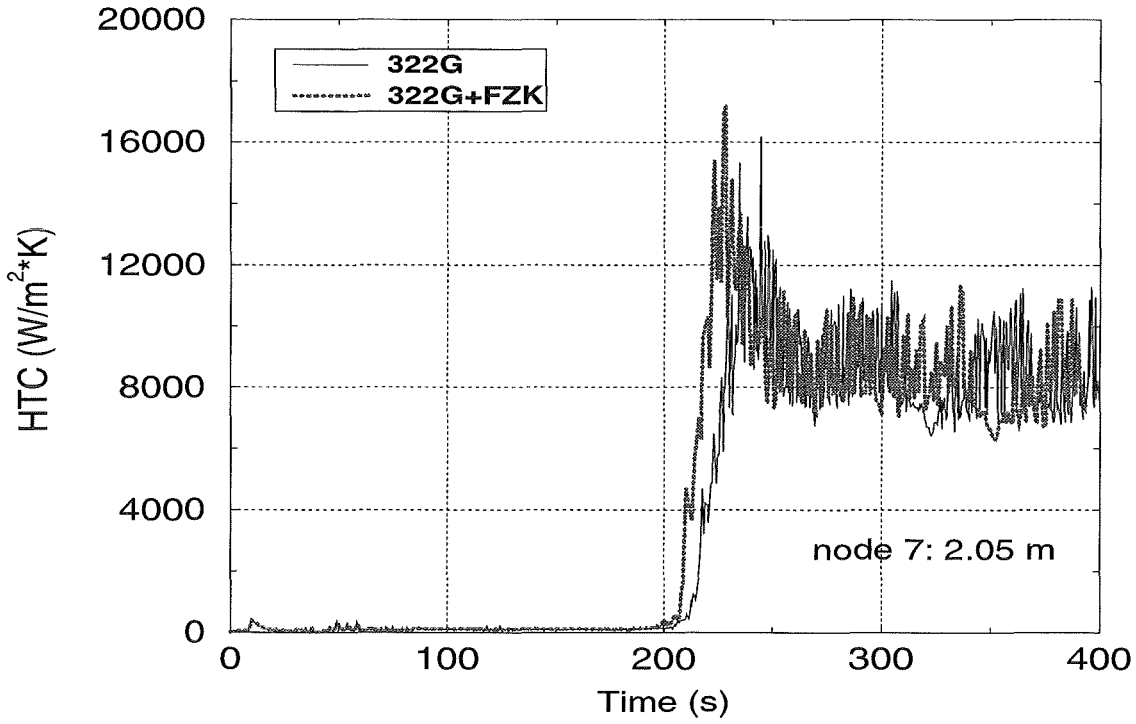

Figure 3 Comparison of calculated heat transfer coefficient for the PKL IIB5 test

1.4 Support of QUENCH experiments

The QUENCH programme at FZK aims at investigating the physico-chemical processes during quenching of overheated rod bundles with water or fast cool-down with steam. At IRS these experiments are supported by numerical analyses before and after the tests, mainly with S/R5 mod 3.2.

1.4.1 QUENCH-05

The test has been run similarly to test QUENCH-04, but the fuel rod claddings have been pre-oxidised up to about 160 µm oxide layer thickness. Important test parameters have been derived from S/R5 calculations. In post-test calculations a comparable agreement between experimental and calculated temperatures and hydrogen production has been obtained as for previous experiments.

1.4.2 QUENCH-06 (ISP-45)

In 2000 OECD/NEA/CSNI decided to accept the experiment QUENCH-06 as the International Standard Problem No. 45. Test QUENCH-06 is similar to test QUENCH-05, but the bundle is quenched with water instead of being cooled down with steam. Finally 22 participants from 15 nations intended to deliver 25 results of 10 different severe core damage codes up to June 11. 2001.

As in the previous ISP cases which were hosted by FZK, the analytical task should be managed by GRS. Due to budget problems GRS was not able to perform this task so that the ISP-45 is the first ISP which runs completely in FZK responsibility. At IRS the experimental task is supported by data analyses and analysts support via E-mail and Web-site information. The ISP-45 initial- and boundary conditions are documented in /10/.

1.4.3 QUENCH-07

This test is supported in the COLOSS project of the 5th EU framework program and scheduled for mid 2001. It was intended to be run similarly to Phebus test FPT3, dedicated to investigate degradation of B_4C absorber rods and production of gaseous reaction products, especially of H_2 and CH_4. For that purpose the steam mass flow should be reduced so that steam starvation occurs at the end of the heated zone and maximum temperatures of about 2000 K are reached for about 20 min, before the bundle is cooled down with steam.

Pre-test calculations (without absorber rod model) showed that, when the steam mass flow is small, the electrical power must be reduced and the argon flow must be increased to avoid premature clad melting.

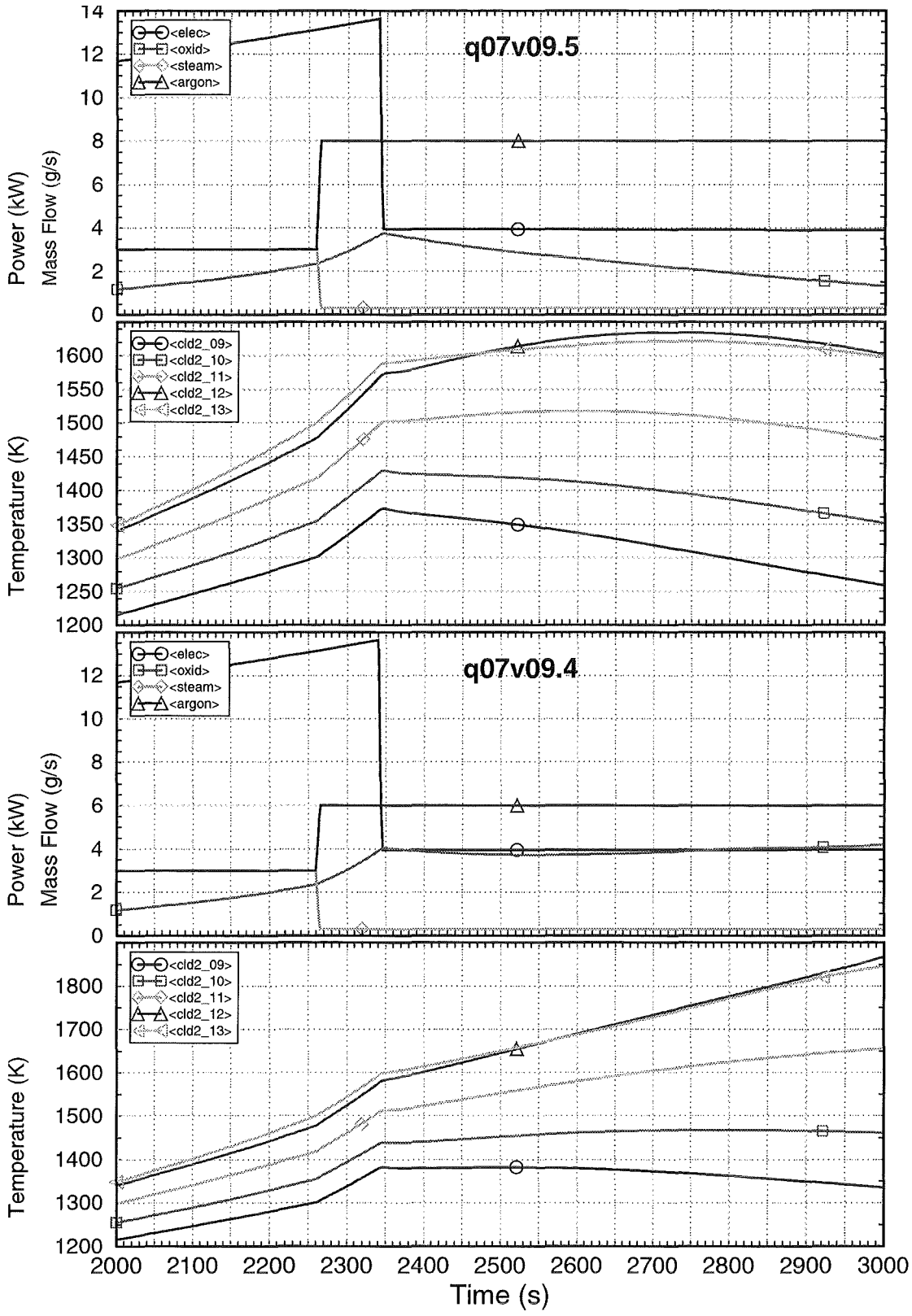

Figure 4 Two calculations showing influence of convective heat sink, in both cases the steam is reduced from 3 g/s to 0.3 g/s and the Argon mass flow rate has been increased to 8 g/s (top), and 6 g/s (bottom).

Due to the low steam mass flow the bundle reacts sensitively to changes of physical parameters: the two cases shown in Figure 4 differ only by the argon mass flow rate. For a value of 8 g/s the bundle temperatures in the upper half of the heated zone have a maximum somewhat above 1600 K, whereas temperatures increase steadily for an argon mass flow rate of 6 g/s, which would lead to clad melting if the calculation were continued. Therefore another test conduct is being investigated.

In the frame of the COLOSS programme a cooperation with PSI was begun for calculations concerning this test and to improve the modelling of S/R5, especially of B_4C absorber rods.

1.4.4 Application of RELAP5 to QUENCH experiments

To compare S/R5 and RELAP5 mod 3.2.γ (stand alone) calculations for QUENCH-04 were made as shown in Figure 5. The modelling of the fuel rod bundle is different in the two programmes. So in RELAP5 heat conduction in the fuel rod simulators is only considered in the radial direction, and the complicated sequence of materials in the rods cannot be modelled adequately.

Despite this restriction the results (Figure 5) show that the modelling of oxidation and hence hydrogen production are different: so in S/R5 a threshold temperature is assumed where oxidation calculation begins. As can be seen clearly in Figure 4 the energy release by oxidation heats up the bundle faster than expected.

The RELAP5 oxidation model is only validated for design basis scenarios in which the additional energy release is only considered conservatively, so that an upper bound is sufficient. When temperatures exceed 1200 K conservative approach becomes rather unrealistic.

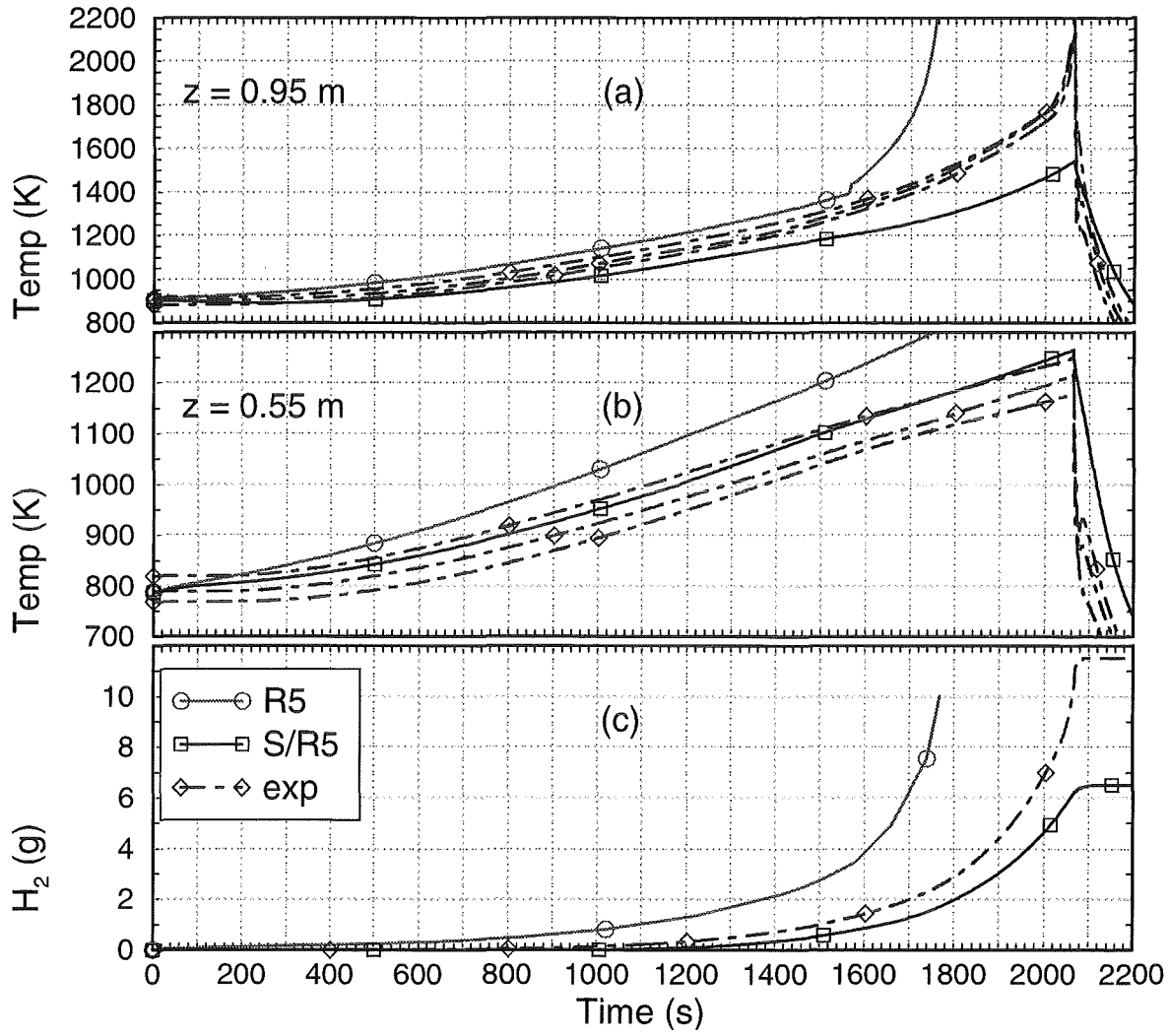

Figure 5 Comparison of RELAP5 (solid lines) with S/R5 results for QUENCH-04: cladding temperatures at 0,95 m (a) and at 0,55 m (b), and hydrogen release from clad oxidation (c).

1.4.5 Application of ICARE2

Within the CEA-FZK co-operation calculations have been made with ICARE2-V3 mod 1.0 for the QUENCH-04 experiment. The axial temperature profiles along the whole length of the fuel rod bundle given in Figure 6 are comparable to those obtained with S/R5.

Besides the ICARE calculations show that a finer nodalisation than used normally (0.1 m long meshes in the heated zone) is necessary to improve the agreement between measured and calculated values, especially in the region of high temperatures at the upper end of the heated zone. Especially in reflood scenarios a finer mesh is required as described in /9/.

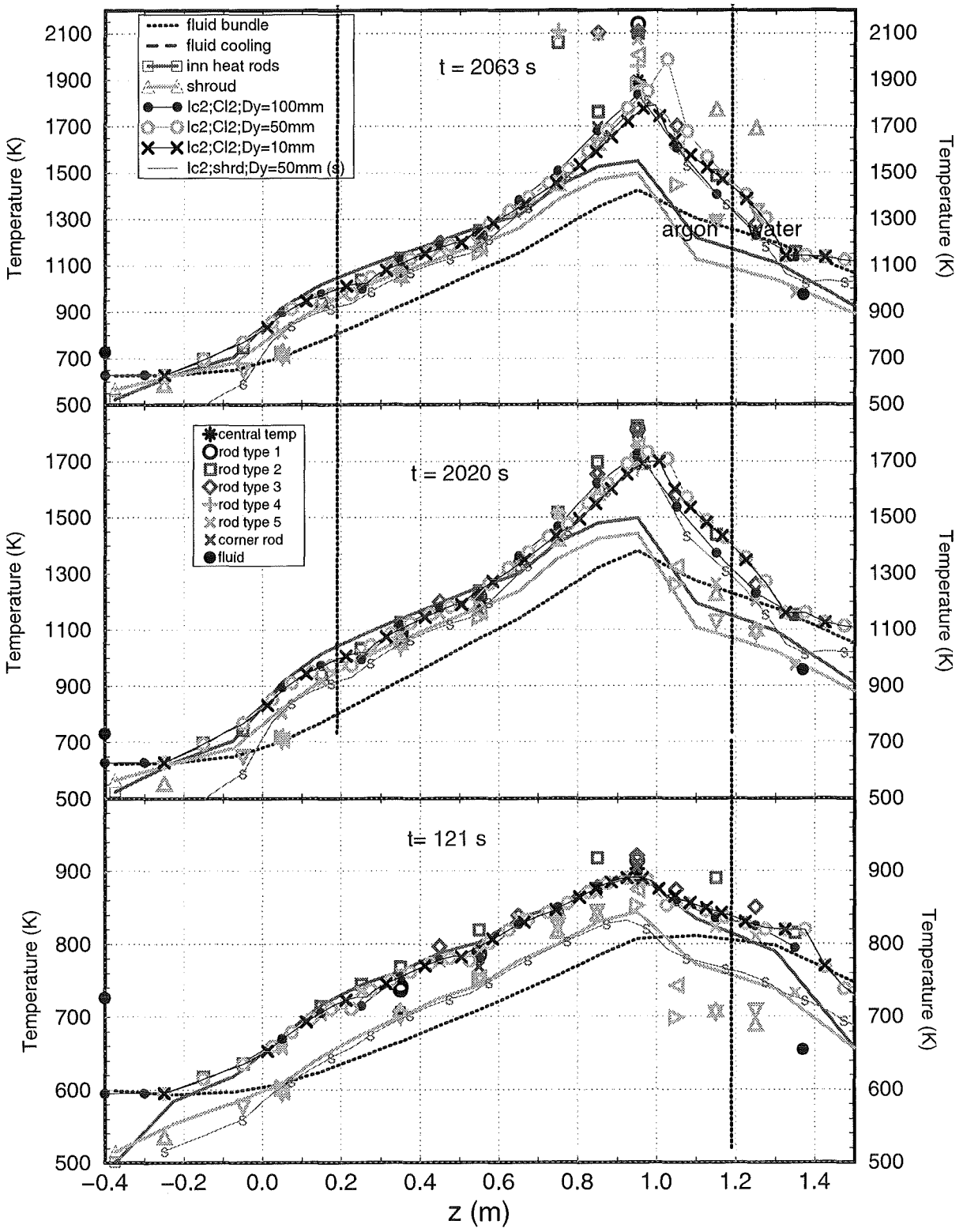

Figure 6 Comparison of calculated temperatures from SCDAP/RELAP5 and ICRE2V3 with measured values for QUENCH-04

1.4.6 Extended axial nodalisation

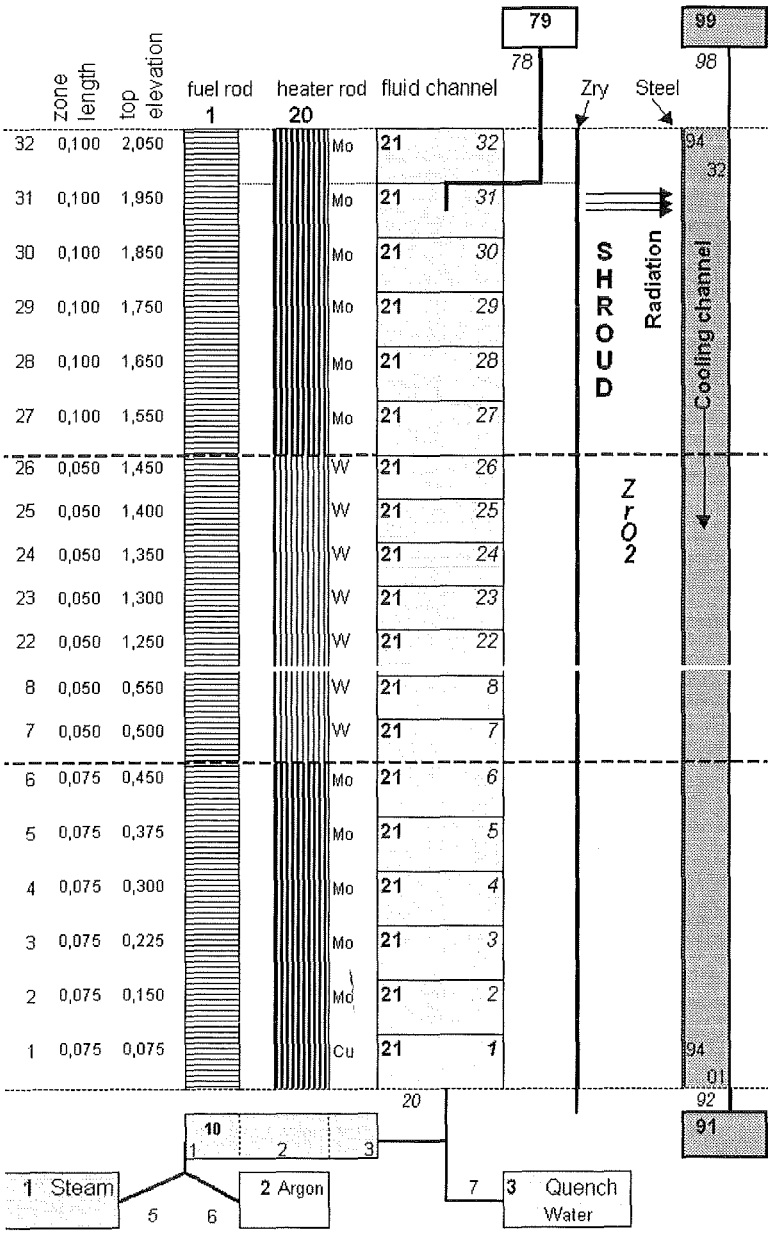

Figure 7 Refined axial nodalisation for QUENCH calculations

For typical reflood conditions it was found /9/ that for axial zone lengths below 3" (0.075m) no significant differences in the results were predicted by the thermal-hydraulic code COBRA. In current CORA and QUENCH analyses the typical zone length is 0.10 m. A refinement of the axial zones was limited by the code restriction to a maximum of 20 axial zones. During work for further axial refinement, several code errors were removed.

With the new S/R5 capabilities, a new model of the facility was developed leading to a refined axial nodalisation scheme shown in Figure 7. The radial heat losses out of the bundle are modeled by appropriate assumptions of the cooling channel. For the new input deck, the initial axial subdivisions of the three bundle zones were doubled.

This leads to a mesh length of 0.075 m in the lower electrode zone and of 0.05 m in the heated section. As an example S/R5 results for QUENCH-01 pre-oxidation phase are shown in Figure 8 in comparison with results of the coarse nodalisation of the whole facility. The reflood phase also show some improvements with respect to the quench time measured in the experiment, however, there is still some deviation which cannot explained easily. One possible cause may be that the dedicated PSI reflood model is not activated for SCDAP components as foreseen. This explains the different heat

transfer values calculated for S/R5 components and RELAP5 heat structures in the same RELAP5 volume.

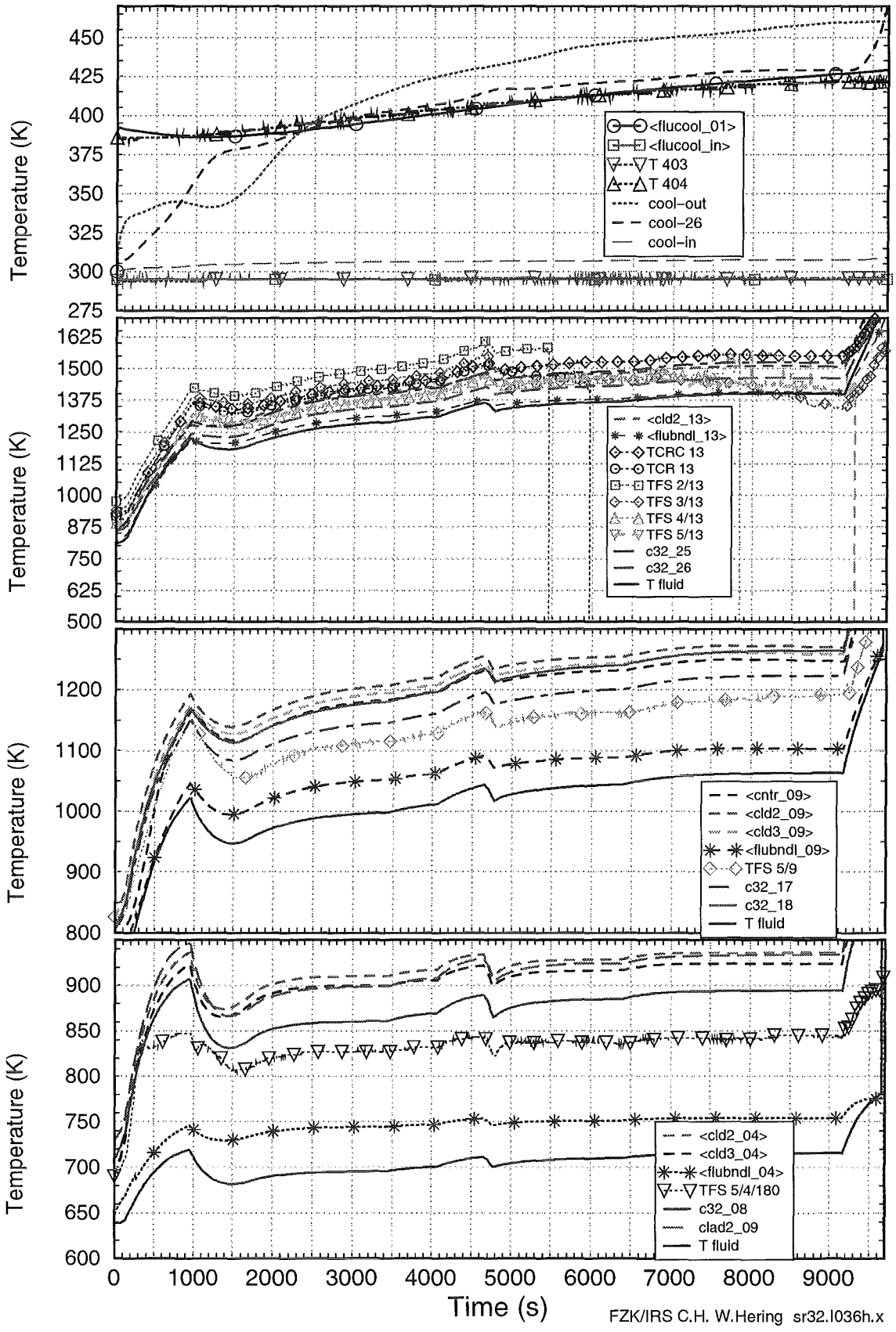

Figure 8 Results of two calculations with 16 and 32 axial nodes compared to the experimental results of QUENCH-01

1.5 Literature

/1/ The SCDAP/RELAP5 Development Team: SCDAP/RELAP5/MOD 3.2 Code Manual, NUREG/CR-6150, INEL-96/0422, Idaho Fall, Idaho, USA,1997.

/2/ Hering W., Messainguiral Ch., Sengpiel W., Investigation of the Melt-down Behaviour of Massive Radial Core Enclosures during LWR accidents, FZKA-6315, November 2000.

/3/ Hering W., Investigation of In-vessel Core Degradation for the European Pressurised Water Reactor with SCDAP/RELAP5 mod 3.2, FZKA-6567, März 2001.

/4/ Gonzales R., Chatelard D., Jacq F., ICARE2 Version 2 Mod 1, Description of physical models, Note Technique DRS/SEMAR 92/43, 1996.

/5/ Hering, W.: Improvement of the SCDAP/RELAP5 Simulator Model with respect to FZK Facilities, FZKA Report 6566, published 2001.

/6/ Elias E., Sanchez V.H., Hering V.; Development and validation of a transition boiling model for RELAP5/MOD3 reflood simulations, NEDEA 183 177-332 (1998).

/7/ Sanchez, V.H., Homann, Ch.: Validation of the improved RELAP5 transition boiling model against the full-length FLECHT-SEASET reflood test. FZKA-..... in preparation. 1998.

/8/ Sanchez V.H., "Validation of the Reflood Model Implemented in the Code RELAP5/MOD3.2.2□ the Integral Test LOFT-LP-LB-1, FZKA Report 6426, 2001.

/9/ C. Frepoli, L.E. Hochreiter, J. Mahaffy, F.B. Cheung, A noding sensitivity analysis using COBRA-TF and the effect of spacer grids during core reflood, ICONE-8711, Proceedings of ICONE-8, April 2-6, 2000, Baltimore, MD, USA.

/10/ Hering W., Homann Ch., Miassoedov A., Steinbrück M., Specification of the International Standard Problem ISP-45 (QUENCH-06), Internal Report 3355, OECD/NEA/ CSNI/R(2001)1.

32.21.09 Entwicklung von Methoden zur Abschätzung und Minimierung der radiologischen Folgen von Reaktorunfällen

(G. Benz*, J. Ehrhardt, F. Fischer, Ch. Haller*, I. Hasemann, E. Hesselschwerdt, C. Landman, A. Lorenz, J. Päsler-Sauer, M. Rafat*, W. Raskob*, T. Schichtel, A. Steidlinger, IKET)

Abstract

Work on the real-time on-line decision support system RODOS for off-site emergency management after nuclear accidents has concentrated on the preparation of the operational version PV 4.0; it has been released by the end of 2000. The hardware and software components of the RODOS system for operational use at a central place in Germany were installed, configured and tested at FZK together with the on-line connections to the German Weather Service and to the radiological and meteorological data providers from the Federal States and the Federal Government. In parallel, the installation of the RODOS system in emergency centres of West and East European countries continued with support from the European Commission. Training courses for RODOS operators have been developed and performed on the national and European level.

Zusammenfassung

Die Arbeiten zum Echtzeit- und On-line-Entscheidungshilfesystems RODOS für den Notfallschutz nach kerntechnischen Unfällen konzentrierten sich auf die Fertigstellung der operationellen Version PV 4.0; sie wurde Ende 2000 fertiggestellt. Die Hardware- und Softwarekomponenten des RODOS Systems zum operationellen Betrieb an zentraler Stelle in der Bundesrepublik Deutschland wurden im FZK installiert, konfiguriert und zusammen mit den Datenverbindungen zum Deutschen Wetterdienst und den Lieferanten radiologischer und meteorologischer Daten des Bundes und der Länder getestet. Parallel wurden die Installationen des RODOS Systems in Notfallschutzzentralen ost- und westeuropäischer Länder mit Unterstützung der europäischen Kommission fortgesetzt. Es wurden Trainingskurse für RODOS Operateure entwickelt und sowohl national als auch auf europäischer Ebene durchgeführt.

---

*Fa. D.T.I., Dr. Trippe Ingenieurgesellschaft m.b.H., Karlsruhe

Rechnergestützte Entscheidungshilfeinstrumentarien für den Notfallschutz (RODOS)

1 Entwicklungsarbeiten

Basierend auf den Erfahrungen der Benutzer und unter Einbeziehung der Ergebnisse der F&E-Arbeiten des 4. Rahmenprogramms der Europäischen Kommission wurde die operationelle Version PV 4.0 des Entscheidungshilfesystems RODOS für das Notfallschutzmanagement nach kerntechnischen Unfällen entwickelt. Sie steht ab Dezember 2000 zum Einsatz in Notfallschutzzentralen europäischer Länder zur Verfügung. Sie enthält Verbesserungen und Erweiterungen des Betriebsabwicklungssystems (Benutzerschnittstelle, Dateninitialisierung, Integrations- und Graphiktools, Messdatenerfassungs- und Real-time Datenbankverwaltung, Programmdatenbankverwaltung) und der Anwendungssoftware (Komplettierung und Integration der Modellkette für die atmosphärische Ausbreitung im Nah- und Fernbereich, der radioökologischen und Dosismodelle für terrestrische und hydrologische Expositionspfade, der Simulationsmodelle für Katastrophenschutz- und Strahlenschutzvorsorgemaßnahmen sowie der Modelle zur Abschätzung von gesundheitlichen und monetären Konsequenzen). Insbesondere wurde die Deposition auf der Basis der Oberflächenbeschaffenheit und der atmosphärischen Turbulenz wie in den Nahrungskettenmodellen auch in den Ausbreitungsmodellierung realisiert. Bei allen Softwarearbeiten wurde besonderer Wert gelegt auf die Stabilität der einzelnen Module unter den verschiedenen Betriebsweisen des RODOS Systems. Das zu RODOS Version 4.0 zugehörige Benutzerhandbuch und die Testprozeduren für die System- und Anwendungssoftware wurden fertiggestellt, das Systemhandbuch liegt in einer vorläufigen Version vor.

Die Weiterentwicklung des RODOS Systems erfolgt im 5. Rahmenprogramm der Europäischen Kommission. Zwei entsprechenden F&E-Verträge begannen im Oktober 2000; der Vertrag FIKR-CT-2000-00077 („RODOS MIGRATION") mit 5 Vertragspartnern wird vom IKET koordiniert. Zum gleichen Zeitpunkt begann ein Netzwerkvorhaben über den operationellen Betrieb von Entscheidungshilfesystemen für kerntechnische Notfälle mit 35 Institutionen in Europa und Übersee („DSSNET"). Das Netzwerk (siehe Abb. 1) besteht jeweils zur Hälfte aus derzeitigen und zukünftigen Benutzern derartiger Systeme und Vertretern der beteiligten F&E Institute. Zielsetzung ist der gemeinsame Informationsaustausch im Hinblick auf die Verbesserung

und breitere Akzeptanz der Entscheidungshilfesysteme im operationellen Einsatz. Um die Wechselwirkung und den Erfahrungsaustausch zwischen Entwicklern und Benutzern zu stimulieren werden jährlich für speziellen Zielsetzungen entwickelte Notfallschutzübungen mit allen Netzwerkteilnehmern durchgeführt. Darüber hinaus werden die Rückmeldungen nach national oder international initiierten Notfallschutzübungen ausgewertet.

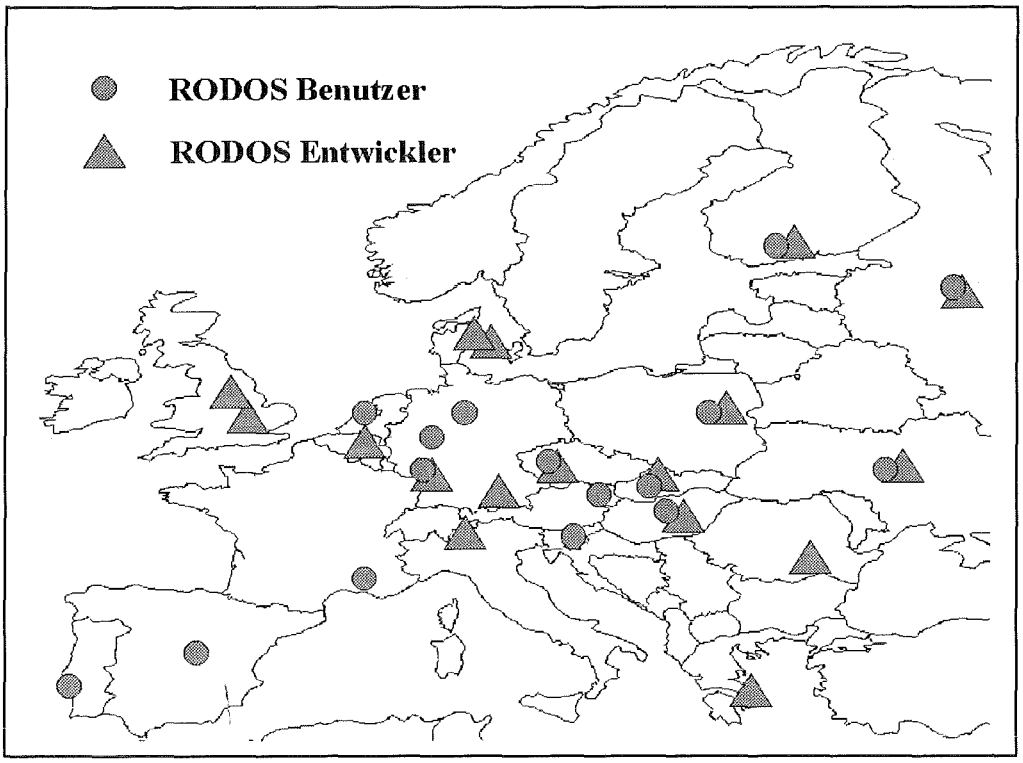

Abb.1 RODOS Teilnehmer am DSSNET

Real-Time Datenverarbeitung

In Abstimmung mit JRC Ispra und BfS/IAR wurde das Real-Time Datenbankkonzept von RODOS modifiziert und überarbeitet, um die Variabilität der Datenstrukturen in EURDEP- und IDF- Datenfiles berücksichtigen und verwalten zu können. Die Software-Erweiterungen sind inzwischen weitgehend abgeschlossen. Weiterhin wurden die technischen Details des Datenaustauschkonzepts zur Anbindung von IMIS/PARK an RODOS festgelegt.

Sowohl die System- als auch die Anwendungssoftware musste für die Verarbeitung der on-line Daten angepasst werden. Hierzu gehörten u.a. die regelbasierte Filterung der eingehenden KFÜ-Daten zur Unterscheidung und Aufbereitung der meteorologischen Messdaten als Eingabe für den meteorologischen Präprozessor und der

Emissionsdaten (Kaminfreisetzungen) als Quellterminformation für Ausbreitungsrechnungen. Die Prozeduren wurden in umfangreichen Tests mit KFÜ-Daten aus Schleswig-Holstein auf ihre operationelle Funktionalität hin überprüft.

2 Installation von RODOS zum operationellen Betrieb in Notfallschutzzentralen

Installation von RODOS in der Bundesrepublik Deutschland

Mit Unterstützung des BMU (Vorhaben St. Sch. 4168) wurde das RODOS System zum zentralen Betrieb bei der Stabsstelle AR des Bundesamtes für Strahlenschutz (BfS), Bonn, vorbereitet. Die in der RODOS Zentrale installierten Rechner mit unterschiedlichen Aufgabenstellungen sind über ein lokales Netzwerk miteinander verbunden (Abb. 2). Das eigentliche RODOS System läuft auf einem Server-Cluster, das hohe Ausfallsicherheit bei Hardware- oder Softwarefehlern sicherstellt (Segment II). Im RODOS Vorrechner werden die einlaufenden meteorologischen und radiologischen Daten externer Datenlieferanten (DWD, KFÜs, IMIS) gespeichert, geprüft und zur Weiterverarbeitung im RODOS System soweit notwendig aufbereitet (Segment I).

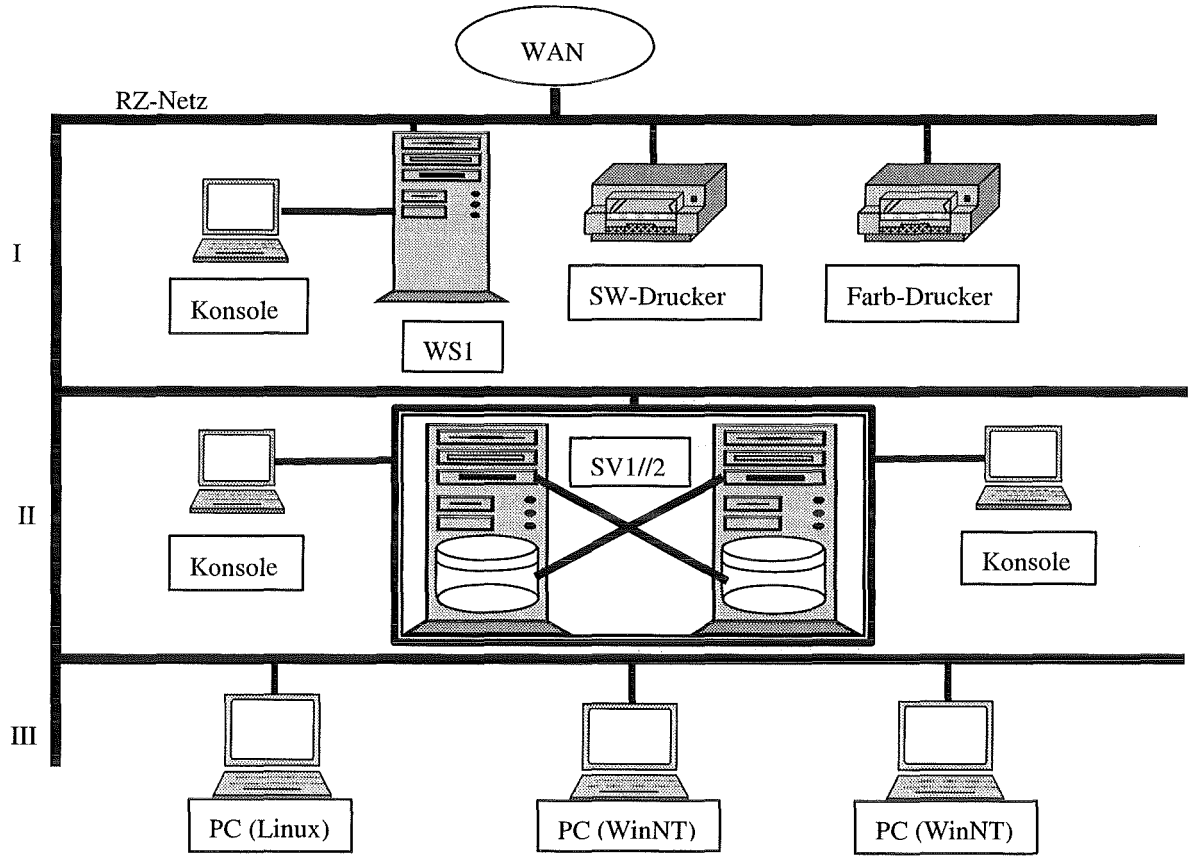

Abb. 2 Konfiguration des Rechnersystems in der RODOS Zentrale

Der direkte Zugriff auf das RODOS System erfolgt über X-Windows-fähige Arbeitsplätze für die Bedienmannschaft in der RZ, über die Ergebnisse des RODOS Systems ausgewählt, zusammen mit geographischen Informationen dargestellt und sowohl graphisch als auch alphanumerisch ausgedruckt werden können (Segment III).

Das Segment I besteht aus einer Workstation HP J5000 und zwei Laser Druckern. In diesem Segment ist die Netzverwaltung, die Back-up-Verwaltung sowie die Erfassung, Speicherung und Steuerung des ankommenden Messdaten und Meldungen implementiert.

Das Segment II stellt den Konfigurationsplan zur Konzeption einer Rechner-Platten-Redundanz dar. Sie besteht aus zwei unabhängigen Servern SV1 und SV2 des Typs HP L2000 und Disk-Arrays. In dieses Segment ist außerdem für jeden Server eine unterbrechungsfreie Stromversorgung mitintegriert, um den kontinuierlichen Betrieb im Falle einer Fehlfunktion der Versorgungsspannung zu gewährleisten.

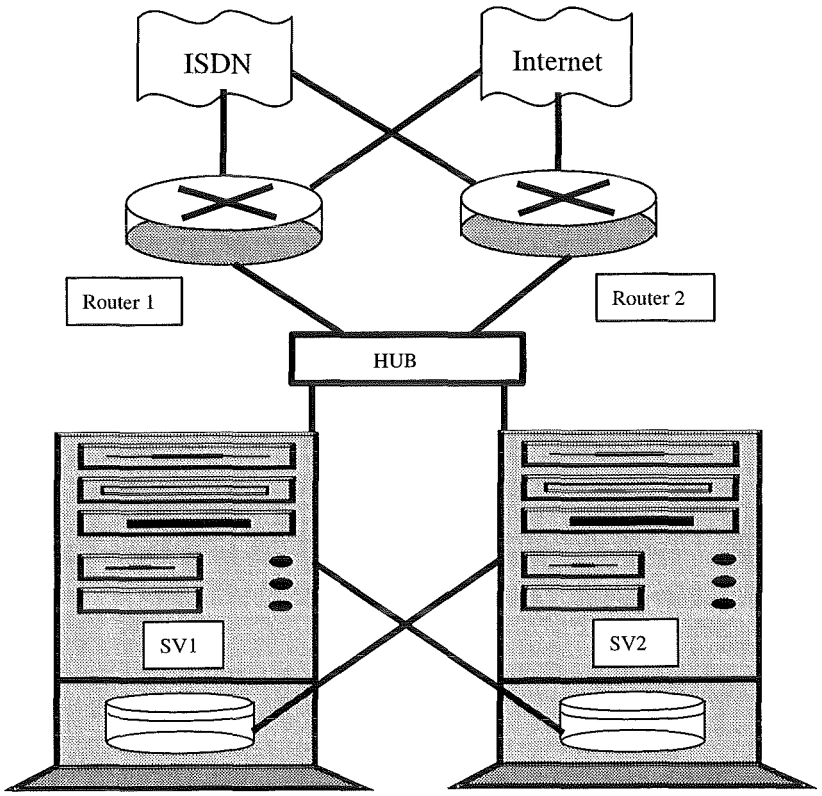

Abb. 3. Realisierung der Netzwerk-Rechner-Platten-Redundanz

Zum Erreichen der vollen Redundanz ist das System über zwei Router mit der Außenwelt (ISDN, Internet) verbunden (Abb. 3). Die Überwachung der Systemereignisse und die Steuerung der Funktionen bei jeder Art von Ausfällen (Netzwerk, Platten, Prozessoren, usw.) erfolgt durch ein kommerzielles Redundanz-Software-Package (Hewlett Packard). Es stellt sicher, dass das Verfügbarkeitskriterium „Verlust aller Information in nur einem Verarbeitungszyklus" erfüllt wird.

Der Betrieb des RODOS Systems basiert auf der Verfügbarkeit von aktuellen Daten zur radiologischen und meteorologischen Lage. Insbesondere im Notfallbetrieb sind diese Daten für die aktuelle Diagnose des Ist-Zustandes notwendig. Als Real-Time Daten werden hier solche Informationen betrachtet, die sich aus den Daten der festen und mobilen Messnetze ergeben. Alle Real-Time Daten für das RODOS System werden aus den zuständigen Datenzentralen des Bundes (IMIS Daten) und der Länder (KFÜ Daten) abgerufen. Für die Übertragung der Daten wird die WAN Anbindung des RODOS Systems an diese Datenzentralen genutzt. Als Format wird bei der Übertragung von IMIS Daten das EURDEP Format benutzt, die Übertragung von KFÜ Daten erfolgt im IDF-Format.

Durch die Datenzentralen der Länder werden die ausgewählten Real-Time Daten im o.g. standardisierten Format auf einem File-System zum Transfer bereitgestellt, von dem die RODOS Zentrale diese Daten kontinuierlich abruft. Im Unterauftrag durch FZK wurden in den Datenzentralen von Schleswig-Holstein, Niedersachsen, Hessen und Bayern die hardware- und softwaretechnischen Voraussetzungen für die Auskopplung und Bereitstellung der KFÜ Daten geschaffen. In ausführlichen Tests wurde die Übertragung der Daten sowie deren Speicherung und weitere Verarbeitung im RODOS System untersucht und sichergestellt. In gleicher Weise wurde die Behandlung von IMIS Daten in einer Reihe von Tests auf fehlerfreie Funktion überprüft.

Meteorologische Prognosedaten werden im Bedarfsfall über eine Datenverbindung zwischen der RZ und dem DWD von der RZ abgerufen. Die Modelle in RODOS nutzen die Daten des Lokal-Modells LM mit einer Auflösung von ca. 7 km, welches zweimal täglich Prognosedaten mit einstündigen Intervallen über einen Zeitraum von 48 h im in der folgenden Tabelle angegebenen Bereich berechnet.

Linke untere Ecke	5.46°W	39.07°N
Rechte untere Ecke	19.68°E	39.39°N
Linke obere Ecke	14.42°W	58.49°N
Rechte obere Ecke	25.55°E	59.86°N

Bei Standorten im Prognosebereich des LM, insbesondere also in Deutschland und dem grenznahen Ausland, werden mit der Datenanforderung die geographischen Koordinaten des Standorts mitgeteilt. Hierdurch wird ein Gebiet von 160 km x 160 km definiert, für das die Prognosedaten aus dem Gesamtdatensatz extrahiert und an die RZ übermittelt werden. Dabei werden immer die 12 Stunden zurückliegenden Prognosedaten mitgesandt.

Zur Prognose der Auswirkungen im Fernbereich liefert der DWD die Ergebnisse seiner großräumigen Ausbreitungsrechnungen zur Nutzung im RODOS System (Ergebnisse des numerischen Wettervorhersagemodells LM und des Ausbreitungsmodells LPDM). Es wurde ein Modul entwickelt, der es erlaubt, Ausbreitungsergebnisse des DWD im RODOS System weiter zu verarbeiten. In mehreren Abstimmungsgesprächen zwischen FZK, DWD und BfS wurden das Konzept, die Inhalte und die technischen Schnittstellen der Datenübertragung festgelegt. Von der RODOS Zentrale werden über Anforderungsnachrichten (E-mail, Telefon) Ergebnisse von Prognoserechnungen (meteorologische Felder, Ausbreitungsrechnungen) des DWD angefordert. Sowohl die Datenanforderung als auch die Schnittstellen zwischen Prognosedaten des DWD und dem RODOS System wurden intensiv getestet.

Dass gesamte RODOS Rechnersystem einschließlich Netzwerkankopplungen wurde im Januar 2001 dem BfS, Stabsstelle AR, Bonn, überstellt.

Installation von RODOS im europäischen Raum

Die Europäische Kommission fördert finanziell die Installation des RODOS Systems in Notfallschutzzentralen osteuropäischer Länder. Dies schließt die Beschaffung der notwendigen Hardware- und Software-Komponenten, die Einrichtung aller Netzwerkverbindungen zu Datenlieferanten und RODOS-Nutzern und die Anpassung des RODOS Systems an nationale Gegebenheiten ein. Die entsprechenden Arbeiten in Polen und der Slowakischen Republik wurden mit Unterstützung des IKET im Mai

2000 abgeschlossen. Die Projekte zur Installation in Ungarn und der Ukraine begannen im November 2000. Als weitere Länder werden die Tschechische Republik und Slowenien in 2001 sowie später Russland, Weißrussland, Rumänien und Bulgarien folgen. Die Ausschreibungen und Vertragsverhandlungen werden vom IKET unterstützt. In einer Reihe von westeuropäischen Ländern ist die (test-) operationelle Installation des ROSOS Systems bereits erfolgt bzw. befindet sich in Vorbereitung, wie z.B. Finnland, den Niederlanden, Österreich, Spanien und Portugal.

3 Trainingskurse und Übungen

Mit Unterstützung der Europäischen Kommission wurde ein Trainingskurs für RODOS Operateure im europäischen Raum entwickelt und erstmals im Dezember 2000 mit 20 Teilnehmern im FZK/FTU durchgeführt. Weitere Kurse sind in 2001 und 2002 geplant. Die gesamten Kursunterlagen werden den Teilnehmern zur Verfügung gestellt als Basis zur Durchführung entsprechender Kurse in ihren Ländern.

Zur Vorbereitung des zentralen RODOS Betriebs des RODOS Systems in Deutschland wurde ein einwöchiger Trainingskurs für zukünftige RODOS Operateure der Benutzerkategorie A entwickelt und Ende November 2000 für 12 Teilnehmer von Bundes- und Länderinstitutionen im FZK/IKET durchgeführt. Weitere Kurse für A-Benutzer werden nach Abschluss der Einführungsphase bei der Stabsstelle AR des BfS frühestens im 2. Halbjahr 2001 möglich sein. Nach Fertigstellung des Web-Servers durch FZK wird die Schulung für B-Benutzer ebenfalls erst im Herbst 2001 stattfinden.

Im Juni 2000 wurde eine erste gemeinsame Notfallschutzübung von IPSN (F) und BfS in Cadarache durchgeführt. Zielsetzung der Übung war der Vergleich der Entscheidungshilfesysteme und Entscheidungsgrundlagen beider Länder. Zur Vorbereitung der Übung wurden Datenschnittstellen zwischen RODOS und dem IMIS-System bzw. dem französischen Rechencode ASTRAL erstellt und Software zur Simulation von Detektorsignalen im Hinblick auf einen zukünftigen Übungsmodul entworfen und implementiert. Alle drei Systeme lieferten während der Übung Ergebnisse ihrer radiologischen Simulationsrechnungen als Entscheidungsbasis für die beteiligten Notfallteams. Die vergleichenden Ergebnisse der Übung werden Anfang 2001 publiziert.

Literatur

Goossens, L.H.; Harper, F.T.; Ehrhardt, J.; Jones, J.A.
Lessons learnt from the EC/USNRC expert judgement study on probabilistic accident consequence codes applied in the COSYMA uncertainty analyses
Proceeding PSAM 5 conference, Osaka, 27. November – 1. Dezember 2000

Goossens, L.H.; Ehrhardt, J.; Kraan, B.; Cooke, R.
Expert judgement of uncertainties in modelling emergency actions after nuclear accidents
Proceeding PSAM 5 conference, Osaka, 27. November – 1. Dezember 2000

Jones, J.A.; Ehrhardt, J.; Goossens, L.H.; Brown, J.; Cooke, M.; Fischer, F.; Hasemann, I.; Kraan, B.
Probabilistic accident consequence uncertainty assessment using COSYMA: Methodology and processing techniques
EUR-Bericht: EUR 18827; FZK-Bericht: FZKA-6313

Jones, J.A.; Ehrhardt, J.; Goossens, L.H.; Brown, J.; Cooke, M.; Fischer, F.; Hasemann, I.; Kraan, B.; Khursheed, A.; Phipps, A.
Probabilistic accident consequence uncertainty assessment using COSYMA: Uncertainty from the dose module
EUR-Bericht: EUR-18825, FZK-Bericht: FZKA-6311

Jones, J.A.; Ehrhardt, J.; Goossens, L.H.; Brown, J.; Cooke, M.; Fischer, F.; Hasemann, I.; Kraan, B.
Probabilistic accident consequence uncertainty assessment using COSYMA: Uncertainty from the early and late health effects module
EUR-Bericht: EUR- 18824, FZK-Bericht: FZKA-6310

Brown, J.; Ehrhardt, J.; Goossens, L.H.; Cooke, R.; Fischer, F.; Hasemann, I.; Jones, J.A.; Kraan, B.; Smith, J.
Probabilistic accident consequence uncertainty assessment using COSYMA: Uncertainty from the food chain module
EUR-Bericht: EUR-18823, FZK-Bericht:FZKA-6309

Jones, J.A.; Ehrhardt, J.; Goossens, L.H.; Cooke, R.; Fischer, F.; Hasemann, I.; Kraan, B.
Probabilistic accident consequence uncertainty assessment using COSYMA: Uncertainty from the atmospheric dispersion and deposition module
EUR-Bericht: EUR-6308, FZK-Bericht: FZKA-18822

Jones, J.A.; Ehrhardt, J.; Goossens, L.H.; Brown, J.; Cooke, R.; Fischer, F.; Hasemann, I.; Kraan, B.
Probabilistic accident consequence uncertainty assessment using COSYMA: Overall uncertainty analysis
EUR-Bericht: EUR-18826, FZK-Bericht: FZKA-6312

Raicevic, J.; Raskob, W.; Merkle, M.; Ninkovic, M.
Stochastic health effects assessment due to short-term external exposure
Yugoslav Nuclear Society Conference (YUNSC 2000), Belgrad, 2. – 5. Oktober 2000

32.21.10 Beteiligung am PHEBUS-Projekt

I. Theoretische Interpretation der experimentellen Ergebnisse

(W. Sengpiel, W.Hering, IRS)

Abstract

FZK/IRS participates in the frame of the international Phebus FP project in the analytical interpretation of the experimental results. Test analyses are performed using SCDAP/ RELAP5 and ICARE2. Post-test analyses of the debris bed experiment FPT4 with ICARE2 show a good agreement with experimental data after some power related adjustments have been introduced. However, for the high temperature phase the temperature evolution both in debris bed and in the shroud also shows significant differences possible origins of which can be interpreted but hardly verified. For the bundle tests Phebus FPT1 und FPT2 the test analyses are continuously updated using SCDAP/RELAP5 and ICARE2.

1. Einleitung

Im Rahmen des internationalen Phebus FP - Projektes, das unter Leitung von IPSN in Cadarache durchgeführt wird, werden die Mechanismen von Spaltproduktfreisetzung und –transport im Primärsystem eines Leichtwasserreaktors unter den Bedingungen eines schweren Kernschmelzunfalles untersucht. Das Projekt umfasst sechs Experimente, von denen vier - FPT0, FPT1 und FPT2 als Bündelversuche - sowie FPT4 als Versuch an einem vordefinierten Schüttbett bereits durchgeführt worden sind. Neben dem Problem von Spaltproduktfreisetzung und –transport stehen Untersuchungen der Mechanik und der physiko-chemischen Vorgänge beim Abschmelzen der Corestrukturen im Vordergrund des Interesses. Diesem letztgenannten Themenbereich widmet sich der sogenannte 'Bundle Interpretation Circle' im Rahmen des Phebus FP-Projekts, in dem FZK/IRS mitarbeitet. Für die Experimentanalyse und –interpretation werden u.a. die Rechenprogramme SCDAP/ RELAP5 und ICARE2 eingesetzt. Im folgenden wird über Ergebnisse von Rechnungen zum Versuch FPT4 mit ICARE2 berichtet.

2. Post-Test-Analysen für das Experiment PHEBUS FPT4 mit ICARE2 V3

Die Versuchsanordnung besteht aus einem aktiven Schüttbett aus einer Mischung aus Brennstoff- und oxidierten Zry-Hüllrohr-Fragmenten (2 bis 5 mm Durchmesser, 3.071 kg UO_2 , 0.76 kg ZrO_2), und einem darunter liegenden passiven Schüttbett aus 2.507 kg abgereicherten UO_2-Fragmenten gleichen Durchmesserbereichs. Das aktive (durch nukleare Wärme aufgeheizte) Schüttbett hat eine Höhe von 240 mm, das passive (mit geringer nuklearer Wärmeerzeugung) von 120 mm. Das gesamte Schüttbett ist von einem wärmeisolierenden Shroud mit einem Innendurchmesser von 70 mm umgeben, der aus mehreren Schichten von Hafnia, Thoria- und Zirkonia zusammengesetzt ist. Abb. 1 zeigt schematisch die Geometrie- und Materialanordnung wie sie für die ICARE2-Rechnungen zugrunde gelegt wird.

Ein erster Vergleich der gemessenen und der gerechneten Temperaturverläufe im Schüttbett ergab große Unterschiede zwischen Experiment und Theorie /1/, die u.a. auf eine von der Versuchsplanung abweichende zeitliche und räumliche nukleare Leistungserzeugung in der Testapparatur zurückzuführen war. Crestia und Repetto /2/ gaben Korrekturen für die tatsächliche nukleare Leistungserzeugung an, die in unseren Rechnungen berücksichtigt wurden. Demnach ist die Leistungsverteilung zwischen aktivem and passivem Schüttbett 85.2 % zu 14.8 % (anstatt 92 % zu 8 %). Abb. 2 zeigt den korrigierten zeitlichen Leistungsverlauf während des Versuchs und den Verlauf des Dampfmassenstromes am unteren Rand. Als Solidus- und Liquidustemperaturen für das (UO_2-ZrO_2) - Gemisch wurden 2750 K bzw. 2850 K angenommen.

Abb. 3 zeigt einen Vergleich der experimentellen und gerechneten Temperaturen im Schüttbett an verschiedenen axialen Positionen, Abb. 4 vergleicht Temperaturverläufe im inneren Thoria-Zirkonia-Ring des Shrouds. Man erkennt entsprechend den ausgeprägten Leistungsplateaus (Abb. 2) ein stufenförmiges zeitliches Temperaturverhalten. Deutliche Abweichungen zwischen Rechnung und Experiment treten ab ca. 12000 s auf (Beginn des lokalen Schmelzprozesses im oberen zentralen Bereich der aktiven Zone), wo der Temperaturanstieg im Schüttbett steiler verläuft als in der Rechnung. Auch die Shroudtemperaturen (Abb. 4) spiegeln dieses Verhalten wieder. Oberhalb des Schüttbetts (410 mm) wird dagegen die Shroudtemperatur in der Rechnung überschätzt. Crestia und Repetto zeigen, dass ein möglicher Bypass des Dampfmassenstromes

durch ein Leck in den Shroud und damit eine schlechtere Kühlung des Schüttbetts den gemessenen steilen Temperaturanstieg im Schüttbett verursacht haben kann /2/; eigene analytische Studien dazu sind noch nicht abgeschlossen. Abb. 5 zeigt den Zustand der Versuchsanordnung am Ende des Versuchs in Form der Verteilung der relativen Materialdichte. Der obere Bereich des aktiven Schüttbetts ist größtenteils abgeschmolzen und in darunter liegenden kälteren Zonen bis in den Bereich des passiven Schüttbetts hinein wiedererstarrt. Die berechnete Masse geschmolzenen und verlagerten (UO_2-ZrO_2)-Gemisches beträgt 1.73 kg. Der experimentelle Wert dürfte darüber liegen, genaue Angaben sind z.Zt. nicht verfügbar.

3. Ausblick

Schwerpunkt der Experimentanalysen in 2000 waren Rechnungen zum Experiment FPT4 mit ICARE2 V3. Diese Arbeiten werden fortgesetzt. Zusätzlich werden die Bündelexperimente FPT1 und FPT2 zur Validierung von SCDAP/RELAP5 und ICARE2 verwendet.

4. Literatur

/1/ Projekt Nukleare Sicherheitsforschung – Jahresbericht 1999, FZKA 6480, August 2000, S. 494-498

/2/ J.-C.Crestia, G.Repetto, PHEBUS FPT4, First Post-Test Calculations of Debris Bed Behaviour using the ICARE2 Code, Phebus Meeting – November 3-4, 1999, Aix-en-Provence (Verteiler eingeschränkt)

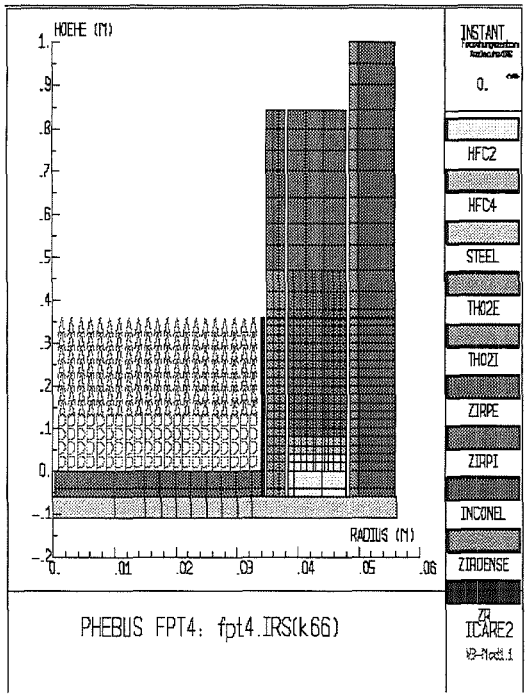

Abb.1: Geometrie und Materialanordnung für ICARE2 V3-Rechnungen von Phebus FPT4 im Ausgangsstadium
(A: aktives Debrisbett,
P: passives Debrisbett)

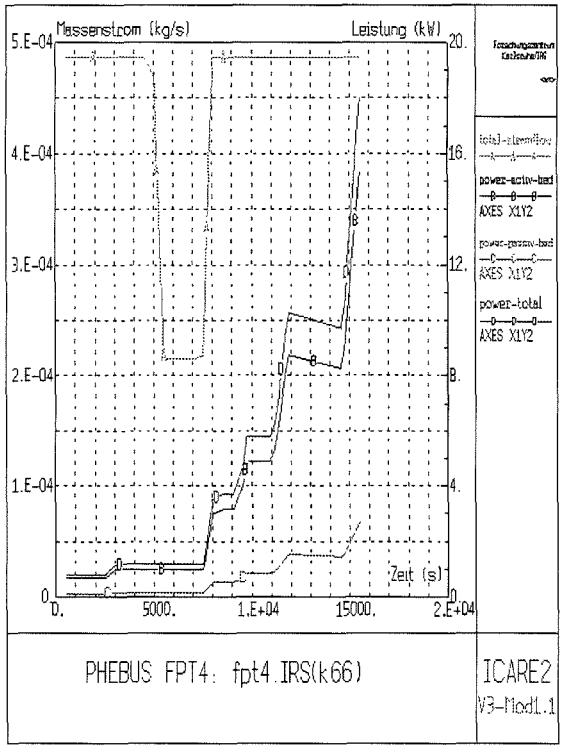

Abb.2: Zeitabhängiger Dampf-Massenstrom und Leistungsverlauf während des Versuchs FPT4

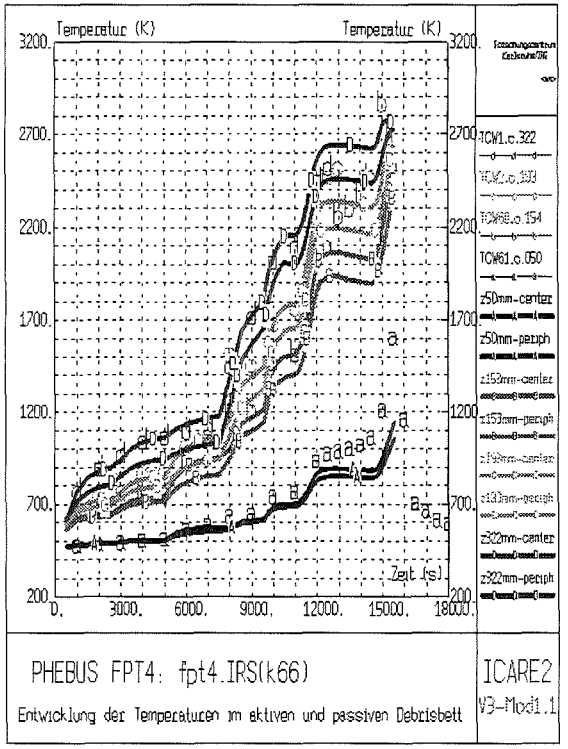

Abb.3: Gemessene (a: 50 mm Höhe im Debrisbett; b: 154 mm; c: 193 mm; d: 322 mm) und gerechnete Temperaturen im Debrisbett (durchgezogene Kurven, A: 50 mm, Mitte und Rand; B: 153 mm, C: 193 mm; D: 322 mm)

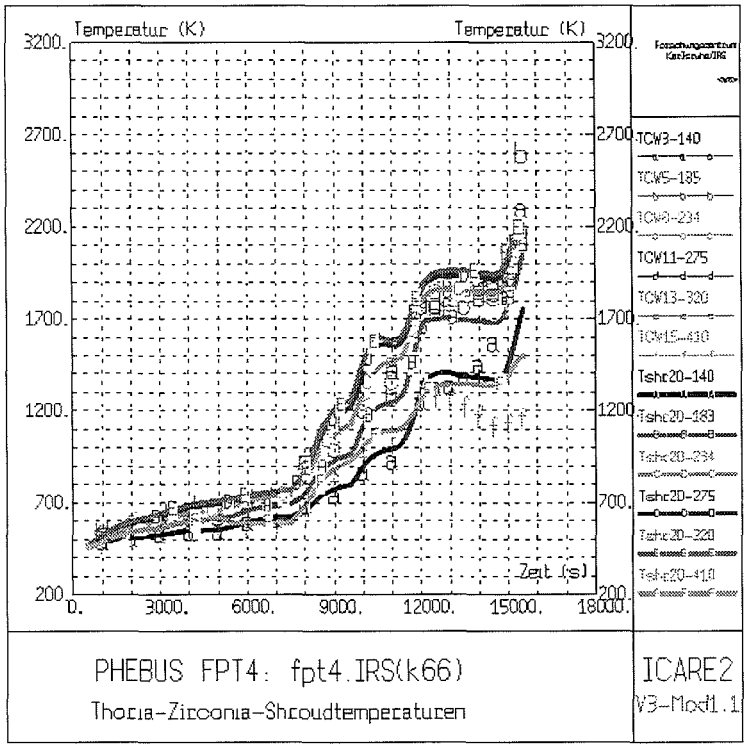

Abb.4: Gemessene (Symbole a bis f) und gerechnete Temperaturen (durchgezogene Kurven A bis F) im inneren Thoria-Zirkonia-Ring des Shrouds (vgl. Abb. 1)

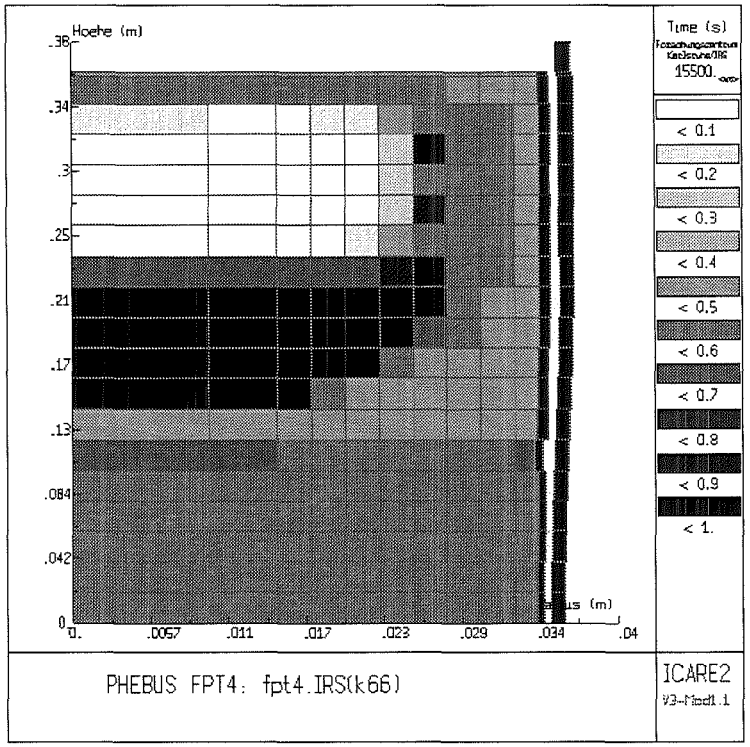

Abb.5: Zustand des FPT4-Testbetts am Ende des Versuchs in Form einer relativen Dichteverteilung, berechnet mit ICARE2 V3. Der obere Teil des aktiven Debrisbetts ist abgeschmolzen und in den darunter liegenden Zonen mit niedrigeren Temperaturen wieder erstarrt. Der Hohlraum wird durch eine gewölbeähnliche feste Struktur nach oben hin abgeschlossen

II. Contribution to PHEBEN2 – Validating Severe Accident Codes Against PHEBUS FP for Plant Applications

(V. Krautschick, P. Schmuck, IKET)

Zusammenfassung

Das internationale PHEBUS FP Programm umfasst eine Reihe von Experimenten zur Sicherheit von Leichtwasserreaktoren. Das EU Projekt PHEBEN2 wurde – basierend auf diesen Experimenten – im Jahr 2000 gestartet. Ziel von PHEBEN2 ist die Validierung von Reaktorsicherheitsrechenprogrammen an PHEBUS FP Tests und die Anwendung der gewonnen Erkenntnisse auf LWR Anlagen. Der FZK Beitrag im Projekt konzentriert sich auf die Iodchemie im Containment. Für FPT1 (Spaltprodukttest 1) wurden post-test Berechnungen durchgeführt, um die Iodverteilung im Gasraum und Sumpf des PHEBUS Containments zu analysieren.

Abstract

The international PHEBUS FP programme comprises a series of tests for the safety of light water reactors. The EU project PHEBEN2 – based on these experiments – was started in March 2000. The objectives of PHEBEN2 are the validation of reactor safety codes against PHEBUS FP tests and the application of the obtained knowledge to LWR plants. The FZK contribution was focused on the iodine chemistry in the containment. Post-test calculations for FPT1 (Fission Product Test 1) with the IMPAIR3 code were performed to analyse the iodine distribution in the gas and water space of the PHEBUS containment.

1. Introduction

FZK participates in the EU project PHEBEN2. The aim of this project in the 5th Euratom Framework Programme is the validation of severe accident codes against PHEBUS FP. A ultimate objective of PHEBEN2 is the transfer of the obtained knowledge to LWRs for plant applications. The project started in March 2000 with a duration of four years. The international PHEBUS FP programme comprises a series of tests for the safety of light water reactors. These experiments are a unique source representing integral source term data. The PHEBUS FP tests have been performed in Cadarache, four tests are completed by now, out of the overall six planned experiments. The FZK contribution to PHEBEN2 is focused on the iodine chemistry in

the containment within three work packages (WP). WP1 includes the validation of integral codes. FZK will use the new version MELCOR 1.8.5 with improved iodine chemistry models. WP2 covers the validation of detailed codes. FZK applies IMPAIR3 for investigations of local PHEBUS conditions and detailed iodine chemistry. The third WP comprises the criteria and code assessment for plant applications. Assessment criteria will be used to quantify the predictive capabilities of the integral code for iodine behaviour [1].

2. WP1: Validation of Integral Codes

In this work package FZK will use the integral code MELCOR 1.8.5. This code version contains a special routine to analyse the chemical iodine behaviour. The code was installed at FZK computers in December 2000. First steps were done to prepare an input deck for FPT1.

3. WP2: Validation of Detailed Codes

FZK has performed iodine chemistry calculations for FPT1 using the IMPAIR3 code [2]. The objective of this study is the investigation of the iodine behaviour in the containment. The calculations are based on input data taken from the PHEBUS FP Data Book [3], the FPT1 Final Report [4] and previous iodine investigations by CIEMAT [5] and PSI [6].

The long term iodine calculation starts at the end of steam injection at the time of 18540s [7]. The input of iodine and silver comes in two steps, the initial phase and the washing phase. For the initial phase the iodine input into the gas space of the containment is taken in form of molecular iodine I_2 (0.0636g). For the water space it is assumed that iodine reaches the sump in form of iodine ions I^- from CsI aerosols. The value is taken from the amount deposited by diffusiophoresis and then washed down to the sump with condensed steam (0.145g). In the washing phase iodine is only sourced into the sump. This iodine minus the deposits in unmeasured sections (recirculation loop) amounts to 0.38g. These deposits and also the iodine trapped in containment samplings and in the unmeasured sections of the washing loop are not included in the calculation. In addition to various chemical reactions silver oxide – iodide, silver metal – iodide and reactions between silver and molecular iodine are taken into account in the code. It is assumed that 2,5% of the silver exists in form of silver oxide and the silver particles are spherical with a mean diameter of 3 µm.

On the basis of these data the local concentrations of iodine species in gas and water space and the deposition on the structures are calculated with IMPAIR3. Figures 1 and 2 show the resulting iodine distributions in the atmosphere and in the sump of the containment, respectively. In the gas space iodine deposited on paint is dominating. It is in good agreement with the experimental amount for painted condensers deposits at the end of the test. The value for the iodine deposited on steel differs more from the experimental vessel walls deposits. The amounts for organic and molecular iodine in the gas space are smaller than the mass of iodine deposited. The dominating iodine product in the whole containment is AgI in the sump. AgI is insoluble and concentrates at the sump bottom. The calculated amount corresponds with the measured sump bottom particulate mass of 0.51g quite well. There are various other iodine species in the sump, but all are much smaller then AgI at the end of the test by some orders of magnitude.

4. WP3: Criteria and Code Assessment for Plant Applications

MELCOR 1.8.5 is the tool for the integral code application. FZK has started to gather information in the descriptions of the new code version in terms of the code assessment criteria.

5. Conclusions and Future Work

The analysis clearly shows that AgI in the sump is the dominating iodine species in FPT1. The concentration of molecular iodine in the gas space is relatively small. One has to be aware that organoiodine data should be taken with caution because of uncertainties in the organoiodine modelling. The analysis also indicates that parameters like temperature, pH, dose rate and the degree of silver oxidation have a strong influence on the iodine distribution. As next steps calculations with MELCOR 1.8.5 for FPT1 will be performed for WP1 and the definition and application of criteria for integral code will be done for WP3.

References

[1] Krautschick, V. and Schmuck, P., "Planned Contributions of Forschungszentrum Karlsruhe to the EU project PHEBEN2", PHEBEN2, Minutes of the Kickoff Meeting, Technical Note No. I.00.61, Ispra, May 2000

[2] Güntay, S. and Cripps, R. "IMPAIR3: A Computer Program to Analyze the Iodine Behaviour in Multi-Compartments of a LWR Containment", Paul Scherrer Institut, Bericht Nr.128, September 1992

[3] Scheurer, H. "PHEBUS FP Data Book FPT1", Doc. PHEBUS PF IS/92/49

[4] Jacquemain, D. et al., "FPT1 Final Report", Doc. PHEBUS PF IP/00/479, 01.12.2000

[5] Jones, A.V. (ed). PHEBEN "Benchmarking Release, Circuit and Containment Codes Against PHEBUS FP", ST-PHEBEN(99)-P09, June 1999, p.99

[6] Ibid. p.105

[7] Krautschick, V. and Schmuck, P., "Contributions of Forschungszentrum Karlsruhe to PHEBEN2 Half-Yearly Progress Report", Half-Yearly Progress Report, Technical Note No. I.00.126, Ispra, Nov. 2000

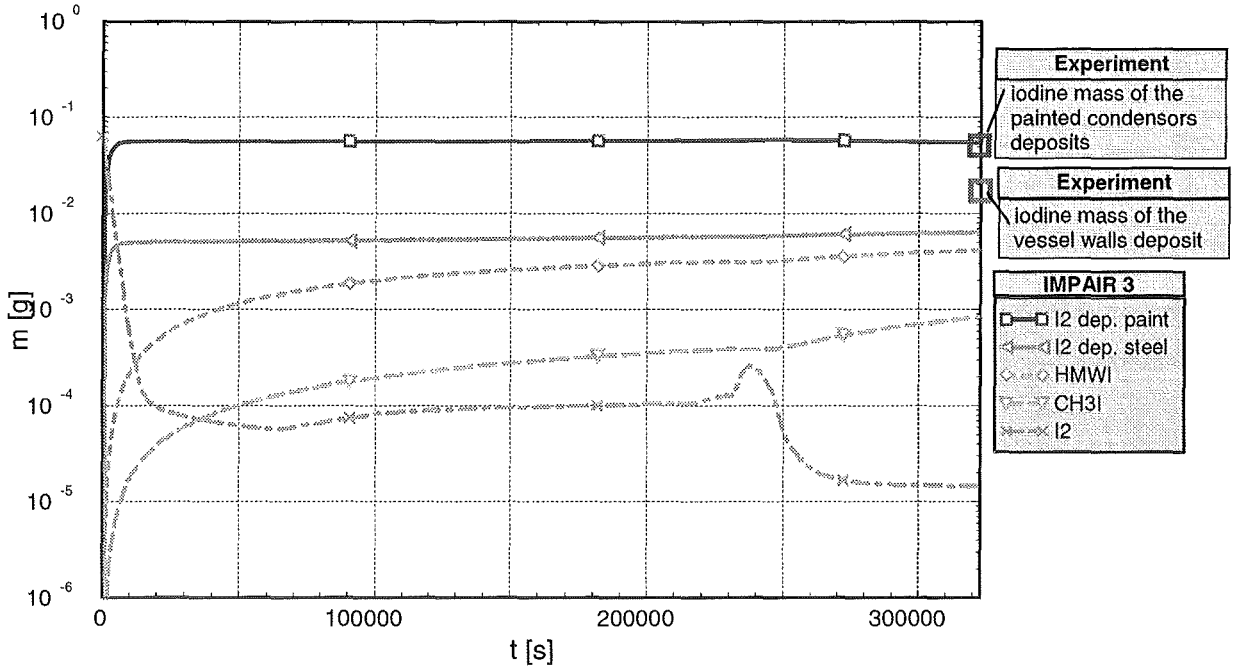

Figure 1: Iodine Distribution in the FPT1 Containment Atmosphere Comparison of Experimental vs. IMPAIR3 Results

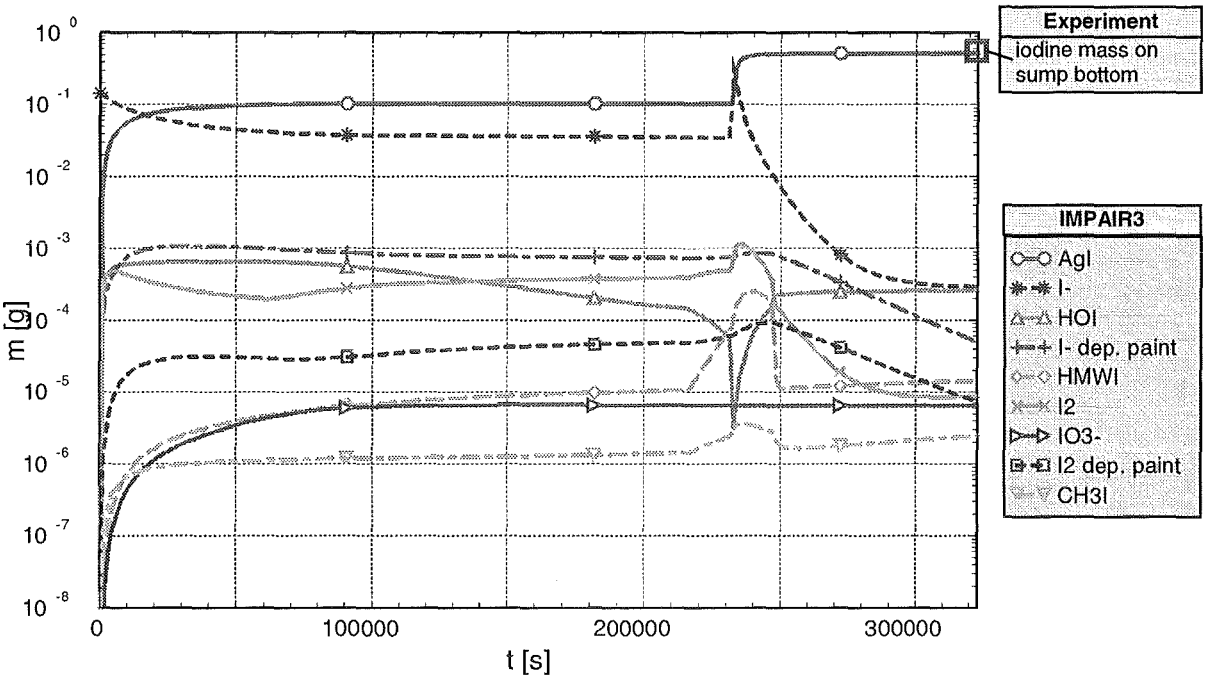

Figure 2: Iodine Distribution in the FPT1 Containment Sump Comparison of Experimental vs. IMPAIR3 Results

32.21.11 Untersuchungen zur Reaktor- und Anlagendynamik

Investigations on Reactor and Plant Dynamics

(D. C. Cacuci, M. Ionescu-Bujor, W. Hering, V. H. Sanchez, IRS)

Abstract

At the Institute for Reactor Safety (IRS) of the Forschungszentrum Karlsruhe (FZK) the thermohydraulic code system RELAP5 is validated and extended as part of the CAMP agreement. The Adjoint Sensitivity Analysis Procedure (ASAP) implemented in RELAP5 is under validation for single- and two-phase conditions. As part of the 5th EU framework program HPLWR, RELAP5 was extended to simulate successfully fluid conditions in the supercritical regime.

Zusammenfassung

Am Institut für Reaktorsicherheit (IRS) des Forschungszentrums Karlsruhe (FZK) wird im Rahmen der CAMP-Vereinbarung das Thermohydraulik-Programm RELAP5 validiert und erweitert. Das in RELAP5 implementierte verfahren "Adjoint Sensitivity Analysis Procedure" (ASAP) wird für ein- und zweiphasige Bedingungen erweitert und validiert. Als Beitrag zum HPLWR Programm im 5. Rahmenprogramm der EU wurde RELAP5 geeignet erweitert, dass Fluidbedingungen im überkritischen Bereich erfolgreich simuliert werden können.

1.1 Status of Implementation of Adjoint Sensitivity Method into RELAP5

The code system RELAP5 mod 3.2 (RELAP5) code system simulates the thermal-hydraulic characteristics of Light Water Reactors (LWR's) by using a non-equilibrium, non-homogeneous two-phase flow model together with conservation equations for boron concentration in the liquid phase and non-condensable gases in the vapor phase. REALP5 is used worldwide for analyzing LWR's under both operational transients and postulated accident conditions. The RELAP5 code contains several hundreds of parameters, associated with correlation relations, flow regimes, geometrical configurations, and water thermodynamic properties. The implementation of efficient methods to analyze exhaustively the sensitivity of results, referred to as *responses*, calculated with the RELAP5 code system would represent a major development towards establishing a

state-of-the-art code system for the analysis of postulated accident scenarios. For this purpose, a research and development program aimed at implementing the *local* Adjoint Sensitivity Analysis Procedure (ASAP) for nonlinear systems into this code has been initiated. The end product of applying this method is the Adjoint Sensitivity Model, denoted as ASM-REL/TF, corresponding to the two-fluid flow model in RELAP5. The adjoint model has been implemented and successfully validated by calculating sensitivities to initial conditions. The next step in the implementation of the ASAP consists in the extension of the ASM-REL/TF model, applied and used until now for the thermal-hydraulic part of the code, to the heat transfer part of RELAP5.

In parallel, typical sensitivities for RELAP5 parameters like those associated with the geometry of the problem, pump and valve parameters and parameters associated with correlation relations of the heat coefficients are calculated and are now in the process of validation. Actually validation of the model is initiated using the experimental data of the QUENCH-04 experiment.

In 2001, after release of RELAP5 mod3.3 to CAMP members, the ASAP formulation has to be revised and adapted to the new code capabilities. After that activity, the RELAP5 base version should be the same for all RELAP5 applications.

1.2 Assessment of Best-Estimate Code Systems with 3D-Neutron Kinetics

At IRS thermohydraulic best-estimate code system RELAP5 coupled with 3D-neutron kinetics capabilities is being evaluated in the frame of international benchmarks and by dedicated applications. In a close co-operation with Siemens/KWU the international OECD/NEA MSLB-Benchmark /2/ was used to validate the Siemens/KWU code system RELAP5/PANBOX /3/ successfully /4/, /5/.

As an example the local power distribution at the elevation of 3,14 m is given in Figure 1 for 6.10 s and 66.0 s after scram. At 66.0 s the calculation shows a local power peak with app. 100 % power for 4-5 fuel elements. The average core power is rather low, but for the energy released in these four fuel elements has to be checked carefully whether or not temperature criteria remain fulfilled. Such detailed analyses can only be obtained by coupled 3D thermohydraulic and neutronics codes.

Even though the results obtained for the MSLB by RELAP5/PANBOX are very good compared to those obtained by similar code systems, PANBOX is restricted to quadratic fuel assemblies commonly used in PWR. Since the core design of innovative reactors concepts may be flexible in geometry (quadratic, hexagonal) and more heterogeneous, it is necessary to have additional tools applicable on a wide range of core designs that allow the evaluation of emerging nuclear concepts from both economical and safety point of view.

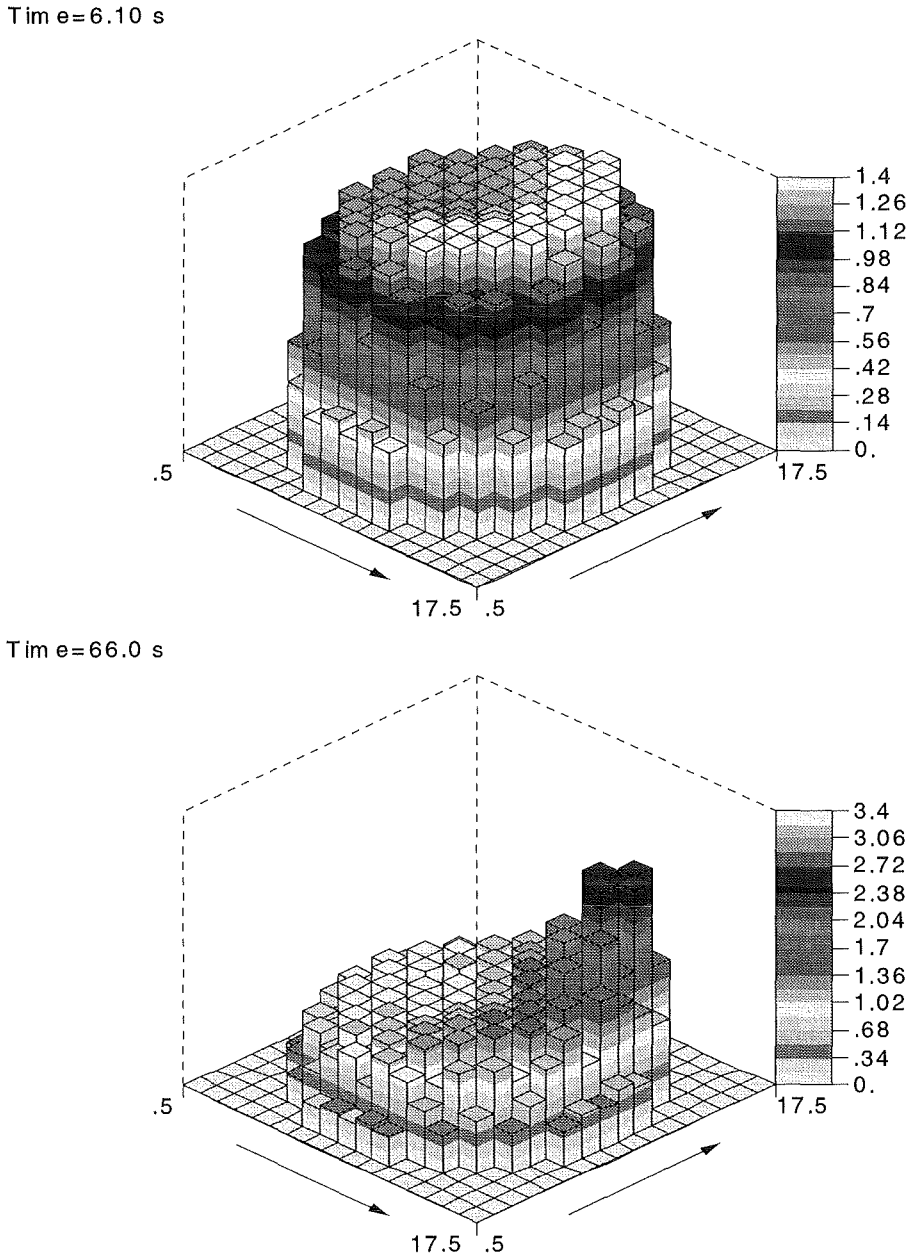

Figure 1 2D relative radial power distribution at the core plane z=3.14 m for 6.1 s and 66.0 s during transient progression

The RELAP5/PARCS code system, developed by the Purdue University sponsored by USNRC /6/, is able to simulate both PWR and BWR with a 3D-neutronic model coupled to 1D-RELAP5 thermal hydraulics. A new version of PARCS is capable to simulate also hexagonal fuel assemblies additionally. This coupled code system uses an internal integration scheme where the system solution and core thermal hydraulics is obtained by RELAP5 and only the spatial kinetics solution is obtained by PARCS. In this approach PARCS takes the thermal hydraulic parameters predicted by RELAP5 to update the cross-sections (feedback) while RELAP5 picks up the thermal power calculated by PARCS to solve the core heat conduction problem. The temporal coupling is explicit. A general interface (GI) is used to manage the passing of variables according too the mapping between the thermal hydraulic and neutronic model from RELAP5 to PARCS and vice versa. Both GI and PARCS are executed as separate processes communicating to each other via the message-passing protocol of the Parallel Virtual Machine (PVM).

1.3 Evaluation of RELAP5 for innovative reactor concepts (HPLWR)

As new reactor concept, the High Performance Light Water Reactor (HPLWR) is being analyzed within 5th Framework Program of the EU /7/. The main advantage is the significantly improved thermodynamic efficiency. Essential for the HPLWR-concept is the operation of the reactor at supercritical pressure of app. 25 MPa while the coolant temperature over the core height varies from 553 K to 778 K. Under such conditions the single phase coolant changes from single phase pseudo-liquid to single phase pseudo-vapor. In this supercritical domain is well know that sharp changes of fluid properties like density, heat capacity, etc. /8/, /9/ occur as shown in Figure 2.

At IRS the applicability of the RELAP5 code system on such innovative reactors is being assessed to ensure a reliable simulation of plant conditions during normal operation, operational transients, and accidents. Since RELAP5 was not developed for supercritical fluid conditions and hence never validated for such situations, investigations are focused on evaluation of fluid (water) properties in the supercritical regime and relevant heat transfer correlation. Since some thermodynamic inconsistencies in the ASME-67 steam table were identified that lead to large mass errors, a new formulation of the steam table called IAPWS-95 (scientific formulation, similar to the IAPWS-IF97 /11/, industrial formulation) is being incorporated in the new version RELAP5/MOD3.3 which will be

distributed in 2001 /12/. The consistency of the ASME-67 and IAPWS-IF97 steam tables have been investigated. No large discrepancies of important steam properties were found.

To test the appropriateness of RELAP5 to simulate the HPLWR-reactor a simplified plant model was developed for the RELAP5/MOD3.2.2γ to simulate the stationary plant conditions as a starting point for following study of any kind of transients and accidents.

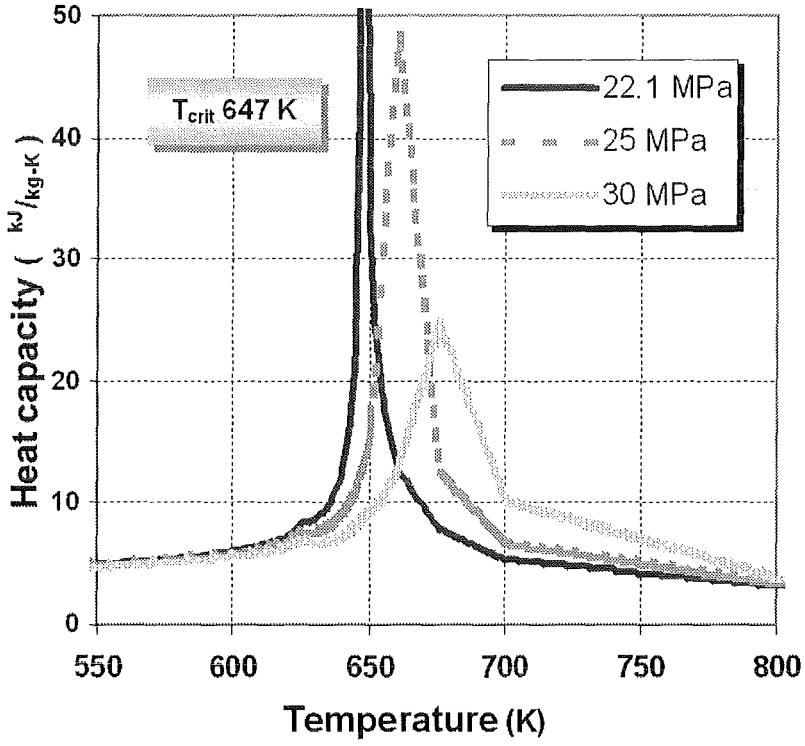

Figure 2 Specific heat capacity of water in the supercritical regime for 3 different pressures.

In the first attempt RELAP5 failed to predict reasonable steady state plant parameters due to numerical errors when the fluid temperature exceeds the pseudo-critical temperature for the given system pressure (25 MPa). After detailed evaluation, it was found that the steam tables, which were optimized for normal operation, did not adequately represent the water properties around critical point due to a rather coarse temperature and pressure mesh used to generate the water properties look-up table. After a rebuilt of the steam tables of RELAP5 (ASME-67 /10/) considering the strong gradients in the vicinity of the critical point adequately with a finer mesh, RELAP5 was enable to calculated conditions in the supercritical regime and to calculate reasonable steady state parameters for the newly developed plant model.

So additional assessment of this RELAP5/MOD3.2.2 γ and/or the new version RELAP5 MOD3.3β seems to be necessary for the HPLWR-project. Furthermore, a re-evaluation of the heat transfer mechanisms between fuel rods and fluid at supercritical conditions is necessary to perform design studies and safety analysis of the HPLWR.

1.3.1 Literature

/1/ Scientec Thermohydraulic Group, RELAP5/MOD3 Code Manuals Vol. 1-8, Formerly NUREG/CR-5535, June 1999.

/2/ K. N. Ivanov, T. M. Beam and A. Baratta; Pressurised Water Reactor main Steam Line Break (MSLB) Benchmark. Volume 1: Final Specifications. NEA/NSC/DOC(99)8. April 1999.

/3/ C. J. Jackson, H. Finnemann, Verification of the Coupled RELAP5/PANBOX2 System with the NEACRP LWR Core Transient Benchmark. International Conference on Mathematics and Computations, Reactor Physics, and Environmental Analyses. Pp.297-306. Portland Oregon. April 30-May 4. 1995.

/4/ V. Sánchez, A. Knoll; Analyses of the International Main Steam Line Break (MSLB)-Benchmark with the Code System RELAP5/MOD3.2 using the Point Kinetics Option. Report FZK-6427, 2001.

/5/ V. Sánchez, Ch. Homann, R. Böer, FZK/Siemens Investigations on MSLB-Phase 3 with the "Best-Estimate" Code System RELAP5/PANBOX . 16 Spring 2000 CAMP-Meeting. 17-19 April 2000. Sicily, Italy.

/6/ D. A. Barber, T. J. Downar, W. Wang; Final Completion of Report for the Coupled RELAP5/PARCS. Report PU/NE-98-31. November 1998.

/7/ G. Heusener, U. Müller, T. Schulenberg, D. Squarer; A European Development Program for a High Performance Light Water Reactor. , SCR-2000, Nov. 6-8, 2000

/8/ Dobashi, K. Oka, Y., Koshizuka, S., Conceptual Design of a High Temperature Power Reactor Cooled And Moderated By Supercritical Light Water; ICONE-6, May 10-15, 1998, ASME, NY.

/9/ Oka, Y. Koshizuka, S., Design Concept of Once-Through Cycle Supercritical-Pressure Light Water Cooled Reactors; SCR-2000, Nov. 6-8, 2000.

/10/ ASME Steam Tables Thermodynamic and Transport Properties of Steam. American Society of Mechanical Engineering. 1967.

/11/ Wagner, W. at al., The IAPWS industrial Formulation 1997 for the Thermodynamic Properties of Water and Steam. IAPWS Secretariat 1997.

/12/ Mortensen, G., RELAP5 Steam Tables. CAMP-Meeting. Sicily april.2000

32.22 INNOVATIVE SYSTEME

32.22.03 Entwicklung von Methoden zur Grobstruktursimulation turbulenter Zweiphasenströmungen

Theoretische Untersuchungen
(M. Wörner, D.G. Cacuci, B. Ghidersa, G. Grötzbach, W. Sabisch, IRS)

Zusammenfassung

Für die detaillierte numerische Simulation von Zweiphasenströmungen wurde das Rechenprogramm TURBIT-VOF entwickelt. Rechnungen mit TURBIT-VOF für Einzelblasen unterschiedlicher Form zeigen eine sehr gute Übereinstimmung mit experimentellen Ergebnissen. Die Leistungsfähigkeit des Rechenprogramms wird insbesondere durch die Simulation einer forminstabilen Blase aufgezeigt, welche einen turbulenten Nachlauf besitzt und auf einer unregelmäßigen Spiralbahn aufsteigt. Die Ergebnisse derartiger Rechnungen werden zukünftig in die Entwicklung von physikalischen Modellen einfließen, wie sie für die Grobstruktursimulation von Zweiphasenströmungen und die auf einer statistischen Beschreibung basierenden ingenieurtechnischen Rechencodes benötigt werden.

1. Einleitung

Ziel dieses Vorhabens ist die Bereitstellung von numerischen Methoden und physikalischen Modellen, mit denen lokale Vorgänge in turbulenter Zweiphasenströmung unter Einbeziehung der Information über die zeitliche Entwicklung der Phasengrenze detailliert simuliert werden können. Die Arbeiten bauen zunächst auf grundlegenden Untersuchungen zu turbulenten Blasenströmungen auf. Die Ergebnisse und Erfahrungen werden verwendet, um die Methode und physikalischen Modelle in anwendungsorientierten Rechenprogrammen für allgemeine Zweiphasenströmungen verfügbar zu machen.

Die numerische Methode stellt eine Erweiterung des von einphasigen Strömungen her bekannten Konzeptes der Grobstruktursimulation auf zweiphasige Strömungen dar. Für den durch das Rechengitter aufgelösten Anteil erfolgt sowohl eine lokale, momentane Beschreibung der Turbulenz als auch eine detaillierte Beschreibung der Dynamik der

Phasengrenzfläche. Die Methodenentwicklung konzentriert sich zunächst auf den Grenzfall eines sehr feinen Rechengitters, bei dem sowohl die kleinsten Wirbel als auch die kleinsten Blasen aufgelöst werden („DNS-RBS" = direct numerical simulation - resolved bubble simulation).

2. Rechenprogramm TURBIT-VOF

Die DNS-RBS Methode wurde im Rechenprogramm TURBIT-VOF realisiert [1]. Die mathematische Beschreibung der zeitlichen Entwicklung der Phasengrenzfläche erfolgt mit der Volume-of-Fluid-Methode (VOF). Dabei wird die Phasenverteilung im Rechengebiet durch den Volumenanteil der Flüssigkeit in einer Gitterzelle beschrieben. Für diese Volumenfraktion gilt $0 \leq f \leq 1$, wobei in reinen Gaszellen $f = 0$, in reinen Flüssigkeitszellen $f = 1$ und in zweiphasigen Zellen $0 < f < 1$ ist. Für die Rekonstruktion der Phasengrenzfläche aus der räumlichen Verteilung der diskreten Werte des Flüssigkeitsanteils in den Maschen wurde der EPIRA-Algorithmus [1,2] entwickelt, der eine beliebig orientierte ebene Grenzfläche stets exakt rekonstruiert.

Die Kontinuitäts- und Impulsgleichungen sind in TURBIT-VOF dimensionslos und für inkompressible Phasen formuliert [3]. Die Gleichungen werden mit hochauflösenden numerischen Verfahren gelöst, die die Anwendung auf die direkte numerische Simulation turbulenter Strömung erlauben. Die Oberflächenspannung wird als lokale Volumenkraft beschrieben. Die Verifizierung von TURBIT-VoF erfolgte anhand verschiedener Testprobleme für ein- und zweiphasige Strömungen. Dabei wurde jeweils eine sehr gute Übereinstimmung mit analytischen Lösungen oder Arbeiten aus der Literatur erzielt [1].

3. Vergleich der Rechenergebnisse für Einzelblasen mit Experimenten

Für Einzelblasen, die im Schwerefeld in einer Flüssigkeit frei aufsteigen, gibt es acht Einflussgrößen $(\rho_l, \rho_g, \mu_l, \mu_g, \sigma, g, d_{Bl}, U_{Bl})$ mit drei Basisdimensionen (kg, m, s) [4]. Dabei ist ρ die Dichte, μ die dynamische Viskosität, σ die Oberflächenspannung, g die Schwerebeschleunigung, d_{Bl} der äquivalenter Blasendurchmesser, U_{Bl} die Aufstiegsgeschwindigkeit der Blase und der Index l kennzeichnet die flüssige und der Index g die gasförmige Phase. Nach dem Π-Theorem von Buckingham gibt es somit $8 - 3 = 5$ unabhängige dimensionslose Kennzahlen, die das physikalische Problem beschreiben. Dies sind die Reynolds-Zahl Re_{Bl}, die Eötvös-Zahl $Eö_{Bl}$, die Morton-Zahl M

$$\mathrm{Re_{Bl}} = \frac{\rho_l d_{Bl} U_{Bl}}{\mu_l}, \quad \mathrm{Eö_{Bl}} = \frac{g d_{Bl}^2 (\rho_l - \rho_g)}{\sigma}, \quad \mathrm{M} = g\mu_l^4 \frac{\rho_l - \rho_g}{\rho_l^2 \sigma^3},$$

sowie das Dichteverhältnis $\Gamma_\rho = \rho_g / \rho_l$ und das Viskositätsverhältnis $\Gamma_\mu = \mu_g / \mu_l$.

Mit TURBIT-VOF wurden Simulationen für vier verschiedene Kombinationen von Morton-Zahl M und Eötvös-Zahl $\mathrm{Eö_{Bl}}$ durchgeführt [1,2], siehe Tabelle 1. Diese Rechnungen erfolgten für einen Kanal zwischen zwei vertikalen parallelen Wänden. Bei den hier vorgestellten Ergebnissen ist das würfelförmige Rechengebiet in 64^3 Maschen unterteilt. Für Fall ❶ startet die Simulation mit einer kugelförmigen Blase in Kanalmitte. Flüssigkeit und Gas sind anfangs in Ruhe. Der Blasendurchmesser d_{Bl} ist ein Viertel des Wandabstandes und damit mit 16 Maschen aufgelöst. Der Gasgehalt im Rechengebiet ist etwa 0,8 %. Um Rechenzeit zu sparen wird bei den Fällen ❷, ❸ und ❹ die Lösung von Fall ❶ als Startwert vorgegeben. In Aufstiegs- (*x*) und Spannweitenrichtung (*y*) werden periodische Randbedingungen verwendet. Dadurch wird nicht eine Einzelblase, sondern ein regelmäßig angeordnetes Feld unendlich vieler Blasen mit vorgegebenem Abstand abgebildet. Jede Blase steigt in ihrem eigenen Nachlauf auf. Damit ist i.a. ein Vergleich mit Experimenten für Einzelblasen nur qualitativ sinnvoll. Geeigneter für einen Vergleich wären Experimente mit Blasenfolgen, bei denen die Blasenbildungsfrequenz so eingestellt ist, dass der vertikale Abstand aufeinanderfolgender Blasen genau der Periodenlänge in Aufstiegsrichtung bei der Simulation entspricht. Für eine Untersuchung des Einflusses von Gitter (128^3) und Größe des Rechengebietes verweisen wir auf [1].

Die Rechnungen wurden mit $\Gamma_\rho = 1/2$ und $\Gamma_\mu = 1$ durchgeführt. Durch schrittweise Verkleinerung von Γ_ρ gelingt es, ausgehend von der zuvor berechneten Lösung als neue Anfangsschätzung, eine Lösung auch für sehr kleine Dichteverhältnisse zu erreichen. Allerdings benötigen sehr kleine Dichteverhältnisse aus numerischen Gründen sehr kleine Zeitschrittweiten und bewirken damit sehr hohe Rechenzeiten. Die Rechnungen wurden auf einem Prozessor eines Fujitsu VPP 300 Hochleistungsrechners durchgeführt. Eine Simulation umfasst typischerweise einige tausend bis 10 000 Zeitschritte. Die Rechenzeit liegt je nach Fall bei bis zu einigen hundert CPU-Stunden.

Zum Vergleich der Simulationsergebnisse mit Experimenten dienen Form und Nachlauftyp der Blase sowie $\mathrm{Re_{Bl}}$ als die dimensionslose Steiggeschwindigkeit. Es ist zu beachten,

dass die Ähnlichkeit von $Eö_{Bl}$ und M gegeben ist, nicht jedoch die von Γ_ρ und Γ_μ. Für Fall ❶ stellt sich eine ellipsoidförmige Blase mit geschlossenem Nachlauf ein. Der Vergleich des Verhältnisses der Halbachsen *E* mit der experimentell ermittelten Korrelation $E = 1/\left(1 + 1{,}63\,\mathrm{Eo}^{0{,}757}\right)$, gültig für $Eö_{Bl} < 40$ und $\log_{10} M \leq -6$, aus [5] zeigt eine gute Übereinstimmung, siehe Tabelle 2. Auch Re_{Bl} liegt in dem in Experimenten beobachteten Bereich. Offensichtlich sind die Ähnlichkeitsparameter Γ_ρ und Γ_μ hier nur von untergeordneter Bedeutung.

Die Eötvös- und Morton-Zahl von Fall ❷ entsprechen den Werten in einem Experiment von Bhaga und Weber [6] für eine Luftblase in wässriger Zuckerlösung ($\Gamma_\rho \approx 1/1000$). Abb. 1 zeigt die stationäre Blasenform in Experiment und Rechnung. Es handelt sich um eine abgeflachte ellipsoidförmige Kappenblase („oblate ellipsoidal cap"). Typisch ist die Einbuchtung am Unterteil der Blase. Die Abflachung der Blase ist im Experiment stärker als in der Rechnung. Dies liegt vermutlich an den periodischen Randbedingungen der Simulation, aufgrund derer die Blase im Nachlauf der vorlaufenden Blase einen geringeren Widerstand erfährt. Möglicherweise spielt hier aber auch das unterschiedliche Dichte- und Viskositätsverhältnis in Experiment und Rechnung eine Rolle.

Für Fall ❹, dessen Morton-Zahl der von Luft-Blasen in Wasser entspricht, stellt sich in Übereinstimmung mit Experimenten [7] eine nahezu sphärische Blase ein. Die Tatsache, dass sich in den dreidimensionalen Simulationen auf einem kartesischen Gitter in den Fällen ❶, ❷ und ❹ rotationssymmetrische Blasen einstellen, spricht für die Genauigkeit des numerischen Verfahrens und der Modellierung der Oberflächenspannung.

Von besonderem Interesse ist Fall ❸, für den eine forminstabile oszillierende Blase erwartet werden kann [8]. Tatsächlich wird in der Simulation die als Anfangslösung vorgegebene geradlinige Aufstiegsbahn der Blase von Fall ❶ instabil, wie die Bahnkurve in Abb. 2 zeigt. Man erkennt in den Projektionen, dass die Blase in der *x*-*y*-Ebene zunächst noch geradlinig aufsteigt, während sie in der *y*-*z*-Ebene unmittelbar eine seitliche Schwingung ausführt. Kurz darauf setzt auch in der *x*-*y*-Ebene eine Pendelbewegung ein. In der Projektion von oben (*y*-*z*-Ebene) ergibt dies eine (unregelmäßige) Spiralbahn. Derartige auf einer Schraubenbahn aufsteigende Einzelblasen mit Re_{Bl}=O(1000) wurden z.B. von Brücker [9] experimentell untersucht.

Abb. 3 zeigt Momentanergebnisse der Simulation für Blasenform und Geschwindigkeitsfeld in zwei Schnittebenen zu zwei verschiedenen Zeitpunkten. Zu Beginn der Simulation (Abb. 3 oben) sind die Blasenform und das Geschwindigkeitsfeld noch weitgehend symmetrisch und regelmäßig. Im Verlauf der Simulation oszilliert die Blasenform unregelmäßig und die Strömung im Nachlauf der Blase wird turbulent (Abb. 3 unten).

4. Schlussfolgerungen und Ausblick

Mit den vorgestellten Rechnungen für Blasen mit unterschiedlicher Form und Steigverhalten wurde gezeigt, dass alle wesentlichen physikalischen Phänomene in der Simulation erfasst sind. Das Rechenprogramm TURBIT-VOF ist in der Lage, auch forminstabile Blasen mit offenem turbulentem Nachlauf zu beschreiben, wie sie für viele technische Anwendungen in Apparaten der Energie- und Verfahrenstechnik typisch sind. Die Ergebnisse belegen die Leistungsfähigkeit der Methode und ihr Potenzial zur Erweiterung des physikalischen Verständnisses. Darüber hinaus liegt der besondere Wert der Simulationen in der Bereitstellung einer konsistenten Datenbasis mit hoher räumlich-zeitlicher Auflösung, die für zukünftige Entwicklungen verbesserter physikalischer Modelle und deren Umsetzung in technisch anwendbaren Rechenprogrammen dienen kann.

Literatur

1 W. Sabisch: Dreidimensionale numerische Simulation der Dynamik von aufsteigenden Einzelblasen und Blasenschwärmen mit einer Volume-of-Fluid-Methode. Forschungszentrum Karlsruhe, Wissenschaftliche Berichte FZKA 6478, Juni 2000
(s. a. http://www.fzk.de/hbk/literatur/FZKA_Berichte/FZKA6478.pdf).

2 W. Sabisch, M. Wörner, G. Grötzbach, D.G. Cacuci: 3D volume-of-fluid simulation of a wobbling bubble in a gas-liquid system of low Morton number. 4th International Conference on Multiphase Flow, New Orleans, Louisiana, U.S.A., May 27 – June 1, 2001, paper 244.

3 M. Wörner, W. Sabisch, G. Grötzbach, D.G. Cacuci: Volume-averaged conservation equations for volume-of-fluid interface tracking. 4th Int. Conference on Multiphase Flow, New Orleans, Louisiana, U.S.A., May 27 – June 1, 2001, paper 245.

4 J.R. Grace: Shapes and velocities of bubbles rising in infinite liquids. Trans. Instn. Chem. Eng. 51, 116-120, 1973.

5 R.M. Wellek, A.K. Agrawal, A.H.P. Skelland: Shape of liquid drops moving in liquid media, AIChE Journal *12* (1966) S. 854.

6 D. Bhaga, M.E. Weber: Bubbles in viscous liquids: shapes, wakes and velocities, J. Fluid Mech. 105 (1981) S. 61.

7 G. Grötzbach, V. Heinzel, A. Jianu, P. Philipp, H. Sauter, W. Sengpiel, M. Simon: Experimentelle Untersuchung zum Strömungsumfeld aufsteigender Gasblasen in ruhendendem Fluid und dessen Wechselwirkung mit dem Aufstiegsverhalten der Blasen. Projekt Nukleare Sicherheitsforschung Jahresbericht 1999, Forschungszentrum Karlsruhe, Wissenschaftliche Berichte FZKA 6480, August 2000.

8 R. Clift, J.R. Grace, M.E. Weber: Bubbles, Drops, and Particles. Academic Press, New York, 1978.

9 Ch. Brücker: Structure and dynamics of the wake of bubbles and its relevance for bubble interaction, Physics of Fluids 11 (1999) 7, S. 1781.

Tabelle 1: Eötvös- und Morton-Zahlen der Simulationen.

Fall	Eö	$\log_{10}$ M
❶	3,07	-5,51
❷	243	2,42
❸	0,2	-10,6
❹	3,07	-9,6

Tabelle 2: Vergleich experimenteller und berechneter Werte von Halbachsenverhältnis *E* und Reynolds-Zahl Re_{Bl} für die ellipsoide Blase (Fall ❶).

	Experiment [5]	Simulation
E	0,72	0,71
Re_{Bl}	50...70	61,5

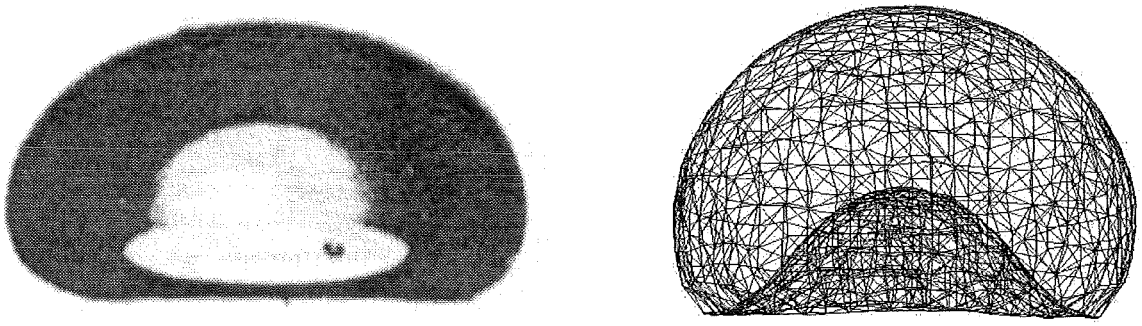

Abb. 1: Stationäre Form der ellipsoiden Kappenblase in Experiment (links, [6]) und Simulation (rechts).

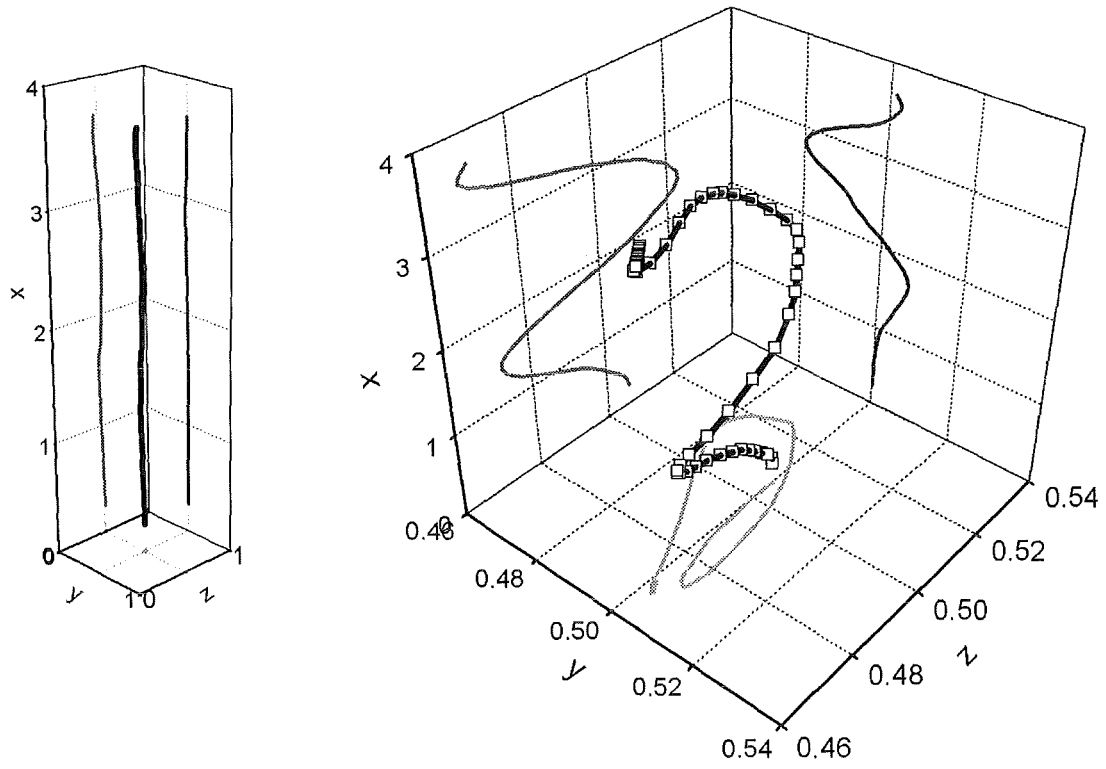

Abb. 2: Bahnkurve des Blasenschwerpunktes (x(t), y(t), z(t)) der forminstabilen Blase (Fall ❸) in perspektivischer Ansicht (dicke Linie) und als Projektion (dünne Linien) in die *x-y*-, *x-z*- und *y-z*-Ebene. Links: Darstellung mit einer Achsen-Skalierung entsprechend der Kanalgeometrie, rechts: Darstellung mit gespreizter *y*- und *z*-Achse.

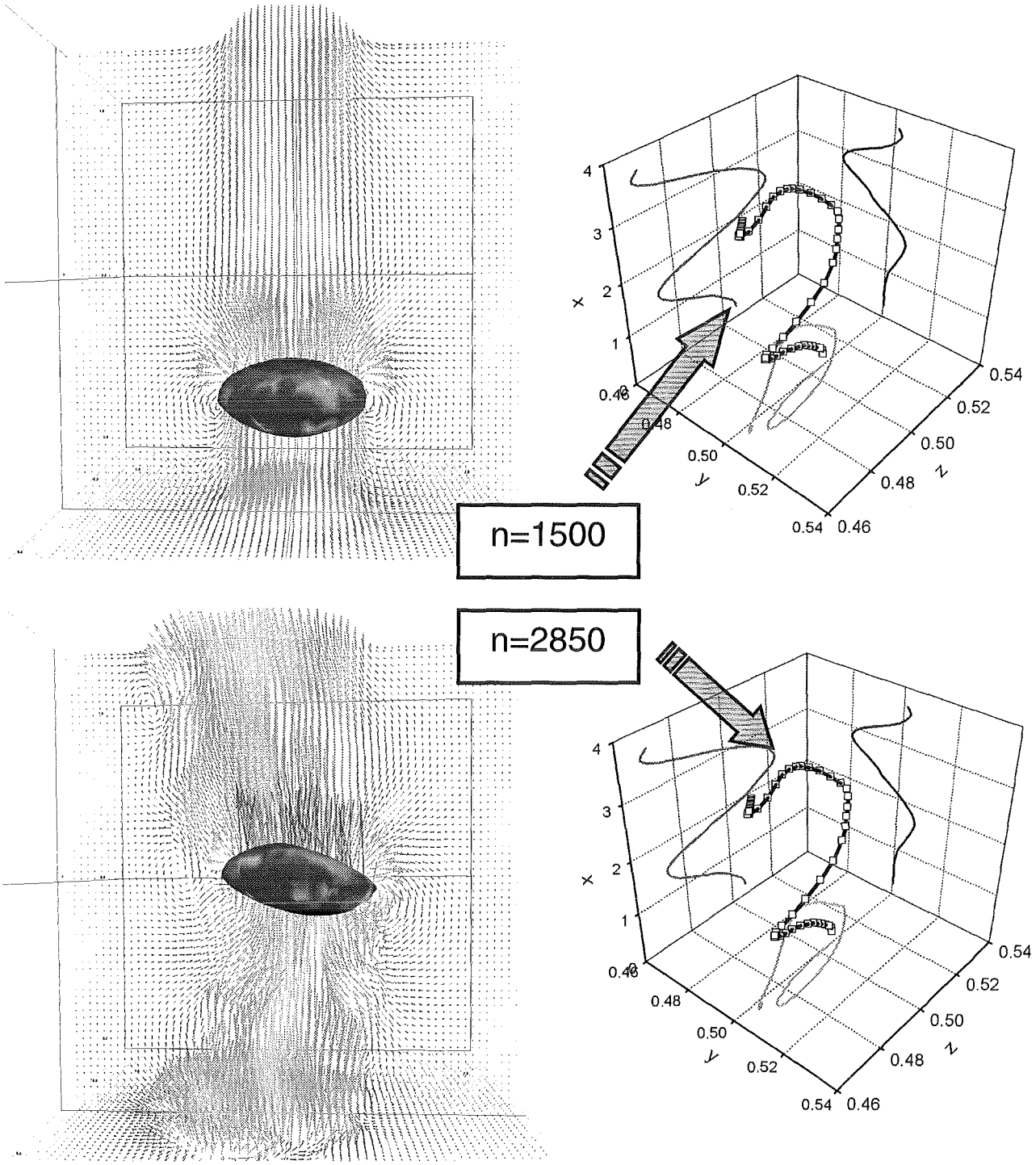

Abb. 3: Forminstabile Blase (Fall ❸): Visualisierung der Phasengrenzfläche und des Geschwindigkeitsfeldes (Vektoren) in den Schnittebenen $x = 0$ und $y = 0.5$ zu zwei verschiedenen Zeitpunkten. Oben: Zeitschritt $n = 1500$, unten: Zeitschritt $n = 2850$. In der rechten Bildhälfte ordnet der Pfeil dem jeweiligen Zeitpunkt den zugehörigen Punkt auf der Trajektorie des Blasenschwerpunktes zu.

32.22.04 Strukturelle Integrität

I. Untersuchungen an Strukturmaterialien der Kerntechnik

(M. Schirra, P. Graf, A. Falkenstein, S. Heger, E. Materna-Morris, IMF I)

Abstract

„Structural integrity" summarises several research activities: The examination of creep and creep rupture behaviour of the austenitic steel 316 L(N)-DIN 1.4919 on low stress levels at 550 and 600°C; Investigations on swelling, irradiation creep and related microstrucutral changes in several austenitic alloys under high-fluence irradiations (PFR-experiment) and the fracture analysis of ferritic and austenitic reactor steels under variable deformation rates and for different sample geometries are further topics of experimental investigations.

Zusammenfassung

In diesem Vorhaben sind mehrere Aktivitäten des IMF I zusammengefasst. Untersuchungen zum Kriech- und Zeitstandfestigkeitsverhalten werden am Werkstoff 316 L(N)-DIN 1.4919 bei 550 und 600°C im anwendungsrelevanten Spannungsbereich unterhalb der 0,2 %-Steckgrenze durchgeführt. Im Bestrahlungsprojekt PFR-M2 sind Untersuchungen zum Schwell- und Kriechverhalten und zur mikrostrukturellen Entwicklung unter Bestrahlung an verschiedenen Stählen abgeschlossen und dokumentiert worden. Das Bruchverhalten zweier LWR-Reaktorstähle wird für unterschiedliche Probengeometrien und stark variierende Verformungsgeschwindigkeiten studiert.

1. Langzeitkriechversuche am Strukturwerkstoff 316 L(N)

1.1 Einleitung

Der in der Reaktortechnik häufig eingesetzte austenitische 17/12/2-CrNiMo-Stahl 316 L(N)-DIN 1.4909 wurde auch für das im europäischen Rahmen geplante Brüterprojekt (EFR) als Anlagenstrukturwerkstoff gewählt. Das Zeitstandfestigkeits- und Kriechverhalten dieses Stahltyps ist im üblichen Spannungs- und Temperaturbereich experimentell gut untersucht, u. a. durch eigene Arbeiten an 3 Chargen im T-Bereich

500 – 750°C und für Standzeiten bis 80000 h. Im auslegungsrelevanten niedrigen Spannungsbereich bei 550 und 600°C ist dagegen ein völliger Mangel an Daten festzustellen, die z. B. eine Aussage zur Spannungsabhängigkeit der minimalen Kriechgeschwindigkeit oder der technisch wichtigen Zeit-Dehngrenzen erlauben würden. Dies hat nicht nur zeitliche, sondern vor allem technische Gründe. In diesem σ/T-Bereich sind die zu erwartenden Kriechraten bzw. Dehnbeträge so gering, dass sie sich im konventionellen Zeitstandversuch messtechnisch kaum erfassen lassen.

Die Bestimmung von Kriechdaten für die Aufstellung zuverlässiger konstitutiver Gleichungen zum Werkstoffverhalten wurde für absolut notwendig erachtet, und das FZK/IMF I erklärte sich bereit, spezielle Langzeitkriechversuche bei 550 und 600°C durchzuführen.

1.2 Stand der Untersuchungen

Im Jahresbericht 1999 (FZKA 6480) ist ausführlich die Versuchsdurchführung und der Stand bis 70000 h beschrieben worden. Erst durch die IMF-Versuche im niedrigen Spannungsbereich konnte die Spannungsabhängigkeit der minimalen Kriechgeschwindigkeit in der europäischen Datensammlung [1] für diesen Stahl im auslegungsrelevanten Spannungsbereich sicher bestimmt werden.

In der Zwischenzeit sind die Versuche weitergeführt worden. Der Stand bis 80000 h Versuchszeit ist ausführlich in einem Beitrag zur Swansea-Conference beschrieben worden [2]. Die Versuche werden in 2001 bis zu einer Gesamtlaufzeit von 85000 h weitergeführt und das Programm qualifiziert abgeschlossen. Bis dahin liegen weitere Daten zu den technologisch wichtigen Zeit-Dehngrenzen vor (0,01 – 1 %), so dass auch die sich ändernde Spannungsabhängigkeit der Zeit-Dehngrenzen klar aufgezeigt werden kann.

Literatur

[1] D. Lehmann; Evaluation of the stress to rupture and creep properties of type 316 L(N) steel for design use. Final report. EUR 16168 EN, 1995

[2] M. Schirra ; Long-term studies on the creep behaviour of the structural material 316-L(N) in the low-stress range at 500 and 600°C, 9th Intern. Conf. on Creep and Fracture, Swansea 1. – 6.4.2001, Proceedings, pp. 669 – 678.

[3] T. Nakazawa, H. Kimura, H. Komatsu, H. Kaguchi, M. Koto, M. Schirra; "Creep rupture properties and microstructure of european and japanese type low-carbon medium nitrogen 316 steel".

2. Fraktografische Untersuchungen an geprüften Zugproben aus ferritischen und austenitischen LWR-Stählen

Die Ergebnisse der Bruchuntersuchungen an zwei LWR-Reaktorstählen mit unterschiedlichen Probengeometrien und Dehngeschwindigkeiten wurden dokumentiert (FZKA 6525, demnächst)

II. Investigations to Size Effects on Deformation and Failure Behavior of Specimens Including a Center Hole

(Aktaa, M. Klotz, M. Pfeifenroth, R. Schmitt, IMF II)

In the European research project LISSAC (**Li**mit **S**trains for **S**evere **A**ccident **C**onditions) the size influence on material properties, e.g. failure strain, needed for the best possible assessment of components failure due to severe accident is investigated.

Tensile tests at room temperature with specimens of similar geometry and different sizes, cut from the wall of a real reactor vessel are performed. The investigations have been started with flat specimens include a central hole. The hole is incorporated to obtain inhomogeneous deformation with high strain gradients, which will be higher in the smaller specimens and might be responsible for size effects. To collect a lot of information about deformations in the hole surrounding area appropriate measuring techniques are used.

Meanwhile the tests with 4, 20, 40 and 80 mm thick specimens were performed. The smaller specimens, 4 and 20 mm thickness, are tested at Forschungszentrum Karlsruhe (FZK) whereas the bigger ones at Staatliche Materialprüfungsanstalt (MPA). For the experiments at FZK servo-hydraulic testing machines are used with a capacity of 160 and 630 kN, respectively. At the MPA, testing machines with capacities up to 100 MN can be applied.

In a first comparison the measured nominal stress (force divided by the initial minimal cross section area) versus the global strain measured by the axial extensometer (elongation divided by the gauge length L_0) is plotted for the four scaled specimens in Fig 1. The curves show up to maximum load no distinctive difference and therewith no size effects on the global deformation behavior. The specimens pronounced yield points for the weakened and the full section could be detected. The yield and the maximum stress in the weakened sections of the 20 and 40 mm thick specimens exceeded slightly the values of standardized material tests (0.2-YS $\approx$ 440 MPa, UTS $\approx$ 600 MPa). After exceeding the elongation before reduction, a drop in loading was found out caused by crack initiation and stable crack growth partly up to final separation depending on the stiffness of the tensile testing machine. However a significant

size effect on failure strain could be identified: The bigger the specimen the lower is the failure strain.

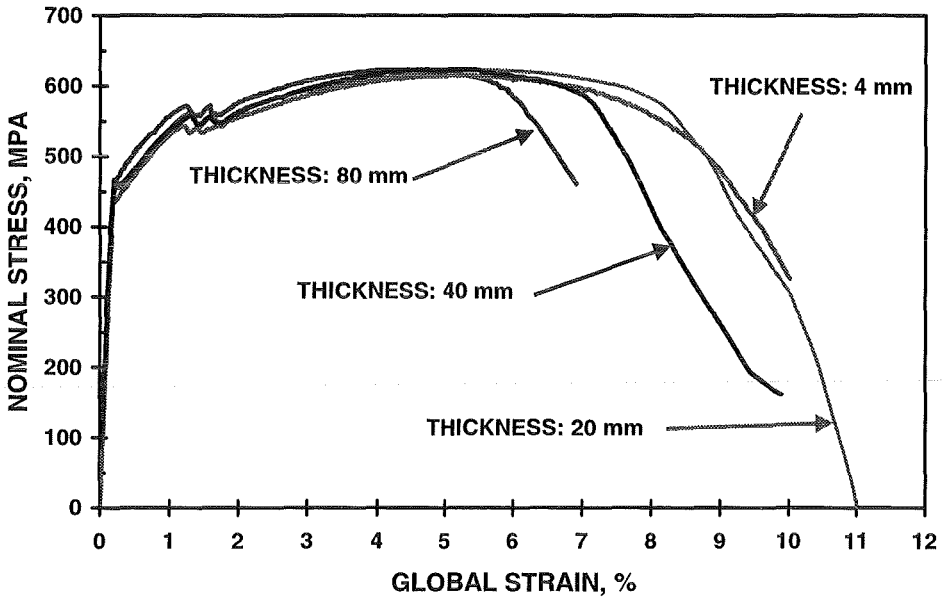

Fig. 1 Nominal stress vs. global strain for the different sized specimens in comparison

32.22.06 Untersuchungen zum Brennstoff- und Brennstabverhalten innovativer Systeme

Theoretische Interpretation der Ergebnisse des CABRI- Programms

(D. Struwe, W. Pfrang, W. Zimmerer, IRS)

Die Untersuchungen zum transienten Brennstabverhalten erfolgen im Rahmen der experimentellen Programme CABRI- FAST und CABRI- RAFT, die in internationaler Zusammenarbeit mit dem französischen IPSN und dem japanischen JNC durchgeführt werden. Diese Programme komplettieren die Arbeiten zur Untersuchung des transienten Brennstabverhaltens konventioneller und innovativer Brennstabkonzepte, die schon im Rahmen der Programme CABRI- 1 und CABRI- 2 begonnen wurden. Im Mittelpunkt der Arbeiten stand die Überprüfung der theoretischen Modelle zum transienten Brennstabverhalten und zu Bestimmung von Versagensschwellen als Folge der unterschiedlichsten Leistungstransienten. Die Ergebnisse dieser neuerlichen Überprüfung der im SAS4A Programm DEFORM integrierten theoretischen Modelle zur Brennstabdynamik sind in den Tabellen zusammengefasst dargestellt. Die in den einzelnen Versuchen experimentell ermittelten Bedingungen des Brennstabversagens sind den theoretisch berechneten Werten gegenüber-gestellt. Für einen weiten Bereich von Brennstabkonzepten und Leistungstransienten kann eine zufriedenstellende Übereinstimmung zwischen Experiment und Theorie festgestellt werden.

Für die Experimente, bei denen Brennstofftabletten mit einem großen Zentralkanal zum Einsatz kamen, konnten die experimentellen Ergebnisse nur dann vernünftig interpretiert werden, wenn der von IPSN bereitgestellte Programm Modul EJECT zum Einsatz kam. Dieser Modul beschreibt die Brennstoffbewegung im Zentralkanal vor und nach Brennstabversagen. Er musste prinzipiell überarbeitet werden. Die unterschiedlichen Modelloptionen wurden an den experimentellen Ergebnissen überprüft. Der heute erreichte Stand der Modellqualifizierung erlaubt es, die experimentellen Befunde mit ausreichender Genauigkeit berechnen zu können.

Results of Fuel Pin Failure Calculations

SAS4A.Ref99.R3-mod FZKA

Experi-ment	Time into the power transient [ms]		Axial location [cm_{bfc}]		Peak fuel ent-halpy (kJ/kg) 10^{-6}	Melt cavity press. MPa	mid wall clad temp. K
	exp.	calc.	exp.	calc.			
AI2	230	238.3 (+8.3)	43-49	47-51	1.12	70.6	1101
AI3	82	81.7 (-0.3)	43-45	47-51	1.18	86.1	962
BI2	79	78.5 (-0.5)	49-53	47-51	1.11	58.9	1150
BI4	88	94.1 (+6.1)	51-53	47-51	1.12	49.0	1347
BI6	63-64	63.7	42; 57	38-42	1.11	43.2	1226
BI3[1]	69-82	78.1	43-51	47-51	0.98	3.5	1686
BI5[1]	55-60	60.7	35-53	51-55	1.02	20.3	1662
AGS3	525	541.3 (+16.3)	45-47	47-51	1.04	160.8	1017
BGS0[1]	500-600	534	32-60	43-47	0.97	7.3	>1700
BGS3	520-548	535.1	31-55	43-47	0.96	11.3	1377
BGS4[1]	500-555	540.3	28-64	43-47	0.96	12.1	>1700

[1] fuel melt fraction dominated

Results of Fuel Pin Failure Calculations

SAS4A.Ref99.R3-mod FZKA

Experi-ment	Time into the power transien [ms] exp.	calc.	Axial location [cm_{bfc}] exp.	calc.	Peak fuel ent-halpy (kJ/kg) 10^{-6}	Melt cavity press. MPa	mid wall clad temp. K
E6	564-567	582.5 (+17.5)	50-54	52-56	0.97	62.2	1116
E2	570	571.5 (+1.5)	48-52	52-56	0.90	38.0	1142
E3[3]	370	(370)[3]	44-60	(50-70)[3]	(0.83)	(10.7)	(1270-1300)
	(475-500)	468.9[1]	(30,70)	48-52	0.90	31.8	1390
E13[1]	250-350	273.5	40-70	52-56	0.97	7.8	>1700
							>1700
E11[1]	(-3600-150)	-282	45-60	57-61	0.98	17.5	
E12	76000	81554 (+5554)	56-65	57-61	0.79	73.1	1000
BCF1	28400	29299 (899)	~60	53-57	0.80	75.5	993
E7	467	472.4 (+5.4)	53-56	50-54	1.42	51.3	1074
E8	523-524[3]	(524)[3]	51-57				
	(527-540)	542.3 (17.3)	51-57	54-58	1.06	35.1	1360
EFM1	380-480	363.2	41-51	42-46	1.00	4.7	>1700
LT4	621	598	63	52-46		12.0	1318
LT1	(385) 535-570	560	52	49-53	0.97	29.4	1254

[1] fuel melt fraction dominated

[3] local fuel melt fraction below 1% fission gas ejection only

Results of Fuel Pin Failure Calculations

SAS4A.Ref99.R3-mod FZKA

Experi-ment	Time into the power transient [ms]		Axial location [cm_{bfc}]		Peak fuel enthalpy (kJ/kg) 10^{-6}	Melt cavity press. MPa	mid wall clad temp. K
	exp.	calc.	exp.	calc.			
AI2	230	238.3 (+8.3)	43-49	47-51	1.12	70.6	1101
AI3	82	81.7 (-0.3)	43-45	47-51	1.18	86.1	962
BI2	79	78.5 (-0.5)	49-53	47-51	1.11	58.9	1150
BI4	88	94.1 (+6.1)	51-53	47-51	1.12	49.0	1347
BI6	63-64	63.7	42; 57	38-42	1.11	43.2	1226
BI3[1]	69-82	78.1	43-51	47-51	0.98	3.5	1686
BI5[1]	55-60	60.7	35-53	51-55	1.02	20.3	1662
AGS3	525	541.3 (+16.3)	45-47	47-51	1.04	160.8	1017
BGS0[1]	500-600	534	32-60	43-47	0.97	7.3	>1700
BGS3	520-548	535.1	31-55	43-47	0.96	11.3	1377
BGS4[1]	500-555	540.3	28-64	43-47	0.96	12.1	>1700

[1] fuel melt fraction dominated

32.22.08 Oberflächenvergütung mit gepulsten Elektronen- und Ionenstrahlen

I. Behandlung von MCrAlY-Schutzschichten und Grundlagenuntersuchungen zur Strahlerzeugung

(G. Müller, R. Huber, G. Schumacher, D. Strauß, F. Zimmermann, IHM; V. Engelko, Efremov Institut, St. Petersburg)

Abstract

The work concerning the surface improvement of turbine blades was continued. Aim of this investigation is to modify the surface of turbine blades in such a way to guarantee the long term bonding of applied thermal barrier coatings (TBC) in a gas turbine. Meanwhile results of steady-state aging experiments at 950 °C for 10.000 h are available. The TBC are still well bonded to the turbine blade after that time.

Last year extensive numerical simulations were performed to improve the homogeneity of the electron beam. The reason for local beam inhomogeneities at the target observed in experiments could be deduced from these simulations. An increase of current density in the center of the beam is caused by ions from the target penetrating focussed in to the accelerating gap. These ions increase the field strength in the center of the cathode locally due to their space charge. Therefore the electron emission is intensified locally. Implementing an ion trap can prevent this ion flux towards the cathode.

Zusammenfassung

Die Arbeiten zur Oberflächenvergütung von Turbinenschaufeln wurden fortgesetzt. Ziel der Arbeiten ist, die Oberflächen der Schaufeln durch Behandlung mit der GESA so zu konditionieren, dass eine lange Haftung von aufgebrachten Wärmedämmschichten (WDS) in der Gasturbine gewährleistet ist. Inzwischen liegen die Ergebnisse der stationären Auslagerung bei 950°C über 10.000 h vor, die zeigen, dass die WDS auch nach dieser Zeit noch einwandfrei auf dem Schaufelmaterial haftet.

Zur Verbesserung der Strahlhomogenität wurde im letzten Jahr umfangreiche Simulationsrechnungen durchgeführt. Aus numerischen Simulationen konnte die Ursache für die experimentell beobachtete örtliche Strahlinhomogenität am Target erklärt werden. Die Erhöhung der Stromdichte im Strahlzentrum wird durch Targetionen verursacht, die fokussiert in den Beschleunigungsspalt eindringen und lokal im

Zentrum der Kathode, aufgrund ihrer Raumladung, die Feldstärke erhöhen und zu einer Verstärkung der lokalen Elektronenemission führen. Durch Implementierung von Ionenfallen kann dieser Ionenfluß in Richtung Kathode verhindert werden.

1. Einleitung

Der Einsatz keramischer Wärmedämmschichten (WDS) auf Gasturbinenschaufeln hat den Betrieb wirtschaftlicherer stationärer Gasturbinen zum Ziel. Dies erfordert eine Optimierung des MCrAlY Coatings, das sowohl den Turbinenschaufelgrundwerkstoff vor Oxidation schützt und gleichzeitig eine gute Anbindung der WDS gewährleisten soll. Im Gegensatz zu den bisherigen Entwicklungen, die hauptsächlich eine Optimierung der Zusammensetzung des MCrAlYs zum Ergebnis hatten, kann mit dem gepulsten Elektronenstrahl der GESA die Mikrostruktur stark verfeinert werden, so dass eine nanoskalige, deutlich homogenere Oberfläche entsteht, auf der sich im Betrieb eine dünne, homogene Oxidschicht bildet [1, 2]. Auf diese Schicht wird die WDS in kolumnarer Struktur aufgebracht.
Für den industriellen Einsatz von gepulsten Elektronenstrahlen benötigt man Strahlen, die zeitlich und räumlich stabil und homogen sind. Die Strahlparameter können durch viele Faktoren beeinflusst werden. So konnte zum Beispiel gezeigt werden, dass bei vorhanden sein eines externen Magnetfeldes, die Leistungsdichte des Strahls durch vom Target reflektierte Elektronen verändert wird [3, 4]. Neben der Leistungsdichte ändern die reflektierten Elektronen auch den Energieeintrag in das zu behandelte Werkstück [3]. Um die experimentell beobachtete räumliche Strahlinhomogenität zu verstehen wurden eine Reihe von theoretischen Grundlagenuntersuchungen zur Strahlerzeugung und Verbesserung der Strahlhomogenität durchgeführt. Wobei sich die Untersuchungen auf den Einfluss von Targetionen fokussieren. Bei der Wechselwirkung des Elektronenstrahls mit dem Target bildet sich auf der Targetoberfläche ein Plasma. Aus diesem Plasma werden Ionen im Eigenfeld des nicht raumladungskompensierten Strahls in Richtung Kathode beschleunigt. Wegen ihrer großen Masse folgen diese Ionen nicht den Magnetfeldlinien und dringen im Zentrum der Kathode in den Beschleunigungsspalt vor. Die positive Raumladung der Ionen kann zu einer erhöhten Emission von Elektronen im Zentrum der Kathode führen. Was sich durch Ausbildung eines Strommaximums in der Strahlmitte bemerkbar macht.

2. Ergebnisse zur GESA – Behandlung von Turbinenschaufelschutzschichten.

Die stationären/zyklischen Oxidationstests an GESA behandelten Proben wurden fortgeführt. Auf Basis der bisherigen Ergebnisse ist ein größeres Versuchsprogramm mit dem Industriepartner gestartet worden mit dem Ziel, eine aussagekräftige Statistik bez. potentieller Standzeitverlängerung zu erreichen. Inzwischen liegen für eine der Schutzschichten Ergebnisse der stationären Auslagerung bei 950°C über 10.000 h vor, die zeigen, dass die WDS auch nach dieser Zeit noch einwandfrei auf dem Schaufelmaterial haftet (Abb.1). Nach 10000 h ist das thermisch gewachsene Oxyd (TGO), das auch als Haftvermittlerschicht für die Wärmedammschicht fungiert, nur ca. 4 µm dick (Abb. 2). Die an Aluminium abgereicherte Zone (β – depletion zone) ist mit ca. 20 µm entsprechend dünn. Der Verbrauch an Aluminium zur Oxidschichtbildung ist der lebensdauerbestimmende Faktor für den Einsatz von MCrAlY – Schutzschichen auf Gasturbinen, so dass nach der GESA – Behandlung, auch ohne Wärmedämmschichten, eine Standzeiterhöhung erreicht wird.

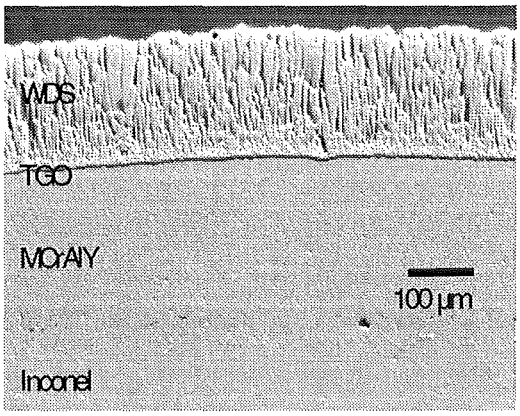

Abb. 1: Querschnitt durch eine Schutzschichtanordnung auf dem Grundwerkstoff (Inconel) einer Turbinenschaufel nach 10000 h Auslagerung bei 950 °C an Luft. Oben die Wärmedämmschicht (TBC), darunter die MCrAlY-Schutzschicht, dazwischen das thermisch gewachsene Oxid (TGO, Al_2O_3).

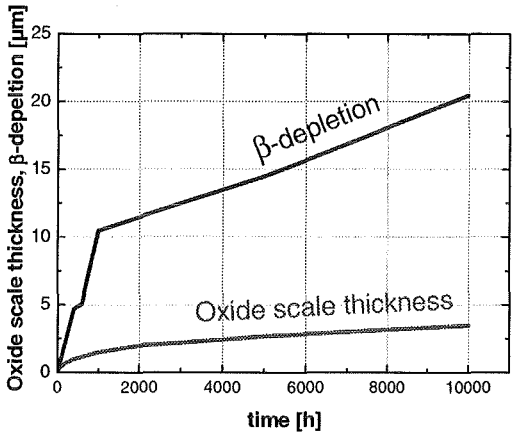

Abb. 2: Oxidschichtwachstum und die entsprechende Aluminiumverarmung bei Auslagerung an Luft bei 950 °C.

In Abstimmung mit dem Industriepartner wurden neue Schutzschichten entwickelt und mit in das Programm aufgenommen. Dabei war das Verhalten bei der GESA-Behandlung (Rissbildung) ein wesentlicher Gesichtspunkt. Zwei der drei neuen Schichten konnten ohne spezielle Vorkehrungen (Vorheizen, Mehrfachpulse) umgeschmolzen werden. Diese Schichten wurden in das Auslagerungsprogramm mitaufgenommen.

Untersuchungen, die für „Regenbogentests" erforderlich sind wurden begonnen. Es konnte gezeigt werden, dass die Austrittsöffnungen für die Oberflächenkühlung (shower heads, Langlöcher, etc.) auf einer Turbinenschaufel nicht deformiert werden.

3. Theoretische Untersuchungen zur Strahlhomogenität in der GESA - Anlage

Experimentelle Untersuchungen zur radialen Verteilung der Elektronenstrahlstromdichte zeigen, dass die Verteilung in der Regel ein Maximum in der Strahlachse aufweist. Dies widerspricht theoretischen Vorhersagen, die grundsätzlich eine homogene Stromdichteverteilung vorhersagen. Durch Berücksichtigung der zusätzlichen positiven Raumladungen von Ionen, die am Target entstehen, konnten die Unterschiede zwischen dem experimentellen Befund und den theoretischen Vorhersagen erklärt werden.

Die Erhöhung der Stromdichte im Strahlzentrum wird durch Targetionen verursacht, die fokussiert in den Beschleunigungsspalt eindringen und lokal im Zentrum der Kathode, aufgrund ihrer Raumladung, die Feldstärke erhöhen und zu einer Verstärkung der lokalen Elektronenemission führen. In Abb. 3 sind die Elektronentrajektorien für den ungestörten Fall, ohne Berücksichtigung der zusätzlichen Raumladung der Ionen dargestellt. In Abb. 4 sind die Trajektorien der Ionen dargestellt. Man sieht

deutlich, dass alle am Target entstehenden Ionen die Kathode nur um die Symmetrieachse treffen. Die entsprechenden Stromdichteverteilungen sind in Abb. 5 dargestellt. Mit Berücksichtigung der Ionen erhält man ein ausgeprägtes Maximum auf der Strahlachse, während im ungestörten Fall die Stromverteilung homogen ist. Des weiteren sieht man, dass die Verteilung weitgehend unabhängig von der jeweiligen Ionensorte ist.

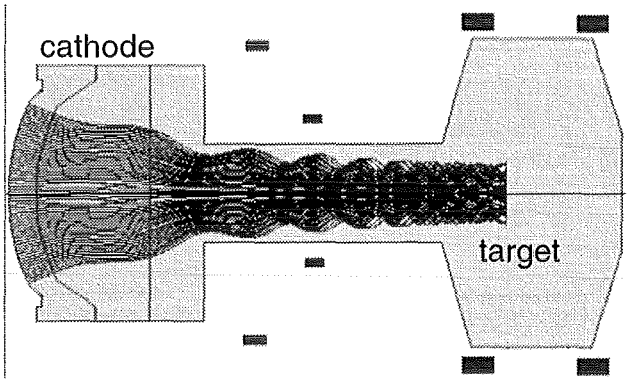

Abb. 3: Simulation Elektronentrajektorien in der GESA I Anlage ohne Berücksichtigung der Targetionen.

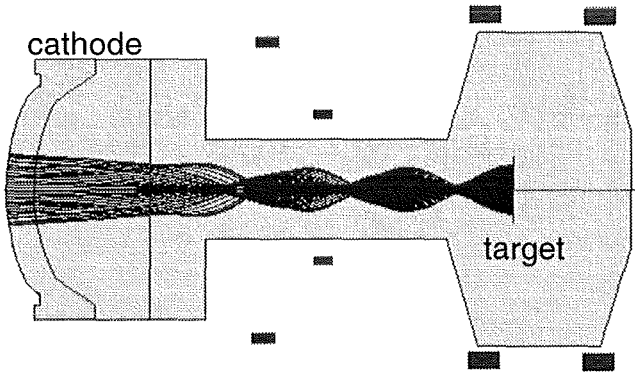

Abb. 4: Simulation der Targetionentrajektorien in der GESA I Anlage.

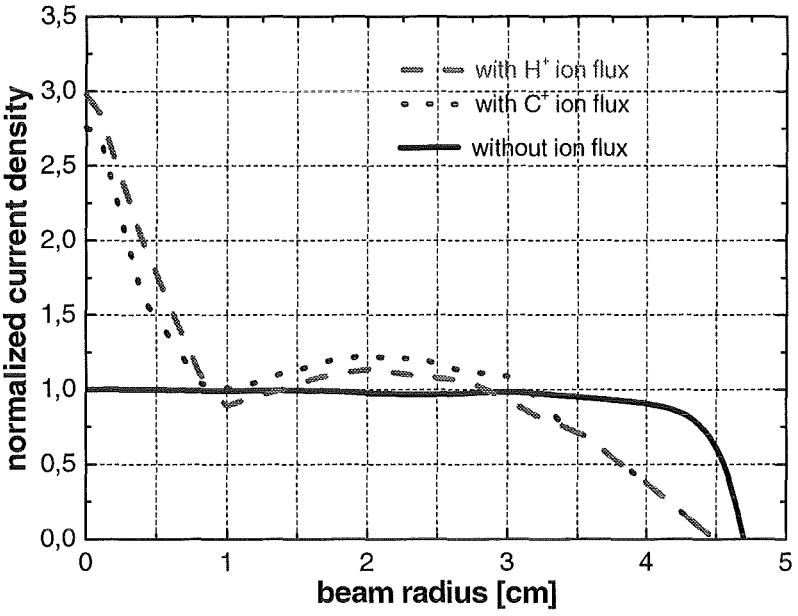

Abb. 5: Strahlstromdichteverteilung mit und ohne Berücksichtigung der Targetionen.

Um eine homogene Stromdichteverteilung in den GESA – Anlagen zu erzielen, muss der Targetionenfluss in Richtung Kathode verhindert werden. Dies kann durch entsprechende Ionenfallen realisiert werden. Die Simulationen hierzu zeigen, dass durch Anlegen eines Gegenpotentials von mindestens 20 kV in Targetraum oder im Transportkanal der Ionenfluß in Richtung Kathode weitgehend gestoppt werden kann (Abb. 6, 7). Experimentelle Untersuchungen hierzu haben begonnen.

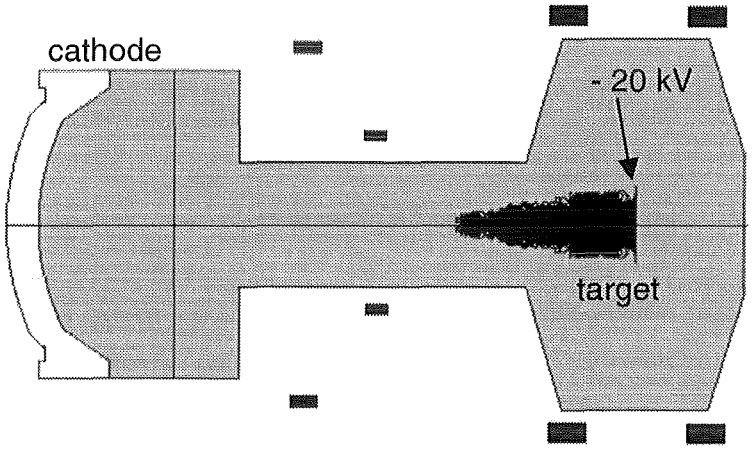

Abb. 6: Simulation der Targetionentrajektorien nach Anlegen eines Potentials von –20 kV an das Target in der GESA I Anlage.

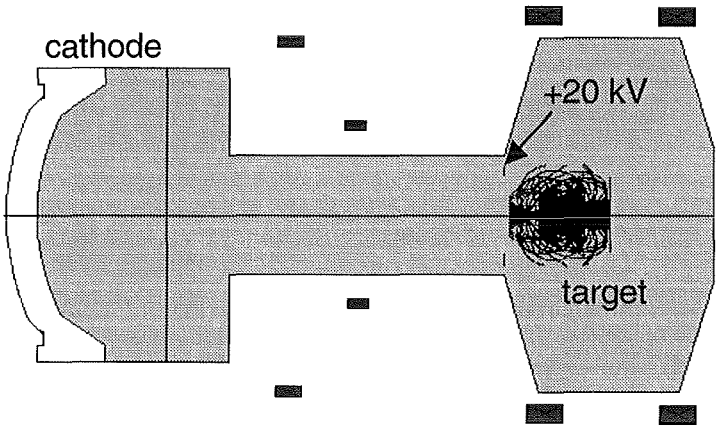

Abb. 7: Simulation der Targetionentrajektorien nach Anlegen eines Potentials von +20 kV an eine zusätzliche Elektrode am Ausgang des Transportkanals in der GESA I Anlage

Literatur

[1] G. Müller, G. Schumacher, D. Strauß, Surface and Coating Technology, 108-109 (1998) 43

[2] D. Strauss, Dissertation, FZKA 6371, Februar 2000

[3] G. Müller, Dissertation, FZKA 6422, Februar 2000

[4] V. Engelko, V. Kusnetsov, G. Viazmenova, G. Müller and H. Bluhm, Journal of Applied Physics, Vol. 88 No.7 1 October 2000, pp. 3879 - 3888

II. Mikromechanische Modellierung von Wärmedämmschichten

(K. Sfar, J. Aktaa, IMF II)

Im Rahmen der mikromechanischen Modellierung von Wärmedämmschichten wurden zunächst die Eigenspannungszustände in 2-Schicht bzw. 4-Schicht-Systemen bestimmt. Dabei wurden die Grenzflächenrauheit, Volumenzunahme durch die Oxidation der Haftvermittlerschicht, Kriechverhalten und nicht-lineare Materialgesetze berücksichtigt. Die Auswertung der Eigenspannungsanalysen liefert die Grundvorstellung des Versagensmodells der Wärmedämmschichten. Die Versagensmodelle werden untersucht durch Modellierung von Rissen im Schichtverbund. Geeignete Methoden zur Rissbewertung, die sich mit der FE-Methode gut kombinieren lassen, sind notwendig. Die experimentellen Beobachtungen und die Literatur zeigen, dass die Risse, die zum Versagen der Schicht führen, eine Mixed-Mode-Situation unterliegen. Diese Risse können Grenzflächenrisse sein oder solche Risse, die sehr nah und parallel zur Grenzfläche sind. Die Untersuchung und Erprobung verschiedener bruchmechanischer Bewertungsmethoden hat gezeigt, dass in Hinsicht auf das Versagen der Wärmedämmschichten, die Rissschließungsmethode sich am besten eignet. Diese Methode wurde anhand vereinfachten Strukturen erfolgreich getestet und wurde zur Auswertung von Rissen in Wärmedämmschichtsystemen eingesetzt. Damit ist es möglich die notwendigen bruchmechanischen Kenngrößen zu bestimmen, die die Grundlage eines Versagenskriteriums darstellen.

32.22.09 High Performance Light Water Reactor (HPLWR)

I. Thermal-Hydraulics of a Supercritical Pressure Light Water Reactor

(X. Cheng, H. Jacobs, E. Kiefhaber, T. Schulenberg, IKET)

Abstract

In Europe, several research institutions and industrial partners are joining in a common research project to develop a High Performance Light Water Reactor (HPLWR) [1], which is cooled by supercritical pressure water and has a thermal efficiency higher than 40%. The main objectives of the HPLWR project are: to review and to assess the existing know how for water cooled reactors at supercritical pressure; to make a design proposal for a European supercritical pressure light water reactor; to assess the technical and economic feasibility of a supercritical pressure light water reactor. In the frame of this project, a thorough literature review on heat transfer in supercritical water is performed. The experimental studies as well as prediction methods in the open literature were analysed and assessed related to their application to the HPLWR condition.

Zusammenfassung

Ein europäisches Projekt, unter der Beteiligung von mehreren Forschungsinstitutionen und Industriepartnern, ist initialisiert worden, um einen sogenannten 'High Performance Light Water Reactor (HPLWR)' zu entwickeln [1], der mit Wasser unter überkritischen Drücken gekühlt wird und einen thermischen Wirkungsgrad von über 40 % hat. Die wesentlichen Zielsetzungen des HPLWR-Projekts sind: (a) Zusammenstellung und Bewertung vorhandener Auslegungskonzepte der mit überkritischem Wasser gekühlten Reaktoren; (b) Vorschlag eines europäischen Auslegungskonzeptes des HPLWR; (c) Untersuchung der technischen und wirtschaftlichen Machbarkeit eines HPLWR. Im Rahmen dieses Vorhabens wird eine gründliche Literaturstudie über den Wärmeübergang bei überkritischen Drücken durchgeführt. Die in der Literatur vorhandenen experimentellen sowie theoretischen Arbeiten werden analysiert und bezüglich ihrer Anwendung auf ein HPLWR-Brennelement bewertet.

1 Thermal Physical Properties of Supercritical Water

Heat transfer at supercritical pressure is mainly characterized by the thermal physical properties which vary strongly as a function of pressure and temperature, especially near the pseudo-critical line. Figure 1 shows the specific heat in dependence on pressure and temperature.

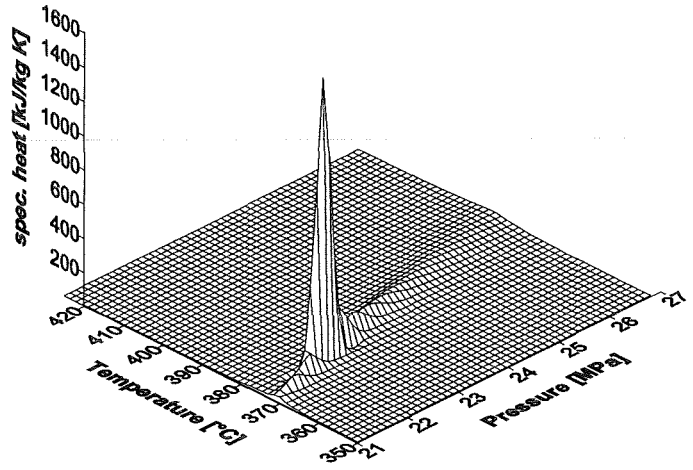

Figure 1: Specific heat of water [2]

It is seen that at each pressure there is a local maximum of the specific heat capacity. In the sub-critical pressure range the maximum specific heat locates on the saturation line. At the critical point (P =22.1 MPa, T = 374°C) specific heat has its maximum value. In supercritical pressure range, the line connecting the maximum values of the specific heat is called pseudo-critical line (PCL). It is seen that the pseudo-critical temperature increases with increasing pressure. At a pressure of 25 MPa the pseudo-critical temperature is 384°C. The specific heat at the critical point is as high as 5600 kJ/kg K which is more than 1000 times higher than that at room temperature. Figure 2 shows the density of water versus temperature at supercritical pressures. Near the pseudo-critical line the density decreases dramatically. There exists a large peak of thermal expansion coefficient which behaves very similar to the specific heat.

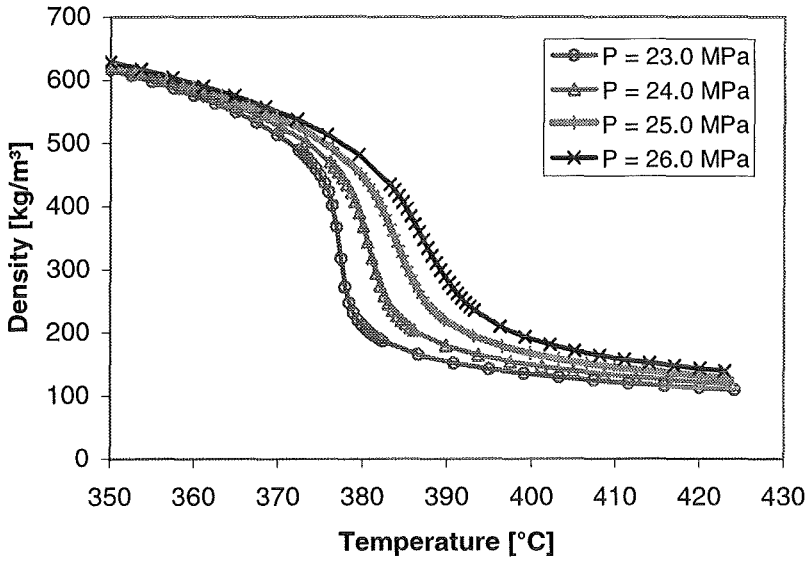

Figure 2: density of SC water

2 General Features of Heat Transfer at Supercritical Pressures

As indicated in chapter 1, a large variation of thermal physical properties occurs near the pseudo-critical line. This would lead to a strong variation in heat transfer coefficient. Taking into account the Dittus-Boelter equation

$$Nu = 0.023 \cdot \mathrm{Re}^{0.8} \cdot \mathrm{Pr}^{1/3} \qquad (1)$$

for turbulent water flow in a circular tube, and using the bulk temperature for calculating the properties, the heat transfer coefficient is shown in Figure 3 as function of the bulk temperature at a mass flux of 1.1 Mg/m²s, pressure of 25MPa, heat flux of 0.8 MW/m² and a tube diameter of 4.0 mm. It is seen that at the pseudo-critical point (T = 384°C) the Dittus-Boelter equation gives a heat transfer coeffcient of about 40 kW/m²K, more than twice of that at low temperature (e.g. 300°C) and five times of that at high temperature (e.g. 500°C). This shows clearly that due to the variation in thermal physical properties, the heat transfer coefficient varies strongly near the pseudo-critical line. The closer the pressure to the critical point is, the higher is the peak of the heat transfer coefficient.

It was agreed in the open literature that the real heat transfer coefficient deviates from the Bittus-Boelter equation, especially near the pseudo-critical line. At low heat fluxes, the heat transfer coefficient is higher than the values predicted by equation (1). This phenomenon is called heat transfer enhancement. At high heat fluxes the heat transfer coefficient is lower than that computed by the Dittus-Boelter equation. Figure 4 shows schematically the ratio of heat transfer coefficient α to the value calculated by the Dittus-Boelter equation α_0. It has been observed that under some specific conditions a very low ratio has been obtained. In this case a sharp increase in the temperature of the heated wall can occur. This large increase in the wall temperature is referred to '*heat transfer deterioration*'. In the literature there is still no unique definition for the onset of heat transfer deterioration, because the reduction in heat transfer coefficient, or the increase in the wall temperature behaves rather smoothly, compared to the behaviour of the boiling crisis in the range below the critical point where a much sharper increase in the wall temperature takes place.

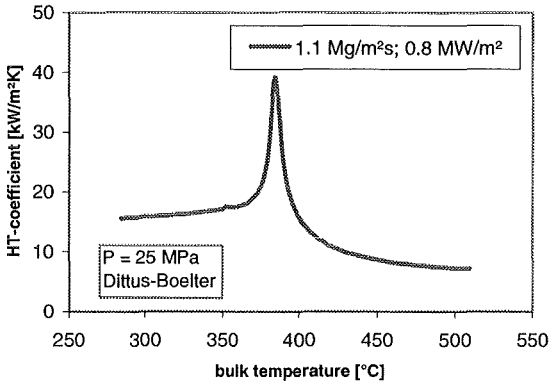

Figure 3: heat transfer coefficient according to the Dittus-Boelter equation

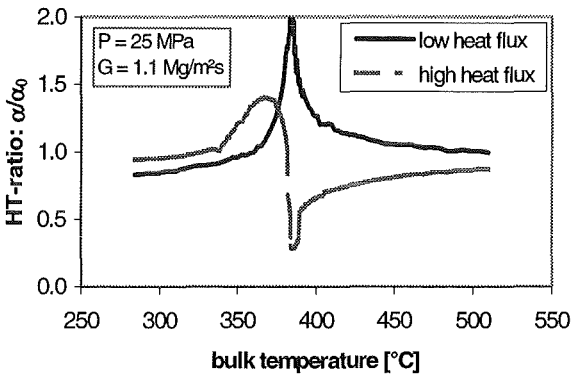

Figure 4: ratio of heat transfer coefficient α to that calculated using equation (1) α_0

3 Literature review

A lot of experimental works are available in the open literature. Details of the literature review are summarized in [3]. The main conclusions drawn are summarized as follows:

- The experimental studies in the literature covers a large parameter range:

  Pressure: 22.0 – 44.1 MPa

  Mass flux: 0.1 – 5.1 Mg/m²s

  Heat flux: 0.0 – 4.5 MW/m²

  Diameter: 2.0 – 32.0 mm

  Bulk temperature: ≤ 575°C

  However, it has to be kept in mind that this parameter matrix is not completely filled with test data. Further checks are necessary to find out those parameter combinations at which no test data are still available.

- Heat transfer deterioration is only observed at low mass fluxes and high heat fluxes with the following temperature condition:

  $$T_B \leq T_{PC} \leq T_W$$

  Here the subscript '*B*' stands for bulk, '*PC*' for pseudo-critical and '*W*' for wall.

- At low heat fluxes a heat transfer enhancement was obtained as the bulk temperature is approaching the pseudo-critical point.
- The experimental works are mainly restricted to circular tube geometry. No publications are available dealing with heat transfer in a flow channel other than circular tubes.
- Some special effects have been studied, i.e. entrance effect, channel inserts, flow channel orientation and heat flux distribution.
- Large deviation was obtained between the Dittus-Boelter equation and the test data with the bulk temperature or the wall temperature near the pseudo-critical value.
- Several empirical correlations have been derived based on the test data.

Most of the prediction methods in the literature were derived empirically based on experimental results. A detailed information about the correlations available in the open literature is provided in [3].

Figure 5 compares the heat transfer coefficient computed using different correlations. The flow parameters selected correspond well to the condition of an HPLWR.

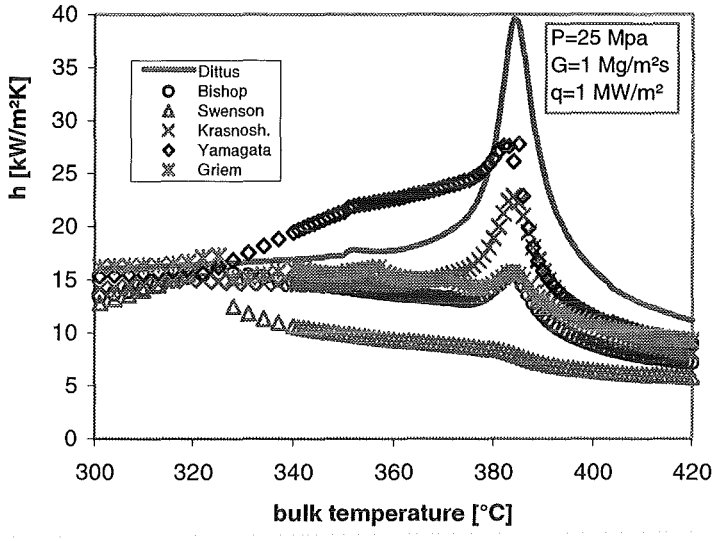

Figure 5: heat transfer coefficient according to different correlations [4-8]

All correlations show a maximum value at a bulk temperature near (or lower than) the pseudo-critical temperature (384°C). For the bulk temperature far away from the pseudo-critical temperature, a satisfactory agreement is obtained between different correlations, whereas a big deviation is observed as the fluid bulk temperature approaches the pseudo-critical value. For the parameter combination considered, the Dittus-Boelter equation gives the highest heat transfer coefficient which occurs when the fluid bulk temperature is equal to the pseudo-critical value. The correlation of Swenson [5] shows the lowest peak of the heat transfer coefficient. At the pseudo-critical temperature, the heat transfer coefficient determined by the Swenson correlation is about 5 times lower than that of Dittus-Boelter equation, about 3 times lower than that of Yamagata [7] and is about 50% of that of Bishop [4].

4 Recommendation for HPLWR application

The relevant condition in sub-channels are summarized as below [3]:

- pressure [MPa]: 25
- mass flux [kg/m²s]: 700 - 1600
- bulk temperature [°C]: 280 - 620
- hydraulic diameter [mm]: 1.9 - 4.5

- heat flux [MW/m²]: 0.0 – 1.5

When checking the valid parameter range of different correlations [3], it is found that the correlation of Bishop [4] is the most suitable ones for the sub-channel condition of the HPLWR. One of the most important parameters is the hydraulic diameter. All other correlations, except that of Bishop and of Krasnoshchekov [6], are derived for larger hydraulic diameters. The correlation of Krasnoshchekov should be valid for a diameter down to 1.6 mm. However, the maximum heat flux is limited to a much lower value than the maximum value in an HPLWR fuel assembly. The correlation of Bishop was developed for tube diameters between 2.5 mm to 5.1 mm, which covers approximately the hydraulic diameter range of an HPLWR fuel assembly. Except for the bulk temperature, all other parameters in an HPLWR fuel assembly are well covered by the valid parameter range of the Bishop correlation. As mentioned before, at a temperature far away from the pseudo-critical value, a satisfactoriy agreement is expected between different correlations. Therefore, the present authors recommend the application of the Bishop correlation to the HPLWR condition due to the deficiency in more reliable prediction methods.

The recommendation made above has to be restricted to the HPLWR project at the present stage. It has to be emphasized again that all the correlations discussed in this study were derived for circular tubes. Application of these correlations to the rod bundle geometry needs further modification which can only be achieved by using experimental data in rod bundles.

5 Summary

The main purpose of the common European project HPLWR, joined by European research institutions and industrial partners, is to assess the technical and economic feasibility of a supercritical pressure light water reactor, the so-called HPLWR. It is well agreed that heat transfer is one of the important items affecting the design of the reactor core. To gather a detailed knowledge about the heat transfer at supercritical pressures, a thorough literature survey has been carried out at the Forschungszentrum Karlsruhe. The applicability of some heat transfer correlations available in the open literature to the sub-channel condition of an HPLWR has been assessed.

For the present stage where a large deficiency exists in accurate knowledge of the heat transfer in the rod bundle geometry, the correlation of Bishop is recommended for calculating the heat transfer coefficient in an HPLWR fuel assembly.

6 References

[1] G. Heusener, U. Müller, T. Schulenberg, D. Squarer
A European development program for a high performance light water reactor (HPLWR)
Proc. of SCR-2000, Nov.6-8, 2000, Tokyo, pp..23-28

[2] W. Wagner, A. Kruse
The industrial standard IAPWS-IF97 for the thermodynamic properties and supplementary equations for other properties, - Properties of water and steam
Springer Verlag, Heidelberg, 1997

[3] X. Cheng, T. Schulenberg
Heat Transfer at Supercritical Pressures - Literature Review and Application to an HPLWR
FZKA-6609, Forschungszentrum, Karlsruhe, April 2001

[4] A.A. Bishop, R.O. Sandberg, L.S. Tong
Forced convection heat transfer to water at near critical temperatures and supercritical pressures
WCAP-2056-P, Part-III-B, February, 1964

[5] H.S. Swenson, J.R. Caever, C.R. Kakarala
Heat transfer to supercritical water in smooth-bore tube
Journal of Heat Transfer, Vol .C 87 (1965), pp.477-484

[6] E.A. Krasnoshchekov, V.S. Protopopov
Experimental study of heat exchange in carbon dioxide in the supercritical range at high temperature drops
Teplofizika Vysokikh Temperatur, Vol. 4, No.3, pp.389-398, May 1966

[7] K. Yamagata, K. Nishikawa, S. Hasegawa, T. Fujii, S. Yoshida
Forced convection heat transfer to supercritical water flowing in tubes
Int. J. Heat Mass Transfer, Vol.15 (1972), pp.2575-2593

[8] H. Griem
Untersuchungen zur Thermohydraulik innenberippter Verdampferrohre
Dissertation an der Technischen Universität München, Februar, 1995

II. Neutronenphysikalische Untersuchungen zum HPLWR

(C.H.M. Broeders, R. Dagan, B. Merk, V. Sanchez, IRS; I. Broeders, E. Stein, IKET).

Die Arbeiten hierzu sind unter dem Vorhaben 32.23.05 beschrieben; siehe dort Beitrag

III. Physics Investigations for Innovative Nuclear Reactor Systems

32.23 STUDIEN ZUR AKTINIDENUMWANDLUNG

32.23.01 Neutronenphysikalische Untersuchungen zur Transmutation von Aktiniden und Spaltprodukten

Upgrading of tools for core design studies and safety analyses

(G. Buckel, S. Fujita*, W. Götzmann, E. Kiefhaber, A. Rineiski, D. Thiem, H.-W. Wiese, D. Woll, IKET)

Zusammenfassung

Der Neutronik-Teil des Programmpakets SIMMER-III wurde bzgl. Zuverlässigkeit und Robustheit weiter verbessert und hinsichtlich der Behandlung der Neutronenaufwärtsstreuung erweitert. Die verbesserten Optionen wurden erprobt bei der iterativen Berechnung von Zeiteigenwerten und bei Fremdquellenproblemen in ADS-Rechnungen sowie bei der Nachrechnung von CRAC-Experimenten und des JCO-Kritikalitäts-Unfalls. Für die grafische Darstellung der umfangreichen Ergebnisse von Core-Auslegungsrechnungen musste, wegen des Wegfalls der bisher eingesetzten Basis-Software, durch Umstellung auf das UNIX-Betriebssystem, ein neues Plotprogramm, HEXAGON, erstellt und erprobt werden. Die Fortschritte bei der Weiterentwicklung des Abbrandprogramms KORIGEN und der Visualisierung der damit erzielten Ergebnisse sollen im nächsten Jahresbericht genauer beschrieben werden.

Abstract

The reliability and robustness of the neutronic part of SIMMER-III was further improved. A new capability was implemented allowing to deal with neutron cross sections and, in particular, scattering matrices taking into account neutron up-scattering processes. The new options were tested for the iterative determination of the asymptotic time eigenvalue of the neutron transport equation and for various cases of source driven problems for accelerator driven systems (ADSs). The CRAC-09 experiment and the JCO criticality accident, both representing thermal systems with neutron upscattering, were recalculated with reasonably good agreement between measurements and calculations. Due to changes in the computer environment and the application of the

* delegated from JNC/Japan

UNIX operation system, the previously used software was no longer available so that a new plot package, HEXAGON had to be prepared for representing the copious results of core design calculations for reactors with hex-z geometry. Improvement and advanced capabilities regarding updating of the burn-up code package KORIGEN establishing the new option of visualization of the results of KORIGEN calculations will be presented in the next annual progress report.

1. TWODANT Upgrading for SIMMER-III

A particular aspect of upgrading the TWODANT part of the SIMMER-III code package [1] was the improvement of the robustness for general purpose applications. Furthermore, we were aiming at making it more user-friendly. The necessity for the associated modifications resulted mainly from the conditions of safety analyses, namely fairly stringent accuracy requirements and fairly coarse spatial mesh grids. These conditions were beyond the conventional range of routine applications of TWODANT where the accuracy of k_{eff} was usually about $1 \cdot 10^{-4}$ and the mesh sizes were most times in the range of 1 to 5 cm. Such reasonably fine meshes were usually not acceptable in safety analyses because of the enormous CPU-time that would be needed. On the other hand, convergence problems during the multitude of TWODANT runs within one SIMMER-III run should be avoided as far as possible because in such a case user interaction and partial or full repetition of the run would become necessary. For a single TWODANT run, such a stop due to an error condition would be less severe and a new run with suitably modified input could be started easily.

As an example for establishing a more user-friendly version, the determination of the eigenvalue, λ, of the neutron transport equation on the asymptotic time eigenvalue, α, is shown in the Figure below. It is obvious that this so-called α-iteration has to take into account a pronounced nonlinear relationship $\lambda(\alpha)$ which is already characterized in the TWODANT-Manual [2] by "...the automatic search procedure may fail dramatically". This difficult situation could be handled successfully by fairly elaborated damping techniques.

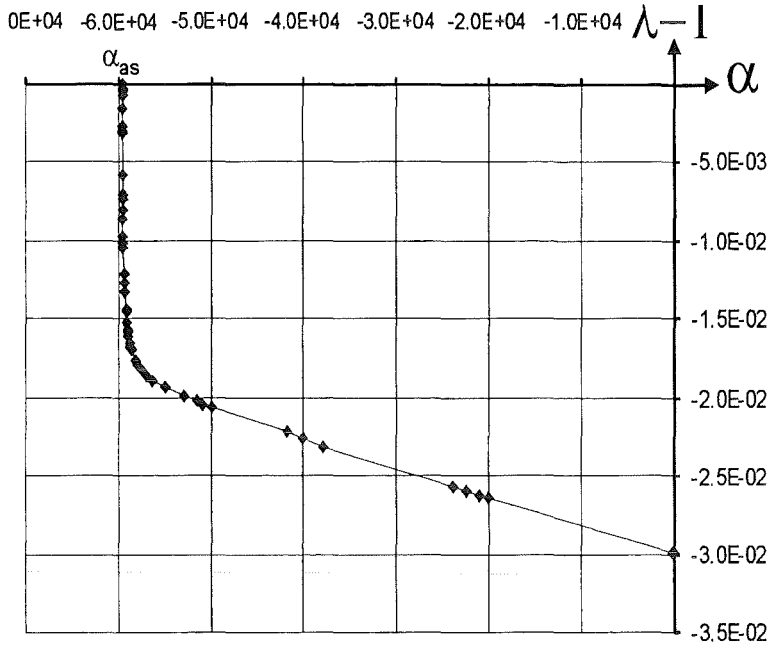

Nonlinear dependence of the eigenvalue, λ, of the neutron transport equation on the asymptotic time eigenvalue

Up to now the application of the TWODANT part of SIMMER-III was restricted to problems without neutron upscattering. This feature was sufficient and adequate for all studies related to reactors with a fast neutron energy spectrum, the traditional field of SIMMER safety analyses. In order to extend the range of use of the TWODANT part and to bring it in accordance with the previously applied but now outdated TWOTRAN part, the capability was now implemented to treat cross section files taking into account neutron upscattering processes. Although the solution of the neutron transport equation in TWODANT already allowed the treatment of neutron upscattering, the coupling between the standard cross section preparation in the existing SIMMER package and the recently supplemented TWODANT part had to be adapted for that purpose.

Proper working of the extended version was verified for two cases, the analysis of the initial phase of the JCO criticality accident [3] and of the initial phase of the CRAC-09 experiment [4]. Results of this experiment were used by our Japanese colleagues for adjusting parameters relevant for radiolytic gas production and bubble coalescence in fissile solutions. Due to the support of our Japanese partner, JNC, we could use the associated models and improved subroutines and a suitable nuclear data library. The following Figure shows that the TWODANT results agree fairly well with corresponding TWOTRAN results determined before by JNC and both calculations agree reasonably well with the experimental data. Still existing discrepancies may be due to minor

modeling deficiencies for the fairly complex phenomena associated to power excursions in fissile solutions (see e. g. [5]).

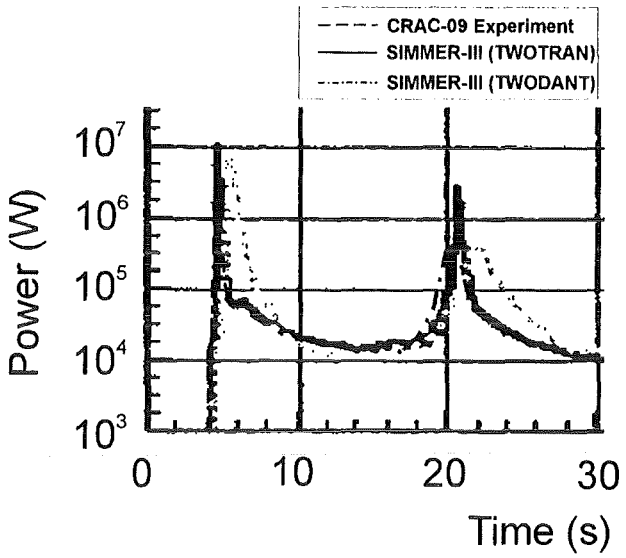

Comparison of SIMMER-III calculations and measurements for the initial phase of the CRAC experiment

The solution of the inhomogeneous neutron transport equation becomes particularly difficult for cases where the eigenvalue, k_{eff}, of the corresponding homogeneous equation approaches unity (from below). The existing solution scheme of TWODANT was not very efficient for such cases. An improved solution scheme described for the diffusion equation in chapter B.5.2.1 of [6] and in Ref. F.2.14 given there, and termed "Loehr-scheme" was now incorporated in the upgraded SIMMER-III version. Although limited up to now to using only scalar neutron fluxes, i. e. not angular neutron fluxes, it proved to be very efficient, reducing the calculation time by even more than one order of magnitude for typical cases (with $k_{eff} \approx 1.0$). Presently this feature has only been tested for isotropic sources. However, this assumption is valid for most practical applications so that this limitation may be no severe drawback in usual safety analyses for accelerator driven systems (ADSs).

2. Upgrading of data and tools for design calculations

For the cooperation with external partners the exchange of neutron cross section libraries has to be accomplished on a routine basis. Unfortunately, a variety of formats is existing for such libraries, so that the subroutines for using these libraries had to be adapted to cope properly with all various format options.

When dealing with the transmutation of minor actinides (MAs) the delayed neutron parameters of these MAs become more important than for conventional reactor designs. For that reason the data for some U-, and Pu-isotopes were determined and incorporated in the calculation tools used for the design and analysis of cores dedicated for MA transmutation.

For nuclear design and burnup calculations usually a vast quantity of results is accumulated. In order to check the correctness of the determined values and of the correlated input data, their graphical presentation is very helpful or almost a necessity. Due to changes in the computer environment and the resulting application of the UNIX operation system instead of the MVS system used in the past, the previously available software could no longer be used. It had to be replaced by a completely new plot package, HEXAGON, capable of representing the copious results of core design calculations for reactors with hex-z geometry.

The numerous improvements implemented in the upgraded version of the burnup code package KORIGEN and the advanced capabilities for visualization of the KORIGEN results, both using user-friendly new options for input preparation will be presented in the next annual report.

References

[1] G. Buckel et al.: A New SIMMER-III Version with Improved Neutronics Solution Algorithms. FZKA-6290, 1999

[2] RSIC COMPUTER CODE COLLECTION; DANTSYS 3.0, One-, Two-, and Three-Dimensional, Multigroup, Discrete Ordinates Transport Code System, contributed by: Los Alamos National Laboratory, Los Alamos, New Mexico, 1995 http://www-xdiv.lanl.gov/XTM/

[3] Y. Tobita et al.: Space-Time Kinetics Simulation of an Early Burst Phase of the Criticality Accient, International Workshop on the Safety of the Nuclear Fuel Cycle, Tokyo, J, May 29-31, 2000

[4] P. Lecorche, R. L. Seale: A Review of the Experiments Performed to Determine the Radiological Consequences of a Criticality Accident, Y-CDC-12, Oak Ridge Y-12 Plant, 1973

[5] C. C. Pain et al.: Transient Criticality in Fissile Solutions – Compressibility Effects, Nucl. Sci. Eng. 138, 78, 2001

[6] B. Stehle: D3D and D3E Zweige eines FORTRAN-Programms zur Lösung der stationären dreidimensionalen Multigruppenneutronendiffusionsgleichungen in Rechteck-, Zylinder und Dreieckgeometrie, KfK-4764, 1991

32.23.02 Abtrennverfahren für Aktiniden aus hochradioaktiven Abfällen

(A. Geist, M. Weigl, U. Müllich, K. Gompper, INE)

Zusammenfassung

Es wurden weitere Versuche zur Aktiniden(III)-Lanthaniden-Trennung in Hohlfasermodulen durchgeführt. Dabei konnte Americium als Vertreter für die dreiwertigen Minoren Aktiniden zu 99,99 % abgetrennt werden. Auch Versuche zur Rückextraktion aus der beladenen organischen Phase wurden unternommen. Zu allen Versuchen wurden Modellrechnungen durchgeführt, welche auf Gleichgewichtsdaten und kinetischen Untersuchungen basieren. Die Übereinstimmung mit den Experimenten ist sehr gut.

Einleitung

Die Radiotoxizität abgebrannter Kernbrennstoffe wird über einen Zeitraum von einigen 10^5 Jahren durch den Gehalt an Plutonium und Minoren Aktiniden (Neptunium, Americium, Curium) bestimmt. Mit der Partitioning&Transmutation-Strategie [1] soll die Langzeitradiotoxizität vermindert werden, indem diese Elemente abgetrennt (Partitioning) und anschließend zu kurzlebigen und schließlich stabilen Nukliden umgewandelt werden (Transmutation). Die Abtrennung der dreiwertigen Minoren Aktiniden Americium und Curium von den Spaltlanthaniden ist dabei aufgrund deren chemischer Ähnlichkeit ein Schlüsselschritt.

Das Vorhaben wird im Rahmen des EU-Projekts *Partitioning: New Solvent Extraction Processes for Minor Actinides* (Vertrag FIKW-CT2000-00087) bearbeitet. Gemäß der Arbeitsaufteilung innerhalb des EU-Programms liegt der Schwerpunkt unserer Arbeiten in der Untersuchung des Einsatzes von Hohlfasermodulen als neuartige Extraktionsapparate [2, 3] sowie der Stoffaustauschkinetik der eingesetzten Extraktionssysteme [4, 5].

Es wurden weitere Versuche zur Abtrennung dreiwertiger Aktiniden von den Spaltlanthaniden in Hohlfasermodulen durchgeführt. Dazu wurde als Extraktionsmittel eine synergistische Mischung von 0,5 M Bis(chlorphenyl)dithiophosphinsäure + 0,25 M TOPO (Tri-n-octylphosphinoxid) in tert.-Butylbenzol verwendet [6, 7]. Weiterhin wurde begonnen, die Stoffaustauschkinetik in diesem System zu untersuchen. Es

sollten zunächst Daten gewonnen werden für die Modellierung, welche die Extraktionsversuche im Hohlfasermodul begleitet.

Stoffaustauschkinetik

Es wurden Rührzellenversuche zur Extraktion von Am-241 und Eu-152 in 0,1 M Salpetersäure mit dem o.g. Extraktionssystem durchgeführt. Apparat und Vorgehensweise sind in [5] beschrieben. Die Ergebnisse sind in Abbildung 1 gezeigt. Die Extraktionsrate steigt linear mit der Rührerdrehzahl an. Das bedeutet, dass die Extraktionsrate im untersuchten Strömungsbereich durch diffusive Transportvorgänge bestimmt ist. Dieser Befund ist für die Vorgehensweise bei der Berechnung der Stoffaustauschleistung im Hohlfasermodul wichtig [2, 3].

Aktiniden-Lanthaniden-Trennung im Hohlfasermodul

Es wurden weitere Versuche zur Americium(III)-Lanthaniden-Trennung [8] durchgeführt. Verwendung als Extraktionsmittel fand die o.g. synergistische Mischung.

Zunächst wurde ein Extraktionsversuch durchgeführt, der sich von dem in [8] vorgestellten lediglich durch die Phasenführung unterscheidet. Es wurde nun die wässrige Phase in den Hohlfasern statt im Mantelraum geführt. Dies hat einen gewaltigen Einfluss auf die Extraktionsleistung: Es konnten bei einem Durchsatz von 300 ml/h 99,99 % Americium (gegenüber ca. 98 %) abgetrennt werden, und dies bei praktisch unveränderter Koextraktion der Lanthaniden von ca. 30 % (Abbildung 2). Der Grund für dieses Verhalten ist die Abhängigkeit der Stofftransportkoeffizienten vom Durchsatz, welche in den Hohlfasern eine andere ist als im Mantelraum. Eine detaillierte Erklärung hierzu findet sich an anderer Stelle [9].

Weiterhin wurden zwei Versuche zur Rückextraktion unternommen. Dazu wurde die mit Americium und den Lanthaniden beladene organische Phase im Hohlfasermodul mit 1,5 M [9] bzw. 2,0 M [10] Salpetersäure kontaktiert. Bei der Rückextraktion in 1,5 M Salpetersäure konnten bei einem Volumenstrom von 300 ml/h Americium zu 80 %, die Lanthaniden zu 93 % und Yttrium zu 88 % rückextrahiert werden (Abbildung 3). Durch die Erhöhung der Säurestärke auf 2,0 M konnte die Rückextraktionsleistung etwas verbessert werden: Es konnten nun bei einem Durchsatz von 320 ml/h Americium zu 88 % und die Lanthaniden einschließlich Yttrium zu 93-95 % rückextrahiert werden (Abbildung 4).

Weiterhin wurde zu allen Versuchen die Extraktionsleistung berechnet [2, 3]. Es zeigte sich eine sehr gute Übereinstimmung der gerechneten Werte mit den experimentellen Ergebnissen (Abbildungen 2–4). Die Tatsache, dass alle Versuche mit einem konsistenten Satz an Daten gerechnet wurden, ist wichtig für die Verwendung der Rechnungen für eine Verfahrensauslegung. So konnten Bedingungen für ein Lanthanidenscrubbing gefunden werden, welche experimentell bestätigt wurden [10]. Weiterhin zeigen die Rechnungen zur Rückextraktion (Abbildung 4), dass, um z.B. eine Rückextraktionsleistung von 99 % zu erreichen, ein maximaler Durchsatz von 100 ml/h gefahren werden kann.

Literatur

[1] *Actinide and Fission Product Partitioning and Transmutation, Status and Assessment Report.* OECD-NEA, Paris (1999).

[2] U. Daiminger, A. Geist, W. Nitsch, P. Plucinski, *The Efficiency of Hollow Fiber Modules for Nondispersive Chemical Extraction.* Ind. Eng. Chem. Res. 35, 184 (1996).

[3] A. Geist, P. Plucinski, W. Nitsch, *Separation of Multi-Cation Mixtures by Non-Dispersive Chemical Extraction Using Hollow Fiber Modules.* Submitted to J. Membr. Sci.

[4] A. Geist, P. Plucinski, W. Nitsch, *Mass Transfer Kinetics of Reactive Multi-Cation Co-Extraction Into Bis(2-ethylhexyl) Phosphoric Acid.* Solvent Extr. Ion Exch. 18(3), 493 (2000).

[5] M. Weigl, A. Geist, K. Gompper, J. I. Kim, *Kinetics of Lanthanide/Actinide Co-extraction with N,N'-dimethyl-N,N'-dibutyltetradecylmalonic diamide (DMDBT DMA).* Solvent Extr. Ion Exch. 19(2), 215 (2001).

[6] G. Modolo, R. Odoj, *Synergistic Selective Extraction of Actinides(III) over Lanthanides From Nitric Acid Using New Aromatic Diorganyldithiophosphinic Acids and Neutral Organophosphorus Compounds.* Solvent Extr. Ion Exch. 17(1), 33 (1999).

[7] C. Madic, M.J. Hudson, J.O. Liljenzin, J.P. Glatz, R. Nannicini, A. Facchini, Z. Kolarik, R. Odoj, *New Partitioning Techniques for Minor Actinides.* EUR 19149, European Commission, Luxembourg (2000).

[8] A. Geist, M. Weigl, U. Müllich, K. Gompper, *Abtrennverfahren für Aktiniden aus hochradioaktiven Abfällen.* Projekt Nukleare Sicherheitsforschung, Jahresbericht 1999. Wissenschaftliche Berichte, FZKA-6480 (2000).

[9] A. Geist, M. Weigl, K. Gompper, *Actinide(III)/Lanthanide(III) Separation in a Hollow Fiber Module with a Synergistic Mixture of bis(Chlorophenyl)dithiophosphinic Acid and TOPO.* To be presented at GLOBAL 2001, September 9-13, 2001, Paris, France.

[10] A. Geist, M. Weigl, U. Müllich, K. Gompper, *Application of Novel Extractants for Actinide(III)/Lanthanide(III) Separation in Hollow Fiber Modules.* To be presented at ISEC 2002, March 18-21, 2002, Cape Town, RSA.

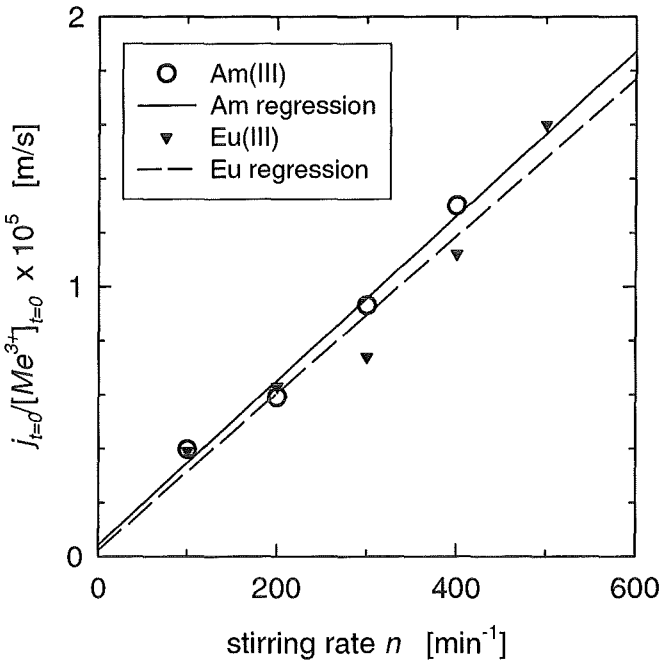

Abbildung 1: Drehzahlabhängigkeit der normierten Extraktionsraten für die Extraktion von Am^{3+} und Eu^{3+} aus 0,1 M Salpetersäure.

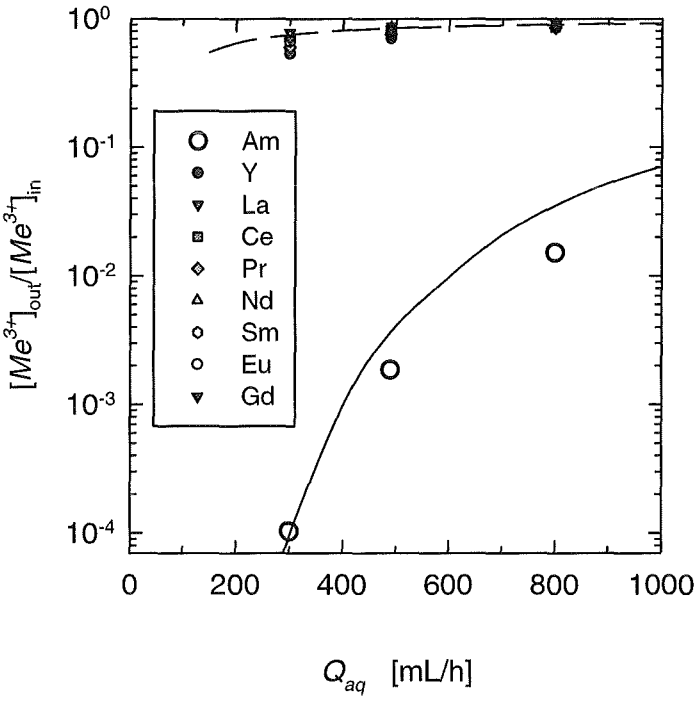

Abbildung 2: Americium(III)-Lanthaniden-Trennung im Hohlfasermodul mit einer synergistischen Mischung aus Bis(chlorphenyl)dithiophosphinsäure 0,5 M + TOPO 0,25 M in tert.-Butylbenzol. Am(III) + Ln(III) in HNO_3 0,5 M. Q_{org} = 300 ml/h. Wässrige Phase in den Hohlfasern. Symbole: Experiment; Linien: Berechnung.

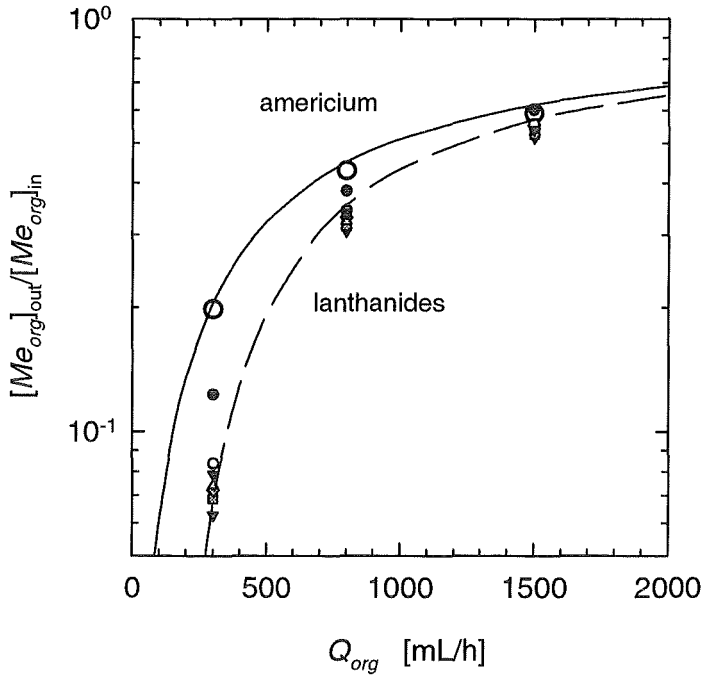

Abbildung 3: Rückextraktion der beladenen organischen Phase in 1,5 M Salpetersäure. Organische Phase in den Hohlfasern. $Q_{aq} = Q_{org}$. Symbole: Experiment; Linien: Berechnung.

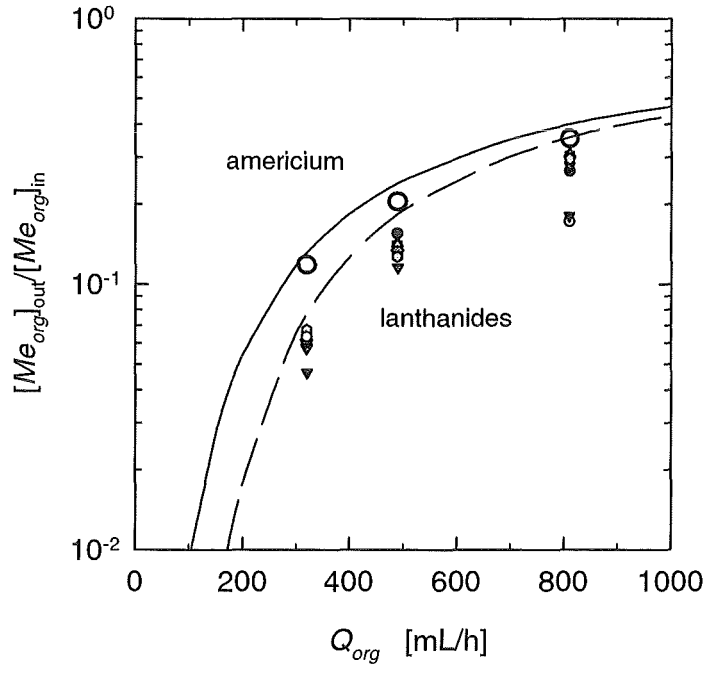

Abbildung 4: Rückextraktion der beladenen organischen Phase in 2,0 M Salpetersäure. Organische Phase in den Hohlfasern. $Q_{aq} = Q_{org}$. Symbole: Experiment; Linien: Berechnung.

32.23.03 Sicherheitsuntersuchungen zum dynamischen Verhalten von Kernen mit Aktinidenanteil

Analysis of the Safety Behavior of Accelerator Driven Transmutation Systems

(W. Maschek, A. Rineiski, K. Morita, IKET; M. Flad, D.T.I. GmbH)

I. Introduction

The incineration/transmutation of plutonium (Pu) and minor actinides (MAs) can be performed with critical reactors and Accelerator Driven Systems (ADS). Different scenarios exist how to achieve an efficient destruction of the nuclear waste /1/. For highest transmutation/incineration rates, the fuel should consist of pure MAs mixed with Pu, but without fertile materials as U238 or Th232. This so-called 'dedicated' fuel is still to be developed and programs have to be initiated to fabricate, investigate and test these innovative fuels. Insertion of such fuels into a reactor core could lead to a strong deterioration of safety relevant parameters as e.g. the void worth, the Doppler and the kinetics quantities as the neutron generation time and β_{eff} . In addition, dedicated fuels might possess high reactivity potentials. These fertile free fuels may also suffer from deteriorated thermal or thermo-mechanical properties, as reduced melting points, reduced thermal conductivities or even thermal instabilities /2/. Safety reasons possibly prohibit the use of dedicated fuels in critical reactors /3, 4/. However, for ADSs the salient hope has been promoted that due to the subcriticality of the system the poor safety features of such fuels could be coped with.

The following investigations deal with the generic safety behavior of an ADS with dedicated fuel. Results of this study are compared to a similar ADS system fueled with U233/Th232 oxide. Investigations of a U233/Th232 ADS core, which corresponds to the original proposal for an energy amplifier /5/, generally showed a very promising safety behavior of the ADS /6, 7/. Based on these analyses a very high safety potential has been attributed to the ADS /8/. The investigations of an ADS as a nuclear waste burner with dedicated fuel, containing high masses of Pu and MAs for efficient transmutation, reveal potential safety problems. Work has been started to develop and propose improvements for this type of ADS to assure an adequate safety level.

II. The SIMMER-III code

The analyses presented here have been mainly performed with the SIMMER-III code /9/, a safety code originally developed for liquid metal cooled critical reactors but now extended to accelerator driven systems /10/. The SIMMER-III code is developed by JNC (Japan Nuclear Cycle Development Institute, O-arai Engineering Center) in co-operation with Forschungszentrum Karlsruhe and CEA (Commissariat à l'Energie Atomique, CEN Grenoble and CE Cadarache). The application of the SIMMER code to ADS is of special interest for the European partners in this cooperation. SIMMER-III is a two-dimensional, three-velocity-field, multi-phase, multi-component, Eulerian, fluid-dynamics code coupled with a structure model (fuel pins etc.) and a space-, time- and energy-dependent neutron dynamics model. SIMMER-III uses an elaborate scheme of equation of state functions for fuels, steel, coolants (light and heavy liquid metals), absorber and simulation materials. In neutronics, the transient neutron flux distribution is calculated with the improved quasistatic method /11/. For the space dependent part, a TWODANT based flux shape calculation scheme has been implemented recently /12/. For ADS application, an external time- dependent neutron source has been implemented in the kinetics equations /13, 14/. For the calculation of the different kinetics quantities different weighting functions can be chosen.

III. Safety Analyses Performed for ADS with Different Cores

A general target in developing new reactor systems as the ADS should be the inclusion of strong inherent and passive safety features. They should help to prevent any escalation into severe accident scenarios. The 'subcriticality' of the core is a corner stone of this concept. The composition of fuel (Pu and MA vector) depends on the envisioned fuel cycle with the Pu content varying over a large range /2/. Therefore, there does not exist a single 'dedicated' fuel. The important point for this safety evaluation is the identification of a reactor with 'dedicated' fuel to be synonymous with a reactor having a small prompt negative Doppler feedback, a small β_{eff} , a short prompt neutron lifetime and large inherent reactivity potentials.

III.1 Core Behavior under Transients

The behavior of a core with 'dedicated' nitride fuel (MAs(Np,Am,Np)+Pu/N) has been compared with a U233/Th232 oxide core of the same power level. The dedicated fuel contains 25 % Pu (CAPRA /4/ type: 5.6/39.1/26.7/13.0/14.3) and 75 % MAs embedded in an ZrN matrix. The thermal power of the ADS is 1200 MW. Both the dedicated and the thorium cores have a subcriticality level of k_{eff} = 0.97. The β_{eff} in the dedicated core is ~150 pcm and the neutron generation time $\Lambda \sim 2.0\ 10^{-7}$ s. In the thorium core both values are higher by a factor of about 2 and 3 respectively. The total core void is strongly positive in the case of the dedicated fuel, but negative for the U/Th core.

The different behavior of a dedicated core and a core with fertile Th232 fuel is demonstrated here with a defined operational transient and a severe transient with core melting. In the operational transient, the neutron source strength is constant initially, than it is rapidly (within 1 ms) doubled, then almost shut off (to 1 % of the original level) and then returned (within 1 ms) to its initial value (Fig. 1). Any pin failure has been suppressed in this calculation. These analyses show, that under intact core system conditions in an ADS even strong source perturbations lead to only minor differences in the power evolution, though the safety parameters of both cores (dedicated versus thorium) deviate considerably. For a reactivity perturbation within the subcriticality level of the ADS a larger difference can however be noted in the power evolution due to the coolant density effect (Fig. 2).

In the second step of calculations the core behavior under severe accident conditions including core-melting has been analyzed. The recriticality potential of the dedicated core has at first been assessed by calculating the number of critical masses, giving a rough idea if under core melt conditions a potential for a recriticality exists. The dedicated core contains about 60 'critical' masses, while the thorium core contains only two. Thus under local core melt conditions with subsequent fuel compaction there would exist a potential to overcome the built-in sub-criticality of the ADS with dedicated fuel, driving the reactor into a critical state.

The safety parameters and the inherent 'recriticality' potential of the fuel decisively influences the response of the core to a severe reactivity perturbation. The core response has been investigated for a range of fuel disruption scenarios and subsequent compaction ramp rates. As a general tendency, the nuclear power

excursions in the dedicated core are much more severe than those in the thorium core with reasonable negative feedback effects. The power excursion in the dedicated core is not stopped by a prompt negative reactivity feedback as the Doppler effect, but only by the delayed feedback of a core disassembly. The high nuclear power excursions in the dedicated ADS core could lead to significant fuel vaporization, pressure build-up and could imply a severe challenge for containment structures. A fuel vapor bubble generated within msec would accelerate the lead coolant surrounding the core. In such a case the high lead density and low compressibility would result in significant impact shock pressures on vessel structures.

In the analyzed core with 'dedicated' fuel a pronounced 'cliff-edge' behavior can be noted. During 'normal operation' the influence of the deteriorated safety parameters is masked by the source dynamics. In the case of a severe accident leading to core disruption and melting, the phenomena in the accident event chain are enhancing the damage potential.

III.2 Influence of Inherent Reactivity Potentials on the ADS Design

In an ADS an essential inherent safety feature is the subcriticality level of the core. One can speculate if and which reactivity potentials and material rearrangements could cause the elimination of the subcriticality level under transient conditions. The coolant voiding problem is relieved by the high boiling point of Pb or Pb/Bi. However, core voiding can take place by a gas release from breached pins or a massive gas blow-down from the fission gas plenum. The production of He by the Am and Cm decay could be a major source for plenum pressurization. Calculations show that with about 5000 pcm the total core void could be considerable in a dedicated core. The gas release from the plena is calculated in a special model of the SIMMER-III code /15/. In Fig. 3 the void front formation in a subassembly triggered by a multiple pin failure at core mid-plane and the subsequent gas blow-down from the upper plenum is displayed.

Besides the reactivity effects, resulting from density changes of the coolant, another requirement for the subcriticality level may come from the clad steel worth. Over-heating transients could lead to clad melting and clad relocation /6, 7/. As the density ratio of liquid steel to lead is ~ 0.7, the clad will be swept upwards. The clad worth of

the core analyzed is 2200 pcm. The steel floating upwards could block the exit regions above the core and cause severe cooling problems. There could exist a generic problem of enhanced blockage formation (caused e.g. by corrosion products, PbO plate-out or by the fore-mentioned steel relocation) related to the design of lead cooled systems. The necessary larger p/d ratio requires grid spacers in the core. As is known from former investigations /16/ these grid spacers enhance the blockage formation problem significantly compared to wire wraps. In Fig. 4 the results of a mechanistic simulation of an unprotected (beam-on) loss of flow accident (ULOF) in a dedicated oxide core is displayed. Though in the mechanistic accident simulation not the whole core is voided via the gas blow-down after local pin failure, the reactivity introduced by voiding is sufficient to drive the core disruption process. The lack of a significant negative Doppler effect finally leads to the unhampered power increase. This is a totally different behavior compared to a thorium core with a negative core void worth and a significant prompt negative feedback effect /17/ (for thorium cores also see /6, 7/). No power excursion takes place in the thorium core.

IV. Conclusions and Final Remarks

The cliff-edge behavior observed in the safety analyses of the dedicated ADS core will not be tolerable. Therefore some proposals are made to eliminate this undesired behavior. The main target is to assure a 'reasonable' core behavior also under severe accident conditions and the removal of cliff-edge effects. With this goal achieved, necessary mitigative measures, as containment measures, can also be defined more reasonably. In addition, specific safety margins can be attributed to the built-in subcriticality, directly related to severe accident prevention. The subcriticality level thus covers reactivity effects from burn-up, operational temperature effects etc. plus a specially devised safety margin for severe transients.

- **Fuel worth:** As the fuel of the dedicated core should consist of Pu and MAs the neutronic worth of the fuel will be high and the core will contain a high number of 'critical' masses. A limit should be posed that a single subassembly does not contain multiple critical masses.
- **Fuel stability:** The fuel worth and spectrum related reactivity quantities can change dramatically in a core disruptive situation if the fuel is not stable in its

matrix under melting conditions and fuel and matrix could separate. Fuel stability is therefore essential.

- **Coolant void worth:** In the case of Pb or Pb/Bi, boiling processes will be of low importance, but voiding e.g. by a gas bubble passage caused by a gas blow-down from the plena must be taken into account. The maximum positive void worth should be less than the subcriticality margin to cope with a potentially additional clad worth contribution.
- **Clad worth:** Due to the high boiling point of lead; steel melting might occur first in accident scenarios. The steel worth of the core should therefore additionally be taken into account by the subcriticality level.
- **Feedback effects/kinetics:** For limiting any nuclear excursion in case the built-in subcriticality level might be consumed by local fuel compaction processes and/or voiding etc., a reasonable Doppler feedback effect should be available. For curbing excursion energetics also the neutron lifetime Λ should not fall much below the values of a conventional critical core. Note that in case of a small Doppler effect the accident energetics is proportional to $1/\Lambda^x$ ($x<1$).

A deep subcriticality level, covering the coolant void and clad worth may eliminate the threat of various accident initiators, but the concern related to the fuel worth will persist. The inherent fuel reactivity potential in a dedicated core is generally much higher than the built-in subcriticality level. To cope with the potential of possible excursions, therefore a reasonable Doppler effect and adequate kinetics parameter values are required.

Complying with these proposals should guarantee the necessary safety potential for an ADS waste burner, especially they devise a clear safety function to the subcriticality level, limit any excursion energetics by inherent feedback effects and facilitate the discussion of containment measures. To fulfill most of the above mentioned requirements, the integration of U238 or Th232 into the fuel matrix would be reasonable. This would reduce transmutation/incineration rates and it would mean a change in the transmutation strategy. Nevertheless it might be worthwhile to consider and investigate dedicated fuel alternatives with fertile fuel included for safety reasons.

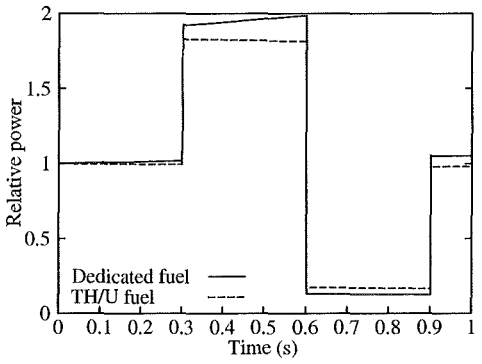

Fig. 1 Comparison of a beam trip transient in an ADS reactor core either with dedicated fuel and U233/Th232 oxide fuel

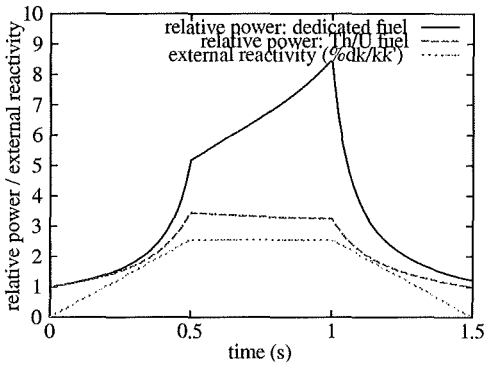

Fig. 2 Comparison of a reactivity transient within the subcriticality margin in an ADS reactor with dedicated fuel and U233/Th232 oxide fuel

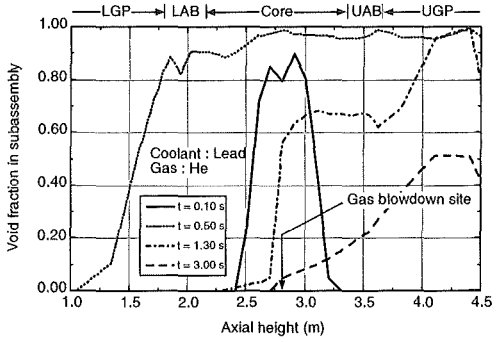

Fig. 3 Axial void front in an inner ring subassembly after helium gas blowdown

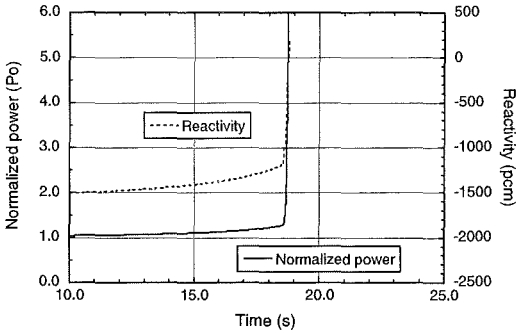

Fig. 4 Mechanistic simulation and nuclear power trace of an unprotected (beam-on) LOF in a dedicated core

V. References

/1/ M. Salvatores et al., Nucl. Instr. And Methods in Phys. Research A 414, 1, 5, (1998)

/2/ Fuel Fabrication and Processing Subgroup of the Technical Working Group on ADS (2000)

/3/ J. Tommasi et al, GLOBAL'99, Jackson Hole, USA (1999)

/4/ W. Maschek et al., ICONE-4, New Orleans, USA (1996)

/5/ C. Rubbia et al., CERN/LCH/96-11 (EET) (1996)

/6/ H.U. Wider, 2 nd Int. Conf. on ADS Transm. Techn. and Application., Kalmar, Sweden (1996)

/7/ W. Maschek et al., AccApp'98, Gatlinburg, USA (1998)

/8/ H.U. Wider et al., ICENES2000, Bruxelles (Belgium) (2000)

/9/ S. Kondo et al., ANP'92, Tokyo, Japan (1992)

/10/ W. Maschek et al., AccApp'00, Washington, USA (2000)

/11/ K.O. Ott et al., Nuclear Reactor Dynamics, ANS, La Grange Park, USA (1985)

/12/ G. Buckel et al., FZKA 6290 (1999)

/13/ R. Rineiski et al., ADDTA'99, Praha (1999)

/14/ R. Rineiski et al., OECD/NEA Workshop on the Utilization and Reliability of High Power Proton Accelerators, Cadarache, France (1999)

/15/ Y. Tobita, JNC, personal communication (2000)

/16/ C.v. Minden et al., GKSS 82/E/50 (1982)

/17/ K. Morita et al., SIMMER-III Analyses of Transients in ADS, ICONE-9, Nice, France (2001)

32.23.04 Bestrahlungsexperimente zur Transmutation von Aktiniden im HFR

(H. Plitz, NUKLEAR)

FZK is participating in the CAPRA programme (Consommation Accrue de Plutonium dans les Rapides), which is mainly conducted by CEA (France). The main objective is to evaluate the performance of a fast neutron reactor core which is dedicated to burn plutonium and to burn or transmute long-living actinides. An enrichment of up to 45 % plutonium is chosen to remain compatible with current fuel cycle technology (dry route fabrication and Purex process). To implement a mixed oxide fuel pin with a maximum Pu-enrichment of 45 % means that the fraction of fuel in a given volume (fuel pin) has to be reduced, i.e. it requires a low smeared density in the fuel pin (annular fuel pellets).

In order to demonstrate the good performance of such a CAPRA mixed oxide fuel pin an irradiation programme has been launched. The High Flux Reactor (HFR) at Petten (NL) was chosen to perform an experimental irradiation programme within specially designed irradiation devices called TRABANT (Transmutation And Burning of Actinides iN TRIOX) which can contain 3 fuel pins which are independently cooled.

The first experiment TRABANT 1 was irradiated in 1995/1996.

The main objectives of TRABANT 1 were to demonstrate the performance of high plutonium content fuel up to 10 % burnup in respect to clad corrosion attack, thermal behaviour and mechanical behaviour of the hollow pellet columns under several startup and shutdown periods imposed by the HFR reactor cycles. In cooperation with the Commissariat à l'Energie Atomique (CEA), Forschungszentrum Karlsruhe and the Institute for Transuranium Elements (ITU), the TRABANT 1 fuel pins have been designed, specified and manufactured:

Pin 1, a CAPRA reference high-plutonium-content (45 % Pu) oxide fuel pin manufactured by CEA

Pin 2, another reference oxide fuel pin with 40 % Pu content plus 5 % Np, manufactured by ITU

Pin 3, a Pu without U oxide fuel pin with $(Pu_{0.44},Ce_{0.56})O_2$ pellets, containing two tightly separated short fuel columns of different O/M ratios and densities, manufactured by ITU.

The fuel pin 1 failed, but despite this failure it was concluded that the fuel pin reference concept is feasible. In consequence another experiment TRABANT 2 was planned, but the heat rating will be lower than in TRABANT 1 because the experienced failure of the pin TRABANT 1/1 was traced back to too high heat rating leading to melting /1/.

The TRABANT 2 irradiation vehicle was ordered already in 1998, but the manufacturing of the 3 test fuel pins was rather delayed. The 3 CAPRA type pins, all with annular pellets, were manufactured at ITU, using both mechanical mixing (MM) of powders and the SOL-GEL method. The main data are given in Table I.

Table I: Fuels prepared for the TRABANT2 irradiation experiment

Pin No.	Fuel	Fabrication Process	Pu content Pu / (U+Pu)	O/M	Density (% dt)
2/1	$(U,Pu)O_2$	MM	0.40	1.971	94.18
2/2	$(U,Pu)O_2$	MM	0.40	1.995	93.40
2/3	$(U,Pu)O_2$	SOL-GEL	0.45	1.990	86.36

The transport of these fuel pins was also delayed due to formalities and non-availability of transport containers.

Pin 2/3 has a rather low fuel density. Due to the poor thermal conductivity, this might result in high fuel centre temperatures. Therefore, it was recommended to load and irradiate this pin later.

The TRABANT 2 capsule was ready in autumn 2000, but due to other circumstances (available manpower, post irradiation examination, waste disposal, etc.), the irradiation of TRABANT 2 was suspended end of December 2000. A final decision to irradiate the completely assembled TRABANT 2 irradiation vehicle has been postponed.

Reference

/1/ E. Picard, H. Noirot, H. Plitz
High Plutonium Content Oxide Fuel for Pu Burning in Fast Reactors. CAPRA Irradiation Programme and First In-pile Experimental Results.
Global '97, Oct. 5-10, 1997, Yokohama, Japan, Proc. Vol. 1, 528-536.

32.23.05 Untersuchungen zu Beschleuniger getriebenen, unterkritischen Anlagenanordnungen (ADS)

I. Thermalhydraulic Layout of the MEGAPIE Spallation Target

(N.-I. Tak, X. Cheng, J.U. Knebel, IKET)

Abstract

The heavy liquid metal spallation target is an innovative module of an accelerator driven system (ADS). In the framework of the MEGAPIE Initiative, FZK is participating in the design of a spallation target with a proton beam power of 1 MW which is going to be operated in the SINQ complex at PSI, Switzerland.

A thermalhydraulic analysis of the active part of the MEGAPIE spallation target has been performed using the CFX 4.3 code. Three types of geometric configurations, i.e. flat guide tube, slanted guide tube, and additional injection bypass pipe are investigated. The main emphasis is on the coolability of the beam window and the heat removal from the active part of the target. In the case of the flat guide tube, flow stagnation occurs in the region near the center of the beam window. This leads to an excessive hot spot on the surface of the beam window. In the case of the slanted guide tube, the axis-symmetry of the flow is destroyed and the zone of flow stagnation is reduced. However, the improvement of heat transfer is insufficient to keep the temperature of the window below the design value. Therefore, two different kinds of bypass pipes are introduced in order to remove the zone of flow stagnation, i.e. a rectangular pipe and a circular pipe. The calculations with a circular bypass pipe give promising results: a sufficient cooling of the beam window is possible.

Kurzfassung

Das Flüssigmetall-Spallationstarget ist eine innovative Komponente eines Beschleuniger getriebenen Systems (ADS). Im Rahmen der MEGAPIE Initiative nimmt das Forschungszentrum Karlsruhe an dem Entwurf eines Spallationstargets teil, das eine Protonenstrahlleistung von 1 MW hat, und das in den SINQ Beschleunigerkomplex am PSI in der Schweiz eingesetzt wird.

Mit dem Code CFX 4.3 wurden numerische Untersuchungen zum thermohydraulischen Verhalten des aktiven Teils des MEGAPIE Spallationstargets durchgeführt. Drei unterschiedliche geometrische Konfigurationen des Targets wurden untersucht:

flaches Führungsrohr, schräg angeschnittenes Führungsrohr und zusätzliche Bypass-Strömung durch ein Rohr. Die Untersuchungsschwerpunkte waren die Kühlbarkeit des Strahlfensters und die Wärmeabfuhr aus dem Spallationstarget. Für den Fall des flachen Führungsrohrs entsteht ein großer stagnierender Bereich nahe des Fensterzentrums. Dies führt zu einer extrem hohen lokalen Temperatur an der Fensteroberfläche. Für den Fall des schräg angeschnittenen Führungsrohrs wird die Symmetrie der Strömung zerstört und der stagnierende Bereich wird reduziert. Trotzdem kann die Kühlung des Fensters nicht gewährleistet werden. Deshalb werden zwei unterschiedliche Geometrien von Bypass-Rohren eingeführt, um den stagnierenden Bereich zu entfernen: ein rechteckiges Rohr und ein kreisförmiges Rohr. Die Ergebnisse für ein kreisförmiges Bypass-Rohr sind vielversprechend: Eine ausreichende Kühlung des Strahlfensters ist möglich.

1. Introduction

Transmutation is a promising and feasible technology world-wide for significantly reducing the amount, and thereby, the long-term radiotoxicity of highly radioactive waste produced by the operation of nuclear power plants such as light water reactors. The maximum, long-term reduction of radiotoxicity could be by a factor of about 100. Transmutation is an alternative to the direct deposition of large volumes of highly radioactive waste. Transmutation presents the possibility of closing the fuel cycle including minor actinides. Plutonium, minor actinides and long-lived fission products can be transmuted in an Accelerator Driven System (ADS). Sketches of two different types of ADS are given in figure 1.1.

A key component of both types of ADS is the spallation target which uses the heavy liquid metal Pb or Pb-Bi both as spallation material and as coolant. Such a heavy liquid metal (HLM) spallation target has never been tested before.

In a collaborative effort, the MEGAPIE founding members CEA, FZK and PSI together with their partners CNRS, ENEA, JAERI, SCK-CEN and SUBATECH agreed to design, build, operate, explore and decommission an exploratory liquid lead-bismuth spallation target for 1 MW of beam power, taking advantage of the existing spallation neutron facility and accelerator complex SINQ.

The major objective of the MEGAPIE Initiative is the full design and feasibility demonstration of a spallation target system. MEGAPIE is to be operated in 2004.

MEGAPIE will be a first decisive step towards the realization of a heavy liquid metal spallation target, Bauer (2000).

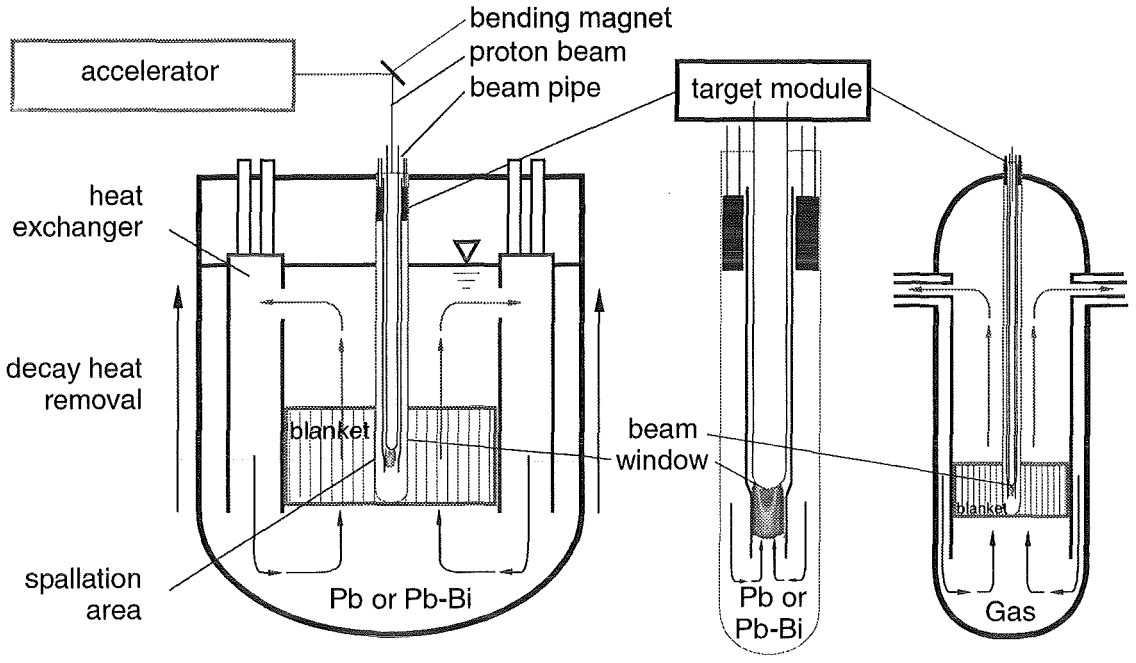

Figure 1.1: Sketch of an accelerator driven system (ADS) with liquid metal cooled (left) and gas cooled (right) blanket.

Here, the major results of a thermal-hydraulic analysis of the active part of the MEGAPIE target for three different types of geometric configurations are discussed. *Further relevant results in the field of ADS technology are given in 32.23.06.*

The applied CFD code is the CFX 4.3 code, AEA (1998).

2. Boundary Conditions and Investigated Configurations

It is known that about 60% of the proton beam energy is released as heat in the active part of the target, being the spallation area and the beam window. Because of a small beam window thickness, the heat deposition in the beam window can be approximated by the following Gaussian distribution, Dury (2000):

$$q''' = 1.3\times10^{9}\, exp[-(\frac{x}{\sigma_x})^2 - (\frac{y}{\sigma_y})^2]\ \text{W/m}^3 \qquad (2.1)$$

with $\sigma_x = 0.019m$, $\sigma_y = 0.033\ m$.

The coordinate used for the present work is shown in Figure 2.1.

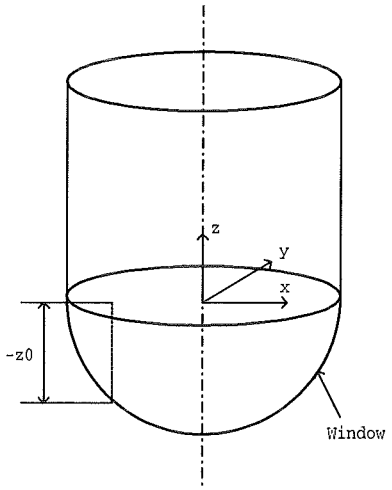

Figure 2.1: Coordinate system used in the present work.

According to eq. (2.1) about 5.44 kW heat is generated in the window. By neglecting the thermal radiation heat transfer and the azimuthal heat conduction inside the window, the heat flux on the window surface can be expressed by

$$q'' = q''' \times \delta \tag{2.2}$$

where δ is the window thickness. The local heat deposition in the target material is determined by:

$$q''' = 1.58 \times 10^9 \exp[-(\frac{x}{\sigma_x})^2 - (\frac{y}{\sigma_y})^2] \exp[-\frac{(z - z_o)}{L}] \text{ W/m}^3 \tag{2.3}$$

with $L = 0.21$ *m*. Here $z - z_0$ is the z axial distance from the window for a given point. According to equation (2.3) about *650 kW* heat is released in the active part of the target.

According to equations (2.1) and (2.2) the maximum heat flux on the window surface is about *2.6 MW/m²*. This requires a special care to ensure a proper cooling. Thus, the design of the active part is one of the main tasks in the design phase of the MEGAPIE target. From the thermal-hydraulic point of view, many design criteria have to be defined. Two of them are crucial for the present study, i.e. the maximum temperature of the window surface T_{max}, and the maximum velocity of Pb-Bi U_{max}. The maximum velocity of Pb-Bi should not exceed the value of about *1.5 m/s* and the maximum temperature of the window surface should be kept below about *400°C*. The main reason for these design limits is due to structure material problems, such as corrosion and erosion.

Three types of configurations are considered, as indicated in Figure 2.2. In the first configuration a flat guide tube is used. For this type of design it is expected that a

large flow stagnation zone occurs near the window center because of axis-symmetry of the flow. This leads to a poor cooling of the beam window and, subsequently, to an excessive hot spot on the center of the beam window. In order to improve the cooling performance, two other configurations are proposed. The first method, indicated as (1) in figure 2.2, is to cut the lower end of the guide tube (slanted guide tube). In this way the axis-symmetry of the flow is destroyed and the zone of flow stagnation near the center of the beam window can be reduced. The second method, indicated as (2) in figure 2.2, is to introduce a injection pipe. The bypass-flow through this pipe is used to remove the zone of flow stagnation near the center of the beam window.

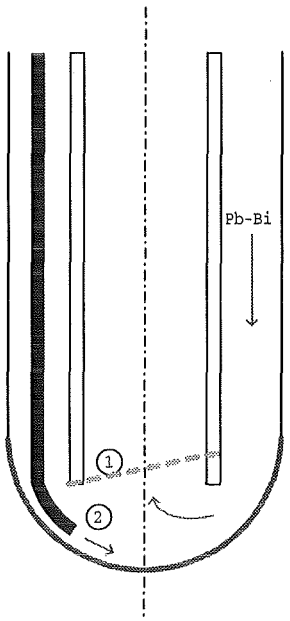

Figure 2.2: Active part of the spallation target considered in the present work.

The present numerical analysis has been performed using the CFX 4.3 code, which is a general purpose thermal-hydraulic code developed by AEA Technology. The solution method of CFX is based on the finite volume method (FVM).

The following assumptions are made:

- Fluid is incompressible.
- Flow is highly turbulent and steady-state.
- Boussinesq approximation is valid.The standard k-ε model with logarithmic wall functions was used. Attention was paid to keep the first mesh size close to a solid wall in the range of $30 \leq y^+ \leq 100$. Here y^+ is the dimensionless distance from the wall.

The mesh generation in the CFX 4.3 code is based on the "body-fitted" and "multi-block" approach. "Body-fitted" means that the grid boundaries fit the geometry

boundary considered. This feature of CFX4 is of crucial importance for the present work because of the curved window surface.
The database of the thermal-physical properties of Pb-Bi is still not complete. There exists deviation between different sources. In Europe many institutions have agreed on using a unique database, Buono (1999).

3. Configuration Variations

3.1 Spallation Target with a Slanted Guide Tube

3.1.1 Geometry and boundary condition

It has been found that in the spallation target with a flat guide tube, a large region of flow stagnation occurs near the center of the beam window and leads to an excessive high temperature in the center of the beam window. One method to destroy the axis-symmetric flow, to reduce the flow stagnation region and, subsequently, to improve the coolability of the window, is to introduce a slanted guide tube. In this case the lower end of the inner cylinder is cut with an inclined cross section, see Figure 3.1.

It was agreed among the partners of the MEGAPIE Initiative that the effect of the gap size h, the inclination angle α and the direction of the cutting cross section on the coolability of the beam window has to be investigated. In the present study, one calculation was carried out with the following conditions:

- gap size (h) : 10 mm
- cutting angle (α) : 8°
- direction of the cutting surface: normal vector parallel to the x-z plane.

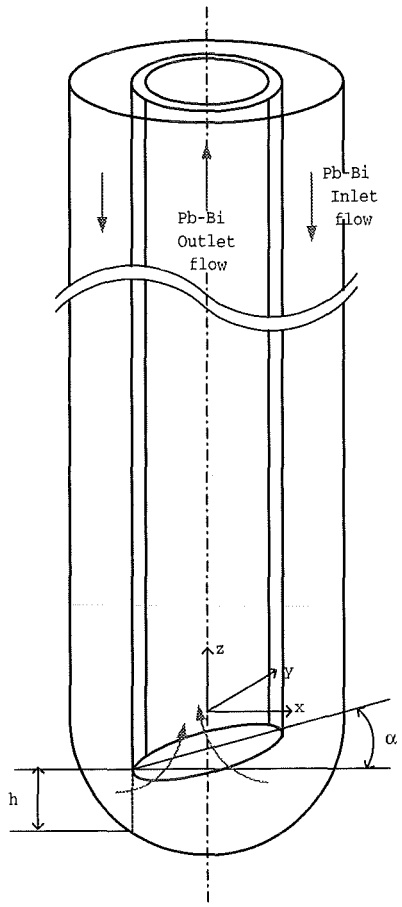

Figure 3.1: Target with a slanted guide pipe.

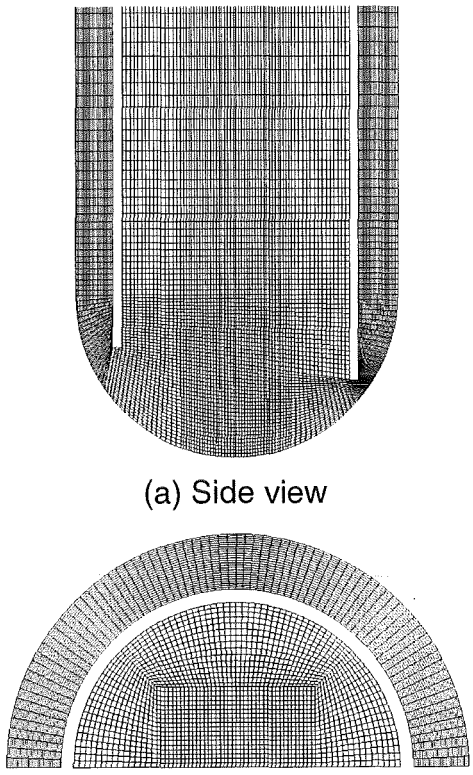

(a) Side view

(b) Top view

Figure 3.2: Meshes for the target with a slanted guide pipe.

The main purpose of this calculation is to show in general the coolablity of the window in the target with a slanted guide pipe. For this configuration, 3-D calculations are required. To avoid an excessive large number of volume cells and some numerical difficulties, the height of the computation domain is reduced to 30 cm. In this case about 300,000 volume cells are generated. Figure 3.2 shows the grid cells generated for the target with a slanted guide pipe.

3.1.2 Results and discussion

For this calculation the heat deposition rate in the beam window and in the spallation area was determined by eqs. (2.1) and (2.3). The guide tube has a thermally insulating wall.

Figure 3.3 shows the distribution of the velocity and the temperature in the target. It is seen that the zone of flow stagnation around the center of the beam window is significantly reduced compared to that in the target with a flat guide pipe. The Pb-Bi flow from the larger gap passes through the center region and meets the flow from

the smaller gap. A region of high flow velocity is observed near the guide tube wall which forms the small gap. A small flow recirculation zone occurs around the small gap and near the larger gap, respectively. In spite of a strong reduction in the maximum temperature, the coolability of the beam window remains insufficient. The maximum temperature of the surface of the beam window is about 550°C, far beyond the design limit of 400°C.

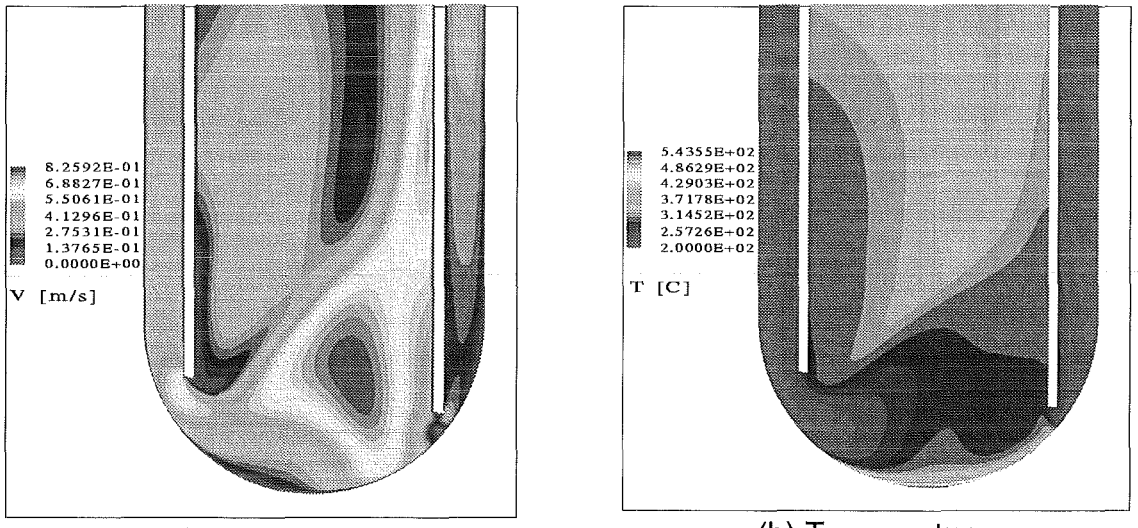

(a) Velocity (b) Temperature

Figure 3.3: Results for the spallation target with a slanted guide pipe.

3.2 Spallation Target with a Rectangular Bypass Pipe

3.2.1 Geometry and Boundary Conditions

In this chapter a bypass injection is adopted to improve the coolabilty of the beam window, as shown in Figure 3.4.

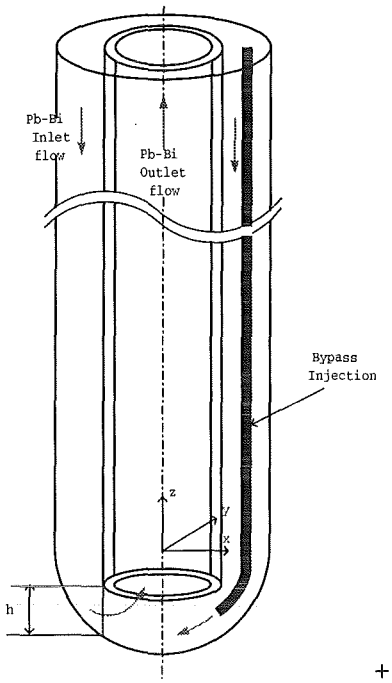

Figure 3.4: Target with an injection bypass pipe.

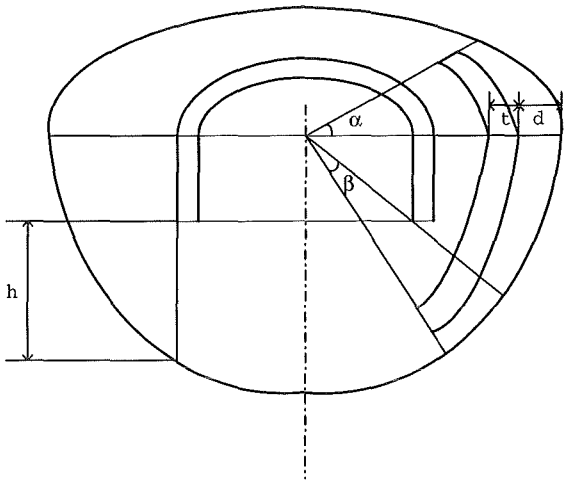

Figure 3.5: Main design parameters of the target with a rectangular bypass pipe.

Two different types of injection bypass pipes are considered, i.e. a rectangular and a circular pipe. With a rectangular bypass pipe a large injection flow area can be achieved. However, a circular shape is easier to fabricate and to install in the target.

Major design parameters of the rectangular bypass pipe are illustrated in Figure 3.5. The reference line for the angle α is the x-axis. The reference line of the angle β is the line connecting the sphere central and the lower end of the guide tube. To achieve an optimum performance of the target, the effects of the geometric parameters of the bypass pipe are investigated to provide a first information for the design optimisation. The parameters considered in the present study are: the injection velocity (V_b), the position of the nozzle end (β), the distance from the wall (d), the depth of the bypass pipe (t), the bypass width (α),the injection direction and the gap size (h). The reference values are summarized as below:

- gap size: h = 30 mm
- injection velocity: V_b = 1.0 m/s
- position of nozzle end: $\beta = 0^o$
- distance from the wall d: d = 5 mm
- depth of the bypass pipe t: t = 5 mm
- bypass width: $\alpha = 20^o$

- location of the bypass injection: on y-axis

With the reference values, the flow rate of the injection bypass is about 10% of the total flow rate. The height for the computation domain is about 30 cm, to avoid an excessive large expenditure in computation. The guide tube wall is considered as thermally insulating. For the simplicity the thickness of the bypass pipe wall is neglected.

About 200,000 meshes are generated for this 3-D calculation. The distance of the first fluid node from solid walls is about 1 mm.

More recently, the following equations for the heat deposition have been provided by Nie (2000), i.e.

$$q''' = 0.696\times 10^{9}\, exp[-\frac{1}{2}\{(\frac{x}{\sigma_x})^2 + (\frac{y}{\sigma_y})^2\}] \tag{3.1}$$

for the heat deposition in the window and

$$q''' = 1.1136\times 10^{9} e^{-\frac{z-z_0}{B}} \times \left[1 - e^{-\frac{z-z_0-Z_a}{\lambda}}\right] \times e^{-\frac{1}{2}\left\{\left(\frac{x}{\sigma_x^*(z)}\right)^2 + \left(\frac{y}{\sigma_y^*(z)}\right)^2\right\}} \tag{3.2}$$

for the heat density in the spallation material. The parameters in equations (3.1) and (3.2) are summarized as below:

$$\sigma_x = 0.020188\, m \tag{3.3}$$

$$\sigma_y = 0.033505\, m \tag{3.4}$$

$$\sigma_x^* = 0.019 + 0.00035\times(z - z_0),\ m \tag{3.4}$$

$$\sigma_y^* = 0.0331 + 0.00035\times(z - z_0),\ m \tag{3.5}$$

$B = 0$

For the numerical calculations in chapters 3.2 and 3.3, equations (3.1) and (3.2) are used to calculate the heat deposition rate.

3.2.2 Results and discussion

Figure 3.6 shows the velocity distribution for the reference case. A high injection velocity from the bypass pipe is obtained. The flow stagnation zone disappears

around the center of the beam window. The bypass flow penetrates into the central region and affects the flow in the opposite side of the annular gap.

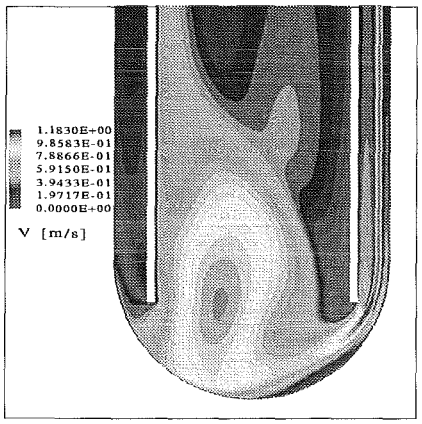

Figure 3.6: Velocity distribution for the reference design.

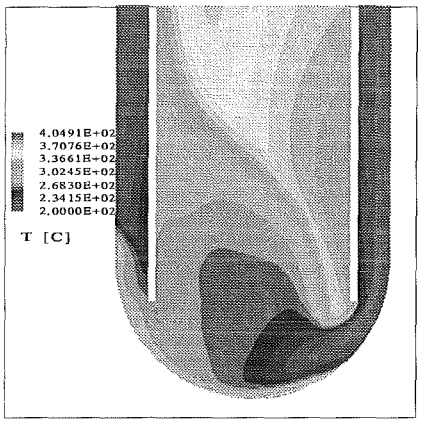

Figure 3.7: Temperature distribution for the reference design.

Figure 3.7 shows the temperature distribution. The maximum temperature is about 400°C. Compared to the previous designs, i.e., the targets with flat or slanted guide pipe, the coolability of this design is improved significantly. Further reduction in the maximum window temperature can be achieved by optimizing the design parameters. Here, one parameter variation is discussed: The injection velocity of the bypass is changed to 0.6 m/s and 1.4 m/s, respectively. Figure 3.8 shows the velocity and temperature profiles for the case with an injection velocity of 0.6 m/s. Obviously, the bypass injection is not high enough to eliminate the flow stagnation zone completely. The maximum window temperature exceeds 500°C. Figure 3.9 shows the velocity and temperature profiles for the case with a higher the injection velocity of 1.4 m/s. In this case the high injection velocity removes completely the stagnation region near the window center. However, it creates a large flow recirculation in the riser. Thus, the position of the maximum temperature is moved to the riser, apart from the window. The maximum temperature of the window surface is reduced to about 330°C. The maximum temperature of Pb-Bi increases slightly, and the maximum velocity of Pb-Bi is about 1.65 m/s, which slightly exceeds the design limit of 1.5 m/s. More optimization studies are thus required.

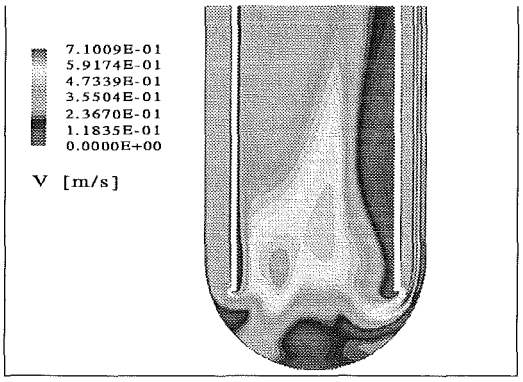

(a) Velocity

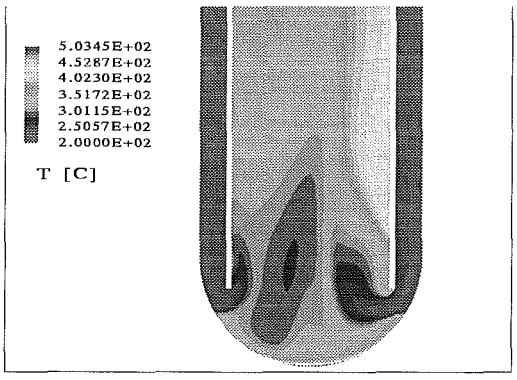

(b) Temperature

Figure 3.8: Results for V_b = 0.6 m/s.

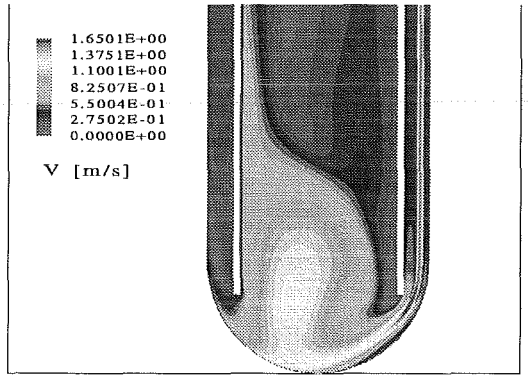

(a) Velocity

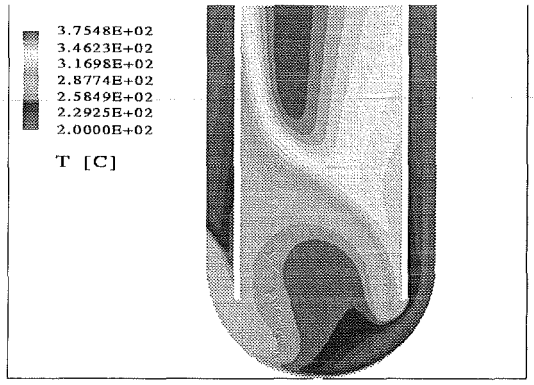

(b) Temperature

Figure 3.9: Results for V_b = 1.4 m/s.

3.3 Target with a Circular Bypass Pipe

3.3.1 Geometry and Boundary Conditions

Rectangular bypass pipe may be preferred due to the flexibility in varying the bypass flow area. However, in terms of fabrication and thermal stresses, a circular tube is more advantagable. In order to check the coolability óf the beam window in case of a circular bypass pipe, one calculation was carried out applying the parameters indicated in figure 3.10 and summarized below:

- gap size: h = 40 mm
- injection velocity: V_b = 1.0 m/s
- position of nozzle end: $\beta = 0^\circ$
- bypass pipe diameter: D = 10 mm
- distance from the wall: δ = 5 mm
- direction of injection: on x-axis

In this case the bypass mass flow rate is only 2.7% of the total mass flow rate, which is about 20% of the flow rate in case with a rectangular bypass pipe. For simplicity the thickness of the bypass pipe is neglected in this calculation.

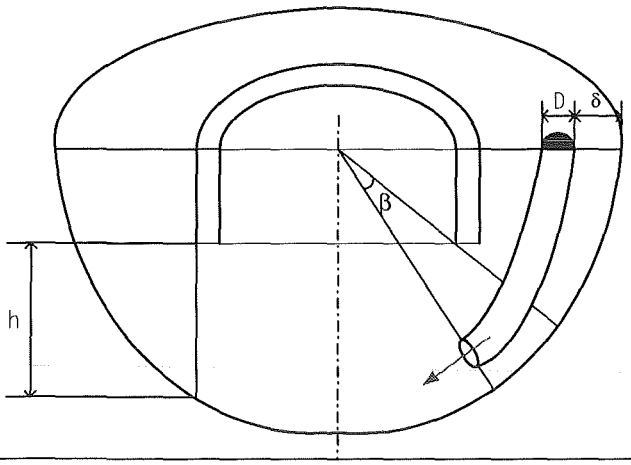

Figure 3.10: Main parameters of the spallation target with a circular bypass injection pipe.

3.3.2 Results and Discussion

Figure 3.11 shows the temperature and the velocity profiles in the target with a circular bypass pipe. The maximum velocity is less than 1.2 m/s, well below the design limit. The maximum surface temperature of the beam window is 387°C, which is at the same level as in the case with a rectangular bypass pipe, although the mass flow rate is much lower. Obviously, with a circular bypass pipe the beam window can be sufficiently cooled down and the spallation heat can be safely removed from the active part of the target. The design with a circular bypass pipe is proven to be a promising design concept which has to be further investigated in the future.

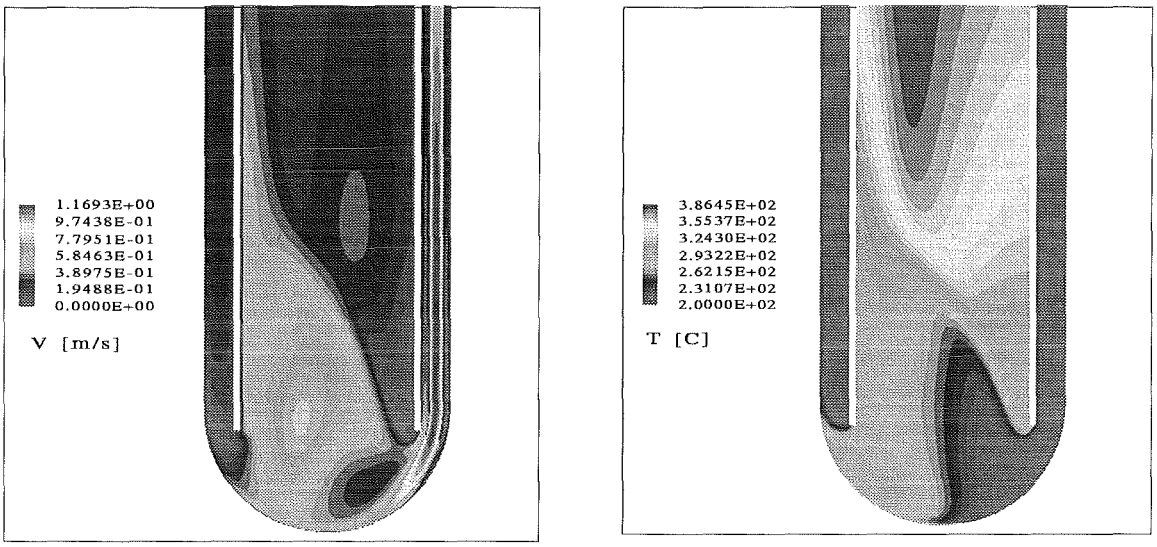

(a) Velocity (b) Temperature

Figure 3.11: Velocity and temperature profiles for a circular bypass pipe.

4. Conclusions

A thermal-hydraulic analyses of the active part of the MEGAPIE spallation target has been performed using the CFX 4.3 code. Three different geometric configurations were considered, i.e. flat guide tube, slanted guide tube, rectangular and circular bypass pipe. From the numerical results the following conclusions can be drawn:

- In the MEGAPIE spallation target with a flat guide tube an excessive hot spot on the surface of the beam window occurs. The maximum temperature is far beyond the design limit of about 400°C.
- By using a slanted guide tube instead of a flat guide tube the zone of flow stagnation near the center of the beam window is reduced. The coolability of the beam window is improved significantly. Nevertheless, the maximum temperature is still far beyond the design limit.
- With either a rectangular or a circular bypass pipe, the beam window can be cooled sufficiently and the heat deposited in the target can be safely removed.
- Compared to a thermally insulating wall, a thermally conducting wall of the guide tube results in an increase of the temperature of the window surface by about 50 K. This should be taken into consideration when designing the MEGAPIE target.

- A higher injection velocity through the bypass-pipe reduces the temperature of the beam window. However, it causes a large recirculation in the spallation area and, subsequently, leads to a higher temperature of the Pb-Bi in the spallation area.
- Due to the asymmetric distribution of the heat deposition in the window as well as in the target, it is recommended to install the bypass pipe on the axis with the smallest spreading length of the proton beam.
- For the case with a circular bypass pipe, a much smaller bypass flow rate is required. However, the coolability of the beam window is comparable to the case with a rectangular bypass pipe. A further systematical study is necessary to optimize the geometrical parameters of such a circular bypass pipe.

References

G. Bauer, 2000
Description of SINQ and Boundary Conditions for MEGAPIE, 1st MEGAPIE General Meeting, CEA, Cadarache, 14.-15., June 2000

T. Dury, 2000
Personal Communication, September, 2000

AEA Technology, 1998
CFX 4.3 User Guide

S. Buono, 1999
Thermal-physical properties of liquid Pb-Bi, First Meeting of the Benchmark Working Group on Heavy Liquid Metal Thermal-Hydraulics, June 29-30, 1999, CERN, Geneva

L.P. Ni, 2000
Personal Communication, November, 2000

II. Liquid metal corrosion

(J. Konys, H. Glasbrenner, IMF III; G. Müller, A. Heinzel, IHM; A. Rusanov, IPPE Obninsk, Russia)

Abstract

Experiments were conducted in a liquid lead pumped loop at 400 °C and 550 °C to examine the corrosion behaviour of ferritic and austenitic steels. The aim of this work is to identify suitable structural containment materials for a lead cooled accelerator driven transmutation reactor (ADS). During exposure to liquid lead containing 3 - $4 \cdot 10^{-5}$ wt% oxygen, protective oxide layers grow on the surface of each candidate alloy. The total thickness of the multiphase layers increases parabolically with increasing exposure time. After 3000 h, they reach a maximum of 50 µm on one ferritic steel (Optifer) and of 30 - 40 µm on electron pulse treated austenitic steels. Austenites with an untreated surface develop oxide layers of just 1-2 µm thickness. In each case the oxide layers prevent the dissolution attack of liquid lead.

Zusammenfassung

Es wurden Auslagerungsversuche bei 400 °C und 550 °C in einem Bleikreislauf durchgeführt, um das Korrosionsverhalten von ferritischen und austenitischen Stählen zu untersuchen. Ziel ist es Stähle zu identifizieren, die für den Einsatz in bleigekühlten beschleunigergetriebenen Reaktoranordnungen (ADS) eingesetzt werden können. Während der Auslagerung im flüssigen Blei, das einen Sauerstoffgehalt von $3 - 4\ 10^{-5}$ wt% aufweist, haben sich auf allen Stählen schützende Oxidschichten gebildet. Die Zunahme der Oxidschichtdicke, die aus unterschiedlichen Lagen besteht, folgt einem parabolisch Wachstum. Nach 3000 h beträgt die maximale Schichtdicke 50 µm auf einem ferritischen Stahl (Optifer) und 30-40 µm auf austenitischen Stählen, die mit gepulsten Elektronen behandelt wurden. Austenite, die an der Oberfläche nicht behandelt wurden, weisen Oxidschichtdicken von nur 1 – 2 µm auf. In allen Fällen schützen die Oxidschichten vor dem Lösungsangriff durch das flüssige Blei.

1. Introduction

Transmutation of plutonium, minor actinides and long-lived fission products can be accomplished in an Accelerator Driven System (ADS) to reduce the half-life of these elements [1]. For this purpose protons are injected into a spallation target through a vacuum beam pipe in order to generate free nucleons (neutrons) by a spallation process. The spallation neutrons convert non-fissile isotopes into fissile ones (transmutation). A heavy liquid metal like lead or the eutectic lead-bismuth alloy is needed for the spallation target material to ensure efficient production of neutrons. Furthermore, the molten metal is intended to be used not only as a target but also as a coolant in the accelerator system. It is known that the heavy metals lead and bismuth are much more corrosive than alkali metals [2-4]. As a consequence the behaviour of possible structural containment materials in heavy liquid metal has to be investigated.

The alloy elements nickel and chromium have a high solubility in lead at elevated temperatures [5], which leads to a strong dissolution corrosion attack by leaching of nickel and chromium contained in the steel. The formation of a protective oxide layer on the surface of the structural materials can prevent dissolution corrosion attack of liquid lead [6,7]. To maintain the oxide layer stability, the oxygen content in lead should not drop below a critical value which would lead immediately to dissolving of the oxide layer and subsequently to a dissolution corrosion attack. Hence, a continuous monitoring of the oxygen content in the melt is required to avoid corrosion.

2. Experimental section

2.1 Materials

Two ferritic-martensitic steels (Optifer IVc and EM 10) and two austenitic steels (1.4948 and 1.4970) have been selected for corrosion testing in circulating lead. The ferritic-martensitic steels were developed in the framework of the Fusion Technology Project to achieve low activation steels as structural materials. Both austenitic steels tested have good mechanical properties at the loop temperatures [8]. Significant experience exists with the steel 1.4948 which was used as a material for tubes, pressure vessels and other structural components in sodium cooled fast breeder reactors. The chemical composition of the austenitic steels is taken out of the

Stahlschlüssel [8] and the chemical composition of the ferritic steels was given by the suppliers. All data are summarised in table 1.

Material	C%	Mn%	Si%	Cr%	Ni%	Mo%	W%	V%	Nb%
1.4970	0.08-0.12	1.6-2.0	0.25-0.45	14.5-15.5	15-16	1.05-1.25	--	--	--
1.4948	0.04-0.08	0-2.0	0-0.75	17-19	10-12	--	--	--	--
Optifer IVc	0.13	0.52	--	9.05	--	--	1.0	0.25	--
EM 10	0.10	0.51	0.37	8.8	0.2	1.0	--	0.03	0.01

Table 1: The chemical composition in wt% of the steels tested in Pb.

2.2 Specimen preparation

Cylindrical specimens were machined of the as received material with a length of about 110 mm and a diameter of 8 mm.

About 1/3 of the specimens were treated by the pulsed electron beam of GESA (Gepulste Elektonen-Strahl-Anlage). In this process, a thin surface layer (50 cm^2) can be melted and cooled in a very short time. The rapid solidification after the pulse (cooling at 10^7 K/s) results in a very fine grained structure. The GESA installation is described elsewhere [9].

2.3 Lead corrosion loop

The corrosion tests were carried out in a non-isothermal pumped lead loop at IPPE Obninsk. The flow loop consists of a main heater, a cooler, a hot and a cold test section, an electromechanical pump, a purification system, a flow meter and two oxygen meters. Two test sections are available, one at 400 °C, the other at 550 °C.

The volume of the liquid lead in the loop is around 60 l, and the steady state flow velocity is 1.9 m/s. The temperature is maintained by electrical resistance heating. This heating zone is positioned just upstream of the hot test section. For cooling the circulating lead, a three-wall cooler construction is applied: cooling water – stagnant Pb-Bi alloy – pumped lead. The cooler is placed directly upstream of the cold test section.

The loop consists of tubes with an inner diameter of 30 mm and 4 mm wall thickness. The tubing of the hot section is made of austenitic chromium nickel 20Cr14Ni2Si steel whereas in the cold section (less than 460 °C) an ordinary austenitic stainless steel 18Cr10Ni1Ti is employed.

In the present corrosion test the oxygen content in lead was monitored by two oxygen meters placed in the two temperature zones. The oxygen activity in the liquid lead is measured by the electrochemical cells of the oxygen meters. The error of E.M.F. measurements in the Pb-O system with an oxygen meter does not exceed 2 % [10]. Up to now the oxygen meters used are not described in the literature and hence no details are available.

2.4 Experimental conditions

The specimens to be tested were fit together in the test sections with fixing their tails by pins in adapter bushes and in upper and bottom grids. The temperature of the hot test section was 550 °C, the temperature in the cold test section 400 °C. The concentration of oxygen dissolved in the liquid metal was around 3 – 4 x 10^{-5} wt%. The exposed materials and the corresponding test conditions are summarised in table 2. Specimens were cleaned after exposure in hot oil to remove residues of lead. Post-test analysis consisted of: (1) weighing of the cleaned specimens, (2) X-ray spectral microanalysis of the surface of the specimens, (3) metallurgical examination and (4) EDX line scan analysis on the cross-sections of the specimens.

Material	**400 °C**	**550 °C**	**400 °C**	**550 °C**	**400 °C**	**550 °C**
1.4970	1027 h	1027 h	2000 h	2000 h	3027 h	3027 h
1.4970 - GESA	--	1027 h	--	2000 h	--	3027 h
1.4948	1027 h	1027 h	2000 h	2000 h	--	3027 h
1.4948 - GESA	1027 h	1027 h	--	2000 h	--	3027 h
Optifer IVc	1027 h	1027 h	2000 h	2000 h	3027 h	3027 h
Optifer IVc-GESA	--	1027 h	--	--	--	--
EM 10	--	1027 h	--	--	--	3027 h

Table 2: A list of the materials exposed to flowing lead at 400 °C and 550 °C.

3. Results

The cleaned specimens showed no sign of damage (i.e. no surface roughing, no porosity etc.) by dissolution attack. The visual inspection revealed an oxide formation with varying thickness on the surface of each specimen. Austenitic steels exposed to lead up to 2000 h revealed a golden shiny surface even when exposed to 550 °C,

which indicates the existence of a thin oxide layer. With increasing exposure time the colour of the surface turned darker, but even then it remained shiny. The surfaces of the ferritic steels (GESA treated and untreated) and also the GESA treated austentic steels were black coloured without any shiny area, i.e. thick oxide layers were formed.

X-ray diffraction patterns obtained from the surface of the ferritic steels showed the formation of the compound $(Fe,Cr)_3O_4$ already after 1000 h of exposure at 400 and 550 °C. No other compounds could be detected even after longer exposure time. In contrast oxide patterns were not visible in the spectra of the austenitic steels, because the oxide layers were too thin. Metallurgical examination of the austenitic steels showed an oxide layer thickness of about 2 µm after 3000 h of exposure at 550 °C (see fig. 1). This film prevents the dissolution attack of the liquid lead at least during the limited time of exposure.

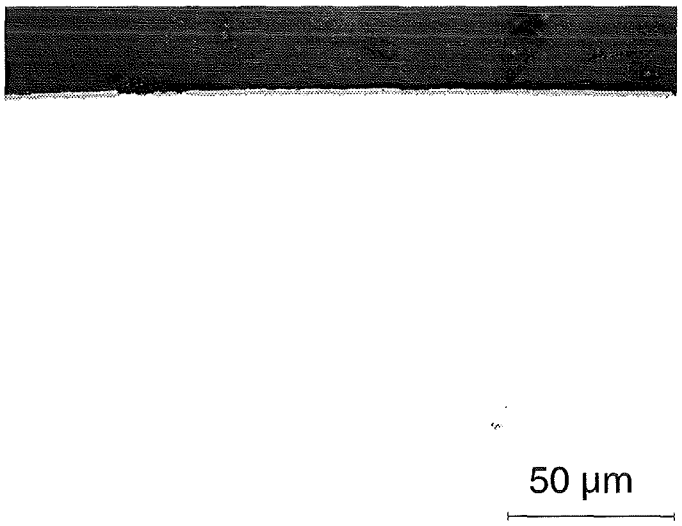

Fig. 1: Metallurgical examination of 1.4970 specimen after 3000 h at 550 °C in flowing lead.

A two phase oxide scale was found on all austenitic steels treated by GESA. Both layers vary in thickness. The adherence seems to be very good. The cross sections of GESA treated 1.4970 and 1.4948 steels after 3000 h of exposure at 550 °C and the corresponding EDX concentration profiles are presented in fig. 2 and 3.

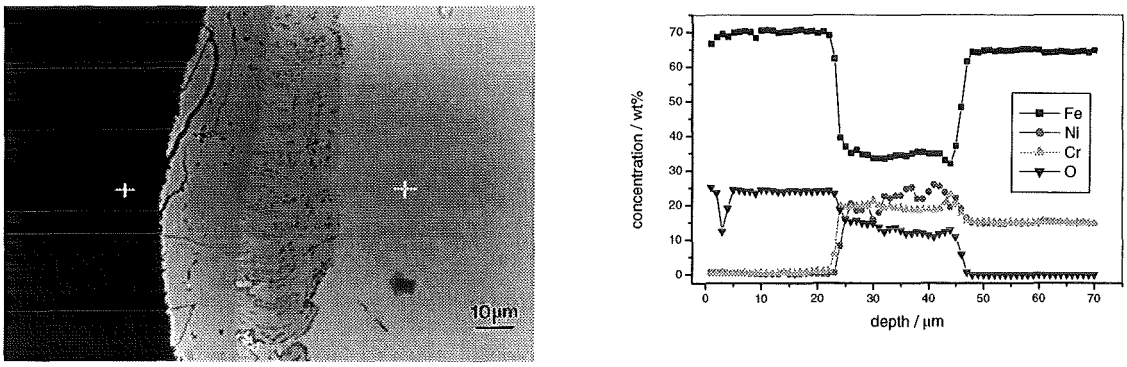

Fig. 2: Micrograph of GESA-treated 1.4970 specimen cross section and EDX concentration profile after 3000 h at 550 °C in flowing lead.

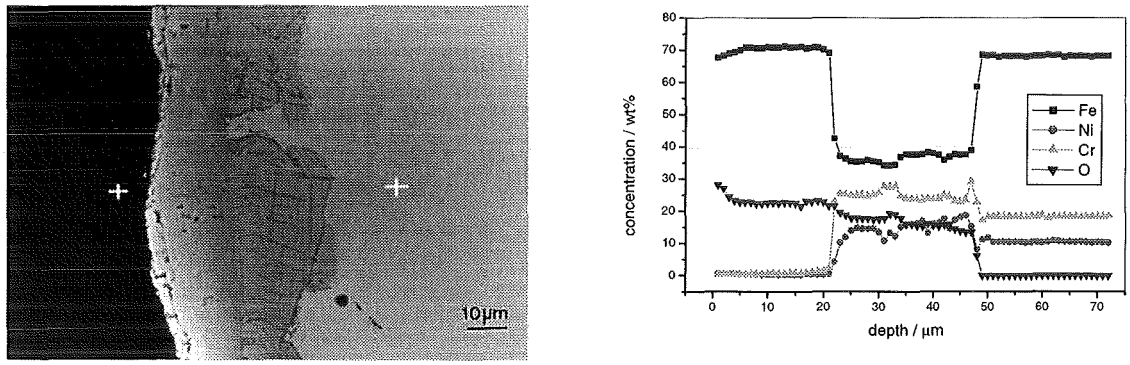

Fig. 3: Micrograph of GESA-treated 1.4948 specimen cross section and EDX concentration profile after 3000 h at 550 °C in flowing lead.

The outer layer has a composition of pure magnetite which is in agreement with the X-ray diffraction results obtained from specimens exposed to stagnant lead [11]. Other alloy steel elements like nickel and chromium were not detected. The inner layer contains iron, chromium nickel and oxygen. This corresponds to an iron chromium spinel plus nickel. The concentration of iron and chromium stays constant in the whole layer whereas the oxygen content decreases slowly and nickel increases slightly towards the steel side. In both austenitic steels the content of chromium and nickel is higher in the internal layer than in the steel matrix because of the release of iron into the magnetite layer.

In ferritic steels no obvious influence of the GESA treatment was observed [11]. The EDX concentration profiles with the corresponding cross sections of Optifer IVc (2000 h at 550 °C in lead) and EM 10 (3000 h at 550 °C in lead) are shown in fig. 4 and fig. 5.

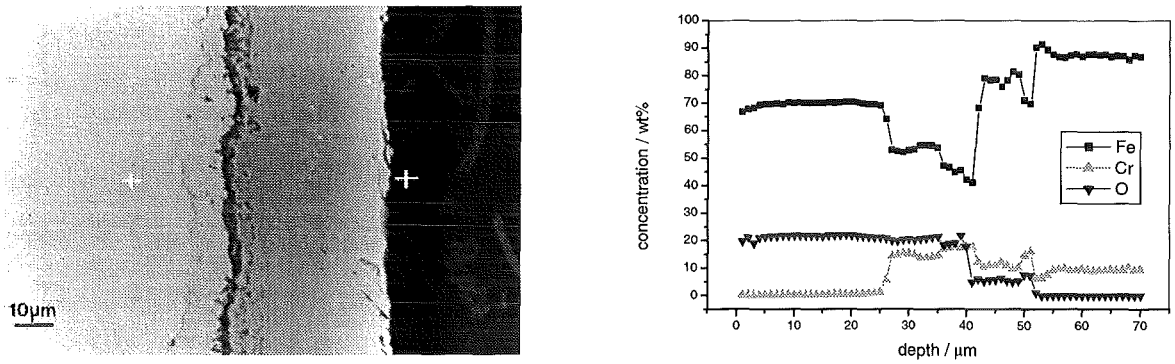

Fig. 4: Micrograph of Optifer IVc specimen cross section and EDX concentration profile after 2000 h at 550 °C in flowing lead.

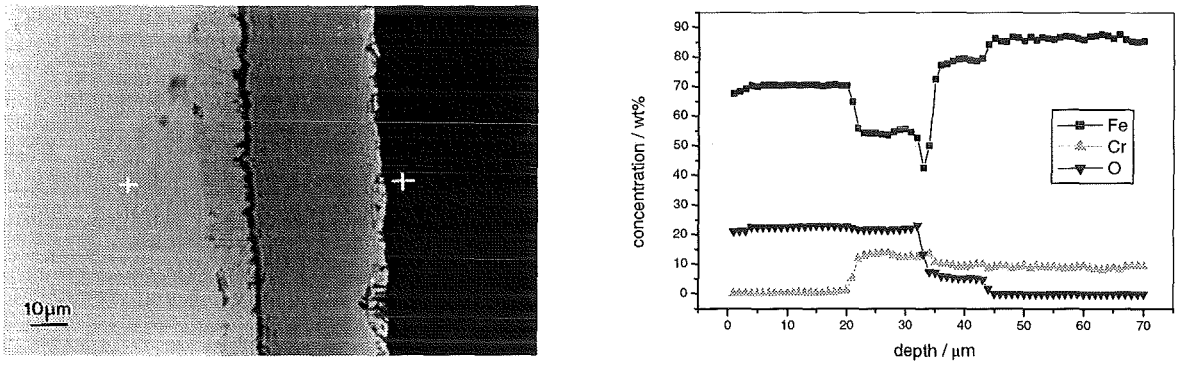

Fig. 5: Micrograph of EM 10 specimen cross section and EDX concentration profile after 3000 h at 550 °C in flowing lead.

The micrographs of the cross sections show the typical corrosion attack with three different zones. The zone at the top consists of magnetite without appreciable chromium concentration. The layer in the middle contains Cr-Fe spinel that roots in a porous belt. Within the spinel zone, the chromium content reaches a maximum that is 1.5 times higher than the concentration in the bulk material due to iron depletion caused by the magnetite scale formation. In the interior, an oxygen diffusion zone can be observed in which oxides precipitate along grain boundaries. In the case of EM 10 the thickness of all three zones formed is smaller than that on Optifer IVc.

The total oxide layer thickness increases with time and temperature, most dramatically for the ferritic steels and GESA-treated austenitic steels. The largest thickness is achieved on Optifer IVc, followed by the GESA treated austenitic steel 1.4948. The steels EM 10 and 1.4970 (GESA treated) showed more or less the same growth rate. The oxide layer thickness versus exposure time in liquid lead at 550 °C is given in fig. 6. It can be seen that the growth of the oxides on the ferritic steels and GESA-treated austenitic steels obeys the parabolic law.

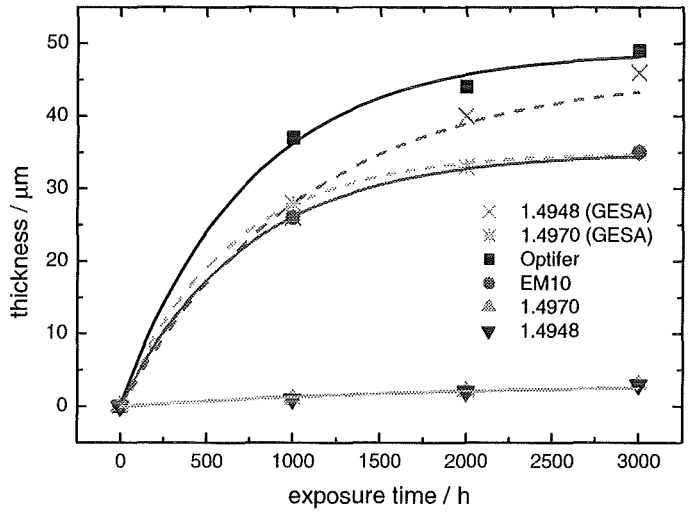

Fig. 6: Total thickness of oxide layers versus the duration of corrosion tests of steels in flowing lead at 550 °C.

4. Discussion

Multiphase oxide scales were formed on the steel surfaces of the ferritic steels and the two GESA treated austenites during exposure to flowing lead. These scales protect the steels against dissolution attack. Lead was not detected in any region of the specimens, i.e. no penetration of lead into the scale or the base material had occurred. Alloy components do not diffuse at the same rate in the oxide layers and the alloy, therefore a multiphase oxide scale is formed during oxidation of the alloys. The stratified oxide layer structure and composition agrees with descriptions by Hauffe [12] and Talbot [13] for oxidation of steels below 570 °C in air.

Three distinct oxidation zones were developed at the steel surfaces: an outer magnetite scale (Fe_3O_4) which is placed on top of the original surface; other than Fe and O, elements do not appear in an appreciable amount in this scale. The intermediate layer below the magnetite scale consists of a spinel $Fe^{2+}(Fe_{1-x}^{3+}Cr_x^{3+})_2O_4$ (+ Ni). The innermost layer is an oxygen diffusion zone with spinel formation along grain boundaries.

The proposed oxidation mechanism for this multiphase oxide scale can be described as follows [14-16]: firstly, oxygen reacts with iron and chromium to form the Fe-Cr spinel. Oxygen has the capability to diffuse inward through the oxide scale and reacts with steel elements to a spinel type structure. As a result of this O-ion diffusion the Fe-Cr spinel grows inward. The outer layer grows by Fe-ion diffusion to the surface,

which creates the magnetite scale that grows on the surface. Cr diffuses more slowly and is only present in the inner part of the scale.

The thickness and compositions of the multiphase oxide scales formed on the ferritic steels with and without GESA treatment do not show any difference. Hence, the additional surface treatment did not have an obvious influence on the oxidation behaviour of Optifer IVc and EM 10. Not so for the GESA treated austenitic steels 1.4970 and 1.4948, in which multiphase oxide scales were developed like observed for the ferritic steels. In the case of untreated austenitic steel surfaces a thin dense oxide layer was formed.

All the oxide scales developed on the examined steels provide protection against dissolution attack at 400 and 550 °C up to an exposure time of 3000 h in a liquid lead loop with controlled oxygen concentration. This corresponds well with the results of corrosion tests in stagnant lead during the same exposure time [11]. Those tests also included austenitic and ferritic steels in which aluminium was alloyed into the surface by GESA pulse heating. In that case, a thin alumina scale appeared during the tests on the surface that prevented not only the dissolution attack of liquid lead but also oxidation of the steel components. This treatment may provide a superior corrosion protection especially for exposure times much longer than 3000 h.

5. Conclusions

Ferritic and austenitic steels appear to be suitable structural materials for liquid lead loops up to 550 °C if the dissolution attack is prevented by a dilute solution of oxygen in the liquid metal. The concentration of oxygen must be controlled at a value at which a protective oxide scale builds up at the steel surface but no PbO is formed. Oxide scales on ferrites that develop under these conditions in lead agree in structure with those for oxidation in air. Austenitic steels have such scales only when the surface is treated by the GESA process. Untreated austenites show only very thin oxide layers of about 1-2 µm. Results obtained so far are representative for exposure times up to 3000 h only. It remains to be determined whether this conclusions is valid for longer times and also whether the thick oxide scales provide a better protection than the thin scale observed on austenitic steel. However, oxidative corrosion may become a problem with long exposure times. Alloying of aluminum into the surface of the steels has to be considered as a prospective treatment for a protection against

corrosion because the alumina scale prevents not only dissolution attack but also oxidation of steel components.

5. Acknowledgement

The work has been performed in the frame work of the Nuclear Research Project of the Research Centre Karlsruhe. The authors wish to thank Mr. Peter Graf for the metallographical examination and Mr. Volker Zibat for the EDX line scan analysis.

6. References

[1] C. Rubbia, J.A. Rubio, S. Buono, F. Carminati, CERN/AT/95-44 (ET), September, 1995.

[2] W.E. Berry in "Corrosion in Nuclear Applications", John Wiley and Sons, New York 1971, p. 308.

[3] G.M. Tolson, A. Taboada, ORNL-TM1437, April 1966.

[4] R.C. Asher, D. Davies, S.A. Beetham, Corr. Sci., 17 (1977) 545.

[5] C. Guminski, Metallkunde, 81 (1990) 105.

[6] B. F. Gromov, Yu. I. Orlov, P. N. Martynov, K. D. Ivanov, V. A. Gulevsky," Liquid Metal Systems", ed. by H. U. Borgstedt and G. Frees, Plenum Press, New York, pp. 339, 1995.

[7] V. Markov, Seminar on the Concept of Lead-Cooled fast Reactor, Cadarache, September 22 - 23, 1997 (unpublished).

[8] Stahlschlüssel 1995, Verlag Stahlschlüssel, Wegst GmbH, Marbach, Germany, Version 1.2.

[9] G. Müller, G. Schumacher, D. Strauß, V. Engelko, A. Andreev, O. Kamarov, K. Shigalichin, Proc. 11th Int. Conf. High Power Part. Beams, Prague (1996) 267.

[10] A. Rusanov, Private Communication.

[11] G. Müller, G. Schumacher, F. Zimmermann, J. Nucl. Mater., 278 (2000) 85.

[12] K. Hauffe, Oxidation of Metals, Plenum Press 1965.

[13] D. Talbot, J. Talbot, Corrosion Science and Technology, CRC Press, 1998.

[14] F. Gesmundo, C. de Asmundis, G. Battilana, E. Ruedl, Werkstoffe und Korrosion, 38 (1987) 367.

[15] K. Kuroda, P.A. Luban, G. Welsch, T.E. Mitchell, Oxid. Metals, 19 (1983) 117.

[16] G. Müller, FZKA Report 6422, February 2000.

III. Physics Investigations for Innovative Nuclear Reactor Systems

(C.H.M. Broeders, R. Dagan, B. Merk, V. Sanchez, IRS; I. Broeders, E. Stein, IKET)

Abstract

In this contribution the actual status at FZK for the physics investigation of proposals for the design of innovative reactor systems is presented. At present two such systems are under investigation: the High Performance Light Water Reactor (HPLWR) and accelerator-driven sub-critical systems (ADS). Available calculation tools, ongoing validation efforts and improvement of the dynamic simulation of ADS are discussed in some detail.

Zusammenfassung

In diesem Beitrag wird der aktuelle Status der Arbeiten im FZK für die physikalische Untersuchung von Entwürfen für innovative Reaktorsysteme beschrieben. Z.Zt. werden zwei solcher Systeme betrachtet: der „High Performance Light Water Reactor" (HPLWR) und Beschleuniger getriebene unterkritische Anordnungen (ADS). Die eingesetzten Rechenprozeduren, die laufenden Validierungsuntersuchungen und Verbesserungen für die dynamische Simulation von ADS werden eingehend diskutiert.

1. Introduction

An important issue of the R&D program NUKLEAR at FZK is to maintain the capability to analyse the physical characteristics of proposals for innovative nuclear reactor systems. For this purpose adequate state-of-the-art calculation tools have to be kept operable and must be validated as well as possible for the intended applications. At present two quite different innovative nuclear reactor systems are under investigation:

- High Performance Light Water Reactor (HPLWR) with main objective to improve the efficiency factor of modern light water reactors (LWR) by the use of supercritical water as coolant, a solution already applied in conventional steam generating power plants.

- Accelerator-driven sub-critical reactor systems (ADS) for use for the incineration of nuclear wastes. ADS may play an important role in the future for closing the back-end of the nuclear fuel cycle.

In section 2 a more general overview of the main calculation tools for reactor physics investigations is presented. In section 3 validation work in progress is discussed. Improvements for the dynamic simulation of ADS are discussed in section 4. Section 5 gives a summary and an outlook for future work.

2. Calculation tools for reactor physics investigations

FZK has a long tradition with own developments of multi-group calculation tools for fast reactor research. The investigation for a high converter LWR with MOX fuel (APWR) in the eighties complemented these procedures with specific solutions for epithermal and thermal reactor systems. For fuel irradiation and depletion calculations the programs KORIGEN [1] and BURNUP [2], based on the well-known one-group code ORIGEN [3] from Oak Ridge, USA, have been developed and extensively validated. All these computer codes and libraries are accumulated in the FZK/INR development of the fully modular code system KAPROS [4] and its sub-system KARBUS [2]. After a long period of strong coupling of these codes with FZK-specific hardware and software resources, which made them practically non-transferable, recently a portable version for UNIX workstations was completed. Actually, KAPROS/KARBUS is running now on IBM RS6000 machines with AIX OS and on INTEL based PC with LINUX OS.

Alternatively to the multi-group procedures, the Monte Carlo methods become of increasing interest due to their ability to describe complex geometries and to utilize continuous energy resolution. The former drawback of Monte Carlo codes to be very computing time consuming is of decreasing importance because of the strongly increasing speed of modern computers. FZK relies since many years on international available Monte Carlo programs, especially on the MCNP code, continuously in development at Los Alamos National Laboratory, USA. At present two lines of MCNP are in use at FZK:

- Version MCNP4C [5] for fission and fusion reactor applications.

- Version MCNPX-2.1.5 [6] for ADS applications. MCNPX combines most of the features of MCNP4C with the Monte Carlo techniques to describe the physics of the spallation processes in the energy regions of interest for ADS. Moreover, FZK participates to beta-testing of MCNPX (actual version MCNPX-2.3.3).

An essential aspect of the use of calculation tools for innovative reactor concepts is their validation for these applications. This can be performed both by comparisons with alternative computation routes and with experimental data. However, confirmation of calcula-

tion procedures by relevant experimental results is indispensable. For this reason a number of actual tasks for the development of reactor physics codes is devoted to experimental validation. For this experimental qualification a number of projects in the framework of international cooperation are in progress, mainly within the 5. framework program (FP) of the European Community (EC) and in collaboration with the International Science and Technology Center (ISTC) in Moscow. The ISTC aims to coordinate the work of eastern nuclear weapon specialists in civilian projects, being partly funded by western partners.

3. Validation work in progress

3.1 HPLWR.

From the neutron physics point of view, the relevant consequence of supercritical water as coolant in a LWR is the strong axial variation of the coolant density. Although counter-measures like isolated water-moderator or solid-moderator rods are considered, these axial and radial variations lead to the need for careful validation of the applied calculation tools. At the present stage no experimental data for such fuel assembly configurations are available and validation work is restricted to code comparisons. At FZK it is planned to utilize multi-group procedures for the HPLWR design investigations, including reactivity coefficients and burn-up behaviour. As a first step benchmark investigations for different axial zones of the fuel assembly are in progress in cooperation with partners from CEA, France, VTT, Finland and KFKI, Hungary within the 5. EC FP [7]. At FZK Monte Carlo calculations with MCNP4C have been started for the complex full layout of a fuel assembly. Comparison with simplified MCNP4C models from VTT show good agreement if the same cross section database is applied. As next steps cross section data influences will be investigated and a simplified model for multi-group calculations has to be defined.

An additional complication for HPLWR design investigations is the strong feedback between the thermo hydraulic and the neutron physics design. For this reason automatic coupling of thermo hydraulic codes like RELAP5 [8], COBRA-IV [9] or other, more simplified models [10], with neutron physics codes is in progress. This will be realized by a loose coupling of the stand-alone thermo hydraulic codes with the modular KAPROS/KARBUS system.

3.2 ADS.

The validation of calculation tools for accelerator-driven sub-critical systems is a challenging task because no real experience is available so far with such systems where the proton beam of a powerful accelerator has to be guided into a high power spallation target within a sub-critical reactor system. Several aspects have to be verified:

- Impact of a strong neutron source in a sub-critical reactor system.

- Characteristics of the spallation target.

- Coupling of the spallation target and the sub-critical reactor system.

At present projects related to these three aspects are in progress.

3.2.1 Impact of a strong neutron source in a sub-critical system

Two complementary experiments for the investigation of the effects of a neutron source in a sub-critical system are in progress:

- In the ISTC project B70, performed in Minsk/Sosny, Belarus, a powerful neutron generator with 14 MeV neutrons is coupled with a low-power sub-critical thermal reactor system with the objective to study the behaviour of the sub-critical system and to perform integral cross section measurements for important isotopes of the back-end of the nuclear fuel cycle. FZK is collaborator in this project. Furthermore, the IAEA has included this project in its on-going ADS Coordinated Research Program. The first experimental results for the sub-critical core show good agreement with MCNP calculations for a detailed core-model [11]. This experiment is complementary to the MUSE project in the next section.

- In the MUSE program the effects of neutron sources with increasing strength in different positions of the experimental low-power fast reactor MASURCA at CEA, Cadarache, France, are investigated. FZK is participating in the MUSE program within the 5. EC FP. One of the first steps in this project was the definition of benchmark models for the MASURCA reactor. Actually, this experimental reactor has some features not yet intensively investigated with KAPROS/KARBUS. The composition of the large reflectors leads to very strong self-shielding effects in structural materials, especially in iron. To investigate these effects, a very strongly simplified benchmark model was proposed by CEA [12]. First calculations at FZK showed large discrepancies up to 8% between the K_{eff} results of continuous energy MCNP calculations and of KAPROS/KARBUS multi-group

calculations with 26- and 69-group constant libraries. After this observation the isotopes of the benchmarks were recalculated for the 69-group library with the actual version of the standard program for group constant calculations NJOY [13], using the JEF2.2 [14] nuclear database. This updating with new JEF2.2 based group cross sections leads to similar results of 69-group calculations and of MCNP4C and is in accordance with results of other participants to the MUSE project [12]. More detailed investigations showed that nearly all new calculated isotopes contribute to the reactivity into the same decreasing direction. It may be concluded that the participation in the MUSE project already has improved the 69-group constant library. After a number of MUSE experiments with neutron sources with relatively small strength, in the presently running experiment MUSE-5 a strong new constructed neutron generator GENEPI with 14 MeV neutrons is utilized.

3.2.2 Investigations for a high power spallation target

Typical ADS design proposals for energy production or spent fuel incineration apply proton beams with energies around 1 GeV and currents larger than 1 mA, sometimes even larger than 100 mA. For the target materials usually heavy metals like tungsten, lead, bismuth are selected. The construction of such a high power device is a challenging task and several aspects like material behaviour, window cooling, and impact of spallation products have to be considered carefully. Most of the input data for these investigations are provided by the physics calculations. As a step towards the construction of a spallation target for ADS, the MEGAPIE initiative of FZK, CEA and PSI, Switzerland, intended to construct a lead-bismuth eutectic (PBE) target as replacement in the existing SINQ accelerator at Villigen, Switzerland [15]. The proton beam at the SINQ target amounts about 575 MeV at 1.74 mA (≈1 MW). In the meantime this project is supported by the EC in its 5. FP. In order to gain confidence in the results of the physics calculations for such a target, a MEGAPIE benchmark investigation was initiated with participation of CEA, PSI, FZK, CNRS (France) and ENEA (Italy) [16]. Parameters to be investigated are: heat deposition in structural materials, decay heat and activation, neutron flux distribution, spallation product yields, damages in structural materials and neutron leakage. After the preparatory investigations in [17], FZK has provided a nearly complete solution for this benchmark [18], mainly using the MCNPX-2.1.5 code with own database and auxiliary programs. First comparisons show that our results usually are in good agreement with the solutions of the other participants. For the analysis of the spallation products a coupling with KAPROS/KARBUS/KORIGEN is in development, using standard output files of MCNPX.

3.2.3 Coupling of a spallation target and a sub-critical reactor system

A real irradiation of a slightly sub-critical system with a proton beam in order to investigate the generic problems with such a coupling is planned at JINR, Dubna, Russia. The proton beam of an existing accelerator with 600MeV, few μA, will be guided into a small sub-critical fast spectrum reactor core with MOX fuel, surrounded by a thick lead reflector. The sub-criticality level will be about $K_{eff} \approx 0.95$ leading to a system-power around 25 W. FZK supports this proposal and has recommended the realization as an ISTC project. The FZK cooperation within this project also resulted in an improvement of the multi-group data libraries of the KAPROS/KARBUS system. The Russian colleagues proposed to utilize Russian critical experiments with fast spectrum fuel with lead reflectors of increasing thickness as a benchmark investigation [19]. During the evaluation of these critical experiments an error on the standard 69-group library was detected: the group constants for the Pb-isotopes were not complete, but contained only data for depletion calculations. After updating as described above the improved library gives satisfactory results.

3.2.4 Enhancements of the nuclear databases

A traditional physics activity of nuclear science is the improvement of the databases. At FZK only minor activities are left in this area, mainly within the programs FUSION and NUKLEAR. The program NUKLEAR supports some activities within the 5. EC FP and collaborates with a number of ISTC projects. Measurements of cross section data for minor actinides and long-lived fission products are supported to improve the database for solving the problems of the backend of the nuclear fuel cycle. For ADS applications neutron and proton cross section measurements for important isotopes in the energy range up to several hundreds of MeV are in progress.

4. Improvements for the dynamic simulation of ADS

The dynamic simulation of ADS is an important application area to gain sufficient knowledge about the system control under normal and perturbed conditions. In ADS a number of characteristics deviate significantly in comparison with critical reactor systems. Moreover, the existence of a high power spallation source in the system is an additional complication. An important observation is shown in figure 1 for the behaviour of the radial power-density profile in ADS with one proton beam in the centre of the core. We may observe a strong increase of the radial peaking factor if the value of K_{eff} decreases. This

means that the basic assumption for the dynamic simulation of critical reactors, namely that during a reactivity change the space-dependent power-shape of the reactor does not change significantly, is not valid. Moreover it can be shown that first order perturbation theory, customarily used for the dynamic simulation of critical reactors, cannot be applied to ADS. For these reasons efforts have been started to provide more adequate computation tools for the dynamic simulation of ADS. The program SAS4A [20] was chosen as the basis for these developments because this code is well established for fast critical reactors and the actual ADS proposals mostly are based on fast spectrum systems.

4.1 Extension of the SAS4A code

The usual application of SAS4A assumes that during a dynamic simulation the space-dependent power-distribution (shape function) does not change and the time-evolution of the neutron-flux is based on the point kinetics model. Reactivity feedback effects, mainly caused by temperature and density changes in the core, are determined on the basis of pre-calculated tables, usually prepared by first order perturbation calculations. For ADS applications the following extensions of the SAS4A procedures are envisaged and to a large extent realized [21]:

- Treatment of the strong external source, including incorporation of source shut-off.

- Preparation of feedback reactivity tables based on ΔK_{eff} calculations. The present application is based on the CITATION [22] diffusion code. If required, the flexible coupling formalisms would enable the application of other flux calculation codes like the nodal transport code VARIANT [23] with moderate efforts.

- Recalculation of the power-distribution and the criticality during the simulation, using the restart options of the SAS4A code. This recalculation requires the feedback of the relevant temperature, composition and possibly geometry changes to the cross section code KARBUS and to the flux calculation code CITATION and has been realized with new KAPROS modules CTFILE and SASADS.

- Time-step selection will be flexible, but frequent power-distribution recalculation should be feasible. For this reason also optimal strategies for cross section calculations must be made available.

The KAPROS/KARBUS system usually utilizes 69-group libraries with the energy group structure of the well-known program WIMS [24]. This structure has been chosen because it is well suited for thermal, epithermal and fast reactor calculations. However, the computing times may become quite large and the use for SAS4A coupling is problematic if many recalculations are required. In such cases a speed-up of the cross section calculations may become mandatory. Several solutions may be considered for this purpose, e.g. the introduction of cross section libraries with a small number of groups or the use of pre-calculated tables with shielded microscopic cross sections. Few group constant cross section libraries are sensitive to the weighting spectrum applied in the group constant generation codes like NJOY [13]. This means that complete multi-group libraries have to be prepared for all systems with significant spectral variations. Preparation and validation of such libraries is a straightforward but tedious procedure. Generation of pre-calculated tables of shielded cross section also have severe drawbacks, e.g. for the calculation of Doppler effect if compositions significantly change. For the coupling of SAS4A with KAPROS/KARBUS a new formalism is under investigation: the creation of collapsed libraries, starting from a 69-group "master-library" and using system-specific weighting spectra. First tests with this new KAPROS module COLLIB show promising results. Systematic investigations with respect to the number of collapsed groups and to the selection of the group boundaries are in progress. The improved SAS4A procedures enable more accurate simulations of ADS but they still incorporate the point-kinetics treatment for the time dependent neutron flux amplitude. The use of small time-steps between succeeding flux and criticality calculations will result in long computing times. The next section describes shortly improved accurate fast calculation methods for the dynamic simulation of ADS.

4.2 Development of fast accurate calculation methods for dynamic ADS simulation

The space-time behaviour of nuclear reactor systems can be described by coupled differential equations for the balance of the neutron population and of the precursors of the delayed neutrons [21]. A commonly used solution method for critical reactors is the separation of a time-dependent amplitude function and a space-dependent shape function, leading to the point-kinetics formulation. The introduction of a weak time-dependency of the shape function by recalculation during the simulation may improve this technique. However, as indicated in figure 1, this synthesis is not well suited for ADS and we have to look for other solutions. Our current research aims at examining alternative methods for the efficient calculation of dynamic parameters for point kinetics and,

subsequently, multi-dimensional kinetics simulation of ADS. In particular, we examine the applicability of variational methods, (as described e.g. in [25]), as well as sensitivity theory for non-linear and non-homogeneous equations as originally developed in [26].

An important point for the dynamic simulation of nuclear systems is the efficiency of the formalisms to reduce the required computation time for acceptable solutions. The characteristics of the space-time behaviour of ADS show parameters varying over wide ranges. For example, as in critical reactors, the time-behaviour is determined by the prompt and delayed neutrons, having strongly different lifetimes. Further the space-dependent variations of the neutron fluxes are in large ADS much faster in the vicinity of the spallation sources than at large distances. In order to utilize such characteristics the application of multi-scale solutions is under investigation. First results for the time-dependent zero-dimensional equations are encouraging.

5. Summary and outlook

The present status of the main activities at FZK for the physics investigation of designs for innovative nuclear reactor systems has been presented. After a short overview of the available calculation tools, ongoing validation work is discussed. For HPLWR investigations coupling of thermo hydraulic and neutron physics codes is in development Especially for the ADS investigations additional experimental data is needed. Benchmark investigations for simplified critical reactor models lead to significant improvements of the available 69-group cross section libraries. An important milestone for the development of ADS is the MEGAPIE initiative, started by FZK, CEA and PSI; the design, construction and utilization of a 1MW spallation device with PBE target and coolant for use in the SINQ neutron source at PSI. A neutronic MEGAPIE benchmark investigation showed good agreement of FZK results with those of other participants. Available methods for the dynamic simulation of ADS have been analysed. Utilization of formalisms developed for critical reactors is doubtful and should be qualified by adequate methods. Modification of the SAS4A code is in progress to enable more accurate dynamic ADS simulation. Proposals for alternative solution techniques are discussed.

6. References

[1] U. Fischer, H.W. Wiese, „Verbesserte konsistente Berechnug des nuklearen Inventars abgebrannter DWR-Brennstoffe auf der Basis von Zell-Abbrandverfahren mit KORIGEN", KfK 3014 (1983)

[2] C.H.M. Broeders, „Entwicklungsarbeiten für die neutronenphysikalische Auslegung von Fortschrittlichen Druckwasserreaktoren (FDWR) mit kompakten Dreiecksgittern in hexagonalen Brennelementen", KfK 5072 (1992)

[3] M.J. Bell, „ORIGEN-The ORNL Isotope Generation and Depletion Code", ORNL-4628, UC-32 (1973)

[4] H. Bachmann, G. Buckel, W. Hoebel, S. Kleinheins, „The Modular System KAPROS for Efficient Management of Complex Reactor Calculations", Proc. Conference Computational Methods in Nuclear Energy Charleston, CONF-750413 (1975)

[5] J.F. Briesmeister, Editor, "MCNP- A General Monte Carlo N-Particle Transport Code Version 4C", LA-13709-M (2000)

[6] L.S. Waters, Editor, "MCNPX USER'S MANUAL", TPO-E83-G-UG-X-00001 (1999)

[7] G. Rimpault, P. Dumaz, "HPLWR WP2 tentative work programme", Private communication (2001)

[8] The Thermal Hydraulics Group, "RELAP4/MOD3 CODE MANUAL", VOLUME I: CODE STRUCTURE, SYSTEM, MODELS AND SOLUTION METHODS", RELAP/MOD3.2.2Gamma, Formerly NUREG/CR-5535 Volume1 (1999)

[9] C.L. Wheeler, C.W. Stewart, R.J. Cena, D.S. Rowe, A.M. Sutey, "COBRA-IV-I: AN INTERIM VERSION OF COBRA FOR THERMAL-HYDRAULIC ANALYSIS OF ROD BUNDLE NUCLEAR FUEL ELEMENTS AND CORES", BNWL-1962, UC-32 (1976)

[10] Y. Oka, "SPROD: single channel code for HPLWR", Private communication (2001)

[11] W. Gudowski, C. Broeders, S. Chigrinov, Y. Kadi, A. Kievitskaja, H. Klippel, I .Slessarev, A. Stanculescu, "IAEA Benchmark on Accelerator Driven System", Paper accepted for AccApp/ADTTA'01 Conference, RENO (2001)

[12] G. Rimpault, Private communication (2000)

[13] R.E.. MacFarlane, The NJOY Nuclear Data Processing System, Version 91, LA-12740-M, LANL (1994)

[14] NEA Data Bank, The JEF-2.2 Nuclear Data Library, JEFF Report 17 (2000)

[15] M. Salvatores, G.S. Bauer, G. Heusener, „The MEGAPIE initiative", PSI Bericht Nr. 00-05 (2000)

[16] Y. Poitevin, R. Enderle, E. Lehmann, „Specifications for a Neutronic Benchmark on the MEGAPIE Spallation Target", SERMA/LCA/RT/00-2862/A (2001)

[17] I. Broeders, C.H.M. Broeders, "Neutron Physics Calculations for ADS Targets", FZKA 6507 (2000)

[18] I. Broeders, C.H.M. Broeders, "FZK contribution to the MEGAPIE neutronic benchmark", Report in preparation

[19] A. Rogov, Private communication (2000)

[20] "The SAS4A LMFBR Accident Analysis Code System", ANL/RAS 83-38 revision 2 (1988)

[21] R. Dagan, C.H.M. Broeders, D. Struwe, "Modifications of the Code SAS4A for Simulation of ADS Designs", FZKA 6334 (2000)

[22] T.B. Fowler, D.R. Vondy, Cunninham, "Nuclear Reactor Core Analysis Code CITATION", ORNL-TM2496, Rev.2 (1971)

[23] G. Palmiotti, E.E Lewis, C.B. Carrico, "VARIANT: VARIational Anisotropic Nodal Transport for Mullti-dimensional Cartesian and Hexagonal Geometry Calculation", ANL-95/40 (1995)

[24] J.R. Askew, F.J. Fayers, P.B. Kemshell,"A General Description of the Lattice Code WIMS", Journal of British Nuclear Energy Society, 5,564 (1966)

[25] W.M. Stacey, "Space time Nuclear Reactor Kinetics", Nuclear Science and Technology, Vol. 5, Academic Press New-York (169)

[26] D.G. Cacuci, "Sensitivity theory for non-linear systems. Parts 1&2", Journal of Mathematical Physics, Vol. 22 (1982)

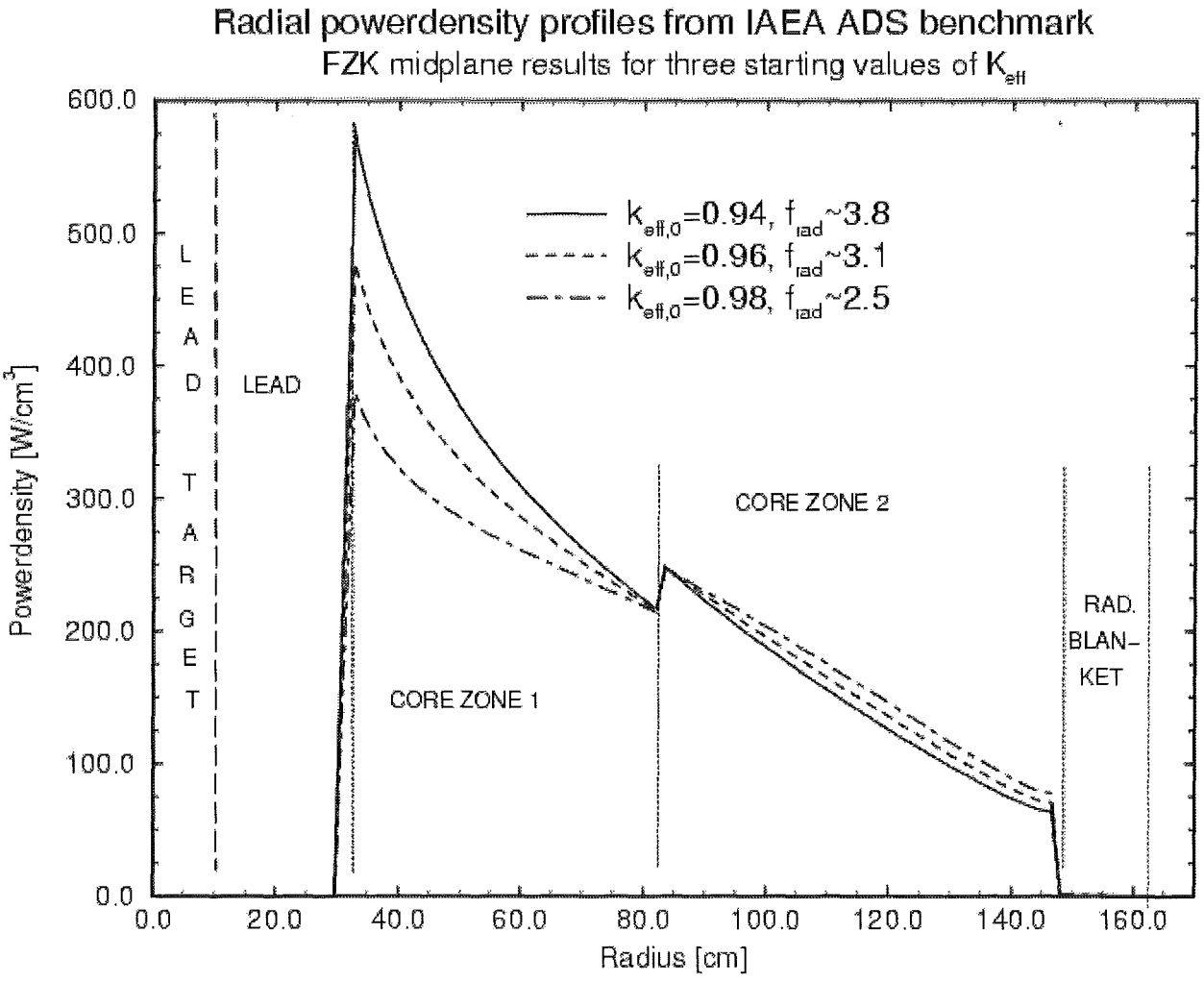

Figure 1: Radial power-density profiles for different levels of K_{eff} in ADS

IV. Entwicklung des Rechenprogramms FLUTAN für thermo- und fluiddynamische Anwendungen – Two and three-dimensional thermal and fluid-dynamical analysis of the complete MEGAPIE-module with the computer code FLUTAN

(L.N. Carteciano, B. Dorr, W. Olbrich, IRS; G. Grötzbach, IKET; X. Jin, Siemens/KWU)

Abstract

2d and 3d simulations of the complete MEGAPIE module were performed using the 3d thermal und fluid-dynamical code FLUTAN. The objective of these first numerical simulations is to investigate the feasibility of using FLUTAN for such calculations and to gain first insight in the flow and cooling behavior in a target module. So, we started with 2d and 3d calculations for a simplified representation of an earlier available module geometry, and switched later, when a new geometry became available, over to a simplified representation of this newer design.

Zusammenfassung

Mit dem 3d thermo- und fluiddynamischen Rechenprogramm FLUTAN wurden 2d und 3d Simulationen des gesamten MEGAPIE-Target-Moduls durchgeführt. Das Ziel dieser ersten numerischen Simulationen ist, die Tauglichkeit des Rechenprogramms FLUTAN für diese Rechnungen zu untersuchen und erste Aussagen zum Verhalten der Strömung und der Kühlung zu gewinnen. Wir haben mit 2d und 3d Simulationen für eine vereinfachte erste Geometrie des Moduls angefangen und später, als eine neue Geometrie verfügbar wurde, mit einem vereinfachten Abbild des neuen Designs weitergearbeitet.

1. Introduction

The results of the KALLA project 32.23.06 with experimental and numerical investigations on the cooling of thin-walled thermally highly-loaded surfaces shall be applied to the development of a target module for an ADS (Knebel et al. 2000). In parallel to this HGF-project, there is at PSI Würenlingen the MEGAPIE project ongoing in which a modeled target is developed for an ADS (Bauer et al. 1999). The target shall be irradiated in the SINQ radiation source (PSI Annual Report 1997). The results gained from

the design, construction, operation, and analysis of that target will provide a valuable basis for the development of an ADS target.

The thermal- and fluiddynamical design of such a target is widely basing on numerical tools like on CFD codes. As the system is rather complex, powerful codes with recent physical modeling, numerical schemes, and pre- and postprocessing tools are required. FLUTAN (Willerding & Baumann 1996) is a transient 3d thermal and fluid-dynamical code with a number of certain physical models like several turbulence models, heat exchanger and thermal structure models (Grötzbach et al. 2000), which make the code attractive to such investigations for a target module. Therefore, the code was already used to analyze the flow separation in the COULI benchmark target (Carteciano et al. 2000a) and to specify a separation-free target geometry (Carteciano et al. 2000b). The recent model extensions are discussed below before we concentrate on the investigations for the MEGAPIE target.

Detailed numerical analyses of the window area of the MEGAPIE-target need sufficiently fine grids. With current computers and codes such detailed numerical analyses can therefore only be performed for small areas around the window. Thus, accurate boundary conditions are required for the inlet and outlet of the relatively small computational domain. Such boundary conditions have to be provided e.g. by approximate 2d and 3d simulations of the complete MEGAPIE module. An other task will be to investigate numerically the principal features of the total target module in case of transients caused by trips of the beam power and by the cooling loops.

The objective of the first numerical simulations for a complete target module is to investigate the feasibility of using FLUTAN for such calculations and to gain first insight in the flow and cooling behavior in a target module. So, we started with 2d and 3d calculations for a simplified representation of an earlier available module geometry, and switched later, when a new geometry became available (Sigg 2001), over to a simplified representation of this newer design.

2. Recent developments for FLUTAN

Analyses of the coolability of targets in ADS systems require CFD codes which are specially adapted to the features of the used heavy liquid metals. An international comparison shows, none of the commercial codes provides turbulence models which are sufficiently accurate with such fluids even without heat transfer. The Turbulence Model for Buoyant Flows (TMBF), which was especially developed for FLUTAN for similar fluids (Carteciano et al. 1999), comes next to the required features. Therefore, the development of FLUTAN was concentrated on improving the physical models for heavy liquid metals, and on improving the efficiency of the numerical schemes used. The work on the turbulence modeling is performed under 32.23.06; there the TMBF in FLUTAN turned out to be widely successful in recalculating some of the TEFLU experiments (Knebel et al. 2001).

To improve the efficiency of the numerics of FLUTAN, a numerical procedure was developed to discretize the transport equations in complex geometries in body-fitted coordinates (Jin 2001). The intention was to improve the numerical accuracy by replacing stepwise discretizations of curved boundaries, which was the only possibility in FLUTAN up to now, by using body-fitted coordinates. The proposed and realized method is basing on a three-dimensional coordinate transformation of the equation system. The calculation of the geometry dependent coefficients for the transformed transport equations were implemented in FLUTAN. The method was carefully tested step by step, e.g. by using not only discretizations with non-rectangular tilted grids, but also with rotated coordinate systems having ordinates non-parallel to any mesh cell surface. The results show that a powerful tool is achieved because convergence and sufficient accuracy is found in contrast to common experience even for grids with highly tilted mesh cells. The transient calculation for a sump cooling experiment from the SUCOS-2D series was used as an application example. The former calculations with the Cartesian FLUTAN version concentrated on the interpretation of the experiments (Carteciano et al. 2000c, 2000d, 2000e, Grötzbach et al. 2000). Here the possibility of using body-fitted tilted grids was used to investigate accurately the possibility to improve the efficiency of the horizontal coolers by small inclinations in the main flow direction. It could be shown, that the critical cooling conditions on the horizontal coolers can indeed be improved by using already very small inclinations of

the cooler surface. The graphical presentations of the results are produced by using specially developed networks of AVS-UCD modules.

Meanwhile FLUATN became a large complex code system, consisting of many programs and tools for pre- and post-processing, data production, data conversion, and maintenance. Therefore, a graphical user interface was developed in which most of the existing programs of the FLUTAN code system were implemented. This user interface is based on the program language Tcl/Tk; thus, it can be used on Windows and on UNIX-based systems. This new graphical user interface improved the handling of the code system considerably.

An other measure to modernize the FLUTAN code was to develop and implement the program ONLIVIS (ONLIne VISualization), which was originally thought to have some control of the convergence behavior of a FLUTAN run. In practical applications with FLUTAN running on the VPP 5000 at FZK and the interactive part of ONLIVIS running on IBM/AIX systems, the program turned out to be a powerful tool to have not only some graphical online access to data of numerical interest, like the values appearing in convergence criteria, but also to several data of physical interest in a running simulation. The first version was programmed on the basis of the graphics software UNIGRAPH, which bounds the application to IBM/AIX systems. Therefore, a second version was programmed on the basis of the program language Tcl/Tk, which allows to use this program also in a heterogeneous Windows and/or UNIX-based computer environment. In addition, the communication between the two engaged computers is in the new version not datagram oriented but stream oriented. The tests with the new Tcl/Tk based ONLIVIS program were successful on all computers used with the FLUTAN code system.

3. Original geometry, 2d natural and forced convection, without bypass

In a first step of analyzing a MEGAPIE target, 2d FLUTAN calculations with a simplified modeling of the complete target module were performed. The geometry is chosen following the construction drawings of February 2000. The heat shall be removed by natural convection without a bypass jet flow across the window. The spatial distribution of the power deposition by the proton beam of 541 kW in the liquid

lead bismuth and in the structures is prescribed using an equation provided by Smith (2000). The window is cooled by liquid lead-bismuth flowing downwards in the annular space and upwards inside the inner pipe (Fig.1). Both channels are separated by the guide tube. The 2d thermal conduction in the guide tube was calculated for several materials with thermal conductivities ranging from 1 to 16 W/(m*K). The annular heat exchanger at the wider upper end of the target module is modeled by a heat sink distributed uniformly over the heat exchanger cross section, by the correct flow area, and by the two horizontal grid plates carrying the (not recorded) heat exchanger pipes. The fluid temperature at the heat exchanger exit is prescribed to be 223 ^{O}C. The standard k-ε model is used.

When the guide tube is modeled as a thermal structure made of 316 L steel with a given heat conductivity of 16 W/(m*K), the FLUTAN calculation shows that a thermal power of 513 kW is conducted through the guide tube from the hot flow inside the guide tube to the cold downcomer flow. This heat input increases the fluid temperature near the window drastically (Fig.1). The maximum temperature in the fluid reaches 2100 ^{0}C at the stagnation point at the window center. This is above the boiling temperature, but we assumed single phase conditions and extrapolated the material property data linearly. On the other hand, the temperature difference between the fluid temperature in the window region and at the heat exchanger inlet is reduced correspondingly. Due to the large radial heat flux, large radial temperature differences occur mainly inside the guide tube and also inside the cold down comer. A mass flow rate of only 13.3 kg/s is achieved; correspondingly, the temperature difference between inlet and outlet of the heat exchanger results in 256 K. So, the large radial heat flux through the guide tube is a consequence of the small mass flow rate and the following high temperature differences inside the module. Such a concept basing on natural convection, even if it would be used as a safety backup measure, is absolutely not acceptable.

When a guide tube with a small thermal conductivity is used, e.g. with a heat conductivity of 1 W/(m*K), the heat conducted through the guide tube decreases to only 70 kW. Therefore, the mean fluid temperature in the window region is clearly reduced in this case to1888 ^{0}C at the window center, in comparison to the previous case (Fig.2). On the other hand, the fluid temperature at the heat exchanger inlet is

increased when the guide tube is almost thermally insulated. This results from the reduced heat conduction from inside the guide tube radially outwards into the heat exchanger. The influence of the thermal conductivity of the guide tube on the mass flow rate is almost negligible.

2d calculations were also performed with FLUTAN for forced convection without a by-pass, using a thermal conductivity of 16 W/(m*K) inside the guide tube. The pump was specified to achieve a mass flow rate of 35 kg/s. The temperature difference across the heat exchanger is now reduced to 105 K (Fig. 3). With the reduced temperature level inside the module the total radial heat flux through the guide tube is reduced to 165 kW; from this, 135 kW occur in the area below the cooler, and 30 kW radially into the cooler. The temperature of the downcoming fluid arriving at the gap near the window is increased correspondingly by 29 K against the heat exchanger outlet temperature. The maximum fluid temperature near the window center remained with 1930 ^{0}C above the boiling value. Thus, also these 2d simulations with forced convection show that a bypass jet flow across the window is absolutely necessary to remove the consequences of the insufficient heat transfer from the stagnation point at the window center.

4. Original geometry, 3d forced convection, with bypass:

Simulations for a MEGAPIE concept with a forced bypass flow across the beam window require 3d representations. We consider a forced convection case with thermal conduction in the guide tube in the old geometry, and natural convection cases for a rough approximation of the new reference geometry with and without thermal conduction in the guide tube.

First 3d calculations were performed following the construction drawings of February 2000. The bypass in form of a jet flow across the window surface is modeled numerically by adding a source term at the position of the outlet nozzle specifying a certain mass flow rate (see the position of the velocity maximum near the center of the window in Fig. 4). The piping system feeding that nozzle is not recorded in the simulation. The spatial distribution of the power deposition of 541 kW in the liquid lead bismuth and in the structures is the same as it is used in the 2d calculations. The 3d

thermal conduction in the guide tube was calculated with two different thermal conductivities of 1 and 16 W/(m*K). The heat exchanger is modeled by a heat sink distributed uniformly over the heat exchanger cross section, by the correct flow area, and by the grid plates carrying the heat exchanger pipes. The fluid temperature at the heat exchanger exit is prescribed to be 223° C. The standard k-ε model is used again with a constant turbulent Prandtl number of σ_t=0.9 to calculate the heat transfer.

The 3d forced convection results from FLUTAN with a bypass flow of 3.5 kg/s, using a thermal conductivity of 16 W/(m*K) inside the guide tube, are shown in Figure 4. The main pump was specified to achieve a mass flow rate of 35 kg/s. Due to the bypass flow, the maximum value of the temperature is now with 483° C far below the boiling temperature. The FLUTAN calculation shows that a thermal power of 152 kW (29 % of the power deposition) is conducted through the guide tube from the hot flow inside the guide tube to the cold downcomer flow. The calculated velocity field shows an asymmetry between the flow field on the left bottom part of the downcomer and the one at the right side. This asymmetry is due to the fact that part of the bypass flow directly injects fluid through the gap between window and guide tube on the left. Some of the injected fluid is rising through the downcomer against the downwards coming cold fluid. The white zero-line in the velocity field in the left part of the annulus separates upwards and downwards coming fluid. Thus, the fluid has to redistribute azimuthally in the annular downcomer and consequently forms there a complex 3d vortex. This lower vortex induces also a vortex with opposite rotation direction in the annulus above, which is the reason for asymmetries in the u and T-field in the downcomer up to the heat exchanger outlet. The vortex may be even stronger in reality because the additional friction forces due to the bypass piping system coming down on the right hand side of the downcomer was not recorded in the calculation. The entity of this secondary flow will depend on the flow rate of the bypass, on the position and form of the nozzle, and on the widths of the vertical gap between guide tube and window. This asymmetry in the downcomer makes any separate local calculation for the window area problematic.

5. New geometry, 3d natural convection, with forced bypass flow:

Meanwhile new construction sketches for the new MEGAPIE target module concept were provided by Sigg (2001). The concept for the upper part of the target with the heat exchanger and the disposition of the pumps was modified in order to reduce the irreversible pressure losses due to the geometry contour inside the guide tube (see geometry in Fig. 5). Thus, 3d calculations were also performed for an approximation of this new geometry. The heat exchanger is again modeled by a heat sink distributed uniformly over the heat exchanger cross section. The outer diameter is adapted to achieve the correct free flow area. The calculations were done for natural convection with a forced bypass flow rate of 1.18 kg/s and with two different thermal conductivities for the guide tube of 16 and 1 W/(m*K).

The results show that the influence of the heat transferred through the guide tube on the temperature field is in this concept with 27.6 % at λ=16 W/(m*K) versus 4.3 % at λ=1 W/(m*K) very small. The temperature level near the window region is for the case of λ=16 W/(m*K) slightly higher in comparison with the other case (Figs. 5 and 6). The maximum value of the fluid temperature remains below the boiling temperature in both cases. In fact, a mass flow rate of about 40 kg/s is achieved inside the guide tube. This value is higher than the mass flow rate given in forced convection for the original geometry. This positive result is due to the reduction of the irreversible pressure losses in the new geometry.

An asymmetry in the downcomer exists also in this design, but it is weaker than in the previous case calculated with the old geometry mainly because of a lower value of the bypass flow rate was chosen in this calculation. Nevertheless, the asymmetries reach again far up in the downcomer towards the heat exchanger area. Thus, also in these cases detailed local numerical investigations for the window area will need special assumptions for the inlet and outlet conditions at the boundaries of the computational domain.

6. Conclusions

2d and 3d FLUTAN calculations were performed with FLUTAN for a simplified modeling of the complete MEGAPIE target module following the construction drawings of February 2000. The results show that without a bypass jet flow across the window the fluid temperature is above the boiling temperature either in natural convection or in forced convection cases. In that geometry and under those flow conditions the thermal conduction inside the guide tube turned out to be a critical feature to determine the coolant temperature at the window.

The 3d investigations with the new geometry and with a bypass jet flow across the window show that the influence of the thermal conduction in the guide tube is small compared to the results for the old geometry concept, and that it may be possible to neglect it under natural convection conditions. The thermal conduction does not considerably influence the fluid temperature near the window. Following the results for this simplified target module one may conclude that this target can now effectively be cooled even by means of a natural convection regime in combination with a forced bypass flow; this is achieved by the reduction of the irreversible pressure losses.

The 3d results show also, that the bypass flow induces vortices in the guide tube which cause asymmetries in the downcomer up to the heat exchanger area. As this asymmetry may be increased by including more accurate geometry information, especially of the bypass flow system, it is an iterative procedure between design and more accurate calculations to provide the information which is necessary to perform local detailed window cooling investigations. E.g., recently a much more detailed design for the heat exchanger became available; for safety reasons, the fluid content was drastically reduced by reducing the free cross section for the fluid on the primary side. Thus, it should be reconsidered numerically whether the heat can also be removed by natural convection in this new design or not.

The next steps should be firstly to analyze for the actual design the influence of using improved turbulence modeling of heat transfer, especially of using the extended Turbulence Model for Buoyant Flows (Carteciano et al. 1999) and then to analyze the dynamical behavior of the MEGAPIE target by means of 3d calculations. Such calcula-

tions are time consuming and expensive. Thus, not too many investigations are possible; they shall only be performed when the MEGAPIE concept is widely settled and more complete detailed information on the new reference concept is available.

References

Bauer, G., Salvatores, M., Heusener, G., 1999. The MEGAPIE initiative – Executive Outline and Status as per November 1999, Paul Scherrer Institut, Würenlingen, Switzerland.

Carteciano, L.N., Wörner, M., Grötzbach, G., 1999. Erweiterte Turbulenzmodelle für technische Anwendung von FLUTAN auf Naturkonvektion. Jahrestagung Kerntechnik 99, Karlsruhe, May 18-20, pp.129-134.

Carteciano, L.N., Dorr, B., Grötzbach, G., 2000a. Development of numerical models for heat transfer in liquid lead-bismuth. World Wide Web-site http://kalla.fzk.de/ (see ADS/Window Layout/Numerics).

Carteciano, L.N., Dorr, B., Grötzbach, G., 2000b. Unveröffentlicht

Carteciano, L. N., Dorr, B., Grötzbach, G., 2000c. Numerical interpretation of the single phase sump cooling experiments SUCOS with the FLUTAN code. Jahrestagung Kerntechnik 2000, Bonn, 23. - 25.5.2000, Kerntechnische Gesellschaft e.V., INFORUM Bonn, S. 153 - 156

Carteciano, L.N., Dorr, B., Grötzbach, G., 2000d. Numerical Investigation of the Natural Convection in Single-Phase SUCOS-Experiments with the FLUTAN Code. Third European Thermal Sciences Conf. (EUROTHERM 2000), Heidelberg, Germany, 10.-13. Sept.

Carteciano, L.N., Dorr, B., Grötzbach, G., 2000e. Numerical Investigation of the Single Phase Natural Convection in Sump Cooling Experiments with the FLUTAN Code. The Tenth Int. Conf. On Emerging Nuclear Energy Systems (ICENES 2000), Petten, The Netherlands, 24.-28. Sept.

Grötzbach, G., Carteciano, L.N., Dorr, B., 2000. Numerical Analysis of Experiments modelling LWR Sump Cooling by Natural Convection. International Atomic Energy Agency, Technical Committee Meeting on "Natural Circulation Data and Methods for Innovative Nuclear Power Plant Design", Vienna, Austria, July 18-21

Jin, X., 2001. Rechenverfahren zur Diskretisierung von Strömungen in komplexer Geometrie mittels körperangepasster Gitter. Dissertation. Forschungszentrum Karlsruhe, FZKA 6596

Knebel, J.U. , Cheng, X., Müller, G., Schumacher, G., Konys, J., Wedemeyer, O., Grötzbach, G., Carteciano, L., 2000. Thermalhydraulic and Material Specific Investigations into the Realisation of an Accelerator Driven System (ADS) to Transmute Minor Actinides – 1999 Status Report. Forschungszentrum Karlsruhe, FZKA 6506

Knebel, J.U. , Cheng, X., Müller, G., Schumacher, G., Konys, J., Wedemeyer, O., Grötzbach, G., Carteciano, L., 2001. Thermalhydraulic and Material Specific Investigations into the Realisation of an Accelerator Driven System (ADS) to Transmute Minor Actinides – 2000 Status Report. Forschungszentrum Karlsruhe, FZKA report to appear.

PSI Annual Report 1997. Annex IIIA, Paul Scherrer Institut, Würenlingen, Switzerland.

Sigg, B., 2001. Personal Information. Paul Scherrer Institut, Würenlingen, Switzerland.

Smith, B., 2000. Personal Information. Paul Scherrer Institut, Würenlingen, Switzerland.

Willerding, G., Baumann, W., 1996. FLUTAN 2.0 Input Specification. Forschungszentrum Karlsruhe, FZKA 5712.

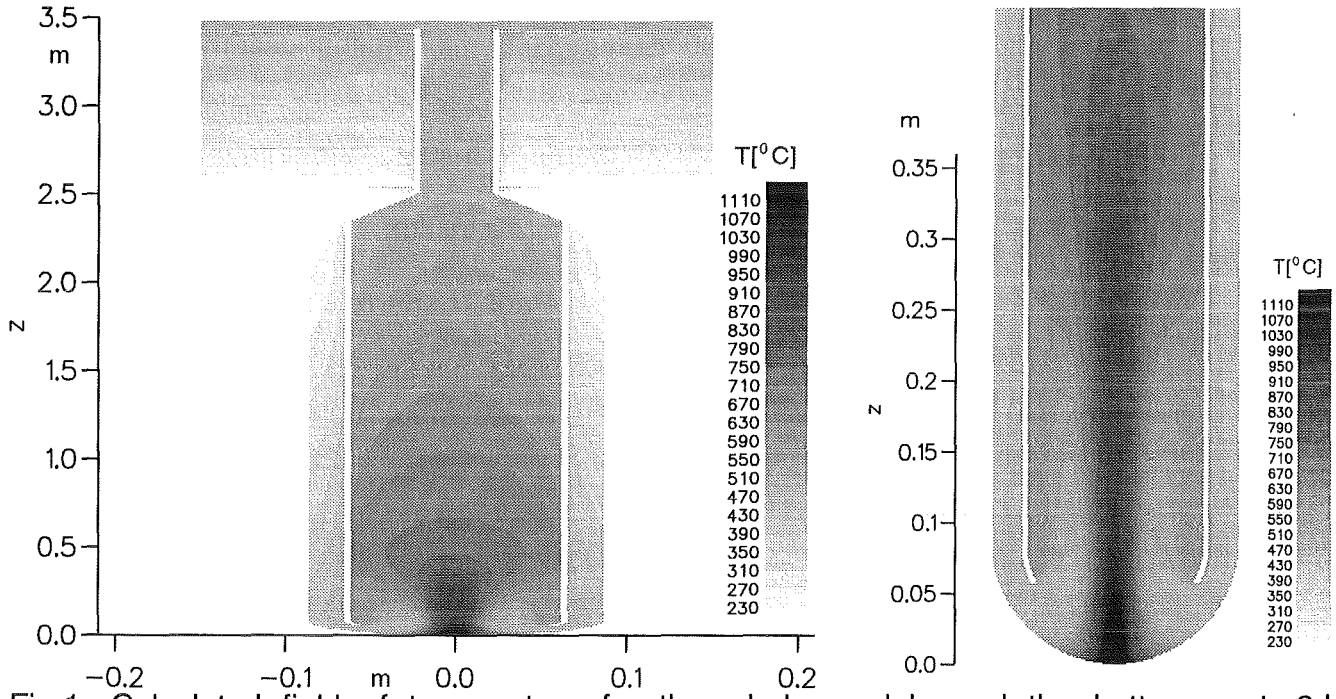

Fig.1: Calculated field of temperature for the whole module and the bottom part. 2d calculation, old geometry, natural convection, thermal conductivity of 16 W/(m*K) inside the guide tube.

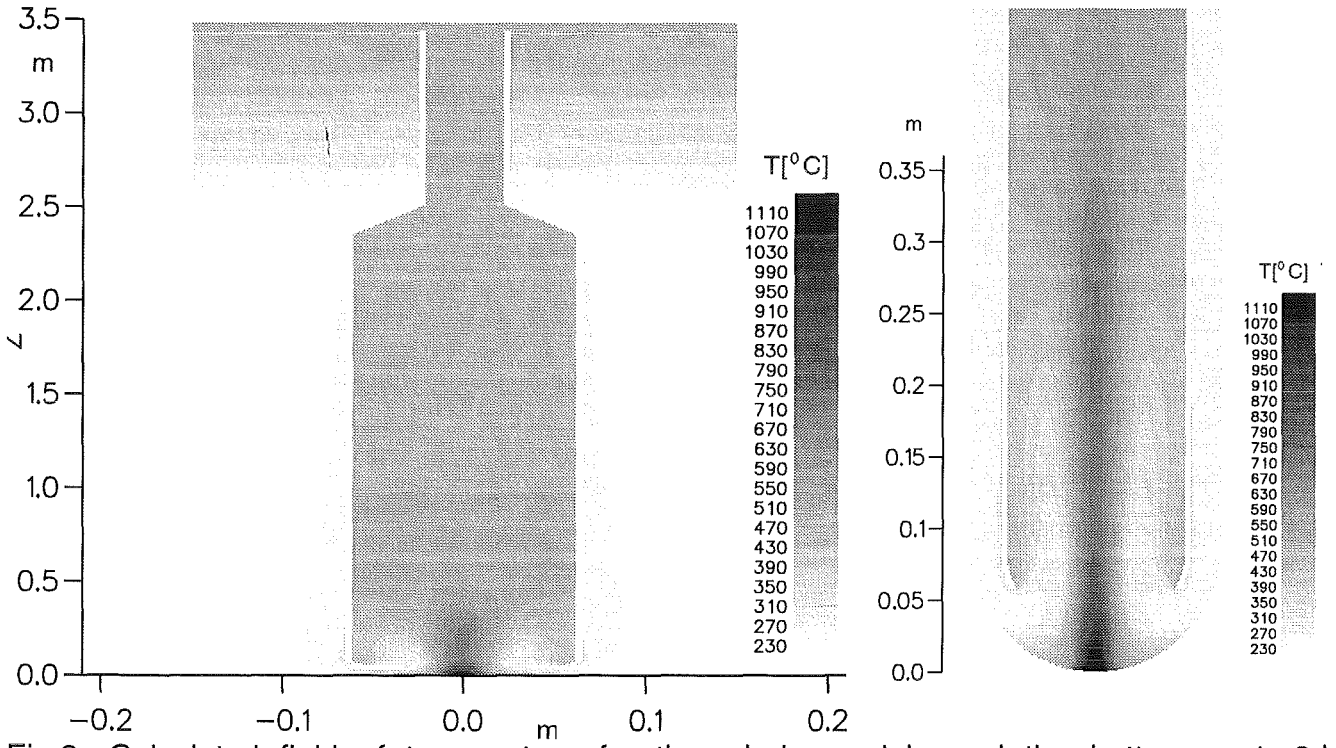

Fig.2: Calculated field of temperature for the whole module and the bottom part. 2d calculation, old geometry, natural convection, thermal conductivity of 1 W/(m*K) inside the guide tube.

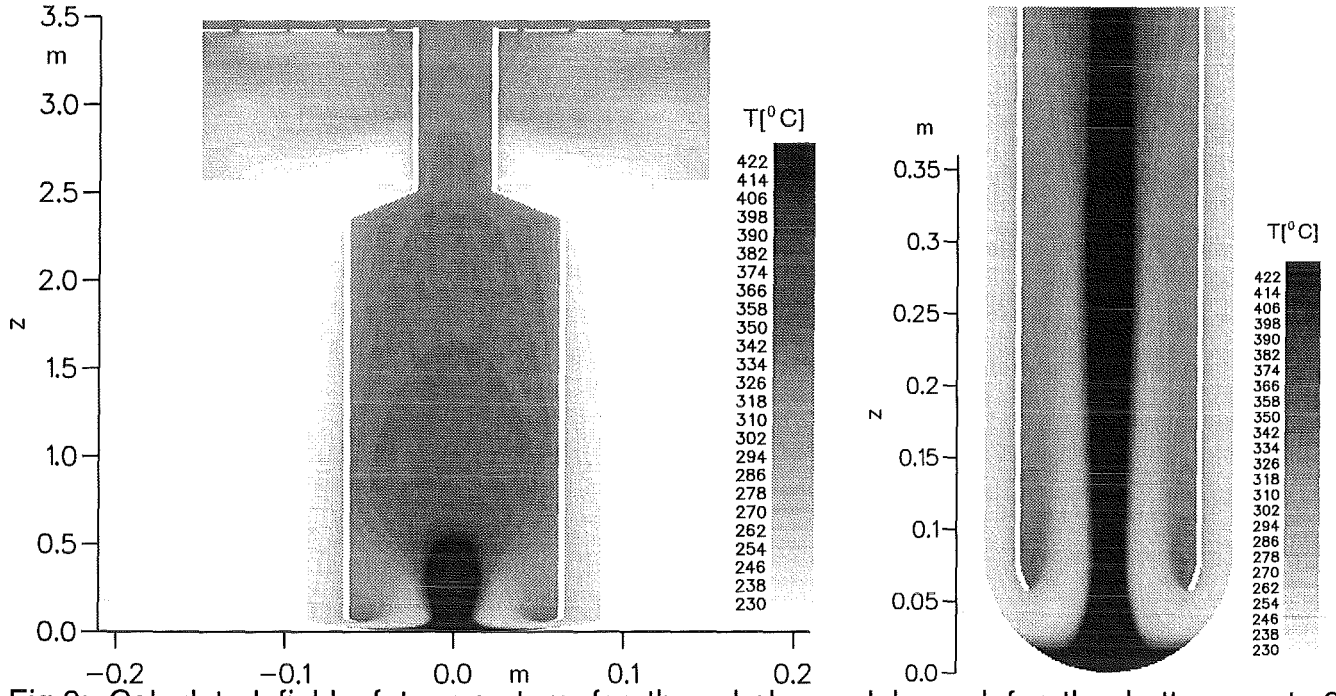

Fig.3: Calculated field of temperature for the whole module and for the bottom part. 2d calculation, old geometry, forced convection, thermal conductivity of 16 W/(m*K) inside the guide tube.

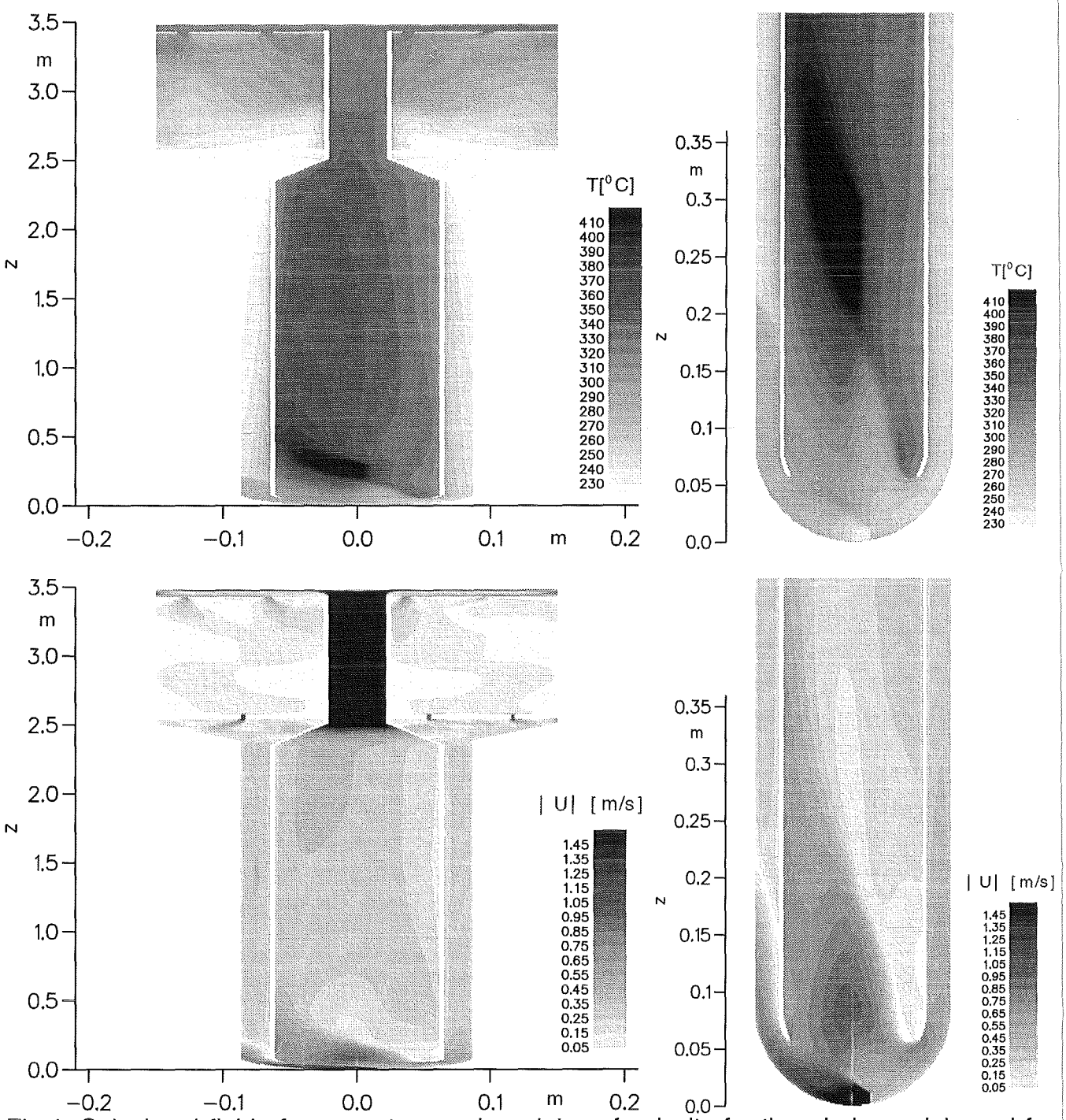

Fig.4: Calculated field of temperature and modulus of velocity for the whole module and for the bottom part. 3d calculation, old geometry, forced convection, mass flow rate of the bypass 3.5 kg/s, thermal conductivity of 16 W/(m*K) inside the guide tube.

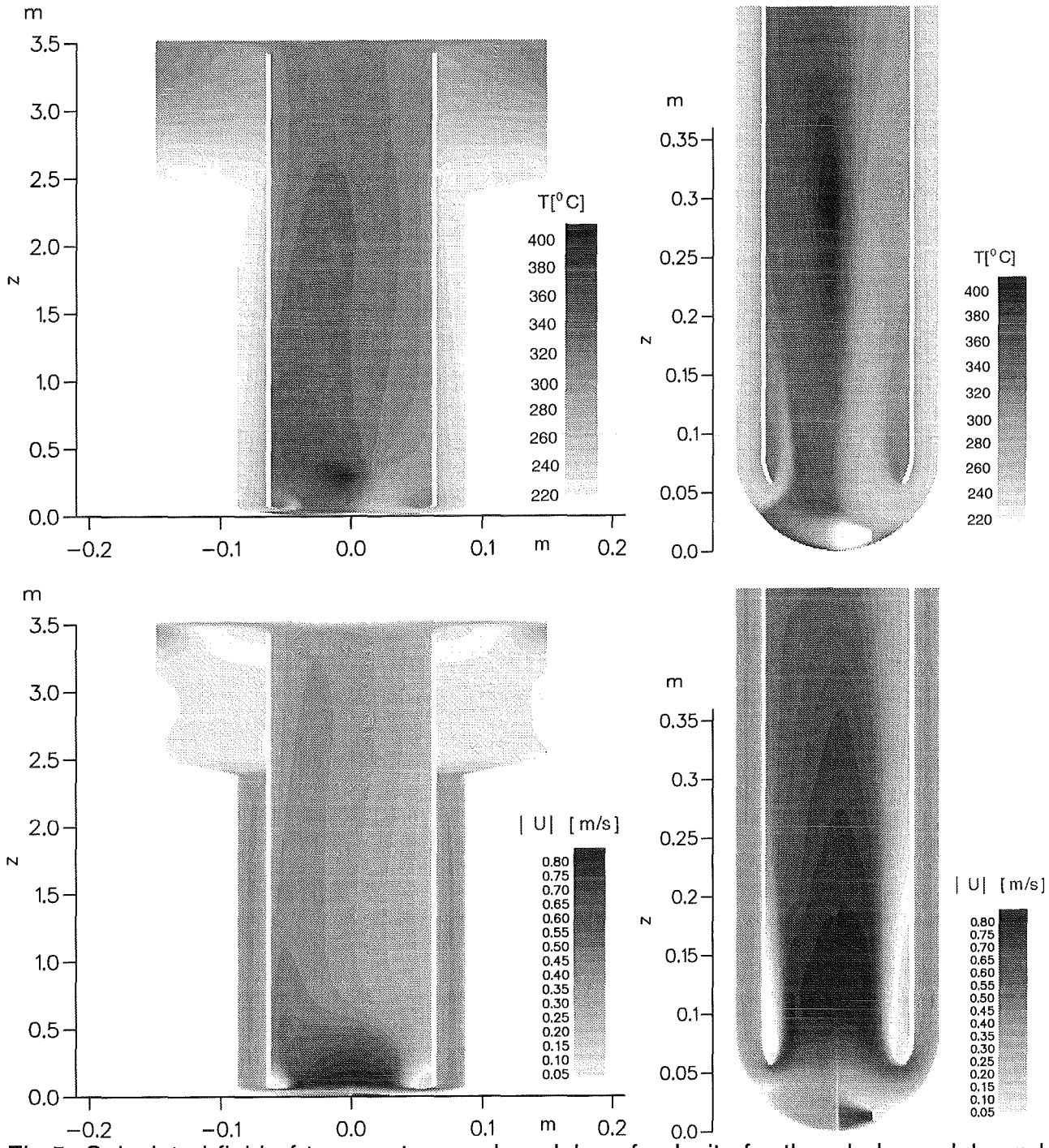

Fig.5: Calculated field of temperature and modulus of velocity for the whole module and for the bottom part. 3d calculation, new geometry, natural convection, mass flow rate of the bypass 1.18 kg/s, thermal conductivity of 16 W/(m*K) inside the guide tube.

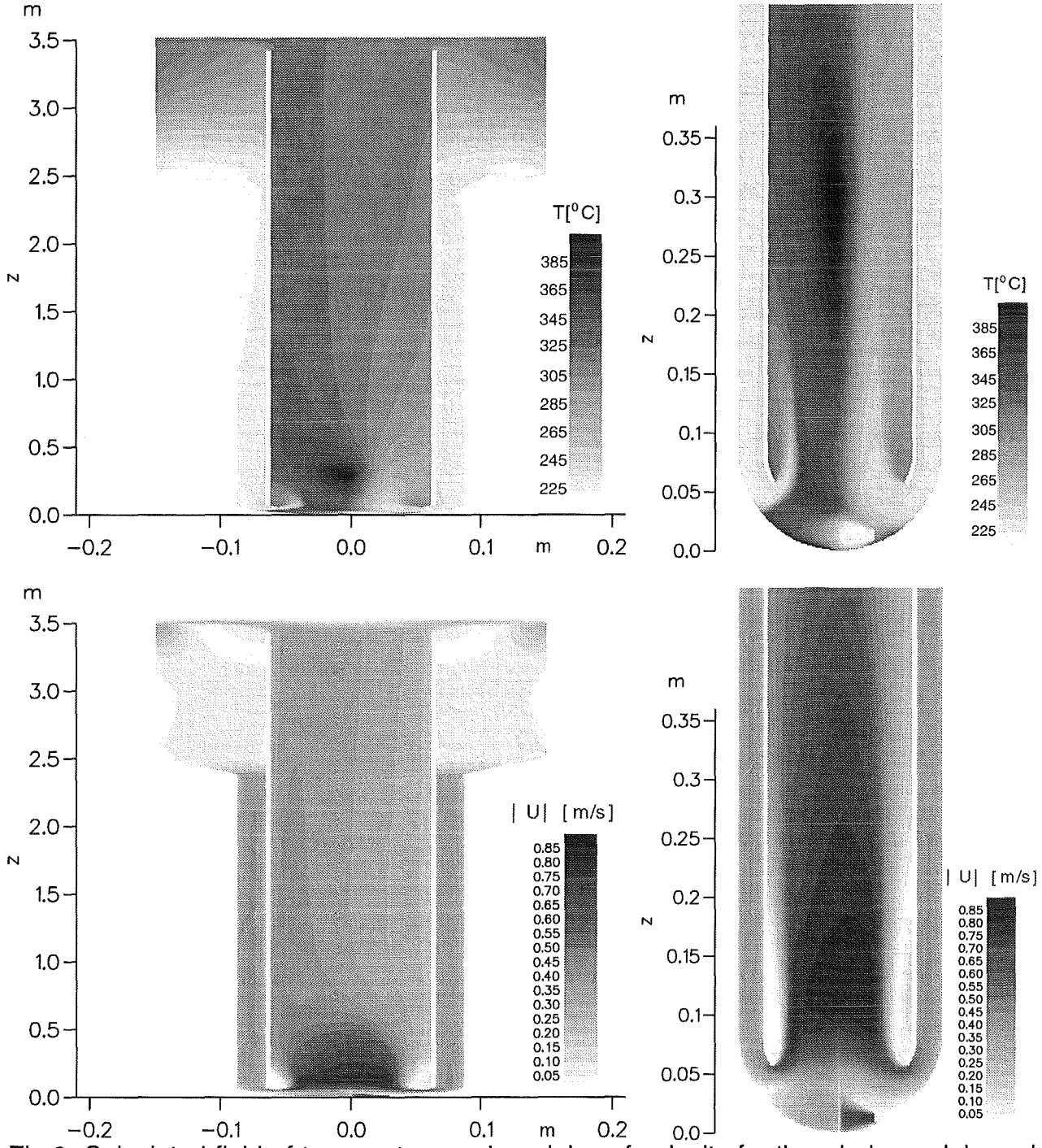

Fig.6: Calculated field of temperature and modulus of velocity for the whole module and for the bottom part. 3d calculation, new geometry, natural convection, mass flow rate of the bypass 1.18 kg/s, thermal conductivity of 1 W/(m*K) inside the guide tube.

V. Assessments of the Transient Behavior of Sub-critical Systems (ADS) in Comparison to Critical Reactor Systems

(M. Schikorr, IRS)

Abstract

The neutron kinetic and the reactor dynamic behavior of Accelerator Driven Systems (ADS) is significantly different from those of conventional power reactor systems currently in use for the production of power. It is the objective of this work to examine and to demonstrate the intrinsic differences of the kinetic and dynamic behavior of accelerator driven systems to typical plant transient initiators in comparison to the known, kinetic and dynamic behavior of critical thermal and fast reactor systems. It will be shown that in sub-critical assemblies, changes in reactivity or in the external neutron source strength lead to an asymptotic power level essentially described by the instantaneous power change (i.e.; prompt jump). Shutdown of ADS operating at high levels of sub-criticality, (i.e.; k_{eff} ~ 0.99), without the support of reactivity control systems (such as control or safety rods), may be problematic in case the ability of cooling of the core should be impaired (i.e.; loss of coolant flow). In addition, the dynamic behavior of sub-critical systems to typical plant transients such as protected or unprotected loss of flow (LOF) or heat sink (LOH) transients are not necessarily substantially different from the plant dynamic behavior of critical systems if the reactivity feedback coefficients of the ADS design are unfavorable.

Introduction

The ADS was originally suggested to burn or transmute considerable quantities of trans-uranic isotopes and/or fission products, and to produce power simultaneously. The inherent safety characteristics of the ADS device is believed to be guaranteed by the sub-criticality of the system and the ability to shut-off on demand the external neutron source (the proton beam) instantaneously making control rod systems unnecessary /1/.

Important safety parameters of the core in form of the reactivity feedback coefficients (i.e.; Doppler and coolant density coefficient) must be anticipated to vary noticeably as transmutation changes the fuel isotopic composition. As a result, an ADS-plant is expected to exhibit a continuously altering behavior in its dynamic response to typical plant transients in different stages of plant operation.

In order to assess the nature and impact of the variation of the important safety parameters during operation of an ADS, a dedicated, dynamic simulation model ("**SIM-ADS**") was developed. The model is applicable to both accelerator driven reactor systems and to critical reactor systems (thermal or fast core design) by simply specifying, among other input parameters, the state of criticality (or sub-criticality), namely k_{eff} of the system.

This model not only incorporates the external neutron source due to the accelerator supplied proton beam, but also the most important temperature dependent reactivity feedback effects (such as Doppler and coolant density effects) by incorporating a dynamic, full-scope thermo-hydraulic model for the transient calculation of the fuel, cladding and coolant temperatures in the core.

SIM-ADS has undergone an extensive validation procedure by comparing **SIM-ADS** results to different sources of available transient data. **SIM-ADS** is to be understood as a generic tool which allows a systematic analysis of the transient behavior of any ADS design (or critical system) if basic data specific to the reactor system under investigation, such as reactor design data and the corresponding reactivity coefficients are known.

In particular, **SIM-ADS** was used to analyze the dynamic behavior of various ADS reactor designs to typical operational plant transient initiators, such as: loss of flow (LOF) and loss of heat sink (LOH), either protected and unprotected, using as a base design the reference FZK 1500 MWth, Pb-cooled, Th-U233 fueled, 3-beam source, ADS plant design /2/. Of special interest here will be the comparison of these results to those assuming the cores would operate as critical reactors.

It should be emphasized, however, that the single node dynamic simulation model **SIM-ADS** should not be misunderstood as a replacement of the detailed, 3-D space-time kinetic code systems, such as SAS4A /3/ or SIMMER /4/. It should be rather understood as a supplementary tool that allows a relative quick, qualitative estimation of the transient behavior of the reactor system under investigation. When the design of the core becomes more refined, or even finalized, **SIM-ADS** definitely needs to be complemented by detailed 3-D, space-time kinetic analyses.

The Point Kinetic Model for ADS and Critical Systems

The underlying assumption in the development **SIM-ADS** is the applicability of the point kinetic equation for sub-critical system with an external source. This assumption is supported by the fact, that the point kinetic equation can be derived in a more general fashion from the transport equation itself in which the assumptions of one-speed diffusion approximation and the time-independence of the spatial flux shape are not necessary /5/ . This derivation leads to the same set of point kinetic equations in which only the definition of β , l_{pr}, and ρ are slightly modified when compared to the derivation assuming one-speed and separability of space and time /6/.

The neutron density in a critical, or sub-critical assembly can be written as :

$$\frac{dn}{dt} = k_{eff}\left(\frac{k_{eff}-1}{k_{eff}} + \rho(t) - \beta\right)\frac{n}{l_{pr}} + \sum_{i=1}^{6}\lambda_i C_i + Q \qquad \text{(Eq.1)}$$

The corresponding concentration of the neutron precursors is written as:

$$\frac{dC_i}{dt} = k_{eff}\frac{\beta_i}{l_{pr}} n - \lambda_i C_i \qquad \text{(Eq.2)}$$

where

n = neutron density [n/cm^3]

C_i = neutron precursor concentration [atoms/cm^3]

$\rho\ (t)$ = time dependent reactivity insertion into assembly [fr]

k_{eff} = state of criticality of assembly

for critical assemblies : k_{eff} = 1.000

for sub-critical assemblies : $k_{eff} \approx$ 0.95 - 0.99

β = fraction of delayed neutrons

for ADS/FBR: $\beta \approx$ 0.00350 = 0.35 [%] = 350 [pcm]

for LWR : $\beta \approx$ 0.00650 = 0.65 [%] = 650 [pcm]

l_{pr} = prompt neutron lifetime [sec]

for ADS/FBR: $l_{pr} \approx 10^{-7}$ [sec

for LWR : $l_{pr} \approx 10^{-5}$ - 10^{-3} [sec]

λ_i = decay constant of precursor i

Q = external neutron source strength density [$\frac{n}{cm^3 * s}$]

For external source driven, sub-critical assemblies (i.e.; k_{eff} < 1.0), a proton beam usually provides the source for the "external" neutrons. The following functional relationship between proton beam, I_{prot} in units of [ma], ADS power level P_{fiss}[MW_{th}], and state of sub-criticality k_{eff} can be derived:

$$I_{prot} = \frac{P_{fiss} * \nu}{0.20 * \eta_{prot}} \left(\frac{(1 - k_{eff})}{k_{eff}} \right) \qquad \text{(Eq.3)}$$

with

I_{prot} = proton beam current [mA]

P_{fiss} = fission power of ADS [MW_{th}], see Equation 8 below

ν = neutrons released per fission [n/fission]

for thermal systems : ν ~ 2.5

for fast systems: from ν ~ 2.5 to 2.9

η_{prot} = number of spallation neutrons released per proton [n/p]

$\eta_{prot} \cong$ 20 [n/p] for Pb(lead)-target, 1.2 [GeV] proton beam /7,2/ .

In the normal case, 6 groups of delayed neutrons are used to describe the time-characteristics of the neutron precursors in the above set of coupled kinetic equations. For our simulation model, 6 groups of delayed neutrons are considered. For the simplified case, in which the 6 delayed neutron groups are represented by 1 effective delayed neutron group with an average decay constant lambda, the set of coupled kinetic equations can appropriately be reduced and analytic solutions can be found for both the critical case (i.e.; k_{eff} = 1 and the external source Q = 0) /8/ and the sub-critical case (k_{eff} < 1.0 and $Q \neq 0$) /9/. A comparison of the results of our numerical simulation model to the these analytic solutions for both the critical and sub-critical case allows verification and validation of our numerical simulation model in the kinetic operating range. This validation procedure has been performed successfully with our simulation model.

Thermo-hydraulic Simulation

In the operating, or power range (i.e.; full-power), temperature dependent feedback effects in reactivity need to be considered. Before temperature reactivity feedbacks

can be calculated, our kinetic simulation model first needs to be extended with a full-scope, thermo-hydraulic model which allows an accurate transient description of the fuel-cladding-coolant temperature distribution in an average fuel pin. The equations below describe the transient behavior of temperatures in the fuel, the cladding, the coolant in the core region, and the coolant in the ex-core, or primary system.

For the gradient of the average fuel temperature T_{fuel}^{av}:

$$c_{p,fuel}\, M_f\, \frac{d\,T_{fuel}^{av}}{dt} = P_{tot} - k_{fc}\left(T_{fuel}^{av} - T_{clad}^{surf}\right) \qquad \text{(Eq. 4)}$$

For the gradient of the cladding surface temperature T_{clad}^{surf}:

$$c_{p,clad}\, M_{clad}\, \frac{d\,T_{clad}^{surf}}{dt} = k_{fc}\left(T_{fuel}^{av} - T_{clad}^{surf}\right) - h_s^{c,c}\left(T_{clad}^{surf} - T_{cool}^{av}\right) \qquad \text{(Eq. 5)}$$

where

$c_{p,fuel}$ = heat capacity of fuel [kJ/kg*K]

$c_{p,clad}$ = heat capacity of cladding material [kJ/kg*K]

M_f = fuel mass [kg]

M_{clad} = cladding mass [kg]

P_{tot} = total power generated by fission and decay heat [MW_{th}]

where

$$P_{tot} = P_{fiss} + P_{decay} \qquad \text{(Eq. 6)}$$

$$P_{decay} \equiv 0.0675 * P_{tot} \quad , \quad \text{(see discussion below)} \qquad \text{(Eq. 7)}$$

$$P_{fiss} = P_{tot} - P_{decay} = (1-0.0675) * P_{tot} = 0.9325 * P_{tot} \qquad \text{(Eq. 8)}$$

T_{cool}^{av} = average coolant temperature in core [C]

k_{fc} = a combined total heat transfer coefficient [W/K] from fuel to clad surface, consisting of the thermal conductivity of the ThO_2 / UO_2 fuel k_{fuel} [W/mK], the gap conductivity k_{gap} [W/mK], and the thermal conductivity of the clad material k_{clad} [W/mK].

$h_s^{c,c}$ = convective heat transfer coefficient between cladding- coolant [W/K]

where

$$h_s^{c,c} = A_{h,core}\left(\frac{k_{cool}}{D_e}\right)Nu \qquad \text{(Eq. 9)}$$

$A_{h,core}$ = total heat transfer area of cladding - coolant [m^2]

k_{cool} = heat conductivity of the coolant [W/mK]

D_e = equivalent hydraulic diameter of the fuel pin assembly [m]

For liquids such as water and He we assume the Dittus-Boelter correlation for the Nusselt number Nu /6/ :

$$Nu = 0.023\,\mathrm{Pr}^{0.4}\,\mathrm{Re}^{0.8} \qquad \text{(Eq. 10)}$$

For liquid metals (such as Na and Pb) we assume the Lyon – Martinelli correlation for the Nusselt number Nu /3,6/ :

$$Nu = 6.3 + 0.030\left(\mathrm{Re\,Pr}\right)^{0.8}. \qquad \text{(Eq. 11)}$$

The coefficients needed in the above equations, k_{cool}, $c_{p,fuel}$, $c_{p,cladd}$, $c_{p,cool}$ (heat capacity of the coolant [J/kgK]), μ (viscosity of the coolant) are all functions of specific material properties, such as fuel type (see discussion below), cladding material type (Zr, SS etc.), coolant type (i.e. H_2O, Na, Pb, gas etc), and combinations of temperatures, pressures, enthalpies, fuel burn-up etc. These, sometimes very complicated, material specific functional inter-relationships are usually expressed in forms of higher order polynomials. The coefficient k_{fc} , describing a combined heat transfer coefficient from fuel to clad surface is a function of several parameters, foremost of the type of fuel (i.e. metal, oxide, isotopic composition of U^{238}, Th^{232}, U^{233}, U^{235}, Pu-vector, minor actinides, etc.), the temperature of the fuel - which itself is dependent on the power level, or linear rod power [W/cm] -, the width of the gap between fuel surface and cladding, and the cladding material itself. k_{fc} is determined in our case by using a separate, multi-zone fuel pin model which describes in detail the temperature distribution from the center of the fuel (solid or annular fuel pin) to the clad surface, in which the geometry of the pin, the burn-up characteristics of the type of fuel (i.e.; porous, oxide fuel in our particular case), the flow rate of the coolant and the power level serve as input.

For the gradient of the average coolant enthalpy in the core we can write:

$$\frac{dh_{cool}}{dt} = \frac{1}{M_{cool}}\left[h_s^{c,c}\left(T_{clad}^{surf} - T_{cool}^{av}\right) + w\left(h_{in} - h_{out}\right)\right] \qquad \text{(Eq. 12)}$$

h_{cool} = average coolant enthalpy in the core [J/kgK]

M_{cool} = coolant mass inventory in the core region [kg]

h_{in} = core inlet enthalpy of the coolant [J/kgK]

h_{out} = core outlet enthalpy of the coolant [J/kgK] .

w = coolant flow rate through the core [kg/sec]

Knowing the average core enthalpy of the coolant h_{cool} , one can infer from the material property tables of the coolant the corresponding average coolant temperature T_{cool}^{av}.

The total decay heat generated, Equation 7, is simulated using 4 decay heat groups describing accurately the generation of decay heat about 10 minutes after reactor shut-down. Under 100 [%] operating load conditions, 6.75 [%] of the heat generated is assumed due to the accumulated decay of the fission product inventory /10/.

$$P_{decay} = \sum_{k=1}^{N} \lambda_{d,k} C_{d,k} \equiv 6.75\ [\%] \text{ of rated power } P_{tot} , \qquad \text{(Eq. 13)}$$

N can be up to 13 decay heat groups describing the long term decay heat generation characteristics (up to 1 year after shut-down)

$C_{d,k}$ = particle concentration of decay heat group k

$\lambda_{d,k}$ = decay constant of decay heat group k

Reactivity Coefficients

If the reactivity coefficients (Doppler etc) of a particular core design under investigation are known, changes in reactivity as a result of changes in fuel and coolant temperatures, caused, for example, by a change in plant load, can be calculated. In general we know, that the total reactivity insertion (feedback) is a complicated, time dependent function, namely :

$$\rho(t) = \rho_{Doppler}\left(T_{fuel}(t)\right) + \rho_{coolant}\left(Den_{coolant}(t)\right) + \rho_{clad}\left(T_{clad}(t)\right) + \rho_{rods}\left(T_{\mathrm{mod}}(t)\right)$$

$$+ \rho_{fuel-\exp}\left(T_{fuel}(t)\right) + \rho_{boron}\left(T_{\mathrm{mod}}(t)\right) + \rho_{xenon}(t) + \rho_{burnup}(t) \ldots . [pcm] \quad \text{(Eq.14)}$$

In our case, we are only interested in those reactivity feedbacks which are important during the time-interval of our typical plant transient (namely up to about 5-10 minutes into the transient). The most important are the Doppler effect (fuel temperature dependent), the coolant density (i.e.; temperature), fuel axial expansion, cladding material removal from the core, and boron (only for thermal rectors). Control rod effects are simulated by inserting into the model a step reactivity which is handled as a simple input parameter with no temperature feedbacks. The effects of Xenon poisoning and other feedbacks can be added to the model if deemed necessary.

The reactivity coefficient Γ of a particular reactivity feedback component ρ in Equation 14, which is required as input information into **SIM-ADS**, usually exhibits some functional dependency in either a temperature, some other material property, or a design specific dependency (such a core location). For example, for fast, or thermal water-cooled reactor systems the relationship between Doppler reactivity component $\rho_{Dopppler}$ [pcm] and the Doppler temperature coefficient $\Gamma_D(T_{fuel})$ [pcm/C] is given by :

$$\rho_{Doppler}(T_{fuel}) \equiv \int_{T_{1,fuel}}^{T_{2,fuel}} \Gamma_D(T_{fuel}) * dT_{fuel} = \int_{T_{1,fuel}}^{T_{2,fuel}} \left[\frac{A}{a * T_{fuel}^{\ b}} \right] * dT_{fuel} \qquad \text{(Eq. 15)}$$

where

$A \equiv$ so called "Doppler constant" [pcm], to be determined by curve fitting to data (see Figure 4a), a = constant, a = 1 for fast reactor systems, a = 2 for thermal water-cooled reactors, b = constant, b = 1.0 for fast reactor systems, b = 1.5 for fast ThO_2/UO_2 – fueled systems for T_{fuel} < 1100 [K], b to be determined by curve fitting to data (see Figure 4a), b = 0.5 for thermal water-cooled reactors, and T_{fuel} = fuel temperature [K],

For example, for thermal systems, the coolant density coefficient has a density (i.e.; temperature, pressure) and a boron concentration dependency, whereas in fast systems, the coolant density coefficient has a temperature as well as a spatial, or core location dependency that explicitly needs to be taken into consideration when performing transient response analyses for fast reactor systems.

The procedure for determining the various reactivity coefficient for a particular reactor design under investigation are usually very involved and time-consuming, requiring detailed nuclear design calculations, which themselves require extensive, nuclear data libraries, multi-group, 3-D, nuclear core analysis code systems, and access to corresponding computation facilities.

The Doppler, coolant density (or coolant temperature), and clad removal reactivity coefficients have been determined for the FZK reference 1500 MW_{th}, Pb-cooled, Th-U233 fueled, 3-source ADS design /2/, using the KARBUS /11/ code system and its associated nuclear data library set for the generation of few-group cross-section sets, and CITATION /12/ as the Nuclear Core Analysis Code.

Figure 1 depicts the fuel assembly arrangement of the FZK 1500 MW_{th}, 3-source ADS reference design /2/. The fuel assemblies have been assigned into 11 "fuel channels" of similar power loading. The fuel elements in the central zone experience the highest power loading (form factor ~ 2.45 /13/) and are assigned fuel channel 1. Fuel elements assigned to fuel channel 5 exhibit "average" fuel power loading characteristics.

For the determination of the coolant reactivity coefficient, the usual procedure of using perturbation analyses was explicitly not used because of the formal difficulty in defining the adjoint function in the case an external neutron source. The 11 fuel channels were partitioned into 15 equal-spaced axial nodes. A k_{eff} calculations was then performed in which for one specific fuel channel (i.e.; the central fuel channel 1) one of the 15 axial node was perturbed (i.e. coolant, clad or fuel was removed or the corresponding temperature was appropriately modified) and the result compared to the unperturbed calculation. Similar k_{eff} calculations were then performed for all remaining axial nodes in the fuel channel. The results were then plotted in Figure 2 which shows the spatial, or local coolant reactivity coefficient of the lead (Pb) coolant for the above described 1500 MW_{th} ADS. The results calculated for total core voiding compare quite well with the results of another Pb-cooled, fast reactor design /14/. As can be observed, the temperature reactivity coefficient for fast systems has a significant spatial, or local dependency. The coefficient can becomes quite positive in the central zone of the core whereas in the outer core zones it becomes even negative. This fact is of significant importance since the transient response of our

ADS design to plant transients will be shown to be primarily influenced by sign and magnitude of this local reactivity coefficient.

A second set of coolant coefficients was calculated for the central fuel region (channel 1) in the same manner as described above by replacing the coolant lead (Pb) with sodium (Na), Figure 3, assuming the coolant volume fraction remains unchanged. The data obtained for Na coolant displays the same spatial distribution as observed for Pb, however, the magnitude of the Na temperature coefficient was lower by a factor of 2.5 than that of Pb. This result is explained by the harder neutron spectrum encountered when using Pb as coolant in comparison to using Na as coolant /15/.

Figure 4 shows the Doppler coefficient of our 1500 MW_{th} ADS design calculated in similar manner. For orientation and comparative purposes, some typical Doppler data of some other critical core design is also depicted. This data serves as input into SIM-ADS in form of a 3^{rd} or 4^{th} order polynomial.

In fast reactor systems, removal of cladding material from the core by means of clad melting will add substantial amounts of positive reactivity. For Pb-cooled systems, melting and removal of clad material from the core by means of buoyancy will commence at the melting temperatures of steel, i.e. ~ 1200 [C], well below the boiling point of lead at ~ 1750 [K]. The total loss of cladding from the core will add up to ~ 7 [$] of positive reactivity /16/. Since this effect of clad material removal from the core region for Pb-cooled fast reactors is recognized to be an important phenomena we included a simplified clad reactivity insertion model in SIM-ADS by assuming a total clad reactivity insertion of 5 [$], or ~ 2000 [pcm], linearly released into the core over an arbitrarily chosen temperature interval of 200 [C] above the clad melting temperature.

The reactivity associated with the thermal expansion of fuel is another important reactivity component in Equation 14 for fast reactors operating under full power conditions. Based on the experience operating fast reactors we assumed $\Gamma_{fuel-\exp}(T_{fuel})$ = - 0.25 [pcm/C] for our an analyses.

Numerical Simulation Model ("SIM-ADS")

The numerical procedure in solving the set of coupled linear equations in Sections II and III is straight forward. For a specified steady state condition, i.e. reactor power [MW_{th}] and state of sub-criticality (or criticality) k_{eff}, certain thermo-hydraulic constants and coefficients are initialized and the proton beam current I_{pr} as well as the time derivatives of neutron density (i.e.; neutron flux), fuel, cladding, coolant and loop temperatures etc. are calculated in the sequential manner as given by the equations above. For the steady state case, all state variables remain unchanged during any subsequent time step (derivatives remain essentially zero) and the power level as well as all temperatures remain constant. The selected model time step is primarily determined by the prompt neutron life time (input) and chosen to be as large as possible (i.e. model remains stable).

Dynamic Transient Analyses of ADS systems

During normal load conditions, variations in plant temperatures will lead to reactivity changes due to various temperature dependent reactivity feedback effects. These fuel and coolant temperature dependent feedback effects determine to a very significant degree the dynamic behavior of any nuclear power plant. The response of the plant operating in the power range to any reactivity perturbation will therefore exhibit a substantially different behavior when compared to the behavior in the kinetic, or zero power range. In principle, the temperature dependent reactivity effects in the power range can be understood to be superimposed on the basic, kinetic behavior of the systems, thereby masking the kinetic characteristics of the system. Using reactivity coefficient data and other relevant design data as input into **SIM-ADS**, the dynamic response of our 1500 MW_{th} ADS to typical plant transient initiators was analyzed and the results compared to other critical core and ADS designs.

For our analysis of the fast 1500 MW_{th} ADS core it was assumed that the transient behavior of this large ADS can be represented by two separated set of simulation runs. One set of runs assumes the axially averaged coolant temperature reactivity coefficient of fuel channel 5 as SIM-ADS input, representing the "average" behavior of this ADS, and the other set assumes the much larger positive coefficient from the core center zone, namely fuel channel 1 as input into SIM-ADS, representing the

transient response in the central region of the core. The applicability of this procedure of core decoupling for large ADS core design is suggested by previous experience in the detailed SAS4A analysis of other large, fast critical cores (CAPRA project). In order to asses the influence of different ADS designs, several ADS designs were "mimicked" in the following manner where each of the "designs" is assumed to be either operable as a critical, i.e.; k_{eff} = 1.00, or sub-critical system, i.e.; k_{eff} < 1.00, by just changing the input parameter k_{eff} in Equation 1:

Design Case	Reactor Type	Coolant Type	Description
Case : **1**	Thermal LWR	H_2O	3600 MW_{th} thermal LWR of typical PWR-design (SIEMENS), where it is assumed that it can be operated as a sub-critical assembly with an external neutron source,
Case : **2**	Fast	Pb	1500 MW_{th} Pb-cooled, fast system (Th-U233 oxide-fueled) with nuclear and thermal characteristics represented by the "average" fuel zone (fuel channel 5) in Figure 1,
Case : **3**	Fast	Pb	1500 MW_{th} Pb-cooled, fast system (Th-U233 oxide-fueled) with nuclear and thermal characteristics represented by the central, or "maximum" loaded fuel region (fuel channel 1) in Figure 1,
Case : **4**	Fast	Na	1500 MW_{th} Na-cooled, fast system (Th-U233 oxide-fueled) with nuclear and thermal characteristics represented by the central, or "maximum" loaded fuel region (fuel channel 1) in Figure 1.

More detailed thermal and nuclear data of the above cases is listed in Table 1

From the many conceivable plant transient initiators, the following initiators were chosen in this study for more detailed analysis, representing a wide spectrum of the most challenging plant transients, namely 1.) normal shutdown, 2.) protected and unprotected loss of flow, and 3.) protected and unprotected loss of heat sink. The transient initiators were purposely selected to challenge the various "designs", critical or sub-critical, to severe loading conditions in order to be able to asses the actual influence of the additional margin of safety associated by making reactor systems sub-critical (i.e. "reactivity window", see previous discussion in section VI).

Each of the above "designs" was subjected for the critical and sub-critical configuration to each of these transient initiators. In order to reduce the number of possible combinations of transients to be analyzed , only two states of sub-criticality,

namely k_{eff} = 0.99 and k_{eff} = 0.95 were chosen. This yielded the following matrix of transients for analysis :

	Transient Initiator :	Criticality k_{eff} 1.00 (critical sys.)	0.99	0.95 (sub-critical sys.)	Comments
1	**Shutdown**	yes	yes	not anal.	
2	**Loss of Flow**				For all LOF cases, w = 10 [%] at start of transient (t=0) simulating natural convection conditions
	PLOF (protected)	yes	yes	yes	
	ULOF (unprotected)	yes	yes	yes	
3	**Loss of Heat Sink**				For all LOH cases, Q_{HX} = 0 [%], only heat sink is radiation losses from vessel and primary system piping surfaces
	PLOH (protected)	not anal.	yes	not anal.	w = 100 [%]
	PLOH (protected)	not anal.	yes	not anal.	w = 15 [%]
	ULOH (unprotected)	not anal.	yes	not anal.	w = 100 [%]

Nomenclature: yes = case was analyzed, not anal.= case not analyzed

Thus for each of the above 4 "designs", 11 different transients were analyzed in this study.

Since **SIM-ADS** does not take into consideration mechanical or structural failure of core fuel materials, the following temperature limits in core fuel material properties should be assumed as model limits beyond which the simulation should not be considered physically realistic. Coolant boiling and the associated voiding of the core and core sweep out of molten clad material beyond the melting point are simulated in SIM-ADS. Mechanism associated with loss of structural integrity of the fuel itself and effects due to loss of core geometry (fuel rearrangement) are not considered.

Critical Core Conditions	Material	Critical Temperature [C]	Comment
Fuel Melting :	UO_2/PuO_2	~ 2800	
	ThO_2/UO_2	~ 3200	
Cladding Melting :	SS	~ 1200	
	Zr	~ 800	
Coolant Boiling :	Pb	~ 1750	
	Na	~ 880	
	H_2O	~ 346	P = 157 [bar]

As an overview of the importance of k_{eff} and the coolant temperature coefficient, Figures 5 and 6 show the results of an ULOF transient (flow was reduced to 10% at the initiation of the transient at t = 0) for the "average" (channel 5) and the center fuel region (channel 1) for the Pb-cooled, fast ADS system described above.

For the average zone (channel 5), the temperature coefficient was slightly positive (see Figure 2) but not large enough to counterbalance the negative Doppler coefficient. The total net reactivity insertion into the system as a result of the ULOF transient is negative in this case, and the power level decrease for all states of sub-criticality, but clearly for high k_{eff} ~ 0.99, the decrease to 83 % power is larger than for low k_{eff} ~0.95 which corresponds to the information that for a certain negative reactivity insertion, the power level of the under-power transient drops further for high k_{eff} ~0.99 assemblies than for low k_{eff} ~ 0.95 assemblies /17/. The critical system drops lowest in power.

For the central fuel region case (channel 1), the temperature coefficient of the coolant is too large positive to be compensated by the Doppler coefficient. The net reactivity insertion into the system as a result of the ULOF transient is positive, and the resulting overpower response is shown in Figure 6. Again the flow was reduced to 10% nominal flow at t=0, and in the critical system case, it took only 5 sec of transient time before the net reactivity insertion increased to 1 $ and above resulting in a steep increase in power. For the sub-critical cases, for low k_{eff} ~ 0.95 it took about 18 sec into the transient until sufficient positive reactivity (in excess of 8 $) was accumulated and inserted into the system before a significant power rise was observed; for high k_{eff} ~0.99, the required excess reactivity was only about 2.5 $ until the steep overpower transient was observed. This can simply be understood in the following manner: as the coolant temperature rises during the loss of flow transient, positive reactivity is inserted into system. Since it takes larger amounts of positive reactivity to be inserted for systems with k_{eff} ~ 0.95, it correspondingly takes a longer time until the coolant is heated up to the higher temperatures before sufficient positive excess reactivity is accumulated.

Figure 6 also clearly demonstrates, that a critical system with a relatively large coolant temperature coefficient will not essentially become "safer" if the assembly is made sub-critical. Even for sub-critical assemblies of relatively low k_{eff} it is seen that power excursion can occur if the corresponding "safety" coefficients are unfavorable. What is gained in making these assemblies with unfavorable safety coefficients sub-critical is time, namely in the neighborhood of 20 – 50 sec, (if a realistic pump coast down is taking into consideration instead of just decreasing the flow by a step function to 10 % nominal as has been done in the above experiment) before the power excursion takes place.

It is known, that in sub-critical assemblies with high k_{eff} ~ 0.99, normal shutdown might be an issue because the power after source shut-off does not drop down to decay heat levels fast enough /18/. Figure 7 displays similar information along with corresponding fuel, cladding and coolant temperatures by assessing the transient response of the 4 different ADS design cases described above. As can be observed, in all 4 ADS designs, the power level does not decrease below 20 % after source shut-off, but fuel, clad and coolant temperatures decrease after source shut-off as long as the coolant flow is maintained. Should the coolant flow be impaired, however, then some of our ADS design may breach maximum temperature limits even though the source does shut off. This is observed in Figure 8, which displays the results in case of a protected (source shut-off) loss of flow (PLOF) for a state of k_{eff} ~0.99. In the case of the LWR ADS and the "average" Pb-cooled, fast ADS no temperature limits are breached, whereas in the central fuel zone of the fast Pb-cooled ADS the melting of cladding material must be expected. For the Na-cooled ADS, boiling of the sodium coolant must be expected with the corresponding insertion of relatively large amounts of positive reactivity. These results clearly illustrate, that certain ADS systems of high k_{eff} ~0.99 might breach temperature limits subsequent to coolant flow impairment even when the source shut-off does shut-off right after flow impairment. Should the state of sub-criticality be however low, such as k_{eff} ~0.95, Figure 9, then a loss of flow with source shut-off will cause a rise in clad and coolant temperatures for about 5 sec into the transient, the power level, however decreases far enough to below 20 % (due to low k_{eff} ~0.95) preventing a continuous increase in clad and coolant temperatures. After the initial temperature rise, all temperatures decrease again, breaching no temperature limits in this case.

The next sequence of Figures 10 to 12 displays the results of "unprotected" loss of flow transients (ULOF). Here it is assumed, that a loss of flow occurs at t=0, the flow decreases again to 10% nominal, and the source does not shut off in the case of the sub-critical assemblies. Since it is known from previous fast reactor core designs that even critical, fast reactors do exhibit overpower transient characteristics for this type of transient, Figure 10 displays the results of our 4 different designs assuming they are operated as critical assemblies. Here it is clearly seen, that for both the Pb-cooled and the Na-cooled fast, critical cores, maximum temperatures in fuel, clad and coolant are quickly reached, i.e.; about 10 seconds into the transient in the central core zones. For the "average fuel zone" Pb-cooled, fast assembly, no critical temperatures are reached but a relatively high cladding and Pb-coolant temperature steady state level is reached about 100 sec into the transient because of the relatively high steady state power level of 50%. In the thermal system, the very large negative coolant temperature (void) coefficient assures a low power level of ~20 % which can be maintained as long as the heat transport system remains intact to condense the steam that is exiting the core.

Again assuming an ULOF transient but making our critical system sub-critical with a k_{eff} ~ 0.99, Figure 11, we observe that the power level in the sub-critical case stays quite high in case the transient is under-power (for thermal ADS and "average" fuel zone of the Pb-cooled system) when compared to the critical systems (again see Figure 5), but for both Pb and Na-cooled "central core zone" cases, an overpower transient is observed with a breach of all critical temperatures about 15 sec into the transient.

Assuming ULOF with k_{eff} = 0.95, as seen in Figure 12, we observe a similar transient response as for the k_{eff} ~0.99 case, only delayed in time by some 10-20 sec.

A different category of transient initiators are the loss of heat sink (LOH). Here it is assumed that the heat transport path out of the primary system becomes impaired, either by the loss of the secondary heat transport system or some other mechanisms which do not allow heat removal from the primary system. The only heat removal mechanism remaining is radiation from the reactor vessel surface. Figure 13 displays

the transient PLOH results of our 4 ADS designs for k_{eff} ~ 0.99 assuming the coolant flow in the primary system is maintained and the source does shut-off. The time response of these type of transient is much longer, up to 400 sec and longer, but as can be observed in Figure 13, critical cladding temperatures in excess of 1300 [C] are reached in the Pb-cooled "central zone" about 400 sec into the transient. Should the coolant flow also become impaired to w=15% nominal, then critical fuel, cladding and coolant boiling will set in about 200 sec into the transient in the Pb and Na-cooled "central core zones" as shown in Figure 14.

Should under loss of heat sink conditions also source shut-down fail, then the corresponding transient ULOH results are displayed in Figure 15. Here it is clearly observed, that all ADS designs will breach critical material property temperatures, with overpower excursion taking place in the central fuel region for both Pb and Na-cooled fast system.

The information of the above discussed transients is collected and summarized in Table 2, in which all the transient initiators are listed in the left column, and the various reactor designs in the following four columns. For each reactor design, the critical configuration as well as two sub-critical states are listed, namely k_{eff} ~ 0.99 and 0.95. An arbitrary categorization has been adopted by assigning a value of 0.5 to a transient response if critical temperatures of either fuel, clad or coolant have been touched. A value 1 is assigned if these boundaries are clearly breached, and a value of 2 is assigned if the transient leads into an overpower situation.

As can be inferred by looking at this somewhat arbitrary categorization, critical reactor systems that show unfavorable transient behavior, as illustrated in the ULOF case, are most likely also to display these unfavorable characteristics when these systems are made sub-critical as seen in the cases k_{eff} ~ 0.99 and k_{eff} ~ 0.95. Thus, careful attention should be placed on the design of sub-critical cores, especially as regards their safety temperature coefficients, in particular the coolant temperature coefficient and the Doppler, since it is these two coefficients, that primarily determine the dynamic response of any reactor design to plant transient initiators.

Table 3 summarizes the above results by listing the preferred level state of sub-criticality k_{eff}. Again, from the perspective of shut-down, a low k_{eff} ~ 0.95 is preferred, for "protected" transient, again a low k_{eff} ~ 0.95 is preferred since all of these transient will be under-power transient. For "unprotected" transient, the issue is not as clear cut, since for under-power transient, - and this is definitely the preferred direction any transient should take, a high k_{eff} ~ 0.98 or 0.99 is desirable, whereas in case the transient should be overpower, a low k_{eff} ~ 0.95 is definitely advantageous.

Conclusions of the Dynamic Behavior Analysis of ADS Systems

The dynamic behavior of sub-critical systems has been shown to be substantially different from that of critical systems to typical plant transient initiators. It has been shown, that the field of open design parameters is increased for ADS systems compared to critical systems, and that the state of sub-criticality is a very important parameter that substantially determines the dynamic behavior of sub-critical systems. Thus k_{eff} needs careful monitoring during the various burn-up stages during the fuel cycle. This is accomplished in a fairly simple manner by monitoring the proton current required to maintain a certain power level (see Equation 3).

Table 3 clearly demonstrates, that the preferred state of sub-criticality k_{eff} of an ADS is not clear-cut, since for some transients a relatively low k_{eff} ~ 0.95 is preferable, whereas for different transients, a rather high k_{eff} ~ 0.99 is preferable.

It has also been demonstrated, that an ADS design with unfavorable safety coefficients, in particular with a large, positive coolant temperature coefficient, will exhibit unfavorable dynamic characteristics even if the assembly is made relatively large sub-critical with k_{eff} ~ 0.95. Careful attention should therefore be placed during the core design of these assemblies, that their safety coefficients, in particular their local coolant temperature coefficient does not become too positive.

It could also be shown during the course of these assessments, that the local coolant temperature coefficient appears to show some dependence on the state of sub-criticality; implying, as the burn-up proceeds, and k_{eff} changes, the safety coefficients also change. Careful assessment of these coefficients and their functional depend-

ence on k_{eff} as well as burn-up is therefore absolutely necessary during the design phase of any ADS core.

In large size, fast ADS cores, lead (Pb) as coolant has a considerably larger positive local coolant temperature coefficient than sodium (Na). This implies, that in order to assure a relatively small coolant coefficient, Pb-cooled, fast assemblies should be of relatively small core size, or their core geometry should be such, that a high neutron leakage component assures that this coefficient remains small, or even becomes negative.

For lead cooled, fast systems, melting temperatures of cladding material of ~ 1200 [C] will be reached before boiling of the Pb coolant set in at 1750 [C]. The melting of cladding will cause this molten material to be swept outside the core region. The loss of this neutron absorber material will lead to a significant insertion of positive reactivity (up to 7 $) into the core. Thus for lead cooled systems, the melting temperature of lead, or the resulting voiding, is of secondary importance since at temperatures below lead melting, namely at 1200 to 1300 [C] large positive reactivity insertions need to be addressed.

The above discussion has clearly demonstrated, that making a critical assembly sub-critical will not assure automatic safety. On the contrary, careful analysis and assessment is required for each different ADS core design, to assure that its combination of reactivity coefficients (Doppler and coolant temperature coefficient) does not lead to an unacceptable dynamic ADS plant behavior in case typical plant transient initiators such as loss of coolant pumping (loss of flow) or loss of heat sink should be encountered during operation of the ADS.

References

/1/ Rubia, C., "A Comparison of the Safety and Environmental Advantages of the Energy Amplifier and of Magnetic Confinement Fusion", CERN/AT/95-58(ET), 1995.

/2/ Gudowski, W.(editor), "Impact of accelerator –based technologies of nuclear fission safety", EUR-19608EN, 2000.

/3/ Bohl, W.R.; et. al., "The SAS4A LMFBR Accident Analysis Code System", ANL/RAS 83-38, May 1985

/4/ Bohl, W.R., Luck, L.B. SIMMER-II: A Computer Program for LMFBR Disrupted Core Analyses, LA-11415-MS 1990

/5/ Akcasu, A.Z., Lellouche, G.S., Shotkin, L.M., "Mathematical Methods in Nuclear Reactor Dynamics", Academic, New York , 1971.

/6/ Duderstadt, J., Hamilton, L.J., "Nuclear Reactor Analysis", John Wiley & Sons, New York, 1976

/7/ Zucker, M.S., et. al.; "Spallation Neutron Production Measurements", Nuclear Science and Eng.:129, pp.180-186 , 1998

/8/ Glasstone, S., Sessonske,A., "Nuclear Reactor Engineering", Van Nostrand Reinhold Company, p. 237, 1981

/9/ Belle, G.I., Glasstone S., 1970. Nuclear Reactor Theory, Van Nostrand Reinhold Company, New York, p. 478.

/10/ American Nuclear Society, American National Standard for Decay Heat Power in Light Water Reactors, ANSI/ANS-5.1 – 1979.

/11/ Broeders, C.H.M., "Entwicklungsarbeiten für die neutronenphysikalische Auslegung von Fortschrittlichen Druckwasserreaktoren ...", KFK-5072, August 1992

/12/ Fowler, T.B., et.al., "Nuclear Reactor Core Analysis Code : CITATION", ORNL-TM2496, Rev.2, 1971.

/13/ Dagan, R., Broeders, C.H.M., Struwe, D., "Modifications of the Code SAS4A for Simulation of ADS Designs", FZKA-6334, Juli 2000

/14/ Gandini, A., Salvaltores, M., Slessarev, I., "Balance of Power in ADS operation and safety", Anals of Nuclear Energy 27, pp. 71-84, 2000

/15/ Liaw, J.R., Fujita, E.K., Wade, D.C., "Comparative Neutronic Analysis of Pb-versus Na-Cooled LMR Cores", Proc. Topl. Mtg. Advances in Reactor Physics, Charleston, South Carolina, March 8-11,1992, p. 578, ANS(1992)

/16/ Tobita, Y., "Preliminary Safety Comparison of Lead/Gas/Light Water concepts", JNC Specialist Meeting at FzK, Karlsruhe, March 2001

/17/ Schikorr, W.M., Minutes of the "CAPRA/CADRA Neutronic Specialist Meeting" CEA, Cadarache, 16-17 January 2001

/18/ Dagan, R., Schikorr, M., Broeders, C.H., "The Kinetic and Dynamic Behavior of ADS versus Critical Systems", KTG -Jahrestagung, Dresden, Juni 2001

Reactor System Data :	Units	Thermal PWR Reactor	Fast Pb-cooled Average Zone	Fast Pb-cooled Central Zone	Fast Na-cooled Central Zone
Global Data:					
Total thermal Power	[MW_{th}]	3765	1500	1500	1500
Form Factor		1	1	2.47	1.5
Coolant Flow rate	[kg /s]	18000	68870	68870	5114
Core Volume	[cm^3]	3.53E+07	1.11E+07	1.11E+07	1.11E+07
Fuel Fraction	[fr]	0.334	.3195	.3195	.3195
Avg. Linear Power	[W/cm]	211.1	167.5	413.7	251.2
Fuel Pin Geometry:					
No. subassemblies [SA]	[#]	193	148	148	148
No. of pins/SA	[#]	236	397	397	397
Pin diameter (cold)	[cm]	1.077	0.820	0.820	0.820
Pin pitch	[cm]	1.436	1.138	1.138	1.138
Pin height	[cm]	391.6	150	150	150
Hex diameter	[cm]	0	27.816	27.816	27.816
Hex or Square side length	[cm]	23.11	12.045	12.045	12.045
Fuel diameter (cold)	[cm]	0.9178	0.730	0.730	0.730
Gap width (cold)	[cm]	0.007	0.01	0.01	0.01
Annulus radius (cold)	[cm]	0	0.055	0.055	0.055
Fuel Porosity	[%]	5.11	4.5	4.5	4.5
ThO_2 /UO_2	[%]	0/100	90/10	90/10	90/10
M_cp_fuel	[W-sec/C]	3.668E+07	1.035E+7	1.035E+7	1.035E+7
M_cp_clad	[W-sec/C]	8.700E+6	4.85E+6	4.85E+6	4.85E+6
Mass coolant core	[kg]	3.035E+4	73860	73860	5907
Mass prim. sys factor	[fact]	20	20	20	20
Boron Concentration	[ppm]	1020	0	0	
100 [%] load data:					
Avg. Fuel Temp.	[C]	669.6	931.4	1516.1	1313.9
Max. Fuel Temp.	[C]	905.9	1121.8	2160.5	1698.6
Clad surface Temp.	[C]	331.8	523.7	668.6	586.7
Avg. Coolant Temp.	[C]	310.8	501.5	613.9	569.2
Inlet Cool. Temp.	[C]	292.8	425.8	425.8	395.0
Outlet Cool Temp.	[C]	329.45	575.0	800.9	744.4
Nuclear data:					
Delayed neutron fraction	[fr]	0.00765	0.00386	0.00386	0.00386
Prompt neutron life-time	[sec]	2.5E-05	8.33E-07	8.33E-07	8.33E-07
Reactivity feedback poly coefficients:					
Dop_a0	[pcm/C]	-4.247	-2.9508	-2.9508	-2.9508
Dop_a1		3.8412E-3	2.4074E-03	2.4074E-03	2.4074E-03
Dop_a2		-1.8502E-6	-7.45414E-07	-7.45414E-07	-7.45414E-07
Dop_a3		0	7.6356E-11	7.6356E-11	7.6356E-11
Cool_dens_a0	[pcm/kg/m^3	251.59	-0.272	-1.12	-2.39
Cool_dens_a1		-0.9873	0	0	0
Cool_dens_a2		0.0013751	0	0	0
Cool_dens_a3		-6.53E-7	0	0	0
Fuel_exp_a0	[pcm/C]	0	-0.25	-0.25	-0.25
Fuel_exp_a1		0	0	0	0
Clad_max_react.	[$]	0	5	5	5
Clad_react_window	[ΔC]		200	200	200

Note: Coolant reactivity coefficients are expressed in terms of coolant density [kg/m^3] and not temperature [C], where the following conversion equation is applicable: Γ_{cool}^{Temp} [pcm/C] = $\Gamma_{cool}^{density}$ [pcm/kg/m^3] * ($\Delta den / \Delta T$), where ($\Delta den / \Delta T$)^{Pb} = -1.177 [kg/m^3/C], ($\Delta den / \Delta T$)^{Na} = -0.2319 [kg/m^3/C], and ($\Delta den / \Delta T$)^{H_2O} = (–27.7+0.19762*T-3.7428E-04*T^2) [kg/m^3/C] for 245<T [C]<345.6 at P=157 [bar].

Table 1: Power Reactor Data for the Reactor Design Cases

Breach of Critical Temperature Boundaries:

Fuel Temp: > 3200 [C]
Clad Temp: > 1300 [C]

Coolant Temp :
Na > 880 [C]
Pb > 1750 [C]
H20 > 345 [C]

Nomenclature :
- - case analyzed
- 0.5 - boundaries are touched
- 1 - boundaries clearly breached
- 2 - power excursion likely
- ( ) - flow = 100 %

Transient	3760 MWth LWR k_eff			Fast 1500 MWth Pb -cooled ADS *average* fuel zone k_eff			Fast 1500 MWth Pb -cooled ADS *central* fuel zone k_eff			Fast 1500 MWth Na -cooled ADS *central* fuel zone k_eff		
	1 (crit.)	0.99	0.95	1 (crit.)	0.99	0.95	1 (crit.)	0.99	0.95	1 (crit.)	0.99	0.95
P-Shutdown		-			-			-			-	
PLOF	-	-	-	-	-	-	-	0.5	-	-	0.5	-
PLOH		-			-			2 (1)			2 (-)	
ULOF	-	-	1		0.5	0.5	2	2	2	2	2	2
ULOH		1			1			2			2	
Sum		1	1		1.5	0.5	2	6.5 (5.5)	2	2	6.5 (4.5)	2

Table 2. Categorization of the Transient Behavior of different Sub-critical and Critical Systems to different Transient Initiators such as Shutdown, LOF, ULOF, LOH, and ULOH.

Prefered State of Sub-criticality for ADS from Perspective of Transient Behavior :

Type of Transient	low k_eff (~ 0.95)	high k_eff (> 0.98)
Shutdown :	X	
"Protected" Transients :	X	
"Unprotected" Transients :		
a. Overpower	X	
b. Underpower		X

Table 3. Preferred State of Sub-criticality for ADS from the Perspective of ADS Transient Behavior to different Transient Initiators

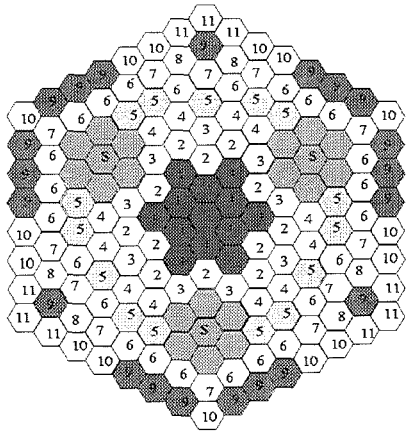

Assignment of Sub-assemblies [SA]
Fuel Channel 1 : central SA
Fuel Channel 5 : average SA
Fuel Channel 9 : external SA

S = Source location
148 active fuel SA
21 empty SA (source loc.)

Fig. 1. Assignment of Subassemblies to Fuel Channels for Reactivity Coefficient Calculations (using CITATION) for 1500 MW_{th} Pb-cooled ADS (FzK 3-source ref. Design [3], ThO_2/UO_2 fuel)

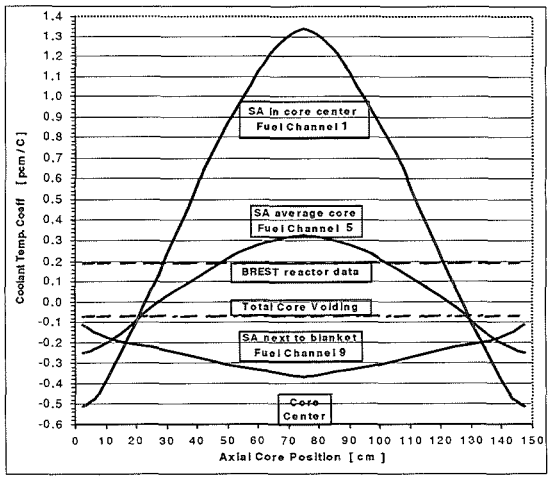

Fig. 2. Spatial Coolant Temperature Coefficient for 1500 MW_{th} Pb-cooled ADS (fresh ThO_2/UO_2 fuel) as a Function of Axial and Radial Core Position.

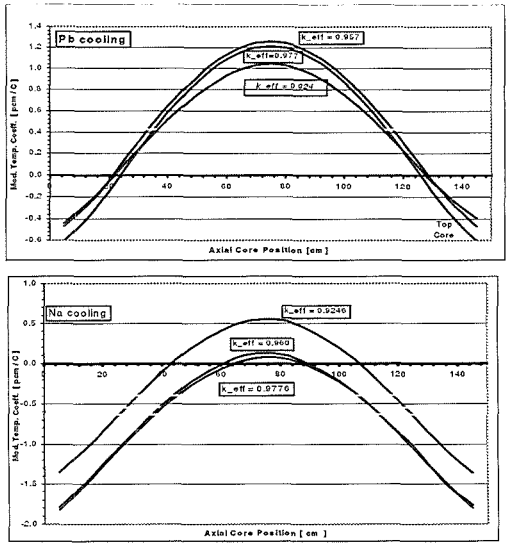

Fig. 3 Spatial Coolant Temperature Coefficient for 1500 MW_{th} ADS (fresh ThO_2/UO_2 fuel) using Pb (lead) or Na (sodium) as coolant for different sub-criticalities as Function of Axial Core Position.

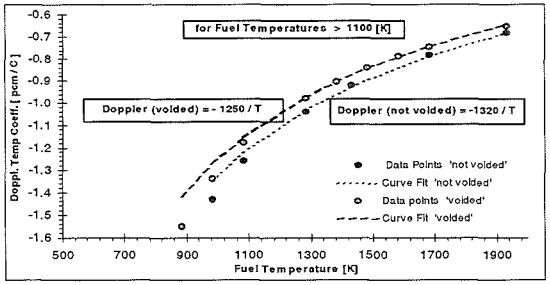

Fig. 7a. Determination of Coefficients of Eq. 4 of Doppler Temperature Coefficient for 1500 MW_{th} Pb-cooled ADS (fresh ThO_2/UO_2 fuel). Curve fitting of data in higher fuel temperature range.

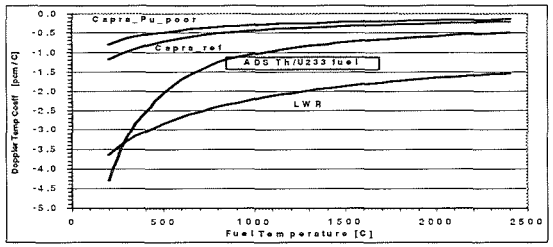

Fig. 7b. Doppler Temperature Coefficient for various fuels of Fast Reactor Designs and Reactor Types

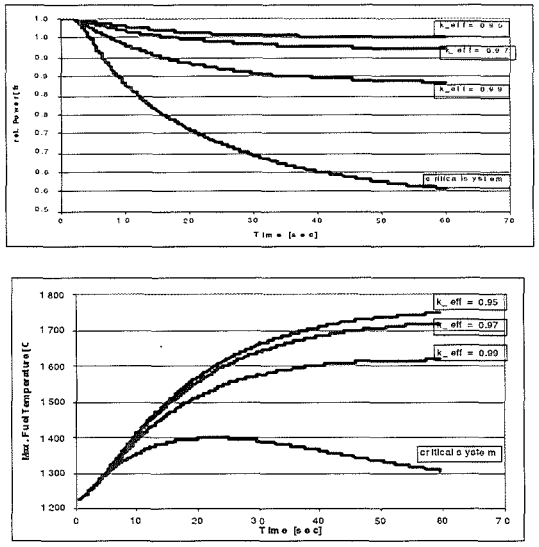

Fig. 5. Power and Temperature Response of Sub-critical and Critical Systems to "Unprotected" Loss of Flow (ULOF) Transient (flow reduced to 10% nominal) assuming Average Fuel Channel (Channel 5) nuclear and thermal characteristics of 1500 MW_{th} Pb-cooled ADS.

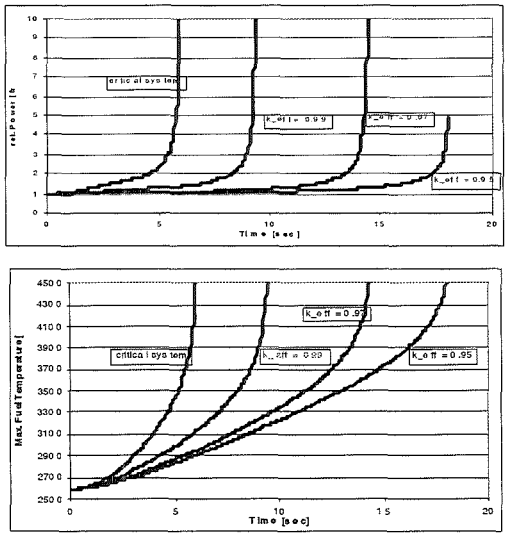

Fig. 6. Power and Temperature Response of Sub-critical and Critical Systems to "Unprotected" Loss of Flow (ULOF) Transient (flow reduced to 10% nominal) assuming Central Fuel Channel (Channel 1) nuclear and thermal characteristics of 1500 MW_{th} Pb-cooled ADS.

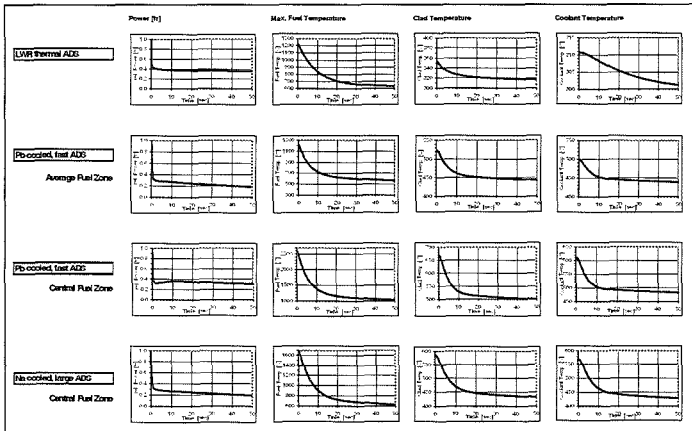

Fig. 7 Shutdown Transient for different ADS designs, k_eff = 0.99, neutron source shuts off

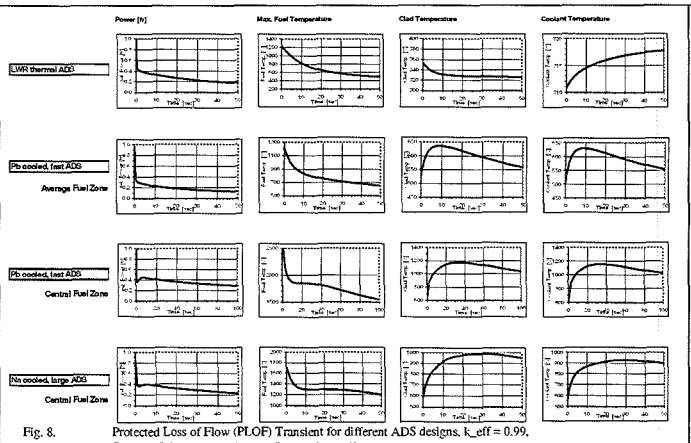

Fig. 8. Protected Loss of Flow (PLOF) Transient for different ADS designs, k_eff = 0.99, Flow = 10 % nominal, Neutron Source shuts off

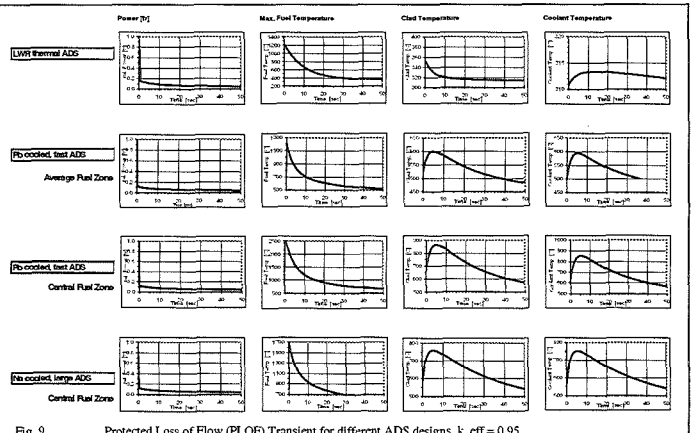

Fig. 9. Protected Loss of Flow (PLOF) Transient for different ADS designs, k_eff = 0.95, Flow = 10 % nominal, Neutron Source shuts off

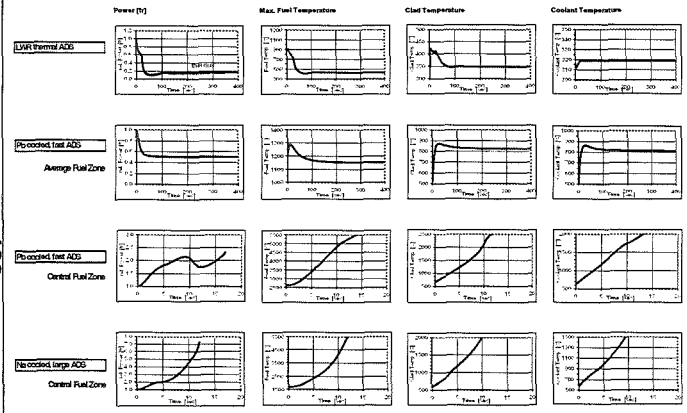

Fig. 10. Unprotected Loss of Flow (ULOF) Transient for different ADS designs, k_eff = 1.00, Flow = 10 % nominal, Control Rods not inserted

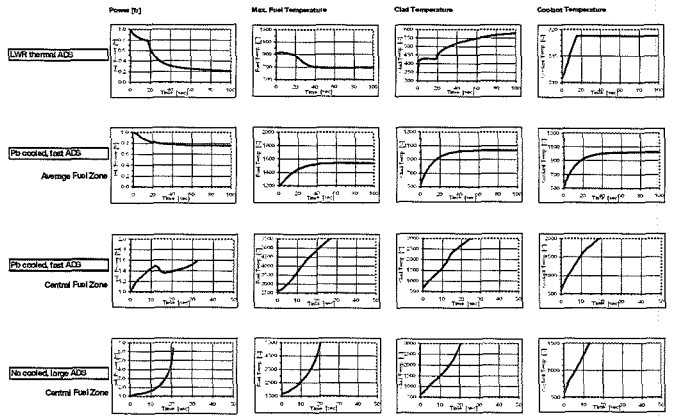

Fig. 11. Unprotected Loss of Flow (ULOF) Transient for different ADS designs, k_eff = 0.99, Flow = 10 % nominal, Neutron Source does not shut off

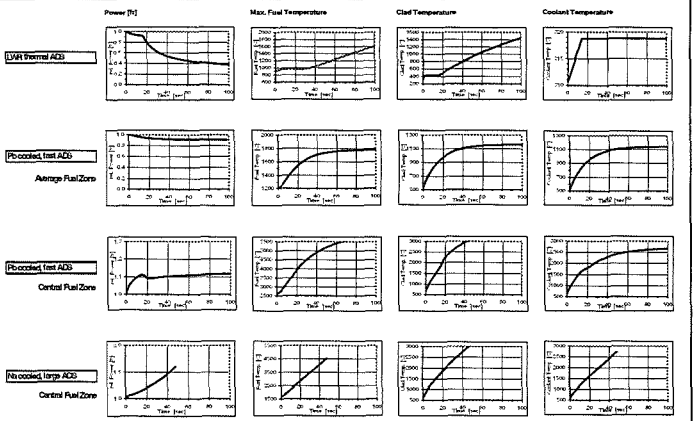

Fig. 12. Unprotected Loss of Flow (ULOF) Transient for different ADS designs, k_eff = 0.95, Flow = 10 % nominal, Neutron Source does not shut off

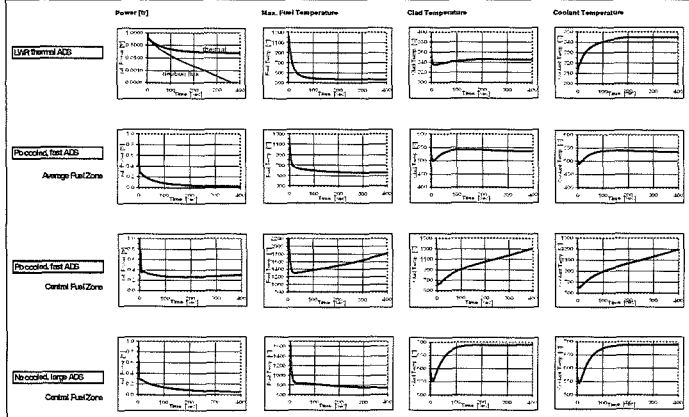

Fig. 13. Protected Loss of Heat Sink (PLOH) Transient for different ADS designs, k_eff = 0.99, Flow = 100 % nominal, Heat Sink: only radiation to ambient, Neutron Source shuts off

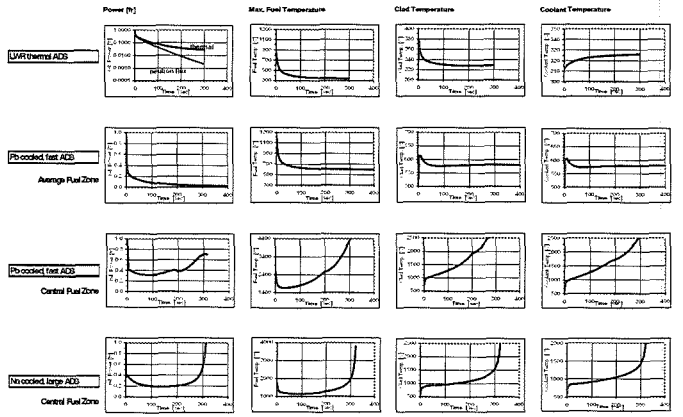

Fig. 14. Protected Loss of Heat Sink (PLOH) Transient for different ADS designs, k_eff = 0.99, Flow = 15 % nominal, Heat Sink: only radiation to ambient, Neutron Source shuts off

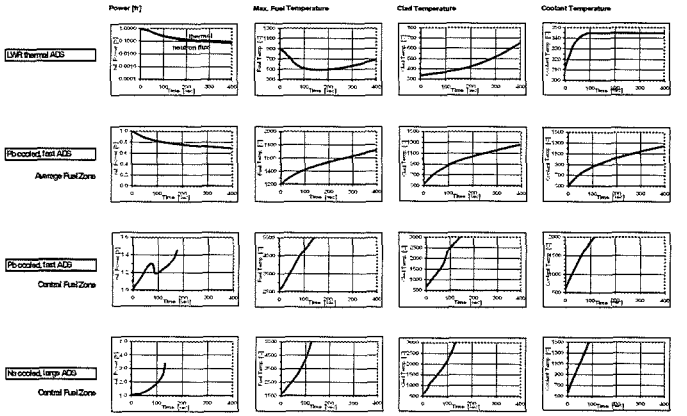

Fig. 15 Unprotected Loss of Heat Sink (ULOH) Transient for different ADS designs, k_eff = 0.99, Flow = 100 % nominal, Heat Sink: only radiation to ambient, Neutron Source does not shut off

32.23.06 HGF Strategy Fund Project 99/16: Thermalhydraulic and Material Specific Investigations into the Realization of an Accelerator Driven System (ADS) to Transmute Minor Actinides

(J.U. Knebel, IKET; Ch. Adelhelm, IMF I; G. Müller, IHM; J. Konys, IMF III; G. Grötzbach, IRS)

Abstract

The objective of this HGF Strategy Fund Project is the development of new methods and technologies to design and manufacture thin-walled and thermally highly-loaded surfaces which are cooled by a corrosive heavy liquid metal (lead-bismuth eutectic). The beam window is a vital component of an ADS spallation target.
The results of this project will provide the scientific-technical basis which allows the conception and the design of an ADS spallation target and later on a European Demonstrator of an ADS system. The work performed at Forschungszentrum Karlsruhe is embedded in a broad European research and development programme on ADS systems.

The project is divided in three sub-projects:
Sub-Project SP1: *Thermalhydraulic Investigations*
Sub-Project SP2: *Material Specific Investigations*
Sub-Project SP3: *Oxygen Control System*

The experimental investigations are performed in the KArlsruhe Lead LAboratory KALLA.
This report gives the some representative results achieved during the year 2000.

Kurzfassung

Ziel dieses HGF-Strategiefondsprojektes ist es, neue Methoden und Technologien zur Auslegung und Herstellung dünnwandiger, thermisch hochbelasteter Oberflächen, die von einem korrosiven schweren Flüssigmetall (eutektisches Blei-Wismut) gekühlt werden, zu entwickeln. Das Strahlfenster ist eine entscheidende Komponente eines Spallationstargets für einen ADS.
Das Ergebnis dieses Projektes ist ein wissenschaftlich-technisches Instrumentarium zur Konzeption und zur detaillierten Auslegung zunächst eines Spallationstargets

und später einer Europäischen Demonstrationsanlage eines ADS. Die Arbeiten am Forschungszentrum sind in ein breites europäisches Forschungs- und Entwicklungsprogramm zu Beschleuniger getriebenen Anordnungen (ADS) eingebunden.

Das Projekt gliedert sich in drei Teilprojekte:
Teilprojekt 1: Thermohydraulische Untersuchungen
Teilprojekt 2: Materialspezifische Untersuchungen
Teilprojekt 3: Sauerstoffkontrolle

Die experimentellen Untersuchungen werden im Flüssigmetalllabor KALLA (KArlsruhe Lead LAboratory) durchgeführt.
Dieser Bericht gibt einige wesentliche im Jahr 2000 erzielten Ergebnisse wieder.

1. Introduction and Objectives

The long-term strategy of the European reseach and development programme in the area of the peaceful utilization of nuclear energy for electricity production is based on scenarios, which consider the importance of the CO_2 emissions and the emission of other greenhouse gases, and the importance of the reduction of fossil fuel. These scenarios are balancing all possible energy resources. Supposing that nuclear energy shall provide a considerable amount of the electric energy produced in Europe, criteria such as energy security, economic efficiency and environmental sustainability are important.
If the option of nuclear energy for electricity production is to be kept open, a research and development programme has to be proposed which covers the following two aspects:

1. Plant life management dealing with the assurance of the high safety level of existing nuclear power plants. This includes risk analysis work which quantifies safety features leading to safety criteria.
2. Development of new reactor systems (evolutionary or innovative) according to market rules, considering: economic aspects, safety assessment, waste management strategies, inherent non-proliferation features and ease of safeguards' measures applications.

Independent of any scenario considered (revival of nuclear energy or not), a third aspect is of major importance and is expected to grow, Allgeier (2000):

3. *Nuclear waste management*, including non-proliferation and disarmament.

To face facts, the nuclear waste is already existing in large quantities and will be produced continuously in the operating nuclear power plants. This is independent of the future of nuclear energy. As a consequence projects on fundamental actinide research, *partitioning and transmutation (P&T)*, spent fuel behaviour and fuel storage safety evaluations are required.
All these topics have a high degree of promising and future characteristics. They exhibit a national and European challenge to governments / polititians, industry and research. Finally the important aspect of communication and of public perception has to be improved by developing effective strategies.

Transmutation is considered a promising technology worldwide for significantly reducing the amount and, thereby, the long-term radiotoxicity of highly active waste (HAW). Transmutation is the treatment of nuclear waste with an intense neutron flux in order to transmute transuranium (TRU) isotopes (plutonium and minor actinides) and long-lived fission products into short-lived radioisotopes or stable nuclei. The maximum reduction of radiotoxicity could be by a factor of about 100 (Knebel and Heusener (2000)). Transmutation is thus an alternative to the direct deposition of large volumes of highly radioactive waste. Transmutation presents the possibility of closing the fuel cycle including the minor actinides. Plutonium, minor actinides and long-lived fission products can be transmuted in a so called *Accelerator Driven System (ADS)*, which consists of an accelerator, a target module and a subcritical blanket.

The *target module* for ADS application is a technologically new component, the technical feasibility of which has to be assessed and experimentally proved. This report is concentrating on the development of a spallation target and on the solution of accompagnying questions.

The *short-term objective of this HGF Strategy Fund Project* is the development of new methods and technologies to design and manufacture thin-walled and thermally

highly-loaded components which are cooled by a corrosive heavy liquid metal. Such a component is the beam window which is cooled by liquid lead-bismuth eutectic. The beam window is a vital component of an ADS spallation target and thus of an Accelerator Driven System (ADS).

The project is divided in three sub-projects (SP):

- SP1: Thermalhydraulic investigations
  Thermalhydraulic investigations of thin-walled, thermally highly-loaded surfaces (beam window and spallation target module) with liquid lead-bismuth as coolant,
- SP2: Material specific investigations
  Investigation of corrosion mechanisms and development of an instruction to condition metals in flowing lead-bismuth,
- SP3: Oxygen control system
  Oxygen concentration measurement and oxygen control in lead-bismuth loops.

The strategy of the project is based both on a theoretical / numerical approach and on an experimental approach.
The summary of the results of the three sub-projects contributes to the method and technology to realize critical and system-relevant components of an Accelerator Driven System (ADS), such as the beam window and the spallation target. The safe design of these components relative to heat transfer, material selection and corrosion control is a basic requirement to guarantee the integral funtionality of an ADS.

The *medium-term objective of this HGF Strategy Fund Project* is the participation in the MEGAPIE Initiative which aims at the development and operation of the exploratory heavy liquid metal spallation target MEGAPIE with a beam power of *1 MW*. MEGAPIE will be implemented in the existing spallation neutron source SINQ at Paul Scherrer Institute (PSI), Switzerland.

The *long-term objective of this HGF Strategy Fund Project* is – on the basis of the newly developped methods and technologies – to provide the scientific-technical tool

which allows, now, the conceptual design and, at a later stage, the detailed design of a European Experimental Demonstrator of an ADS.
The Experimental Demonstrator with a thermal power of about 80 to 100 MW(th) is a milestone towards the long-term realization of a prototypical ADS with a thermal power of about 1500 MW(th).

2. Accelerator Driven System (ADS)

An *accelerator driven system (ADS)* consists of three main parts: an *accelerator* for primary particles (protons), a *spallation target (or target module)* in which the protons produce free nucleons (neutrons) in a spallation reaction (external neutron source), and a *subcritical blanket* in which, first, the fission reaction, producing fission neutrons (internal neutron source) and thermal energy, and second, the transmutation reaction occur, Bowman (1992). The protons are injected into the spallation target through a vacuum beam pipe, the beam pipe being closed by a window at the end. The target is a heavy liquid metal (e.g. lead Pb or eutectic lead-bismuth Pb-Bi). The spallation neutrons produced in the spallation target are completely independent of the subcritical blanket. A shut-down of the accelerator or an interruption of the proton beam immediately stops the fission reaction. Safety aspects of such a subcritical system are discussed in Wider (1998), Maschek, Thiem, Heusener (1999), Klügel et. al. (1999). A sketch of an ADS is given in figure 1.

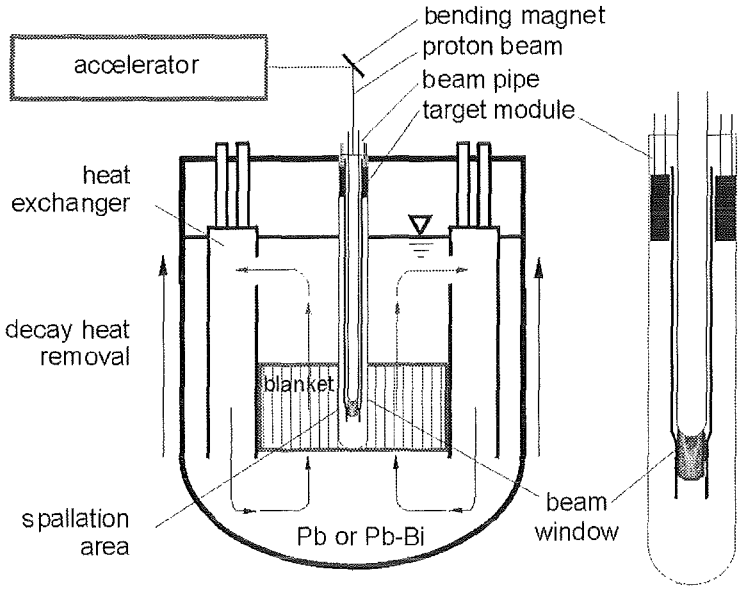

Figure 1: Sketch of an accelerator driven system (ADS).

The *strategic objective* of an ADS is to transmute long-lived radioactive waste and, thus, to close the fuel cycle including minor actinides, (Heusener and Salvatores (1998), Carminati et al. (1993), Rubbia et al. (1995)). The waste which is treated in an ADS can be divided into two parts: the minor actinides such as Neptunium, Americium und Curium and some long-lived fission products such as technetium 99 and iodine 129. The two latter species can diffuse in the biosphere in the long run where they can be selectively incorporated by organisms.
The ADS technology is a natural extention to the existing park of light water reactors (LWR). The use of ADS reduces the amount and the radiotoxicity of radioactive waste which has to be transported and stored in a final repository. Such considerations are formulated for Europe, TWG (2001), the United States, US-DOE (1999) and van Tuyle (2000), Japan, Takizuka et al. (1998), and Korea, Park (1999).

The evaluation commission of the Bundesministerium für Wirtschaft (BMWi) considers the strategic work on transmutation a priority task. The evaluation commission considers it as required to fundamentally investigate the physical and technical conditions for the technological realization of the ADS technology, Evaluierungskommission (2000).

This HGF Strategy Fund Project provides an essential scientific contribution to the application-oriented fundamental research work within the energy technology of an ADS as mentioned above.

3. Results during 2000

Here, only a brief overview of the main results is given. A detailed description of the achieved results is given in the 2000 status report, Knebel et al. (2001).

3.1 KArlsruhe Lead LAboratory KALLA

The KArlsruhe Lead LAboratory KALLA summarizes all experimental activities at Forschungszentrum Karlsruhe which use the fluid lead-bismuth eutectic, (KALLA (2001)). The involved institutes are Institute for Nuclear and Energy Tech-

nologies (IKET), Institute for Pulsed Power and Microwave Technology (IHM), Institute for Materials Research III (IMF III).
The experimental activities of KALLA can be divided in two groups:

- Stagnant experiments:
  - COSTA 1 to 3 (COrrosion test stand for STagnant liquid lead Alloys)
  - KOSIMA 1 to 6 (Karlsruhe Oxygen Sensor In Molten Alloys)
  - KOCOS (Kinetics of Oxygen COntrol Systems)

- Loop experiments:
  - THESYS (Technologies for HEavy metal SYStems)
  - THEADES (THErmalhydraulics and Ads DESign)
  - CORRIDA (CORRosion In Dynamic lead Alloys)
  - K4T (Karlsruhe 4 MW Target experiment)

The Technical Working Group (TWG) proposes to establish only a few larger laboratories for experimental investigations in liquid lead-bismuth within the European Union. With the KArlsruhe Lead LAboratory KALLA at Forschungszentrum Karlsruhe there will be a strategic focal point in the field of lead-bismuth technologies in Germany.

In this sense, KALLA is meant to be an open user laboratory for experiments which are relevant for ADS applications. KALLA shall enhance international collaboration and encourage scientific staff exchange. In addition, your scientists can be educated and trained in heavy liquid metal technologies and applications. This is in agreement with the newly proposed direction of EURATOM research in the Framework Program 2002-2006, which will strengthen both integrated projects and networks of excellence, EURATOM (2001).

A brief explanation of each experiment, giving the objectives, the experimental set-up, the parameter range and a representative photograph, can be found in *http:// www.kalla.fzk.de.*

Parallel to the lead-bismuth experiments in KALLA, model experiments with water as fluid are performed in the test facility HYTAS (HYdraulic behaviour in spallation TArget Systems). HYTAS allows for hydraulic and heated experiments in various lucid test sections, the measurement techniques being a 4-beam 2-component fiber optical Laser Doppler Anemometer (LDA) and Laser light sheet for the velocity field and thermocouples and shadow graph for temperature field. The application of particle image velocimetry (PIV) and ultrasonic velocimetry technique (UVP) is envisaged.

3.2 Data Acquisition and Control Scheme

In the KArlsruhe Lead LAboratory KALLA a distributed measurement and automation system consisting of several personal computers and measurement devices is used. All PCs are linked over a 100 Base-TX switched Ethernet and are connected to a central server, which provides connectivity to the intranet and internet. The configuration and data storing is managed by a central database server running IBM DB2 V7 for Linux, attached to a Level 5 RAID with backup to obtain highest possible reliability and data security. The programming based on National Instruments LabVIEW 6.0i including the Datalogging and Supervisory Control Modules (DSC) which allows to share measurement values in the internal network and so to remote access any data from any PC.

The process control is managed by one Siemens S5 processor per loop connected over serial AS511 interface to a control PC running National Instruments Lookout OPC Server. Target values for heating temperatures, pump power and other process equipment can be entered by the operator using a graphical human machine interface (HMI) on these PCs. Historical process data are logged continuously to the database and can be reviewed at any time. By this means a user friendly, long term state monitoring for the test facilities is made available.

To acquire the measurement data of the extensive loop instrumentation, mainly three different devices come into operation. First Schlumberger Integrated Measurement Pods (IMPs) are used for logging of the internal Pb-Bi temperatures in the loops and for acquisition of voltage and currency as scaled outputs of arbitrary devices. Second the Beckhoff Fieldbus with different types of terminals and controllers is installed to operate the Oxygen Control Systems (OCS) in combination with external control equipment. Third fast data acquisition cards (DAQ) in a National Instruments PXI

rack are used for special measurement tasks at the test sections. The resulting data are collected by personal computers and also filed in the central database for later analysis.

In addition to the above described features a very new technique in the field of data acquisition and control is used at KALLA. A wireless local area network (WaveLAN) is installed at the laboratory which gives the possibility to use one or more laptops as mobile maintenance and measurement units. With this installation one can control an experiment from "within" the test facility always having direct access to the desired measurement data and control operations.

Figure 2 gives a schematic view of the distributed measurement and automation network in the Karlsruhe Lead Laboratory KALLA. Online data displays are given on *http:// www.kalla.fzk.de/kalla*.

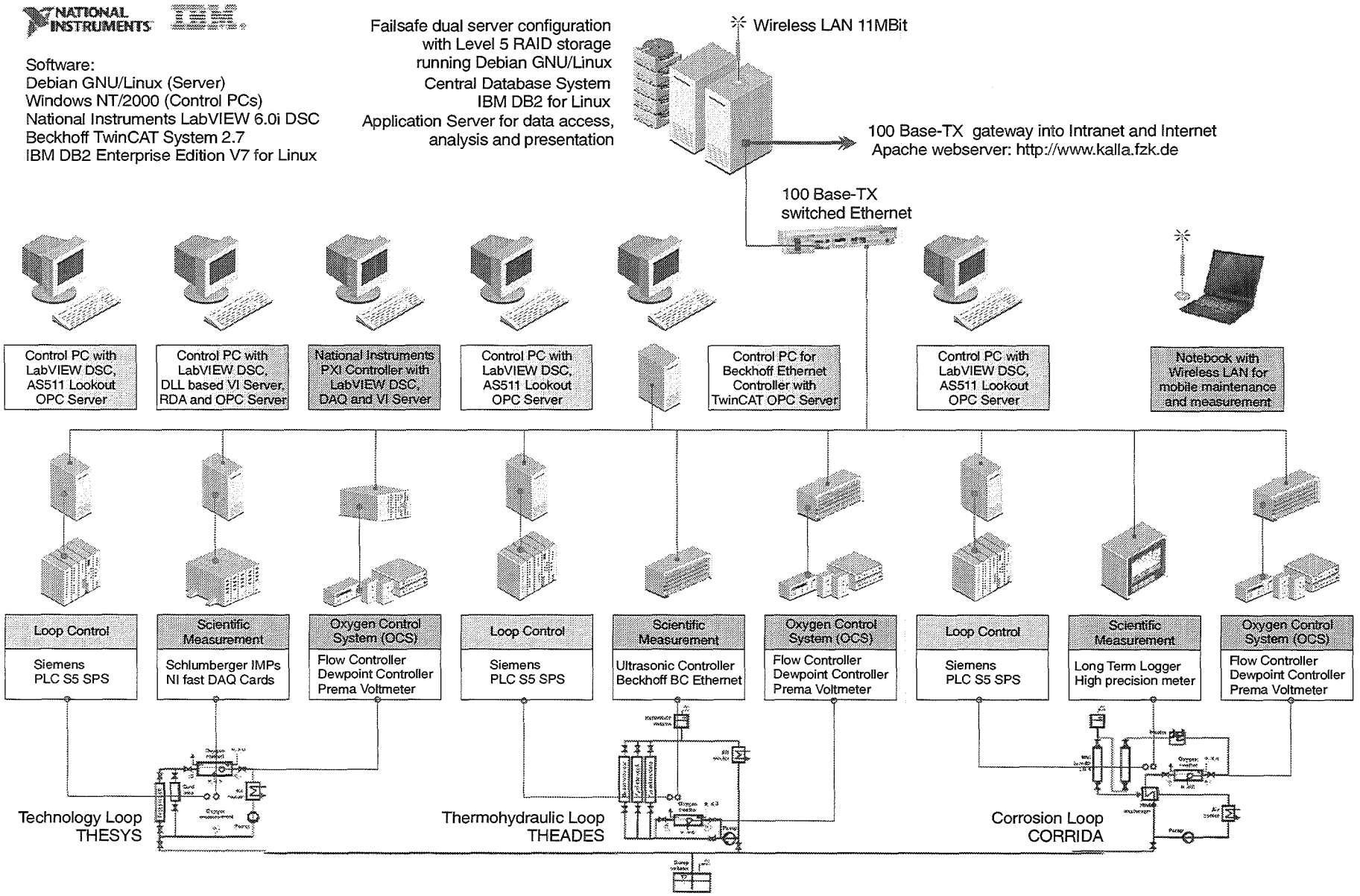

Figure 2: Automization scheme of KALLA.

3.3 Sub-Project SP1: Thermalhydraulic Investigations

A three steps strategy has been proposed for the research activities accompagnying the spallation target design.

In the *first step* a numerical analysis is carried out with available CFD codes (the commercial codes CFX and FIDAP, and the Forschungszentrum Karlsruhe code FLUTAN), to provide a fundamental knowledge about the steady-state and transient thermalhydraulic behaviour of a spallation target, and to develop evaluation criteria which are to be applied to a design selection procedure at a later stage.

In the *second step* model experiments are performed, to provide an experimental data base for physical model development and code improvement and validation (reported here). At the present stage a certain deficiency in applied Pb-Bi technology exists so that experimental investigations both with a model fluid, e.g. water, and with the realistic coolant, Pb-Bi eutectic, are recommended. A model experiment using water as fluid allows to both perform a systematical study of the physical phenomena involved and to apply sophisticated measurement techniques, which is not the case with the prototypical fluid (reported here). To this purpose the water test facility HYTAS (HYdraulic behaviour in spallation TArget Systems) has been erected. However, the results obtained in a water model experiment cannot be directly transferred to the prototype conditions as far as heat transfer characteristics and buoyancy effects are concerned.

In the *third step* experimental studies in liquid Pb-Bi are performed in the KArlsruhe Lead LAboratory KALLA for the final design of a beam window. The design of the complete spallation target module is done numerically first (reported here). The experimental investigations of a target module is beyond the scope of this HGF Strategy Fund Project.

3.3.1 Design of a Beam Window Based on Numerical Simulations and Model Experiments with Water as Fluid (Experimental Study on the ISTC 559 Target)

Test Facility HYTAS:

The main purpose of the HYTAS experiment is to study the hydraulic behaviour of the flow around the beam window of a spallation target. It is well known that the hydraulic behaviour of a liquid metal flow in a prototype geometry can be exactly

simulated in a model experiment using water, as long as the Reynolds numbers in both the prototype and the model are identical.

The water test facility HYTAS is a pump driven water loop, which is capable of circulating a maximun volumetric flow rate of 100 m^3/h with a maximum pressure drop of 0.4 MPa. Test sections with a maximum vertical length of 3.5 m can be integrated in the test facility.

Test Section for ISTC Target:

During the reported time period experiments have been carried out for the ISTC 559 target. More details about the ISTC 559 project can be found in Cheng and Slessarev (2000). The design of the active part (beam window and spallation area) is one of the main tasks in the target design. Figure 3 shows a sketch and a photograph of the ISTC 559 model test section. The beam window has a semi-spheric surface, the diameter being 110 mm. The active part consists of two coaxial cylinders with inner diameters of 130 mm and 185 mm, respectively. The coolant flows into the annular gap between the two cylinders, makes a U-turn at the top, passes along the window surface, and then exits the active part via the central cylinder. To reduce the flow stagnation zone near the center of the beam window (stagnation point), where the heat deposition by the proton beam has its maximum, a perforated steel plate with distributed holes is installed close to the beam window. The plate has a thickness of 5 mm. The porosity is highest on the centerline and decreases with increasing distance from the center line. The flow resistance increases with increasing distance from the centerline. In this way, the coolant flow and the heat transfer near the center of the beam window is significantly enhanced.

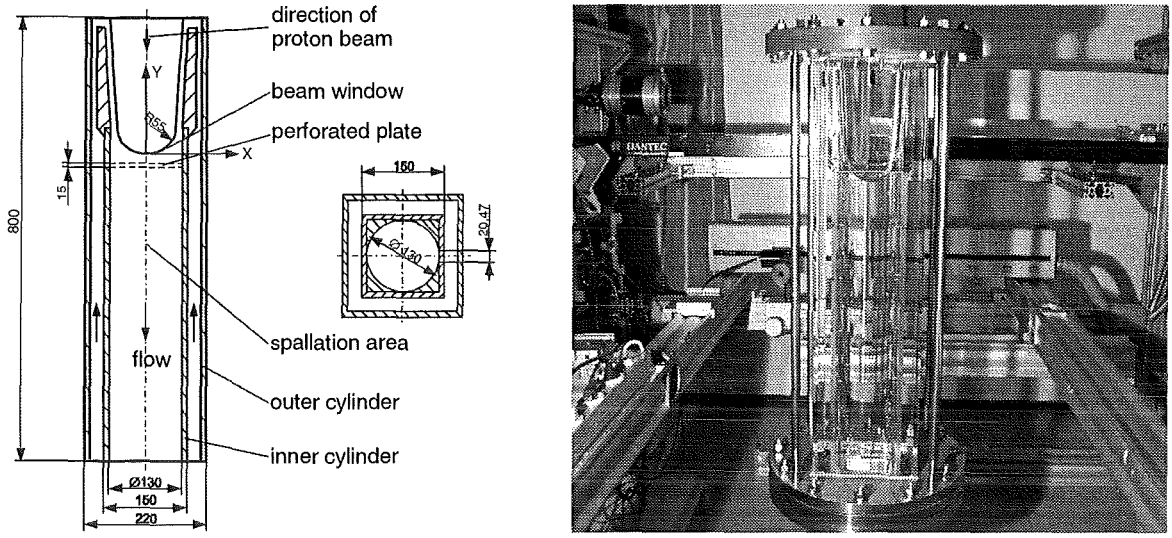

Figure 3: Test section of the ISTC 559 beam window geometry.

Results:

The local velocities are measured with a 2-D Laser-Doppler Anemometer (LDA). To present the results, a coordinate system is chosen, the origin of which is located on the center of the window surface, see figure 3. The x-axis is in the radial direction. The y-axis is parallel to the axis of the target, the positive direction being towards the direction of the proton beam. Figure 4 shows the distribution of the mean axial velocity u versus the radial direction of the test channel with a perforated plate. The distance between the perforated plate (5 mm thick) and the center of the beam window is 15 mm. It is found that there is no detachment of the boundary layer from the window surface, i.e. at both elevations (y = 0 and y = 10 mm) the axial velocity is negative for all radial positions. Close to the perforated plate (e.g. at y = -10 mm) a strong increase in the axial velocity is obtained around the axis of the target. As indicated in figure 4, the axial velocity on the centre line (x = 0) is about -0.8 m/s at 5 mm upstream of the plate, e.g. at y = -10 mm, and -1.5 m/s at 10 mm downstream of the plate, e.g. at y = -30 mm. Flow recirculation occurs both downstream of the plate and between the holes.

Figure 5 compares the radial profile of the axial velocity at y = 0 mm for both cases: with and without perforated plate. It is seen that the introduction of the perforated plate leads to a strong increase in the axial velocity near the beam window. The stagnation zone close to the beam window is reduced significantly. In the outer region, i.e. $x \geq 40$ mm, flow recirculation occurs. In order to avoid a hot spot in the

fluid for the case of a proton beam shift, an optimization of the distribution of the holes in the perforated plate is required.

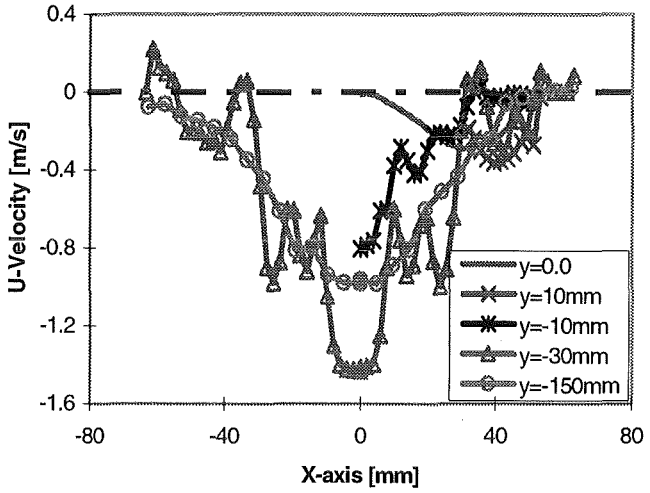

Figure 4: Axial velocity profiles with downward flow through the central channel and a perforated plate, V = 10 m³/h.

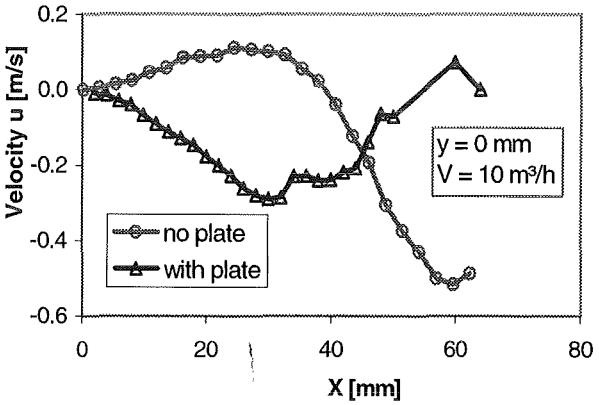

Figure 5: Axial velocity profiles with downward flow through the central channel at y = 0 mm: comparison of the experimental results with and without perforated plate.

3.3.2 Fundamental Experiments in Liquid Lead-Bismuth on Heat Transfer and Model Development / Model Validation (TEFLU Benchmark)

Introduction:

The temperatures in the structures of a spallation target reach critical values at the beam window. In order to determine these structure temperatures accurately, turbulence models are required to predict the temperature field in the cooling fluid. Standard turbulence models, which are used in commercial codes, are not suitable for the adequate simulation of turbulent heat transfer in heavy liquid metal flows, with buoyancy effects being important: the models using a turbulent Prandtl number to describe the turbulent heat transport assume the Reynolds analogy between the turbulent transport of momentum and heat. This assumption is not valid for liquid

metals because the momentum field is mainly turbulence dominated and has only thin wall layers governed by molecular viscous forces, whereas the temperature field is less turbulence dominated and has thick wall layers governed by molecular conduction.

Improved turbulent heat transfer modeling for liquid metals requires more sophisticated measures, than are usually applied for momentum transfer. This means that additional transport equations have to be used which characterize the statistics of the temperature fluctuations. In Carteciano (1996) the TMBF turbulence model is described, which consists of a combination of a low–Reynolds number k-ε model and a second order 5–equation heat flux model. Certain model extensions for liquid metal flows are reported which were developed based on the analysis of data from direct numerical turbulence simulations (Carteciano et al. (1999)).

The objective of the last year activity was to investigate in more detail the advantages of the extended TMBF model and possible necessities for additional model extensions. For this purpose, a heated turbulent sodium jet was chosen by the Benchmark Working Group in order to test the capabilities of CFD codes at simulating liquid metal turbulent flows with heat transfer. The corresponding experiments were performed in the test facility TEFLU at Forschungszentrum Karlsruhe (Knebel et al. (1998)); a detailed description of the experimental setup is given there. Three different flow regimes being a forced jet, a buoyant jet, and a plume are considered for the TEFLU Benchmark (Maciocco (2000)).

The FLUTAN calculations (Carteciano and Grötzbach (2001)) are performed using two different turbulence models: the standard k-ε-σ_t model and the TMBF model. The calculations with the k-ε-σ_t model are performed using the standard value for the turbulent Prandtl number σ_t=0.9. The results are compared with experimental data in order to show how the TMBF improves the k-ε-σ_t model and to show the limits of applicability of an eddy diffusivity approach to liquid metal flows. In addition results are deduced from the TMBF calculations on the spatial distribution of the turbulent Prandtl number σ_t which are required to approximate the experimental temperature field with a k-ε-σ_t model.

The case specifications such as numerical grid, symmetry conditions, inlet profiles, convergence criterion parameter, and discretization method are given in Carteciano and Grötzbach (2001).

Results:

The TMBF and the k-ε-σ_t model can adequately simulate the turbulent transport of momentum using the standard values of the empirical coefficients for the buoyant jet and for the plume regime, Figure 6 is given as a representative result. However, the value of c_μ must be reduced to 0.06 in the case of the forced jet in order to damp the well known attitude of the k-ε model to overestimate the rate of spread of an axi-symmetric jet, (Rodi (1980)). The fact that the TMBF simulates the same velocity field as calculated by the k-ε-σ_t model signalizes that the temperature influence on the velocity field by means of the turbulent transport of heat is negligible even in the case of the plume regime. In fact, both models describe the turbulent transport of momentum using the same transport equations of k and ε. The only difference in this description is in the model of the buoyancy term which is obviously of negligible order in all the calculations.

The TMBF is a significant improvement in comparison to the k-ε-σ_t model in the simulation of the turbulent transport of heat (Figure 7 is given as a representative result). The TMBF can reproduce the mean temperature field well by using the standard values of empirical coefficients in all experiments. This good agreement is due to the separate treatment of the turbulent transport of heat and momentum in the TMBF using the transport equations for the three heat fluxes instead of using the isotropic Fourier assumption.

In contrast, the k-ε-σ_t model cannot accurately simulate the mean temperature field when the standard turbulent Prandtl number is used. As a result of a strong anisotropy in the field of the temperature gradient which shows very high values perpendicular to the flow direction, the turbulent heat flux acting perpendicular to the flow direction has very high values as they are calculated being proportional to the temperature gradient according to the Fourier assumption. For this reason the k-ε-σ_t model shows an unsatisfactory simulation of the turbulent heat fluxes overestimating the values calculated from the TMBF model.

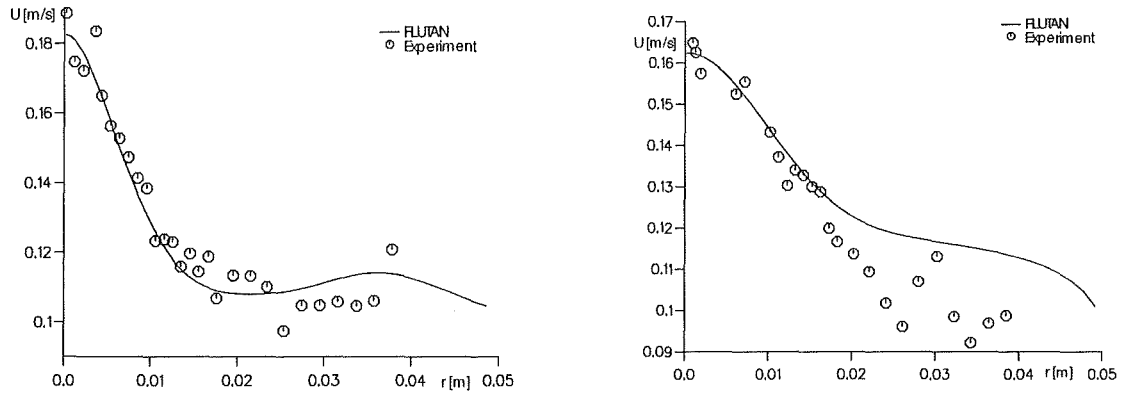

Figure 6: Radial velocity profiles at x/d=12. Plume. Calculation with the k-ε-σ_t model (left) and TMBF model (right).

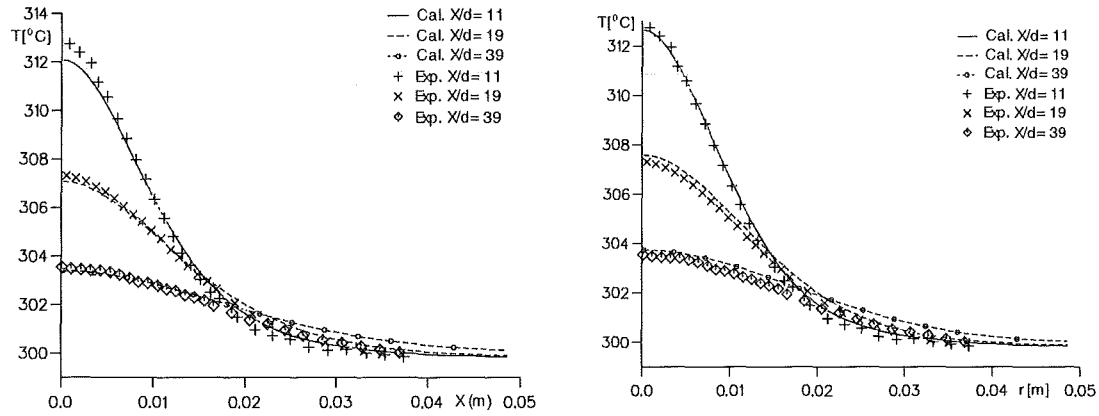

Figure 7: Radial temperature profiles. Plume. Calculation with the k-ε-σ_t model (left) and with the TMBF model (right).

The k-ε-σ_t model can give a good simulation only by adjusting the value of σ_t reducing the turbulent heat flux acting perpendicularly to the flow direction. The fields of σ_t can be calculated by the TMBF model. They represent approximate values because σ_t is calculated using the turbulent heat fluxes, which are modelled by transport equations, and the turbulent shear stresses, which are modelled like in the k-ε model by velocity gradients. The calculated fields show that the turbulent Prandtl number depends not only on the fluid but also on the flow regime and on the position (Figure 8).

From the turbulent Prandtl number distributions it is obvious that the influence of the overestimation of the turbulent radial heat flux on the temperature field by the k-ε-σ_t model is negligible in the plume regime due to the high turbulent conductivity λ_t. In all three flow regimes the turbulent conductivity is lower than the molecular one. The turbulent heat transport by becomes less and less important compared to the molecular one when going from the forced to the plume regime. This can explain the

acceptable simulation of the temperature field performed by the k-ε-σ_t model in case of the plume regime.

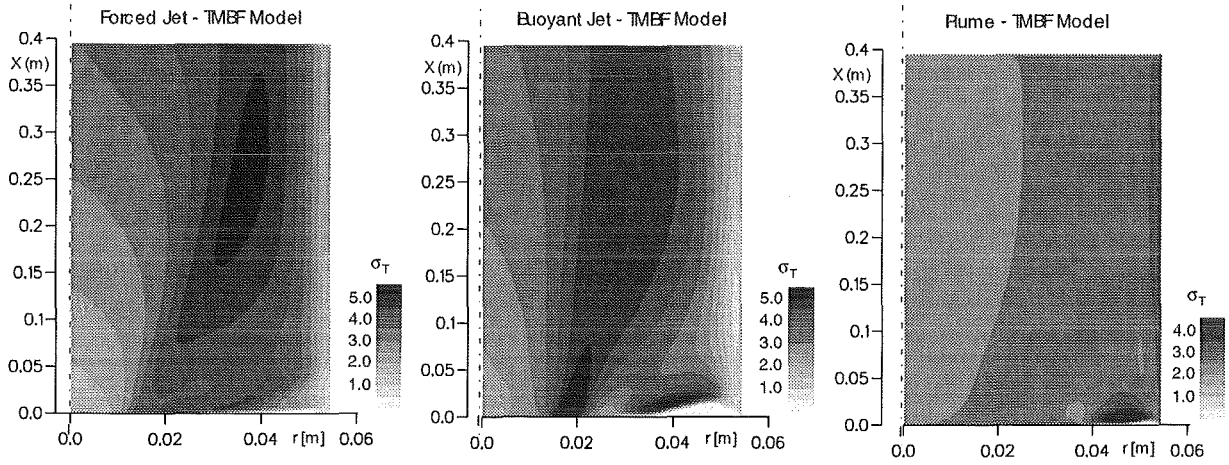

Figure 8: Field of the turbulent Prandtl number calculated with the TMBF model.

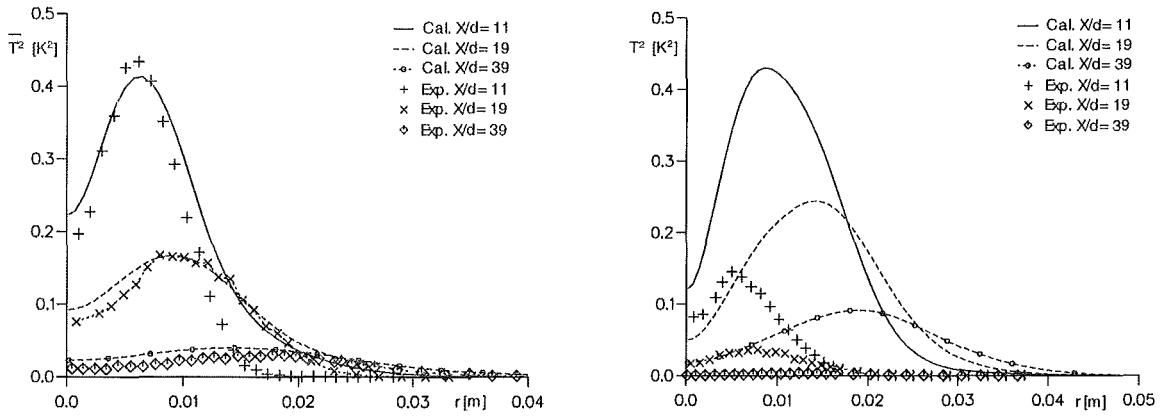

Figure 9: Radial profiles of the temperature variance. Forced Jet (left) and Plume (right). Calculation with the TMBF model.

The TMBF properly simulates the variance of temperature fluctuations $\overline{T'^2}$ in all experiments with the exception of the plume regime (Figure 9). Due to the use of a transport equation for $\varepsilon_{T'}$, a local non-constant value of the turbulent time-scale ratio

$$R=0.5*(\overline{T'^2}/\varepsilon_{T'})/(k/\varepsilon) \quad (1)$$

can be calculated which is otherwise needed to model the sink term in the $\overline{T'^2}$ equation.

Conclusions:

The recalculations of the TEFLU experiments show the limits of the applicability of an eddy diffusivity approach used by the widely used k-ε-σ_t model to buoyant liquid

metal flows. The TMBF which is a compromise between the classical k-ε-σ_t model and the Reynolds stress model is clearly an improvement of the k-ε-σ_t model for turbulent flows where the turbulent transport of heat is complex and the Reynolds analogy is not valid, such as in buoyant liquid metal flows. A further development of the TMBF model should still be carried out as the radial profiles of $\overline{T'^2}$ in the plume regime are overestimated. In fact, a new modeling depending on the Peclet number should be developed for the transport equation of $\varepsilon_{T'}$ (Wörner et al. (1996) and (1999)). Further validation of the TMBF model for heavy liquid metals has to be carried out for flow regimes in which the velocity field is considerably influenced by the turbulent heat transport, this means for buoyant flows.

3.3.3 Simulation Experiments for the Optimized Beam Window in Lead-Bismuth and Numerical Simulation of Beam Window and Spallation Target
(One-dimensional analysis of the flow behaviour within a 4 MW spallation target)

Introduction:

The overall objective of this HGF Strategy Fund Project is to design a large-scale spallation target which can be implemented in an ADS demonstrator. Before starting to design a test rig for such a large-scale spallation target, simple one-dimensional calculations have to be performed, in order to clarify the general layout and geometry of the major components of such a spallation target (cf. figure 10) and its heat removal chain (cf. figure 11), together with the dimensions and the total driving heights needed. The heat removal considered here is by natural circulation only. These data are important as they have to be technically feasible and to match with the dimensions defined within the design of the ADS demonstrator.
The major objectives of the integral experiment on a large-scale spallation target are:

- Demonstration of the beam window coolability,
- Demonstration of the heat removal from the spallation area and the beam window by natural circulation,
- Steady-state and transient characteristics of heat transport in a coupled loop system under natural circulation,
- Demonstration of oxygen control system,

- Corrosion behaviour of structural and window materials,
- Set-up of a data base for physical model and code validation,
- Simulation of fluid flow phenomena using CFD codes.

Investigated Geometry:

The considered heat removal system consists of three coupled loops, see figure 11. The heat transport between spallation area and environment is done by natural circulation only.

- Primary loop or spallation target itself (fluid: Pb-Bi),
- Secondary loop (fluid: Pb-Bi),
- Tertiary loop (fluid: air).

The main components of the heat removal system are the following:

- Spallation area and beam window,
- Primary-secondary heat exchanger (see figure 12),
- Secondary-tertiary heat exchanger (see figure 13),
- Stack (see figure 11).

A detailed geometrical description of the components is given in Knebel and Neitzel (2000).

A modification to this design could be a forced convection heat removal system utilizing pumps in the primary and secondary loop, and an air blower in the tertiary loop. In this case, the fluid of the secondary loop could be an organic fluid, as proposed for the EA Demonstrator by ___ (19__). These modifications are not considered here.

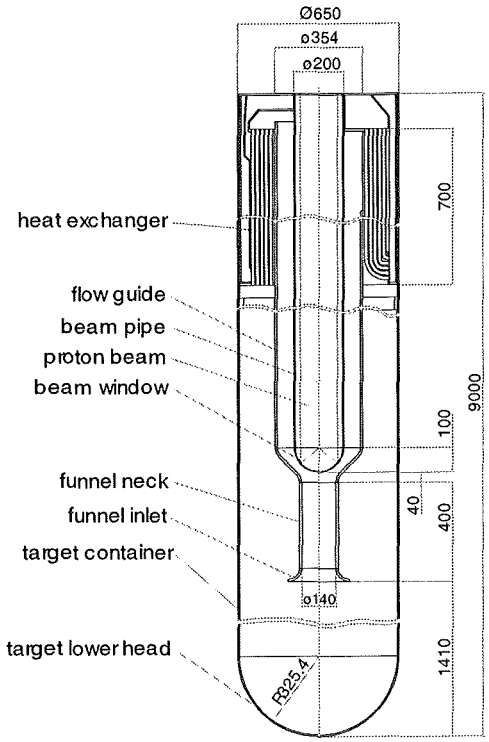

Figure 10: Sketch of a spallation target module of 4 MW beam power.

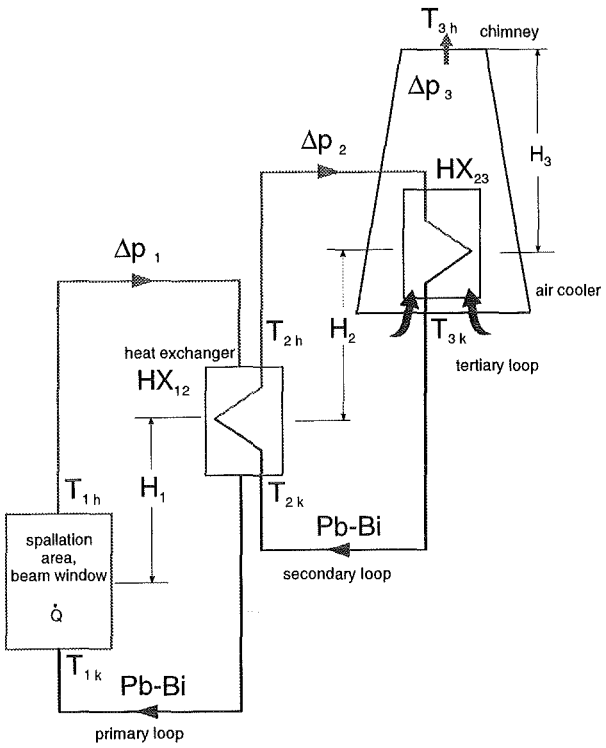

Figure 11: Natural circulation heat removal chain for the integral experiment K4T: primary Pb-Bi loop, secondary Pb-Bi loop, tertiary air loop.

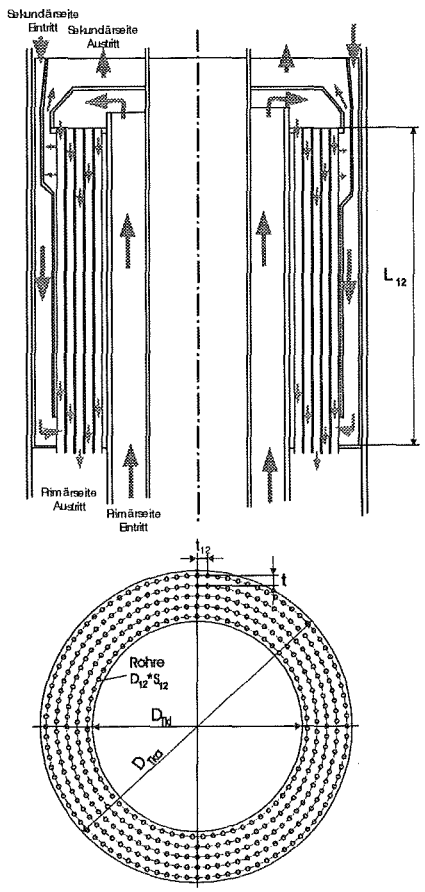

Figure 12: Sketch of primary-secondary heat exchanger.

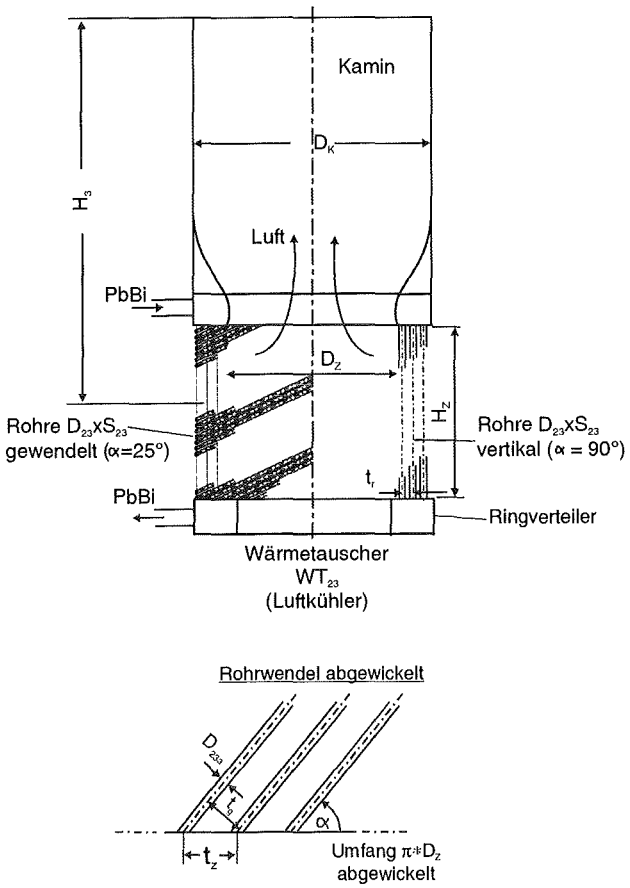

Figure 13: Sketch of secondary-tertiary heat exchanger.

Results:

According to the one-dimensional calculations in Neitzel and Knebel (2000) the main results for a spallation heat of 4 MW are summarized in table 1.

Table 1: Main results for the design of a 4 MW spallation target.

	Primary loop	Secondary loop	Tertiary loop
Power	$\dot{Q} = 4\ MW$		
Fluid	Pb-Bi	Pb-Bi	Air
Temperature hot leg / cold leg	$T_{1h} = 500°C$ $T_{1k} = 350°C$	$T_{2k} = 200°C$ $T_{2h} = 350°C$	$T_{3h} = 150°C$ $T_{3k} = 30°C$
Mass flux	$\dot{m}_1 = 181\ kg/s$	$\dot{m}_2 = 181\ kg/s$	$\dot{m}_3 = 33\ kg/s$
Pressure drop	$\Delta p_1 = 9130\ Pa$	$\Delta p_2 = 19300\ Pa$	$\Delta p_3 = 13\ Pa$
Driving height	$H_1 = 5.17\ m$	$H_2 = 10.36\ m$	$H_3 = 4.05\ m$

As shown in table 1 the overall dimensions such as temperature levels, mass fluxes, pressure drops and, above all, geodetic driving heights for the natural circulation heat removal can be realized with technically reasonable efforts in an ADS demonstrator. Thus, a spallation target with 4 MW of spallation power is a technically feasible design for normal, steady-state operation conditions.

Conclusions:

From the calculated pressure drops and required driving natural circulation heights it can be concluded that a natural circulation heat removal from a closed spallation module of 4 MW beam power is feasible. This holds for steady-state conditions.
Future emphasis will be on the transient characteristics of the complete heat removal chain from the spallation area to the environment under normal operation and decay heat removal conditions. Limitations of such a heat removal system, which is entirely relying on natural circulation forces, have to be specified.
In addition, the technical implementation of a full scale spallation target with heat removal system, being the Karlsruhe 4 MW Target experiment K4T, into KALLA will be investigated in more detail.

3.4 Sub-Project SP2: Material Specific Investigations

3.4.1 Investigation of the Corrosion and Erosion of Structure and Window Materials in Flowing Lead-Bismuth (Dynamic corrosion experiments with oxygen control)

Introduction:

This work package WP1 is divided into three steps which systematically describe the mechanisms of corrosion and erosion: first, stagnant experiments without oxygen protection, second, stagnant experiments with oxygen protection (reported here), and, third, dynamic experiments in flowing lead. The applied techniques and methods for the improvement of corrosion resistivity are, first, the surface protection applying an oxygen control system (OCS), and, second, the surface modification using the pulsed electron beam facility GESA.

Within the reported period, some corrosion experiments have been carried out in collaboration with IPPE in Obninsk, Russia. Two ferritic-martensitic and two austenitic steels in original condition and with a surface treatment by GESA were exposed to Pb in a loop at 400°C and 550°C resp. for 1027, 2000 and 3000 h, respectively. First results of specimens exposed for 1027 h are available and discussed here.

Materials and experimental conditions:

Different types of steel were selected for corrosion tests in the Pb loop: two ferritic-martensitic steels (Optifer IVc and EM10) and two austenitic steels (1.4948 and 1.4970).

The specimens (cylindrical shaped, about 110 mm total length, 8 mm diameter) to be tested were machined at Forschungszentrum Karlsruhe. The original specimens were not heat treated before exposure. Some specimens were treated by GESA (Pulsed Electron Beam Facility GESA) on approximately one third of the total length. The degreased samples were weighed before the corrosion testing. After the exposure, the specimens were washed to remove adherent Pb at 170 to 180°C in a special fluid which is not interacting with steels and oxide films.

The corrosion tests were carried out in a non-isothermal forced lead loop at IPPE Obninsk. The oxygen content in the lead was monitored by two oxygen meters placed in the loop. The exposed materials and the corresponding test conditions are summarised in table 2.

Table 2: Materials exposed to flowing lead at 400°C and 550°C.

Material	400°C	550°C	400°C	550°C	400°C	550°C
1.4970	1027 h	1027 h	2000 h	2000 h	3027 h	3027 h
1.4970 - GESA	--	1027 h	--	2000 h	--	3027 h
1.4948	1027 h	1027 h	2000 h	2000 h	--	3027 h
1.4948 - GESA	1027 h	1027 h	--	2000 h	--	3027 h
Optifer IVc	1027 h	1027 h	2000 h	2000 h	3027 h	3027 h
OptiferIVc-GESA	--	1027 h	--	--	--	--
EM 10	--	1027 h	--	--	--	3027 h

The applied analysis techniques consisted of:

- weighing of the cleaned specimens,
- X-ray spectral microanalysis of the surface of the specimens,
- metallurgical examination,
- EDX line scan analysis on the cross-sections of the specimens.

Results:

The cleaned specimens showed no sign of damage by dissolution attack. The visual inspection revealed an oxide formation with varying thickness on the surface of each specimen. Austenitic steels exposed to lead up to 2000 h still have a golden shiny surface even when exposed to 550°C, which indicates the existence of a thin oxide layer. With increasing exposure time the colour of the surface turned darker, but even then it was still shiny. The surfaces of the ferrites (GESA treated and untreated) and also the GESA treated austentic steels were black coloured without any shiny area, i.e. thick oxide layers were formed.

X-ray diffraction patterns obtained from the surface of the ferritic steels showed the formation of the compound Me_3O_4 already after 1000 h of exposure at 400°C and 550°C. No other compounds could be detected even after longer exposure time. In contrary to this, oxide patterns were not visible in the spectra of the austenitic steels, because the oxide layers were too thin.

Metallurgical examination of these steels showed an oxide layer thickness of about 2 µm after 3000 h of exposure at 550°C. This prevents the dissolution corrosion attack of the liquid lead at least during the limited time of exposure.

A two phase oxide scale was found on all austenitic steels treated by GESA. Both layers vary in thickness. The adherence seems to be very good. The cross sections

of GESA treated 1.4970 and 1.4948 steels after 3000 h of exposure at 550°C and the corresponding EDX concentration profiles are presented in figures 14 a,b and 15 a,b. The external layer has a composition of pure magnetite which is in agreement with the X-ray diffraction results obtained from specimens exposed to stagnant lead [9]. Other steel elements like nickel and chromium are not detected. The internal layer contains iron, chromium nickel and oxygen. This corresponds to an iron chromium spinel plus nickel. The concentration of iron and chromium stays constant in the whole layer whereas the oxygen content decreases slowly and nickel increases slightly towards to the steel side. In both austenitic steels the content of chromium and nickel is higher in the internal layer than in the steel matrix because of the release of iron into the magnetite layer.

In ferritic steels no obvious influence of the GESA treatment was observed. The EDX concentration profiles with the corresponding cross sections of Optifer IVc (2000 h at 550°C in lead) and EM 10 (3000 h at 550°C in lead) are shown in figures 16 a,b and 17 a,b. The micrographs of the cross sections show the typical corrosion attack with three different zones. The zone at the top consists of magnetite without appreciable chromium concentration. The layer in the middle contains Cr-Fe spinel that roots in a porous belt. Within the spinel zone, the chromium content reaches a maximum that is 1.5 times higher than the concentration in the bulk material due to iron depletion caused by the magnetite scale formation. In the interior, an oxygen diffusion zone can be observed in which oxides precipitate along grain boundaries. In the case of EM 10 the thickness of all three zones formed is smaller than that on Optifer IVc.

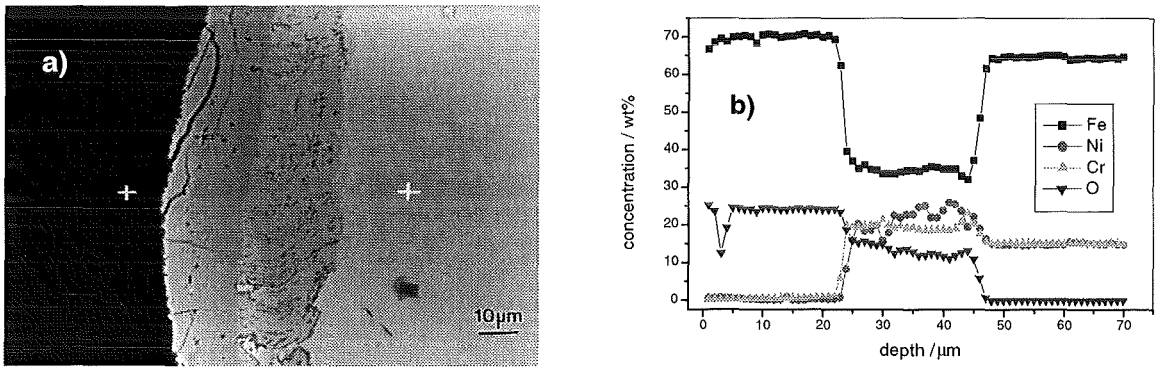

Figure 14: Micrograph of GESA-treated 1.4970 specimen cross section (a) and EDX concentration profile after 3000 h at 550°C (b).

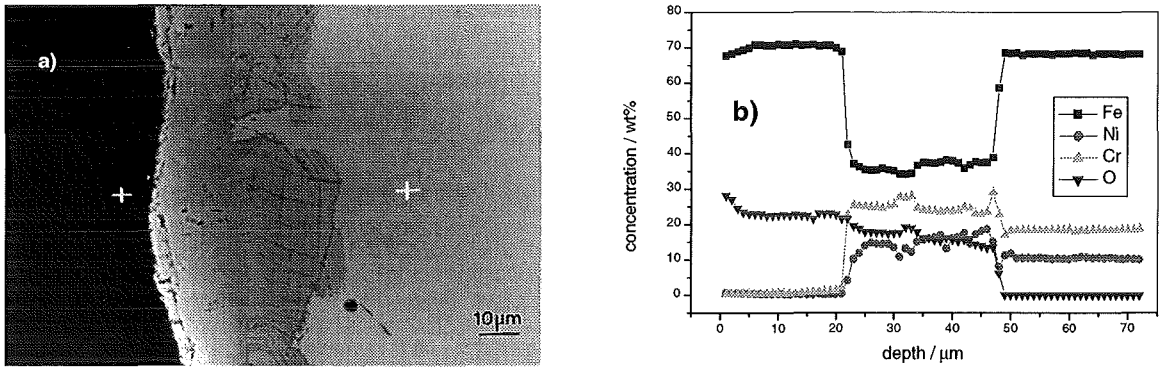

Figure 15: Micrograph of GESA-treated 1.4948 specimen cross section (a) and EDX concentration profile after 3000 h at 550°C (b).

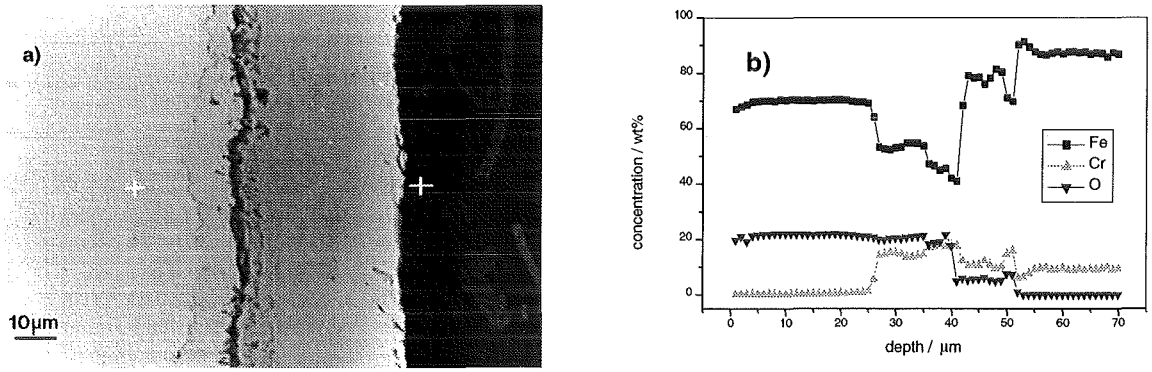

Figure 16: Micrograph of Optifer IVc specimen cross section (a) and EDX concentration profile after 2000 h at 550°C (b).

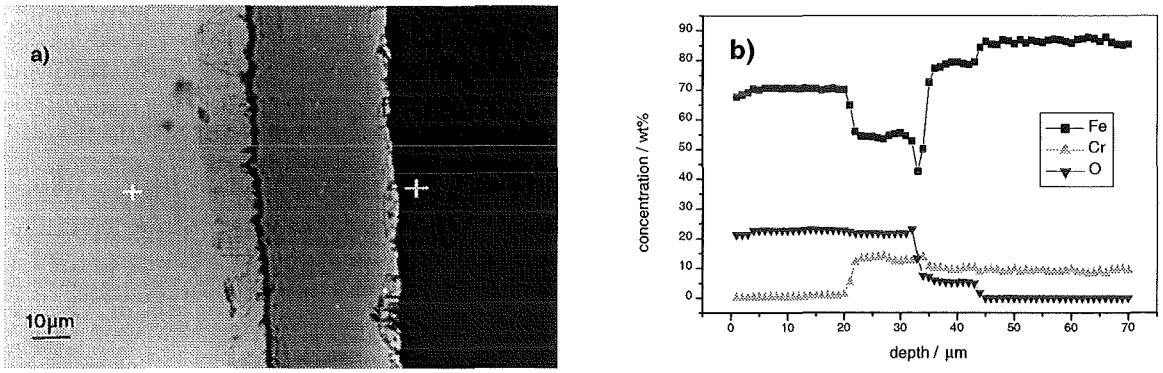

Figure 17: Micrograph of EM 10 specimen cross section (a) and EDX concentration profile after 3000 h at 550°C (b).

The oxide layers increase with time and temperature. The largest thickness is achieved on Optifer IVc, followed by the GESA treated austenitic steel 1.4948. The steels EM 10 and 1.4970 (GESA treated) showed more or less the same growth rate. The oxide layers thickness versus exposure time in liquid lead at 550°C is given in figure 18. It can be seen that the growth of the oxides on all steels obeys the parabolic law.

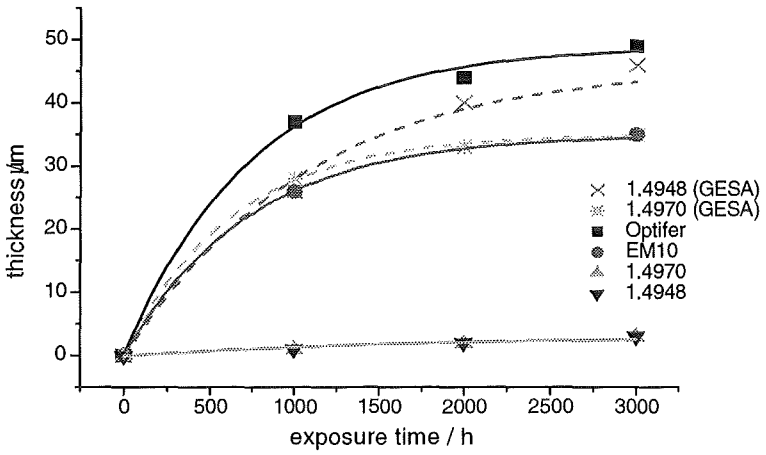

Figure 18: Total thickness of oxide layers versus the duration of corrosion tests of steels in flowing lead at 550°C.

Discussion of results:

Multiphase oxide scales were formed on the steel surfaces of the ferritic steels and the two GESA treated austenitic steels during exposure to flowing lead. The scales protect the steels against dissolution attack. Alloy components do not diffuse at the same rate in the oxide layers and the alloy. Therefore, a multiphase oxide scale is formed during oxidation of the alloys. The stratified oxide layer structure agrees with descriptions by Hauffe (1965) and Talbot and Talbot (1998) for oxidation of steels below 570°C in air.

Three distinct oxidation zones are developed at the steel surfaces: an outer magnetite scale (Fe_3O_4) which is placed on top of the original surface. Besides Fe and O other elements do not appear in an appreciable amount in this scale. The intermediate layer below the magnetite scale consists of a spinel $Fe^{2+}(Fe_{1-x}^{3+}Cr_x^{3+})_2O_4$ (+ Ni). This layer is an oxygen diffusion zone with spinel formation along grain boundaries.

The proposed oxidation mechanism for this multiphase oxide scale can be described as follows (Kuroda et al. (1983), Gesmundo et al. (1987), Müller (2000)): firstly, oxygen reacts with iron and chromium to form the Fe-Cr spinel. Oxygen has the capability to diffuse inwards through the oxide scale and reacts with steel elements to a spinel type structure. As a result of this O-ion diffusion the Fe-Cr spinel grows inwards. The outer layer grows by Fe-ion diffusion to the surface, which creates the magnetite scale that grows on the surface. Cr diffuses more slowly and is only present in the inner part of the scale.

The thickness and composition of the multiphase oxide scales formed on the ferritic steels with and without GESA treatment do not show any difference. Hence, the additional surface treatment did not have an obvious influence on the oxidation behaviour of Optifer IVc and EM 10. Not so for the GESA treated austenitic steels 1.4970 and 1.4980 in which multiphase oxide scales were developed like observed for the ferritic steels. In the case of untreated austenitic steel surfaces a thin dense oxide layer was formed.

All the oxide scales developed on the examined steels provide a good protection against the dissolution attack at 400°C and 550°C up to an exposure time of 3.000 h in a liquid lead loop with controlled oxygen concentration. This corresponds with the results of corrosion tests in stagnant lead during the same exposure time, Müller et al. (2000). Those tests include also austenitic and ferritic steels in which aluminium was alloyed into the surface by GESA pulse heating. In this case a thin alumina scale appeared during the tests on the surface that prevented not only the dissolution attack of liquid lead but also oxidation of the steel components. This treatment may provide a better corrosion protection especially for exposure times much higher than 3.000 h.

Conclusions:

Ferritic and austenitic steels appear to be suitable structural materials for liquid lead loops up to 550°C if the dissolution attack is prevented by a dilute solution of oxygen in the liquid metal. The concentration of oxygen must be controlled at a value at which a protective oxide scale builds up at the steel surface but no PbO is formed. Oxide scales on ferrites that develop under these conditions agree in structure with those for oxidation in air. Austenitic steels have such scales only when the surface is treated by the GESA process. Untreated austenites show only very thin oxide layers of about 1 µm. Results obtained so far are representative for exposure times up to 3.000 h. It has to be prooved whether this holds for longer exposure times and also whether the thick oxide scales provide a better protection than the thin scale observed on austenitic steel. However, oxidative corrosion may become a problem with high exposure times. Alloying of aluminum into the surface of the steels has to be considered as a prospective treatment for a protection against corrosion. This is because the alumina scale prevents not only dissolution attack but also oxidation of steel components.

3.5 Sub-Project SP3: Oxygen Control System (OCS)

3.5.1 Oxygen measurement in flowing lead-bismuth

Introduction:

In Knebel et al. (2000) a detailed description about the theoretical background of the electrochemical oxygen meter, the possible reference electrodes and the oxygen meter design was given. First results of measurements of the temperature dependency of the EMF of oxygen meters with Pt/air and In/In_2O_3 reference electrodes have shown that the theoretical predictions are fulfilled for oxygen saturated and pure lead-bismuth. Here, results about the response behavior of the EMF signal against changes in the oxygen concentration in the eutectic lead-bismuth and data about the long term stability of the EMF signal will be presented.
The experiments were performed in the stagnant experiment KOSIMA of KALLA.

Results:

Figure 19 describes the response of a oxygen meter with Pt/air reference system during bubbling of reducing and oxidizing gases through the Pb-Bi melt. First $Ar+5\%H_2$, then air ($p = 0.21$ bar) with subsequent $Ar+5\%H_2$ bubbling was performed. The rate of the meter response to oxygen activity changes in the Pb-Bi has been found to be very rapid. The transient response to step changes of the oxygen activity in Pb-Bi exhibit no unusual behavior. The excellent time response of the EMF values after replacing of the $Ar+5\%H_2$ with air bubbling (no time delay) is obvious. By changes in the opposite direction there is some phase shift detected. The intrinsic temperature fluctuations at the beginning of the curve (Figure 19, lower part) are due to the reaction enthalpies of oxide scales degradation (oxygen removed by $Ar+5\%H_2$) and growth of oxides (air bubbling) respectively, whereas at the end of the curve only the noise level of the control unit was measured.

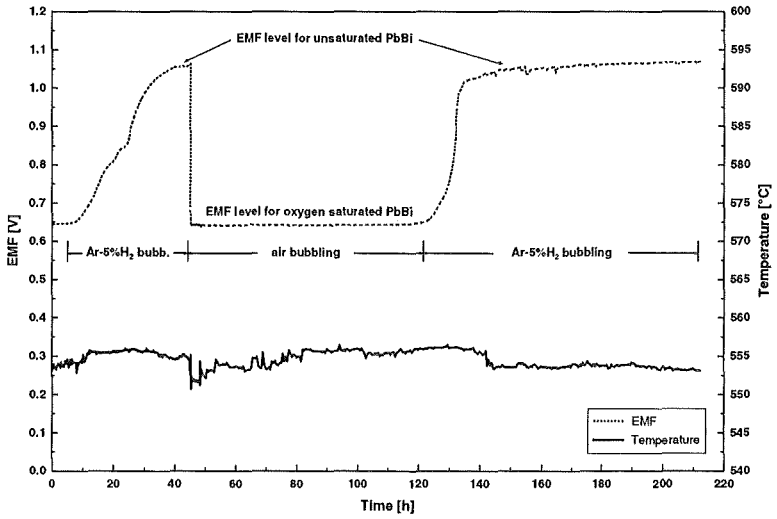

Figure 19: Changes of EMF for a cell with Pt/air reference system due to bubbling of reducing and oxidizing gases through the Pb-Bi melt.

A very similar behavior was seen for the In/In_2O_3 cell at 552°C. Shortly after starting of Ar+5%H_2 bubbling from a intermediate oxygen level, a strong increase of the EMF, corresponding to a decrease in oxygen activity in the Pb-Bi, was measured. After about 5 hours, an EMF level of about 0.95 V was reached, which stayed nearly constant for the rest of the bubbling period.

Figure 20 shows the mid-term-stability of the EMF of a cell with Pt/air reference electrode at 555°C over about 4 months of continuous collecting of data during the immersion of the oxygen-meter in the Pb-Bi melt. Regardless of the high level of the EMF during and after the equilibration, the long-time stability within a small range of 75 mV over months without any intermittencies buried in noise seems to be very good. The ascending of the EMF at the beginning of the experiment was due to the chemical reaction of the dissolved oxygen with the steel of the container wall.

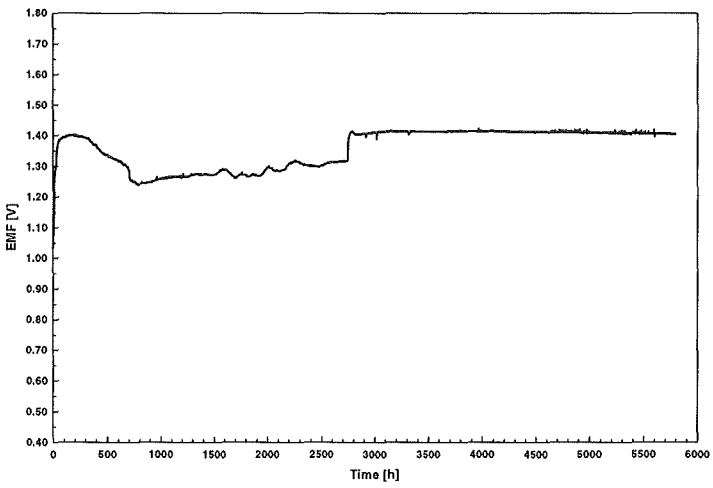

Figure 20: Mid-term behavior of EMF at 555°C for a cell with Pt/air reference system.

Conclusions:

Electrochemical oxygen meters with Pt/air and In/In_2O_3 reference systems can be used as in-situ devices for measuring the chemical activity of dissolved oxygen in liquid Pb-Bi. The data obtained confirm the feasibility of using oxygen meters for the purposes of oxygen control in Pb-Bi.

The Pt/air system is a suitable reference electrode capable of maintaining stable EMF values over a long time of immersion in liquid Pb-Bi. Pt/air offers both a fast response-kinetics and a very good mid-term stability. Successful performance has been demonstrated in a lot of experiments. Calibration slopes EMF versus temperature for Pt/air were fitting to theoretical calculations very well.

Similar results have been obtained for oxygen meters with In/In_2O_3 reference systems. The operational experiences are less good, compared to Pt/air results, regarding to the theoretical estimations. The deviations in the slopes of the EMF-temperature curves, especially in unsaturated Pb-Bi, might be due to a more pronounced sensibility to the time to reach thermodynamic equilibrium during cooling.

The current results from mid-term stability tests indicate a very satisfactory behavior for cells with a Pt/air reference system. Up to nearly 6.000 h, no degradation of the oxygen sensor was detected. Comparable results for In/In_2O_3 cells are not existing at the moment.

Sensors with both types of reference electrodes revealed an excellent response to changes in the oxygen activity of the Pb-Bi. The response time for significant reactions of the EMF was in the range of minutes. The reproducibility of this behavior was very good for cells with Pt/air reference system, when cycling between reducing and oxidizing gases.

The results from the EMF-temperature dependency tests have shown, that the minimum operational temperature of the oxygen sensor is about 400°C for Pt/air. This is much lower than the measured about 480°C for In/In_2O_3. The reason for such differences could be due to higher internal resistances of the In/In_2O_3 electrode.

3.5.2 Oxygen control in flowing lead-bismuth

Introduction:

Liquid metal corrosion is a serious problem for systems using a Pb or Pb-Bi as spallation material and as coolant like an ADS system. Because of the partially high

solubility of some steel components strong corrosion effects could be observed, Massalski (1990). One way to protect the metal surface is by an oxide layer that has the ability to slow down the dissolution of the protected metal components to tolerable values, Markov (1997) and Orlov (1998).

The Oxygen Control System (OCS) developed at FZK gives the possibility to control the oxygen content in the liquid metal. A detailed description is given in Lefhalm et al. (2001). As stated in Knebel et al. (1999) an oxygen concentrations between 10^{-6} at% and 10^{-7} at% in lead is desired to prevent both liquid metal corrosion and oxygen corrosion due to excessive oxidation of the steel surface.

One key question to an oxygen control system (OCS) is the physical description of its kinetics. The time which is needed to reach the desired oxygen concentration in a Pb-Bi system of a given liquid volume is crucial for the applicability to systems of industrial size.

With the OCS the oxygen concentration is controlled via a gas atmosphere above the liquid metal with a definite oxygen partial pressure p_{O_2} that determines the chemical potential of oxygen within the liquid metal. To prevent PbO precipitation and to support Fe_3O_4 formation the following condition must be established:

$$2\,\Delta G^0_{PbO} > RT\,\ln p_{O_2} > 0.5\,\Delta G^0_{Fe_3O_4} \quad . \tag{2}$$

The standard values ΔG^0 of the Gibbs energies are known for the oxides in question, so the oxygen partial pressure that retains the stable condition can be calculated. To set the desired oxygen partial pressure in the gas phase a mixture of hydrogen and water vapour within the carrier gas argon is used. The H_2/H_2O ratio determines the oxygen potential as shown by the following relation:

$$p_{O_2} = \frac{p^2_{H_2O}}{p^2_{H_2}}\,exp\,\frac{2\,\Delta G^0_{H_2O}}{RT} \quad . \tag{3}$$

For the safe operation of a PbBi- or Pb-loop with ADS relevant temperatures the typical working conditions are between $p_{O_2}=10^{-31}$ bar at *400°C* and $p_{O_2}=10^{-24}$ bar at *550°C*, respectively. This results in a corresponding H_2/H_2O ratio of *0.4.* In the case of stagnant Pb-Bi or Pb, iron oxide is formed at both temperatures that prevents liquid metal corrosion. However, no PbO is formed. In the case of a liquid Pb-Bi- or Pb-loop

(flowing liquid metal), there is no equilibrium across the temperature region via the H_2/H_2O ratio but via the oxygen dissolved in the flowing liquid Pb-Bi or Pb.

Theoretical Background:

The physical process found to determine the timescale of the oxygen control process via OCS is the diffusion. The exchange of oxygen atoms through the interface between the gas phase and the liquid metal can be modelled with solutions of the diffusion equations, Fick's laws:

$$j = -D\frac{\partial c}{\partial x} \quad \text{and} \quad \frac{\partial c}{\partial t} = D\frac{\partial^2 c}{\partial x^2}. \tag{4}$$

In this case a solution can be obtained by the use of Laplace transformation. Here a rigid plane of stagnant liquid metal (height *l*) with a given oxygen concentration at the surface is assumed, which is given according to the H_2/H_2O ratio in the gas phase. The time dependent solution for oxygen sorption or desorption with a constant diffusion coefficient results in:

$$\frac{M_t}{M_\infty} = 1 - \sum_{n=0}^{\infty} \frac{8}{(2n-1)^2\pi^2} exp\left\{-\frac{D(2n+1)^2\pi^2 t}{4l^2}\right\}, \tag{5}$$

where M_t is the amount of oxygen exchanged between the gas phase and the liquid metal in the time t according to the concentration difference. In /4/ the value for the diffusion constant D of oxygen in liquid lead is given as $D=1.2\cdot10^{-5}$ *cm²/s*. With this value a change of the H_2/H_2O ratio from 0.57 (equivalent to $8.85\cdot10^{-7}$ at%) to 0.19 (equivalent to $2.66\cdot10^{-}$ at%) in the gas phase results in a duration of about 2 hours for desorption of oxygen at the surface.

However this model seems to be too simple to describe the experimental findings. Further calculations with more complex boundary conditions (stagnant liquid metal plane with variable oxygen concentration on the surface with respect to the concentration-dependent diffusion coefficient) were made. The final solution (Jost (1970), Crank (1975))

$$\frac{M_t}{2lc_1} = 1 - \sqrt{\frac{D}{\beta l^2}}\tan\sqrt{\frac{\beta l^2}{D}}e^{-\beta t} - \frac{8}{\pi}\sum_{n=0}^{\infty}\frac{exp\left(-D(2n+1)^2\pi^2 t/4l^2\right)}{(2n+1)^2\left[1-(2n+1)^2\left(D\pi^2/4\beta l^2\right)\right]} \tag{6}$$

fits the experimental results, see figure 22.

Results

The oxygen control test stand KOCOS (Kinetics of Oxygen COntrol Systems) is installed within the KArlsruhe Lead Laboratory. KOCOS allows the investigation of kinetics of the oxygen control process via the gas phase as described above in theory. A mixture of Ar and Ar/5%H_2 allows to adjust the hydrogen concentration in the gas. The water vapour is added by passing the gas through water at a given temperature. By changing the gas flow of Ar/5%H_2 the H_2/H_2O ratio can be controlled. The gas is guided through a chilled mirror moisture sensor and over the surface of 680g stagnant liquid Pb-Bi at a constant temperature of 430°C. The liquid metal is held in a crucible of aluminium oxide to prevent contact to the steel wall of the oven. So it is ensured that no oxide formation other than PbO can take place. The moisture and the oxygen partial pressure in the escaping gas is measured. A constant total gas flow rate of 18 l/h is set.

For the experimental investigations a stepwise change of the H_2/H_2O ratio from 0.053 to 1.725 is established and observed until thermodynamic equilibrium is reached (figure 21). Due to limitations in the sensibility of the measurement equipment for the oxygen partial pressure in the gas phase, one has to take into account that the concentration in the liquid metal bath is not homogeneous throughout the bath, even when the thermodynamic equilibrium on the interface seems to be already stable. Therefore the given results are related to the exchange of oxygen at the interface between the gas phase and the liquid Pb-Bi only. However, this is the process that determines the kinetics of the gas phase oxygen control system (OCS).

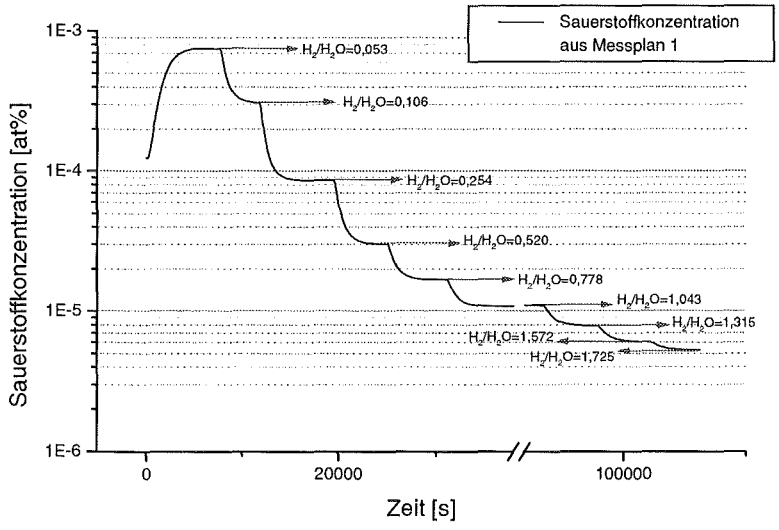

Figure 21: Oxygen concentration versus time for a stepwise change of the H_2/H_2O ratio.

Beside the issue that the oxygen control process is reversible in time, three important results have been found. First, the measured values for the H_2/H_2O ratio in equilibrium conditions are in very good agreement with the values calculated from the given gas flows and dew point (moisture). The error is less than 2 %. So the control of the partial oxygen pressure is guaranteed even at low gas flow rates, especially for hydrogen (figure 22).

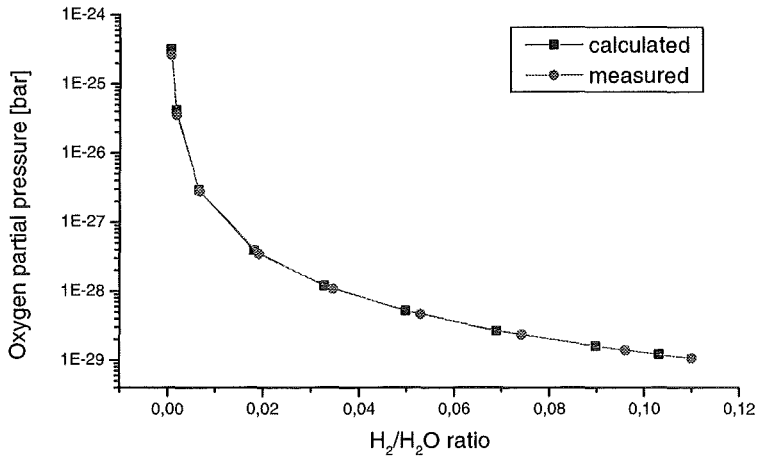

Figure 22: Oxygen partial pressure versus H_2/H_2O ratio. Measured and calculated values at a Pb-Bi temperature of 430°C.

Second, the physical model of the diffusion process, which considers a variable oxygen concentration on the surface of the liquid metal as described above, fits the experimental findings. After a change of the H_2/H_2O ratio the desorption of oxygen was observed and compared with the calculations (figure 23). Applying this model (equation 6) a prediction of the time is possible that is needed in order to reach a desired concentration in the liquid metal bath using the oxygen control system. To the author's knowledge, this is the first theoretical approach to the description of the process of oxygen exchange between gas phase and liquid metal under oxygen control with respect to variable surface concentrations.

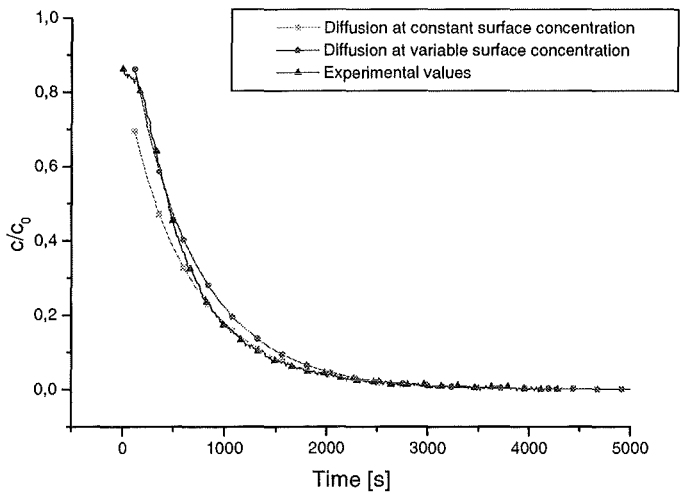

Figure 23: Comparison between diffusion models and experimental data: concentration versus time.

Third, the diffusion coefficient is found to be concentration dependent. From the data of the experiments with stepwise change of the H_2/H_2O ratio, (see figure 21), the diffusion coefficient for oxygen desorption is calculated. For each step of concentration difference another diffusion coefficient is evaluated. One important consequence of this result is the different time behaviour of sorption and desorption of oxygen. In the experiments, the process of desorption is found to be always faster than the process of sorption of oxygen. Furthermore, the expected dependency of the diffusion on the ratio between surface and volume is viewed (figure 24).

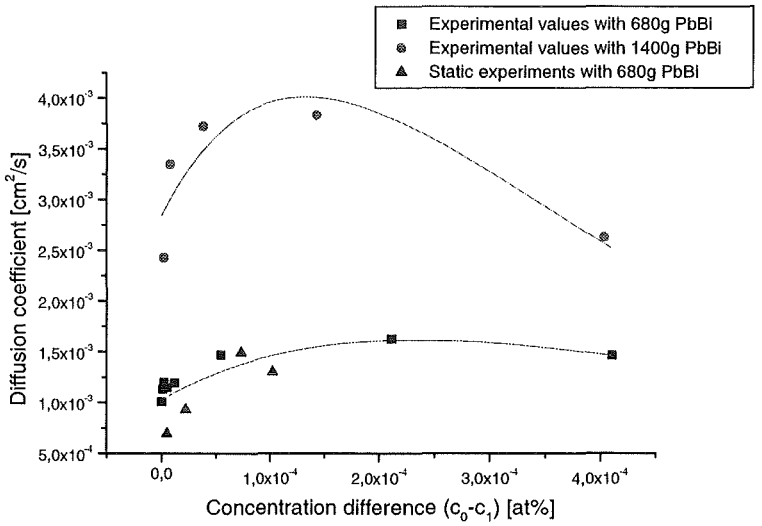

Figure 24: Dependency of diffusion coefficient on concentration difference for different Pb-Bi masses (ratio surface/volume).

Summary:

Liquid metal loops with Pb or Pb-Bi as spallation material and as coolant are only feasible if the problem of steel corrosion by liquid Pb-Bi at the relevant temperatures is solved. At Forschungszentrum Karlsruhe, this is done by applying an OCS which controls the oxygen concentration in the liquid metal under thermodynamic equilibrium conditions by controlling the H_2/H_2O ratio in the gas atmosphere.

The exchange of oxygen between gas phase and liquid metal is limited by the process of diffusion. The physical model of the kinetics betwen the gas phase and the liquid phase is given. Experimental findings at the oxygen control test stand KOCOS are in excellent agreement with the results of the developed diffusion model. Dependencies on the variable oxygen concentration in the gas phase and the total concentration differences are determined.

4. Overall Conclusions And Perspectives

The objective of the HGF Project is to provide the scientific-technical basis which allows the conception and the design of a spallation target. The application of a spallation target is in the fields of, first, spallation neutron source for material investigations and, second, transmutation of highly radioactive waste.

The HGF Strategy Fund Project is divided into three sub-projects:

- SP1: Thermalhydraulic investigations,
- SP2: Material specific investigations,
- SP3: Oxygen control system.

Each sub-project consists of several work packages. All results and deliverables that were due in 2000, could be delivered successfully.

The major results are:

- KALLA:
  The stagnant experiments COSTA, KOSIMA and KOCOS are in operation. The loop experiment THESYS is in operation; THEADES and CORRIDA are in the commissioning phase.

- SP1: Thermalhydraulic investigations
  Experimental (HYTAS test facility) and numerical (CFX and FIDAP) results for a beam window with water as the model fluid were performed for two international reference designs: the ISTC 559 and the MEGAPIE spallation target. A good agreement between measurement and calculation is achieved. The numerical optimization and the detailed design of a beam window in Pb-Bi (cf. COULI) is in progress.
  A fundamental liquid metal heat transfer experiment is performed, a numerical simulation using FIDAP is finished.
  The benchmark exercise TEFLU (buoyant liquid metal jet) is finished for the TMBF turbulence model in FLUTAN. Deficiencies and further modelling work are outlined.

A stepwise numerical analysis (1D, 2D and 3D) of a complete spallation target is in progress. The general technical feasibility of the heat removal chain is demonstrated. The integral experiment K4T is proposed and preliminarily designed in order to simulate the thermalhydraulic behaviour of a spallation target including the heat removal chain.

- SP2: Material specific investigations

  The protection of ferritic and austenitic steels is experimentally investigated and proven for exposure times up to 3.000 h, as long as the dilute solution of oxygen in the liquid metal is kept in a representative region (cf. SP3: Oxygen Control System).

  Using the GESA test facility, several steel specimens were prepared by surface restructuring and surface aluminium alloying. First experimental results are obtained: Under a cover gas atmosphere with $H_2/H_2O = 0.4$ (equilibrium oxygen concentration of 8×10^{-6} at%), oxide scales develop on OPTIFER IVc and 1.4970 steel which prevent the dissolution attack of Pb at 550°C. Pb/Bi eutectic alloy appears to be considerably more aggressive: a severe dissolution attack on OPTIFER IVc under the same conditions after 800 h is observed. Surface alloying of Aluminium by GESA provides the best protection due to a thin, dense alumina scale on top of the base material.

- SP3: Oxygen control system (OCS)

  It is successfully demonstrated that electrochemical oxygen meters with Pt/air and In/In_2O_3 reference systems are an in-situ device to measure the chemical activity of dissolved oxygen in liquid lead or lead-bismuth.

  A physical model to describe the kinetics of the exchange of oxygen between the gas atmosphere and the liquid heavy metal is developped and validated with experiments performed in KOCOS.

  The oxygen control system (OCS) is successfully applied to experiments with stagnant lead or lead-bismuth. The next step is the application of the OCS to a loop system.

5. Literature

A complete list of references is given in „Thermalhydraulic and Material Specific Investigations into the Realization of an Accelerator Driven System (ADS) to Transmute Minor Actinides, 2000 Status Report", Forschungszentrum Karlsruhe, Wissenschaftliche Berichte FZKA 6618, 2001 by J.U. Knebel, X. Cheng, G. Müller, G. Schumacher, J. Konys, O. Wedemeyer, G. Grötzbach, L. Carteciano, 2000

6. Acknowledgements

The co-authors and co-workers, who significantly contributed to this work, are listed together with the institute in alphabetical order:

Institute for Nuclear and Energy Technologies (IKET)
X. Cheng, M. Daubner, F. Fellmoser, J.U. Knebel, V. Krieger, C.H. Lefhalm, K. Mack, P. Miodek, H.J. Neitzel, C. Pettan, H. Piecha, H. Schmidt, R. Stieglitz, R. Vollmer, Nam-Il Tak (KAERI, Korea)

Institute for Pulsed Power and Microwave Technology (IHM)
A. Heinzel, R. Huber, G. Müller, G. Schumacher, F. Zimmermann

Institute for Materials Research I (IMF I)
Ch. Adelhelm, M. Heinle

Institute for Materials Research III (IMF III)
H. Glasbrenner, J. Konys, W. Krauss, H. Muscher, J. Novotny, Z. Voss, O. Wedemeyer

Institute for Reactor Safety (IRS)
L. Carteciano, B. Dorr, G. Grötzbach

Veröffentlichte Berichte

Schriftliche Veröffentlichungen

ADROGUER, B.; BARRACHIN, M.; AZARIAN, G.; BOTTOMLEY, D.; HOFMANN, P.; STEINBRÜCK, M.; STUCKERT, J.; HAYWARD, P.; VESHCHUNOV, M.; BERDYSHEV, A.; BOLDYREV, A.
Dissolution of fuel rods and related effects. Status report.
INV-CIT(99)-D004 (July 2000)
IPSN/DRS/SEMAR 00/65 (48638)

ADROGUER, B.; BARRACHIN, M.; BOTTOMLEY, D.; HOFMANN, P.; MIASSOEDOV, A.; STUCKERT, J.; CHEVALIER, P.Y.; CHEYNET, B.; FISCHER, M.; HELLMANN, S.; SEILER, J.M.; GOGNET, G.; SUDREAU, F.; BELLON, M.; TOCI, F.; FORCEY, K.; PACENTI, P.; NANNICINI, R.; AZARIAN, G.; HAYWARD, P.; VESHCHUNOV, M.; VRTILKOVA, V.; LOPUKH, D.
Corium interactions and thermochemistry (CIT).
Van Goethem, G. [Hrsg.]
FISA 99 : EU Research in Reactor Safety ; Conclusion Symp. on Shared-Cost and Concerted Actions, Luxembourg, L, November 29 - December 1, 1999
Luxembourg : Office for Official Publ. of the European Communities, 2000 S.202-10
EUR-19532-EN (48537)

AKTAA, J.; KLOTZ, M.; PFEIFENROTH, M.; SCHMITT, R.; SCHNEIDER, H.
Untersuchung des Größeneinflusses auf das Verformungs- und Versagensverhalten von gelochten Flachzugproben im Rahmen des LISSAC-Programms.
Projekt Nukleare Sicherheitsforschung. Jahresbericht 1999.
Wissenschaftliche Berichte, FZKA-6480 (August 2000) S.555-56 (48191)

AKTAA, J.; SFAR, K.
Mikromechanische Modellierung von Wärmedämmschichten.
Projekt Nukleare Sicherheitsforschung. Jahresbericht 1999.
Wissenschaftliche Berichte, FZKA-6480 (August 2000) S.581 (48195)

ALBRECHT, G.; BRÜGGEMANN, H.; JENES, E.; RAUPP, D.; SCHÜTZ, W.
Untersuchungen zum EPR-Konzept - KAJET Versuche.
Projekt Nukleare Sicherheitsforschung. Jahresbericht 1999.
Wissenschaftliche Berichte, FZKA-6480 (August 2000) S.301-09 (48169)

ALBRECHT, G.; JENES, E.; KAISER, A.; SCHÜTZ, W.
KAJET experiments on pressurized melt jets with view to their interaction with substratum materials.
Proc.of the OECD Workshop on Ex-Vessel Debris Coolability, Karlsruhe, November 15-18, 1999
Wissenschaftliche Berichte, FZKA-6475 (Mai 2000) S.54-65 (47480)

ALBRECHT, G.; JENES, E.; KAISER, A.; SCHÜTZ, W.
KAJET experiments on pressurized melt jets and their interaction with substratum materials.
Jahrestagung Kerntechnik 2000, Bonn, 23.-25.Mai 2000
Bonn : INFORUM GmbH, 2000 S.125-30
(Auch auf CD ROM) (47900)

ALLELEIN, H.J.; TURLAND, B.; SDOUZ, G.; FISCHER, K.; GIORDANO, P.; DOMINGUEZ, T.; SICCAMA, A.; PASSALACQUA, R.; HERING, W.; BUERGER, M.; JONES, A.V.; SEHGAL, B.R; PLANK, B.; STEINRÖTTER, T.; PEKKARINEN, E.
Validation strategies for severe accident codes with special emphasis given to integral codes.
Van Goethem, G. [Hrsg.]
FISA 99 : EU Research in Reactor Safety ; Conclusion Symp.on Shared-Cost and Concerted Actions, Luxembourg, L, November 29 - December 1, 1999
Luxembourg : Office for Official Publ.of the European Communities, 2000 S.520-28
EUR-19532-EN (47978)

ALSMEYER, H.
Proceedings of the OECD workshop on ex-vessel debris coolability, Karlsruhe, 15-18 November 1999
Wissenschaftliche Berichte, FZKA-6475 (Mai 2000) (47463)

ALSMEYER, H.; ADELHELM, C.; BENZ, H.; CRON, T.; DILLMANN, G.; TROMM, W.; SCHMIDT-STIEFEL, S.; SCHNEIDER, H.; SCHUMACHER, G.; WENZ, T.; FERDERER, F.
Corium cooling by bottom flooding: results of the COMET investigations.
Proc. of the OECD Workshop on Ex-Vessel Debris Coolability, Karlsruhe, November 15-18, 1999
Wissenschaftliche Berichte, FZKA-6475 (Mai 2000) S.345-55 (46623)

ALSMEYER, H.; ALBRECHT, G.; FIEG, G.; STEGMAIER, U.; TROMM, W.; WERLE, H.
Controlling and cooling core melts outside the pressure vessel.
Nuclear Engineering and Design, 202(2000) S.269-78 (48931)

ALSMEYER, H.; BENZ, H.; CRON, T.; TROMM, W.; WENZ, T.; FERDERER, F.
CometPC: first results for a simplified

cooling concept based on porous concrete.
Proc. of the OECD Workshop on Ex-Vessel Debris Coolability, Karlsruhe, November 15-18, 1999
Wissenschaftliche Berichte, FZKA-6475 (Mai 2000) S.356-64 (46622)

ALSMEYER, H.; BENZ, H.; CRON, T.; TROMM, W.; WENZ, T.; FERDERER, F.
Experimental investigations on the simplified CometPC core catcher.
Jahrestagung Kerntechnik 2000, Bonn, 23.-25.Mai 2000
Bonn : INFORUM GmbH, 2000 S.139-42
(Auch auf CD ROM) (47025)

ALSMEYER, H.; CRON, T.; SCHMIDT-STIEFEL, S.; SCHNEIDER, H.; TROMM, W.; WENZ, T.; ADELHELM, C.; DILLMANN, H.G.; PASLER, H.; SCHÖCK, W.; BENZ, H.; GREHL, C.; MERKEL, G.; RATAJCZAK, W.
COMET-Concept.
Projekt Nukleare Sicherheitsforschung. Jahresbericht 1999.
Wissenschaftliche Berichte, FZKA-6480 (August 2000) S.256-87 (48167)

BAN, C.H.; HERING, W.
Assessment of RELAP5 reflood models using PKL-IIB5 test.
Wissenschaftliche Berichte, PSF Report 3322 (März 99) (47138)

BAUMANN, W.
Measured turbulence data compared to FLUTAN calculations.
Projekt Nukleare Sicherheitsforschung. Jahresbericht 1999.
Wissenschaftliche Berichte, FZKA-6480 (August 2000) S.48-63 (48157)

BENZ, G.; EHRHARDT, J.; FISCHER, F.; HALLER, CH.; HASEMANN, I.; HESSELSCHWERDT, E.; LANDMANN, C.; LORENZ, A.; PÄSLER-SAUER, J.; RAFAT, M.; RASKOB, W.; SCHICHTEL, T.; STEIDLINGER, A.
Entwicklung von Methoden zur Abschätzung und Minimierung der radiologischen Folgen von Reaktorunfällen.
Projekt Nukleare Sicherheitsforschung. Jahresbericht 1999.
Wissenschaftliche Berichte, FZKA-6480 (August 2000) S.485-93 (48183)

BIELERT, U.
Numerical simulation of ignition processes in H_2-air-steam mixtures.
Projekt Nukleare Sicherheitsforschung. Jahresbericht 1999.
Wissenschaftliche Berichte, FZKA-6480 (August 2000) S.64-96 (48158)

BIELERT, U.; BREITUNG, W.; KOTCHOURKO, A.; ROYL, P.; SCHOLTYSSEK, W.; VESER, A.; BECCANTINI, A.; DABBENE, F.; PAILLERE, H.; STUDER, E.; HULD, T.; WILKENING, H.; EDLINGER, B.; PORUBA, C.; MOVAHED, M.
Multidimensional simulation of hydrogen distribution and turbulent combustion in severe accidents.
Van Goethem, G. [Hrsg.]
FISA 99 : EU Research in Reactor Safety ; Conclusion Symp.on Shared-Cost and Concerted Actions, Luxembourg, L, November 29 -December 1, 1999
Luxembourg : Office for Official Publ.of the European Communities, 2000 S.450-58
EUR-19532-EN (46698)

BORGSTEDT, H.U.; GUMINSKI, C.
Solubilities and solution chemistry in liquid alkali metals.
Monatshefte für Chemie/Chemical Monthly, 131(2000) S.917-30 (48489)

BREITUNG, W.; BIELERT, U.; NECKER, G.; VESER, A.; WETZEL, F.J.; PEHR, K.
Numerical simulation and safety evaluation of tunnel accidents with a hydrogen powered vehicle.
Mao, Z.Q. [Hrsg.]
Hydrogen Energy Progress XIII : Proc.of the 13th World Hydrogen Energy Conf., Beijing, China, June 12-15, 2000
Vol. 2 S.1175-81 (47188)

BREITUNG, W.; CHAN, C.K.; DOROFEEV, S.B.; EDER, A.; GELFAND, B.E.; HEITSCH, M.; KLEIN, R.; MALLIAKOS, A.; SHEPHERD, J.E.; STUDER, E.; THIBAULT, P.
Flame acceleration and deflagration-to-detonation transition in nuclear safety. State-of-the art report by a group of experts.
NEA/CSNI/R(2000)7 (August 2000) (48589)

BREITUNG, W.; DOROFEEV, S.B.
Criteria for deflagration-to-detonation transition (DDT) in nuclear containment analysis.
Proc. of the Seminar on Containment of Nuclear Reactors held in Conjunction with the 15th Internat. Conf. on Structural Mechanics in Reactor Technology, Seoul, Korea, August 23-24, 1999, S.51-87 (46724)

BREITUNG, W.; ROYL, P.
Procedure and tools for deterministic analysis and control of hydrogen behavior in severe accidents.
Nuclear Engineering and Design, 202(2000) S.249-68 (48930)

BROEDERS, I.; BROEDERS, C.H.M.
Neutron physics calculations for ADS targets.
Wissenschaftliche Berichte, FZKA-6507 (Oktober 2000) (48699)

BROEDERS, C.H.M.; BROEDERS, I.
Neutron physics analyses of accelerator-driven subcritical assemblies.
Nuclear Engineering and Design, 202(2000) S.209-18 (48927)

BROEDERS, C.H.M.; KIEFHABER, E.; WIESE, H.W.
Burning transuranium isotopes in thermal and fast reactors.
Nuclear Engineering and Design, 202(2000) S.157-72 (48925)

BRÜGGEMANN, H.H.; CHERDRON, W.; JENES, E.; KAISER, A.; KORNELSON, I.; PROTHMANN, N.; RAUPP, D.; SCHÜTZ, W.; WILL, H.
PREMIX and ECO, Experimente zur Schmelze/Wasser-Wechselwirkung.
Projekt Nukleare Sicherheitsforschung. Jahresbericht 1999.
Wissenschaftliche Berichte, FZKA-6480 (August 2000) S.152-72 (48161)

BUCKEL, G.; KIEFHABER, E.; RINEISKI, A.
THREEDANT test calculations for a particular FCA VIII-2 assembly.
Projekt Nukleare Sicherheitsforschung. Jahresbericht 1999.
Wissenschaftliche Berichte, FZKA-6480 (August 2000) S.612-19 (48201)

BURGETH, B.F.
On the hydrogen-air adiabatic isochoric complete combustion pressure.
Projekt Nukleare Sicherheitsforschung. Jahresbericht 1999.
Wissenschaftliche Berichte, FZKA-6480 (August 2000) S.136-51 (48160)

CACUCI, D.G.
Innovative features in the RELAP5/PANBOX/ COBRA neutron-kinetics/thermal-hydraulics code system.
Proc.of the 8th Internat.Conf.on Nuclear Engineering (ICONE-8), Baltimore, Md., April 2-6, 2000
New York, N.Y. : ASME, 2000 CD-ROM 8774, track 7.27 (47812)

CACUCI, D.G.; IONESCU-BUJOR, M.
Adjoint sensitivity analysis of coupled neutronics/thermal-hydraulics codes.
Wechselwirkungen Neutronenphysik und Thermofluiddynamik, Fachtagung der KTG, Forschungszentrum Rossendorf, Dresden, 31.Januar - 1.Februar 2000
Proc. S.3.14-3.24 (47536)

CACUCI, D.G.; IONESCU-BUJOR, M.
Adjoint sensitivity analysis of the RELAP5/ MOD3.2 two-fluid thermal-hydraulic code system. I: Theory.
Nuclear Science and Engineering, 136(2000) S.59-84 (47920)

CACUCI, D.G.; IONESCU-BUJOR, M.; HERING, W.; SANCHEZ, V.H.
Investigations on reactor and plant dynamics.
Projekt Nukleare Sicherheitsforschung. Jahresbericht 1999.
Wissenschaftliche Berichte, FZKA-6480 (August 2000) S.499-507 (48185)

CARTECIANO, L.N.
Implementation of a concentration equation for the turbulent transport of Boron in FLUTAN.
Projekt Nukleare Sicherheitsforschung. Jahresbericht 1999.
Wissenschaftliche Berichte, FZKA-6480 (August 2000) S.508-12 (48186)

CARTECIANO, L.N.; DORR, B.; GRÖTZBACH, G.
Numerical interpretation of the single phase sump cooling experiments SUCOS with the FLUTAN code.
Jahrestagung Kerntechnik 2000, Bonn, 23.-25.Mai 2000
Bonn : INFORUM GmbH, 2000 S.153-56
(Auch auf CD ROM) (47715)

CARTECIANO, L.N.; DORR, B.; GRÖTZBACH, G.
Rechenprogramm FLUTAN für thermo- und fluiddynamische Anwendungen.
Projekt Nukleare Sicherheitsforschung. Jahresbericht 1999.
Wissenschaftliche Berichte, FZKA-6480 (August 2000) S.345-62 (48174)

CARTECIANO, L.N.; DORR, B.; GRÖTZBACH, G.
Numerical investigation of the single phase natural convection in sump cooling experiments with the FLUTAN code.
Van Dam, H. [Hrsg.]
ICENES 2000 : The 10th Internat. Conf. on Emerging Nuclear Energy Systems, Petten, NL, September 24-28, 2000
CD ROM S.296-304 .....(48318)

CHARPENEL, J.; LEMOINE, F.; SATO, I.; STRUWE, D.; PFRANG, W.
Fuel pin behavior under the slow power ramp transients in the CABRI-2 experiments.
Nuclear Technology, 130(2000) S.252-71 .....(48735)

CHENG, X.; BAZIN, P.; CORNET, P.; HITTNER, D.; JACKSON, J.D.; LOPEZ-JIMENEZ, J.; NAVIGLIO, A.; ORIOLO, F.; PLANK, H.
Common experimental data base for the development of physical models and correlations for thermal-hyraulic containment analysis (DABASCO).

Van Goethem, G. [Hrsg.]
FISA 99 : EU Research in Reactor Safety ; Conclusion Symp. on Shared-Cost and Concerted Actions, Luxembourg, L, November 29 - December 1, 1999
Luxembourg : Office for Official Publ. of the European Communities, 2000 S.490-99
EUR-19532-EN (46700)

CHENG, X.; ERBACHER, F.J.; NEITZEL, H.J.
Passive containment cooling by natural air convection and thermal radiation after severe accidents.
Nuclear Engineering and Design, 202(2000) S.219-29 (48928)

CHENG, X.; NEITZEL, H.J.; SCHMIDT, H.; KNEBEL, J.U.
Passive containment cooling (PASCO-Programme).
Projekt Nukleare Sicherheitsforschung. Jahresbericht 1999.
Wissenschaftliche Berichte, FZKA-6480 (August 2000) S.363-68 (48175)

CHENG, X.; PETTAN, C.; KNEBEL, J.U.; CHEN, H.Y.
Thermalhydraulic investigations on spallation target systems.
Jahrestagung Kerntechnik 2000, Bonn, 23.-25.Mai 2000
Bonn : INFORUM GmbH, 2000 S.91-94
(Auch auf CD ROM) (47185)

CHENG, X.; SLESSAREV, I.
Thermal-hydraulic investigations on a pilot liquid metal target.
Nuclear Engineering and Design, 202(2000) S.297-310 (48933)

COGNET, G.; ALSMEYER, H.; TROMM, W.; MAGALLON, D.; WITTMAACK, R.; SEHGAL, B.R.; WIDMANN, W.; DE CECCO, L.; OCELLI, R.; AZARIN, G.; PINEAU, D.; SPINDLER, B.; FIEG, G.; WERLE, H.; JOURNEAU, C.; CRANGA, M.; LAFFONT, G.
Corium spreading and coolability (CSC project).
Van Goethem, G. [Hrsg.]
FISA 99 : EU Research in Reactor Safety ; Conclusion Symp. on Shared-Cost and Concerted Actions, Luxembourg, L, November 29 - December 1, 1999
Luxembourg : Office for Official Publ. of the European Communities, 2000 S.269-78
EUR-19532-EN (45871)

COGNET, G.; TROMM, W.; MAGALLON, D.; WITTMAACK, R.; SEHGAL, B.R.; DE CECCO, L.; OCELLI, R.; PINEAU, D.; SPINDLER, B.; FIEG, G.; WERLE, H.; JOURNEAU, C.; CRANGA, M.; LAFFONT, G.
Corium spreading phenomena: results obtained from the EU CSC project.
Proc. of the OECD Workshop on Ex-Vessel Debris Coolability, Karlsruhe, November 15-18, 1999
Wissenschaftliche Berichte, FZKA-6475 (Mai 2000) S.138-47 (46350)

DAGAN, R.; BROEDERS, C.H.M.
Optimization of a multiple source system for ADS.
20th Conf. of the Nuclear Societies in Israel, Dead Sea, IL, December 20-21, 1999
Final Program and Book of Abstracts S.241-44 (47062)

DAGAN, R.; BROEDERS, C.H.M.; STRUWE, D.
Modifications of the code SAS4A for simulation of ADS designs.
Wissenschaftliche Berichte, FZKA-6334 (Juli 2000) (47979)

DOLENSKY, B.; GÖLLER, B.; HAILFINGER, G.; JONATZKE, O.; JORDAN, J.; KORNELSON, I.; KRIEG, R.; LANG, K.H.; MALMBERG, T.; MESSEMER, G.; STRATMANS, E.; VORBERG, G.
Mechanische Auswirkungen auf den Reaktordruckbehälter.
Projekt Nukleare Sicherheitsforschung. Jahresbericht 1999.
Wissenschaftliche Berichte, FZKA-6480 (August 2000) S.369-77 (48176)

EHRHARDT, J.; JONES, J.A.; GOOSSENS, L.
Probabilistic accident consequence uncertainty analysis of the whole program package COSYMA.
Workshop on Expert Judgement and Accident Consequence Uncertainty Analysis (COSYMA), Avifauna, NL, June 21-24, 1999
Radiation Protection Dosimetry, 90(2000) S.365-72 (45599)

EHRHARDT, J.; WEIS, A.
RODOS: decision support system for off-site nuclear emergency management in Europe.
EUR-19144-EN (2000) (48470)

EHRLICH, K.
Die Untersuchung mikrostruktureller Änderungen in bestrahlten Stählen mittels Transmissions- und Rasterelektronen-mikroskopie.
Bauteilprüfung im Mikro- und Nanobereich : 19.Tagung des DVM Arbeitskreises MNP, Mülheim, 28.-29.November 2000
Berlin : Deutscher Verband für Materialforschung und -prüfung e.V., 2000 S.9-18
(DVM-Berichte ; 519) (49004)

ENGEL, G.; EPPINGER, B.; FELLMOSER, F.; FIEG, G.; MESSAINGUIRAL, C.; MASSIER, H.; SCHMIDT-STIEFEL, S.
KAPOOL experiments to simulate molten corium sacrificial-concrete interaction and gate

opening in the EPR core catcher concept.
Proc. of the OECD Workshop on Ex-Vessel Debris Coolability, Karlsruhe, November 15-18, 1999
Wissenschaftliche Berichte, FZKA-6475 (Mai 2000) S.66-74 (47481)

ENGEL, G.; EPPINGER, B.; FIEG, G.; SCHMIDT-STIEFEL, S.; MESSAINGUIRAL, C.; PROTHMANN, N.; RAUPP, D.; SCHÜTZ, W.; STEGMAIER, U.; MASSIER, H.; STERN, G.; VESER, A.
Investigations for the EPR concept - KAPOOL and KATS experiments.
Projekt Nukleare Sicherheitsforschung. Jahresbericht 1999.
Wissenschaftliche Berichte, FZKA-6480 (August 2000) S.288-300 (48168)

ENGEL, G.; FIEG, G.; MASSIER, H.; STEGMAIER, U.; SCHÜTZ, W.
KATS experiments to simulate corium spreading in the EPR core catcher concept.
Proc. of the OECD Workshop on Ex-Vessel Debris Coolability, Karlsruhe, November 15-18, 1999
Wissenschaftliche Berichte, FZKA-6475 (Mai 2000) S.148-55 (47482)

ENGELKO, V.; GIESE, H.; MÜLLER, G.; SCHALK, S.; SCHULTHEISS, C.; WÜRZ, H.
Quelle zur Erzeugung von großflächigen, gepulsten Ionen- und Elektronenstrahlen.
DE-OS 19 621 874 (11.12.1997)
DE-PS 19 621 874 (22.5.2000) (44254)

ENGELKO, V.; KUZNETSOV, V.; VIAZMENOVA, G.; MUELLER, G.; BLUHM, H.
Influence of electrons reflected from a target on the operation of triode-type electron sources.
Journal of Applied Physics, 88(2000) S.3879-88 (48473)

EPPINGER, B.; FELLMOSER, F.; FIEG, G.; MASSIER, H.; STERN, G.
Experiments on concrete erosion by a corium melt in the EPR reactor cavity: KAPOOL 6-8.
Wissenschaftliche Berichte, FZKA-6453 (März 2000) (47361)

EPPINGER, B.; FIEG, G.
KAPOOL experiments to simulate gate opening in the EPR core catcher concept.
Jahrestagung Kerntechnik 2000, Bonn, 23.-25.Mai 2000
Bonn : INFORUM GmbH, 2000 S.131-34
(Auch auf CD ROM) (47026)

EYINK, J.; FISCHER, K.; HEITSCH, M.; REHM, W.; SCHOLTYSSEK, W.
Research on hydrogen risk mitigation resulting from hypothetical severe accident.
Atomwirtschaft-Atomtechnik, 45(2000) S.740-49
(48959)

FIEG, G.; MASSIER, H.; SCHÜTZ, W.; STEGMAIER, U.; STERN, G.
Simulationsexperiment zum Fluten von Kernschmelzen: KATS-9.
Wissenschaftliche Berichte, FZKA-6554 (November 2000) (48679)

FISCHER, E.A.
Density of liquid uranium and derived equation of state.
Wissenschaftliche Berichte, FZKA-6387 (Februar 2000) (47219)

FISCHER, F.; HASEMANN, I.; JONES, J.A.
Techniques applied in the COSYMA accident consequence uncertainty analysis.
Workshop on Expert Judgement and Accident Consequence Uncertainty Analysis (COSYMA), Avifauna, NL, June 21-24, 1999
Radiation Protection Dosimetry, 90(2000) S.317-23 (45601)

FOIT, J.J.; TROMM, W.
Analysis of FARO spreading experiments.
Projekt Nukleare Sicherheitsforschung. Jahresbericht 1999.
Wissenschaftliche Berichte, FZKA-6480 (August 2000) S.315-23 (48171)

FOIT, J.J.; VESER, A.
Spreading with variable viscosity. CORFLOW validation and analysis of KATS experiments.
Proc. of the OECD Workshop on Ex-Vessel Debris Coolability, Karlsruhe, November 15-18, 1999
Wissenschaftliche Berichte, FZKA-6475 (Mai 2000) S.212-20 (46728)

FRUTOS, R.; GIDO, D.; HENNEGES, G.; SCHMUCK, P.
Calculation of fission product behaviour in an advanced containment in case of a severe accident.
Nuclear Engineering and Design, 202(2000) S.173-78 (48926)

FZKA-MITARB.; U.A.
INTERNATIONAL ATOMIC ENERGY AGENCY
Transient and accident analysis of a BN-800 type LMFR with near zero void effect.
WIEN : IAEA, 2000
IAEA-TECDOC-1139 (May 2000) (48770)

GARGALLO, M.; GREULICH, M.; KIRSTAHLER, M.; MEYER, L.; SCHWALL, M.; WACHTER, E.; WÖRNER, G.
Experimente zur Dispersion von Corium.
Projekt Nukleare Sicherheitsforschung. Jahresbericht 1999.
Wissenschaftliche Berichte, FZKA-6480 (August 2000) S.215-26 (48164)

GEIST, A.; PLUCINSKI, P.; NITSCH, W.
Mass transfer kinetics of reactive multi-cation co-extraction into bis(2-ethylhexyl) phosphoric acid.
Solvent Extraction and Ion Exchange, 18(2000) S.493-515 (48358)

GEIST, A.; WEIGL, M.; MÜLLICH, U.; GOMPPER, K.
Abtrennverfahren für Aktiniden aus hochradioaktiven Abfällen.
Projekt Nukleare Sicherheitsforschung. Jahresbericht 1999.
Wissenschaftliche Berichte, FZKA-6480 (August 2000) S.593-97 (48197)

GOOSSENS, L.H.J.; EHRHARDT, J.; KRAAN, B.C.P.; COOKE, R.M.
Expert judgement of uncertainties in modelling emergency actions after nuclear accidents.
Kondo, S. [Hrsg.]
PSAM 5 : Probabilistic Safety Assessment and Management ; Proc. of the 5th Internat. Conf., Osaka, J, November 27 - December 1, 2000 Vol.2/4 S.971-76
Tokyo : Universal Acad. Pr., 2000
(Frontiers Science Series ; 34) (47960)

GOOSSENS, L.H.; HARPER, F.T.; EHRHARDT, J.; JONES, J.A.; KRAAN, B.C.; COOKE, R.M.
Lessons learnt from the EC/USNRC expert judgement study on probabilistic accident consequence codes applied in the COSYMA uncertainty analyses.
Kondo, S. [Hrsg.]
PSAM 5 : Probabilistic Safety Assessment and Management ; Proc. of the 5th Internat. Conf., Osaka, J, November 27 - December 1, 2000 Vol.2/4 S.965-70
Tokyo : Universal Acad. Pr., 2000
(Frontiers Science Series ; 34) (47959)

GOOSSENS, L.H.J.; WAKEFORD, R.; LITTLE, M.; MUIRHEAD, C.; HASEMANN, I.; JONES, J.A.
Probabilistic accident consequence uncertainty analysis of the late health effects module in the COSYMA package.
Workshop on Expert Judgement and Accident Consequence Uncertainty Analysis (COSYMA), Avifauna, NL, June 21-24, 1999
Radiation Protection Dosimetry, 90(2000) S.359-64 (45596)

GRUPA, J.B.; HASEMANN, I.
Probabilistic accident consequence uncertainty analysis of the early health effects module in the COSYMA package.
Workshop on Expert Judgement and Accident Consequence Uncertainty Analysis (COSYMA), Avifauna, NL, June 21-24, 1999
Radiation Protection Dosimetry, 90(2000) S.353-58 (45595)

GRÖTZBACH, G.; CARTECIANO, L.; DORR, B.; LEHMANN, N.; OLBRICH, W.; JIN, X.
Entwicklung des Rechenprogramms FLUTAN für thermo- und fluiddynamische Anwendungen.
Projekt Nukleare Sicherheitsforschung. Jahresbericht 1999.
Wissenschaftliche Berichte, FZKA-6480 (August 2000) S.652-55 (48206)

GRÖTZBACH, G.; HEINZEL, V.; JIANU, A.; PHILIPP, P.; SAUTER, H.; SENGPIEL, W.; SIMON, M.
Experimentelle Untersuchungen zum Strömungsfeld aufsteigender 527 Gasblasen in ruhendem Fluid und dessen Wechselwirkung mit dem Aufstiegsverhalten der Blasen.
Projekt Nukleare Sicherheitsforschung. Jahresbericht 1999.
Wissenschaftliche Berichte, FZKA-6480 (August 2000) S.527-40 (48189)

GRÖTZBACH, G.; WÖRNER, M.; ALEF, M.; BAUMANN, W.
Entwicklung von Thermofluiddynamikprogrammen für ingenieurtechnische Anwendungen.
Projekt Nukleare Sicherheitsforschung. Jahresbericht 1999.
Wissenschaftliche Berichte, FZKA-6480 (August 2000) S.513-15 (48187)

GÖLLER, B.
On experiments to validate computational models to describe liquid structure impact.
Jones, N. [Hrsg.]
Structures under Shock and Impact VI : SUSI VI ; 6th Internat. Conf., Cambridge, GB, July 3-5, 2000
Southampton [u.a.] : WIT Press, 2000
S.341-50 (48322)

HENNEGES, G.
Parameterstudien für einen EPR-ähnlichen PWR.
Projekt Nukleare Sicherheitsforschung. Jahresbericht 1999.
Wissenschaftliche Berichte, FZKA-6480 (August 2000) S.397-414 (48178)

HENNIES, H.H.; KESSLER, G.; KRAFFT, G.; MÜLLER, G.; SCHUMACHER, G.
Turbinenschaufel.
DE-OS 19 609 690 (18.9.1997)
DE-PS 19 609 690 (28.7.2000) (42078)

HERING, W.; HOMANN, CH.; SENGPIEL, W.; STRUWE, D.; MESSAINGUIRAL, CH.
Severe accident investigations.
Projekt Nukleare Sicherheitsforschung. Jahresbericht 1999.
Wissenschaftliche Berichte, FZKA-6480 (August

Engineering (ICONE-8), Baltimore, Md., April 2-6, 2000
New York, N.Y. : ASME, 2000 CD-ROM 8730, track 11 (47813)

IONESCU-BUJOR, M.; CACUCI, D.G.
Adjoint sensitivity analysis of the RELAP5/MOD3.2 two-fluid thermal-hydraulic code system. II: Applications.
Nuclear Science and Engineering, 136(2000) S.85-121 (47921)

IONESCU-BUJOR, M.; CACUCI, D.G.
New capabilities for coupled neutron-kinetics/thermal-hydraulics code systems: adjoint sensitivity analysis.
Proc. of the 4th Internat. Conf. on Supercomputing in Nuclear Applications (SNA 2000), Tokyo, J, September 4-7, 2000
CD ROM S.114
Tokyo : SNA2000 Office, 2000 (48331)

JACOBS, G.; NÖBEL, R.; WENDTLANDT, T.
Nachrechnungen der SNL-Experimente Sup1 und Sup2 mit CONTAIN 2.0.
Projekt Nukleare Sicherheitsforschung. Jahresbericht 1999.
Wissenschaftliche Berichte, FZKA-6480 (August 2000) S.239-55 (48166)

JACOBS, H.; RUATTO, P.; STEHLE, B.; STEIN, E.; BÖTTCHER, M.; IMKE , U.; LUMMER, M.; STRUWE, D.
Theoretische Arbeiten zur Schmelze-Kühlmittel-Wechselwirkung.
Projekt Nukleare Sicherheitsforschung. Jahresbericht 1999.
Wissenschaftliche Berichte, FZKA-6480 (August 2000) S.173-83 (48162)

JANSOHN, W.; RITTER, B.; TSAKMAKIS, CH.
Energy dissipated in elastic-plastic and elastic-viscoplastic solids.
2nd Euroconf. and Internat. Symp.on Material Instabilities in Deformation and Fracture, Thessaloniki, GR, August 31 - September 4, 1997
Journal of the Mechanical Behaviour of Materials, 11(2000) Nr.1-3, S.69-71 (48115)

JANSSENS-MAENHOUT, G.; DAUBNER, M.; KNEBEL, J.U.; MÜLLER, U.
Boiling driven mixed convection in a L-shaped slab geometry.
Misale, M. [Hrsg.]
Single and Two-Phase Natural Circulation : Proc. of EUROTHERM Seminar N.63, Genova, I, September 6-8, 1999
Genova : Editore Genovaviva, 1999 S.189-98
Heat and Mass Transfer, 36(2000) S.517-24 (45897)

JANSSENS-MAENHOUT, G.; KNEBEL, J.U.; MÜLLER, U.
Two-phase flow modelling of passive safety cooling loops.
Proc. of the OECD Workshop on Ex-Vessel Debris Coolability, Karlsruhe, November 15-18, 1999
Wissenschaftliche Berichte, FZKA-6475 (Mai 2000) S.498-507 (45894)

JANSSENS-MAENHOUT, G.; UMEKAWA, H.; DAUBNER, M.
Criteria for geysering in two dimensions.
Internat. Workshop on Current Status and Future Directions in Boiling Heat Transfer and Two-Phase Flow, Osaka, J, October 5-6, 2000
Proc. S.159-64 (47264)

JANSSENS-MAENHOUT, G.; UMEKAWA, H.; DAUBNER, M.; MÜLLER, U.; SCHULENBERG, T.
Two-dimensional geysering.
Projekt Nukleare Sicherheitsforschung. Jahresbericht 1999.
Wissenschaftliche Berichte, FZKA-6480 (August 2000) S.336-44 (48173)

KAISER, A.; SCHÜTZ, W.; WILL, H.
Study of the mixing behaviour of a hot melt released into subcooled water.
Jahrestagung Kerntechnik 2000, Bonn, 23.-25.Mai 2000
Bonn : INFORUM GmbH, 2000 S.175-81
(Auch auf CD ROM) (47898)

KIEFHABER, E.
Updating of an 11-groups nuclear cross section set for transmutation applications.
Projekt Nukleare Sicherheitsforschung. Jahresbericht 1999.
Wissenschaftliche Berichte, FZKA-6480 (August 2000) S.582-92 (48196)

KLEIN, R.; BREITUNG, W.; COE, I.; HE, L.; OLIVIER, H.; REHM, W.; STUDER, E.
Models and criteria for prediction of deflagration-to-detonation transition (DDT) in hydrogen-air-steam systems under severe accident conditions.
Van Goethem, G. [Hrsg.]
FISA 99 : EU Research in Reactor Safety ; Conclusion Symp. on Shared-Cost and Concerted Actions, Luxembourg, L, November 29 - December 1, 1999
Luxembourg : Office for Official Publ. of the European Communities, 2000 S.480-89
EUR-19532-EN (46699)

KNEBEL, J.U.; CHEN, H.Y.; CHENG, X.; JANSSENS-MAENHOUT, G.; MACK, K.J.; NEITZEL, H.J.; SCHMIDT, H.
Thermohydraulic investigations on accelerator driven systems (ADS).

Projekt Nukleare Sicherheitsforschung.
Jahresbericht 1999.
Wissenschaftliche Berichte, FZKA-6480 (August 2000) S.624-36 (48203)

KNEBEL, J.U.; CHENG, X.; LEFHALM, C.H.; MÜLLER, G.; SCHUMACHER, G.; KONYS, J.; GLASBRENNER, H.
Design and corrosion study of a closed spallation target module of an accelerator-driven system (ADS).
Nuclear Engineering and Design, 202(2000) S.279-96 (48932)

KNEBEL, J.U.; CHENG, X.; MÜLLER, G.; SCHUMACHER, G.; KONYS, J.; WEDEMEYER, O.; GRÖTZBACH, G.; CARTECIANO, L.
Thermalhydraulic and material specific investigations into the realization of an accelerator driven system (ADS) to transmute minor actinides. 1999 status report.
Wissenschaftliche Berichte, FZKA-6506 (Oktober 2000) (48483)

KNEBEL, J.U.; CHENG, X.; NEITZEL, H.J.; ERBACHER, F.J.; HOFMANN, F.
Investigations of passive containment cooling.
The Nuclear Engineer, 41(2000) S.158-63 (48568)

KNEBEL, J.U.; EHRHARD, P.; [HRSG.]
Zusammenfassung der zwischen März 1995 und Februar 2000 unter Leitung von Herrn Professor Dr.-Ing. Ulrich Müller abgeschlossenen Dissertationen.
Herrn Professor Dr.-Ing. Ulrich Müller zum 65.Geburtstag am 28.Februar 2000.
Wissenschaftliche Berichte, FZKA-6450 (Februar 2000) (47360)

KNEBEL, J.U.; FELLMOSER, F.; LEFHALM, C.; MACK, K.; PETTAN, C.; PIECHA, H.; KONYS, J.; ADELHELM, C.; GLASBRENNER, H.; MUSCHER, H.; NOVOTNY, J.; VOSS, Z.; WEDEMEYER, O.; MÜLLER, G.; HEINZEL, A.; SCHUMACHER, G.; HUBER, R.; ZIMMERMANN, F.; GRÖTZBACH, G.; DORR, B.; CARTECIANO, L.N.
HGF-Strategiefonds-Projekt: Thermohydraulische und materialspezifische Untersuchungen zur Realisierung einer Beschleuniger getriebenen Anlagenanordnung zur Transmutation von Aktiniden.
Projekt Nukleare Sicherheitsforschung.
Jahresbericht 1999.
Wissenschaftliche Berichte, FZKA-6480 (August 2000) S.656-82 (48207)

KNEBEL, J.U.; HEUSENER, G.
Research on Transmutation and Accelerator-Driven Systems at the Forschungszentrum Karlsruhe.
Atomwirtschaft-Atomtechnik, 45(2000) S.350-58 (47661)

KOCH, M.K.; VOSSNACKE, A.; STARFLINGER, J.; SCHÜTZ, W.; UNGER, H.
Radionuclide re-entrainment at bubbling water pool surfaces.
Journal of Aerosol Science, 31(2000) S.1015-28 (47894)

KONYS, J.; GLASBRENNER, H.; MÜLLER, G.; SCHUMACHER, G.; RUSANOV, A.
Liquid metal corrosion.
Projekt Nukleare Sicherheitsforschung.
Jahresbericht 1999.
Wissenschaftliche Berichte, FZKA-6480 (August 2000) S.640-51 (48205)

KOTCHOURKO, A.; BREITUNG, W.
Numerische Simulation der turbulenten Verbrennung von vorgemischten Gasen in komplexen 3D-Geometrien.
Nachrichten - Forschungszentrum Karlsruhe, 32(2000) S.222-42 (48094)

KOTCHOURKO, A.; BREITUNG, W.
Numerische Simulation der turbulenten Verbrennung von vorgemischten Gasen in komplexen 3d-Geometrien.
Projekt Nukleare Sicherheitsforschung.
Jahresbericht 1999.
Wissenschaftliche Berichte, FZKA-6480 (August 2000) S.97-135 (48159)

KRAUSS, W.; SCHANZ, G.
Reaktionsverhalten von Zircaloy-4 in Luft.
Projekt Nukleare Sicherheitsforschung.
Jahresbericht 1999. Wissenschaftliche Berichte, FZKA-6480 (August 2000) S.472-84 (48182)

KRAUSS, W.; SCHANZ, G.
Air ingress experiments.
Oxidation Phenomena in Severe Accedents (OPSA)
Final Report
EUR-19528-EN (2000) S.27-33
INV-OPSA(99)-P008 (48560)

KRAUTSCHICK, V.; SCHMUCK, P.
Planned contributions of Forschungszentrum Karlsruhe to the EU project PHEBEN2.
Haste, T.J. [Hrsg.]
PHEBEN2 : Validating Severe Accident Codes Against Phebus FP for Plant Applications ; Minutes of the Kickoff Meeting, Marseille, F, March 22, 2000
SAM-PHEBEN2-M001 (May 2000) Annex 9 (48885)

KRAUTSCHICK, V.; SCHMUCK, P.
Contributions of Forschungszentrum Karlsruhe

to PHEBEN2 half-yearly progress report.
PHEBEN2 Progr. Meeting, Aix-en-Provence, F, October 4, 2000
Jones, A.V. [Hrsg.]
PHEBEN2 : Validating Severe Accident Codes Against Phebus FP for Plant Applications : Half-Yearly Progress Report. No.1 (March-August 2000)
SAM-PHEBEN2-P001/0 (October 2000)
(48886)

KRIEG, R.
RPVSA: Behaviour of the reactor pressure vessel under mechanical and thermal loadings caused by core melt-down and steam explosion accidents - INV.
EUR-19115/1-EN (1999) S.143-48 (47135)

KRIEG, R.
Risiken der Technik : Ein kritischer Dialog über neue, am Menschen orientierte Denk- und Lösungsansätze.
Stuttgart [u.a.] : Raabe Verl., 2000
(DUZ-Edition) (48601)

KRIEG, R.
Schalen und Behälter unter komplexen Aufprall-Belastungen - ein praxisnahes Lösungskonzept.
Technische Überwachung, 41(2000) Nr.11/12, S.53-55 (48915)

KRIEG, R.; MESSEMER, G.; HAILFINGER, G.; JORDAN, T.
Pressure vessel head loaded by internal liquid impact - mitigating influence of internal structures.
Jones, N. [Hrsg.]
Structures under Shock and Impact VI : SUSI VI ; 6th Internat. Conf., Cambridge, GB, July 3-5, 2000
Southampton [u.a.] : WIT Press, 2000
S.363-72 (48323)

KRONENBERG, J.; GANDRILLE, P.; HERING, W.
Hydrogen production during the reflood of a hot PWR core.
Jahrestagung Kerntechnik 2000, Bonn, 23.-25.Mai 2000
Bonn : INFORUM GmbH, 2000 S.207-11
(Auch auf CD ROM) (47716)

LEFHALM, C.H.; MACK, K.J.; KNEBEL, J.U.
Investigations into accelerator driven systems (ADS) at FZK within the HGF-strategy fund project 99/16: reduction of radiotoxicity.
Jahrestagung Kerntechnik 2000, Bonn, 23.-25.Mai 2000
Bonn : INFORUM GmbH, 2000 S.567-72
(Auch auf CD ROM) (47186)

LÄMMER, H.; DIEGELE, E.
On material modelling, identification of material parameters and application to two benchmark exercises.
Projekt Nukleare Sicherheitsforschung. Jahresbericht 1999.
Wissenschaftliche Berichte, FZKA-6480 (August 2000) S.184-214 (48163)

MAGALLON, D.; HUHTINIEMI, I.; DIETRICH, P.; BERTHOUD, G.; VALETTE, M.; SCHÜTZ, W.; JACOBS, H.; KOLEV, N.; GRAZIOS, G.; SEHGAL, R.; BÜRGER, M.; BUCK, M.; BERG, E.V.; COLOMBO, G.; TURLAND, B.; DOBSON, G.; MONHARD, D.
Characterisation of molten-fuel coolant interaction processes (MFCI). Summary final report.
EUR-19566-EN (2000)
INV-MFCI(99)-P006 (47922)

MAGALLON, D.; HUHTINIEMI, I.; DIETRICH, P.; BERTHOUD, G.; VALETTE, M.; SCHÜTZ, W.; JACOBS, H.; KOLEV, N.; GRAZIOSI, G.; SEHGAL, R.; BÜRGER, M.; BUCK, M.; BERG, E.V.; COLOMBO, G.; TURLAND, B.; DOBSON, G.; MONHARD, D.
Characterisation of molten-fuel coolant interaction processes (MFCI). Final report.
EUR-19567-EN (2000)
INV-MFCI(99)-P007 (47923)

MAGALLON, D.; HUHTINIEMI, I.; DIETRICH, P.; BERTHOUD, G.; VALETTE, M.; SCHÜTZ, W.; JACOBS, H.; KOLEV, N.; GRAZIOSI, G.; SEHGAL, R.; BÜRGER, M.; BUCK, M.; BERG, E.V.; COLOMBO, G.; TURLAND, B.; DOBSON, G.; MONHARDT, D.
Molten fuel coolant interaction (MFCI).
Van Goethem, G. [Hrsg.]
FISA 99 : EU Research in Reactor Safety ; Conclusion Symp. on Shared-Cost and Concerted Actions, Luxembourg, L, November 29 - December 1, 1999
Luxembourg : Office for Official Publ. of the European Communities, 2000 S.211-19
EUR-19532-EN (47977)

MANSEL, A.; MONTAVON, G.; SEIBERT, A.; ARTINGER, R.; KELLER, H.; KIM, J.I.; KRATZ, J.V.; MARQUARDT, C.M.; SCHERBAUM, F.;TRAUTMANN, N.
Complexation studies of actinides with humic acids at very low metal concentrations.
Marquardt, C.M. [Hrsg.]
Influence of Humic Acids on the Migration Behaviour of Radioactive and Non-Radioactive Substances under Conditions Close to Nature. Final Report.
Wissenschaftliche Berichte, FZKA-6557 (November 2000) S.23-78 (48682)

MARQUARDT, C.M. [HRSG.]
Influence of humic acids on the migration behaviour of radioactive and non-radioactive substances under conditions close to nature. Final report.
Wissenschaftliche Berichte, FZKA-6557 (November 2000) (48681)

MARQUARDT, C.; PIRLET, V.; KIM, J.I.
Initial studies on the complexation of tetravalent neptunium with fulvic acid.
Effects of Humic Substances on the Migration of Radionuclides: Complexation and Transport of Actinides
Third Technical Progress Report
Wissenschaftliche Berichte, FZKA-6524 (Oktober 2000) S.45-70 (48712)

MASCHEK, W.
Status of SIMMER-III and SIMMER-IV code development.
Projekt Nukleare Sicherheitsforschung. Jahresbericht 1999.
Wissenschaftliche Berichte, FZKA-6480 (August 2000) S.598-601 (48198)

MASCHEK, W.; KONDO, S.; COSTE, P.; LOUVET, J.
Status of SIMMER-III code verification.
Projekt Nukleare Sicherheitsforschung. Jahresbericht 1999.
Wissenschaftliche Berichte, FZKA-6480 (August 2000) S.602-05 (48199)

MASCHEK, W.; RINEISKI, A.; KIEFHABER, E.; BUCKEL, G.; MORITA, K.; FLAD, M.; COSTE, P.; PIGNY, S.; LOUVET, J.; CADIOU, T.; RIMPAULT, G.; KONDO, S.; TOBITA, Y.; SUZUKI, T.
SIMMER-III code development for accelerator driven systems (ADS).
Proc. from the 6th CAPRA/CADRA Seminar, Windermere, GB, June 26-28, 2000
CD ROM, Paper 3.2 (47823)

MASCHEK, W.; STRUWE, D.
Accident analyses and passive measures reducing the consequences of a core-melt in CAPRA/CADRA reactor cores.
Nuclear Engineering and Design, 202(2000) S.311-24 (48934)

MEYER, L.
Experiments to investigate the low pressure corium dispersion in EPR geometry.
Proc. of the OECD Workshop on Ex-Vessel Debris Coolability, Karlsruhe, November 15-18, 1999
Wissenschaftliche Berichte, FZKA-6475 (Mai 2000) S.36-44 (46454)

MEYER, L.; JACOBS, G.; WILHELM, D.; GARGALLO, M.; BLANCHAT, T.K.
Experiments on corium dispersion after lower head failure at moderate pressure.
Proc. of the Seminar on Containment of Nuclear Reactors held in Conjunction with the 15th Internat. Conf. on Structural Mechanics in Reactor Technology, Seoul, Korea, August 23-24, 1999; S.245-65 (45896)

MIASSOEDOV, A.; HOFMANN, P.; LEILING, W.; PIEL, D.; SCHMIDT, L.; SEPOLD, L.; STEINBRÜCK, M.; HERING, W.; HOMANN, C.
Flooding experiments on the investigation of the hydrogen source term (QUENCH test results).
Jahrestagung Kerntechnik 2000, Bonn, 23.-25.Mai 2000
Bonn : INFORUM GmbH, 2000 S.203-06
(Auch auf CD ROM) (47974)

MIETTINEN, J.; HERVIOU, K.; SCHMUCK, P.
A process model for fast prediction of radioactive releases from a LWR.
Proc. of the 8th Internat. Conf. on Nuclear Engineering (ICONE-8), Baltimore, Md., April 2-6, 2000
New York, N.Y. : ASME, 2000 CD-ROM 8190 (47201)

MINGES, J.; SCHÜTZ, W.
Experimente zur Resuspension schwerflüchtiger Substanzen aus Wasservorlagen.
Jahrestagung Kerntechnik 2000, Bonn, 23.-25.Mai 2000
Bonn : INFORUM GmbH, 2000 S.193-96
(Auch auf CD ROM) (47899)

MINGES, J.; SCHÜTZ, W.; KOCH, M.K.
KAREX-Experimente zum radiologischen Quellterm infolge Resuspension.
Projekt Nukleare Sicherheitsforschung. Jahresbericht 1999.
Wissenschaftliche Berichte, FZKA-6480 (August 2000) S.561-68 (48193)

MITRAN, S.M.
Closure models for the computation of dilute bubbly flows.
Wissenschaftliche Berichte, FZKA-6357 (April 2000) (47382)

MOVAHED, M.A.; TRAVIS, J.R.; BREITUNG, W.
Hydrogen mitigation concept and its justification method for the European pressurized water reactor (EPR).
Proc.of the Seminar on Containment of Nuclear Reactors held in Conjunction with the 15th Internat.Conf.on Structural Mechanics in Reactor Technology, Seoul, Korea, August 23-24, 1999
S.91-138 (46725)

MÜHL, B.; [HRSG.]
Projekt Nukleare Sicherheitsforschung.
Jahresbericht 1999.
Wissenschaftliche Berichte, FZKA-6480 (August 2000) (48154)

MÜHLING, G.; DELPECH, M.; TOMMASI, J.; MALDAGUE, T.; BRUSSELAERS, P.; KLOOSTERMAN, J.L.; DAMEN, P.M.G.; VETTRAINO, F.; MASCHEK, W.; STRUWE, D.; THIEM, D.; PFRANG, W.; SCHIKORR, M.; WEBER, W.; GEWEHR, K.; HESSE, U.; HUMMELSHEIM, K.; QUADE, U.; WHYMAN, E.K.; ALLEN, K.G.; SUNDERLAND, R.E.; MAZZOLA, A.; PADOVANI, E.; SANJUST, V.
Evaluation of possible partitioning and transmutations strategies and of means for implementing them. Part B - Feasibility of transmutation.
EUR-19128-EN (2000) B 1-63 (47769)

MÜLLER, G.
Korrosionsverhalten von Stählen in flüssigem Blei nach Behandlung mit hochenergetischen gepulsten Elektronenstrahlen.
Wissenschaftliche Berichte, FZKA-6422 (Februar 2000)
Dissertation, Universität Karlsruhe 2000 (46939)

MÜLLER, G.; ENGELKO, V.; KUZNETZOV, V.; VIAZMENOVA, G.
Influence of electrons reflected from target on operation of diode and triode electron sources.
Markovits, M. [Hrsg.]
High-Power Particle Beams : Proc.of the 12th Internat.Conf., Haifa, IL, June 7-12, 1998 ; BEAMS Vol.1 S.404-07
Piscataway, N.Y. : IEEE Service Center, 1998 (43467)

MÜLLER, G.; SCHUMACHER, G.; STRAUSS, D.;
ZIMMERMANN, F.; ENGELKO, V.I.
Oxide scale growth on MCrAlY coatings after pulsed electron beam treatment.
Markovits, M. [Hrsg.]
High-Power Particle Beams : Proc.of the 12th Internat.Conf., Haifa, IL, June 7-12, 1998 ; BEAMS 98 Vol.2 S.1008-11
Piscataway, N.Y. : IEEE Service Center, 1998 (43463)

MÜLLER, G.; SCHUMACHER, G.; ZIMMERMANN, F.
Investigation on oxygen controlled liquid lead corrosion of surface treated steels.
Journal of Nuclear Materials, 278(2000) S.85-95 (47956)

PETZOLD, K.G.; BREITUNG, W.
Present status of hydrogen control and mitigation in a future PWR containment.
Jahrestagung Kerntechnik 2000, Bonn, 23.-25.Mai 2000
Bonn : INFORUM GmbH, 2000 S.219-23
(Auch auf CD ROM) (47713)

PFRANG, W.; STRUWE, D.; ZIMMERER, W.
Untersuchungen zu Brennstoff- und Brennstabverhalten innovativer Systeme.
Projekt Nukleare Sicherheitsforschung.
Jahresbericht 1999.
Wissenschaftliche Berichte, FZKA-6480 (August 2000) S.557-60 (48192)

PLITZ, H.
Bestrahlungsexperimente zur Transmutation von Aktiniden im HFR.
Projekt Nukleare Sicherheitsforschung.
Jahresbericht 1999.
Wissenschaftliche Berichte, FZKA-6480 (August 2000) S.620-23 (48202)

POPP, M.
Kompetenzsicherung in der Kerntechnik im Rahmen der Verbundforschung.
Atomwirtschaft-Atomtechnik, 45(2000) S.652-57 (48627)

PÄSLER-SAUER, J.; JONES, J.A.
Probabilistic accident consequence uncertainty analysis of the atmospheric dispersion and deposition module in the COSYMA package.
Workshop on Expert Judgement and Accident Consequence Uncertainty Analysis (COSYMA), Avifauna, NL, June 21-24, 1999
Radiation Protection Dosimetry, 90(2000) S.331-37 (45594)

RASKOB, W.; EHRHARDT, J.
The RODOS system: decision support for nuclear off-site emergency management in Europe.
Harmonization of Radiation, Human Life and the Ecosystem : Proc.of the 10th Internat.Congress of the Internat.Radiation Protection Association (IRPA-10), Hiroshima,J, May 14-19, 2000
CD-ROM T-16-3, P-11-292 (47191)

REDLINGER, R.
Numerische Simulation von Gasdetonationen in komplexen 3D-Geometrien.
Nachrichten - Forschungszentrum Karlsruhe, 32(2000) S.243-49 (48095)

REINKE, N.; KOCH, M.K.; SCHÜTZ, W.; FIEG, G.; UNGER, H.
The code MECO for the numerical simulation of free surface flows with phase change.
Jahrestagung Kerntechnik 2000, Bonn, 23.-25.Mai 2000
Bonn : INFORUM GmbH, 2000 S.135-38
(Auch auf CD ROM) (47714)

SCHULTHEISS, C.; ENGELKO, V.; KRAFFT, G.; SCHUMACHER, G.; MÜLLER, G.
Gepulste Elektronenstrahlquelle und deren Verwendung.
DE-OS 19 541 510 (15.5.1997)
DE-PS 19 541 510 (6.4.1999)
EP-PS 59 603 887 (8.12.1999) (42068)

SCHULZ, B.; SEVERLOH, P.
Viscosity and characterisation of samples of the KATS and Premix experiments.
Projekt Nukleare Sicherheitsforschung. Jahresbericht 1999.
Wissenschaftliche Berichte, FZKA-6480 (August 2000) S.324-35 (48172)

SFAR, K.; AKTAA, J.; MUNZ, D.
Analysing the failure behaviour of thermal barrier coatings using the finite element method.
24th Annual Conf. on Composites, Advanced Ceramics, Materials, and Structures, Cocoa Beach, Fla., January 23-28, 2000
Ceramic Engineering and Science Proceedings, 21(2000) Nr.3, S.203-11 (48382)

SPINDLER, B.; JOURNEAU, C.; BRAYER, C.; ALSMEYER, H.; WERLE, H.; FIEG, G.; STEGMAIER, U.; TROMM, W.; MAGALLON, D.; WITTMAACK, R.; FISCHER, M.; SEHGAL, B.R.; YANG, Z.L.; WIDMAN, W.; DE CECCO, L.; OCELLI, R.; AZARIAN, G.; PINEAU, D.
Corium spreading and coolability (CSC project). Final summary report.
EXV-CSC(00)-P008 (August 2000) (48591)

STARFLINGER, J.
Assessment of in-vessel hydrogen sources.
Projekt Nukleare Sicherheitsforschung. Jahresbericht 1999.
Wissenschaftliche Berichte, FZKA-6480 (August 2000) S.1-6 (48155)

STEINER, H.; HECK, M.
The code CALUMO a tool for the analysis of temperature transients in QUENCH tests.
Wissenschaftliche Berichte, FZKA-6501 (September 2000) (48153)

STEINER, H.; HECK, M.
Recalculation of the temperature transient in QUENCH-03 with the code CALUMO.
Projekt Nukleare Sicherheitsforschung. Jahresbericht 1999.
Wissenschaftliche Berichte, FZKA-6480 (August 2000) S.442-47 (48180)

STRAUSS, D.
Verbesserung des Oxidationsverhaltens von MCrAlY-Schutzschichten für Gasturbinen-schaufeln durch Oberflächenbehandlung mit großflächigen, gepulsten Elektronenstrahlen.
Wissenschaftliche Berichte, FZKA-6371 (Februar 2000)
Dissertation, Universität Karlsruhe 2000 (47222)

TENCHINE, D.; BERTHOUX, M.; KNEBEL, J.U.; JACKSON, J.D.; AN, P.; NAVIGLIO, A.; CARUSO, G.
Thermalhydraulics of passive decay heat removal systems (POOLTHY).
Van Goethem, G. [Hrsg.]
FISA 99 : EU Research in Reactor Safety ; Conclusion Symp. on Shared-Cost and Concerted Actions, Luxembourg, L, November 29 - December 1, 1999
Luxembourg : Office for Official Publ. of the European Communities, 2000 S.711-20
EUR-19532-EN (45603)

TRAVIS, J.R.
A computationally efficient thermal radiation transport model for the GASFLOW code.
Proc. of the Seminar on Containment of Nuclear Reactors held in Conjunction with the 15th Internat. Conf. on Structural Mechanics in Reactor Technology, Seoul, Korea, August 23-24, 1999
S.3-25 (46723)

TROMM, W.; FOIT, J.J.
The FARO spreading experiment on small water layer and theoretical analysis.
Jahrestagung Kerntechnik 2000, Bonn, 23.-25.Mai 2000
Bonn : INFORUM GmbH, 2000 S.149-52
(Auch auf CD ROM) (47024)

TROMM, W.; FOIT, J.J.; MAGALLON, W.
Dry and wet spreading experiments with prototypic material at the FARO facility and theoretical analysis.
Proc. of the OECD Workshop on Ex-Vessel Debris Coolability, Karlsruhe, November 15-18, 1999
Wissenschaftliche Berichte, FZKA-6475 (Mai 2000) S.178-88 (46621)

VASILE, A.; VAMBENEPE, G.; LEFEVRE, J.C.; HESKETH, K.; MASCHEK, W.; DE RAEDT, CH.; HAAS, D.
The CAPRA - CADRA programme.
Proc. of the 8th Internat. Conf. on Nuclear Engineering (ICONE-8), Baltimore, Md., April 2-6, 2000
New York, N.Y. : ASME, 2000 CD-ROM 8143 (47325)

VESER, A.; FOIT, J.J.
Nachrechnung des KATS15-Experiments mit CORFLOW.
Projekt Nukleare Sicherheitsforschung. Jahresbericht 1999.
Wissenschaftliche Berichte, FZKA-6480 (August 2000) S.310-14 (48170)

REINKE, N.; SCHÜTZ, W.; UNGER, H.; KOCH, M.K.; FIEG, G.
Numerical modelling of melt spreading phenomena.
Proc. of the 8th Internat. Conf. on Nuclear Engineering (ICONE-8), Baltimore, Md., April 2-6, 2000
New York, N.Y. : ASME, 2000 CD-ROM Track 7 (47187)

RINEISKI, A.; KIEFHABER, E.; MERK, B.; MASCHEK, W.; FLAD, M.
Neutron kinetics of the SIMMER-III safety code for ADS application.
Projekt Nukleare Sicherheitsforschung. Jahresbericht 1999.
Wissenschaftliche Berichte, FZKA-6480 (August 2000) S.606-11 (48200)

ROYL, P.
Wasserstoffverhalten und Gegenmaßnahmen.
Projekt Nukleare Sicherheitsforschung. Jahresbericht 1999.
Wissenschaftliche Berichte, FZKA-6480 (August 2000) S.39-47 (48156)

ROYL, P.; ROCHHOLZ, H.; BREITUNG, W.; TRAVIS, J.R.; NECKER, G.
Analysis of steam hydrogen distribution with mitigation in large reactor containments.
Proc. of the Seminar on Containment of Nuclear Reactors held in Conjunction with the 15th Internat. Conf. on Structural Mechanics in Reactor Technology, Seoul, Korea, August 23-24, 1999
S.27-50 (46592)

ROYL, P.; ROCHHOLZ, H.; BREITUNG, W.; TRAVIS, J.R.; NECKER, G.; VESER, A.
GASFLOW-Analysen zur Wirksamkeit eines Rekombinatorkonzepts bei einem postulierten Surge-line LOCA im Kernkraftwerk Neckarwestheim-2.
Wissenschaftliche Berichte, FZKA-6333 (März 2000) (47356)

ROYL, P.; ROCHHOLZ, H.; BREITUNG, W.; TRAVIS, J.R.; NECKER, G.
Analysis of steam and hydrogen distributions with PAR mitigation in NPP containments.
Nuclear Engineering and Design, 202(2000) S.231-48 (48929)

ROYL, P.; TRAVIS, J.R.; BREITUNG, W.
GASFLOW analysis of hydrogen recombination in a Konvoi type PWR containment under hypothetical small break and large break LOCA conditions.
Jahrestagung Kerntechnik 2000, Bonn, 23.-25.Mai 2000
Bonn : INFORUM GmbH, 2000 S.213-18
(Auch auf CD ROM) (47712)

SABISCH, W.
Dreidimensionale numerische Simulation der Dynamik von aufsteigenden Einzelblasen und Blasenschwärmen mit einer Volume-of-Fluid-Methode.
Wissenschaftliche Berichte, FZKA-6478 (Juni 2000)
Dissertation, Universität Karlsruhe 2000 (47595)

SABISCH, W.; WÖRNER, M.; GRÖTZBACH, G.; CACUCI, D.G.
An improved volume of fluid method for numerical simulation of clusters of bubbles.
Sommerfeld, M. [Hrsg.]
Proc. of the 9th Workshop on Two-Phase Flow Predicitons, Merseburg, April 13-16 1999
Halle : Martin-Luther-Univ., Lehrstuhl f. Mechanische Verfahrenstechnik, 2000
S.175-94 (45985)

SABISCH, W.; WÖRNER, M.; GRÖTZBACH, G.; CACUCI, D.G.
Dreidimensionale Numerische Simulation von Einzelblasen und Blasenschwärmen mit einer Volume-of-Fluid Methode.
Tagung des GVC-Fachausschusses CFD, Bamberg,
28.Februar - 1.März 2000
Chemie Ingenieur Technik, 72(2000) S.1065 (47537)

SANCHEZ-ESPINOZA, V.; HERING, W.; KNOLL, A.; BÖER, R.
Main steam line break (MSLB) analysis for the TMI-1 nuclear power plant with the best-estimate code system RELAP5/PANBOX.
Jahrestagung Kerntechnik 2000, Bonn, 23.-25.Mai 2000
Bonn : INFORUM GmbH, 2000 S.11-14
(Auch auf CD ROM) (47717)

SCHIRRA, M.; FALKENSTEIN, A.; HÜBNER, R.; MATERNA-MORRIS, E.; BENNEK-KAMMERICHS, B.; EHRLICH, K.
Untersuchungen an Strukturmaterialien der Kerntechnik.
Projekt Nukleare Sicherheitsforschung. Jahresbericht 1999.
Wissenschaftliche Berichte, FZKA-6480 (August 2000) S.541-54 (48190)

SCHMUCK, P.
Analyses of severe accidents for the EPR using MELCOR.
Projekt Nukleare Sicherheitsforschung. Jahresbericht 1999.
Wissenschaftliche Berichte, FZKA-6480 (August 2000) S.378-96 (48177)

WEICK, M.; AKTAA, J.; MUNZ, D.
Inbetriebnahme und Optimierung einer biaxialen Prüfmaschine zur Durchführung von nicht-proportionalen, mehrachsigen Ermüdungs-versuchen an Rohrproben.
Kolloquium des DFG-Schwerpunktprogramms Lebensdauervorhersage, Universität Bremen, 24.-25.Februar 2000
Berlin : Deutscher Verband für Material-forschung und -prüfung, 2000 S.179-86 (47837)

WIESE, H.W.
Equilibrium in pools of PWRs and burner reactors with homogeneous recycling of plutonium and minor actinides.
The 1999 Frederic Joliot/Otto Hahn Summer School in Reactor Physics : Modern Reactor Physics and the Modelling of Complex Systems, Karlsruhe, August 18-27, 1999
Proc. S.236-79 (46233)

WIESE, H.W.
Determination of equilibrium in reactor scenarios.
Proc. from the 6th CAPRA/CADRA Seminar, Windermere, GB, June 26-28, 2000
CD ROM, Paper 2.3 (47824)

WIESE, H.W.
Berechnung der Bildung von Tritium aus Bor 10 in Steuerelementen von Kernreaktoren mit TRIBOR.
Wissenschaftliche Berichte, FZKA-6500 (Oktober 2000) (48217)

WILHELM, D.
Transient code models for low pressure corium dispersion.
Proc. of the OECD Workshop on Ex-Vessel Debris Coolability, Karlsruhe, November 15-18, 1999
Wissenschaftliche Berichte, FZKA-6475 (Mai 2000) S.45-53 (46291)

WILHELM, D.
Rechnungen zur Dispersion der Kernschmelze.
Projekt Nukleare Sicherheitsforschung. Jahresbericht 1999.
Wissenschaftliche Berichte, FZKA-6480 (August 2000) S.227-38 (48165)

WINTRUFF, I.
Ein adaptives Bewegte-Gitter-Verfahren zur Berechnung von Aufschmelz- und Erstarrungsvorgängen.
Dissertation, Universität Karlsruhe 2000
Wissenschaftliche Berichte, FZKA-6449 (April 2000) (47461)

WINTRUFF, I.; GÜNTHER, C.
Numerical simulation of the stability of solidified core melt accumulations.
Proc. of the OECD Workshop on Ex-Vessel Debris Coolability, Karlsruhe, November 15-18, 1999
Wissenschaftliche Berichte, FZKA-6475 (Mai 2000) S.259-66 (46718)

WÖRNER, M.; CACUCI, D.G.; GHIDERSA, B.; GRÖTZBACH, G.; MITRAN, S.; MÜLLER, A.; OBERHOF, A.; SABISCH, W.; DUNKER, T.
Entwicklung von Methoden zur Grobstruktur-simulation turbulenter Zweiphasenströmungen. Theoretische Untersuchungen.
Projekt Nukleare Sicherheitsforschung. Jahresbericht 1999.
Wissenschaftliche Berichte, FZKA-6480 (August 2000) S.516-26 (48188)

Veröffentlichungen in elektronischen Medien

CARTECIANO, L.N.; DORR, B.; GRÖTZBACH, G.
Development of numerical models for heat transfer in liquid lead-bismuth.
http://www.kalla.fzk.de/kalla/ads/window_num.html (E48660)

WILHELM, D.; COSTE, P.
Experience with the multiphase code SIMMER and its models for interfacial area convection.
Trends in Numerical and Physical Modeling for Industrial Multiphase Flows, Cargese, F, September 27-29, 2000 (E48258)

Vorträge, die nicht in gedruckter Form vorliegen

BIELERT, U.; BURGETH, B.; KOTCHOURKO, A.
Turbulent combustion simulation with adaptive mesh refinement on parallel computers.
8th Internat.Conf.on Numerical Combustion, Amelia Island, Fla., March 5-8, 2000(V47266)

BIELERT, U.; KOTCHOURKO, A.; BURGETH, B.; BREITUNG, W.
Numerical simulation of large scale hydrogen explosions in complex geometries.
Jahrestagung der Gesellschaft für Angewandte Mathematik und Mechanik, Göttingen, 2.-7.April 2000
Book of Abstracts S.14-15 (V47268)

BUNK, M.; EHRHARD, P.
Model for the plane spreading of solidifying oxidic melts.
Vortr.: Cornell University, Ithaca, N.Y., 16.März 1999
GAMM-Jahrestagung, Metz, F, 12.-16.April 1999 (V46947)

BURGETH, B.F.
The assumed PDF-approach: efficient calculation of integrals involving the β-PDF.
28th Internat. Symp. on Combustion, Edinburgh, GB, July 30 - August 4, 2000
Abstracts of Work-in-Progress S.219 (V48493)

BURGETH, B.; KOTCHOURKO, A.
Assumed β-PDF model for turbulent reacting flows: calculation of mean reaction rates.
8th Internat. Conf. on Numerical Combustion, Amelia Island, Fla., March 5-8, 2000(V47267)

CACUCI, D.G.
Sensitivity and uncertainty analyses in reactor physics.
Vortr.: Universität Stuttgart, 18.Juli 2000 (V47973)

CARTECIANO, L.N.; DORR, B.; GRÖTZBACH, G.
Numerical investigation of natural convection in single phase SUCOS experiments with the FLUTAN code.
EUROTHERM 2000, Heidelberg, September 11-13, 2000 (V48237)

CHAWLA, R.; HAGER, H.; PARATTE, J.M.; SEILER, R.; WILLIAMS, T.; BERGER, H.D.; BÖHME, R.
Analysis of fuel enrichment effects investigated in the PROTEUS-LWHCR phase II experiments.
10th Internat. Conf. on Emerging Nuclear Energy Systems (ICENES 2000), Petten, NL, September 25-28, 2000 (V48760)

EHRHARD, P.
Modell und Experimente zur ebenen Ausbreitung oxidischer Schmelzen bei gleichzeitiger Erstarrung.
Vortr.: Universität Siegen, 9.November 2000 (V48327)

EHRHARD, P.; BUNK, M.
Zur ebenen Ausbreitung oxidischer Schmelzen auf kalten horizontalen Platten bei simultaner Erstarrung.
Sitzung des GVC-Fachausschusses Wärme- und Stoffübertragung, Bad Kissingen, 1.-3.März 1999 (V46948)

EHRHARD, P.; BUNK, M.
Ausbreitung von Schmelzen auf horizontalen Platten bei gleichzeitiger Erstarrung.
Vortr.: Technische Universität Wien, A, 19.September 2000 (V48329)

EHRHARD, P.; RICHTER, F.
Achsensymmetrische Schmelzeausbreitung bei simultaner Erstarrung.
Jahrestagung der Gesellschaft für Angewandte Mathematik und Mechanik, Göttingen, 2.-7.April 2000
Book of Abstracts S.34 (V46949)

EHRHARD, P.; RICHTER, F.
Axisymmetric spreading of melts with basal solidification.
EUROMECH Colloquium 408: Interactive Dynamics of Convection and Solidification, Chamonix, F, March 18-22, 2000 (V48131)

ENGELKO, V.; MÜLLER, G.; BLUHM, H.
Influence of particle fluxes from target on characteristics of intense electron beams.
13th Internat. Conf. on High-Power Particle Beams, Nagaoka, J, June 25-30, 2000 (V47993)

GLASBRENNER, H.; KONYS, J.; MÜLLER, G.; RUSANOV, A.
Corrosion investigations of steels in flowing lead at 400 and 550^{0}C.
4th Internat. Workshop on Spallation Materials Technology (IWSMT-4), Schruns, A, October 8-13, 2000 (V48498)

GRÖTZBACH, G.
DNS- und LES-Ansätze für Impuls- und Wärmeübertragung in turbulenten Ein- und Zweiphasenströmungen.
Graduiertenkolleg-Klausurtagung 'Modellierung und numerische Beschreibung technischer Strömungen' der TU Darmstadt, Lufthansa-Zentrum Seeheim, 30.Juni - 1.Juli 2000 (V47890)

GRÖTZBACH, G.
Stand der Direkten Numerischen und Grobstruktursimulationsmethode und von deren Anwendungen in der Kernreaktortechnik.
Vortr.: Universität Siegen, 8.Juni 2000 (V47891)

GRÖTZBACH, G.
Stand der Direkten Numerischen und Grobstruktur-Simulationsmethode und deren Anwendungen am Beispiel der Kernreaktortechnik.
Vortr.: Technische Universität Dresden, 24.November 2000 (V48671)

GRÖTZBACH, G.; CARTECIANO, L.N.
FZK benchmark calculations for experiments with various fluids.

Workshop on Heavy Liquid Metal Thermal-Hydraulic, CERN, Geneve, CH, June 29-30, 1999 (V46999)

GRÖTZBACH, G.; CARTECIANO, L.N.; DORR, B.
Numerical analysis of experiments modeling LWR sump cooling by natural convection.
IAEA Technical Committee Meeting on Natural Circulation Data and Methods for Innovative Nuclear Power Plant Design, Wien, A, July 18-21, 2000 (V47962)

HARMS, M.; GOSCHNICK, J.
Selective hydrogen detection with a tungsten trioxide microarray over a concentration range of 6 magnitudes.
8th Internat.Meeting on Chemical Sensors, Basel, CH, July 3-5, 2000 (V47731)

HERING, W.; HOMANN, C.; MEIER, A.; STEGMAIER, U.; STEINBOCK, L.; STEINBRÜCK, M.; STUCKERT, J.; HECK, M.; KRAUSS, W.; LAIER, J.; LEILING, W.; MIASSOEDOV, A.; MOCH, J.; PIEL, D.; SCHANZ, G.; SCHMIDT, L.; SEPOLD, L.; STEINER, H.; VOURIOT, R.; WERNER, I.; PLITZ, H.
Status of the QUENCH program.
6th Internat.Quench Workshop, Karlsruhe, October 10-12, 2000 (V48963)

HERING, W.; HOMANN, CH.; SANCHEZ, V.; SENGPIEL, W.; STRUWE, D.; MESSAINGUIRAL, CH.
Code validation and core degradation analyses with S/R5 and ICARE2.
CSARP Meeting (CSARP = Cooperative Severe Accidents Research Programme), Bethesda, Md., May 8-12, 2000 (V47895)

HEUSENER, G.; MÜLLER, U.; SCHULENBERG, T.; SQUARER, D.
A European development program for a high performance light water reactor (HPLWR).
SCR-2000 Meeting, University of Tokyo, J, November 7-8, 2000 (V48536)

HOFMANN, P.; HOMANN, CH.; LEILING, W.; MIASSOEDOV, A.; PIEL, D.; SCHANZ, G.; SCHMIDT, L.; SEPOLD, L.; STEINBRÜCK, M.
The hydrogen generation during reflood of an overheated reactor core. QUENCH experiments results.
Seminario de la ARN 'Comportamiento de Materiales del Nucleo Durante Accidentes Severos', Buenos Aires, RA, 22 Marzo, 2000 (V48532)

JIANU, A.V.; HEINZEL, V.; CHERDRON, W.
Investigation of flow behaviour in the near vicinity of a gas bubble by laser-Doppler-anemometry.
7th Internat.Conf.on Optimization of Electrical and Electronic Equipment (OPTIM 2000), Brasov, R, May 11-12, 2000 (V48737)

KNEBEL, J.U.
Übersicht über die FZK-Arbeiten zum ADS.
Vortr.: Forschungszentrum Jülich, 10.Januar 2000
Vortr.: Forschungszentrum Rossendorf, Institut für Sicherheitsforschung, 2.März 2000 (V47039)

KNEBEL, J.U.
Übersicht über die Arbeiten zur Transmutation und Beschleuniger getriebenen Anlagen (ADS) am Forschungszentrum Karlsruhe.
Vortr.: DESY Hamburg, Linear Collider Project, 28.Juli 2000 (V47966)

KNEBEL, J.U.
Transmutation: Perspektiven und berufliche Chancen.
Tagung für die Junge Generation in der Kerntechnik, Kerntechnische Gesellschaft, GKN Neckarwestheim, 10.November 2000 (V48707)

KNEBEL, J.U.; LEFHALM, C.H.
Oxygen control system OCS and its application to MEGAPIE.
Vortr.: Paul Scherrer Institut, Villigen, CH, 14.Februar 2000 (V47202)

KONYS, J.; MUSCHER, H.; VOSS, Z.; WEDEMEYER, O.
Development of oxygen meters for the use in lead-bismuth.
4th Internat. Workshop on Spallation Materials Technology (IWSMT-4), Schruns, A, October 8-13, 2000 (V48499)

KOTCHOURKO, A.; BURGETH, B.F.
Turbulent reactive flows simulation with presumed β-PDF combustion model.
8th Internat. Conf. on Numerical Combustion, Amelia Island, Fla., March 5-8, 2000(V47265)

KRAUSS, W.; SCHANZ, G.
Thermogravimetric analyses towards B_4C oxidation mechanisms and kinetics.
6th Internat. QUENCH Workshop, Karlsruhe, October 10-12, 2000 (V48783)

KRAUSS, W.; STEINER, H.; SCHANZ, G.
Separate effect tests on Zry-4/air and Zry-4/O_2 reaction towards air ingress scenarios, including first modelling work.
6th Internat. Quench Workshop, Karlsruhe, October 10-12, 2000 (V48791)

MASCHEK, W.; RINEISKI, A.; MORITA, K.; MÜHLING, G.; FLAD, M.; KONINGS, R.J.M.
Safety analyses for ADS cores with dedicated fuel and proposals for safety improvements.
Technical Committee Meeting on Core Physics and Engineering Aspects of Emerging Nuclear Energy Systems for Energy Generation and Transmutation, Argonne National Laboratory, Argonne, Ill., November 28 - December 1, 2000 (V48708)

MIASSOEDOV, A.; HOFMANN, P.; LEILING, W.; PIEL, D.; SCHMIDT, L.; SEPOLD, L.; STEINBRÜCK, M.
Large-scale bundle experiments on the determination of the hydrogen source term. Results of the QUENCH program.
Cooperative Severe Accident Research Program Meeting, Bethesda, Md., May 8-12, 2000 (V48797)

MÜLLER, G.; ENGELKO, D.V.; ANDREEV, A.; KOMAROV, O.; STRAUSS, G.; SCHUMACHER, G.; ZIMMERMANN, F.; BLUHM, H.
Pulsed electron beam facility GESA-2 for treatment of material surface.
13th Internat. Conf. on High-Power Particle Beams, Nagaoka, J, June 25-30, 2000 (V47994)

MÜLLER, G.; KNEBEL, J.; KONYS, J.; GLASBRENNER, H.
Corrosion investigations of steels in Pb and Pb/Bi at FZK.
Pb-Bi Internat.Meeting, JNC, Tokyo, J, December 12-15, 2000 (V48773)

MÜLLER, G.; KNEBEL, J.; KONYS, J.
The oxygen control system (OCS) at FZK.
Pb-Bi Internat.Meeting, JNC, Tokyo, December 12-15, 2000 (V48774)

MÜLLER, G.; SCHUMACHER, G.; STRAUSS, D.; ZIMMERMANN, F.; BLUHM, H.; ENGELKO, V.
Improvement of the corrosion resistance of steels and MCrAlY coatings by application of a pulsed electron beam.
13th Internat. Conf. on High-Power Particle Beams, Nagaoka, J, June 25-30, 2000 (V47992)

SABISCH, W.
Numerische Untersuchungen zum Aufstiegsverhalten von Blasen mit TURBIT-VoF.
Seminar Ausgewählte Themen über Strömungsmaschinen und -anlagen, Universität Karlsruhe, 25.Mai 2000 (V47889)

SABISCH, W.; WÖRNER, M.; GRÖTZBACH, G.; CACUCI, D.G.
Three-dimensional numerical simulation of bubbles by a volume-of-fluid method.
Jahrestagung der Gesellschaft für Angewandte Mathematik und Mechanik, Göttingen, 2.-7.April 2000 (V47538)

SABISCH, W.; WÖRNER, M.; GRÖTZBACH, G.; CACUCI, D.G.
Dreidimensionale Numerische Simulation von Einzelblasen und Blasenschwärmen mit dem Rechenprogramm TURBIT-VoF.
Workshop 'CFD in der Praxis', Bad Dürkheim, 12.-13.September 2000 (V48236)

SANCHEZ, V.; HERING, W.; KNOLL, A.; BÖER, R.; FINNEMANN, H.
FZK/Siemens final results of the MSLB-benchmark investigations with the best-estimate code RELAP5/PANBOX.
4th Internat. OECD/NEA Main Steam Line Break Workshop, Paris, F, January 24-25, 2000 (V47540)

SANCHEZ, V.; HOMANN, C.; KNOLL, A.; BÖER, R.
FZK/Siemens investigations on MSLB-PHASE 3 with RELAP5/PANBOX2.
16th Internat. Spring 2000 CAMP Meeting, Terrasini, I, April 17-20, 2000 (V48321)

SCHANZ, G.; STEGMAIER, U.
Metallographic post-test examination of the QUENCH-03 test bundle. Actual evaluation of QUENCH-04.
6th Internat. QUENCH Workshop, Karlsruhe, October 10-12, 2000 (V48790)

SCHMUCK, P.
MELCOR 1.8.4 assessment of lower head failure: creep rupture failure modeling for PWRs without lower head penetrations.
CSARP Meeting (CSARP = Cooperative Severe Accidents Research Programme), Bethesda, Md., May 8-12, 2000 (V47533)

SCHMUCK, P.
Current capabilities of severe accident codes for plant applications.
CSARP Meeting (CSARP = Cooperative Severe Accidents Research Programme), Bethesda, Md., May 8-12, 2000 (V47534)

STEINBRÜCK, M.; HOFMANN, P.; MIASSOEDOV, A.; STEGMAIER, U.
Cladding behavior during reflood of an overheated core. Recent results of separate-effects tests performed at FZK.
CSARP Meeting (CSARP = Cooperative Severe Accidents Research Programme), Bethesda, Md., May 8-12, 2000 (V48531)

STEINBRÜCK, M.; HOFMANN, P.; MIASSOEDOV, A.
Hydrogen uptake and release by zircaloy (Zr 1% Nb) at elevated temperatures. Separate

effects test.
Seminario de la ARN 'Comportamiento de Materiales del Nucleo Durante Accidentes Severos', Buenos Aires, RA, 22 Marzo, 2000 (V48533)

STEINBRÜCK, M.; STEGMAIER, U.
Hydrogen absorption by Zry-4 in steam and steam/hydrogen atmosphere.
6th Internat. QUENCH Workshop, Karlsruhe, October 10-12, 2000 (V48530)

STEINBRÜCK, M.; STEINBOCK, L.; MEIER, A.; STEGMAIER, U.; STUCKERT, J.
Oxidation of B_4C at high temperatures.
6th Internat. QUENCH Workshop, Karlsruhe, October 10-12, 2000 (V48529)

STEINER, H.
Interpretation and analysis work for QUENCH-03 and QUENCH-04.
6th Internat. QUENCH Workshop, Karlsruhe, October 10-12, 2000 (V48497)

STUCKERT, J.; STEINBRÜCK, M.; STEGMAIER, U.
Single rod quench tests with Zr1%Nb cladding.
6th Internat. QUENCH Workshop, Karlsruhe, October 10-12, 2000 (V48637)

TOBITA, Y.; KONDO, S.; YAMANO, H.; FUJITA, S.; MORITA, K.; MASCHEK, W.; LOUVET, J.; COSTE, P.; PIGNY, S.
Current status and application of SIMMER-III, an advanced computer program for LMFR safety analysis.
2nd Japan-Korea Symp. on Nuclear Thermal Hydraulics and Safety (NTHAS2), Fukuoka, J, October 15-18, 2000 (V48257)

VERFONDERN, K.; MOORMANN, R.; BREITUNG, W.; VESER, A.
Contribution to a safety analysis for a hydrogen production system with HTGR.
OECD/NEA Information Exchange Meeting on the Nuclear Production of Hydrogen, Paris, F, October 2-3, 2000 (V48832)

VOSSNACKE, A.; REINKE, N.; KOCH, M.K.; SCHÜTZ, W.; UNGER, H.
Aerosol generation by bubble collapse at ocean surface.
6th Internat. Conf. on Air-Surface Exchange of Gases and Particles, Edinburgh, GB, July 3-7, 2000 (V47785)

WEIGL, M.
Kinetik der Lanthaniden/Actiniden Koextraktion mit DMDBTDMA (N,N'-dimethyl-N,N'-dibutyltetradecylmalonsäurediamid).
GVC-Fachausschuss 'Extraktion', Bremen, 7.September 2000 (V48355)

WÖRNER, M.
Direkte Numerische Simulation von turbulenter Naturkonvektion in horizontalen Fluidschichten.
Kolloquium Thermo- und Fluiddynamik, Technische Universität Ilmenau, 24.Mai 2000 (V47496)

WÖRNER, M.
Direkte Numerische Simulation von turbulenter Naturkonvektion in horizontalen Fluidschichten.
Vortr.: Universität Erlangen-Nürnberg, 18.Februar 2000 (V47539)